Coaxial Artefact Standard for Specific Absorption Rate 100 kHz to 400 MHz

B. G. Loader, A. G. Gregory, and Daniel Bownds
National Physical Laboratory, UK

Abstract— A new artefact standard to calibrate electric field probes in liquid has been developed at the National Physical Laboratory to cover the frequency range 100 kHz to 400 MHz, as required for the traceable measurement of the specific absorption rate of energy (SAR) in phantoms at these frequencies. The system is a calorimeter consisting of a short-circuited coaxial transmission line in which the liquid forms part of the inner conductor. This arrangement gives a good input match for the system, high efficiency, and results in a uniform field distribution in the liquid, thus limiting thermal gradients. A thermometer measures the rate of temperature rise in the liquid due to the applied RF power, and the liquid density and specific heat capacity are used to calculate the SAR level. Substituting an electric field probe for the thermometer allows its calibration factor to be measured.

1. INTRODUCTION

To avoid biological effects, it is necessary to limit the heating of tissues caused by exposure to electromagnetic fields (EMF), and this heating is related to the specific absorption rate (SAR) of energy (units Wkg^{-1}). SAR forms the basic restriction of the International Commission on Non-Ionizing Radiation Protection (ICNIRP) for human exposure to EMF [1] over the frequency range 100 kHz to 10 GHz. The SAR from a transmitter can be determined by placing a liquid phantom having similar electrical properties to human tissues next to the transmitter, and measuring the electric field distribution in the phantom. SAR is related to the electric field, E, and rate of increase in temperature, dT/dt, by

$$SAR = \frac{E^2\sigma}{\rho} = k\frac{dT}{dt} \tag{1}$$

where E is the electric field in a liquid phantom having conductivity σ, density ρ, and specific heat k. Measuring the electric field yields higher sensitivity than measuring the resulting temperature rises in the liquid, and facilitates volume scanning as required to determine 1 g or 10 g mass-averaged values. However, the calibration factor of the electric field probe is dependent on the complex permittivity of the liquid phantom, so the probe needs to be calibrated in the liquid.

The method for calibrating the electric field probe in liquid are well established for at wireless communications frequencies, and NPL has such systems for 450 MHz, 900 MHz, 1800 MHz, 2450 MHz, 5200 MHz and 5800 MHz, with calibration uncertainties as low as 6.5% at $k = 2$, which gives approximately 95% confidence interval [2–4]. These systems are based on waveguides, and establish calculable field distributions in the liquid. Power is fed to a waveguide via a waveguide to coaxial adapter, and the liquid phantom terminates the waveguide. A ceramic or plastic spacer separates the liquid from the adapter, and acts as a matching section to provide efficient power transfer into the liquid, and thus good input match for the system. However, these systems have the disadvantage that they are narrow-band, due to the tuned nature of the matching spacer, and cannot practically be used below 380 MHz, due to the size of the waveguide required and also the associated volume of the liquid phantom required for the calibration.

The directive EC/40/2004 of the European Parliament [5] will makes ICNIRP occupational exposure limits for EMF mandatory for workers, and this is due to be adopted into the National Law of member states by 2011. This legislation will impact some industries using high power RF processing, plastic welding and medical applications such Magnetic Resonance Imaging (MRI) and radio frequency (RF) physiotherapy, where high exposures to EMF can occur. Also device measurement standards are being extended to cover frequencies down to 30 MHz [6, 7]. This has created an urgent requirement for SAR calibration standards for frequencies in the range 100 kHz to 400 MHz, particularly at the Industrial Scientific and Medical (ISM) frequencies. This paper describes the development of a low frequency SAR standard based on a coaxial line calorimeter, in which the SAR in the liquid phantom is determined from the rate of temperature rise at the calibration point, and the electric field probe is then used to measure the electric field at this position. In this way the calibration factor of the electric field probe can be measured. The system provides continuous frequency coverage from 100 kHz to 400 MHz.

2. DESIGN OF THE SYSTEM

The aim was to design a system that gave continuous frequency coverage and low uncertainties for calibrating electric field probes in liquids over the frequency range 100 kHz to 400 MHz. To avoid potential interference effects with the probe meters, which are high sensitivity voltmeters, the calibration system should not radiate fields into the laboratory. Also, the fields at the probe sensors should be higher than those at the position of the high-impedance lines connecting the diodes to the meter, as signal pickup on these lines can occur. Three calibration methods were considered: Calculable field methods, where the SAR distribution in the liquid can be determined analytically, methods that determine the ratio of probe calibration factor in liquid compared to that in air [8], and also calorimeter methods in which temperature measurements in the liquid determine the SAR. A calorimeter approach was chosen, as this method can yield a broadband system with low measurement uncertainties. To achieve a high accuracy for this system, the rate of temperature rise should be linear with time, so it is important that the liquid is well insulated from the surroundings and that thermal gradients in the liquid should be limited. The latter requires the RF power is absorbed uniformly in the liquid, and this also reduces positional errors when substituting the SAR probe for the temperature probe, and errors due to the different size of the thermal and electric field sensors.

The SAR calibration system, Fig. 1(a), is a short-circuited 50 Ω coaxial transmission line of length 700 mm with a shield inner diameter of 203 mm, and inner conductor diameter of 88 mm, in which the liquid forms part of the inner conductor. The phantom liquid is contained within a Perspex cylinder with metal ends Fig. 1(b), which can be removed from the system when changing liquids. The liquid acts as the load to terminate the coaxial line, and absorbs most of the power put into the system. A thermometer is inserted to the centre of the liquid volume, through an aperture at the top of system, Fig. 1(c), and this measures the rate of temperature rise in the liquid due to the applied RF power. Substituting an electric field probe for the thermometer allows its calibration factor, CF, to be determined using

$$SAR = k\left(\frac{dT}{dt}\right) = CF(V_{linX} + V_{linY} + V_{linZ}) \tag{2}$$

where dT/dt is the rate of increase in temperature in the liquid having specific heat k, and $V_{linX}, V_{linY}, V_{linZ}$ are the linearised output voltages from the three orthogonal sensors in the electric field probe.

(a) (b) (c)

Figure 1: Low frequency SAR system (a) photo of system, (b) container for liquid phantom removed from the system, (c) SAR probe inserted into the liquid.

Figure 2(a) shows a cross-section through the system, and gives the electric field distribution at 30 MHz, simulated with CST Microwave Studio. The electric field distribution and SAR are uniform in the liquid, thus limiting thermal gradients, and the electric field is aligned with the axis of the cylinder. This arrangement provides good input match over the operating frequency of the system, as shown in Fig. 2(b).

By limiting the thermal gradients in the liquid, the temperature increases at a constant rate over many minutes, and this improves the accuracy of the calibration. However, it is important

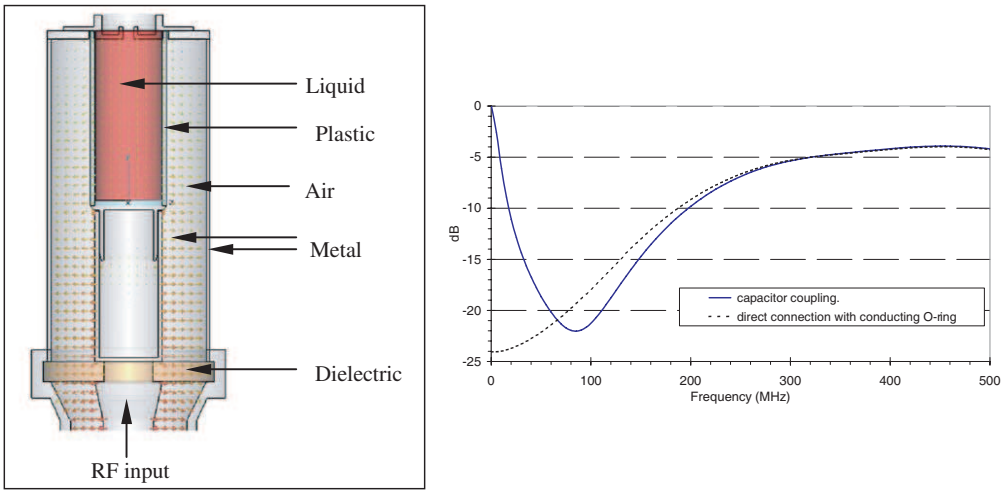

(a) (b)

Figure 2: (a) Cross-section through system showing computed electric field distribution, (b) measured input return loss for the system.

to limit the liquid temperature rise to around 1°C, since the conductivity of the liquids phantoms changes by between three percent and five percent per degree Celsius.

3. UNCERTAINTY ESTIMATES FOR SAR

Table 1 gives the estimates for the calibration uncertainties for SAR in the low frequency system. Because the system uses temperature measurements to establish the SAR, the absolute power input to the system need not be known, but directional power sensor is used to monitor the power during the thermal measurement and E-field measurement. The main uncertainties relate to the temperature coefficient of the liquid, that is the change in conductivity with temperature. It is essential that the liquid temperature rise is limited to 1°C for to achieve accurate calibration. The uncertainty is similar to that for the calculable waveguide standards that are used at higher frequencies.

Table 1: Estimated uncertainties for SAR.

Source of uncertainty	Value (±%)	Probability Distribution	Divisor	Sensitivity coefficient C_i	Standard Uncertainty u_i (±%)
Linearity and drift of the power sensor	1.5	Normal	1	1	1.5
Temperature coefficient of liquid	5.0	Rectangular	$\sqrt{3}$	1	2.9
Specific heat capacity of liquid	2.0	Normal	2	1	1.0
Linearity of temperature probe	2.0	Normal	2	1	1.0
Thermal effects giving rise to non-linear temperature rise	4.0	Rectangular	$\sqrt{3}$	1	2.3
Positional errors	0.6	Normal	2	1	0.3
Measured liquid density	1.0	Normal	2	1	0.5
Combined uncertainty		Normal			4.3
Expanded uncertainty U_i		$k = 2$			8.6

4. CONCLUSIONS

A new low frequency artefact standard for SAR has been built and tested which gives continuous frequency coverage from 100 kHz to 400 MHz, with best measurement uncertainty of 8.6% at $k = 2$. This system allows the calibration factor of electric field probes when used in liquid phantoms to be measured, as required for the assessment of specific absorption rate. It is based on a 50 Ω coaxial in which the liquid forms part of the inner conductor that terminates the line. In this way the power input to the system is absorbed uniformly in the liquid sample, and this reduces thermal gradients. The SAR in the liquid is determined by measuring the rate of change of temperature, and the electric field probe is then substituted for the temperature probe. Applications for this standard include patient SAR assessment during magnetic resonance imaging and assessment of worker exposures for compliance with EU directive EC/40/2004. Future work will compare SAR to induced current standards below 110 MHz.

ACKNOWLEDGMENT

This work was funded under the UK National Measurement System. This work forms part of a collaborative project (EURAMET) with seven European partners that will establish standards for electromagnetic exposure. The work of Yvonne Johnson at Bristol University on developing the new phantom mixes for use in the system is also acknowledged.

REFERENCES

1. "Guidelines of limiting exposure to time-varying electric, magnetic, and electromagnetic fields (up to 300 GHz)," *Health Physics*, Vol. 74, No. 4, 494–522, April 1998.
2. Loader, B. G. and K. Lees, "Calibrating SAR probes in liquid at 2.45 GHz," *BEMC*, Teddington, November 14–17, 2005.
3. Loader, B. G., K. Lees, and R. N. Clarke, "Calibration of implantable field probes for specific absorption rate measurements at TETRA frequencies (380 MHz to 460 MHz) in waveguide cells," *Antenna Measurements and SAR Conference*, Loughborough, May 2002.
4. Loader, B. G, " Dosimetry for the mobile telecommunications and health research (MTHR) program," *4th International Workshop on Biological Effects of EMFs*, Limin Hersonissou, Crete, Greece, October 16–20, 2006.
5. "Directive 2004/40/EC of the European Parliament and of the Council of 29 April 2004, on the minimum health and safety requirements regarding the exposure of workers to risks arising from physical agents (electromagnetic fields)," *Official Journal of the European Union*, 2004.
6. IEC Draft Standard IEC-62209-2-CD, "Human exposure to radio frequency fields from handheld and body-mounted wireless communication devices — Human models, instrumentation, and procedures — Part 2: Procedure to determine the specific absorption rate (SAR) for mobile wireless communication devices used in close proximity to the human body (frequency range of 30 MHz to 6 GHz)".
7. Federal Communications Commission, "Evaluating compliance with FCC guidelines for human exposure to radiofrequency electromagnetic fields additional information for evaluating compliance of mobile and portable devices with FCC limits for human exposure to radiofrequency emissions," David L. Means, Kwok W. Chan, *FCC OET Bulletin 65, Supplement C*, June 2001.
8. Liang, W., P. West, B. Loader, K. Lees, A. P. Gregory, and R. N. Clarke, " Traceable calibration of specific absorption rate (SAR) for mobile phone dosimetry," *Conference on Precision Electromagnetic Measurement*, 283–284, Sydney, May 14–19, 2000.

Effects of Losses Due to Human Phantoms on 3-dimensional Electromagnetic Field Distribution in Elevators

Y. Kawamaura[1], **T. Hikage**[1], **T. Nojima**[1], **A. Simba**[2], **and S. Watanabe**[2]

[1]Hokkaido University, Japan
[2]National Institute of Information and Communications Technology, Japan

Abstract— The purpose of this study is to estimate the Electromagnetic field (EMF) distributions emitted by Cellular radios in environments surrounded by conductive surfaces, e.g., elevators using precise numerical analysis based on the FDTD method. Since portable radios may be used in various environments, accurate and reliable estimations of EMF in practical environments are required. In this paper, we discuss the EMF absorption effects due to lossy materials being present in elevators. Simplified field histograms and cumulative ratios are derived from 3-dimensional EMF distributions throughout the inner space of the elevator. The lossy material consisted of almost the same volume as a human body and can decrease the strength of EMF distributions inside the elevator by about 20 dB.

1. INTRODUCTION

With regard to the EMC of the portable radio terminals such as cellular phones and data communication transceivers that transmit RF waves, one of the most important and substantial issues is to prevent the occurrence of unwanted effects on human health due to RF exposure from such radio devices. The Bioelectromagnetics effects and RF interferences on implantable medical devices are the major subjects to be considered. Since portable radios may be used in various environments, accurate and reliable estimations of EMC in practical environments are required. For example, places surrounded by conductive surfaces, e.g., trains or elevators, are typical environments requiring assessment. There is a concern that the use of cellular phone in elevator might cause unexpectedly high exposure levels due to the reflection and accumulation of RF waves [1, 2]. A report from a primitive study, which ignored energy absorption effects due to lossy material inside elevators, states that there is an effect due to signal reflection in elevators that can cause EMI to impact implantable cardiac pacemakers [3]. In the actual environment, however, the effects of losses due to the human body cannot be disregarded. Previously, in order to examine more realistic and complicated situations where humans are present in elevators, we have carried out precise numerical simulations applying homogeneous human phantom models and some elevator models [4–6]. Based on the results of our study, a quantitative evaluation of the EMI risk to pacemakers by cellular radio transmission has been performed.

In this paper, we discuss the EMF absorption effects due to the lossy materials which have different volume being present in elevators using precise numerical analysis based on the FDTD method. The computation method is used in order to obtain 3-dimensional spatial electric field distributions throughout the inner space of the elevator. Finally, cumulative ratios are derived from the spatial distributions to estimate the percentage of the area having the same strength, and the effects of losses due to humans in elevators are discussed.

2. METHOD

The numerical simulations are carried out using the Finite-Difference-Time-Domain (FDTD) Method. The FDTD technique is a versatile and efficient tool for the solution of Maxwell's equations in complex structures, and is used in order to obtain spatial electric field distributions throughout the inner space of the elevator. Additionally, the simplified cumulative ratio is used to deal with the complicated EMF distributions. These methods are useful for carrying out a complete estimation in the whole area.

A 3-D representation of the numerical model of the elevator is shown in Figure 1. The elevator model's dimensions are $1.4\,\mathrm{m} \times 1.35\,\mathrm{m} \times 2.3\,\mathrm{m}$ (Length × Width × Height). In creating the model to represent the elevator's body, the material whose physical properties were used is Perfect Electric Conductor (PEC). The elevator door is closed. The openings in the roof of the elevator are the means by which cellular signals are able to propagate into and out of the elevator. We use a half-wavelength dipole antenna to represent a cellular radio operating in the 800 MHz, 1.5 GHz

and 2 GHz bands. The antenna is set 1.15 m from the floor. The details of the FDTD analysis configurations are summarized in Table 1.

To achieve quantitative estimation of the absorption effects due to the lossy material inside the elevator, some simplified rectangular phantoms that have homogeneous electric parameters are applied in the analysis, as shown in Figure 2. The phantom sizes are 0.05 m × 0.4 m × 0.4 m (Phantom 1) and 0.1 m × 0.4 m × 1.8 m (Phantom 2), respectively. Phantom 2 is considered to be the average height and weight of male adults. The phantom material corresponds to 2/3 muscle-equivalent tissue of human for each frequency band [7]. The locations of the lossy materials are varied in order to observe the position dependency of the absorption effect inside the elevator.

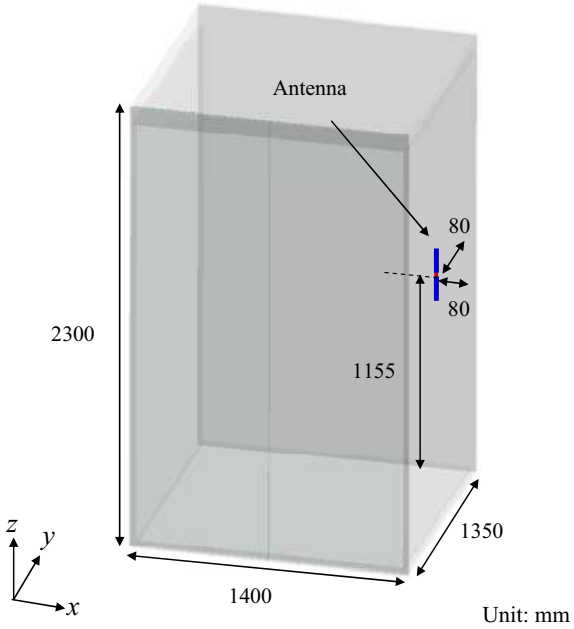

Figure 1: Elevator model.

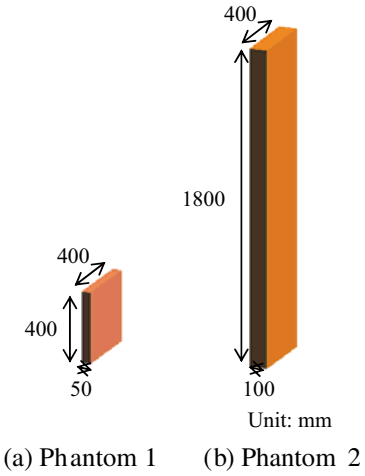

Figure 2: Phantom models.

Modeling the scenario when there is only a single antenna but no lossy material present allowed the background electric field distribution to be determined in the absence of materials whose physical properties disturb the electric field being measured. Following this, the case where Phantom 1

Table 1: FDTD analysis configuration.

Frequency	800 MHz	1500 MHz	2000 MHz
Cell size (cubic)	10 mm		
Total program space	148 x 143 x 246 cells		
Absorbing B.C.	UPML (4 layer)		
Elevator	PEC		
Phantom	Material: 2/3 Muscle		
	ε_r 40.68	ε_r 39.68	ε_r 39.18
	σ 0.641	σ 0.845	σ 1.030
Cellular radio model	Dipole antenna Continuous wave		
Iteration	350 times	600 times	900 times

or Phantom 2 is present in the elevator is modeled. This is followed by additional cases where the phantom model's position is changed to be in one of the corners of the elevator. In the elevator models, the cellular radio has identical values for each frequency. For each of these scenarios, cumulative ratios are used to estimate the percentage of areas having the same field strength inside the elevator.

3. RESULTS

The estimation results for the absorbing effects due to a simplified rectangular phantom are shown in Figure 3. The x axis denotes the relative value of electric field strength normalized by 100 V/m. In these cases, a dipole antenna is set 0.08 m from a metallic wall near the corner of the elevator as shown in Figure 1. The input voltage of the dipole antenna is 1 V. The absorption effects due to two kinds of phantoms existing in the elevator are estimated by comparing with the case of no phantom existing. These figures suggest that a small phantom (Phantom 1) results in a decrease of about 10 dB of the field strength in the elevator. In addition, the position dependency of the absorption effect inside the elevator is ±5 dB.

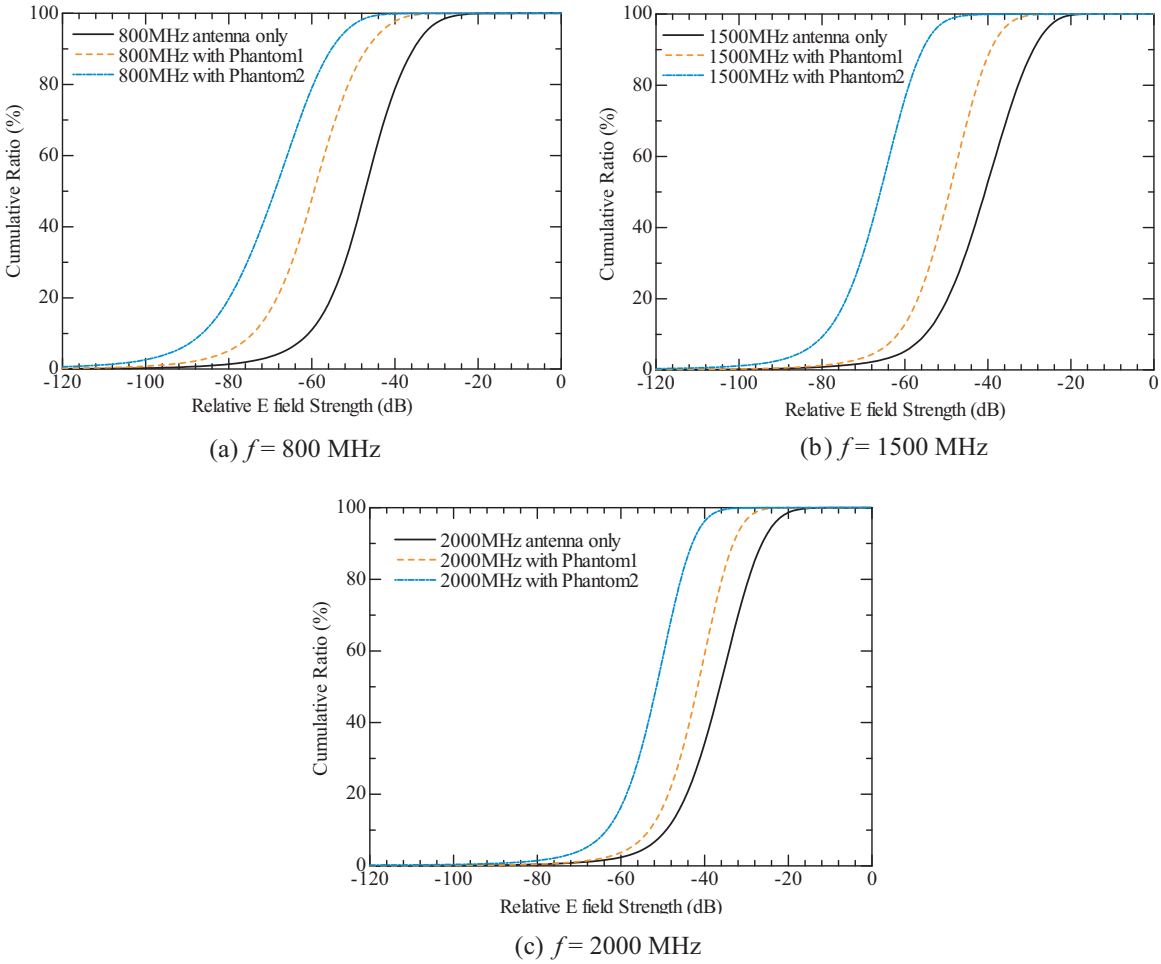

(a) f = 800 MHz

(b) f = 1500 MHz

(c) f = 2000 MHz

Figure 3: Absorption effects due to lossy materials in the elevator.

Also, comparing the cases when no phantom is present, and when Phantom 2 is present, the field strength inside the elevator is seem to decrease by 20 dB (800 MHz), 24 dB (1.5 GHz) and 17 dB (2 GHz), respectively. The absorption of the Phantom 2 is increased by about 10 dB in each frequency band when compared with that of Phantom 1, in proportion to volume of lossy material.

4. DISCUSSION AND CONCLUSIONS

In this paper, the EMF absorption effects due to the presence of lossy materials having different volumes in an elevator were discussed using precise FDTD analysis and cumulative ratio estimations.

From our study, even if there is a small lossy material in the elevator, the energy absorption effect due to the material is not small and it should not be ignored. The material consisted of almost the same volume and same electrical parameters as the human body can decrease the strength of EMF distributions inside the elevator by about 20 dB throughout the inner space.

ACKNOWLEDGMENT

This study was partially supported by the Electromagnetic Environment Committee of ARIB JAPAN.

REFERENCES

1. Frhlich, K. J. and N. Kuster, "Towards danger of mobile phones in planes, trains, cars and elevators," *Journal of the Physical Society of Japan*, Vol. 71, 3100, Dec. 2002.
2. Tropainen, A., "Brief communication human exposure by mobile phones in enclosed areas," *Bioelectromagnetics*, Vol. 24, No. 1, 63–65, Jan. 2003.
3. Hondou, T., et al., "Passive exposure to mobile phones: Enhancement of intensity by reflection," *Journal of the Physical Society of Japan*, Vol. 75, No. 8, 084801, Aug. 2006.
4. Hikage, T., et al., "Electric-field distribution estimation in a train carriage due to cellular radios in order to assess the implantable cardiac pacemaker EMI in semi-echoic environments," *IEICE Trans. Commun.*, Vol. E88-B, No. 8, 3281–3286, Aug. 2005.
5. Harris, L., et al., "A precise electromagnetic field estimation in elevator considering of implantable cardiac pacemaker EMI from cellular radios," *Progress In Electromagnetics Research Symposium Abstract*, 123, Tokyo, Japan, 2006.
6. Abiko, Y., L. Harris, T. Hikage, T. Nojima, A. Simba, S. Watanabe, and T. Shinozuka, "Electromagnetic field estimations considering of implantable cardiac pacemaker EMI from cellular radios in elevators," *Progress In Electromagnetics Research Symposium Abstract*, 100, Mar. 2007.
7. Gabriel, C., "Compilation of the dielectric properties of body tissues at RF and microwave frequencies," Brooks Air Force Report, 1996.

Temperature Rise in the MRI Head Models Exposed to Commercial Mobile Phones

Jafar Keshvari

Corporate Development Office, Nokia Corporation Itämerenkatu 11-13
Helsinki 00180, Finland

Abstract— The physiological adverse health effects to humans through electromagnetic-wave exposure are induced by temperature increases although the safety standards at the moment are regulated in terms of the local peak specific absorption rate (SAR). The temperature rise the Magnetic Resonance Imaging MRI based adult and child head models following exposure to two commercially available mobile phones are calculated. Also the temperature rise in child and adult head models were compared. Four (MRI) based head models; one female, one adult, two child head models aged 3 and 5 years were used. The finite-difference time-domain method (FDTD) was employed for calculating the temperature. The results show that the temperature rise in the brain region remains below 0.15°C.

1. BACKGROUND AND OBJECTIVES

When RF electromagnetic energy is transmitted into a body tissue or a lossy medium it causes energy dissipation in the tissue in the form of heat. This is a well-known phenomenon which is characterized by the SAR distribution. SAR distribution is then transformed into a distribution of temperature, T, based on the thermal properties of the tissue. It is temperature which ultimately causes tissue damage. Consideration of thermal effects in setting standards for limiting human exposure to non-ionizing radiation is playing very important role. That is why the assessment of the temperature increase inside tissues under various exposure conditions has been gaining more attention. The relationship between RF energy absorption rate, SAR, and induced temperature change, ΔT, in biological tissues are very complex biophysical phenomenon.

Normal body temperature is maintained by a complex control system of heat loss or gain responses, at a value of around 37°C. Body temperature is maintained within a narrow range of 0.5°C fluctuation by the processes of sweating and/or increasing metabolic heat production. The blood circulation beneath the skin, local metabolism and heat exchange between the skin and its environment controls body surface temperature. Changes in any of these parameters can induce variation of temperature and heat flux at the skin surface, reflecting the physiological state of human body. For calculating the temperature increase in the human head, the Bio-Heat equation [1], which takes into account the heat exchange mechanisms such as heat conduction, blood flow, and EM heating was used. The Bio-Heat equation is as follows:

$$C_t \rho_t \frac{dT}{dt} = k_t \nabla^2 T - c_b W_b (T - T_{art}) + P$$

where ρ_t is tissue density, C_t tissue specific heat capacity, k_t tissue thermal conductivity, W_b the blood perfusion, T_{art} the temperature of the arterial blood entering the discritized volum and P the power density. Minus sign in front of the second term in the right hand side of the equation represents the cooling effect of the blood entering the volume.

2. METHODS

2.1. Numerical Technique

Simulations were performed using a commercially available EM solver, SEMCAD-X, which is based on the FDTD technique. The numerical technique used by the thermal solver of the software employed in this study was the FDTD method. The numerical solution of a differential equation like bioheat equation consists of a limited set of numbers, from which the distribution of the dependent variable T can be reconstructed. Thus, when solving a differential equation numerically, the basic unknowns are the values of T at a discrete number of locations in the calculation domain.

2.2. Head Models

I. The High Resolution European Female head was generated from magnetic resonance images (MRI) taken of a 40 year old female volunteer. During the MRI scan the ear was slightly compressed against the surface of the head in order to simulate the correct shape of the pinna while using a mobile phone. The MRI data consist of 121 different slices. In the ear region, the slices have a thickness of 1 mm; all other slices have a thickness of 3 mm. The high resolution of the ear region allows the accurate representation of the pinna as well as the anatomical details of the inner ear. 15 different tissues are distinguished.

II. The adult male head model is based on the data set provided by the Visible Human Project. The slices were taken normal to the body axis at distances of 2 mm ($\pm$0.2 mm) considering more than 100 different tissue or organ types. The ear reference point is set 15 mm above and behind the auditory canal opening. The outer range of the pinna is cut of such that the overall thickness of the ear does not exceed 6 mm.

III. The CAD model of the SAM head phantom was also used in this study. The SAM CAD model in SAT format has been made available for download from the IEEE TC34 SC2 website.

2.3. Commercial Mobile Phone as Exposure Source

The CAD model of Nokia 8310 mobile phone (Figure 1) was used as exposure source. Nokia 8310 mobile phone is a dual band transceiver unit designed for the GSM 900 (including EGSM) and GSM 1800 networks. The original model contained approximately 850 subparts including almost all Integrated Circuits (IC) on the Printed Circuit Board (PCB). A stepwise approach was used to import and arrange the model logically in the simulation platform. First, the most significant parts were identified (antenna, feed structure, PCB) and used for harmonic and transient simulations to determine relevant gridding parameters and verify the excitation modes. The complexity of the model was then increased by adding the remaining parts according to their RF significance. This enabled a construction of a reliable exposure source with all key material parameters and essential electrical properties, which well represented the original phone model. Components with dimensions less than 1 mm were removed from the model due to their insignificant role in the RF simulations. The final models which were used in the simulations are shown in Figure 2, together with the phantoms. Target power levels of the mobile phones used in this study are shown in Table 1.

Table 1: Target levels for the phones' power amplifiers with different bands. Transmitted power is calculated assuming standing wave ratio, i.e., SWR=2.

Frequency Band	Forward power	Transmitted power (SWR=2)
GSM900	32 dBm	31.49 dBm
GSM1800	29 dBm	28.49 dBm

Figure 1: Nokia 8310 mobile phone.

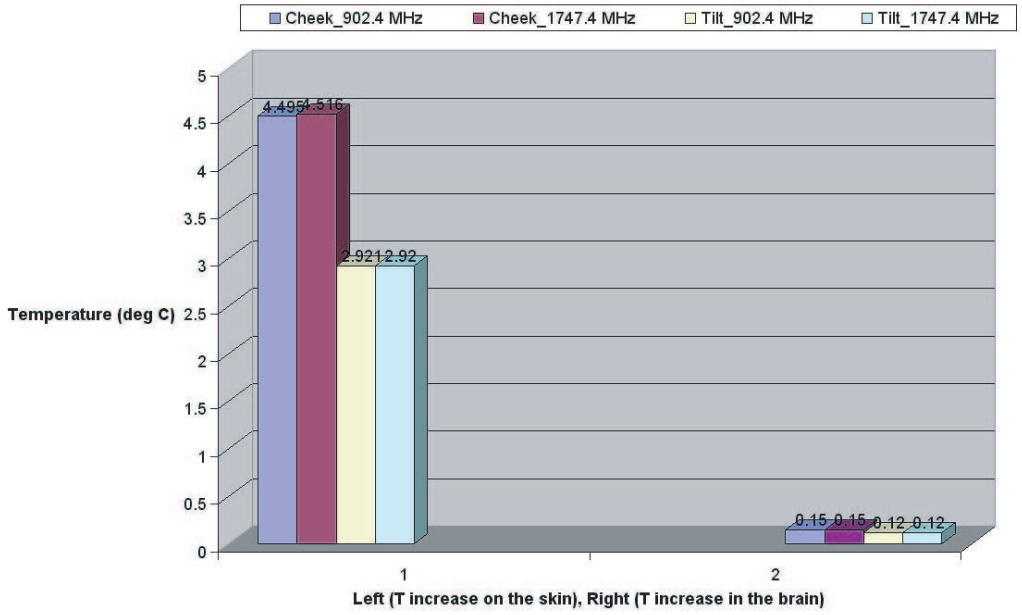

Figure 2: Temperature increase on the skin (left) and in the brain of the adult mal head model.

2.3.1. Phone Position next to the Head

Each simulation is carried out with the phone on the right side of the head model in both the Cheek (Touch) and Tilted positions as described in IEEE-1528.1.

3. RESULTS

Part of the results presented here is shown as bar graphs. Each bar represents the temperature rise for specified position and the frequency. The temperature rise on the skin and in the brain region is presented (Figures 2, 3 and 4).

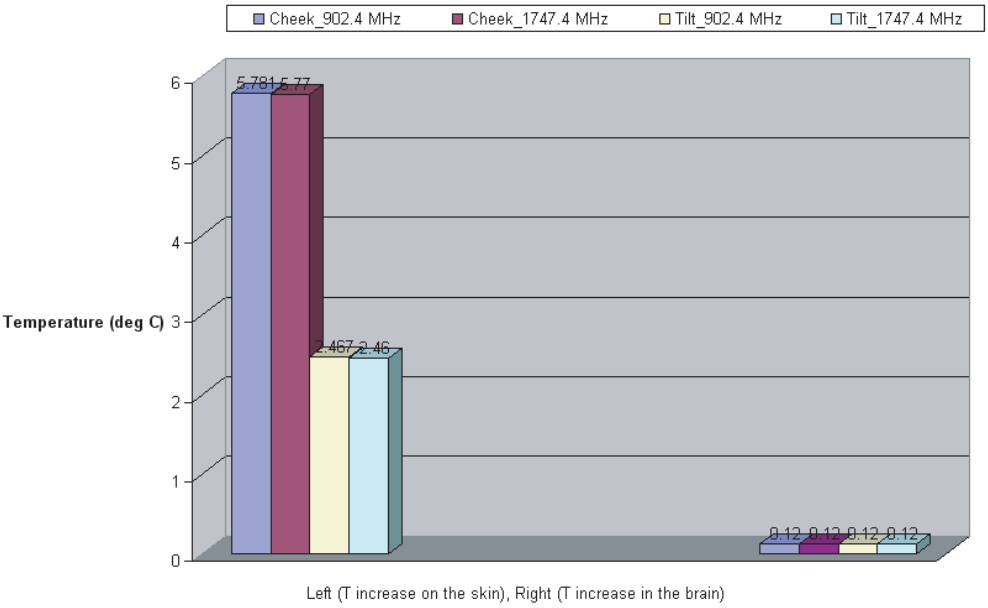

Figure 3: Temperature increase on the skin (left) and in the brain of the adult female head model.

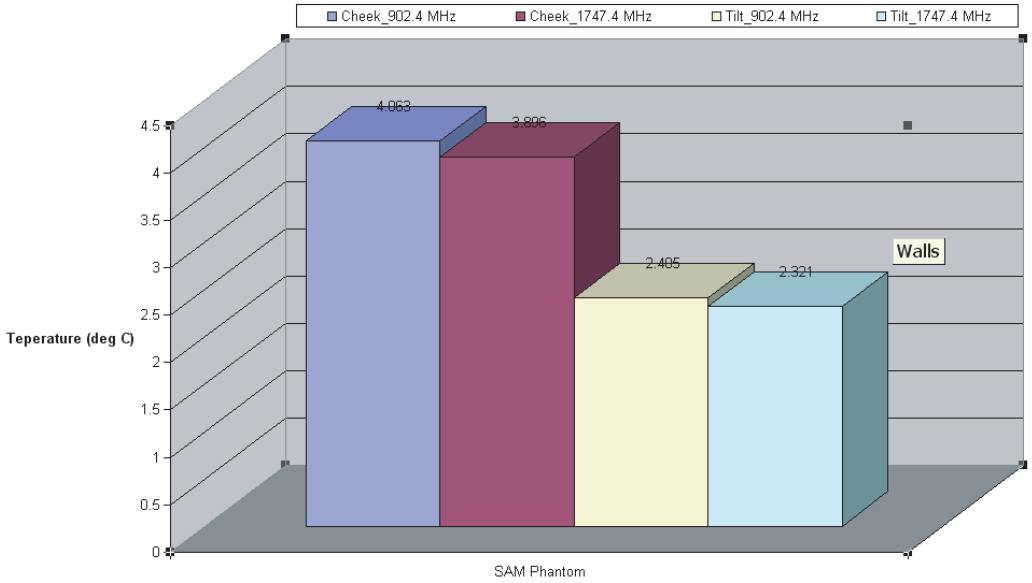

Figure 4: Temperature increase in the SAM phantom exposed to 8310 Nokia phone.

4. CONCLUSIONS

The results of this study show that the temperature increase on the skin in both models may increase over 5 degrees centigrade, but in the brain region the temperature increase remain below 0.15 degrees centigrade. The temperature increase in the SAM phantom is too high compared to the temperature increase in the brain region of MRI based models used in this study. This could mean that for temperature evaluation the SAM phantom is too conservative.

REFERENCES

1. Pennes, H. H., "Analysis of tissue and arterial blood temperature in esting forearm," *J. Appl. Phys.*, Vol. 1, 93–122, 1948.
2. "Practice for determining the peak spatial-averaged specific absorption rate (SAR) in human head from wireless communications devices: Computational techniques," IEEE Std 1528, Part II (draft).

Design of a Broadband Microwave Amplifier Using Fuzzy Logic Performance Data Sheets with a Artificial Immune System

Yavuz Cengiz[1], **Fırat Yücel**[2], **and Filiz Güneş**[3]

[1]Department of Electronics and Communication Engineering,
Süleyman Demirel University, Isparta, Turkey
[2]International Computing Institute, Ege University, İzmir, Turkey
[3]Department of Electronics and Communication Engineering,
Yıldız Technical University, Istanbul, Turkey

Abstract— Optimization is one of the fundamental processes frequently encountered in the engineering problems and is highly nonlinear in terms of the descriptive parameters of the system. In this work, the fuzzy logic performance data sheets of the transistor are employed to determine the feasible design target space in the optimization of a microwave amplifier. The potential gain characteristics with the associated source $Z_S(\omega)$ and load $Z_L(\omega)$ terminations functions are utilized combined with the artificial immune data processing in the design of the microwave amplifiers. A typical example is given and its resulted performance ingredients are compared with the design targets.

1. INTRODUCTION

Optimization is one of the fundamental processes frequently encountered in the engineering problems and is highly nonlinear in terms of the descriptive parameters of the system. Nowadays, microwave amplifier design is doubtlessly one of the major interests of microwave engineering. Considering all the stringent requirements which include high gain, low input VSWR together with the low-power consumption from the low- battery, the wideband miniature LNA design is one of the biggest challenges to UWB transceiver integrations. An optimization process generally contains two fundamental problems: (i) The first is to form a feasible Design Space which is defined in terms of the design variables and targets; (ii) The second is that the global minimum of the error (objective) function governing the optimization must be obtained with respect to the design variables within the feasible design space.

For optimization of a microwave amplifier, design variables are generally the matching circuit parameters whose lower and upper limits are very often determined by the technology to be utilized in the realization stage of the design. Certainly, within the optimization process one can easily embed the desired performance goals without knowing the physical limits and/or compromise relations among F, V_i and G_T appropriately. Unfortunately this process often fails to attain the desired goals. However, the Fuzzy Performance Data Sheets (FPDS) of the transistor overcomes all the above — mentioned handicaps and embeds the compatible (F, V_i, G_T) triplets with their source (Z_S) and load (Z_L) terminations together over a predetermined frequency band of operation. Thus, combining this performance characterisation with the Fuzzy Logic model of the device [1, 2], the compatible (Noise Figure F, Input VSWR V_i, Gain G_T) triplets together with their source Z_S, and load Z_L terminations can be obtained as the functions of the operation variables V_{DS}, I_{DS}, f of the device (Fig. 1).

2. MICROSTRIP AMPLIFIER

Block Diagramme of the microwave amplifier is given in the Fig. 2(a), where the input matching (IMC) and output matching circuits (OMC) are lossless and reciprocal, which are designed by the elements of distributed or lumped parameters in the various configurations. In these matching circuits, two types of distibuted element are employed: (i) The series line (ii) The shunt type of shorted line.

Circuit analysis is based upon the modular structure using either $ABCD$ or wave-amplitude transmission parameters. So the $ABCD$ parameter matrices of the series and shunt line can be given, respectively as follows:

$$A = \cos\beta l, \quad B = jZ_0 \sin\beta l, \quad C = j\sin\beta l/Z_0, \quad D = \cos\beta l \tag{1.1}$$

$$A = 1, \quad B = 0, \quad C = -j/Z_0 \mathrm{tg}\beta l, \quad D = 1 \tag{1.2}$$

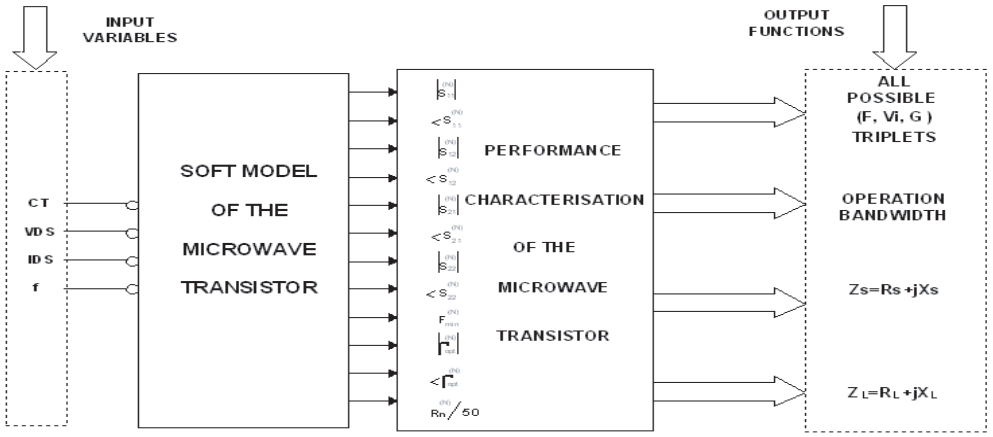

Figure 1: A block diagram for the compatible performance triplets of a microwave transistor.

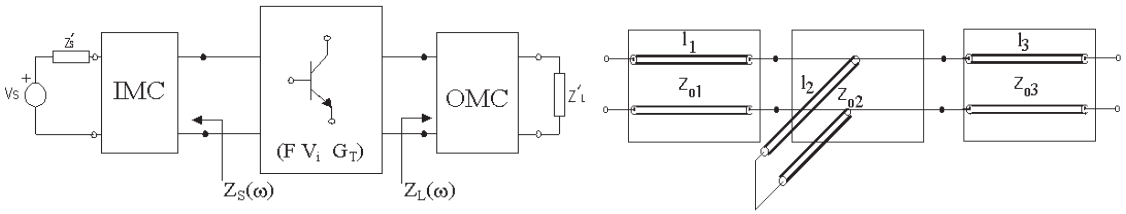

(a) (b)

Figure 2: (a) The two-port representation of a single-transistor microwave amplifiers. (b) T-type matching circuit structure used in the amplifier.

Similarly, wave-amplitude transmission matrices of the series and shunt lines can be expressed.

Scattering and noise parameters of the transistor are approximated by a simple neural network having one hidden layer using the manufacturer's supplied data [3]. The total $ABCD$ or wave-amplitude transmission matrix of the network can be obtained by multiplying each respective matrix; the circuit functions employed in the objective functions can be expressed in either the transfer of port impedance forms in terms of the network parameters. So the transducer power gain of a two-port in term of $ABCD$ parameters can be given as

$$G_T = \frac{4R_S R_L}{P} \tag{2.1}$$

where

$$P = |AZ_L + B + Z_S(CZ_L + D)|^2 \tag{2.2}$$

with $R_S = \mathrm{Re}\{Z_S\},\ R_L = \mathrm{Re}\{Z_L\}$, and Z_S and Z_L are the complex source and load impedances respectively. The noise performance measure function can be expressed as follows:

$$F = \frac{(S/N)_i}{(S/N)_o} = F\{R_S, X_S\} = F_{\min} + \frac{R_N}{|Z_{opt}|^2}\frac{|Z_S - Z_{opt}|^2}{R_S} \tag{3.1}$$

which can be reexpressed in terms of loss of the input matching circuit terminated by Z^*_{opt}, $1/G_{TF}$ as

$$F = F_{\min} + \frac{4R_N R_{OPT}}{|Z_{opt}|^2}\left(\frac{1}{G_{TF}} - 1\right) \tag{3.2}$$

So, the non-negative inequality noise constraint can be written as

$$E_N = 1 + \frac{F_{ref} - F_{\min}}{4R_N R_{opt}}|Z_{opt}|^2 - \frac{1}{G_{TFC}} > 0 \tag{3.3}$$

where $1/G_{TFC}$ is the calculated loss of the input matching circuit terminated by Z^*_{opt}.

The input VSWR is defined at the generator port as the measure of the mismatching of the input impedance with respect to the source impedance

$$V_i = \frac{1+|\rho_i|}{1-|\rho_i|}, \qquad \rho_i = \frac{Zi - Z_s^*}{Zi + Z_s} \tag{4}$$

Here we define a logarithmic inequality constrain function as follows

$$E_{vi} = \log_{10}|\rho_{iref}|^2 - \log_{10}|\rho_{ic}|^2 > 0 \tag{5}$$

3. ARTIFICIAL IMMUNE SYSTEMS

Drawing inspiration from the vertebrate immune system, a new research field of Artificial Immune Systems (AIS) is springing up. The vertebrate immune system is a rich source of theories and acts as an inspiration for computer-based solutions. Over the last few years there has been an increasing interest in the area of artificial immune system [4]. AIS uses ideas gleaned from immunology in order to develop systems capable of performing tasks in various engineering applications [5]. Artificial Immune Systems have come on the scene in the 1990s as a new system consolidating a number of biologically-based calculating methods such as Artificial Neural Networks and Artificial Life [6, 7].

The artificial immune system has been formed on the basis of the working principles of the natural immune system found in the human body. Tissues and organs related with the natural immune system in the body are the thymus gland, the bone marrow, the lymph nodes, the spleen and the tonsils. A central organ coordinating the functions of the associated tissue, the organ, the molecule and the cells does not exist in the immune system. The immune system, via its special cells, recognizes the foreign (external) cells filtering through the body and neutralizes them. The basic immunity cell is the lymphocyte [8]. The lymphocytes are grouped into two categories: "T" and "B" cells. The "B" cells can recognize the antigens without restraint in liquid solutions whereas the "T" cells need the recognition of antigens by means of other assisting cells [9]. A natural immune response is given simply as follows: When an external molecule enters the body, the special molecules (macrophages) surround that external molecule and get other immunity cells to notice it. When the assisting "T" cells notice the special cells, they forewarn the white blood cells and these cells become larger in number. The "B" cells begin to produce chemical substances called antibodies; the antibodies combining with the antigens exterminate the antigens with ease. The exterminating "T" cells alerted by the assisting "T" cells make it possible for the antigen to be exterminated. The body needs to be able to distinguish between its own cells and external cells plus molecules (antigens) in order for the natural immune system cells to carry out the activities defined above. The cells belonging to the body itself are called the "self" cells and the external cells are called the "non-self" cells. It is important to keep the "self" cells unharmed in the course of exterminating the "non-self" cells.

These problem-solving methods that are used in artificial immune systems thoroughly imitate the mechanisms found in the natural immune system that the human body possesses. We used a Clonal Selection algorithm (CLONALG) to solve the optimization problem at this study.

4. COMPUTED RESULTS

NE329S01 is biased at $I_C = 5\,\text{mA}$ and $V_{CE} = 10\,\text{V}$, for which the termination functions $Z_S(\omega_i)$, $Z_L(\omega_i)$ for $F_{req}(\omega_i) = 0.46\,\text{dB}$, $V_{ireq}(\omega_i) = 1.0$, $G_{Treq}(\omega_i)) = 12\,\text{dB}$, $i = 2, \ldots 11$ are supplied into the optimization process as the target values over the operation bandwidth. These target values are the physically realizable $Z_S(\omega_i) = R_S(\omega_i) + jX_S\omega_i)$; $Z_L(\omega_i) = R_L(\omega) + jX_L(\omega_i)$, $i = 2, \ldots 11$ termination solutions to the simultaneous nonlinear equations of $F\ (R_S,\ X_S) = F_{req}$, $V_i(R_S,\ X_S,\ R_L,\ X_L) = V_{ireq}$, $G_T = (R_S,\ X_S,\ R_L,\ X_L) = G_{Treq}$ for the transistor. Since the optimization process also find out the approximately solution set to the same equations in terms of the predetermined variables, so the resulted values will no longer be equal to the target values, but will be values nearly to the target values, ruled by the objective function and its data processing method. So Figs. 3(a), 3(b) and 3(c) give the resulted $G_T(\omega)$, $F(\omega)$, $V_i(\omega)$-frequency variations. Bandwidth of amplifier is between 2 GHz and 11 GHz.

T-type matching circuit parameters for NE329S01 transistor are found as follows:

$\ell_1 = 14.99\,\text{cm}$, $\ell_2 = 1.23\,\text{cm}$, $\ell_3 = 0.32\,\text{cm}$, $Z_{o1} = 5\,\Omega$, $Z_{o2} = 150\,\Omega$, $Z_{o3} = 89.78\,\Omega$;
$\ell_4 = 13.76\,\text{cm}$, $\ell_5 = 0.69\,\text{cm}$, $\ell_6 = 1.02\,\text{cm}$, $Z_{o4} = 135.8\,\Omega$, $Z_{o5} = 148.8\,\Omega$, $Z_{o6} = 88.25\,\Omega$

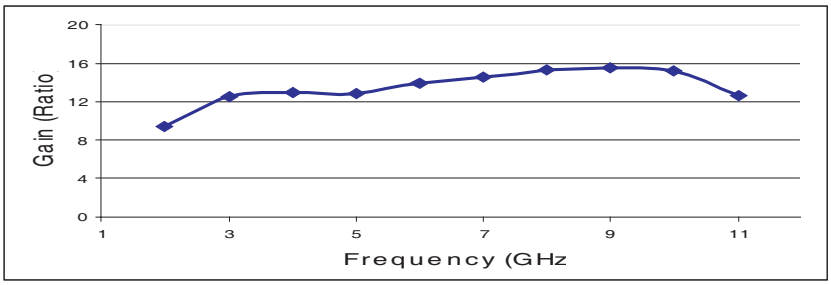

(a)

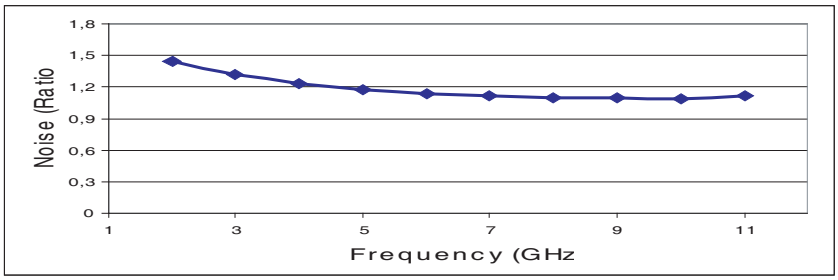

(b)

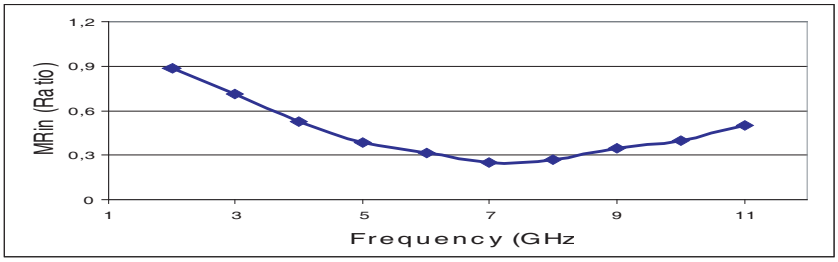

(c)

Figure 3: (a) G_T (ratio) variation of the microwave amplifier (G_{Treq} (ratio) = 15.85; V_{ireq} (ratio) = 1.0; F_{req} (ratio) = 1.11). (b) Noise(ratio) variation of the microwave amplifier (G_{Treq} (ratio) = 15.85; V_{ireq} (ratio) = 1.0; F_{req} (ratio) = 1.11). (c) Input reflection coefficient variation of the microwave amplifier (G_{Treq} (ratio) = 15.85; V_{ireq} (ratio) = 1.0; F_{req} (ratio) = 1.11).

5. CONCLUSIONS

Quality of the microwave amplifier performance can be determined by the flat gain level as well as the percent of the maximum power delivered into the input port, which is characterized by the module square of the input reflection coefficient, over the operation bandwidth. Noise figure is also important performance ingredient depending on the position of the amplifier in system order. So this work may have the following originalities:

Gain, Input VSWR and Noise Figure are taken into account simultaneously over a pre-determined operation bandwidth in a Multi- Objective Error Function;

Manufacturers Data Sheets of the transistor utilized are replaced by the Fuzzy Performance Data Sheets to determine the Feasible Design Space;

Novel Soft Computing Methods of Fuzzy Logic, Artificial Immune Algorithm are utilized;

The Resulted Design Space can be utilized efficiently in the realization by the MMIC (Monolithic Microwave Integrated Circuit) technology.

REFERENCES

1. Güneş, F., H. Torpi, and F. Gürgen, "A multidimensional signal-noise neural network model for microwave transistors," *IEE Proceedings — Circuits Devices and Systems*, Vol. 145, No. 2, 111–117, April 1998.

2. Güneş, F., N. Türker, and F. Gürgen, "Signal-noise support vector model of a microwave transistor," *Int. J. of RF and Microwave CAE*, Vol. 17, No. 4, 404–415, July 2007.
3. Güneş, F., H. Torpi, and F. Gürgen, "A multidimensional signal-noise neural network model for microwave transistor," *IEE Proceedings — Circuits Devices and Systems*, Vol. 145, No. 2, 111-7, 1998.
4. Zhang, L., Y. Zhong, and P. Li, "Applications of artificial immune systems in remote sensing image classification," *Proc. 20th Congress. Int. Soc. for Photogrammetry and Remote Sensing*, 2004.
5. De Castro, L. N. and F. J. Von Zuben, "Learning and optimization using the clonal selection principle," *IEEE Transactions on Evolutionary Computation, Special Issue on Artificial Immune Systems*, Vol. 6, No. 3, 239–251, 2002.
6. Engin, O. and A. Döyen, "Artificial immune systems and applications in industrial problems," *G.U. Journal of Science*, Vol. 17, No. 1, 71–84, 2004.
7. Nasaroui, O., D. Dasgupta, and F. Gonzales, "The promise and challenges of artificial immune system based web usage mining: Preliminary results," *Workshop on Web Analytics at Second SIAM International Conference on Data mining(SDM)*, Arlington, VA, April 11–13, 2002.
8. Trojanowski, K. and S. T. Wierzchon, "Searching for memory in artificial immune system," *The Elevent International Symposium on Intelligent Information Systems*, June 3–6, 2002.
9. De Castro, L. N. and J. Timmis, "A novel approach to pattern recognition," *Artificial Neural Networks in Pattern Recognition*, L. Alonso, J. Corchado, and Fyfe, Editors, 67–84, University of Paisley, 2002.

Design of a Patch Antenna with Integration Cellular Automata and Genetic Algorithm

Y. Cengiz[1] **and H. Tokat**[2]

[1]Suleyman Demirel University, Isparta, Turkey
[2] Turk Telekom, Isparta, Turkey

Abstract— Microstrip patch antennas are used in many communication systems as they are low-weight, low-cost and as they have multi band properties and effective performances. Microstrip antennas gain importance because they have a great range of usage area such as, GSM, space vehicles, planes, radars, satellite communication in many military services and their production is easy with printed circuit technology [1].

At the antenna design, small changes affects the performance of the antenna. While optimizing the shape, the probality of the finding best configuration is very low, because of possible wide range geometries. If the geometry can be determined by formulations, then optimized geometry range can be more computable.

Cellular Automata, is a geometri determination method which has a system with simple rules and becomes from stages affecting by themselves mentioned at 1982 by Stephen Wolfram. Through this method, beginning from black box, it is possible to reach the whole different rules that models the system.

1. INTRODUCTION

The concept of CA was initiated in the early 1950's by J. Von Neumann and Stan Ulam [2]. Von Neumann showed that a cellular automaton can be universal and devised a CA, each cell of which has a state space of 29 states, and showed that the devised CA can execute any computable operation. However, due to its complexity, Von Neumann rules were never implemented on a computer. Von Neumann's research pointed to a dichotomy in CA research. It was proven that a decentralized machine can be designed to simulate any arbitrary function [3, 4].

Cellular automata are simple mathematical idealizations of natural systems. They consist of a lattice of discrete identical sites, each site taking on a finite set of, say, integer values. The values of the sites evolve in discrete time steps according to deterministic rules that specify the value of each site in terms of the values of neighboring sites. Cellular automata may thus be considered as discrete idealizations of the partial differential equations often used to describe natural systems. Their discrete nature also allows an important analogy with digital computers: cellular automata may be viewed as parallelprocessing computers of simple construction. As a first example of a cellular automaton, consider a line of sites, each with value 0 or 1 (Figure 1). Take the value of a site at position i on step t to be $a^{(t)}$. One very simple rule for the time evolution of these site values is

$$a_i^{(t+1)} = a_{i-1}^{(t)} + a_{i+1}^{(t)} \mod 2 \tag{1}$$

where mod 2 indicates that the 0 or 1 remainder after division by 2 is taken. According to this rule, the value of a particular site is given by the sum modulo 2 (or equivalently, the Boolean algebra "exclusive or") of the values of its left- and right- and nearest neighbor sites on the previous time step. The rule is implemented simultaneously at each site. Even with this very simple rule quite complicated behavior is nevertheless found.

Figure 1: Cellular automata design with the binary form of the cellular automata rule.

The simplest nontrivial CA would be one-dimensional, with two possible states per cell, and a cell's neighbors defined to be the adjacent cells on either side of it. A cell and its two neighbors form a neighborhood of 3 cells, so there are $2^3 = 8$ possible patterns for a neighborhood. There are then $2^8 = 256$ possible rules. These 256 CAs are generally referred to using Wolfram notation, a

standard naming convention invented by Wolfram. The name of a CA is the decimal number which, in binary, gives the rule table, with the eight possible neighborhoods listed in reverse counting order. For example, below are tables defining the "rule 30 CA" and the "rule 110 CA" (in binary, 30 and 110 are written 11110 and 1101110, respectively) and graphical representations of them starting from a 1 in the center of each image:

Table 1: Rule 30 cellular automata.

current pattern	111	110	101	100	011	010	001	000
new state for center cell	0	0	0	1	1	1	1	0

Table 2: Rule 110 cellular automata.

current pattern	111	110	101	100	011	010	001	000
new state for center cell	0	1	1	0	1	1	1	0

A table completely defines a CA rule. For example, the rule 30 table says that if three adjacent cells in the CA currently have the pattern 100 (left cell is on, middle and right cells are off), then the middle cell will become 1 (on) on the next time step. The rule 110 CA says the opposite for that particular case.

A number of papers have analyzed and compared these 256 CAs, either individually or collectively. The rule 30 and rule 110 CAs are particularly interesting.

Rule 30 generates apparent randomness despite the lack of anything that could reasonably be considered random input. Wolfram proposed using its center column as a pseudorandom number generator (PRNG); it passes many standard tests for randomness, and Wolfram uses this rule in the Mathematica product for creating random integers [3–5].

2. METHODS OF ANALYSIS

While analyzig antenna using MoM based on RWG, the surface of a metal antenna is divided into seperate triangels, each pair of triangles, and each pair of triangles has a common edge constituting the corresponding RWG edge element. Figure 1 shows two triangles, one has a plus sign and the other a minus sign, to the nth edge of a triangulated surface modeling a scatterer. A basis function associated with the nth edge is given as below (2).

$$\mathbf{f}(\mathbf{r}) = \begin{cases} (l/2A^+)\rho^+(r) & r \text{ in } T^+ \\ (l/2A^-)\rho^-(r) & r \text{ in } T^- \\ 0, & \text{otherwise} \end{cases} \tag{2}$$

where l is the edge length and $A^\pm$ is the area of triangle $T^\pm$ Vector ρ connects the free vertex of the triangle $T^\pm$ to the observation point r, while vector ρ^- connects the observation point to the free vertex of the triangle T^-. The surface current density on the antenna surface is the sum of basis functions over all edge elements, with unknown coefficients. These unknown coefficients are found by using the MoM. The surface current density (3) for a given triangle k is obtained in the

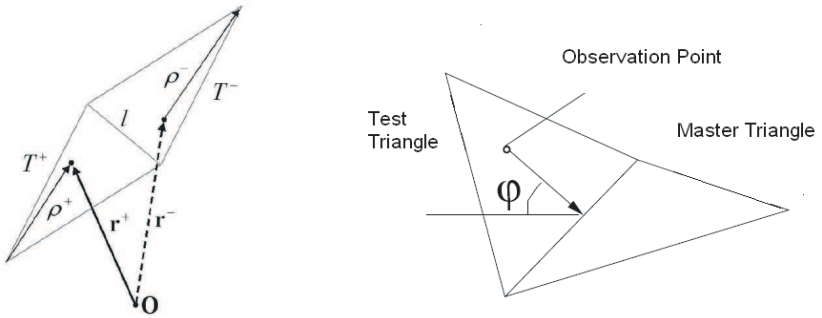

Figure 2: Schematics of a RWG edge element.

form;

$$\mathbf{J}_k = \sum_{m=1}^{M} I_m f_m(r) \tag{3}$$

where $\mathbf{J}$ is the vector sum of surface currents, and I_m are the unknown coefficients. The expansion coefficients, I_m, form vector $\mathbf{I}$, which is the unique solution of the moment equation, and the solution can be obtained using matrix inversion as at (4);

$$\mathbf{I} = \mathbf{Z}^{-1}\mathbf{V} \tag{4}$$

where $\mathbf{Z}$ is the impedance matrix and $\mathbf{V}$ is the voltage excitation vector [7, 8].

3. ANTENNA DESIGN

In its most basic form, a Microstrip patch antenna consists of a radiating patch on one side of a dielectric substrate which has a ground plane on the other side. The patch is generally made of conducting material and can take any possible shape. As the cellular automata algorithm is the geometri determination method, the genetic algorithm can be used to choose the best configuration of patch. Dimensions of the antennas are configured as $L = 0.10$; $W = 0.05$; and the height of the patch from the ground is $h = 0.0150$.

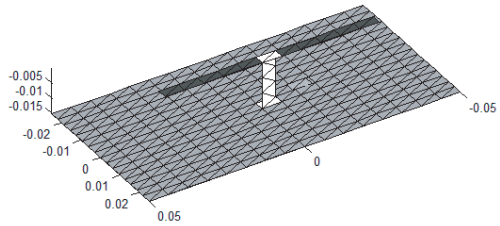

Figure 3: Feeding patch configuration.

The following examples Figures 4 and 5 are designed with the CA. To increase the active regions on antenna, feeding point is configured as Figure 3.

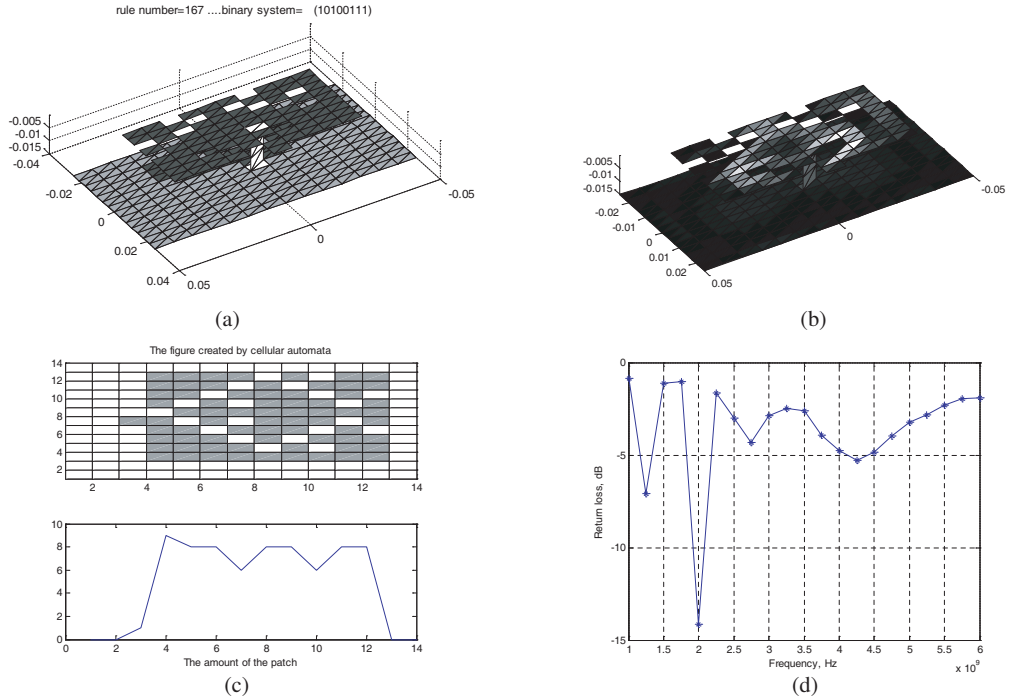

Figure 4: (a)Antenna designed by the rule number 167. (b) The active regions on antenna. (c) Rule 167 cellular automata design. (d) Rule 167 return loss graph.

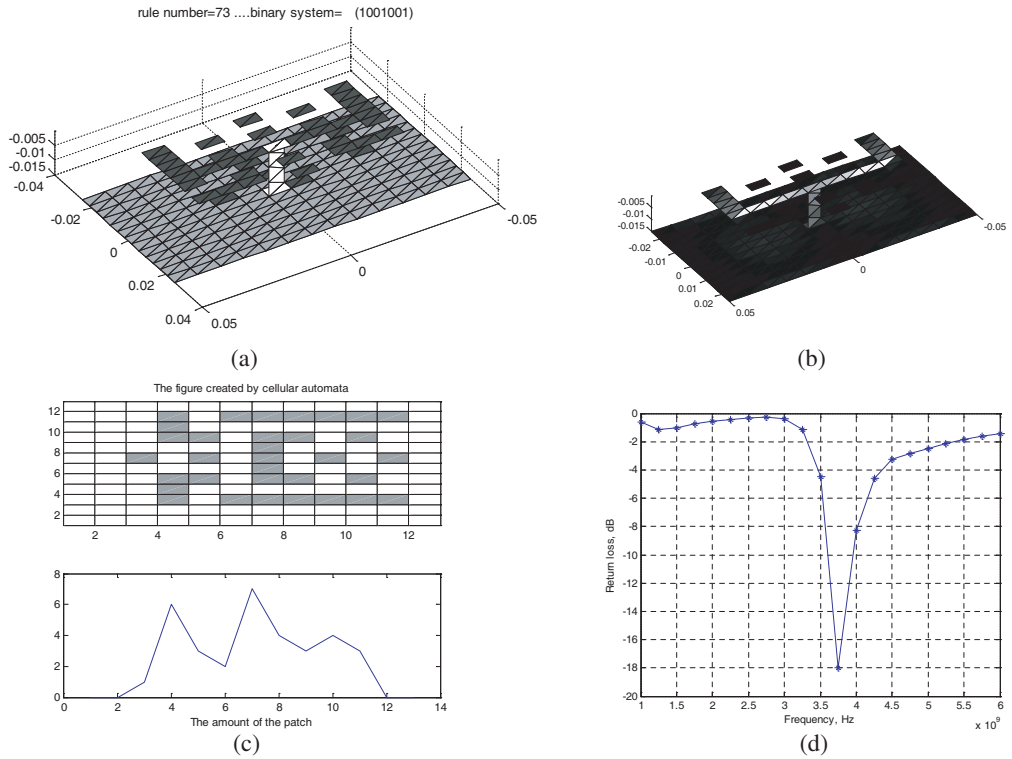

Figure 5: (a) Antenna designed by the rule number 73. (b) The active regions on antenna. (c) Rule 73 cellular automata design. (d) Rule 73 return loss graph.

4. GENETIC OPTIMIZATION

The evolutionary process of a population in GA is based upon the principle of "survival of the fittest" and directed to genetic operators after the genetic operations emerging naturally. The most widely used genetic operators are recombination, crossover and mutation. The individuals from the population to be worked on must be selected in order to apply the genetic operators. The optimized fitness funcion value is the rule number of the cellular automat of the individuals in the population, will be employed by following algorithm Figure 6.

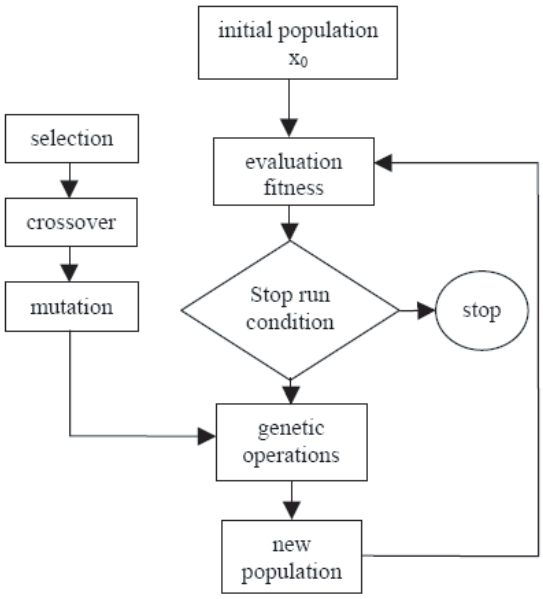

Figure 6: Genetic optimization algorithm.

With GA and CA the design and result are shown at Figures 5(a), (b), (c), (d). 4.5 GHz 33 dB. The dimensions of the antennas are configured as $L = 0.10$; $W = 0.05$; and the height of the patch from the ground is $h = 0.0150$. The patch of the area is 15×15 squares configured with cellular automata.

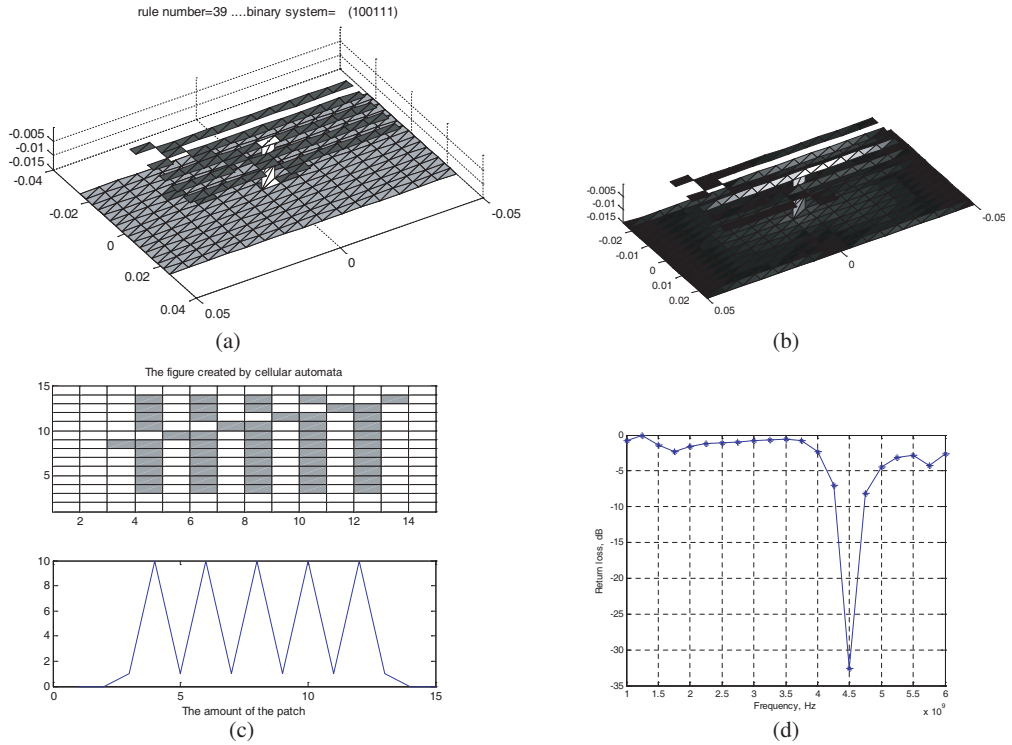

Figure 7: (a) Three band antenna designed by the rule number 39. (b) The active regions on antenna. (c) Rule 39 cellular automata design. (d) Rule 39 return loss graph.

5. RESULTS AND CONCLUSION

At this work, the three methods, CA, MoM anaylsis and GA has been configured to work to gether, Some different examples has been given at the Figures 3, 4, 5. Figure 3 shows three band antenna configuration. Works at 1.7 GHz with 12 dB, 2.5 GHz with 16 dB and 3 GHz 16.7 dB created with the cellular automata 333. Figure 4 shows an antenna works at 2 GHz with 14 dB created with the cellular automata rule 167. Figure 5 shows an antenna works at 3.7 GHz with 16 dB created with the cellular automata rule 73. Lastly the optimized figure as shown at the Figure 7 with cellular automata rule 39 works at 4.5 GHz with 34 dB.

At this work CA is used for saving the iteration number of GA, by selecting the best geometry among the figures created with CA, by using the rule number as a fitness function value.

REFERENCES

1. Yazgan, E., "Mikroşerit antenler," *Elektrik Mühendisliği Dergisi*, September 1987.
2. Neumann, J. V., *The Theory of Self-Reproducing Automata*, A. W. Burks (ed.), Univ. of Illinois Press, Urbana and London, 1966.
3. Joel, L., *Cellular Automata: A Discrete View of the World*, Schiff, Wiley & Sons, Inc., ISBN 047016879X (0-470-16879-X).
4. Chopard, B. and M. Droz, *Cellular Automata Modeling of Physical Systems*, Cambridge University Press, 1998, ISBN 0-521-46168-5.
5. Von Neumann, J., "Neighbourhood survey includes discussion on triangular grids, and larger neighbourhood Cas," *The Theory of Self-Reproducing Automata*, A. Burks, ed., Univ. of Illinois Press, Urbana, IL, 1966.
6. Wolfram, S., "Statistical mechanics of cellular automata," *Reviews of Modern Physics*, Vol. 55, 601, 1983.

7. Namkung, J., E. L. Hines, R. J. Green, and M. S. Leeson, "Probe-fed microstrip antenna feed point optimization using a genetic algorithm and the method of moments," *Microwave and Optical Technology Letters*, Vol. 49, No. 2, 325–329, Wiley Periodicals, 2006.
8. Rao, S. M., D. R. Wilton, and A. W. Glisson, "Electromagnetic scattering by surfaces of arbitrary shape," *IEEE Trans. Antennas Propagat.*, Vol. 30, 409–418, May 1982.
9. Altunkaynak, B. and A. Esin, "The genetıc algorıthm method for parameter estımatıon in nonlınear regressıon," *G.Ü. Fen Bilimleri Dergisi, (G.U. Journal of Science)*, Vol. 17, No. 2, 43–51, 2004, ISSN 1303-9709.
10. Troshkin, M., http://www.econ.umn.edu/ troshkin/misc/_misc.htm.

A 5 GHz LNA Design Using Neural Smith Chart

M. Fatih Çağlar[1] and Filiz Güneş[2]

[1]Department of Electronics and Communication Engineering
Süleyman Demirel University, Isparta, Turkey
[2]Department of Electronics and Communication Engineering
Yıldız Technical University, Beşiktaş, Istanbul

Abstract— This work presents the design of a single-stage, low noise, stable and matched amplifier at 5 GHz. The amplifier is designed around the Agilent ATF-551M4 low noise enhancement mode pseudomorphic HEMT (EpHEMT). An Artificial Neural Network (ANN) model of the Smith Chart is proposed for an alternative solution to impedance matching of this LNA (Low Noise Amplifier) design which has been entitled "Neural Smith Chart (NSC)" shortly. The input and the output impedance matching networks are performed using NSC outputs and MATLAB® RF Toolbox simulation solutions for comparison.

1. INTRODUCTION

In wireless communications, receivers need to be able to detect and amplify incoming low-power signals without adding much more noise. Therefore, a LNA is often used as the first stage of these receivers. As the usage of wireless communication in 2.4 GHz band grows, it causes uncontrolled occupancy by users in that band. Since it is an unregulated frequency, the 2.4 GHz band also suffers from enormous interference effects generated by devices like microwave ovens and 2.4 GHz transmitters that will reduce performance especially in wireless local area networks (WLANs). On the other hand, the 5 GHz band provides lots of unlicensed spectrum and it has less interference. Recently, many researchers have been focused on the 5 GHz standard in the design of wireless transceivers which should be used in 802.11a, HiperLAN2 and HiSWANa applications.

Analysis and design of microwave circuits are generally tedious with their highly nonlinear equations and lack in the insight to their related problems. The Smith Chart provides a very useful graphical tool to these types of the problems with its numerous applications. However, the manual interpretation of the Smith Chart can be error prone. In the literature, works on the computerized Smith Chart took place between 1992–1995 by Prasad and her group in [1–3]. In their work, the Smith Chart is represented firstly by a $(n \times n)$ numerical matrix [1], and then this model has been developed as a massively distributed computing network [3]. Thus, due to this discrete nature of these CAD systems, use of these types of the Smith Chart models remained limited.

Neural networks are universal function approximators [9, 10] allowing reuse of the same modeling technology for both linear and nonlinear problems at both device and circuit levels [8]. Yet neural network models are simple and model evaluation is very fast. Recent works have let to their use for modeling of both active and passive components such as transistors [4, 5], planar transmission line microstrip, coplanar wave (CPW) guides [6], vias, CPW discontinuities, spiral inductors [4]. Furthermore ANNs have found modeling in Smith Chart representation and automatic impedance matching [7].

To design a sample LNA, in this work the available gain design technique is used, which involves selecting a single-stub matching network that provides a suitable compromise between gain and noise. After designing the input and output matching networks using lossless transmission lines, it is verified that the design by analyzing the matched LNA and plotting its gain, noise and return loss. The simulated results of theoretical calculations by MATLAB® RF Toolbox are compared with impedance matching response of NSC.

2. ANN MODEL OF THE SMITH CHART: NEURAL SMITH CHART (NSC)

The black-box model of the Smith Chart for analysis and design of the fundamental transmission line circuit is given in Fig. 1, where the termination $Z_S = R_S + jX_S$; the transmission line with ℓ, Z_0; operation bandwidth **B** between $f_{\min}$, $f_{\max}$ and the dielectric are the inputs, the corresponding outputs are the standing waves, impedance matching and impedance transformation properties of the transmission line. For this purpose, the two fairly simple, similar ANN modules are generated: One is for the standing waves and impedance matching properties of the transmission line and the other is for the modeling of impedance transformation. As given in Figs. 2(a) and 2(b), NSC is

generated by the two ANN modules, each of which is a multilayer perceptron (MLP) with the three inputs of the same termination (R_S, X_S) and the electrical length ($\beta\ell$) [11].

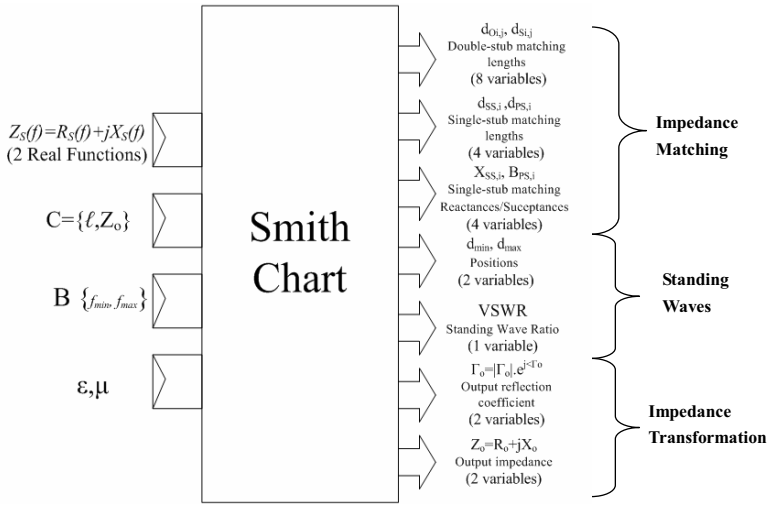

Figure 1: Black-Box Model of the Smith Chart with the variable definitions.

There are four steps designing this model as a view of programmer. Firstly, the input-output data space is mined from the Smith Chart and the analytical equations (formulas) to train and test selected ANN structure. In this session it has obeyed universal data mining rules. The data space is divided into two parts of 50% training and 50% testing data. ANN training and testing are the second and third step, respectively. Unless the testing results satisfy, different types of ANN structures with varied hidden sizes and training algorithms will be tried. These trying operations are being a loop for best test results. At the last step, the fourth step, the targets are compared in the verified error interval.

Three key rules are applied in the data generation from the Smith Chart:

- The whole Smith Chart is divided into the N transmission circles (ideally $N \to \infty$);
- Each transmission circle is divided into the $n(r)$ arcs with adaptive radius r sampling algorithm [11];
- Resistive, capacitive, inductive regions of the Smith Chart can be determined by a rule which may be named as "the $f\ell$ product" [11] depending on the ratio of Z_S/Z_0 which may be either greater or smaller than the unity.

The Levenberg-Marquardt (LM) back-propagation algorithm for the smallest testing error and four layered network with the minimum number of neuron for faster training are performed with the MLP type of network. The performance function of MLP is the Mean Squared Error (MSE).

3. LNA DESIGN AND WORKED EXAMPLE

The LNA design initial specifications are as follows: Bandwidth: 4–6 GHz; Noise Figure $\leq$ 1 dB; Transducer Gain $>$ 11 dB; Operating between 50 Ω load and source terminations. Before proceeding with this design, it is determined the calculated frequencies at which the amplifier is unconditionally stable. μ and μ' defines the distance from the center of the Smith Chart to the nearest output (load) and input (source) stability circle, respectively. Having $\mu > 1$ (or $\mu' > 1$) is necessary and sufficient for the 2-port linear network to be unconditionally stable. This stability factor is given by where $\Delta = s_{11}s_{22} - s_{21}s_{12}$:

$$\mu = \frac{1 - |s_{11}|^2}{|s_{22} - s_{11}^* \cdot \Delta| + |s_{21} \cdot s_{12}|} \quad \left(\text{or} \quad \mu' = \frac{1 - |s_{22}|^2}{|s_{11} - s_{22}^* \cdot \Delta| + |s_{21} \cdot s_{12}|} \right) \tag{1}$$

One way to stabilize an amplifier is to add a shunt resistor at the output of the amplifier. However, this approach will also reduce gain and add noise. The maximum shunt resistor value makes $\mu = 1$ that makes the amplifier unconditionally stable. Fig. 3 shows the stable LNA structure with 50 Ω

terminals, input-output matching networks and shunt resistor. In the Fig. 4, input and output stability, available gain and NF circles at 5 GHz are drawn. A star ($'*'$) and a circle-in-dashed-line will also appear on the Smith Chart. The star represents the matching load reflection coefficient (Γ_L) that is the complex conjugate of Γ_{out}. The gain is maximized when Γ_L is the complex conjugate of Γ_{out}. The data cursor (black square point) represents the matching values of Γ_S and Γ_{out} with high available gain and less NF.

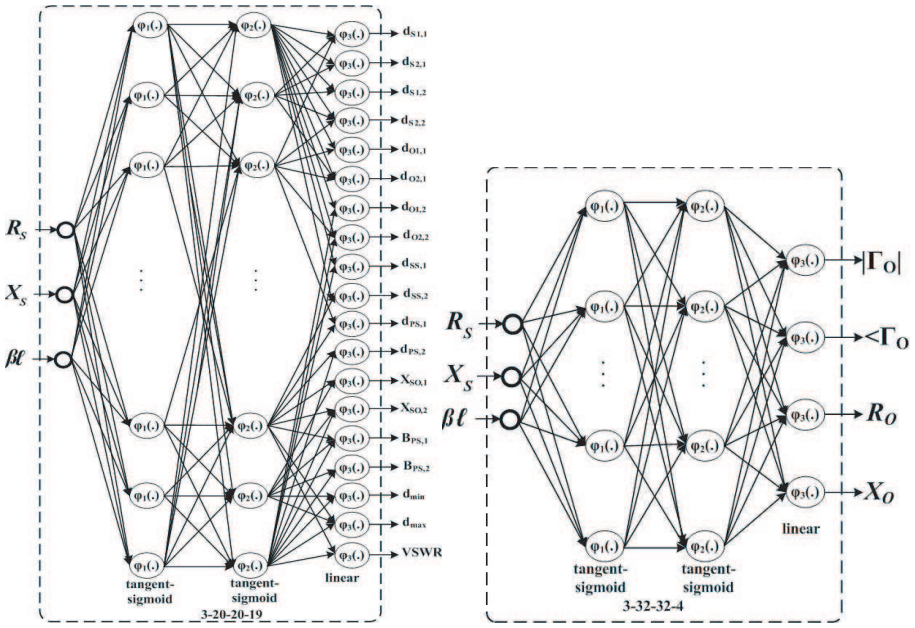

(a) Neural Smith Chart Module-I (b) Neural Smith Chart Module-II

Figure 2: Neural Smith Chart modules.

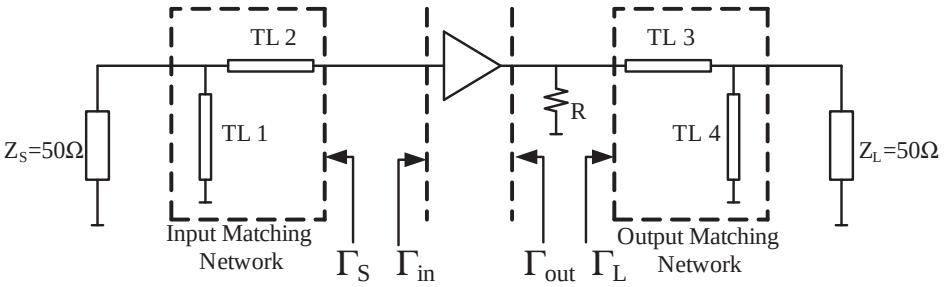

Figure 3: Desired LNA schematic with matching networks.

Table 1: NSC and simulation results of designed LNA.

	G_T [dB]	$\lvert S_{11}\rvert$ [dB]	$\lvert S_{22}\rvert$ [dB]	N_F [dB]
NSC	12.81	−5.15	−76.87	0.77
RF Toolbox	13.00	−4.74	−28.36	0.78

The s-parameters of ATF-551M4 transistor which biased at 2 V and 20 mA are collected from the data sheet and converted to s2p format for LNA analyzing. Then, single-stub lossless transmission line matching network stub positions and lengths are calculated for both input and output by using the data in Fig. 4(b). After finding Z_s and Z_L using Γ_S and Γ_L (conjugate of Γ_{out}), these impedances are inputted to the NSC for achieving short-circuit terminated parallel single-stub matching network positions and lengths for both input and output. In Table 1, performance of NSC matched LNA is compared. Transducer and available gain, noise figure, input and output return losses of both simulated matched LNA and NSC matched LNA are figured in Figs. 5(a), 5(b), 5(c) and 5(d).

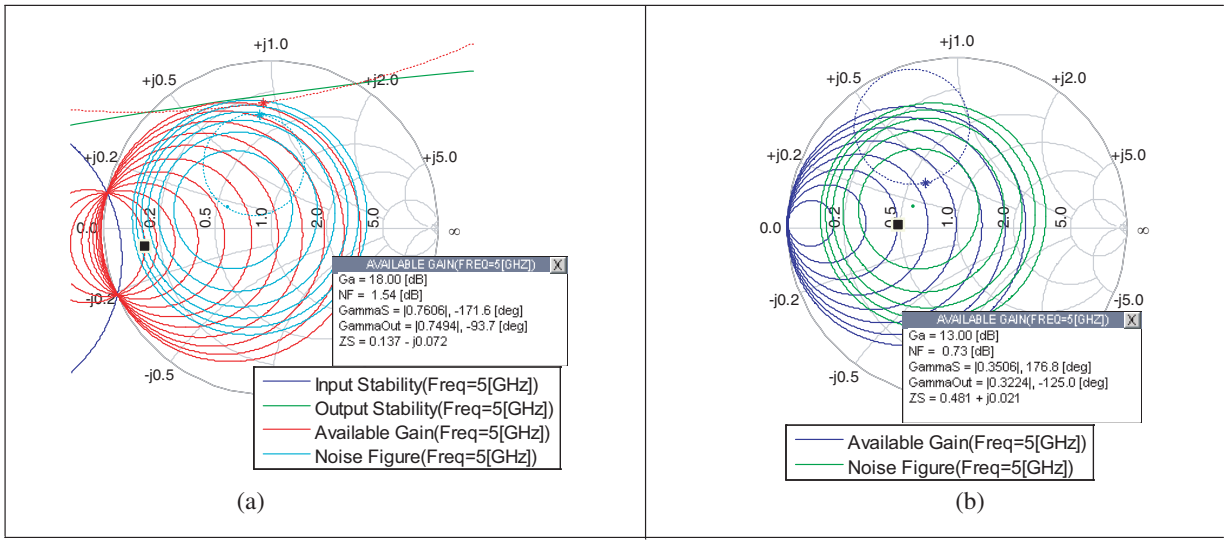

Figure 4: Stability, gain and NF circles at 5 GHz. (a) Without a shunt resistor at the output. (b) With a $R = 150\,\Omega$ shunt resistor at the output.

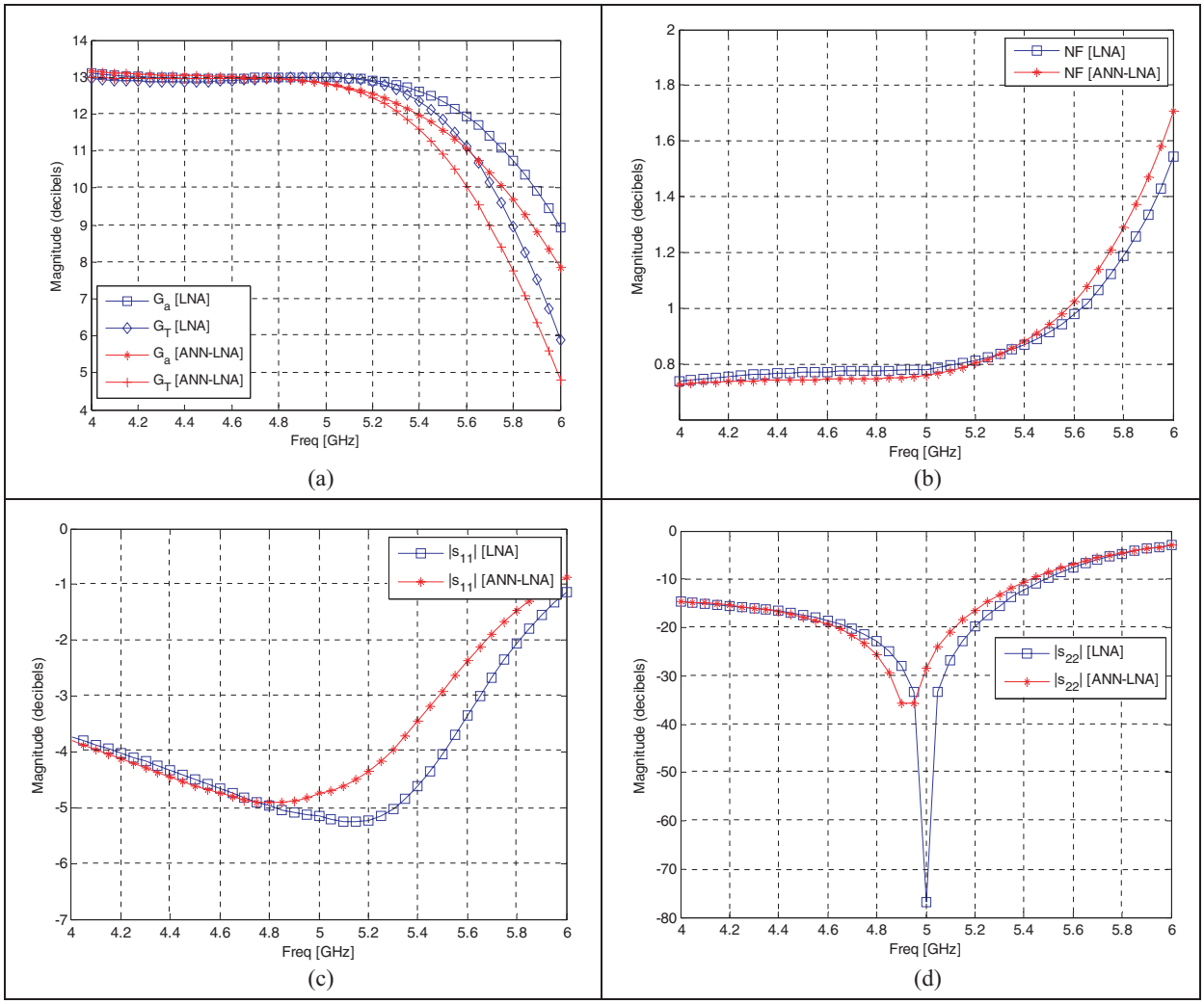

Figure 5: Gain, NF and return loss at 4–6 GHz.

4. CONCLUSIONS

A "Neural Smith Chart" is formed by using the ANNs in the simple MLP structures as the nonlinear learning machines from the input space to the output space [11]. An application of LNA design for above specifications is achieved. Especially it is stressed on matching performance of NSC. The graphics in Fig. 5 show that the NSC matching results of a LNA design procedures ensure similarity and availability when initial specifications reviewed.

REFERENCES

1. Vai, M., S. Prasad, and H. Wang, "A Smith Chart represented by a neural network and its applications," *IEEE MTT-S International Microwave Symposium Digest*, 1565–1568, 1992.
2. Vai, M. and S. Prasad, "Automatic impedance matching with a neural network," *IEEE Microwave and Guided Wave Letters*, Vol. 3, No. 10, 353–354, 1993.
3. Vai, M. and S. Prasad, "Microwave circuit analysis and design by a massively distributed computer network," *IEEE Microwave Theory and Techniques*, Vol. 43, No. 5, 1087–1094, 1995.
4. Günes, F., F. Gürgen, and H. Torpi, "Signal-noise neural network model for active microwave device," *IEE Proc. — Circuits Devices and Systems*, Vol. 143, 1–8, 1996.
5. Günes, F., F. Gürgen, and H. Torpi, "A multidimensional signal-noise naural model for microwave transistor," *IEE Proc. — Circuits Devices and Systems*, Vol. 145, No. 2, 111–117, 1998.
6. Günes, F. and N. Türker, "Artificial neural networks in their simplest forms for analysis and synthesis of RF/microwave planar transmission lines," *The International Journal of RF and Microwave Computer-Aided Engineering*, Vol. 15, No. 6, 587–600, 2005.
7. Zhang, Q. J. and K. C. Gupta, "Models for RF and microwave components," *Neural Networks for RF and Microwave Design*, Artech House, Norwood, MA, 2000.
8. Çaglar, M. F. and F. Günes, "Neural networks as a nonlinear equation set solver in analysis and synthesis of a microwave circuits," *INISTA'2005*, 103–107, Istanbul, Turkey, June 2005.
9. Hornik, K., M. Stinchcombe, and H. White, "Multilayer feedforward networks are universal approximators," *Neural Networks*, Vol. 2, 359–366, 1989.
10. Cybenko, G., "Approximation by superpositions of a sigmoidal function," *Math. Control Signals Systems*, Vol. 2, 303–314, 1989.
11. Günes, F. and M. F. Çaglar, "A novel neural smith chart for use in microwave circuitry," *The International Journal of RF and Microwave Computer-Aided Engineering*, Vol. 9999, No. 9999, 2008.

Effect of Edge-preserving Parameters on GPR Reconstruction

Hui Zhou[1,3], **Zhaolei Wang**[2], **Dongling Qiu**[3], **and Guofa Li**[1,3]

[1]State Key Laboratory of Petroleum Resources and Prospecting
Key Laboratory of Geophysical Prospecting, CNPC, China
[2]Oriental Geophysical Corporation, Zhuozhou, Hebei, China
[3]China University of Petroleum Beijing, Beijing 102249, China

Abstract— The edge-preserving regularization (EPR) method is applied to the reconstruction of physical properties from ground-penetrating radar (GPR) data, and the relation between the regularization parameters and signal to noise ratio (SNR) is discussed. The regularization method is stable and is able to preserve boundaries, and protects resolution. It is necessary to investigate the relationship between the regularization parameters and the error of data because the effect of regularization depends to a great extent on the suitable choice of regularization parameters. Several numerical reconstruction examples are conducted. From the reconstruction examples using different SNR data, the relationship between the regularization parameters and the level of noise is obtained.

1. INTRODUCTION

The key of the application of regularization is to construct a regularization operator and to determine regularization parameters. A simple and well-known regularization method is to suppose the model is globally smooth. However, realistic geological model consists of not only smooth regions, but also evident boundaries that are important characters of the model. These boundaries need be preserved in order to obtain high-resolution reconstruction images with a clear background and boundaries. It is a difficulty to preserve the boundaries and avoid excessive smooth in the effective application of the regularization method [1]. Conventional smooth method cannot overcome the conflict of suppressing noise and preserving edges [2] since the noise and the edges are both high frequency components of a reconstructed image. Conventional smooth method deals with the noise and boundaries equally. As a result the noise is weakened, and the boundaries are blurred. Contrarily, the boundaries are reserved, the ability to resist noise is lowered. In practical reconstructions it is necessary to tradeoff the edge preservation and noise suppression. In this paper we use the edge-preserving method to reconstruct the subsurface.

We try to investigate the relation between the parameters and error of data by theoretical analysis and numerical calculation, in order to find a rule to determine the edge preserving parameters reasonably and efficiently.

2. INVERSE SCATTERING WITH EDGE-PRESERVING

Construct a cost functional $Q(\bar{p},\bar{b})$ with a regularization term [3, 4]

$$Q\left(\bar{p},\bar{b}\right) = Q_1\left(\bar{p}\right) + \bar{\lambda}\cdot\bar{Q}_2\left(\bar{p},\bar{b}\right), \tag{1}$$

$$Q_1(\bar{p}) = \int_0^{cT}\sum_{m=1}^{M}\sum_{n=1}^{N} K_m\left(\bar{r}_n^r,t\right)\left|\bar{v}_m\left(\bar{p};\bar{r}_n^r,t\right)-\bar{\bar{v}}_m\left(\bar{r}_n^r,t\right)\right|^2 d(ct), \tag{2}$$

$$Q_{2i}\left(\bar{p},\bar{b}\right) = \iint_S b_i\left[\left|\nabla p_i/\chi_i\right|^2+\phi\left(b_i\right)\right]ds, i=1,2,\ldots,I, \tag{3}$$

M is the number of illuminations, N is the number of receivers for each source, $K_m(\bar{r}_n^r,t)$ is a weighting function, $\bar{r}_n^r$ is the position vector of the nth receiver, t is time, c is the speed of light in free space, S is the reconstruction region, I is the number of parameters to be reconstructed, $\bar{\bar{v}}_m(\bar{r}_n^r,t)$ is the observed data at $\bar{r}_n^r$corresponding to the mth source, $\bar{v}_m(\bar{p};\bar{r}_n^r,t)$ is the calculated data for the mth source by using the guessed parameter $\bar{p}$, $\bar{v}_m(\bar{p};\bar{r}_n^r,t)$ are electric and magnetic field components. $\bar{p}$ consists of permittivity, permeability and conductivity. $Q_2(\bar{p},\bar{b})$ is the gradient of the model parameters. It acts as a damping factor to control perturbation of error, and to increase the stability. λ_i and χ_i are regularization parameters. λ_i is a smooth parameter used to balance the weight of the data and the prior term. χ_i is a threshold parameter used to determine

the preserved and smoothed gradient. This parameter plays a key role in edge preservation by using the cost functional (1) [5].

This paper uses the potential function proposed by [6]

$$\varphi(x) = \frac{x^2}{1+x^2}. \tag{4}$$

Substitution of (4) into (3) gives

$$\phi\left(b_i\right) = b_i - 2\sqrt{b_i} + 1, \tag{5}$$

where b_i is an auxiliary variable introduced in the half-square regularization method by [7]. The introduction of this variable can simplify the calculation. By derivation if b_i is given by

$$b_i = \varphi'\left(\left|\frac{\nabla p_i}{\chi_i}\right|\right) \Big/ \left(2\left|\frac{\nabla p_i}{\chi_i}\right|\right) = \left[1 + \left|\frac{\nabla p_i}{\chi_i}\right|^2\right]^{-2}, \tag{6}$$

Eq. (3) reaches its minimum.

3. THEORETICAL ANALYSIS

The EPR method used in this paper is different from the traditional Tikhonov regularization method. In the EPR method the prior weight term relates to not only the regularization parameter $\bar{\lambda}$, but also the choice of potential function and the regularization parameter $\bar{\chi}$. From (3) it is seen that the prior term is a function of $\bar{\chi}$, as a result it is impossible to determine the weight only from $\bar{\lambda}$.

Define an auxiliary parameter $\bar{\theta}$

$$\theta_i = Q_1/\lambda_i Q_2. \tag{7}$$

From (7) it is known that $\bar{\theta}$ is a function of $\bar{\lambda}$ and $\bar{\chi}$, and it plays a role to balance the weight between the data and the prior term. It is clear that the function of $\bar{\theta}$ is similar to that of the regularization parameter $\bar{\lambda}$ in the traditional Tikhonov regularization method. Once $\bar{\chi}$ and $\bar{\theta}$ are determined, $\bar{\lambda}$ is determined uniquely too. Therefore we will determine the relationship of the regularization parameter $\bar{\chi}$ and auxiliary parameter $\bar{\theta}$ with other factors.

According to the prior analysis and deviation theory the auxiliary parameter $\bar{\theta}$ is a function of error of data $\bar{\delta}$

$$\bar{\theta} = f\left(\bar{\delta}\right). \tag{8}$$

Since the auxiliary parameter $\bar{\theta}$, which balances the data and prior term, replaces the original regularization parameter $\bar{\lambda}$, if the error of data $\bar{\delta}$ is large, $\bar{\theta}$ increases to enlarge the weight of the prior term. On the contrary, if $\bar{\delta}$ is small, $\bar{\theta}$ decreases to increase the weight of the data.

Figure 1 is the relation of the potential function φ with $\bar{\chi}$ and the gradient $|\nabla p|$. It is seen that the curve consists of two variable sections, one is on the left side with large slopes, and another is on the right side with little slopes, and χ controls the position of the boundary between the two sections. Eq. (4) indicates that the potential function is monotonously increasing and has a horizontal asymptote, its value is in the range of $[0, 1]$. The gradient located in the left section is smoothed and that in the right section is protected.

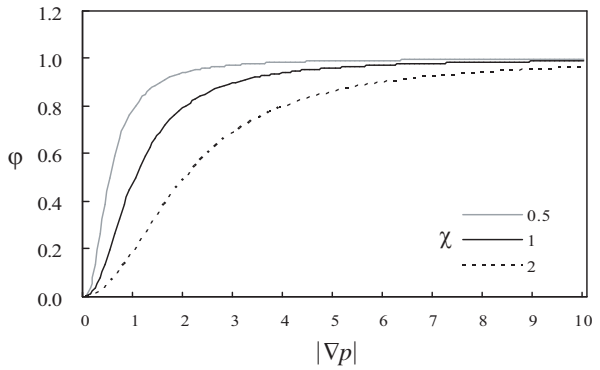

Figure 1: The relation of φ with χ and $|\nabla p|$.

If χ tends to 0 the length of the left section tends to 0 too, the value of the potential function is 1 for all $|\nabla p|$. For this case the prior term is of no effect, and the reconstruction result is equivalent to the least-square solution. With the increase of χ the length of the left section gets long. If χ is large enough, the relation between the potential function and the gradient of the model $|\nabla p|$ is approximately linear. The gradients located in this linear part are smoothed identically. For this case the edge is not protected neither. As a result χ should be selected to let the gradient (be protected) of the actual model be located in the right section, and to let the gradient (be smoothed) created by error and noise be located in the left section.

4. THE RELATION OF REGULARIZATION PARAMETERS AND ERROR

By using two-dimensional numerical reconstruction examples we draw the relation of SNR and regularization parameters. Only permittivity is reconstructed. As shown in Fig. 2 there are two buried objects with relative permittivity of 4 in a background with relative permittivity of 6. The numerals in the x and z directions represent grid number. There are 9 transmitting positions and 19 receivers for each source. The gap between the source and the first receiver is 2 grids, the interval of receiver is 1 grid, the interval of source point is 10 grids. The initial guess of permittivity of the reconstruction region is that of the background. The highest frequency is 1 GHz, grid size is 1.2 cm.

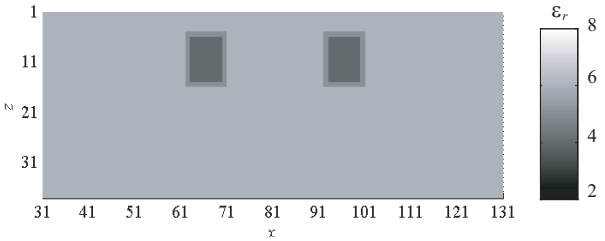

Figure 2: Actual distribution of relative permittivity in the reconstruction region.

Figures 3(a) and 3(b) are the reconstructed result after 100 iterations from noisy data with SNR = 20 dB without and with EPR. Fig. 3(b) is the best result by testing time after time, the regularization parameters are $\theta = 0.1$ and $\chi = 0.08$. It is clear that in Fig. 3(b) the influence of noise on the reconstructed result is weak, however the reconstructed value is not so good, and the edges are not protected quite well. From this example it is deduced that the application of the EPR is not so effective for the case of SNR > 20 dB. Figs. 3(c) and 3(d) are the reconstructed result from the data of SNR = 15 dB without and with EPR. Fig. 3(d) is the best result by testing with $\theta = 0.2$ and $\chi = 0.09$. It is clear from Figs. 3(c) and 3(d) that the effect of the EPR is evident, the background of Fig. 3(d) is less affected by noise and the boundaries are much clearer than those of Fig. 3(c).

Figures 3(e), 3(f) and 3(g) are the reconstructed results the data with SNR = 5 dB without and with EPR. Fig. 3(f) is the result for $\theta = 0.3$ and $\chi = 0.2$, and Fig. 3(g) is the result for $\theta = 0.35$ and $\chi = 0.15$. It is clear from Figs. 3(c) and 3(d) that the effect of EPR is evident, the background of Fig. 3(d) is less affected by noise and the boundaries are clearer than those of Fig. 3(c). Figs. 3(f) and (g) are better than Fig. 3(e). It is almost impossible from Fig. 3(e) to recognize the two objects due to the influence of noise. With the increase of iterations the image becomes even worse. It is noted that with the increase of noise the conventional reconstruction method fails to reconstruct the models. By utilizing the EPR method a stable reconstruction result can be obtained. Fig. 3(f) for $\theta = 0.3$ and $\chi = 0.2$ is more affected by noise than Fig. 3(g) for $\theta = 0.35$ and $\chi = 0.15$. However the boundaries in Fig. 3(f) are protected much better and the value of permittivity is more accurate than those in Fig. 3(g).

Figures 3(h), 3(i) and 3(j) are the result from noisy data with SNR = 0 dB without and with EPR. Fig. 3(i) is the result for $\theta = 0.4$ and $\chi = 0.3$, and Fig. 3(j) is the result for $\theta = 0.4$ and $\chi = 0.25$. The phenomena are almost the same as the case of SNR = 5 dB, but the influence of noise is more evident. It is clearer that the EPR plays a very important role in suppressing noise and protecting boundaries.

By fitting two graphs of θ-SNR and χ-E_N/E_S are plotted in Fig. 4. It shows that θ-SNR and χ-E_N/E_S are nearly linear. Sequentially it is possible to determine θ and χ by SNR. However this paper does not give a regression formula since the regression coefficients of the formula are

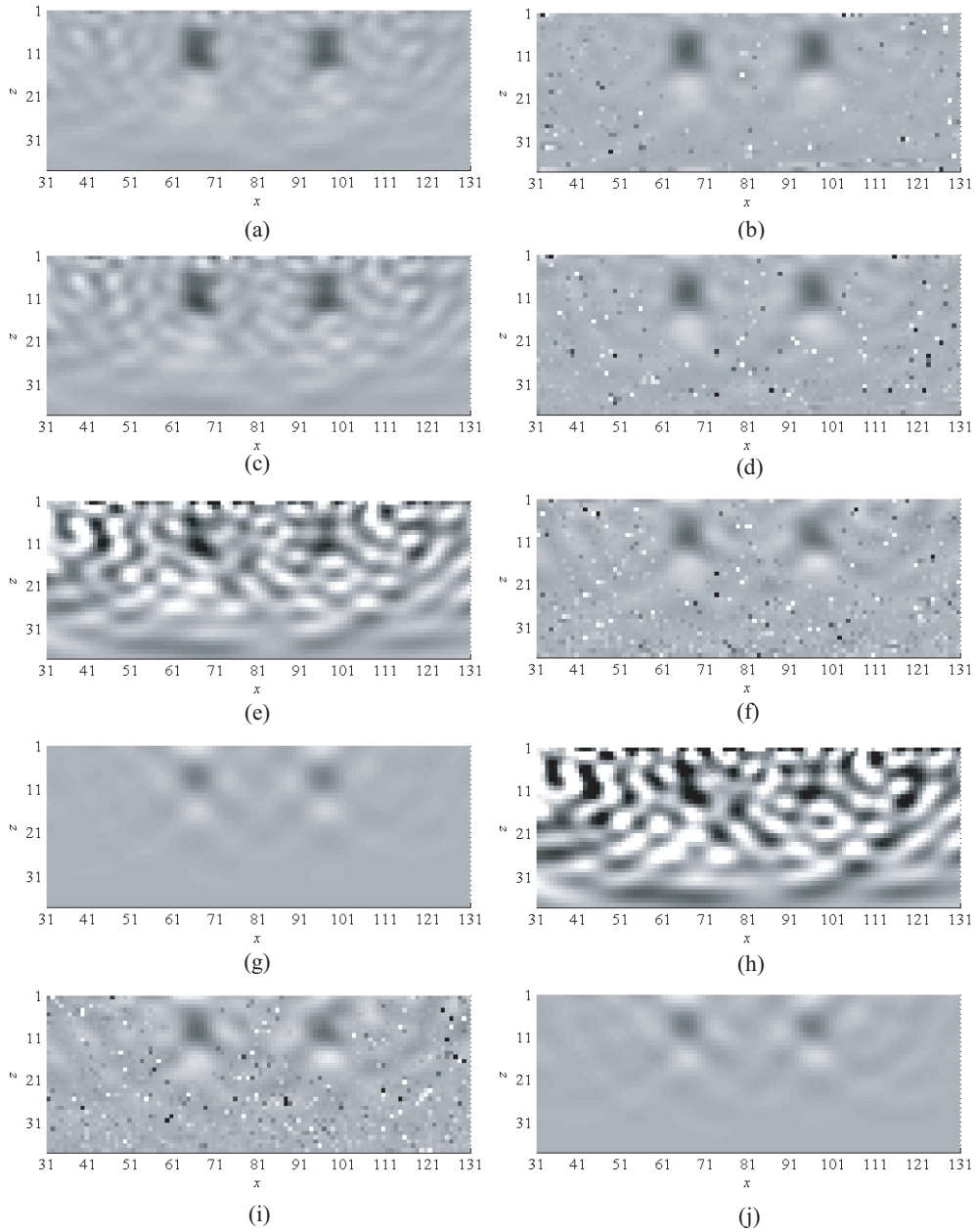

Figure 3: Reconstructed image after 100 iterations from the data of SNR = 20 dB (a) using non-regularization method (NRM), (b) using EPR method for $\theta = 0.1$, $\chi = 0.08$. From 15 dB data (c) using NRM, (d) using EPR method for $\theta = 0.2$, $\chi = 0.09$. From 5 dB data (e) using NRM, (f) using EPR method for $\theta = 0.3$, $\chi = 0.2$, (g) $\theta = 0.35$, $\chi = 0.15$. From 0 dB data (h) using NRM, (i) using EPR method for $\theta = 0.4$, $\chi = 0.3$, (j) $\theta = 0.4$, $\chi = 0.25$.

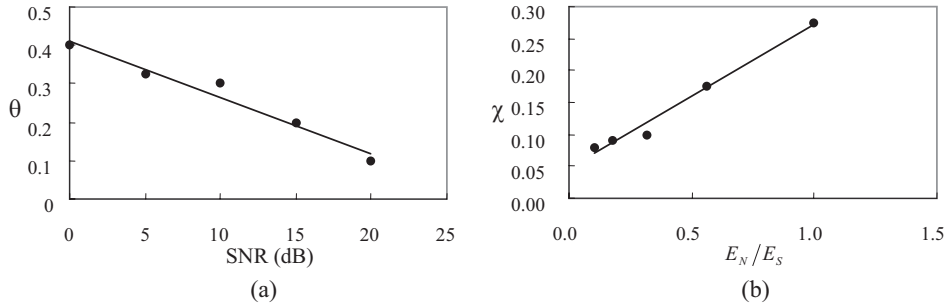

Figure 4: The relation of (a) auxiliary parameter θ and SNR, and (b) regularization parameter χ and E_N/E_S.

strongly related the variance of the model, initial guess of the model, the reconstruction method, the type of noise. For example, if the initial model is very close to the actual one, θ should be large to emphasize the prior term, if the initial model is little bit far from the actual one, θ should be small to emphasize the data term. If variance of model is large, χ is increased to smooth the noise. But the variance and degree of close to the actual model are not estimated as easy as SNR, maneuverability is low.

5. CONCLUSIONS

In this paper the edge-preserving regularization (EPR) method in the reconstruction of physical parameters is discussed. This method can provide a stable, edge protected, and high resolution result. By theoretical analysis and a great deal of numerical computation, this paper finds the relation between the parameter and error of data. Based on these a way to select regularization parameters is given to avoid the blindness and randomness in the applications.

The EPR method used in this paper always protects large gradients and smoothes small gradients. It is based on the assumption that larger gradients are the result of real boundaries, and small gradients are the result of, such as, noise. This assumption is not tenable for the case of low SNR. As a result when the error of data is large, attention should be paid to apply this regularization method. It is better to use other regularization methods and compare these results to judge the quality of the results. In addition, the rule to determine the regularization parameters obtained in this paper is qualitative. Experience and understanding of the regularization method are sometimes needed. As a result this method needs to be researched further more.

ACKNOWLEDGMENT

This work was supported in part by the National Natural Science Foundation of China under Grant-in-Aid 40574053, the Program for New Century Excellent Talents in University, China.

REFERENCES

1. Zhang, H. B. and C. C. Yang, "A constrained impedance inversion method controlled by regularized parameters," *Chinese Journal of Geophysics*, Vol. 46, No. 6, 827–834, Chinese, 2003.
2. Liu, D. and R. C. Zhao, "The method of preserving edge smoothing," *Journal of Northwestern Plytechnical University*, Vol. 18, No. 1, 102–105, Chinese, 2000.
3. Takenaka, T., H. Jia, and T. Tanaka, "Microwave imaging of electrical property distributions by a forward-backward time-stepping method," *Journal of Electromagnetic Waves and Applications*, Vol. 14, 1609–1626, 2000.
4. Takenaka, T., H. Jia, and T. Tanaka, "Microwave imaging of an anisotropic cylindrical object by a forward-backward time-stepping method," *IEICE Trans. Electron.*, Vol. E84, No. 12, 1910–1916, 2001.
5. Pierre, C., B. F. Laure, and A. Gilles, "Michel Barlaud. Deterministic edge-preserving regularization in computed imaging," *IEEE Trans. Image Processing*, Vol. 6, No. 2, 298–311, 1997.
6. Geman, S. and D. E. McClure, "Bayesian image analysis: An application to single photon emission tomography," *Proc. Statistical Computation Section, Amer. Statistical Assoc.*, 12–18, Washington, DC, 1985.
7. Geman, D. and C. Yang, "Nonlinear image recovery with half-quadratic regularization and FFT's," *IEEE Trans. Image Processing*, Vol. 4, 932–946, 1995.

Use GL TM Model Inversion to Detect the Dielectric Parameter

Jianhua Li[1, 2], **Ganquan Xie**[1], **Lee Xie**[1], **Chien-Chuang Lin**[2], **and Michael Oristaglio**[3]

[1]GL Geophysical Laboratory, USA
[2]Da Yeh University, Taiwan
[3]Schlumberger Research, USA

Abstract— The GL TM model inversion is used to detect the dielectric parameter in this paper. A nonlinear operator on the dielectric parameter is defined to present the transverse magnetic model inversion to detect the dielectric parameter. We present to use the GL TM model inversion method to detect the dielectric parameter. The GL TM inversion method can be extended to solve the 2.5D and 3D dimensional inverse problems. The 2D and 3D GL TM inversion with non impulse source excitation is investigated and suitable regularized. The 2D TM synthetic data inversion images are presented.

1. INTRODUCTION

There are several research works for the electromagnetic parameter inversion in frequency domain. Habashy and Oristaglio proposed Born Approximation inversion for the conductivity and permittivity in frequency domain in 1994 [1]. Oristaglio and Habashy proposed the conductivity inversion based on reciprocity in wavefield inversion in 1995 [2]. Xie proposed a new iterative method for solving the coefficient inverse problem of wave equation in time domain in 1986 [3]. Xie and Chen proposed 2D inversion in frequency domain 1985 [4]. Xie and Li proposed the 2D and 3D wave velocity inversion methods in the time domain from 1986 to 1990 [5–11]. Lee and Xie proposed a pesudo wave field tomography inversion in the q domain in 1993 [12]. Xie and Li proposed the GILD, AGILD and GL EM nonlinear inversion in [13–19]. According to [1, 3] and [6–8], in this paper, we use the GL TM model inversion to detect the dielectric parameter in time domain [1, 20]. We present GL TM model inversion method to detect the dielectric parameter. The GL TM inversion method can be used to solve the 2.5D and 3D dimensional inverse problem. The 2.5D and 3D TM inversion with non impulse source excitation is investigated and suitable regularized. The TM inversion method and theory in this paper are from GLGEO technology patent report [20]. The 2D TM synthetic data inversion images are presented.

The description arrangement of this paper is as follows. The introduction is described in Section 1. The 1-D TM forward and inverse problems are presented in Section 2. We present GL TM inversion method for solving the dielectric inverse problem in Section 3. The simulation and discussions are described in Section 4. We conclude this paper in Section 5.

2. THE 1-D TM FORWARD MODELING AND INVERSE PROBLEMS

2.1. The 1-D TM forward Modeling Equation

We describe the one dimensional transversal magnetic (TM) forward modeling equation in this section.

Let $H_y(x,t)$ denote the nonzero y component of the magnetic field, the 1-D TM forward modeling is governed by the following wave equation,

$$\mu\frac{\partial^2 H_y}{\partial t^2} - \frac{\partial}{\partial x}\left(\frac{1}{\varepsilon_e(x)}\frac{\partial H_y}{\partial x}\right) = s(x,t),\ \ x>0,\ \ t>0, \tag{1}$$

where μ is basic permeability constant $\mu_0 = 10^{-7}\times 4\pi = 1.2566\times 10^{-6}\,\mathrm{m\,kg\,s^{-2}A^{-2}}$. The effective dielectric parameter $\varepsilon_e(x) = \varepsilon_r\varepsilon_0$. The ε_0 is the basic permittivity, $\varepsilon_0 = 8.85418\times 10^{-12}\,\mathrm{m^{-3}\,kg^{-1}\,s^4A^2}$. Let $H_y(x,t) = H(x,t)$, $x = cx'$, c is the light speed, the TM model wave Equation (1) is translated to the following wave equation

$$\frac{\partial^2 H}{\partial t^2} - \frac{\partial}{\partial x'}\left(\frac{1}{\varepsilon_r(cx')}\frac{\partial H}{\partial x'}\right) = s\left(cx',t\right),\ \ x'>0,\ \ t>0, \tag{2}$$

Let $\frac{1}{\varepsilon_r(cx')} = \varepsilon^{-1}(x')$, $s(cx',t) = S(x',t)$, and remove the superscript of x' in the Equation (2), we obtain

$$\frac{\partial^2 H}{\partial t^2} - \frac{\partial}{\partial x}\left(\varepsilon^{-1}(x)\frac{\partial H}{\partial x}\right) = S(x,t),\ \ x>0,\ \ t>0, \tag{3}$$

2.2. The 1-D TM Inverse Problem to Find the Dielectric Parameter

Suppose that the magnetic permeability $\mu = \mu_0$, let the source term in right hand of (1) $s(x,t) = 0$, the initial magnetic field and its time derivative are zero at the initial time $t = 0$. The y component of the transverse magnetic field H_y satisfies the following wave equation and initial and boundary conditions,

$$\begin{aligned} &\mu\frac{\partial^2 H_y}{\partial t^2} - \frac{\partial}{\partial x}\left(\frac{1}{\varepsilon_e(x)}\frac{\partial H_y}{\partial x}\right) = s(x,t),\ \ x>0,\ \ t>0,\\ &H_y(x,0) = \frac{\partial}{\partial t}H_y(x,0) = 0,\ \ x>0,\\ &\frac{\partial H_y}{\partial x}(0,t) = h(t),\ \ t>0. \end{aligned} \tag{4}$$

From the magnetic wave y component H_y measurement on the boundary point

$$H_y(0,t) = f(t),\ \ t>0, \tag{5}$$

to find the effective dielectric parameter that is called the 1-D TM dielectric inverse problem. The inverse problem is translated the following TM inversion to find relative dielectric parameter $\varepsilon(x)$ from the following wave equation system:

$$\begin{aligned} &\frac{\partial^2 H}{\partial t^2} - \frac{\partial}{\partial x}\left(\varepsilon^{-1}(x)\frac{\partial H}{\partial x}\right) = s(x,t),\ \ x>0,\ \ t>0,\\ &H(x,0) = \frac{\partial}{\partial t}H(x,0) = 0,\ \ x>0,\\ &\frac{\partial H}{\partial x}(0,t) = g(t),\ \ t>0. \end{aligned} \tag{6}$$

and the measure data on the boundary

$$H(0,t) = f(t),\ \ t>0, \tag{7}$$

to find the relative dielectric permittivity $\varepsilon(x) \geq 1$.

3. 1-D TM INVERSION METHOD FOR SOLVING THE DIELECTRIC INVERSE PROBLEM

When the boundary excitation is exited by the impulse, $g(t) = \delta(t)$, let

$$H_1(x,t) = \frac{\partial a(x)}{\partial x}S(t-\phi(x)) + \frac{\partial}{\partial x}H_s(x,t), \tag{8}$$

$a(x)$ is amplitude, $\phi(x)$ is wave front, $H_s(x,t)$ is the scattering wave solution of the Equation (6) [1, 7, 20].

The GL TM inversion algorithm is proposed by Xie et al. [20] as following steps [20]:
(3.1) Let the start dielectric model be $\varepsilon_0(x) = \varepsilon(0)$, $\varepsilon(0)$ is known boundary value of the $\varepsilon(x)$.
(3.2) By induction, suppose that the $\varepsilon_{k-1}(x)$ is known, to replace $\varepsilon(x)$ by $\varepsilon_{k-1}(x)$ in (6) and solve the Equation (6) and get $H_{k-1}(x,t)$ by GL Method [14–16].
(3.3) Solve the following well posed Second kind of integral equation

$$\varepsilon^{-1}(0)\left(H_{k-1}(0,t) - f(t)\right) = \int_0^\infty \left(\left(\varepsilon_{k-1}^{-2}(x)\right)\delta\varepsilon_k(x)\frac{\partial H_{k-1}}{\partial x} *_t \frac{\partial}{\partial x}\left(G(x,t)\right)\right)dx' \tag{9}$$

and get the increment dielectric $\delta\varepsilon_k(x)$. Where $G(x,t)$ is $Green's$ function [14-20]
(3.4) update

$$\varepsilon_k(x) = \varepsilon_{k-1}(x) + \delta\varepsilon_k(x). \tag{10}$$

4. 2D DIELECTRIC IMAGING

The GL TM dielectric inversion method can be used to make 2-D dielectric imaging. The dielectric model is embedded in to the background medium which is shown in the Figure 1. The magnetic moment dipole source "STAR" is located in $x = 0$, $z = 0$ on the surface boundary in the Figure 1. The Figure 2 shows that the surface magnetic field $Hy(x, z, t)$ wave curve is excited by the magnetic moment dipole source. The dielectric imaging from the first iteration of the 2D TM inversion is shown in the Figure 3. The surface response of the magnetic field through the dielectric medium in Figure 3 is presented in Figure 4. The dielectric imaging from the eighth iteration of the 2D TM inversion is shown in the Figure 5. It scatters the surface response of the magnetic field which is shown in Figure 6. The frequency band is from 1 MHz to 1 GHz.

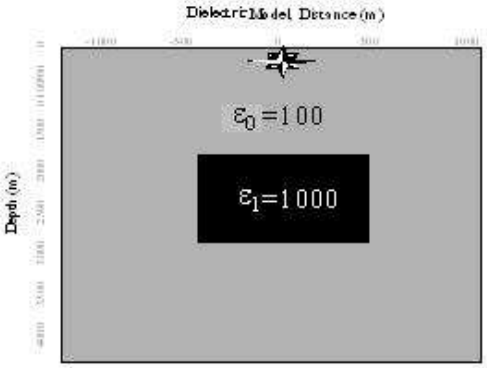

Figure 1: The dielectric bulk model, star is source.

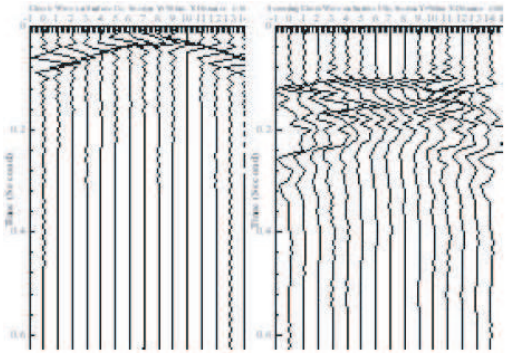

Figure 2: H_y in $Y = 500$ m on surface. Left: H_y, Right: SH_y.

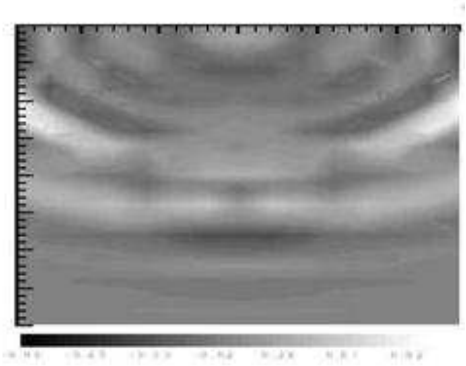

Figure 3: The dielectric imaging from the first iteration of the 2D TM inversion.

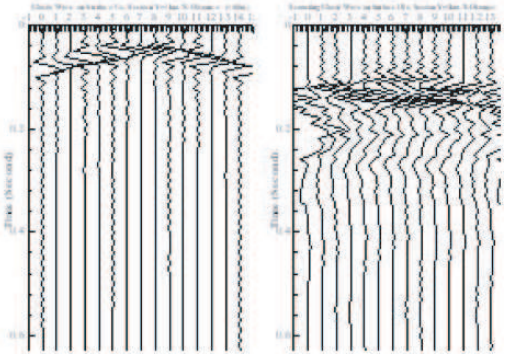

Figure 4: H_y in $Y = 500$ m on surface. Left: U_z, Right: SH_y by first iteration.

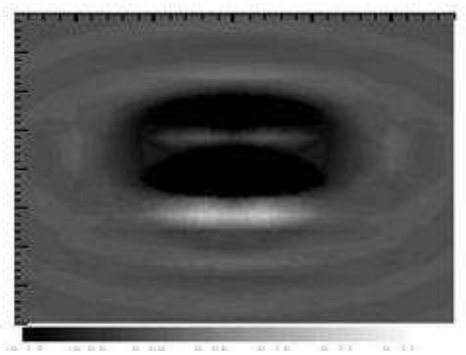

Figure 5: The dielectric image from the eighth iteration of the 2D TM inversion.

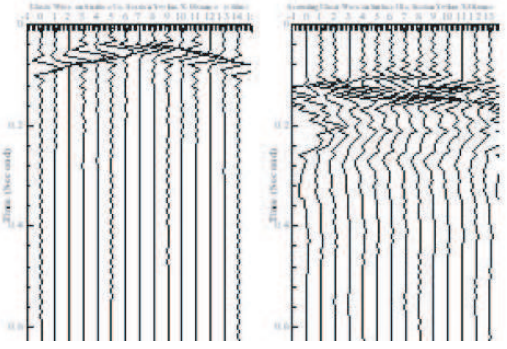

Figure 6: H_y in section $Y = 0$ on surface. Left: H_y, Right: SH_y by eighth iteration.

5. CONCLUSION

The synthetic data interpretations show that the GL TM dielectric inversion is stable and is of high resolution. We use a small and suitable regularizing parameter to control the inversion process stable. The GL EM modeling is used for forward modeling in the inversion. The GL TM inversion method has applications in the geophysical, earthquake, and oil explorations, materials, nanometer and metamaterial dispersion design. The GL modeling and the GL TM inversion are patented to GLGEO and all rights are reserved to GL Geophysical Laboratory.

ACKNOWLEDGMENT

We thank to GL Geophysical Laboratory for this paper is approved to be published. Authors thank to Professor Kong for his encouragements. Authors thank to Professor Jiang Qin for her help.

REFERENCES

1. Habashy, T. M., M. Oristaglio, and de Hoop, "Deep simultaneous nonlinear reconstruction of the two dimensional permittivity and conductivity," *Radio Sci.*, Vol. 29, 1101–1118, 1994.
2. Oristaglio, M. L. and T. M. Habashy, "Some uses of reciprocity in wavefield inversion," Van den Berg, P. M., Blok, H., and Foklema, *Wavefield and Reciprocity*, Delft University Press, 1995.
3. Xie, G., "A new iterative method for solving the coefficient inverse problem of wave equation," *Comm. on Pure and Applied Math.*, Vol. 39, 307–322, 1986.
4. Xie, G. and Y. M. Chen, "A modified pulse spectrum technique for solving inverse problem of two-dimensional elastic wave equation," *Appl. Numer. Math.*, Vol. 1, No. 3, 217–237, 1985.
5. Xie, G., J. Li, and Y. M. Chen, "Gauss-Newton-Regularizing method for solving coefficient inverse problem of PD," *J. Comput. Math.*, Vol. 5, No. 1, 38–49, 1987.
6. Xie, G. and J. H. Li, "A characteristic iteration for solving inverse problems of a wave equation," *J. Comput. Math.*, Vol. 6, No. 3. 1990.
7. Xie, G. and Y. M. Chen, "Nonlinear integral equation of inverse scattering problems of wave equation and iteration," *J. Comput. Math.*, Vol. 9, No. 3, 1989.
8. Xie, G. and J. H. Li, "Nonlinear integral equation of coefficient inversion of acoustic wave equation and TCCR iteration," *Science in China*, Vol. 31, No. 12, 1989.
9. Xie, G and J. H. Li, "3-D nonlinear inversion of the wave equation using integral equation," *Science in China*, Vol. 3, No. 12, 1988.
10. Xie, G. and J. H. Li, "New iterative method for solving inverse scattering problem of 3-D wave equation," *Science in China (Series A)*, Vol. 31, No. 10, 1988.
11. Xie, G. and Q. Zou, "A parallel numerical method for solving 3-D inverse scattering problem," *Computer Physics Communications*, Vol. 65. 320–326, 1991.
12. Lee, K. H. and G. Q. Xie, "A new approach to imaging with low-frequency electromagnetic fields," *Geophysics*, Vol. 58, No. 6, 780–796, 1993.
13. Li, J. H. and G. Xie, "A 3D cubic-hole element and its application in resistivity imaging, 3-D electromagnetic methods," *Proceedings of the International Symposium on Three-dimensional Electromagnetics in Schlumberger-Doll Research*, 415–419, 1995; *SEG book*, 591–599, 1999.
14. Xie, G., F. Xie, L. Xie, and J. Li, "New GL method and its advantages for resolving historical diffculties," *Progress In Electromagnetics Research*, PIER 63, 141–152, 2006.
15. Xie, G., J. Li, L. Xie, and F. Xie, "GL metro carlo EM inversion," *Journal of Electromagnetic Waves and Applications*, Vol. 20, No. 14, 1991–2000, 2006.
16. Xie, G., J. H. Li, L. Xie, and F. Xie, "GL method for solving equations in math-physics and engineering," *Acta Mathmatica Applicane*, Vol. 24, No. 3, 392–404, 2008.
17. Li, J. H., G. Xie, and L. Xie, "A new GL method for solving differential equation in electromagnetic and phys-chemical and financial mathematics," *PIERS Online*, Vol. 3, No. 8, 1151–1159, 2007.
18. Xie, G., J. H. Li, L. Xie, and F. Xie, "GL method for solving equations in math-physics and engineering," *Acta Mathmatica Applicane*, Vol. 24, No. 3, 392–404, 2008
19. Xie, G. and J. Li, "New parallel GILD-SOR modeling and inversion for E-O-A strategic simulation," *IMACS Series Book in Computational and Applied Math.*, Vol. 5, 123–138, 1999.
20. Xie, G., J. H. Li, F. Xie, and L. Xie, "New TE and TM model inversion methods to detect the conductivity, dielectric and permeability," *GL Geophysical Laboratory Technology Patent Report*, GLGEOTP0806, 2008; To be published in *PIERS Proceeding 2009 in Beijing.*

Multi-parameter Inversion of Electrical Array Lateral-logging by Using the Neural Networks

Yueqin Dun, **Jihuan Tian**, **and Jiansheng Yuan**
Department of Electrical Engineering, Tsinghua University, Beijing 100084, China

Abstract— The inversion of the multi-parameters of the electrical array lateral-logging is a nonlinear and multi-solution problem. To avoid the defects of the traditional inversion algorithms and enhance the inversion speed, the three layer back propagation (BP) neural network is built to inverse formation parameters. The inputs of the BP neural networks are the logging responses and the target outputs are the formation parameters. The training results of different networks are given and compared, and the inversion results with trained net are all very close to the real values. Once the BP neural network has been trained successfully, it doesn't need any initial parameters and can be used without any iterative calculation, so the inversion speed can be enhanced greatly.

1. INTRODUCTION

To judge which layer or what depth of the earth is of petroleum or gas, a measurement sonde is put into a borehole and moved down to measure the physical characteristics of the soil, which is called logging. Extracting the electrical and the structure parameters of the formations from the measured data, which is an inversion problem, is the most important objective of logging. The rapid one-dimensional (1-D) inversion is always needed at the logging field to provide real-time and rough formation model parameters, and it also can be used as the initial formation model parameters for the traditional accurate inversion method. The principal parameters need to be inversed involve the resistivity of invasion (Rxo) surrounding the borehole, the resistivity of the true formation (Rt), and the diameter of the invasion (Di).

The inversion of parameters is a nonlinear and multi-solution problem. The linearization methods are often used to solve the problems, which gets a convergent solution by an iterative process with suitable initial parameters. The linearization methods may converge to a local optimal solution if the initial parameters deviate far from the real solution. And the forward problem must be calculated for many times during the iterative process. To avoid calculating forward responses and enhance the inversion speed, the Look-Up Tables of precalculated forward responses are generated over a set of cylindrical 1D earth model covering a large range of resistivity contrasts and invasion length [1–3]. But large numbers of Look-Up Tables must be stored in advance and many interpolations need to be calculated.

To avoid these defects of the iterative algorithms, the back propagation (BP) neural network is applied to inverse the formation parameters in this paper. It doesn't need any initial parameters and can be used without any iterative calculation.

2. BP NEURAL NETWORKS

The backpropagation (BP) neural network is widely used as supervised neural nets in solving nonlinear problems. Its typical architecture is composed of three kinds of layers: input, hidden and output layers. The input layer nodes only receive inputs from the outside. The number of nodes of input and output layers is usually determined by the variables and targets for a particular problem, while the number of nodes in the hidden layer is difficult to determine and is usually determined by experiences or trial and error. Unlike the input and output layers, the number of hidden layers can be any positive number. Studies have shown that one hidden layer is generally sufficient to solve complex problems if enough nodes are used. Here, a three layer network architecture shown in Fig. 1 has been chosen to solve inverse problem.

In Fig. 1, $\mathbf{X} = (x_1, \ldots, x_i, \ldots, x_n)^T$ is the inputs vector of the input layer, $\mathbf{Y} = (y_1, \ldots, y_j, \ldots, y_h)^T$ is the inputs vector of the hidden layer, and the $\mathbf{O} = (o_1, \ldots, o_k, \ldots, o_m)^T$ is the outputs vector of the output layer. x_0 and y_0 are both set to be -1 as the biases for the hidden and output layer. Bias nodes are usually included for faster convergence and better decision. These inputs layer nodes are connected to every node in the hidden layer via weights W_{ij} represented by the lines as shown in the Fig. 1, the output layer nodes are connected to those of hidden layer with

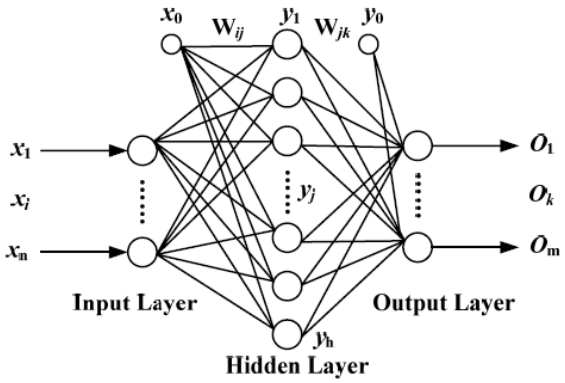

Figure 1: Schematic model of a three layer network.

W_{jk} and they can provide output vector (eg., formation model parameters) according to a given set of input vector (eg., logging responses).

The training is an essential part in using neural networks. This process requires training a number of input samples paired with target outputs. If the target vector is $\mathbf{d} = (d_1, \ldots, d_k, \ldots, d_m)^T$, the aim of training is to minimize the differences between the target outputs for all the training pairs, which can be defined as the error function

$$E = \frac{1}{2}\sum_{k=1}^{m}(d_k - o_k)^2. \tag{1}$$

Before beginning training, some small random values are usually used to initialize the weights and biases. BP neural network is a forward propagation step followed by a backward-propagation step. The forward-propagation step begins by sending the inputs through the nodes of each layer. A nonlinear function, called the sigmoid function, is usually used at each node for the transformation of the inputs to outputs. This process repeats until an output vector is calculated. The backward-propagation step calculates the error vector by comparing the calculated outputs and targets, and the network weights and biases are modified to reduce the error.

The weight adjustment in hidden layer and output layer is:

$$\Delta w_{jk} = -\eta\frac{\partial E}{\partial w_{jk}} = \eta(d_k - o_k)o_k(1 - o_k)y_j = \eta\delta_k^o y_j \quad (j = 0, 1, 2, \ldots, h, \;\; k = 1, 2, \ldots, m) \tag{2}$$

where η is the learning rate, and $\delta_k^o = (d_k - o_k)o_k(1 - o_k)$.
The weight adjustment in input layer and hidden layer is:

$$\Delta w_{ij} = -\eta\frac{\partial E}{\partial w_{ij}} = \eta\left(\sum_{k=1}^{m}\delta_k^o w_{jk}\right)y_j(1 - y_j)x_i = \eta\delta_j^y x_i \quad (i = 0, 1, 2, \ldots, n, \;\; j = 1, 2, \ldots, h) \tag{3}$$

where $\delta_j^y = (\sum_{k=1}^{m}\delta_k^o w_{jk})y_j(1 - y_j)$.

By training, a set of weights and biases will be produced finally and can be used for calculating target values (eg., the formation model parameters) when the actual output is unknown. More details about BP neural network can be found in references [4] and [5].

3. PARAMETERS INVERSION OF ARRAY LATERAL-LOGGING

3.1. The Characteristic of Array Lateral-logging Responses

By the array lateral-logging sonde as shown in Fig. 2, a total of six apparent resistivity (Ra) responses are measured, among which the shallowest apparent resistivity (Ra0) is most sensitive to the mud in the borehole and can be used to estimate Rm, and the other five responses, Ra1 to Ra5, are all sensitive to the formation parameters (Rxo, Di and Rt) as shown in Fig. 2. If the thickness (H) of the formation is quite thick, the shoulder effect to the apparent resistivity Ra1 to Ra5 is very small, and the 2-D formation can be simplified to a 1-D problem. Then, a supervised

BP network can be trained based on the simplified model, here, the logging responses Ra0 to Ra5 are used as the input training samples, and the corresponding formation parameters as the training targets. Therefore, the unknown formation parameters will be calculated with the trained network if the logging responses are given.

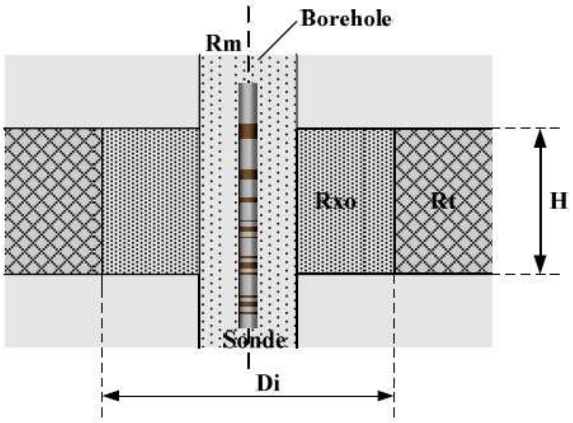

Figure 2: The parameters of formation model.

3.2. Training of BP Neural Networks

Before training, 3166 representative input samples paired with targets according to the practical engineering logging are precalculated by the forward problem solution. The input samples (Ra0 to Ra5) should be preprocessed by two steps. The first is borehole correction which can eliminate the effect of different Rm, and only one set of network needs to be trained under some Rm (such as 1.0). The second step is calculating the logarithm (base 10) of the input samples. While the training targets just need to calculate its logarithm (base 10).

A supervised BP networks with three layers is built to inverse the formation parameters. The transfer function between the input layer and the hidden layer is sigmoid function, between the hidden layer and the output layer is linear function, and the Levenberg-Marquardt method is adopted as the training function. The learning rate of the network is set to 0.05, the stop iteration is set to 2000, and the nodes of hidden layer are 8, 10, 12, ..., 22, respectively. The mean absolute error (MAE) threshold is set to 0.001, and the formula of MAE is as follows

$$\text{MAE} = \frac{1}{pm}\sum_{s=1}^{p}\sum_{k=1}^{m}|d_{sk} - o_{sk}|,$$

where p is the number of training samples, m is the number of output nodes, d_{sk} and o_{sk} are the target output and net output of sample p at output node k. The training result is in Table 1 and 6-8-3 network means 6 inputs, 8 hidden layer nodes and 3 outputs. The error will be lower than 0.001 when the number of hidden layer nodes is 22, so the following calculation is based on the network with 22 hidden layer nodes.

Table 1: Training results of different hidden layer nodes.

Network size	MAE	Network size	MAE
6-8-3	0.006715	6-16-3	0.001998
6-10-3	0.003715	6-18-3	0.001086
6-12-3	0.002722	6-20-3	0.001039
6-14-3	0.002704	6-22-3	0.000928

3.3. Inversion Parameters with BP Neural Networks

To validate the inverse precision of the trained network (the training samples are calculated under Rm = 1.0), ten set of formation models that are all different with the training samples has been

chosen to be inversed with the trained network 6-22-3. The inversion results of two group (under Rm = 1.0 and Rm = 0.5) are given in Table 2 and Table 3, respectively. The Di_real, Rxo_real and Rt_real mean real formation parameters, and the Di_inv, Rxo_inv and Rt_inv are the inversion results. It only takes 0.24 second to inverse 10 set of formation parameters with the trained network, and the inversion formation parameters are all very close to the real values.

Table 2: The comparison between inversion parameters and real values (Rm = 1.0).

No.	Di_inv	Di_real	Rxo_inv	Rxo_real	Rt_inv	Rt_real
1	0.4962	0.5	4.9473	5.0	10.007	10.0
2	0.7021	0.7	4.9936	5.0	29.985	30.0
3	0.8986	0.9	4.9943	5.0	50.049	50.0
4	1.1011	1.1	5.0111	5.0	79.799	80.0
5	1.2984	1.3	5.0056	5.0	99.66	100.0
6	0.5023	0.5	10.1	10.0	20.034	20.0
7	0.6997	0.7	10.093	10.0	29.994	30.0
8	0.8990	0.9	10.036	10.0	50.008	50.0
9	1.0979	1.1	9.9881	10.0	79.943	80.0
10	1.2988	1.3	9.9817	10.0	100.04	100.0

Table 3: The comparison between inversion parameters and real values (Rm = 0.5).

No.	Di_inv	Di_real	Rxo_inv	Rxo_real	Rt_inv	Rt_real
1	0.4971	0.5	5.0152	5.0	9.8971	10.0
2	0.6846	0.7	4.897	5.0	29.483	30.0
3	0.8827	0.9	4.8814	5.0	49.264	50.0
4	1.0914	1.1	4.9019	5.0	78.613	80.0
5	1.2938	1.3	4.9218	5.0	98.584	100.0
6	0.4938	0.5	9.9316	10.0	19.897	20.0
7	0.6918	0.7	9.958	10.0	29.714	30.0
8	0.8912	0.9	9.9255	10.0	49.555	50.0
9	1.0917	1.1	9.8971	10.0	79.256	80.0
10	1.2963	1.3	9.9142	10.0	99.11	100.0

4. CONCLUSIONS

In the study of multi-parameter inversion of array lateral-logging, we adopt the three layer BP neural network to inverse the thick formation parameters. According to the characteristic of the array lateral-logging responses, a great number of preprocessed training samples pared with targets have been trained. The hidden layer nodes has been chosen to be 22 by comparing the training results under different hidden layer nodes, and the supervised BP network was trained under Rm = 1.0. The inversion results under different Rm with the trained net are all very close to the real values. It shows the validity of borehole correction of the logging responses. Once the BP neural network has been trained successfully, it doesnt need any initial parameters and can be used without any iterative calculation. Hence the inversion speed will be quite fast, and it can be used as the rapid inversion at the logging field.

REFERENCES

1. Yin, H. and H. Wang, "Method for 2D inversion of dual lateralog mearsurements," United Stated Patent, Pub. No. US 0040274, 2002.

2. Frenkel, M. A. and A. G. Mezzatesta, "Well logging data interpretation system and methods," United Stated Patent, Pub. No. US 5889729, 1999.
3. Frenkel, M. A., "Real-time interpretation technology for new multi-laterolog array logging tool," *SPE*, 102772, 2006.
4. Ham, F. M., *Principles of Neurocomputing for Science and Engineering*, McGraw-Hill, New York, 2000.
5. Hagan, M. T. and H. B. Demuth, *Neural Network Design*, PWS Publishing Company, United Stated, 1996.

Experimental Study on the Role of Water in the TIR Anomaly before Earthquake

Shanjun Liu[1,2], **Qunlong Chen**[1], **Guoliang Li**[1], **and Lixin Wu**[2]

[1]College of Resources and Environment
Hebei Polytechnic University, Tangshan 063000, China
[2]Institute for GIS/RS/GPS & Digital Mine Research
Northeastern University, Shenyang 110004, China

Abstract— TIR anomaly before tectonic earthquake is becoming a research hotspot for seismology and remote sensing. Past study showed the thermal infrared (TIR) anomaly precursors appear before violent earthquake, and the anomaly appeared mostly in the water area of earth surface. To study the mechanisms of Infrared anomaly a group of contrastive infrared radiation imaging detection experiment of dry rock and wet rock in uniaxially compressing process is carried out. The experimental results show that: The increment of IR radiation temperature of wet rock increases greater than the dry rock in the loading process. AIRT (average infrared radiation temperature)-time curve of the wet rock keeps more accordant variation with the load-time curve. On the basis of the experimental result analysis the mechanism of TIR anomaly before tectonic earthquake are discussed, and some views are also put forward to explain the TIR anomaly phenomenon.

1. INTRODUCTION

TIR anomaly before tectonic earthquake is becoming a research hotspot for seismology and remote sensing. Past study showed the TIR anomaly precursors appeared before violent earthquake, and many anomalies appeared in the water area of earth surface. Even though the earthquake occurred in the land the TIR anomaly appeared frequently in river, lake or the vicinity of sea. Qiang [7], Kong [4], Xu [10], Lu [5] and Yurur [11] reported that there were large area of TIR anomalies in satellite remote sensing images before ocean earthquakes. Cui [1] reported that TIR anomaly appeared on the northwest of Bohai bay in China before Zhangbei Ms 6.2 earthquake. Fig. 1 shows a positive thermal anomaly area appeared on the Northwest of Bohai bay 1 days before the Zhangbei Ms 6.2 earthquake. The highest temperature area limited originally by coastline had broken though the limitation and developed towards the northwest of Bohai bay. Fig. 2 shows TIR anomaly of Hualian Ms 6.8 earthquake appearing in the surrounding sea region of Twaiwan island four days before the earthquake. The color of the anomaly area in the images is wine and its expressive temperature is 2–4°C higher than the background area whose color is yellow.

Why did the TIR anomalies frequently appear in water region? What is the mechanism of this phenomenon?

To answer above question the paper carries out a group of contrastive IR detection experiments of dry rock and wet rock in uniaxially compressing process. Some views are also put forward to explain the TIR anomaly phenomenon based on the experimental results.

2. COMPARATIVE EXPERIMENT OF IR RADIATION OF WET ROCK AND DRY ROCK IN LOADING PROCESS

2.1. Eperimental Design

Three kinds of typical crustal rock, sandstone, marble and granodiorite are processed as standard cylindrical samples of diameter 50 mm and length 100 mm. Every kind of rock samples are divides into two groups, one group is dried and the another group is dipped in water up to saturation. A servocontrol loader, WAW-200, is used to uniaxially load the samples. A modern TIR imaging system, VarioSCAN 3021ST with temperature precision 0.03°C and 360×240 pixel is applied for the TIR radiation detection and image recording. The IR imaging system is aligned in level with the rock sample and approximately 1 m away from it. The loading was displacement controlled at 0.3 mm/min. In order to minimize environmental effects on the detection of TIR radiation from the rock surface, a paper box with a circular hole was used for enclosing both the rock sample and the load platform.

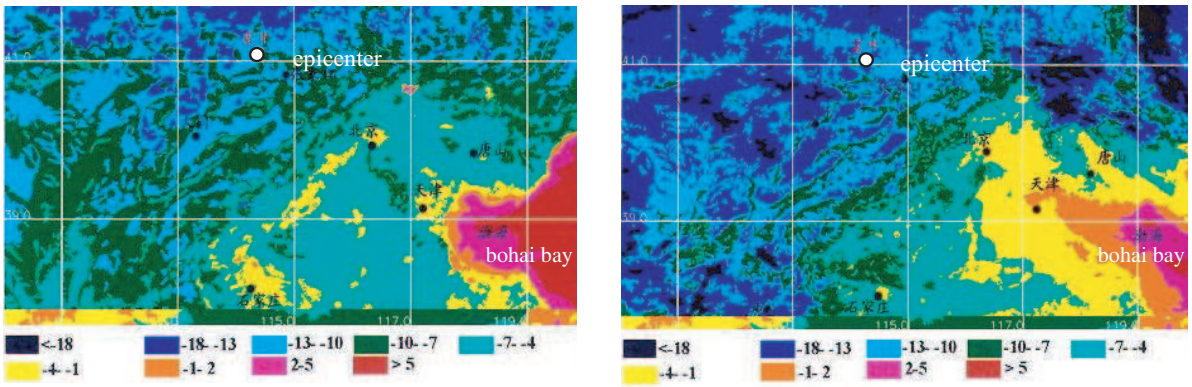

(a) (b)

Figure 1: Satellite thermal IR anomaly images before Zhangbei earthquake (Jan. 10, 1998), (a) TIR image 18 days before earthquake, (b) TIR anomaly image 1 day before earthquake.

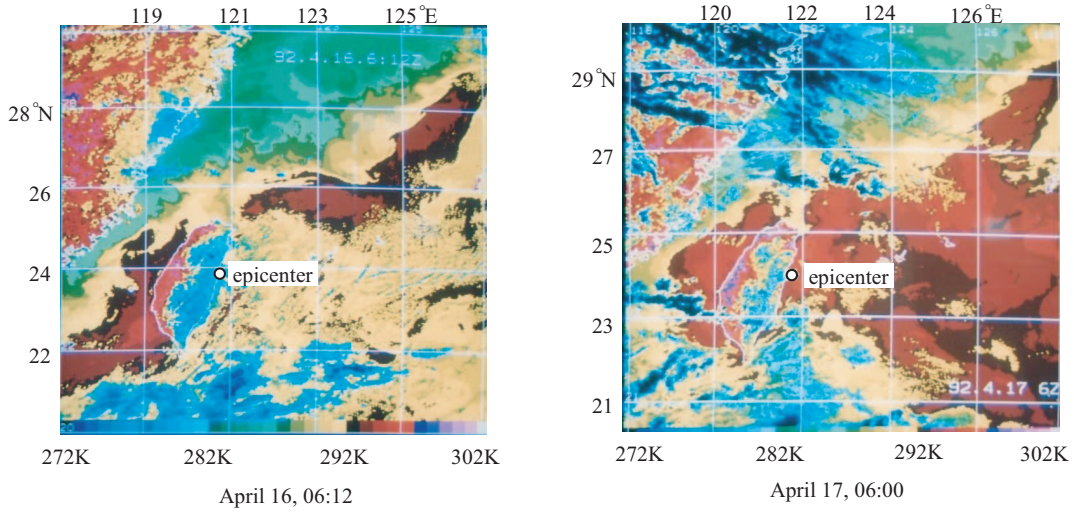

Figure 2: Satellite TIR anomaly distribution before Hualian Ms 6.8 earthquake (April 20, 1991).

2.2. Experimental Results

2.2.1. Comparison of AIRT-time Curve

AIRT (average IR radiation temperature) represents the average TIR radiation energy from the rock sample's surface. The experimental results show that the AIRT variation of wet rock is different from the that of dry rock in the loading process. Fig. 3 shows AIRT-time curve comparison of wet sandstone with dry sandstone in the loading process. The curves show the features:

1) The AIRT-time curve of dry rock fluctuates more strongly than wet rock, which indicates that the IR radiation variation of wet rock is more smooth;
2) AIRT variation of dry rock in initial loading stage is little or the AIRT decreases, but the AIRT of wet rock increases in initial stage;
3) the AIRT variation pattern of wet rock is consistent with the stress variation. But the AIRT-time curve of dry rock departures from its stress-time curve. This indicates that the relationship between IR radiation and stress for wet rock is closer than that for dry rock. The result indicates that infrared detection technique can be applied to monitor the stress change of the wet rock;
4) Under the action of equal load, the IR radiation temperature of wet rock increases greater than the dry rock. Fig. 3 shows that the AIRT of a dry sandstone sample increases about 0.1°C before rock fracture, but the AIRT of a wet sandstone sample increases about 0.5°C. Table 1 shows that the mean AIRT increment of 5 dry sandstone samples before fracture is 0.073°C, whereas that of 5 wet sandstone samples is 0.318°C, which is 4 times of the former. This indicates that the wet rock can give out more quantity of heat when it is loaded.

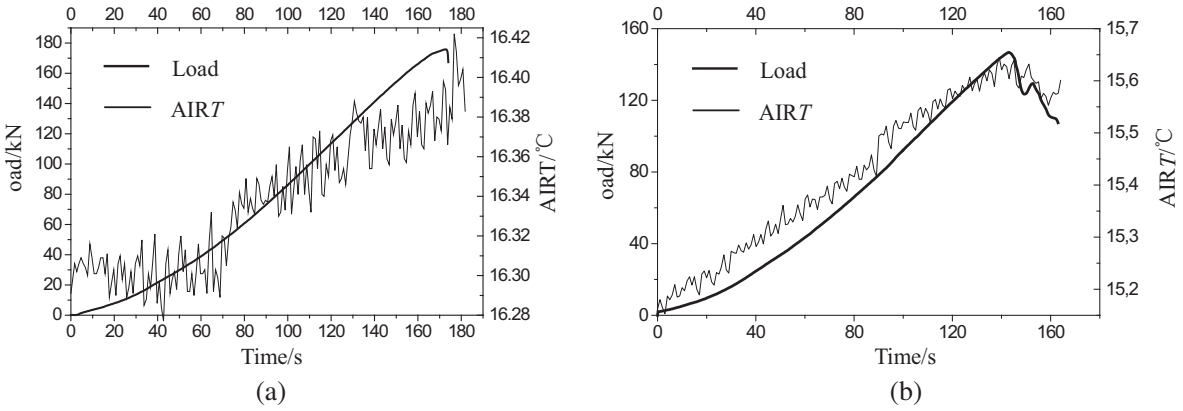

Figure 3: AIRT-time curve comparison of dry sandstone sample with wet sandstone sample, (a) Dry sandstone, (b) Wet sandstone.

Table 1: Statistic result on the AIRT increment of all rock samples before fracture.

Rock type	Wet or dry	Sample number	AIRTincrement before fracture/°C	Mean AIRT increment/°C
Sandstone	Wet	s-01	0.268	0.318
		s-02	0.248	
		s-03	0.314	
		s-04	0.492	
		s-05	0.271	
	Dry	gs-01	−0.044	0.073
		gs-02	0.065	
		gs-03	0.107	
		gs-04	0.161	
		gs-05	0.075	
Granodiorite	Wet	5d-8	0.146	0.130
		5d-10	0.114	
	Dry	5-c5	0.110	0.110
Marble	Wet	2-1	0.209	0.297
		2-2	0.362	
		2-3	0.321	
	Dry	2-g1	0.058	0.0185
		2-g2	−0.021	

2.2.2. Comparison of IR Image

The infrared image reflects the temperature field distribution of rock sample. Fig. 4 shows the comparison result of IR image of wet rock sample with dry rock sample in the loading process. The images of Fig. 4 are got by the difference with the first image.

1) The radiation temperature of rock part near the loading head (top part of sample) is higher than the part far from the loading head for all samples, but the maximal radiation temperature increment of wet rock samples in the top part is higher than that of dry rock samples. Fig. 4 shows that the maximal increment of wet rock sample in the top part is up to 1.04°C, which is 0.6°C higher than that of dry rock sample;

2) The IR image feature of wet rock samples is different from that of dry rock samples at the moment of failure. The IR radiation temperature of most dry rock samples rises obviously along the fracture at the moment of failure, but that of wet rock sample rises lesser. This indicates when the deep and wet rock fractures to result in a earthquake happening, the stress heat effect is not more obvious than that before quake.

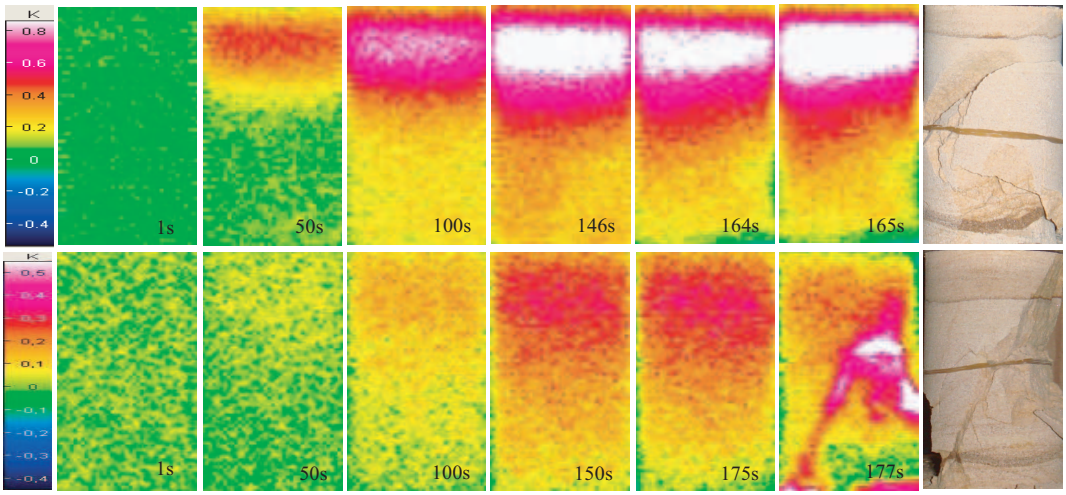

Figure 4: Difference IR image comparison of a wet sandstone sample (top) with a dry sandstone sample (low) in loading process, the right part is the photos of two samples after fracture.

3. DISCUSSION ON THE MECHANISM OF IR ANOMALY BEFORE EARTHQUAKE

Qiang [8] considered that those gases such as CO_2, CH_4, H_2 etc. go up from the deep earth and the cranny of the rock and then enhance the greenhouse effect in the atmosphere though the radiation of the sun and electromagnetic field action. Tronin [9] thought that the temperature increase of the earth surface before earthquake maybe hydro-geologyical factors or the greenhouse effect play a main role in the forming of anomalies. Geng [3] put forward stress-thermal viewpoint based on physical experiment. He deemed that the thermal anomaly before earthquake was caused by tectonic stress. Freund [2] thought the recombination of stress-activated positive hole in rock face resulting in infrared emission. Pulinets [6] thought the near-ground air ionization due to enhanced radon emission leading to the condensation of water vapor from the atmosphere and, hence, to the release of latent heat.

It is well known that earthquake is the result of crustal stress action. Therefore all phenomena related to earthquake is the effect of crustal stress action, including the satellite TIR anomaly. Above experiments indicate that the temperature of wet rock rises more than the dry rock under loading. As the experimental loading mode is uniaxilaly compression the temperature increment under loading is relatively lower. However the actual earthquake occurs in the deep crust where the stress is hundreds times of the experiment's. Thus the temperature increment induced by stress action will be very high. These stress-heat can be transferred by the water or gas of crust up to the surface of earth to make the temperature rise. Meanwhile the greenhouse effect caused by the high-density gases (CO_2, CH_4, H_2 etc.) and the thermal effect caused by the wakening up of electromagnetic field are the factors to sub-effect of stress-thermal effect. Finally multi-factor interaction leads to the TIR anomaly before earthquake.

4. CONCLUSIONS

Many TIR anomaly precursors appear before violent earthquake, and the anomaly appeared mostly in the water area of earth surface. In order to realize the mechanism of this phenomenon the contrastive infrared radiation imaging detection experiment of dry rock and wet rock in uniaxially compressing process is carried out. The experimental results show that the increment of IR radiation temperature of wet rock increases more than the dry rock. Relationship of wet rock between stress and IR radiation temperature is closer than that of dry rock. The results indicate there is a mass of heat produced by the wet rock under stress action. We think that the IR anomaly appearing

before earthquake is mainly due to the stress heat from wet rock in the deep curst, multi-factor interaction leads to the TIR anomaly before earthquake. Water plays a intensifying role in the TIR Anomaly before Earthquake.

ACKNOWLEDGMENT

This work is supported by the National Natural Science Foundations of China (No. 50774017) and the National Outstanding Youth Fund (No. 50525414).

REFERENCES

1. Cui, C. Y., et al., "Monitoring the thermal IR anomaly of Zhangbei earthquake precursor by satellite remote sensing technique," *Proc. 20th Asia RS Congress*, 1179–1184, Hongkong, China, 1999.
2. Freund, F. T., "Rocks that crackle and sparkle and glow: Strange pre-earthquake phenomena," *Journal of Scientific Exploreation*, Vol. 17, 37–71, 2003.
3. Geng, N., P. Yu, et al., "The simulated experimental studies on cause of thermal infrared precursor of earthquake," *Earthquake*, Vol. 18, No. 1, 83–88, 1998.
4. Kong, L. and Z. Qiang, "Anomaly of thermal infrared increase temperature before Taiwan strait earthquake of Ms 7.3," *Journal of Seismology*, No. 3, 34–37, 1997.
5. Lu, Z., Z. Qiang, and B. Wu, "A tentative interpretation of the formation of high temperature anomaly in satellite based thermal infrared scanning images(STISI) of the South China Sea before earthquake," *Acta Geoscientia Sinica*, Vol. 23, No. 1, 42–46, 2002.
6. Pulinets, S., D. Ouzounov, A. Karelin, et al., "The physical nature of thermal anomalies observed before strong earthquakes," *Physics and Chemistry of the Earth*, Vol. 31, 143–153, 2006.
7. Qiang, Z., C. Dian, L. Li, et al., "Satellite thermal infrared anomaly and earthquake prediction in advance and in short-term," *Proceedings of The the 30th International Geological Congress*, 186–194, Beijing, China, 1996.
8. Qiang, Z., "Satellite-based prediction earthquakes," *Earsel Newsletter*, Vol. 47, 21–26, 2001.
9. Tronin, A. A., "Thermal IR satellite sensor data application for earthquake research in china," *Int. J. Remote Sensing*, Vol. 21, 3169–3177, 2000.
10. Xu, X., X. Xu, and Y. Wang, "Satellite infrared anomaly before Nantou Ms = 7.6 earthquake in Taiwan, China," *Acta Seismologica Sinica*, Vol. 22, No. 6, 666–669, 2000.
11. Yurur, M. T., "The positive temperature anomaly as detected by Landsat TM data in the eastern Marmara Sea (Turkey): Possible link with the 1999 Umit earthquake," *International Journal of Remote Sensing*, Vol. 27, No. 5–6, 1205–1218, 2006.

A Novel RSW Antenna

Kai Ma[1], **Di Wu**[1], **and Seo Kazuyuki**[2]

[1]Jiangsu Key Laboratory of Wireless Communications
Nanjing University of Posts & Telecommunications, Nanjing 210003, China
[2]Development 2nd Dept., Nippon Pillar Packing Co. Ltd.
Sanda, Hyogo 669-1333, Japan

Abstract— In this paper, a novel design of reduced-surface wave (RSW) antenna that have minimum surface-wave excitation and radiation at the horizon is presented. The antenna is a rectangular patch which is a classic rectangular patch and has its inner edge shorted by a rectangular conducting wall. Different from other RSW antenna, the upper substrate of the antenna is air substrate. The feed network is achieved by using H-sharp aperture-coupled configuration. These patch designs excite very little surface-wave power, and thus have better radiation characteristics when mounted on finite-size ground planes.

1. INTRODUCTION

Microstrip antennas are one of the most widely used type of antennas in the modern communication systems. Their advantages are simple but very robust construction, low profile and weight, and compatibility with microwave circuits. However microstrip antennas have a series of disadvantages like narrow bandwidth, low directivity and gain, poor front-to-back ratio. One of the methods to obtain a higher gain property of microstrip antenna is to reduce the surface wave power excited by antenna [1–3]. A common property of most microstrip antennas is that the antenna element launches surface wave modes, in addition to the fields radiated into space. The power launched into the surface waves is the power which will eventually be lost, at least for the case of an infinite substrate; hence the excitation of surface waves lowers the overall radiation efficiency of the antenna. In the former work [4–6], some novel types of RSW antennas are presented. In [4] the antenna is annular with its inner edge shorted by a elliptical conducting wall, then the sharp of the antenna is transformed to a square one with its with its inner edge shorted by a square conducting wall in [6]. Our novel antenna is based on the design of [6], we remodel the antenna in [6] to a rectangular one and instead the upper substrate of the antenna of air. The feed network is achieved by using H-sharp aperture-coupled configuration. Due to the shorted wall and the upper air substrate structure, the gain of the antenna is higher than the ordinary RSW antenna. Simulation and designer make use of CST MICROWAVE STUDIO, which is based on the FDTD method. Simulation and measurements of the antenna's return loss, radiation pattern and gain are also deduced. These results show this antenna has better performance on the gain property.

2. CONFIGURATION

According to the transmission-line model and to the equivalence principle, the radiation from a rectangular patch antenna working on the dominant mode, TM10, can be modeled considering two slots with uniform magnetic current along the width of the patch. In general, each slot lunches surface wave modes into the dielectric and even if this phenomenon can be reduced using thin substrates, it can not be completely cancelled [7]. The problem is solved in [6] by has an inner rectangular boundary shorted to the ground plane. In this paper, we present an improved antenna based on [6].

The novel antenna as shown in Fig. 1 is composed of two substrates. The upper substrate is air substrate. The patch is supported with its inner edge shorted rectangular conducting wall, which coupled an H-sharp aperture slot in the ground. The feed network is etched on the lower substrate.

The proposed antenna is designed to resonate at 2.4 GHz. It is printed on a substrate with a dielectric constant of 2.65, a conductor loss ($\tan\delta$) of 0.005. The geometry, parameters, and top and bottom views for the prototype of the proposed antenna are shown in Figs. 2(a)–(c). GL and GW are the length and width of the ground, while L and W are the length and width of the patch. d is the ratio of the inner side of the single patch to the outer side of it. The height of the patch and wall is 0.5 mm. dx is the distance from the end of the feed line to the centre of the patch, while dy is the distance from the centre of the H-sharp aperture to the centre of the single element patch. hx, hy and hz can describe the sharp of the H-sharp aperture wid is the width of the feed line.

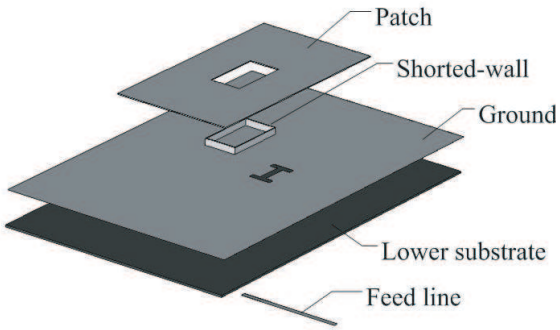

Figure 1: Configuration of the novel RSW antenna.

The dimensions of our antenna are shown in Table 1. The antenna can be viewed as two coupled quarter wavelength resonators consisting of short circuited microstrip lines of width W and length $(L - L * d)/2$. The antenna can be thus designed to cancel the surface wave emissions choosing L to be $\lambda/2$ and adjusting the other parameters to obtain the desired operating frequency and to keep in phase the two radiating edges of the patch [7].

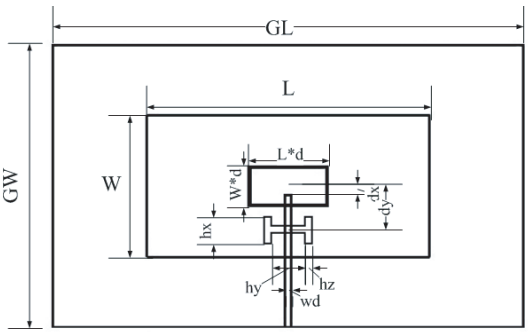

(a)

(b)

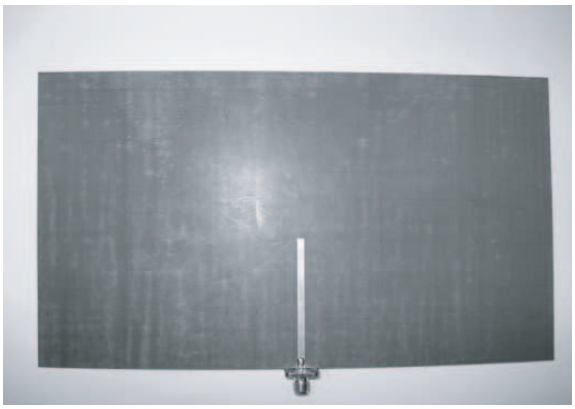

(c)

Figure 2: Antenna geometry, parameters and prototype. (a) Antenna geometry. (b) Prototype top view. (c) Prototype bottom view.

Compared with RSW antenna in Ref. [6], the antenna discussed in this paper has two superior improvements. Firstly, the upper substrate of the antenna is changed to air substrate, which will increase the gain property of the antenna. Secondly, the feed network is achieved by using H-sharp aperture-coupled configuration, which is easily achieved in engineering but will cause huger back lobe. The RSW antenna will get higher gain characteristic than the antenna in Ref. [6].

3. SIMULATION AND MEASUREMENT RESULTS

The novel RSW antenna with air substrate are arrayed; the antenna is designed to resonate at 2.4 GHz. The design is simulated by the CST MICROWAVE STUDIO software and measured in the microwave chamber. Fig. 3 shows the reflection of the 4-element array antenna, the measured S_{11} parameter reach its lowest point (−16.842 dB) when frequency is 2.4 GHz, while the simulated S_{11} parameter reach its lowest point (−16.842 dB) at the same resonating frequency point. The array achieved a 2.9% bandwidth from 2.37 GHz to 2.44 GHz in the measured results, and the simulated bandwidth is 4.37% from 2.345 GHz to 2.45 GHz. The radiation pattern property of the array is shown in Fig. 4. The measured gain of the antenna is 10.66 dB and its cross-polar is lower than −30 dB in the main direction, and the simulated gain of the antenna achieved 11.35 dB. The gain and reflection characteristic of the antenna is lower than the simulated results, which may be due to the processing error. As shown in Figs. 4(a)(b), we can see the cross-polar property of the E-plane direction is better than it of the H-plane direction.

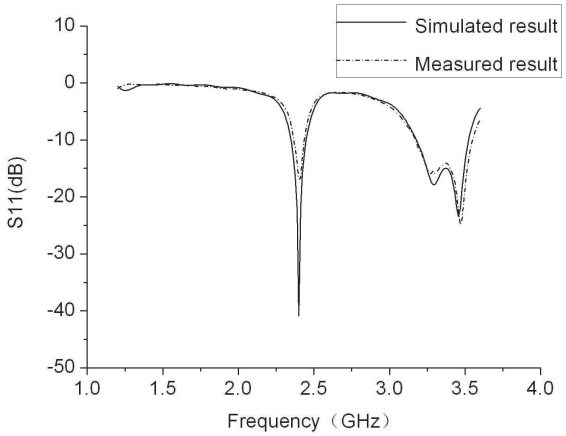

Figure 3: Reflection characteristic (S_{11}).

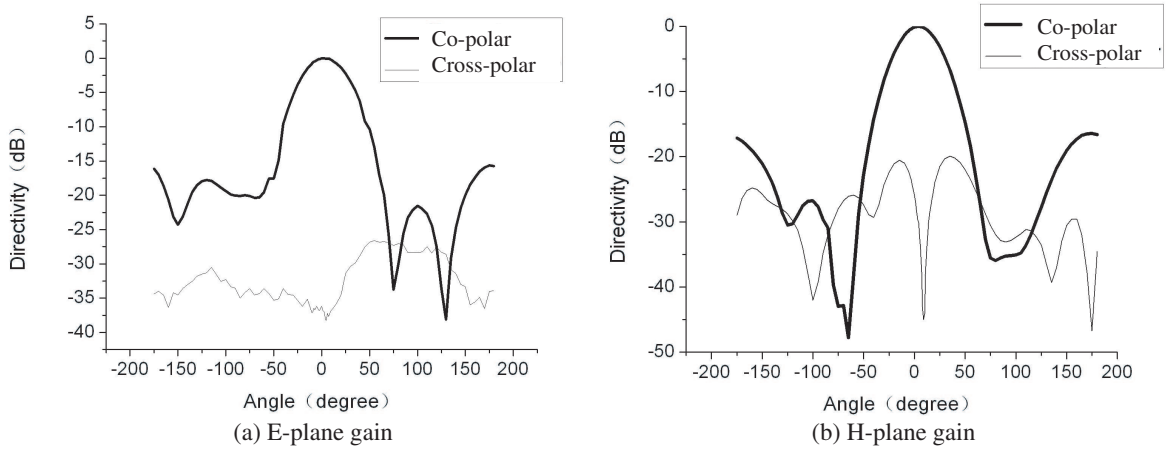

Figure 4: Radiation Pattern of 4-elements array antenna.

4. CONCLUSION

A novel microstrip RSW (Reduced-surface wave) antenna with high gain property is presented. The antenna can achieve high gain property because the novel shorted wall structure effectively reduced the surface wave power excited by the patch. The measured gain of the 4-element array antenna is 10.66 dBi at 2.4 GHz with a 2.9% bandwidth from 2.37 GHz to 2.44 GHz. And its cross-polar is lower than −30 dB in the main direction. The H-sharp aperture-coupled configuration feed network is easily achieved in engineering. The antenna can be used as a department of phased array antennas.

ACKNOWLEDGMENT

This work was supported in part by the Scientific Research Foundation of Nanjing University of Posts and Telecommunications under Grant No. NY207016, in part by Jiangsu provincial research scheme of natural science for higher education institutions under Grant No. 07KJB510080, in part by the National Basic Research Program (973) of China under Grant No. 2007CB310607.

REFERENCES

1. Amendols, G., L. Boccia, and G. Di Massa, "Surface wave radiation from a shorted elliptical patch antenna," *Antennas and Propagation Society International Symposium*, IEEE, 2003.
2. Arnieri, E., L. Boccia, G. Amendola, and G. Di Massa, "A compact high gain antenna for small satellite applications," *Transactions on Antennas and Propagation*, Vol. 55, No. 2, IEEE, February 2007.
3. Arnieri, E., L. Boccia, G. Amendola, and G. Di Massa, "A high gain antenna for small satellite missions," *Antennas and Propagation Society International Symposium*, IEEE, 2004.
4. Jackson, D. R., J. T. Williams, A. K. Bhattacharyya, R. L. Smith, S. J. Buchheit, and S. A. Long, "Microstrip patch designs that do not excite surface waves," *Transactions on Antennas and Propagation*, Vol. 41, No. 8, IEEE, August 1993.
5. Boccia, L., G. Amendola, G. Di Massa, and L. Giulicchi, "Shorted annular patch antennas for multipath in GPS-based attitude determination systems," *Microwave and Optical Technology Letters*, Vol. 28, No. 1, January 5, 2001.
6. Li, Q., D. Wu, and S. Kazuyuki, "Study on a Ku band high-gain microstrip antenna," *CRAM*, 2007.
7. Boccia, L., G. Amendola, and G. Di Massa, "Rectangular patch antennas with reduced surface wave radiation," *Antennas and Propagation Society International Symposium*, IEEE, 2005.

An Improvement to Decrease the Effect of Handset Internal Components on a Dual Band PIFA Performance

M. Pasandehmanesh, D. Arefan, and M. A. Ebrahimi-Ganjeh
Electrical Engineering Department, Sadjad Institute of Higher Education, Iran

Abstract— This paper presents a dual band planar inverted-F antenna (PIFA) which has been designed to get less effect of handset internal components than previous ones in 900 and 1800 MHz. The applied technique based on decreasing the space between radiation plane and ground plane in some parts of the antenna. Two shapes of a handset ground plane, as well as the antenna alone are examined. VSWR and radiation pattern of the antenna has been computed, and compared in each case. All numerical simulations are performed using the Ansoft HFSS software.

1. INTRODUCTION

In the early 20th century, wireless telecommunication hardware was so heavy and large that their equipments would occupy a car carrying the device. Furthermore, the required power to operate these systems was too high, which would lead to a very poor battery life. However, the advent of microelectronics held a revolution in the mobile communication technologies. With this revolution, mobile communication devices became lighter and smaller, and consumed less power to operate [1, 2].

Nowadays, the spread of mobile communications technologies is really remarkable and the handsets are reduced in sized as much as possible. It is well-known that the most significant factor in decreasing the size of a handset is reducing the dimension of its antenna, yet maintaining the good radiation performance. A mobile handset consists of internal components such as a PCB (that may roll as a ground plane), a battery, a locking member for securing the battery, etc. In fact, the various types of these components from handset to handset can remarkably affect the antenna radiation characteristics [3–5].

For instance, [3] presents results from a comprehensive investigation on the performance of a conventional PIFA mounted on ground planes with various shapes and sizes. It has been shown there is significant impact of ground plane size of more than 0.4λ on any radiation characteristics of the PIFA. [4] investigates a modified ground plane to design ultra thin PIFA. It offers a slotted meandered ground plane to gain this specification. It is seen in [5], depending on size and situation, the presence of other components around the antenna may damage the antenna's total radiated power to the far field, and also increase the VSWR quantity. Furthermore, a modified miniature antenna in [6], which operates at 2.45 GHz, exhibits low coupling to the PCB.

The main purpose of this paper is designing a dual band PIFA antenna for various mobile phones with any size and any shape. Therefore, it should get less effect of other handset internal components to be able to work independent from the type of the handsets. This antenna is designed to be used in 900 MHz and 1800 MHz, the typical frequencies in the mobile communication. This antenna also includes other advantages of PIFAs, such as low profile, easy fabrication, etc.

2. DESIGNED ANTENNA

Figure 1 shows the dual band PIFA antenna designed by this paper in the presence of a typical ground plane. In addition to this, the details of the antenna's structure are depicted in Fig. 2. The applied technique, which supports the idea of this paper, based on decreasing the space between radiation and ground plane in some parts of the antenna [6], which is well seen in the figures.

For more studies of the radiation performance in presence of any handset internal components around the antenna, two more other structures have been considered covering this purpose. One without presence of the phone ground plane and the other with presence of both the phone ground plane and the battery, as shown in Fig. 3.

3. RESULTS

Figure 4 and Fig. 5 illustrate the computed VSWR in various cases considered in Section 2 around 900 and 1800 MHz. Normalizing to 900 and 1800, It is seen that there is less than 5% variations

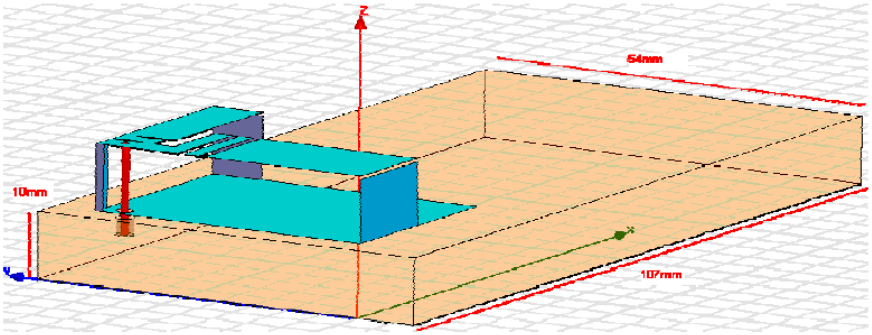

Figure 1: Dual band PIFA antenna in presence of the phone ground plane (phone box).

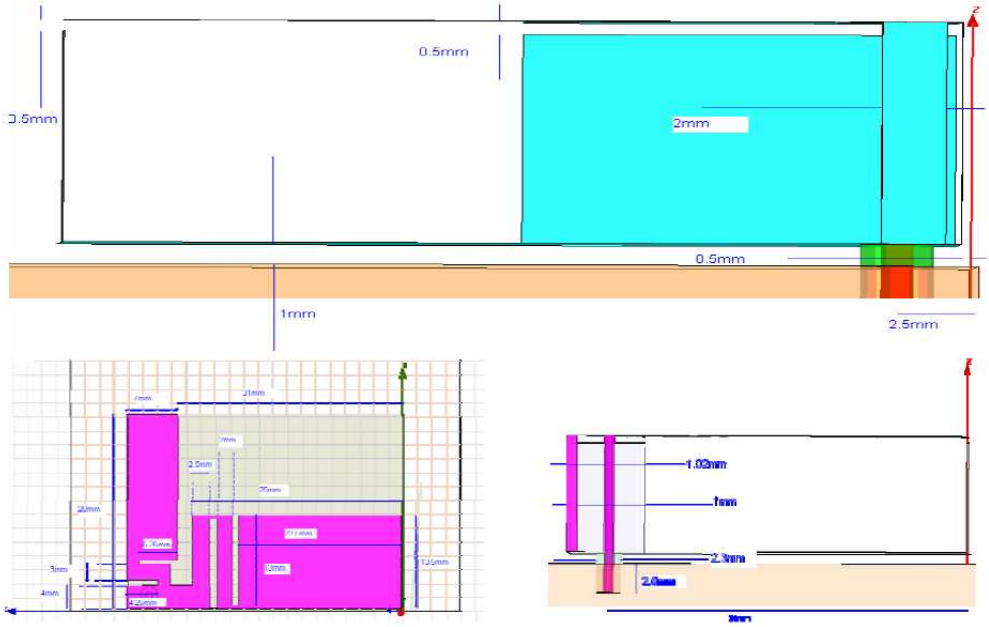

Figure 2: The dimensions and the details of designed antenna in Fig. 1.

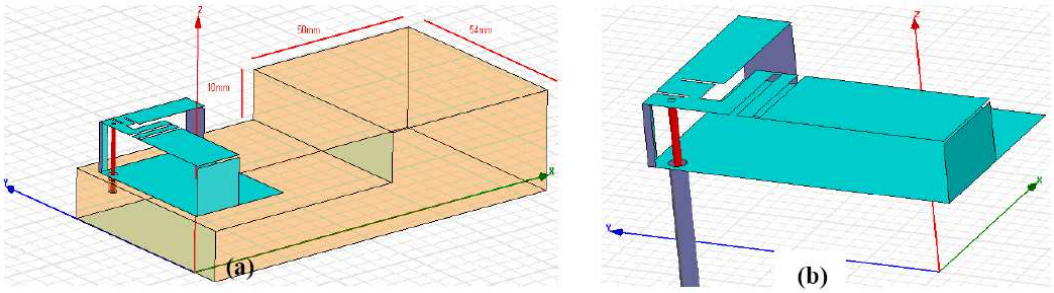

Figure 3: (a) Antenna with phone box and a component like battery; (b) Antenna without phone box.

in the frequency resonances of the designed antenna when the battery is added or even when the handset ground plane is totally removed. Therefore effect of the handset internal components on the frequency resonances at 900 MHz and 1800 MHz can be neglected. Moreover the variation of the bandwidth except in the one case (900 MHz without ground plane) can be neglected.

Radiation patterns of the antenna are shown in Fig. 6. It can be seen the variations of the radiation patterns can be neglected when the battery is added. However the presence of the handset ground plane has great effect on the radiation patterns, which was predictable (it plays reflector roll).

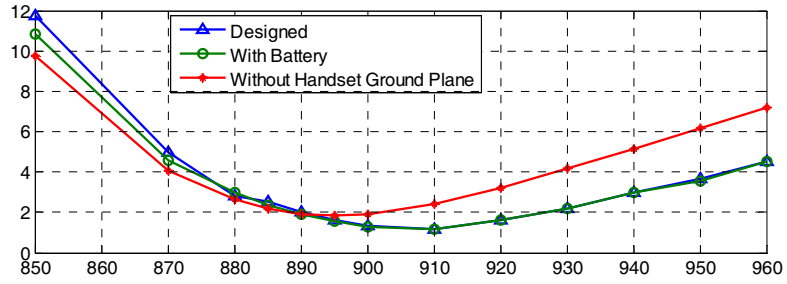

Figure 4: VSWR plots for various cases around 900 MHz.

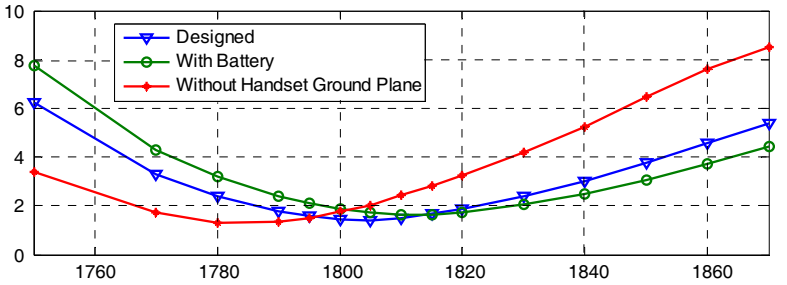

Figure 5: VSWR plots for various cases around 1800 MHz.

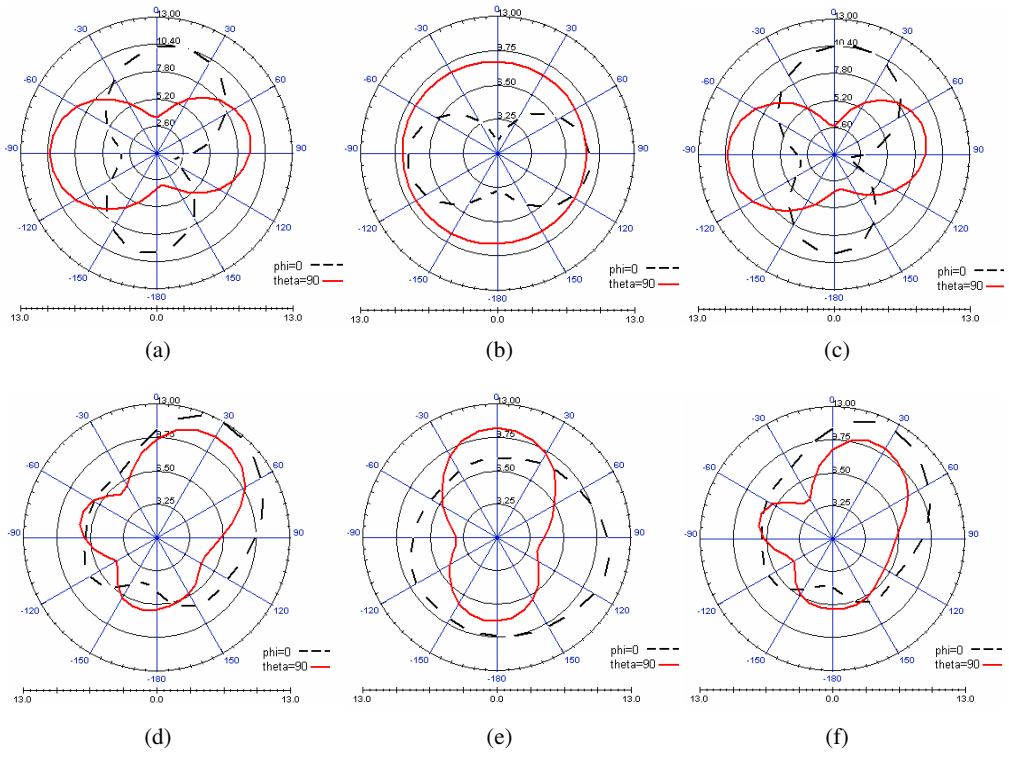

Figure 6: Radiation patters for antenna in three different cases in 900 MHz and 1800 MHz, the coordinate system is shown in Fig. 1. (a) Antenna with phone box in 900 MHz; (b) Antenna without phone box in 900 MHz; (c) Antenna with phone box and battery in 900 MHz; (d) Antenna with phone box in 1800 MHz; (e) Antenna without phone box in 1800 MHz; (f) Antenna with phone box and battery in 1800 MHz.

4. CONCLUSION

In this paper, a dual band PIFA antenna in 900 MHz and 1800 MHz has been designed to get less effect of handset internal components. The obtained results confirmed the idea of the paper. It is seen that there is less than 5% variations in the frequency resonances of the designed antenna

when the battery is added or even when the handset ground plane is totally removed. Moreover, except the one case, the effect on bandwidth is not noticeable. Finally, it is shown the variations of the radiation patterns can be neglected when the battery is added.

REFERENCES

1. Yacoub, M. D., *Foundations of Mobile Radio Engineering*, CRC Press, Boca Raton, USA, 1993.
2. Lecuyer, C., *Making Silicon Valley: Innovation and the Growth of High Tech.*, 1930–1970, MIT Press, Cambridge, 2005.
3. Hyunh, M. C. and W. Stutzman, "Ground plane effects on planar inverted-F antenna performance," *IEE Proc. Microw. Antennas Prop.*, Vol. 150, No. 4, 209–213, 2003.
4. Abedin, M. F. and M. Ali, "Modifying the ground plane and its effect on planar inverted-F antennas (PIFA) for mobile phone handsets," *IEEE Antennas and Wireless Propag. Letters*, Vol. 2, 226–229, 2003.
5. Ebrahimi-Ganjeh, M. A. and A. R. Attari, "Interaction of dual band helical and PIFA handset antennas with human head and hand," *Progress In Electromagnetics Research*, PIER 77, 225–242, 2007.
6. Gao, Y. and X. Chen, "Study of a miniature PIFA," *Asia-Pacific Microwave Conference*, Vol. 4, 2005.

Design of Thin-membrane Printed Dipole

Daqun Yu[1] **and Ruiping Zhu**[1, 2]

[1]Nanjing Research Institute of Electronics Technology, Nanjing 210013, China
[2]China National Key Laboratory of Antenna and Microwave Technology
Nanjing 210013, China

Abstract— Future space-based radar and spaceborne SAR require very large aperture and high-gain phased array antennas. Membrane-based deployable antennas provide a means to reduce mass, stowage volume, and overall cost of radar antenna system. JPL has developed some array antennas which are based on thin-membrane structure, and the elements of these antennas are microstrip antenna. But there are some distinct disadvantages associated with these thin-membrane microstrip antennas, as shown in Section 1 of this paper. As an improved antenna element, a novel printed dipole which based on thin-membrane structure is presented in this paper. This thin-membrane printed dipole is center fed by parallel-strip (PS), which is transformed from coplanar waveguide (CPW) by using a vertical transition balun. This vertical transition between CPW and PS has a wide frequency band due to the two waveguide structures have little or no variation of their characteristic impedance with respect to frequency and can meet the design requirement of thin-membrane printed dipole. The use of CPW in the feed network makes this printed dipole easily be integrated with T/R modules. The whole thin-membrane printed dipole with vertical transition balun is simulated by means of Ansoft HFSS. From the simulation result, it is know that this printed dipole has wide bandwidth of 190 MHz (15.2%) and good radiation characteristic with low cross-polarization (< -30 dB). The thin-membrane printed dipole is a very useful antenna element for future large aperture, lightweight, deployable and high-gain phased array application.

1. INTRODUCTION

The large aperture, lightweight, deployable and high-gain phased array antennas are indispensable for future space-based radar and spaceborne SAR system. At the same time, however, low mass and small stowage volume are emphasized on these antennas, in order to reduce payload weight and size. The deployable array antenna using thin-membrane structure has been identified as one of enabling technology to achieve low-mass, high packaging efficiency, low cost and reliable deployment for future spaceborne high-gain and large aperture antennas. Both the membrane layers and the metal conductors should be thin enough for low mass and deployability considerations. The thin metal conductors are supported by thin membranes. The antenna elements are etched on very thin membrane substrate and the inflatable tubular frame structure to support multilayer membrane.

To keep the antenna low profile and light weight, the elements of array antennas that are developed by JPL are microstrip antennas [1–3]. But the microstrip antennas based on thin-membrane structure also have some limitations. Coplanar microstrip feed that is used in paper [1] need only two thin-membrane layers, and so the structure is simple. But frequency bandwidth of this microstrip antenna is only a few percent and cross-polarization is high due to the radiation from the feed network interfering with the radiation pattern of antenna. Although the aperture coupled microstrip antenna can increase bandwidth beyond the few percent and reduce the cross-polarization, this antenna needs three thin-membrane layers so the structure is complicated, and the characteristics of antenna are sensitive to the flatness of the thin-membrane. Additionally the two type's thin-membrane microstrip antennas are difficult to be integrated with T/R modules. As an improved antenna element, a novel aperture coupled microstrip antenna element that only needs two thin-membrane layers is presented [2, 3]. The feed network and ground plane are on the two sides of the same membrane. This approach allows easier integration with T/R modules where a single-layer CPW transmission line is used. But the microstrip line of this element is so thin that the high loss is unacceptable. Furthermore, the fabricated precision of thin microstrip line and couple slot is too high.

The thin-membrane printed dipole that is based on thin-membrane structure is presented in this paper. This printed dipole has three thin-membrane layers, each made of 5-micro copper on a 0.05-mm Kapton sheet with relative dielectric constant of 3.4. The dipole is etched on the top radiating membrane. The middle ground plane membrane has a cut-out that allows the PS to through. The bottom membrane has the CPW feed network. The configuration of this dipole is

shown in Fig. 1. The CPW on the bottom membrane is transformed to PS transmission line by using a vertical transition balun, and then the printed dipole on the radiating membrane is center fed by the PS. The thin-membrane printed dipole is easily integrated with T/R modules by using CPW in the bottom membrane.

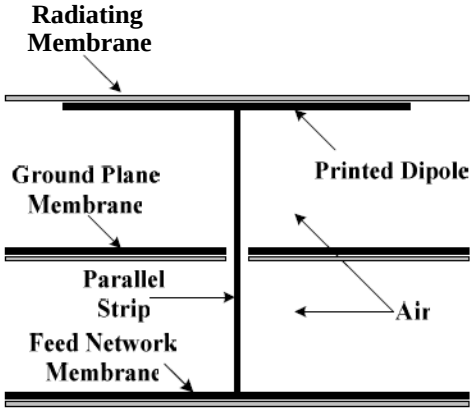

Figure 1: Cross-section configuration of thin-membrane printed dipole.

2. THIN-MEMBRANE PRINTED DIPOLE DESIGN

2.1. Vertical Balun Design

The vertical transition between CPW and PS transmission line is very important for design the thin-membrane printed dipole. The vertical transition balun transform a CPW unbalanced mode to balanced PS mode, and then the balanced PS feeds the printed dipole. This balun is presented by D.-H. Kwon in [5], as shown in Fig. 2 and Fig. 3. The CPW that is fabricated on thin membrane is terminated with the open-circuit discontinuity and two parallel strips are attached vertically at the point of the discontinuity. The two strips can have landing soldering pads formed by sharply bending a small section of the metal strips at their ends for reliable connection, as shown in Fig. 2. It is note that, the two parallel strips are also etched on thin membrane and need foam struts to keep the distance between them. In our study, when the width of the two strips is chosen to be equal to the width of the CPW signal line ($w1 = w2$), the transition realizes unbalanced-to-balanced transformation, which can be useful in driving antenna elements in balanced modes.

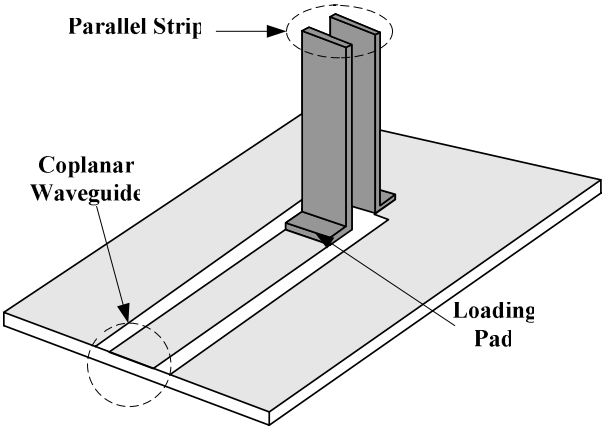

Figure 2: Geometry of the vertical CPW-PS transition.

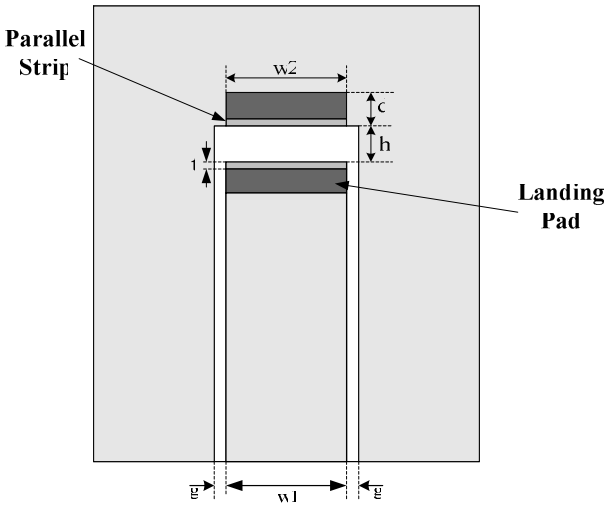

Figure 3: Top view of the CPW-PS transition.

Going through the transition from the CPW to the PS transmission line, the electric field inevitably undergoes reflection at the junction mainly due to two differences. To minimize the

reflection of the signal at the junction, the two distinct transmission lines are designed to have the same characteristic impedance. For given membrane substrate, $w1$ and g are properly chosen to realize particular characteristic impedance for the CPW. The separation h can be adjusted for the parallel strips to match this impedance for given $w1$.

To verify the performance of the CPW-PS transition, back-to-back transition with the characteristic impedance of the CPW and the PS transmission line equal to 80 Ω is simulated in the simulation software Ansoft HFSS. The CPW and PS geometry are given by $w1 = w2 = 6.56$ mm, $g = 0.77$ mm and $h = 2$ mm to realize the required characteristic impedance. The simulated result for $|S_{11}|$ and $|S_{21}|$ of the CPW-PS-CPW transition with 80 Ω characteristic impedance is shown in Fig. 4 from 0.6 to 2.0 GHz. From simulated result shown in Fig. 4, we know that the transition has a wide frequency band due to the two waveguide structures have little or no variation of their characteristic impedance with respect to frequency and can meet the design requirement of thin-membrane printed dipole.

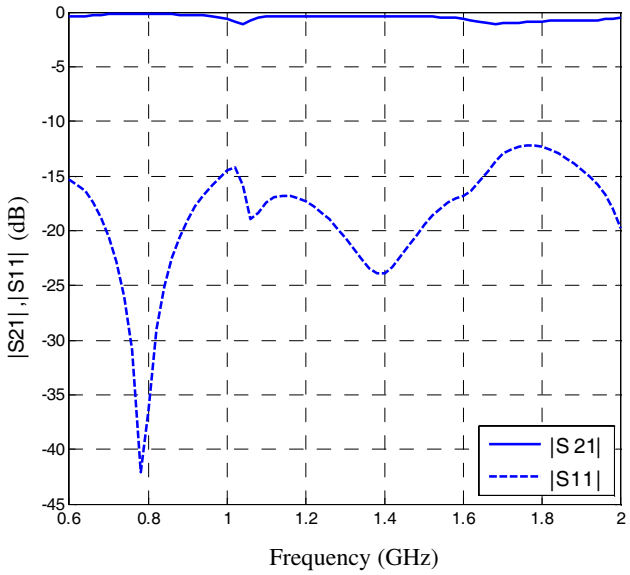

Figure 4: Simulated results for $|S_{21}|$ and $|S_{11}|$ for the CPW-PS-CPW transition.

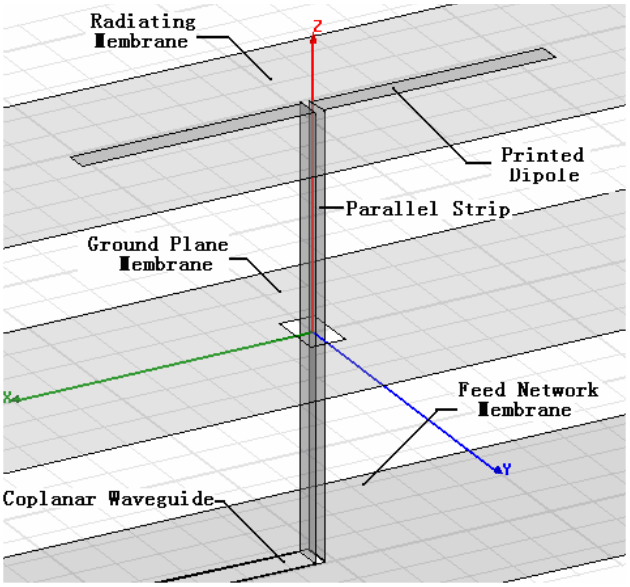

Figure 5: Configuration of thin-membrane printed dipole.

2.2. Printed Dipole Design

The printed dipole that is etched on the top radiating membrane is center fed by PS transmission line, and the distance between top radiating membrane and ground plane membrane is 55 mm ($0.25\lambda_0$, λ_0 is wavelength of free-space). The configuration of thin-membrane printed dipole is shown in Fig. 5.

We can create the coarse model of printed dipole in the simulation software Ansoft HFSS with the length of it is nearly $0.5\lambda_0$ and the width is less than $0.05\lambda_0$. Then the dipole is balanced fed by PS transmission line with characteristic impedance is 80 Ω, and the PS transmission line is transformed from CPW by using the balun that is designed in Section 2.1. The CPW with 80 Ω characteristic impedance is transformed to 50 Ω by adding a quarter-wave transformer. The impedance bandwidth and resonant point is optimized by varying the length and width of the dipole in the simulation software Ansoft HFSS. The optimized configuration is: the length and width of dipole is 104.5 mm and 6 mm.

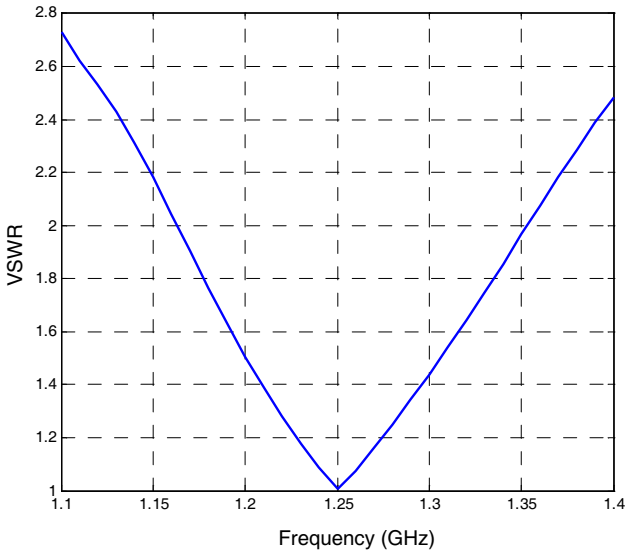

Figure 6: Simulated VSWR of thin-membrane printed dipole.

The simulated VSWR of dipole is shown in Fig. 6. Far field co-polarization and cross-polarization patterns of the E-plane and H-plane at 1.25 GHz are shown in Fig. 7 and Fig. 8. It can be observed that the bandwidth is nearly 15.2% with VSWR of 2 and the radiation characteristic is good with cross-polarization is below −30 dB.

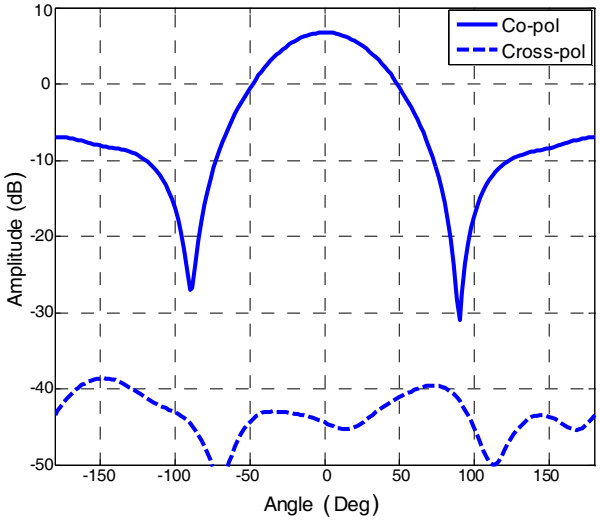

Figure 7: E-plane radiation pattern.

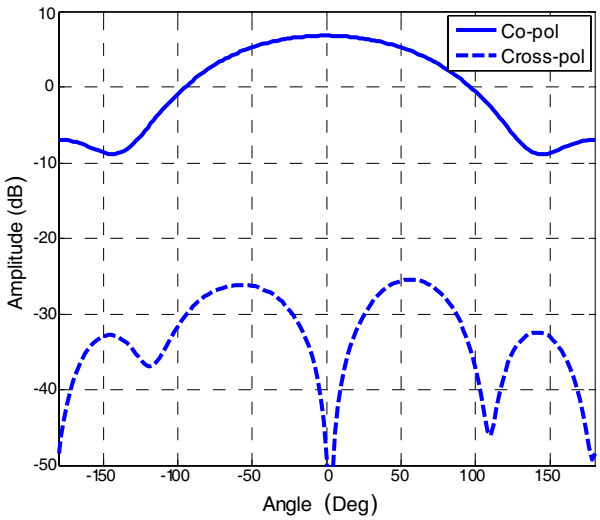

Figure 8: H-plane radiation pattern.

3. CONCLUSIONS

In this paper, the development of thin-membrane printed dipole is presented. This thin membrane printed dipole is center fed by PS, which is transformed from CPW through a vertical transition balun. From the simulation result, we know that this dipole has wide bandwidth (nearly 16%), good radiation characteristic and good cross-polarization ($< -30\,\mathrm{dB}$) due to the shield of ground plane membrane. The use of CPW in the feed network makes the dipole easily integrated with T/R module. The thin-membrane printed dipole is very useful antenna element for future thin-membrane phased array application.

REFERENCES

1. Huang, J., M. Lou, A. Feria, and Y. Kim, "An inflatable L-band microstrip SAR array," *IEEE AP-S Symposium*, Atlanta, Georgia, June 1998.
2. Huang, J. and A. Moussessian, "Thin-membrane aperture-coupled L-band patch antenna," *Proc. IEEE AP-S/URSI Symp.*, Monterey, CA, June 2004.
3. Huang, J., "Paper-thin membrane aperture-coupled L-band antennas," *IEEE Trans. Antennas and Propagation*, 2005.
4. Kwon, D.-H. and Y. Kim, "A wideband vertical transition between co-planar waveguide and parallel-strip transmission line," *IEEE Microw. Wireless Compon. Lett.*, 2005.

CPW-fed Compact Planar UWB Antenna with Circular Disc and Spiral Split Ring Resonators

Li-Ming Si, **Hou-Jun Sun**, **Yong Yuan**, **and Xin Lv**
Department of Electronic Engineering, School of Information Science and Technology
Beijing Institute of Technology, Beijing 100081, China

Abstract— This paper presents a novel compact-size (the diameter of the radiating element is only 0.05λ at the lower end of the operating band, 1.2 GHz) coplanar waveguide (CPW)-fed planar antenna with 10 dB return loss (VSWR < 2) bandwidth from 1.2 to 25 GHz, 182%, for ultra-wideband (UWB) communications. The proposed antenna consists of a circular disc and a spiral split ring resonator displayed on an inexpensive FR4_expoxy substrate. This UWB printed monopole antenna adopts CPW-fed and two tapered transmission lines for improving broadband impedance matching in the required band. Numerical simulations using finite element method (FEM) show that the radiation patterns over the mostly operation band are omni-directional in H-plane and symmetrical in E-plane, with an average gain of 4.5 dB.

1. INTRODUCTION

Federal Communications Commission (FCC) has allocated 7.5 GHz of the spectrum from 3.1 GHz to 10.6 GHz for Ultra wideband (UWB) radio applications from February 2002. Then, UWB have wide applications in short range and high speed wireless systems, such as ground penetrating radars, medical imaging system, high data rate wireless local area networks (WLAN), communication systems for military, and short pulse radars for automotive even or robotics. Recently, due to low-profile, low weight, inexpensive, and easy fabrication and integration with monolithic systems, planar UWB antennas with printed circuit boards (PCB) technology have been widely studied and reported for UWB communications, like circular disc [1], PICA [2], tapered-slot-fed annular slot antenna [3], and so on. However, these antennas have relatively large size or complex structures.

Metamaterials are artificially constructed materials based on the designed structure rather than the constituent materials from which it is composed, so metamaterials can exhibit exotic electromagnetic properties which not be readily found in nature. Because the dimensions of the element structure are less than the wavelengths (usually termed sub-wavelength) of the resonant frequencies, it will open the door to the development of small-size electromagnetic (EM) devices. In our previous work [4], it was shown that by using different circular/ring microstrip resonators (like split-ring resonator, closed-ring resonator, and circular disc resonator), the dimension of antenna can be effectively reduced and overcome the classical half-wavelength size limitation. Split-ring resonator (SRR) is well-known artificial magnetic metamaterial and one of the essential components of left-handed material (LHM). It consists of two metal rings separated by a gap, each with a split at opposite sides. Though it was built up by nonmagnetic conductors (like copper), it can yield negative effective magnetic permeability, which was introduced by Pendry et al. in 1999 [5] and experimentally confirmed by Smith et al. in 2000 [6]. Yang et al. have used an SRR to design an UWB antenna [7]. However, spiral split ring has smaller size than SRR, about half of it, at the same resonant frequency [8].

In this paper, we presents a CPW-fed antenna for the UWB applications that achieves a physically compact planar profile, sufficient impedance bandwidth, high radiation pattern and near omni-directional radiation pattern. The planar antenna consists of a circular disc and a spiral split ring resonator displayed on an inexpensive FR4_expoxy substrate. Properties of the antenna are investigated by three-dimensional (3D) EM full-wave finite element method (FEM) simulation software package High Frequency Structure Simulator (HFSS). The diameter of the radiating element is approximately 0.05λ at the lower end of the operating band. Namely, a 1.2–25 GHz UWB antenna will only have a circular area radiating element with diameter of approximately 26 mm.

2. ANTENNA CONFIGURATION

The configuration of the proposed UWB antenna is illustrated in Figure 1. The proposed antenna consists of a circular disc and a spiral split ring resonator developed on a $H = 1.6$ mm FR4 epoxy substrate with relatively permittivity $\varepsilon_r = 4.4$ and loss tangent $\tan\sigma = 0.025$. A 50 Ω CPW feed line, which has a width of the signal strip w_f fixed at 1.5 mm and a gap of distance between the

strip and the coplanar ground plane g at 0.22 mm, is used to excite the antenna. The metal lines of the resonators and CPW are fabricated with 0.018 mm-thick copper. r_1 and r_2 are the radius of the a circular disc and the outer ring of spiral split ring, respectively. h is the spacing between the feed point and the ground plane. Two tapered impedance transformer lines have been applied for improving impedance matching. The width of the tapered transmission line at the feed point is w_f (equal to 1.5 mm), and the width of two tapered transmission lines can be described as

$$L_n = 0.8^n \times w_f \qquad (n = 1, 2) \tag{1}$$

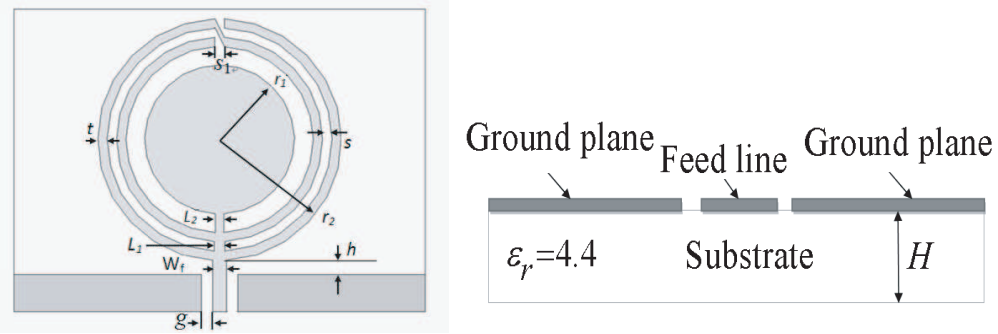

Figure 1: Configuration of the proposed antenna. (a) Top view; (b) Side view.

3. PERFORMANCE OF THE ANTENNA

To find the characterization of the antenna, a 3D EM full-wave technique is required to accurately mode the dimensions and simulate the performance of it. Here, FEM-based Ansoft HFSS, which is a powerful and efficient method for EM problems through subdividing a large problem into individually simple constituent units and then reassembling the solution for the entire problem space as a matrix of simultaneous equations [9], have been carried out to give the characterizations of the antenna.

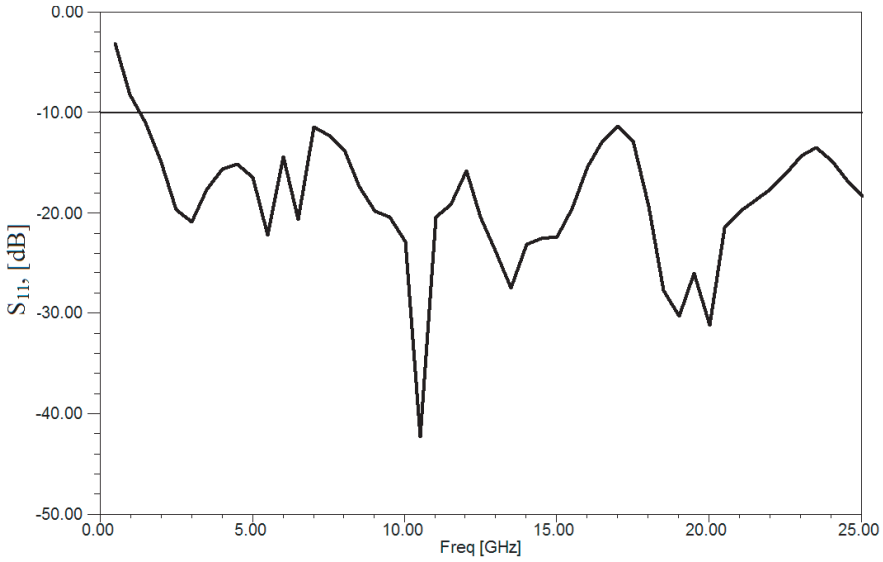

Figure 2: Return loss of proposed antenna with the parameters. $w_f = 1.5,\ g = 0.22,\ r_1 = 8,\ r_2 = 13,\ t = 1,\ s = 1,\ s_1 = 1,\ h = 0.2,\ H = 1.6$, all parameters unit in mm.

Figure 2 shows the return loss for the proposed antenna. As can be seen from this figure, the impedance bandwidth of the proposed antenna for return loss of better than −10 dB is from 1.2 GHz to 25 GHz, which covers the whole FCC-defined UWB frequency region (3.1–10.6 GHz).

Radiation patterns of the antenna in E-plane and H-plane are shown in Figure 3(a)–(d) at four different frequencies, 1.5 GHz, 3.5 GHz, 6.5 GHz, 9.5 GHz, over the operation frequency band.

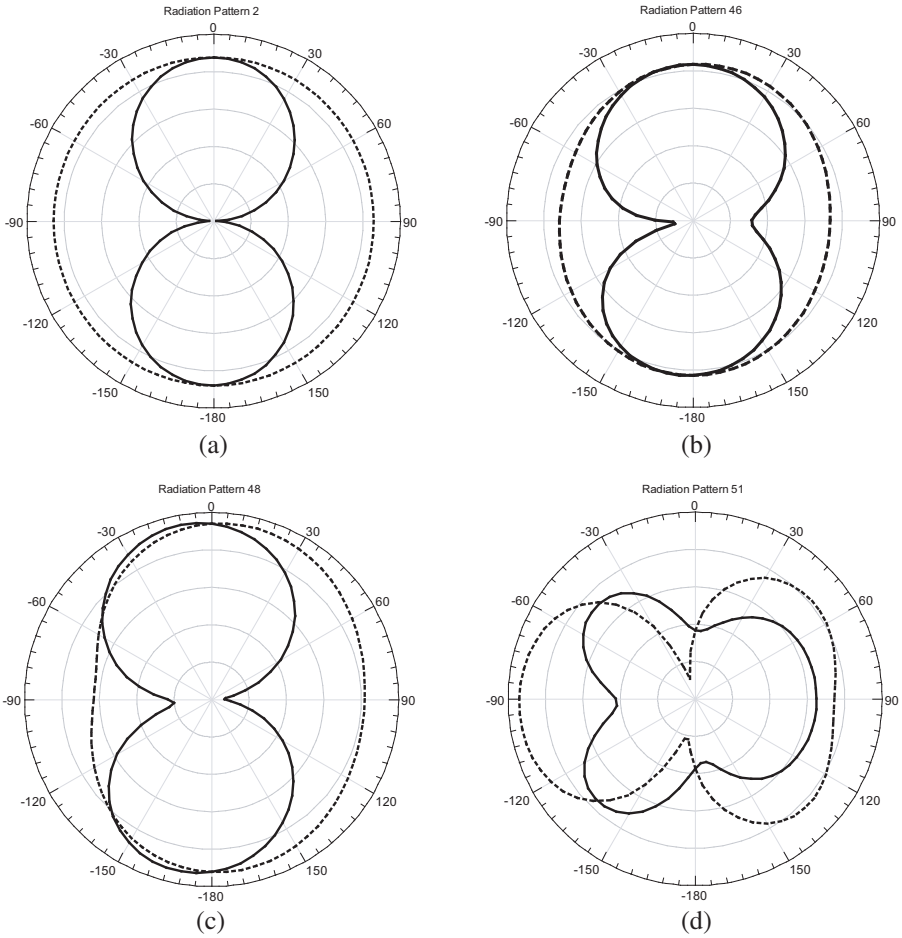

Figure 3: Radiation parrerns in the E-plane (solid line) and H-plane (dotted line) of the proposed antenna at (a) 1.5 GHz, (b) 3.5 GHz, (c) 6.5 GHz, and (d) 9.5 GHz with the same parameters as Figure 2.

As can be seen from Figure 3, the H-plane radiation patterns of the proposed antenna are omni-directional and the E-plane radiation patterns are symetric in the most UWB band. The antenna gain is also calculated by HFSS. From the whole operenting band, the antenna has an average gain of about 4.5 dB.

4. CONCLUSIONS

A novel compact-size configuration of CPW-fed UWB antenna gives large bandwidth has been investigated. The bandwidth of the proposed antenna is from 1.2 to 25 GHz (182%) for return loss of better than 10 dB (VSWR < 2), which covers the required commercial UWB band approved by the FCC. This planar-type antenna has a simple structure, good impedance matching, also an omni-directional radiation pattern in the H-plane during the mostly operation band. Meantime, the antenna size may be scaled to any desired frequencies for other wireless applications. All these advantages make it a very good candidate for UWB applications or even very suitable for wideband array design.

REFERENCES

1. Liang, J., C. C. Chiau, X. Chen, and C. G. Parini, "Study of printed circular disc monopole antenna for UWB systems," *IEEE Trans. Antennas Propag.*, Vol. 53, 3500–3504, 2005.
2. Suh, S. Y., W. L. Stutzman, and W. A. Davis, "A new ultra wide band printed monopole antenna: The planar inverted cone antenna (PICA)," *IEEE Trans. Antennas Propag.*, Vol. 52, 1361–1364, 2004.

3. Ma, T. G. and S. K. Jeng, "Planar miniature tapered-slot-fed annular slot antennas for ultrawide-band radios," *IEEE Trans. Antennas Propag.*, Vol. 53, 1194–1202, 2005.
4. Si, L. M. and X. Lv, "CPW-fed multi-band omni-directional planar microstrip antenna using composite metamaterial resonators for wireless communications," *Progress In Electromagnetics Research*, PIER 83, 133–146, 2008.
5. Pendry, J. B., A. J. Holden, D. J. Robins, and W. J. Stewart, "Magnetism from conductors and enhanced nonlinear phenomena," *IEEE Trans. Microwave Theory Tech.*, Vol. 47, 2075–2084, 1999.
6. Smith, D. R., J. P. Willie, D. C. Vier, S. C. Nemat-Nasser, and S. Schultz, "Composite medium with simultaneously negative permeability and permittivity," *Phy. Rev. Lett.*, Vol. 84, 4184–4187, 2000.
7. Yang, X., Z. Yu, Q. Shi, and R. Tao, "Design of novel ultra-wideband antenna with individual SRR," *Electron. Lett.*, Vol. 44, No. 19, 1109–1110, 2008.
8. Baena, J. D., et al, "Equivalent-circuit models for split-ring resonators and complementary split-ring resonators coupled to planar transmission lines," *IEEE Trans. Microwave Theory Tech.*, Vol. 53, No. 4, 1451–1461, 2005.
9. Jin, J. M., *The Finite Element Method in Electromagnetics*, 2nd edition, Wiley-IEEE Press, 2002.

Design and Fabrication of Wide Band Printed Multi-ring Fractal Antenna for Commercial Applications

M. Kazerooni and A. Cheldavi
College of Electrical Engineering, Iran University of Science and Technology (IUST)
Narmak, Tehran, Iran

Abstract— This paper presents a wideband printed multi-ring fractal antenna. The ground plane is only under part of the feed line. Good performance of S-parameters is obtained. This optimized fractal antenna has the potential of operating in several of the currently broad band commercial existing systems such as, Bluetooth and GSM.

1. INTRODUCTION

Microstrip patch fractal antennas have been rapidly developed for multi-band and broad band in high data rate systems known as wideband communication systems. The use of microstrip fractal geometry antennas in electromagnetic radiations has been a recent topic of interest in the world. It has been shown that fractal shaped antennas exhibit features that are directly associated with the geometric properties of fractals. One property associated with fractal geometry that is used in the design of super special antennas is self-similarity, which means that some of their parts have the same shape as the whole object but at a different scale [1–3]. The construction of many ideal fractal shapes is usually carried out by applying an infinite number of times an iterative algorithm such as the multiple reduction copy machine (MRCM) algorithm [1]. In such iterative procedure, an initial structure called generator is replicated many times at different scales, positions and directions, to grow the final fractal structure. A fractal antenna can be designed to receive and transmit over a wide range of frequencies using the self-similarity properties associated with fractal geometry structures. The applications of fractal shapes are on scattering problems, array techniques, reduced size and multi-band and wide-band antennas. In antenna application, the Minkowski loop [4, 5], the Koch curve monopole [4, 5], the Koch island patch [6], the Sierpinski carpet [7, 8] and the Sierpinski gasket have been reported [9, 10]. Therefore, traditional fractals such as Koch curves, Sierpinski triangles, and Minkowski fractals, etc, have been used to design compact antennas for multiband or broadband operation. D. L. Jaggard et al. [11] showed that the same kind of geometrical similarity relations at several growth stages were found in the electromagnetic behavior of the fractal body. The diffraction of fractally serrated apertures [12], [13] the reflection and transmission coefficients of fractal multilayers [14] and the sidelobe properties of some fractal arrays [15], [16] are other examples of studies currently available in the literature that relate fractals and electromagnetic.

In our work, a simple structure of printed multiple elliptic ring fractal antennas has investigated and also demonstrated. A significant matched bandwidth compared to the conventional multiple ring monopole antenna has obtained. Many possibilities of improved design have been investigated by varying the width of the rings. On the other hand, this type of structure can achieve larger matched bandwidth in comparison to conventional multiple ring monopole antennas. Simulation and experimental results confirm that this type of antenna can achieve better performance than the conventional multiple ring monopole antennas, and obtain very wide bandwidth of more than 14 GHz under -10 dB. By tuning of elliptic ring partial ground size the optimum operation is obtained. The gap between antenna and ground plane is the key point for impedance matching performance of radiation pattern and S-parameters. On the other hand, a novel wide-band fractal patch antenna is designed, measured and analyzed. Based on these concepts, a compact printed fractal antenna has constructed with the aid of an electromagnetic (EM) simulator using Ansoft HFSS (a full wave simulator). The impedance antenna structure bandwidth of the proposed antenna could reach 64%, which has rarely been reported for patch antennas. All results and performance are validated and confirmed experimentally.

2. DESCRIPTION OF THE ANTENNA STRUCTURE

Figure 1 shows the geometry of the fabricated antenna. The exact dimensions for the proposed antenna are also given in Figure 1. The antenna is fed by microstrip line of width of 3.864 mm to match the 50 Ω SMA connector is then attached to end of the microstrip line, under which is

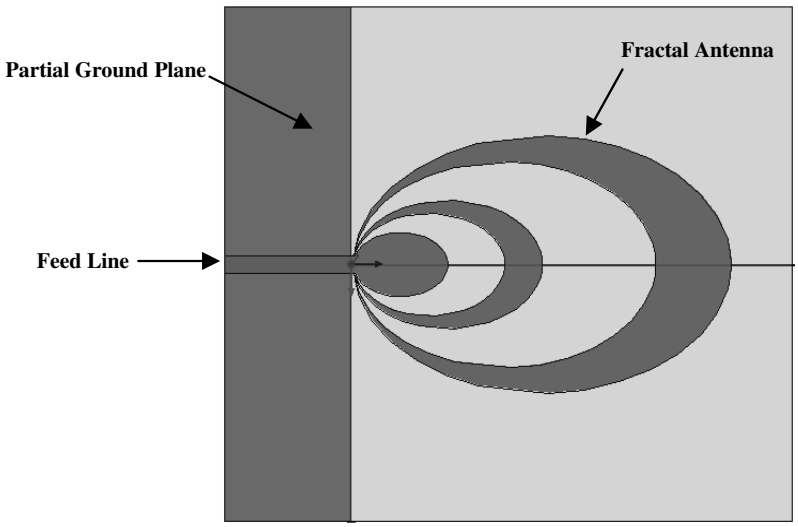

Figure 1: Fractal antenna structure using Ansoft HFSS software.

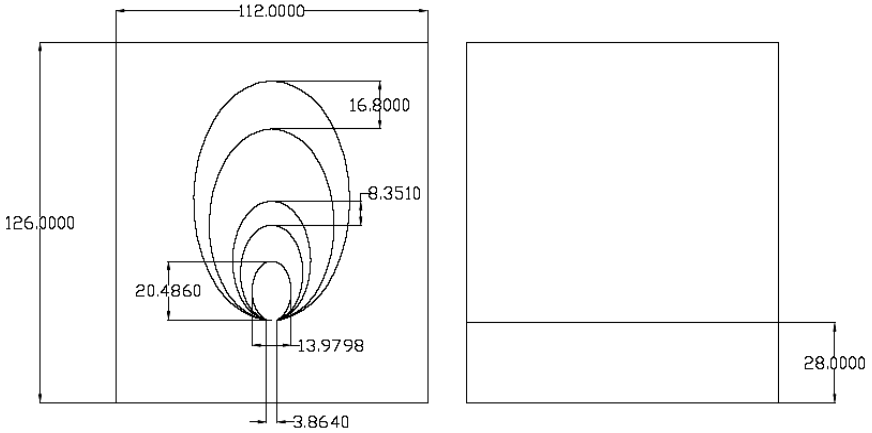

(a)

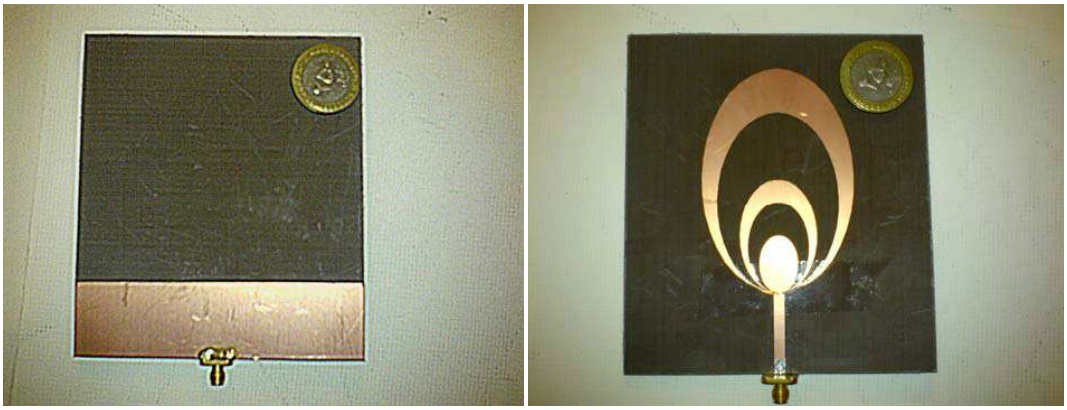

(b) (c)

Figure 2: (a) Exact dimensions of proposed planar microstrip multi-ring fractal antenna in mm, (b) Fabricated antenna structure, (c) Feed and partial ground plane.

the ground plane. There is no plane under antenna and the antenna's ground plane is only under the feed. The gap between ground plane and antenna is 0.663 mm to achieve better performance. The optimized length and width of the ground plane is 28 and 112 mm respectively. The patch is printed on a microwave substrate with low relative permittivity and thickness $H = 0.62$ mil.

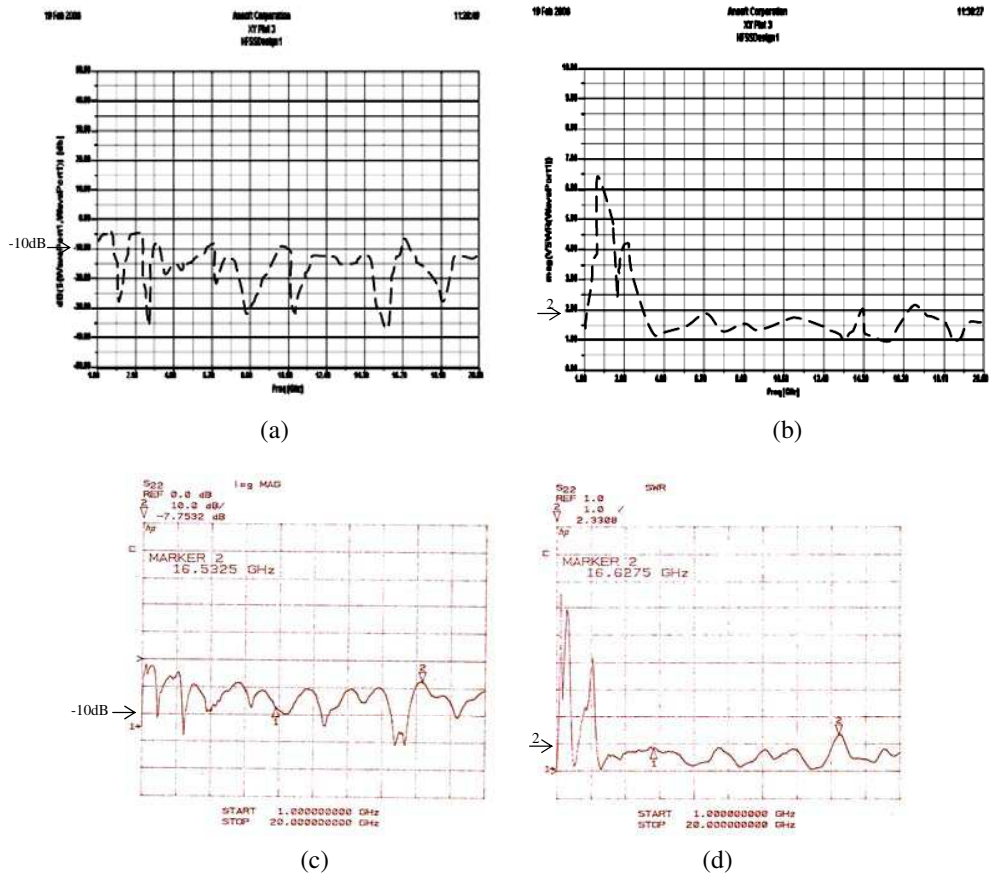

Figure 3: Simulated and measured results for fabricated antenna. (a) Simulated return loss, (b) Simulated VSWR, (c) Measured return loss, (d) Measured VSWR.

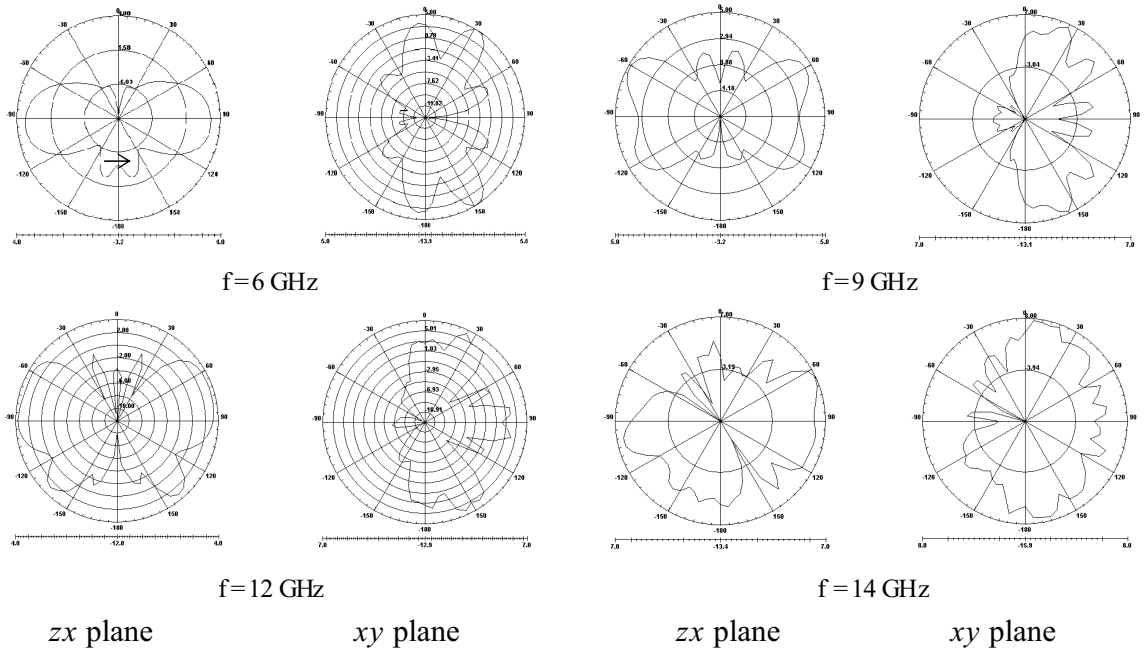

Figure 4: Radiation patterns of proposed antenna in the some operation frequencies.

3. SIMULATED AND EXPERIMENTAL RESULTS

Design procedure and simulation of the proposed antenna is carried out by commercially full wave simulator, Ansoft HFSS (Figure 1) and measured with a vector network analyzer (VNA). The

exact dimensions and fabricated antenna is shown in Figure 2. Figure 3 compares the simulated and measured return loss and VSWR of the antenna. The measured impedance bandwidth of the optimized antenna is approximately 64% (2 GHz–16 GHz). In addition, the Good agreement can be seen between the simulated and measured results. From the measured results, it can be clearly concluded that the antenna has good improved performance for all 2–16 GHz band. In order to determine the antenna's radiation patterns of the antenna in zx-plane and xy-plane at four different frequencies in dB over the operation frequency band are measured in an anechoic chamber and acceptable radiation patterns were obtained and were well controlled over frequency range for this wideband antenna, as shown in Figure 4. It is observed that the results are in good agreement in all the patterns, though some deviations are noticeable due to the interference of the feeding cable during the measurement procedure. The patterns of the bands exhibit some degree of similarity, although it is not strong. It is expected that when operating at higher frequencies, ripples along the plots are inevitable due to the fixed ground plane size. Therefore, The fact that the ground plane is not self-scalable, i.e., its electrical size becomes longer as the frequency increases or on the other hand, as the wavelength becomes smaller, the microstrip feed ground plane begins to look much larger, is responsible for the characteristic ripple displayed at the higher frequencies.

4. CONCLUSION

A novel 2–16 GHz fractal planar microstrip antenna with excellent very wide band performance has been successfully demonstrated. This antenna has VSWR 2 : 1 or better, inherent 50 Ω, linear polarization, SMA center fed, partial ground plane and no balun required. The impedance bandwidth of the antenna is 64%. The antenna is compact, simple to design and easy to fabricate and applicable in wide band communication systems and commercial existing systems such as, Bluetooth and GSM.

ACKNOWLEDGMENT

The authors would like to thank S. O. Mohseni Armaki (for antenna testing), H. Faezi (for the some simulations) and M. Harir Fourush (for VSWR testing). Their assistance is gratefully acknowledged.

REFERENCES

1. Peitgen, H. O., H. Jürgens, and D. Saupe, *Chaos and Fractals*, Springer-Verlag, New York, 1990.
2. Barnsley, M. F., R. L. Devaney, B. B. Mandelbrot, H. O. Peitgen, D. Saupe, R. F. Voss, Y. Fisher, and M. Mc Guire, *The Science of Fractal Images*, Springer-Verlag, New York, 1988.
3. Jones, H., D. E. Reeve, and D. Saupe, *Fractals and Chaos*, A. J. Crilly, R. A. Earnshaw, and H. Jones, Eds., Springer-Verlag, New York, 1990.
4. Cohen, N., "Fractal antenna applications in wireless telecommunications," *Professional Program Proc. of Electronics Industry Forum*, 43–49, 1997.
5. Gianvittorio, J. and Y. Rahmat-Samii, "Fractal element antennas: A compilation of configurations with novel characteristics," *IEEE AP-S International Symposium*, Salt Lake City, 2000.
6. Puente, C., J. Romeu, R. Pous, J. Ramis, and A. Hijazo, "Small but long Koch fractal monopole," *Elect. Lett.*, Vol. 34, 9–10, 1998.
7. Hara Prasad, R. V., Y. Purushottam, V. C. Misrak, and N. Ashok, "Microstrip fractal patch antenna for multiband communication," *Elect. Lett.*, Vol. 36, No. 14, 1179–1180, 2000.
8. Song, C. T. P., P. S. Hall, H. Ghafouri-Shiraz, and D. Wake, "Fractal stacked monopole antenna with very wide bandwidth," *Elect. Lett.*, Vol. 35, No. 12, 945–946, 1999.
9. Puente, C., J. Romeu, R. Pous, and A. Cardama, "On the behavior of the Sierpinski multiband fractal antenna," *IEEE Trans. Antennas and Propagation*, Vol. 46, No. 4, 517–524, 1998.
10. Puente, C., "Fractal antennas," *Ph.D. Dissertation at the Dept. of Signal Theory and Communications*, Universitat Politkcnica de Catalunya, June 1997.
11. Jaggard, D. L. and T. Spielman, "Triadic cantor target diffraction," *Microwave Opt. Technol. Lett.*, Vol. 5, 460–466, Aug. 1992.
12. Beal, M. M. and N. George, "Features in the optical transforms of serrated apertures and disks," *J. Opt. Soc. Amer.*, Vol. 6, No. 12, 1815–1826, Dec. 1989.
13. Kim, Y., H. Grebel, and D. L. Jaggard, "Diffraction by fractally serrated apertures," *J. Opt. Soc. Amer.*, Vol. 8, No. 1, 20–26, Jan. 1991.

14. Sun, X. and D. L. Jaggard, "Wave interactions with generalized cantor bar fractal multilayers," *J. Appl. Phys.*, Vol. 70, No. 5, 2500–2507, Sept. 1991.
15. Kim, Y. and D. L. Jaggard, "The fractal random array," *Proc. IEEE*, Vol. 74, 1278–1280, Sept. 1986.
16. Goutelard, C., "Fractal theory of large arrays of lacunar antennas," *Electromagn. Wave Propagat. Panel Symp. (AGARD-CP-528)*, 35/1–35/15, France, June 1992.

Analysis of the Multi Surface Current Distributed within in a Broadband Printed Monopole Antenna

Sung-Keun Jeon[1], **Nam Kim**[2], **Seung-Woo Lee**[2], **and Liu-Yu Lin**[1]

[1]Department Bio and Information Technology, Chungbuk National University, Korea
[2]Division of Information and Communication Eng., Chungbuk National University, Korea

Abstract— In this study, we developed a novel broadband printed monopole antenna for PCS/IMT-2000/WLAN terminals by widening the current flow. To compensate for the narrow bandwidth characteristic, which is one of the disadvantages of the general printed monopole antenna, we added a diamond shape patch to induce the current to move in various directions. In addition, the frequency characteristics were optimized with various design parameters. The bandwidth of the realized antenna was 1.66∼3.04 GHz (58.72%) at a return loss that was below −10 dB, which contains the bandwidth required for the PCS/IMT-2000/WLAN band.

1. INTRODUCTION

Currently, mobile communication systems have an advantage in that various mobile communication services including voice, data, moving images, and digital TV broadcasting can be easily exchanged without time and spatial limitations. As a result of the convenience of mobile communication, the number of users and the development of mobile communication systems has rapidly increased. The advancement of various mobile communication systems including cellular, PCS, IMT-2000, WLAN (Wireless LAN), PDA, and satellite DMB, requires the development of high-functioning and high-performance personal portable terminals and small, light and thin antennas.

In this study, we developed a novel broadband printed monopole antenna by widening the surface current flow. A diamond shape patch was inserted into the dual band antenna (1.60∼2.32 GHz, 2.73∼3.04 GHz) to resonant the middle band (2.30∼2.73 GHz). The proposed antenna was manufactured and its performance was evaluated.

2. STRUCTURE OF ANTENNA

The antenna proposed in this study has two different types of resonant bands, which originate from the different lengths of the antenna. The diamond shaped patch was added for the resonance of the stopband between the two resonant bands and to extend the current flow. In addition, the diamond patch was designed to operate at the broadband frequency. Figure 1 shows a schematic of the proposed monopole antenna. The size of the antenna was $30 \times 60 \times 1\,\text{mm}^3$ and a substrate with a heritability of 4.62 was used. The size of the ground plane was $30 \times 45\,\text{mm}^2$, and the size of patch was $30 \times 10\,\text{mm}^2$. The height and heritability of the substrate were determined and impedance matching was achieved by adjusting the micro-strip line width. This was done to smooth the current flow identity width of the whole lines. The optimized parameters are shown in Table 1.

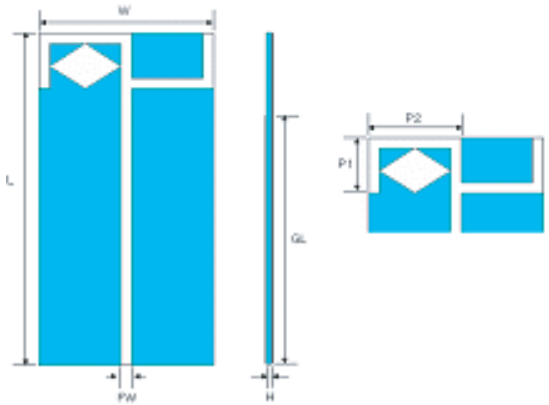

Figure 1: Structure of the proposed printed monopole antenna.

Table 1: Optimized parameter for the proposed antenna.

Parameter	Definition of Parameter	Value (mm)
L	Length of substrate	60
W	Width of substrate	30
FW	Width of feeding line	1.856
H	Height of substrate	1
GL	Length of ground plane	45
P1	Length of patch	10
P2	Width of patch	15

3. DESIGN AND ANALYSIS OF THE PROPOSED ANTENNA

Microwave Studio was used to design and simulate the proposed antenna. Since the proposed antenna was an internal antenna, an antenna size of $30 \times 60\,\text{mm}^2$ was chosen prior to the simulation. In order to guarantee a minimum frequency range we first decided that the longest line would be 40 mm. In addition, in order to design to the dual band structure, the shortest line decided 30 mm.

By using the optimized ground plane length the current flow at each resonance frequency was tested. Figure 2 shows the surface current flow at each resonance frequency, 1.75 GHz and 2.88 GHz. As shown in Figure 2, the first resonance part increased the left patch by 40 mm, and the second resonance part increased the right patch by 30 mm.

There was a -10 dB return loss of the dual band antenna as a result of the optimization process Figure 3. From the results of the simulation, the -10 dB bandwidth of the proposed dual-band antenna was found to have dual-band characteristic.

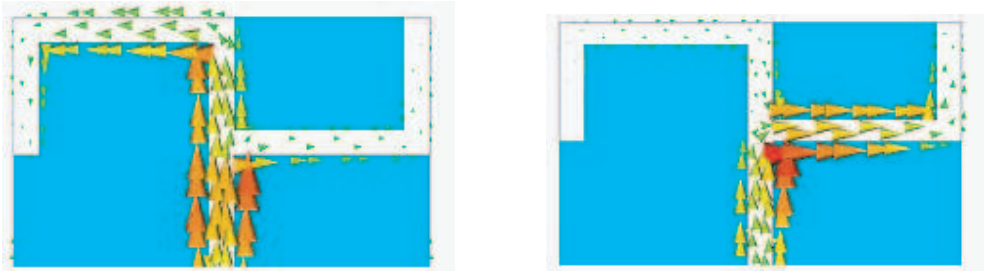

(a) (b)

Figure 2: Surface current on the radiator, (a) $f = 1.75$ GHz, (b) $f = 2.88$ GHz.

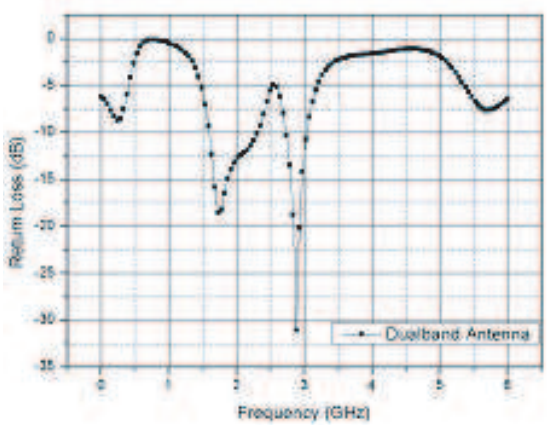

Figure 3: Return loss of the dual band antenna.

In order to achieve a resonance that was not the resonance part in the proposed dual band antenna, we analyzed the dual band antenna from the perspective of the current flow. The resonance length of the monopole antenna must satisfy the following criteria; $\lambda/4$ length of the frequency. However, the band did not satisfy this criterion. Therefore, we inserted a diamond shape patch that did satisfy the resonance length, while not altering the dual band characteristic of the antenna. When this was done we were able to achieve broadband characteristics. We also examined patches that were in the form of a triangle, circle and diamond to create and examine a variety of current paths that have broadband characteristics. From this analysis, we found that the diamond shape patch was optimal. Figure 4 shows the multi current flow and surface current flow at 2.4 GHz. Figure 4(a) shows that the conventional dual band antenna has only the two paths (①, ② Figure 4(a)) but the proposed antenna has other paths (③, ④, ⑤ Figure 4(a)) in addition to the two paths of the conventional dual band antenna (①, ② Figure 4 (a)). Figure 5 shows the −10 dB return loss of the proposed broadband monopole antenna.

As a result of the optimization process, the resonance band was 1.67∼3.02 GHz (57.57%), which satisfies the PCS/IMT-2000/WLAN band.

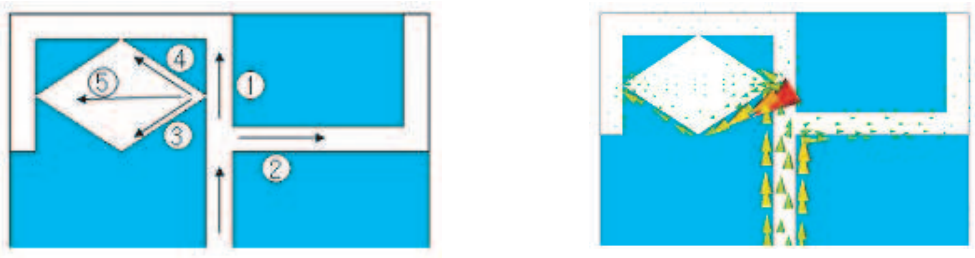

(a) (b)

Figure 4: Current flow of the proposed antenna and surface current at 2.4 GHz. (a) Current flow of the proposed antenna. (b) Surface current at 2.4 GHz.

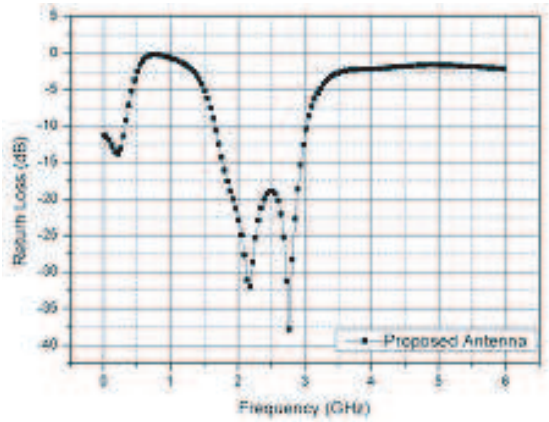

Figure 5: Return loss of the proposed broadband monopole antenna.

4. MANUFACTURING AND MEASUREMENT OF ANTENNA

Figure 6 shows the actual structure of the manufactured antenna. The simulation results and the experimental measurements of the proposed antenna are compared in Figure 7. As shown in Figure 7, the experimental results were very similar to the results obtained from the simulation. The −10 dB return loss in the simulation resulted in a bandwidth of 1.67∼3.02 GHz (57.57%), and the bandwidth determined from the experiments was 1.66∼3.04 GHz. These bandwidths are capable of satisfying PCS (1.750∼1.870 GHz), IMT-2000 (1.920∼2.170 GHz) and WLAN (2.400∼2.480 GHz).

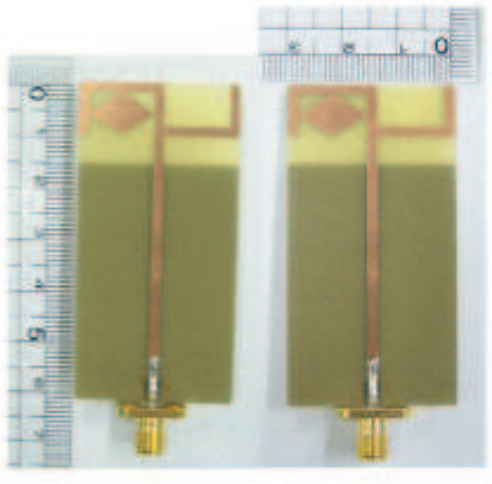

Figure 6: Photograph of the fabricated antenna.

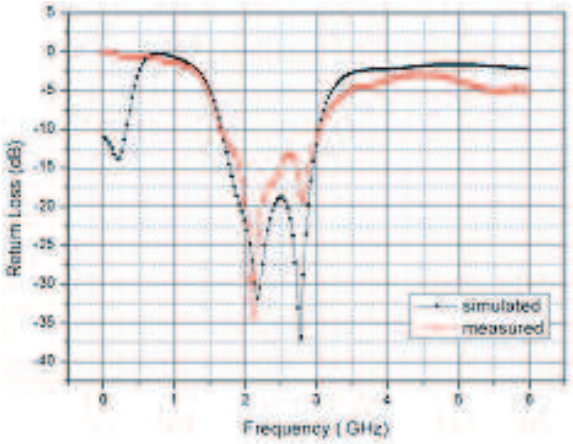

Figure 7: Comparison of the simulated and experimentally measured return loss.

5. CONCLUSION

In this study, we designed and manufactured a broadband monopole antenna that satisfied the PCS/IMT-2000/WLAN band. The current flow of a basic antenna, which has dual resonances, was analyzed by simulation. After analysis, the design of the broadband antenna was modified by adding a diamond shape patch. Using this novel design, the efficiency of the antenna was verified by experimental measurements in an anechoic chamber. From the experimental measurements, the -10 dB bandwidth of the proposed antenna was found to be 1.66∼3.04 GHz (58.72%)

The antenna proposed in this paper has a simple structure and from the point of view of the current flow, this novel design has the potential to greatly expand the field of broadband antenna research.

ACKNOWLEDGMENT

This work was supported by the grant of the Korean Ministry of Education, Science and Technology (The Regional Core Research Program/Chungbuk BIT Research-Oriented University Consortium)

REFERENCES

1. Kuo, Y.-L. and K.-L. Wong, "Printed double-T monopole antenna for 2.4/5.2 GHz dual-band WLAN operations," *IEEE Trans. Antennas Propagation*, Vol. 51, No. 9, Sep. 2003.
2. Liang, J., C. C. Chiau, X. Chen, and C. G. Parini, "Printed circular disc monopole antenna for ultra wideband applications," *Electronics Letters*, Vol. 40, No. 20, Sep. 2004.
3. Huynh, M.-C. and W. Stutzman, "Ground plane effects on planar inverted-F antenna (PIFA) performance," *IEEE Proc.-Microw. Antenna Propagation*, Vol. 150, No. 4, Aug. 2003.
4. Kim, N., S. M. Park, and J. M. Kim, "The design and SAR analysis of the spiral planar monopole antenna for dual-band," *The Journal of Korea Institute of Electromagnetic Engineering and Science*, Vol. 18, No. 12, Dec. 2007

Divided Two-arms Spiral Slot Antenna fed by Coplanar Waveguide Using the Different Magnetic Phase Different

S. W. Park[1], **N. Kim**[1], **S. Y. Rhee**[2], **and S. W. Lee**[1]

[1]Chungbuk National University, Korea
[2]Chonnam National University, Korea

Abstract— In this paper, we proposed a divided two-arms spiral slot antenna fed by coplanar waveguide using the magnetic flow at slots. This antenna has characteristics of which one is to short-circuit at the end of the slot and another is to turn spirals separately. To reduce the offset of the magnetic flow, two spiral slots are fed by the different phase of π (180°). Because we proposed the printed two-arms spiral slot antenna without a balun circuit, the antenna size become smaller substantially. And frequency characteristics are studied by using the various design parameters. The bandwidth of the fabricated antenna is 2.7 GHz ∼ 12 GHz below the return loss of −10 dB.

1. INTRODUCTION

In the last years, there are various demands for high capacity wireless systems. One of the demands is to downsize antennas. There are merits that small antennas are loaded in the portable devices, and then have bad effects that increase the current density and quality factor that seriously decrease the bandwidth. Moreover, an upward trend of working frequency is going up to the ultra high frequency range (3 ∼ 30 GHz) due to Limited frequency resource. Because of these things, although microstrip antennas have long been used as the efficient radiators at microwave frequencies, the coplanar waveguide (CPW) feeding method is compatible for new research trends. The CPW feed is smaller the radiation loss and the dispersion than the microstrip and removes the via holes that deteriorate the antenna performance at high frequencies.

The characteristics of the spiral antenna are wider bandwidth and circular polarization. Advantages of the spiral antenna are various radiation patterns and wide beam width. Recently, multi-functions of the spiral antenna that are wideband, multi-band, beam-control antenna, etc. are actively researched. At the synchronous time, a progress wave between the adjacent arms radiates, and then does not happen as countervailed at the reverse phase.

In this paper, we propose the new spiral slot antenna fed by coplanar waveguide and analyze this antenna by using the FDTD method. Since the magnetic fields are induced with 180° different phase at the starting points of spiral slots, an offset by different phase is minimized, by using this, a balun circuit that limits bandwidth of an antenna is useless unlike the microstrip. Advantages of this antenna are to decrease in 3-dimensional volume and simplify the antenna design or progresses. And one of the characteristics of this structure is that the end of the slots is made of a short circuit at the electric field. So, the magnetic flow is the source of radiations.

2. ANTENNA DESIGN

The planar two-arms Archimedean spiral antenna fed at the center of the spiral plane radiates a circularly polarized wave in the direction normal to the spiral plane. But, the two-arms eccentric spiral antenna generates a circularly polarized wave with a main beam off-normal to the spiral plane. The proposed antenna is similar to the eccentric antenna in that they are fed at the eccentricity. Because of the narrow spaces of the center of arms, the power feeding must be performed by the vertical. This contributes the device to expanding the volume. In addition, two-port feeing needs a balun circuit that complicates a physical processing. To supplement these disadvantages, we attempt to introduce a CPW feeding.

The geometry of the divided spiral slot antenna is shown in Figure 1. The short ends have the higher inductance and lower resonance frequency than the open. The whole size of the antenna is $75 \times 45 \times 1\,\text{mm}^3$, the substrate is FR-4 consist of the copper and the dielectric constant of 4.62. The left and right slot are same size and design but the feed has a phase difference. Usually, An existing two-arms spiral antenna rotates with two adjacent line dependently, and then we proposed that the left and right spiral slot rotate separately, decided the position $S1$, $S2$ to minimize unintended coupling between slots and the feeding line, and frequency characteristics are optimized with various design parameters.

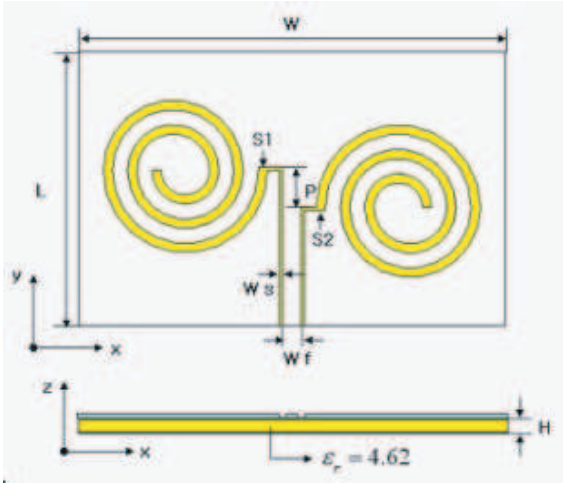

Figure 1: Structure of the spiral antenna.

3. ANTENNA FABRICATION AND MEASUREMENT

Figure 2 is the photograph of the fabricated antenna. The parameters shown in Table 1 represent values optimized through sweeping function of the computer simulation tool. And Figure 3 shows the simulated and measured return loss on the optimized antenna. Between the frequency ranges of 2.7 GHz to 12 GHz, this antenna has a −10 dB return loss response. The simulated results reasonably agree with the experimental results.

Parameters	Value [mm]
W	75
L	45
H	1
P	7
Ws	0.5
Wf	4

Table 1: Optimized parameters for the proposed antenna.

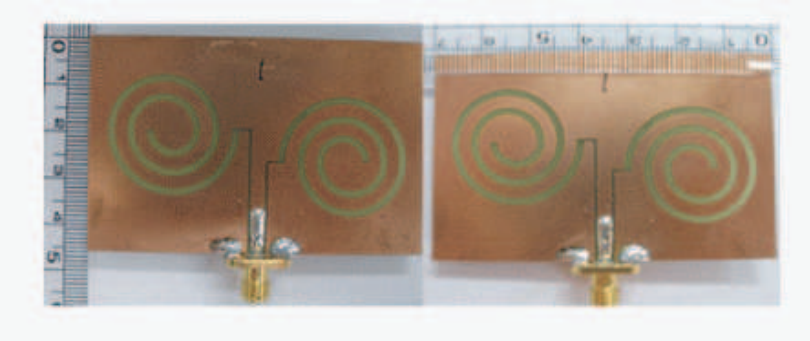

Figure 2: Photograph of the fabricated antenna.

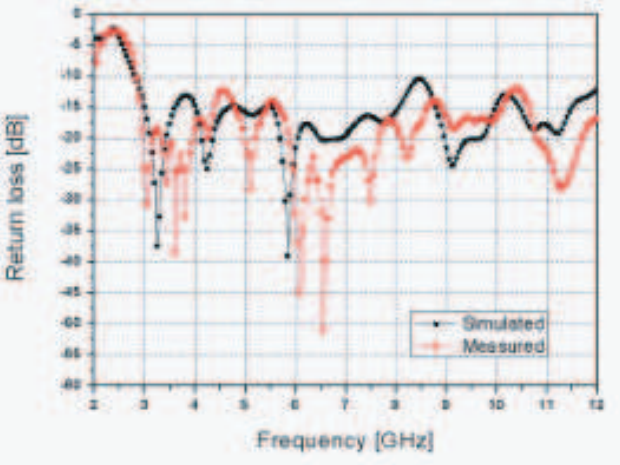

Figure 3: The simulated and measured return loss on the optimized antenna.

Figure 4 shows the measured gain. In the operating frequency range, the gain of this antenna is values from 3.4 to 6.1 dBi, the maximum variation is 6.1 dBi. This results confirm the proposed antenna to apply to UWB (Ultra Wide Band) antenna. Figure 5 shows the axial ratio in the direction of the main beam. A minimum axial ratio level of 0.7 dB was obtained at 6.2 GHz and the 3 dB fractional bandwidth of the axial ratio was 4.2 GHz ∼ 4.7 GHz, 5.9 GHz ∼ 6.8 GHz. Figure 6 presents the measured radiation patterns. This antenna radiates a circularly polarized wave in the vertical direction to the spiral plane at 4.5 GHz, and the higher the operating frequency is, the more horizontal the direction of main beam is.

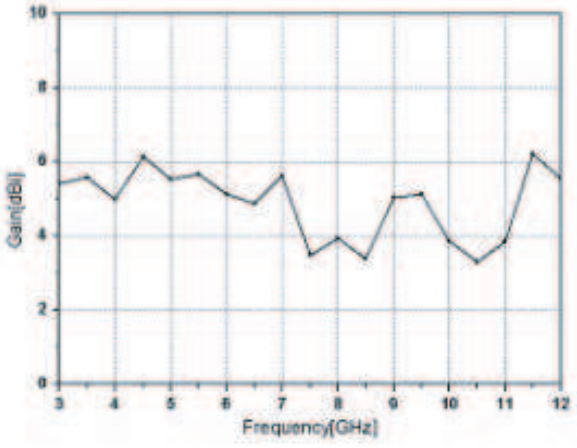

Figure 4: The measured gain of the proposed antenna.

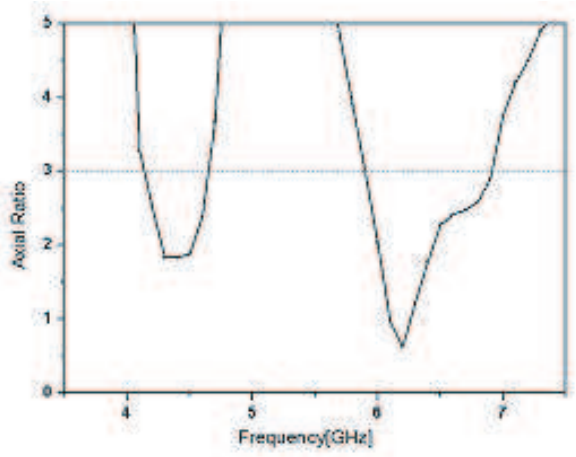

Figure 5: The axial ratio in the direction of the main beam.

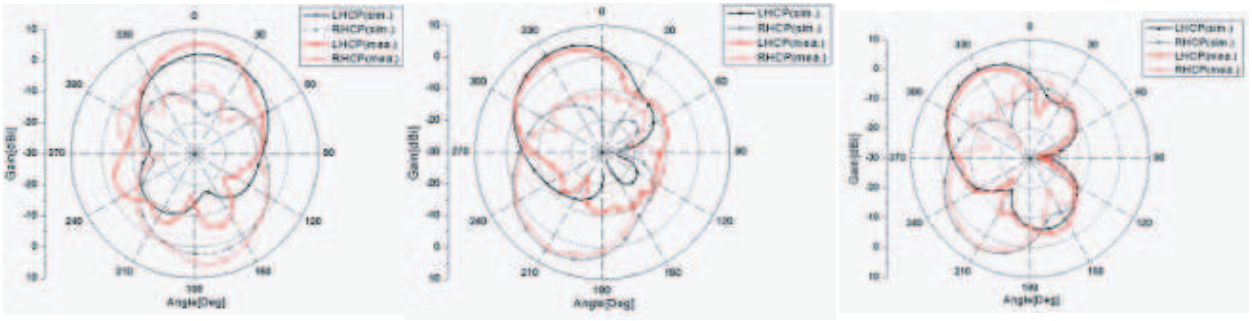

4.5 GHz 6 GHz 6.5 GHz

Figure 6: The measured radiation pattern of the circular polarization.

4. CONCLUSIONS

We designed and fabricated the divided two-arms spiral slot antenna fed by the coplanar waveguide using the magnetic flow. This antenna has characteristics of which one is to short-circuit at the end of the slot and another is to turn spirals separately. Advantages of this antenna are that the 3-dimensional volume is reduced using the CPW structure and the balun circuit is useless. Because two spiral slots are fed by the different phase of π (180°). we are able to minimize the offset caused by the different magnetic flow. And frequency characteristics are studied using the parameter sweeping. The bandwidth of the realized antenna is 2.7 GHz ∼ 12 GHz below the return loss of −10 dB, the gain of this antenna is values from 3.4 to 6.1 dBi, and the 3 dB fractional bandwidth of the axial ratio is 4.2 GHz ∼ 4.7 GHz, 5.9 GHz ∼ 6.8 GHz. We validate the various radiation patterns.

ACKNOWLEDGMENT

"This work was supported by the grant of the Korean Ministry of Education, Science and Technology" (The Regional Core Research Program/Chungbuk BIT Research-Oriented University Consortium) "This research was supported by the MKE (Ministry of Knowledge Economy), Korea,

under the ITRC (Information Technology Research Center) support program supervised by the IITA (Institute of Information Technology Advancement)" (IITA-2008-(C1090-0801-0034)).

REFERENCES

1. Matsuzawa, S. and K. Ito, "Circularly polarised printed antenna fed by coplanar waveguide," *Electron. Lett.*, Vol. 32, No. 22, October 1996.
2. Morgan, T. E., "Spiral antennas for ESM," *IEE Proc., Part H*, Vol. 132, No. 4, 245–251, July 1985.
3. Gloutak, R. T. and N. G. Alexopulos, "Two-arm eccentric spiral antenna," *IEEE Trans. on Antennas Propagat.*, Vol. 45, No. 4, 723–730, April 1997.
4. Kaiser, J. A., "The archimedean two-wire spiral antenna," *IRE Trans. on Antenna Propagat.*, Vol. 8, 312–323, May 1960.
5. Balanis, C. A., *Antenna Theory*, John Wiley & Sons, 2005.
6. Oh, D. Y., M. K. Kim, and I. M. Park, "Two-arm microstrip spiral antenna with a circular slot on the ground plane," *The Journal of Korea Institute of Electromagnetic Engineering and Science*, Vol. 13, No. 5, June 2002.
7. Kim, N., S. M. Park, and J. M. Kim, "The design and SAR analysis of the spiral planar monopole antenna for dual-band," *The Journal of Korea Institute of Electromagnetic Engineering and Science*, Vol. 18, No. 12, December 2007.

Design of Multi-Band Dual-Polarized Two-Port E-shape Microstrip Antenna

A. M. El-Teger[1] and A. M. Abdin[2]

[1]Electronics Department, M. T. C., Cairo, Egypt
[2]Department of Communications and Electronics, Shorouk Academy, Cairo, Egypt

Abstract— In this paper, a novel compact size E-shape microstrip single-layer patch antenna is designed, analyzed, and fabricated for multi-band wireless applications. This E-shape antenna is designed to operate at three sub-bands, namely 5 GHZ, 10 GHz and 20 GHz with about 8% bandwidth at each frequency. It has two ports excited with microstrip line feed mechanism. The physical parameters of the novel structure as well as its partial ground plane are analyzed, and optimized using commercial 3D electromagnetic simulation packages. Return loss at both ports (S_{11}, S_{22}), voltage standing wave ratio (VSWR), and isolation between ports (S_{21}) are carried out. Measurements are in good agreement with simulated results, which validates the design strategy and the proposed structure. Therefore, the proposed antenna is very promising for various modern communication applications.

1. INTRODUCTION

With the increased development of wireless communications, the urgency to design low volume, compact, low profile planar configuration and wideband multi-frequency planar antennas become highly desirable. Such antennas would greatly simplify the installation of multi-band systems and provide a much more aesthetic appearance. The approach of the microstrip antenna can fulfill these requirements because it enjoys all the advantages of printed circuit technology. On the other hand, the drawbacks of basic microstrip structures include narrow bandwidth, loss, half plane radiation and limitation on the maximum gain. For many practical designs, the advantages of microstrip antennas far outweigh their disadvantages [1]. However, research is still continuing today to overcome some of these disadvantages.

To improve the microstrip antenna bandwidth, some techniques may be obtained such as increasing the substrate thickness, introducing parasitic element either in coplanar or in multilayer configuration, and performing slots in radiator patch. The last approach is very promising because it can provide excellent bandwidth improvement and maintain a single-layer radiating structure to preserve the antenna's thin profile characteristic. Therefore, U-slot patch antennas are introduced [2] and finally E-shape patches are developed [3, 4].

Dual frequency operations can be realized by exciting the microstrip patch antenna using a single feed [5] or dual feed [6]. Dual Feed has the advantage of facilitating the use of multi-polarization therefore it attracts many researchers [7, 8]. But most of these introduced antennas are based on multilayer structures. Therefore, this paper, introduces a novel E-shape microstrip patch antenna for multi-band wireless applications and multi-polarization facility using the advantage of a single layer structure.

2. ANTENNA STRUCTURE

The proposed antenna is shown in Fig. 1. The initial rectangular patch is groundless with parameters width W_p and length L_p. It is fed by two microstrip lines at the center of each side with widths W_{f1} and W_{f2}. In this case both lines are chosen to be 50 Ω with the shown ground underneath. The partial ground has width W_{sub} and length L_{sub} with hollow rectangle inside (W_s and L_s). Two parallel slots are incorporated inside the rectangular patch antenna to perturb the surface current path, introducing local inductive effects that are responsible for multi-mode excitation. The two slots and the center arm dimensions of the E-shaped patch control the higher resonant frequencies. On the other hand, the two perpendicular excitation ports are controlling the polarization whether it is linear or circular.

This E-shape antenna is designed to operate at three sub-bands, namely 5 GHz, 10 GHz and 20 GHz with greater than 8% bandwidth at each frequency. Antenna size and performance are compromised at these frequencies by using RT/Duroid 6010 substrate with ($\varepsilon_r = 10.5$ and $h = 1.25$ mm).

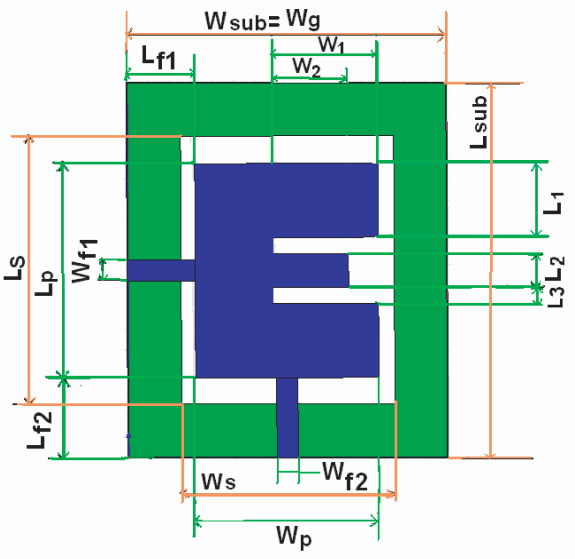

Figure 1: The E-shape microstrip antenna fed by two 50 Ω microstrip lines.

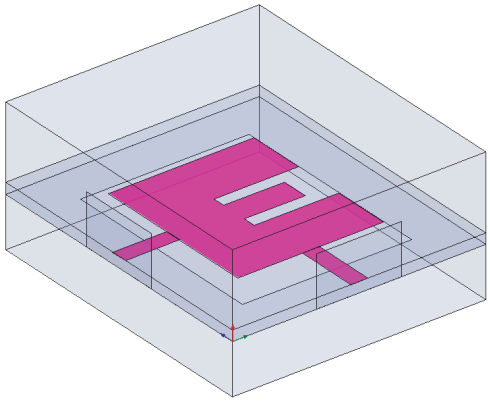

Figure 2: 3D model of the proposed E-shape microstrip antenna.

3. 3D EM MODELING AND OPTIMIZATION

This initial design of the proposed E-shape antenna is modeled using advanced 3D electromagnetic (EM) simulation packages; namely IE3D from Zeland and HFSS from Ansoft. The parameters are optimized to obtain the required specifications. The resultant physical dimensions are shown in Table 1. The created 3D model of the final structure is shown in Fig. 2. Fig. 3 shows the simulated insertion loss and return loss of the proposed E-shape microstrip antenna which guarantee the radiation at 5, 10 and 20 GHz with enough isolation between the two ports.

Table 1: Designed structure parameters (all dimensions are in mm).

L_p	W_p	L_s	W_s	L_{f2}	L_{f1}	$W_{f1} = W_{f2}$	L_3	L_2	L_1	W_2	W_1	L_{sub}	W_{sub}
20	17.2	25	20	7.5	64	2	1.5	3.2	6.9	7.2	10	35	30

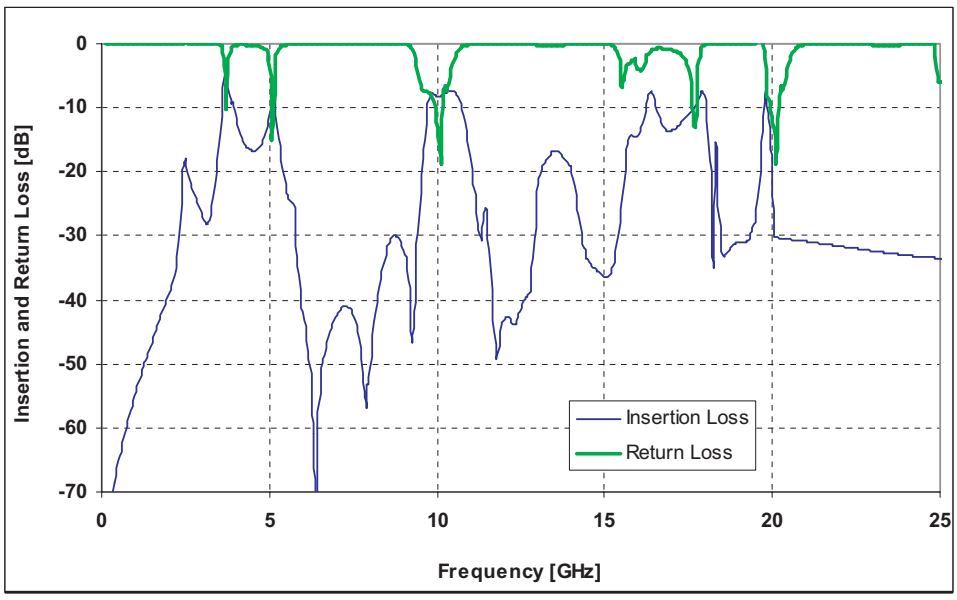

Figure 3: Simulated insertion loss and return loss of the proposed E-shape microstrip antenna.

4. FABRICATION AND MEASUREMENTS

The optimized antenna is fabricated using photolithographic technique. The measurement setup of the fabricated prototype is shown in Fig. 4. The antenna is measured using HP8510C VNA. The measured S parameters are plotted as shown in Fig. 5. S_{11} and S_{22} have many resonating points but they coincide with each other and maintain good isolation between ports at 5, 9.7, and 20 GHz only. This means that the proposed prototype is radiating at these three sub-bands, while other resonating points perform filtration between the 2 circuit ports. Fig. 6 is given as an example to show that there is fair agreement between simulation and measurements at the frequencies of interest. Table 2 summarizes measured S-parameters at each radiating frequency sub-band as well as its associated impedance bandwidth. It shows good agreement between required and achieved results, which validates the proposed prototype. This proposed antenna shows many advantages over the conventional E-shape ones [9], such as multi-band operation and multi polarization facility due to excitation using 2 perpendicular ports. Therefore, it is very promising for modern wireless applications.

Table 2: Measured results at each radiating frequency sub-band.

Frequency [GHz]		**S_{11} [dB]**	**S_{22} [dB]**	**Isolation [dB]**	**Bandwidth [%]**
Required	**Achieved**				
5	5	−17	−20	−27	10
10	9.7	−26	−21	−12	8
20	19.8	−30	−21	−18	7

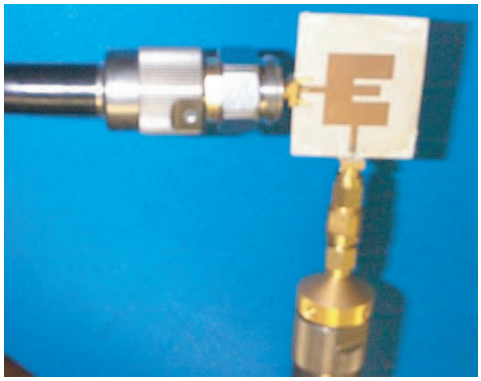

Figure 4: Photograph of the proposed E-shape microstrip antenna.

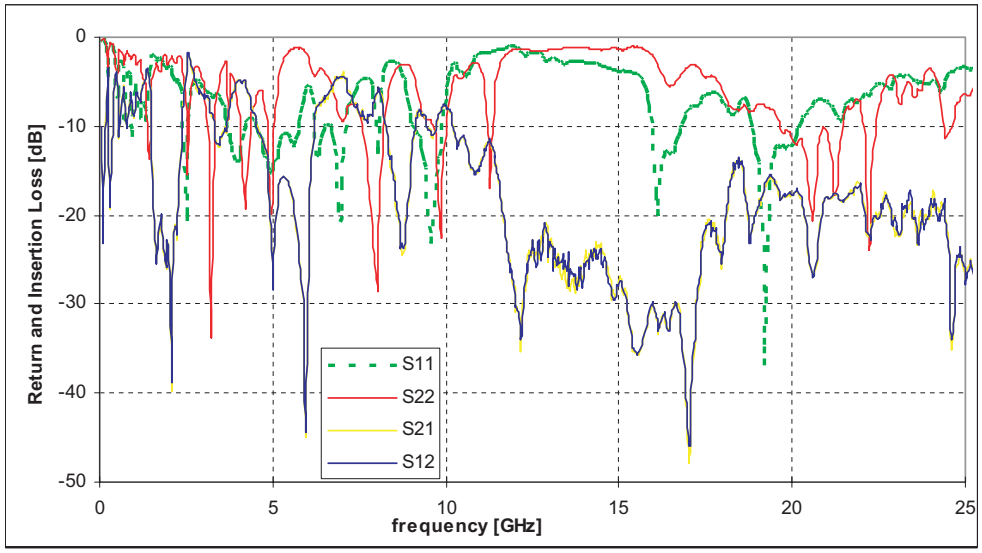

Figure 5: Measured S-parameters of the proposed E-shape microstrip antenna.

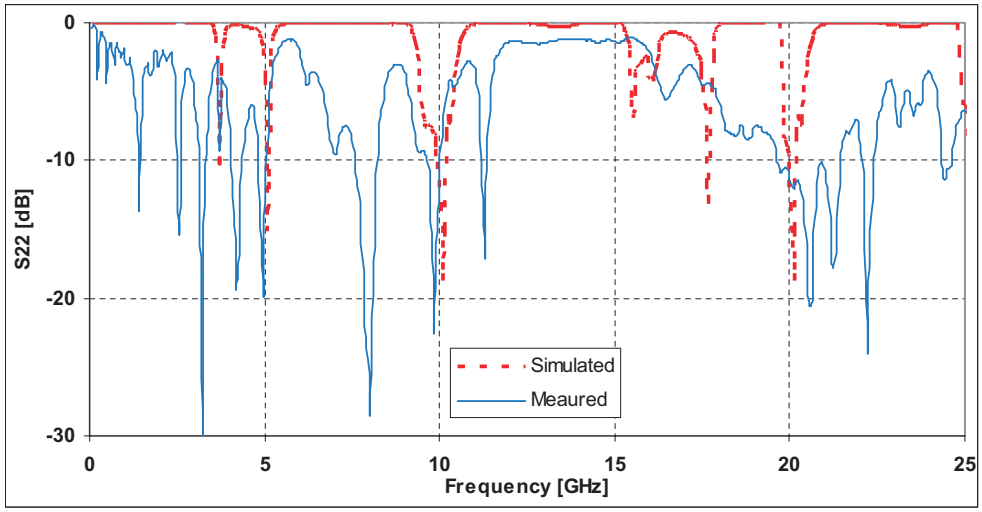

Figure 6: Comparison between simulated and measured return loss at port 2.

5. CONCLUSIONS

This paper introduces a novel E-shape microstrip patch antenna for multi-band and dual-polarization facility using single layer structure. This E-shape antenna operates at three sub-bands, namely 5, 9.7 and 20 GHz with 10%, 8%, and 7% bandwidths respectively. The physical parameters of the novel structure as well as its partial ground plane are analyzed, and optimized using commercial 3D electromagnetic simulation tools. Return loss at both ports (S_{11}, S_{22}) and isolation between both ports (S_{21}) are carried out to fulfill the requirements of the targeted communication system. Measurements are in good agreement with simulated results, which validates the design strategy and the proposed structure. Therefore, the proposed antenna is very promising for various modern communication applications.

REFERENCES

1. Garg, R., P. Bahartia, and A. Ittipiboon, *Microstrip Antenna Design Handbook*, Artech House, Boston, London, 2001.
2. Lee, K. F., et al., "Experimental and simulation studies of the coaxially fed U-slots rectangular patch antenna," *IEE Proc. Microw. Antenna Propag.*, Vol. 144, No. 5, 354–358, Oct. 1997.
3. Wong, K. L. and W. H. Hsu, "Abroad-band rectangular patch antenna with a pair of wide slits," *IEEE Trans. Antennas Propagat.*, Vol. 49, No. 9, 1345–1347, Sept. 2001.
4. Ge, Y., K. P. Esselle, and T. S. Bird, "E-shaped patch antennas for high-speed wireless networks," *IEEE Trans. Antennas Propagat.*, Vol. 52, No. 12, 3213–3219, Dec. 2004.
5. Paulson, M., S. O. Kundukulam, C. K. Aanandan, and P. Mohanan, "A new compact dual band dual polarized microstrip antenna," *Microwave and Opt. Technol. Lett.*, Vol. 29, No. 5, 315–317, Jun. 5, 2001.
6. Paul, B., S. Mridula, C. K. Aanandan, and P. Mohanan, "A new microstrip patch antenna for mobile communications and Bluetooth applications," *Microwave and Opt. Technol. Lett.*, Vol. 33, No. 4, 285–286, May 20, 2002.
7. Zürcher, J.-F., J. R. Mosig, A. K. Skrivervik, Q. Xu, and S. Vaccaro, "Multi-frequency, multi-polarization N-port printed planar antennas," *Microwave Engineering Europe*, Jun. 2000.
8. Paul, B., S. Mridula, C. K. Aanandan, K. Vasudevan, and P. Mohanan, "Octagonal microstrip patch antenna for dual band applications," *Proc. XXVIII URSI General Assembly*, 2005.
9. Ang, B.-K. and B.-K. Chung, "A wideband e-shaped microstrip patch antenna for 5–6 GHz wireless communications," *Progress In Electromagnetics Research*, PIER 75, 397–407, 2007.

A Circularly Polarized Dual-frequency Square Patch Antenna for TT&C Satellite Applications

A. M. El-Tager[1], **M. A. Eleiwa**[1], **and M. I. Salama**[2]

[1]Electronics Department, M. T. C., Cairo, Egypt
[2]Egyptian Armed Forces, Cairo, Egypt

Abstract— In this paper, a circularly polarized, dual-frequency, slotted square patch is designed with probe feeding mechanism to operate as the telemetry, telecommand and control (TT&C) antenna for satellite spacecrafts at 2.25 GHz and 3 GHz. This antenna is designed and optimized using 3D EM modeling. Several optimizations are performed to obtain the optimum values of the antenna physical parameters. Then a prototype is fabricated on a low loss teflon microstrip substrate and measured using VNA. Measurements are in great agreement with simulations, which verifies the design procedure and strongly recommends the proposed structure for TT&C satellite system applications.

1. INTRODUCTION

Due to size reduction of modern spacecrafts, onboard antennas of mini-satellites require a great deal of research and development. The dimensions of mini and microsatellites generally make reflector antennas inadequate, even if they are small [1, 2]. In addition, the placement of mechanical elements needed to deploy such antennas after reaching space is a significant problem. On the other hand, helical antennas were widely used in traditional spacecrafts, because of their wide beam and circular polarization. But, they have become unsuitable for mini-satellites [3]. The protrusion of such antenna on a retractable boom needs mechanical elements especially susceptible to mechanical failure. Inflatable antennas, despite their large dimensions, do not need protrusion mechanisms, but the technology is still in their infancy. Also, the deployment of a large bowl may easily block solar energy. For these reasons, the type of onboard antennas for small spacecraft should be investigated very carefully.

The main feature of minisatellite antennas is the lightweight structure and the high degree of integration. In small satellites, it is preferred to use antennas placed on outer walls, which may easily be bonded with a thermal blanket. Among the different types of low profile antennas, microstrip antennas gained the greatest interest. In this paper, a circularly polarized dual-frequency square patch probe-fed antenna is proposed, designed, fabricated and measured for TT&C satellite applications. The main advantage of CP versus linear polarization is that CP eliminates polarization mismatch losses caused by Faraday's rotation and varies the squint angle of polarization vectors between stations on the Earth.

2. INITIAL DESIGN

The uplink (U/L) depends on the strength of the signal originating on the earth and the manner in which the satellite receives it. The downlink (D/L), on the other hand, depends on how strongly the satellite can transmit the received signal and how good the reception is at the ground station. Thus by calculating a link budget, it can be determined whether the proposed link will function properly or not. This worst case link condition corresponds to the spacecraft being 10° above the horizon. Margin calculations for different kinds of antennas are shown in Table 1 based on the given equations in [4]. As a result, the margin of the microstrip patch antenna is found to be the best after that of the helical antenna. Moreover, single patch is suitable for this kind of satellites due to:

- Smaller size (6 cm × 6 cm).
- Omni directional antenna pattern characteristics with beamwidth > 100°.
- Antenna gain ($\geq$ 5 dB).
- Low and comformal profile.
- Low cost and light weight.
- Fixed antenna (no deployment for small sat.).

Table 1: Spacecraft to ground station link budget (worst case).

		Single Patch	**Monopole**	**Helical**	**Horn**	**2 element patch array**
3 db beam width of transmitting antenna	θ_t	101.4°	77.3°	66°	51.4°	77.2°
Alignment loss (includes the antenna pointing and misalignment losses)	L_{ptx}	−1.92	−3.213	−4.407	−7.26	−3.2216
Transmitting antenna gain	G_{tx}	6.93	2.2	10.18	8.1	7.6
Effective isotropic radiated power	$EIRP$	7.52	1.496	8.28	3.342	6.884
The carrier level	C	−128.37	−134.38	−127.59	−132.53	−129.009
Carrier-to-noise spectral density ratio	C/N_o	81.17	74.99	81.78	76.84	80.37
Energy in a bit relative to noise spectral density	E_b/N_o	30.38	24.38	31.16	26.22	29.75
Margin		14.98	8.98	15.76	10.82	14.35

It is preferable to use dual-frequency antenna for up and downlink to reduce size. In addition, the transmission wave can be circularly polarized to eliminate the effects that craft rotation could have on a linearly polarized wave. Some planar structures are proposed to obtain dual-frequency circular polarization (CP) radiation of a single-feed square microstrip antenna as in [5].

Initially, a square patch is designed. Then, central slot is perturbed to obtain circular polarization, as shown in Figure 1. Its initial design equations are as follows[6]:

$$c = \frac{L}{2.72} = \frac{W}{2.72} \tag{1}$$

$$d = \frac{c}{10} = \frac{L}{27.2} = \frac{W}{27.2} \tag{2}$$

where $L = W$ is the length of the patch, c is the length of the slot, d is the width of the slot.

To get dual-frequency operation, 2 pairs of slots are added to the square patch antenna as shown in Figure 2. The dual-frequency operation in the slotted structure can be interpreted as that associated with two modes that arise from the perturbation of the TM_{100} and of the TM_{300} mode. Let f_{100} and f_{300} be the resonant frequencies associated with the modified TM_{100} and TM_{300} modes, respectively. In order to design for two frequencies, simple semi-empirical formulas, based on physical models, can be used [7].

$$f_{100} = \frac{c}{2(W + \Delta W)\sqrt{\varepsilon_e(L/t, \varepsilon_r)}} G, \tag{3}$$

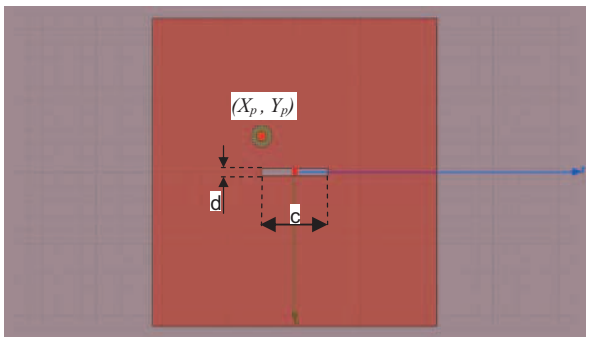

Figure 1: Circular polarized (CP) central slot.

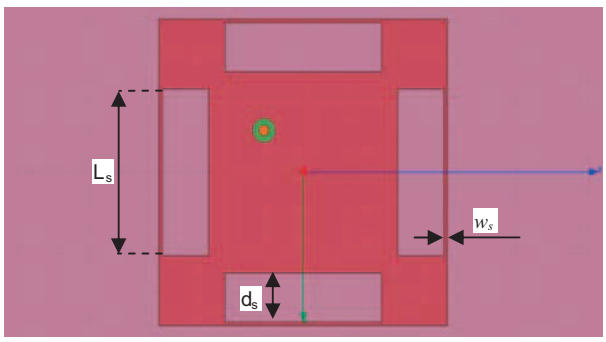

Figure 2: Slotted square-patch antenna.

where c is the free-space speed of light,

$$\varepsilon_e(x,\, y) = \frac{y+1}{2} + \frac{y-1}{2}\left[1+\frac{10}{x}\right]^{-1/2} \tag{4}$$

$$\Delta W = \frac{t}{\pi}\frac{L/t+0.336}{L/t+0.556}\left\{0.28+\frac{\varepsilon_r+1}{\varepsilon_r}\left[0.274+\ln\left(\frac{L}{t}+2.518\right)\right]\right\}, \tag{5}$$

$$G = 1.13-0.19\frac{L_s}{W}-0.73\frac{w}{W} \tag{6}$$

$$f_{300} = \frac{c}{2\,(L-2l+d)\,\sqrt{\varepsilon_e\,(w/t,\varepsilon_r)}} \tag{7}$$

A low-loss teflon substrate with $\varepsilon_r = 2.2$ and $h = 1.6\,\text{mm}$ is employed and Equations (1)–(7) are used to calculate the mentioned parameters of the dual-frequency circularly polarized patch antenna at $f_{100} = 2.25\,\text{GHz}$ and $f_{300} = 3\,\text{GHz}$. The calculated parameters are found to be $W = L = 43\,\text{mm}$, $X_P = 5\,\text{mm}$, $Y_P = 5\,\text{mm}$, $L_s = 32\,\text{mm}$, $d_s = 6.5\,\text{mm}$, $w_s = 0.5\,\text{mm}$, $c = 16\,\text{mm}$, $d = 1.6\,\text{mm}$.

3. 3D MODELING AND OPTIMIZATION

A 3D EM model is built for the initially designed antenna using HFSS10 as shown in Figure 3. The return loss is simulated. The physical parameters of the proposed antenna are optimized to obtain enough impedance bandwidth at the required frequencies. The final optimized physical parameters are: $W = L = 40.6\,\text{mm}$, $X_P = Y_P = 6\,\text{mm}$, $L_s = 19\,\text{mm}$, $d_s = 6.5\,\text{mm}$, $w_s = 0.5\,\text{mm}$, $c = 10\,\text{mm}$, $d = 1\,\text{mm}$.

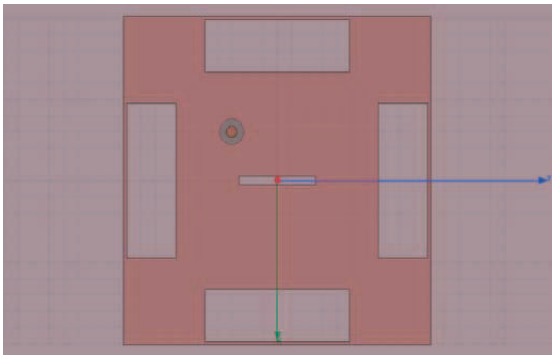

Figure 3: 3D EM model of the proposed antenna.

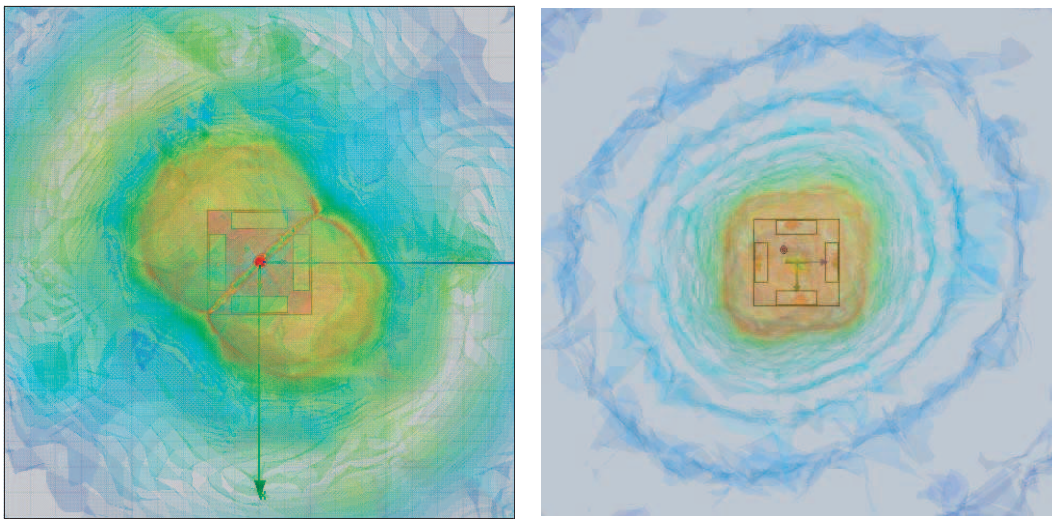

(a) (b)

Figure 4: E-field plots of (a) linearly polarized design of Figure 2 and (b) circularly polarized patch of Figure 3.

Figure 4 compares Electric field magnitude of the linear polarized patch of Figure 2 and that of the CP antenna of Figure 3. Therefore, circular polarization and dual frequency operation are achieved, while maintaining simpler design and lower profile than some other published structures [8, 9].

4. FABRICATION AND MEASUREMENTS

The proposed antenna is fabricated using low loss Teflon microstrip substrate with $\varepsilon_r = 2.2$ and 1.6 mm height. Figure 5 shows a photograph of the fabricated probe-fed dual frequency circularly polarized antenna. Finally, the fabricated antenna is measured suing HP8510c VNA achieving S_{11} of -24 dB at 2.255 GHz and -17.5 dB at 3.01 GHz. Figure 6 shows a comparison between simulated and measured return loss. The measured impedance bandwidth is about 60 MHz at f_1 and 30 MHz at f_2, which are sufficient for both uplink and downlink operations. Measurements are in great agreement with simulations, which verifies the design procedure. Therefore, the proposed structure is very promising in TT&C satellite applications.

Figure 5: Photograph of the fabricated prototype.

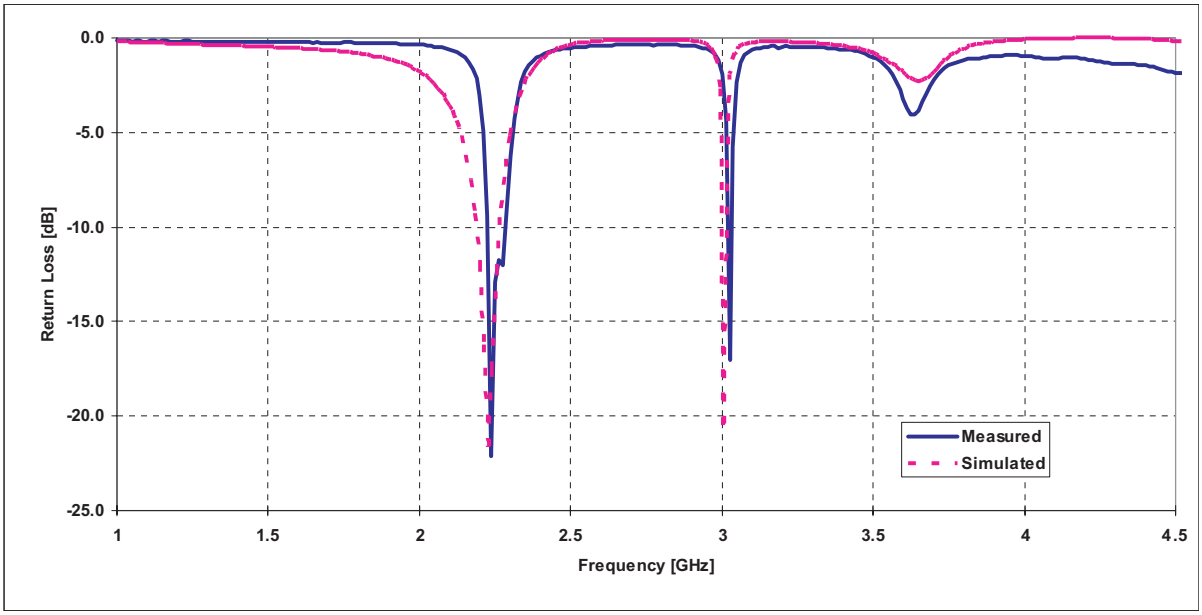

Figure 6: Comparison between measured and simulated return loss of the proposed antenna.

5. CONCLUSIONS

This paper introduces a dual frequency circularly polarized patch antenna to fulfill the requirements of a TT&C antennas for mini satellites. A probe-fed square patch is used with center slot for circular polarization adjustment and edge slots for dual frequency applications. 3D EM modeling

is used to optimize the initially designed antenna, while maintaining simpler design and lower profile than some other published structures. The proposed antenna is fabricated using low loss Teflon microstrip substrate and measured suing HP8510c VNA achieving S_{11} of -24 dB at 2.255 GHz and -17.5 dB at 3.01 GHz with 60 MHz and 30 MHz bandwidth respectively. Measurements are in great agreement with simulations, which verifies the design procedure and make this antenna very promising in TT&C satellite applications.

REFERENCES

1. SSETI project web page http://www.sseti.org.
2. CubeSAT project web page http://cubesat.catpoly.edu/.
3. Curiel, A. S., P. Davies, S. Eves, L. Boland, and M. Sweeting, "Real-time Mosaic — Rapid response high-resolution imaging from space," *2nd Responsive Space Conf.*, Los Angeles, CA, Apr. 19–22, 2004.
4. Chandrasekara, A. and J. E. Gutshall, "The design of the communication and telemetry system used by the ionospheric observation nanosatellite-formation (ION-F) mission," Utah State University, 2002.
5. Yang, K. P. and K. L. Wong, "Dual-band circularly-polarized square microstrip antenna," *IEEE Trans. on Antenna and Propagation*, Vol. 49, 377–382, 2001.
6. Balanis, C. A., *Antenna Theory: Analysis and Design*, John Wiley & Sons, Inc, 1997.
7. Maci, S. and G. B. Gentilli, "Dual-frequency patch antenna," *IEEE Trans. on Antenna and Propagation*, Vol. 39, No. 6, 13–20, Dec. 1997.
8. Bao, X. L. and M. J. Ammann, "Dual-frequency circularly-polarized patch antenna with compact size and small frequency ratio," *IEEE Trans. Antenna Propag.*, Vol. 55, No. 7, Jul. 2007.
9. Wu, G.-L., W. Mu, G. Zhao, and Y.-C. Jiao, "A novel design of dual circularly polarized antenna fed by l-strip," *Progress In Electromagnetics Research*, PIER 79, 39–46, 2008.

Design and Experiment of a Loop Rectenna for RFID Wireless Power Transmission and Data Communication Applications

R. H. Chen, Y. C. Lee, and J. S. Sun
Graduate Institute of Computer and Communication Engineering
National Taipei University of Technology
Taipei, Taiwan

Abstract— This paper presents a low-cost rectifying antenna (rectenna) has been developed and measured at 900–950 MHz (Radio Frequency Identification Device, RFID band) for low-power applications involving wireless power transmission (WPT) and data communication. In order to validate the rectenna, we have been developed a loop antenna which was photo-etched from copper-clad FR-4 material ($\varepsilon_r = 4.4$) with the volume of $60 \times 80 \times 0.8\,\text{mm}^3$. The loop antenna used a meander line structure to reduce its size to 50% of the regular loop antenna and measured operating frequency of 925 MHz with bandwidth of 52 MHz at return loss −10 dB. The maximum antenna gain is 4.22 dBi and radiation efficiency is 97% at 925 MHz. Results show the satisfactory agreement for the loop antenna design to meet the RFID specifications.

Furthermore, to contribute a rectenna for RF power conversion, the back side of the loop antenna is the doubler rectifier circuit with input filter for efficiency optimization and rejects higher order harmonics produced by the rectifying diode. For the Schottky diode we used the commercial Agilent HSMS-285C surface mount zero bias schottky detector diode pair for small signal applications at frequencies below 1.5 GHz was used as the rectifying device, and there are two diodes are mounted into a single package to be the best in reduce the size and the efficiency.

In addition, the rectenna has a RF-DC conversion efficiency of 47% is achieved when 0 dBm RF power is received at 925 MHz. Measured results of rectenna proved that the rectenna is suitable for component of the WPT system.

1. INTRODUCTION

Recently, numerous applications involving radio frequency identification device (RFID) components have been developed (such as cases of product, persons, pets, luggage and electronic devices in order to identify, track, and access control). Considering the RFID tag functionalities and the reading range, available energy is a key point. In order to achieve such a result, a rectifying antenna (rectenna) was used. The rectenna is plays an important role in free space wireless power transmission (WPT) [2], which can efficiently converts radio frequency (RF) energy into useful direct current (DC) power, and typically store it in a capacitor until it is required. In this paper, a planar loop antenna is adopted here as a power receiving part and combined with RF rectifier for RF-DC conversion. Furthermore, the doubler rectifier with match network placed on the back side of the receiving antenna (loop) provides high output voltage as well as great RF-DC conversion efficiency when 0 dBm RF power is received at 925 MHz. The rectenna has been optimized to

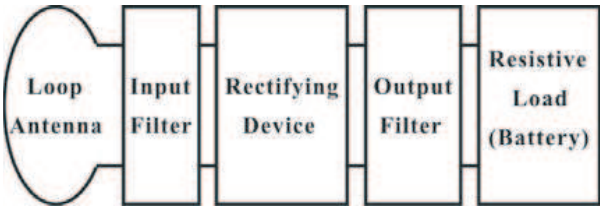

Figure 1: Block diagram of the proposed rectenna.

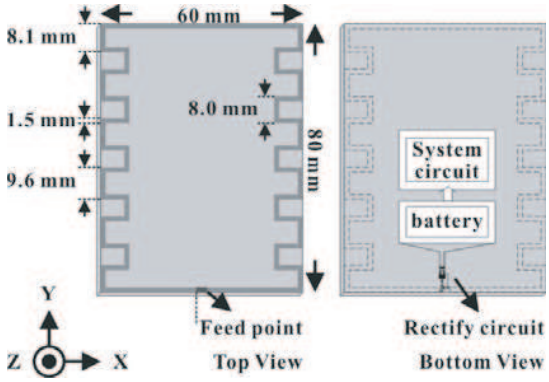

Figure 2: Configuration of the antenna and rectifying circuit of the proposed rectenna.

achieve maximum sensitivity by characterizing both the impedance transformation network and the rectifier circuit and choosing the optimum values for the circuit parameters.

2. RECTENNA ELEMENT DESIGN

The block diagram of the proposed rectenna is shown in Figure 1. And the rectenna developed in this paper is shown in Figure 2. The antenna and the rectifying circuit are fabricated on double sides FR-4 substrate ($\varepsilon_r = 4.4$) with the volume of $60 \times 80 \times 0.8\,\text{mm}^3$. The sections below describe the steps taken to design the rectenna.

2.1. Loop Antenna

The steps taken to design the rectenna begin at the receiving antenna, and a planar loop antenna was designed. The gap between the two extremities of feed point is designed to accommodate the size of the chip elements (inductors, capacitor and diode) package. The loop antenna used a meander line structure to reduce its size to 50% of the regular loop antenna.

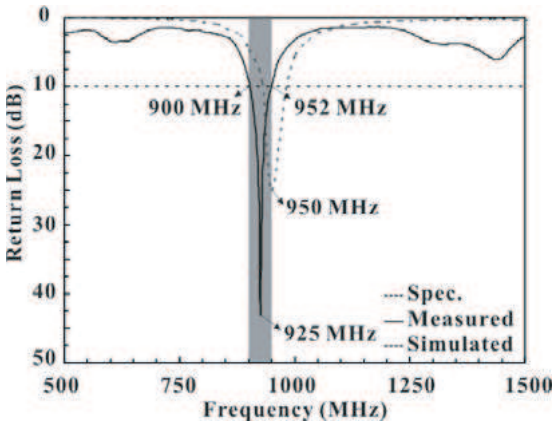

Figure 3: Measured and simulated return loss for the loop antenna.

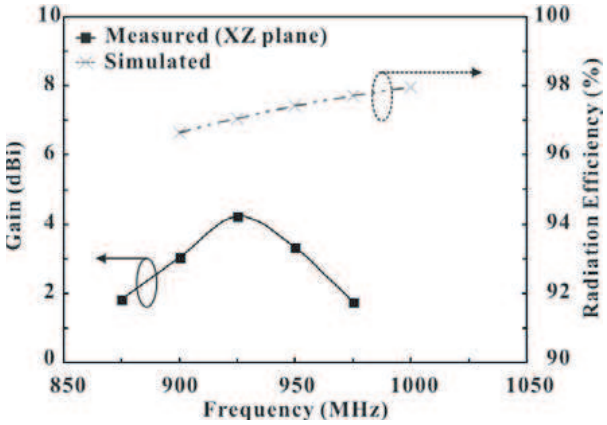

Figure 4: Measured gain and simulated radiation efficiency levels for operating frequency.

The return loss for the loop antenna is shown in Figure 3 and measured operating frequency of 925 MHz with bandwidth of 52 MHz at return loss −10 dB. Figure 4 shows the peak gain and radiation efficiency across the operating band, respectively. The maximum antenna gain is 4.22 dBi and radiation efficiency is 97% at 925 MHz. At last, the radiation patterns of the loop antenna at 925 MHz are plotted in Figure 5. Results show the satisfactory agreement for the loop antenna design to meet the RFID specifications.

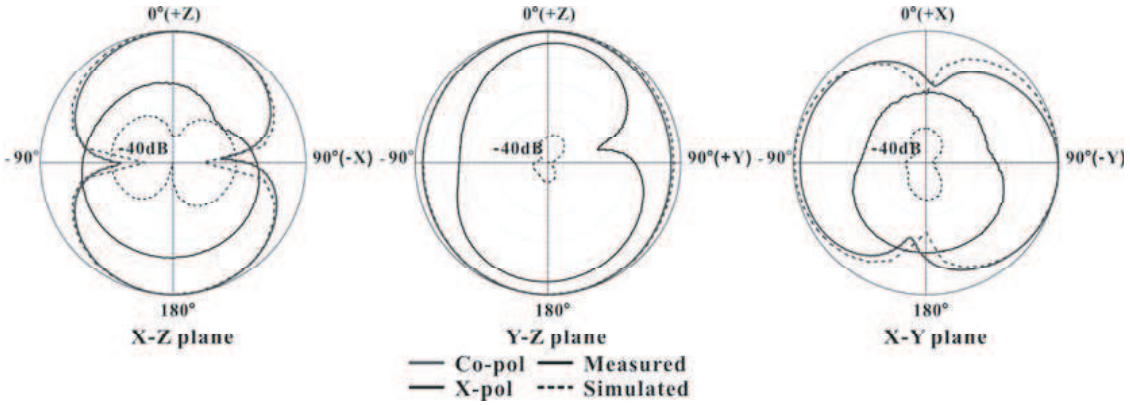

Figure 5: Measured and simulated radiation pattern of the loop antenna.

2.2. Band-pass Filter and Match Network

The antenna integrated with nonlinear circuits, such as diodes and FETs, it is well known that harmonics of the fundamental frequency would be generated. The unwanted harmonics cause problems of harmonics re-radiation and efficiency reduction of rectenna, then the BPF is required to suppress harmonics to improve system performance and prevent harmonics interference. Furthermore, the input filter also transforms the input impedance of the loop antenna to the input impedance of the rectifier.

2.3. Configure of Rectifier

The rectifying circuit with the doubler rectifier with input filter is shown in Figure 6. A commercial Agilent HSMS-285C surface mount zero bias schottky detector diode pair for small signal applications at frequencies below 1.5 GHz was used as the rectifying device, and there are two diodes are mounted into a single package to be the best in reduce the size and the efficiency [6]. It is ideal for RFID and RF tag applications. The return loss of the rectifier with input filter is shows in Figure 7.

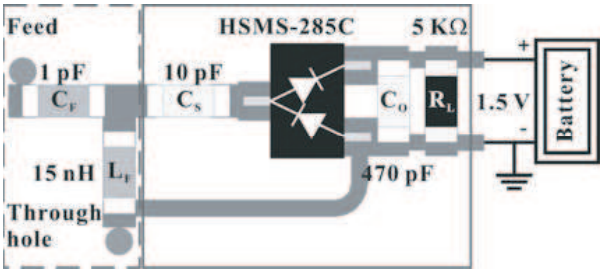

Figure 6: Schematic of doubler rectifier with input filter for rejects higher order harmonics produced by the rectifying diode. The dotted line represents the input filter. The solid line represents the doubler rectifier.

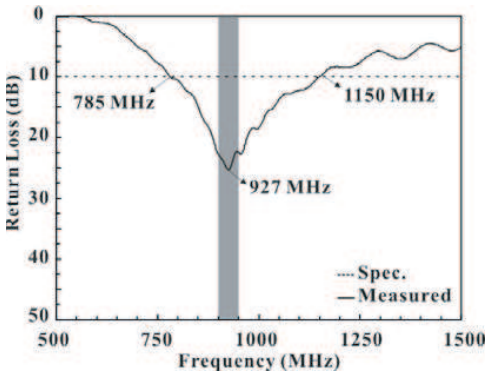

Figure 7: Measured result of return loss for the rectifier with input filter.

2.4. Output DC Pass Filter

The output filter is used to effectively block the RF energy and to pass the DC power to a load or battery [7]. The chip capacitor is also used to maximize the diode's conversion efficiency. The distance between the diode and the output capacitor constitutes an inductance which tunes the capacitance reactance of the diode. Its resonance is needed to maximize the diode efficiency.

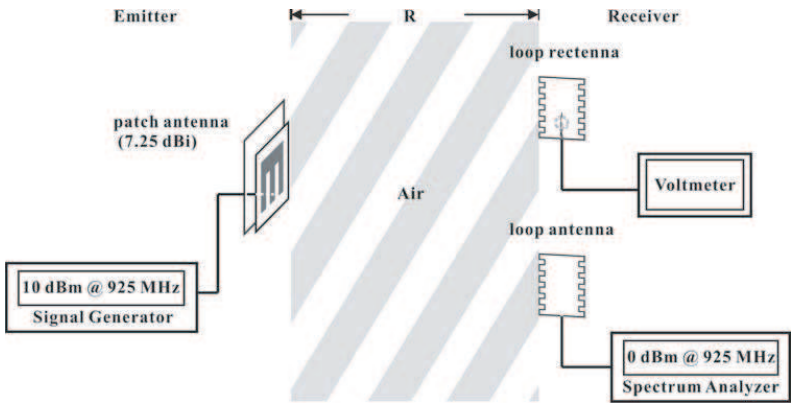

Figure 8: Measurements setup of the proposed rectenna.

3. RECTENNA MEASUREMENTS

After the validation of the rectifying circuit and the planar loop antenna, we have to measure the performances of the rectenna. The rectenna is measured in free space, and the measurement setup is shown in Figure 8. The RF signal generator is used, and allows the power and frequency to be varied. A linear patch antenna is used for provides the RF power to the rectenna. The wireless transmission distance R is equal to 0.5 m.

We measured an RF-DC conversion efficiency of 47% for the rectifying system at the reception level, and an overall conversion efficiency of 4.7% between the emitter and output of the rectenna. Furthermore, the sensitivity if the rectenna can be improved by increasing the gain of the receiving antenna. Figures 9 and 10 are show output voltage and conversion efficiencies of the proposed rectenna when 0 dBm RF power is received with 5 kΩ load.

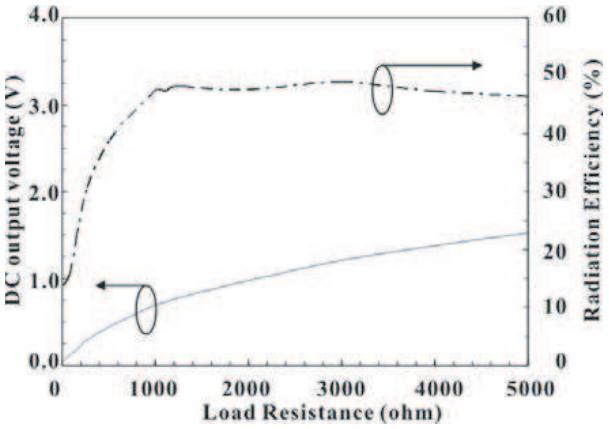

Figure 9: Measured output voltage and conversion efficiency of the proposed rectenna as a function of load resistance when 0 dBm RF power is received.

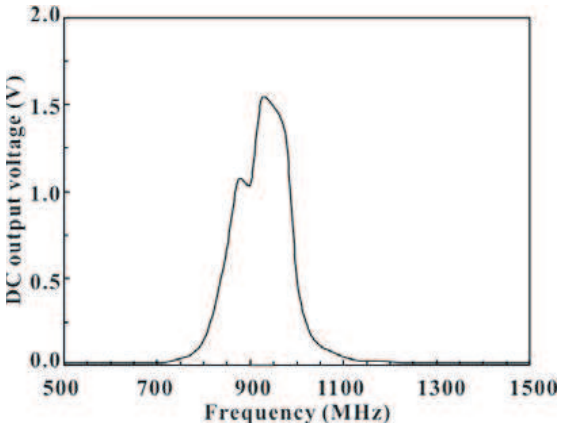

Figure 10: Measured output voltage of the proposed rectenna by sweeping frequency when 0 dBm RF power is received with 5 kΩ load.

4. CONCLUSIONS

A new rectenna with a loop antenna and a designed rectifierby commercial Schottky diode has been developed. The used doubler rectifier provides optimum output DC voltage of 1.54 V as well as 47% RF-DC conversion efficiency is achieved when 0 dBm RF power is received at 925 MHz. The rectifier has good impedance matching with the loop antenna corresponding to its optimum frequency response.

REFERENCES

1. Finkenzeller, K., *RFID Handbook: Fundamentals and Applications in Contactless Smart Cards and Identification*, 2nd ed. Wiley, New York, 2003.
2. Brown, W. C., "The history of power transmission by radio waves," *IEEE Trans. Microw. Theory Tech.*, Vol. 32, No. 9, 1230–1242, 1984.
3. Heikkinen, J., P. Salonenm, and M. Kivikoski, "Planar rectennas for 2.45 GHz wireless power transfer," *Proc. Radio and Wireless Conf.*, 63–66, Denver, CO, 2000.
4. Suh, Y. H. and K. Chang, "A high-efficiency dual-frequency rectenna for 2.45- and 5.8-GHz wireless power transmission," *IEEE Trans. Microw. Theory Tech.*, Vol. 50, No. 7, 1784–1789, 2002.
5. Chin, C. H. K., W. Xue, and C. H. Chan, "Design of a 5.8-GHz rectenna incorporation a new patch antenna," *IEEE Antennas Wireless Propag. Lett.*, Vol. 4, 175–178, 2005.
6. "Surface mount zero bias schottky detector diodes," Agilent Techologies, HSMS-285x Series, 1999.
7. Brown, W. C., "Design definition of a microwave power reception and conversion system for use on a high altitude powered platform," Raytheon Company, Wallops Flight Facility, VA, NASA CR-156866, NASA Contract NAS 6-3006m, 3-16-3-21, July 1980.

Design of a Compact Dual-Band Loop-Slot Antenna

R.-H. Chen, **Y.-C. Lee**, **and J.-S. Sun**
Graduate Institute of Computer and Communication Engineering
National Taipei University of Technology
Taipei, Taiwan

Abstract— This article presents a new compact antenna with loop-slotted structure to achieve the dual-band operation. This loop-slotted structure on the printed antenna is presented, and is measured the impedance bandwidth, radiation patterns, and gain requirements of the 2.4- and 5-GHz wireless local area network (WLAN) applications. The investigated numerically and experimentally results demonstrate that a tunable dual-operating band and an enhancement of the antenna bandwidth are obtained owing to the proposed antenna with compact radiators.

1. INTRODUCTION

Compact design and dual-band operations for the wireless communication systems have been significant investigated and widely developed, which has the strong design advantages over low-profile, easy fabrication, low manufacturing cost, and easy integrating circuit boards. Many compact antennas with broadband and dual-band performances including printed antenna, inverted-F antenna, and planar antenna configurations have been reported [1–3]. These are printed antennas with moderate radiating characteristics and can be operative at dual- and multiple-frequency bands. Moreover, for the antenna fabrication designs, the slot structures are required to provide broadband and dual-band systems including the 2.4- and 5-GHz wireless local area network (WLAN) bands. These antennas based on the slot design configurations and the tunable antenna fabrications have been developed to obtain wide impedance bandwidth and small size, but also have complex designed structure. However, the designed antennas improve multi- and dual-band for the wireless communication operations. The feed point structure of the slot antennas by using CPW-fed and microstrip line fed have been developed to obtain integrating the circuit boards over the wide and dual-bandwidth of operating band. The proposed antenna of this paper is presented and experimented by way of arranging in loop-slot shape and compact metal patch, we could be applied to the dipole antenna, and a wide dual-band characteristic with the slot improves the narrow band of the printed dipole antenna for WLAN dual-band applications.

2. ANTENNA DESIGN

The geometry and configuration of the printed antennas with loop-slot structure is illustrated with Figure 1. The compact design of proposed antenna has a loop-slot structure and a rectangular-shaped plane on the coplanar ground plane. The inner fed conductor and the outer metal sheath of the coaxial line are connected to the feed point and the ground plane and both with a distance of 1.5 mm between two points, respectively. The proposed antenna is printed on the FR4 substrate with thickness of 0.8 mm, dielectric constant of 4.3, and loss tangent of 0.0245 and has a compact dimension of $32 \times 22.5\,\mathrm{mm}^2$ in this study.

3. RESULTS

Figure 2 shows the simulated and measured return loss of the proposed antenna with slotted structure for dual-operating wireless communication applications. It shows the measured return loss of the loop-slot antenna and it is noted that three main resonant modes at around 2.5, 4.6 and 5.7 GHz are excited with -10 dB return loss. The measured return loss of operation bandwidth portion has a 280 MHz within 2.33–2.61 GHz at the lower resonance band. Nevertheless, this resonance bandwidth has the signification operation on the 2.4-GHz WLAN system. The upper resonance band of 1700 MHz within 4.35–6.05 GHz is resulted, which cover the 5-GHz for WLAN operation including 5.2- and 5.8-GHz operating area. The measured bandwidth of loop-slot antenna is covered two impedance bandwidths, 11.3% on the lower bandwidth and 32.7% on the upper bandwidth, respectively.

The measured radiation patterns of the proposed slot antenna at 2.45 and 5.2 GHz are illustrated with Figure 3. It is noticed that the radiation patterns in two main planes are conventional dipole antenna of the same. The x-z plane radiation pattern is omni-directional pattern at two presented

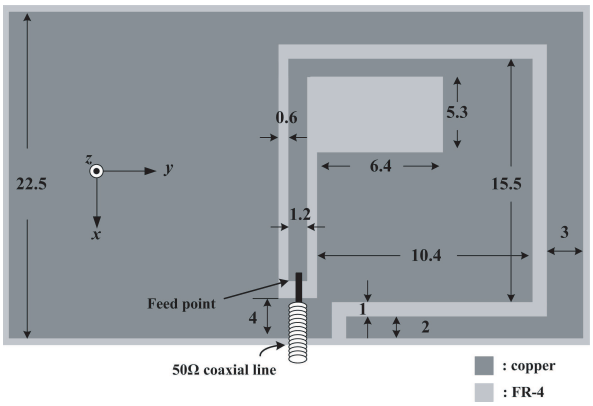

Figure 1: The geometry of proposed antenna.

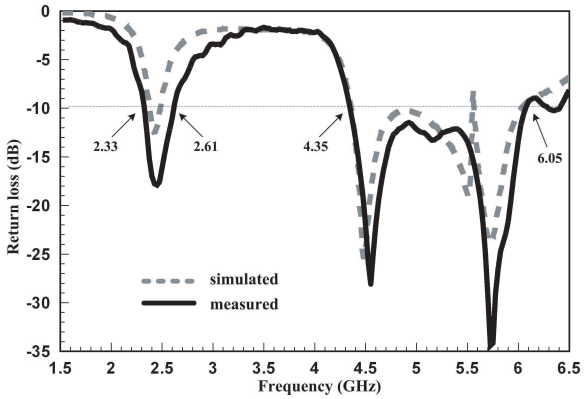

Figure 2: Simulated and measured return loss of the proposed antenna.

operations. So the radiation patterns are generally omni-directional over the entire bandwidth, similar to a conventional antenna for wireless communication systems. As shown in Figure 4, the maximum measured gain at all radiation planes is obtained a 4.98 dBi at the 2.5 GHz within the lower operating frequency band and from 5.16 dBi to 1.86 dBi within 5–6 GHz at the upper operating frequency band, respectively.

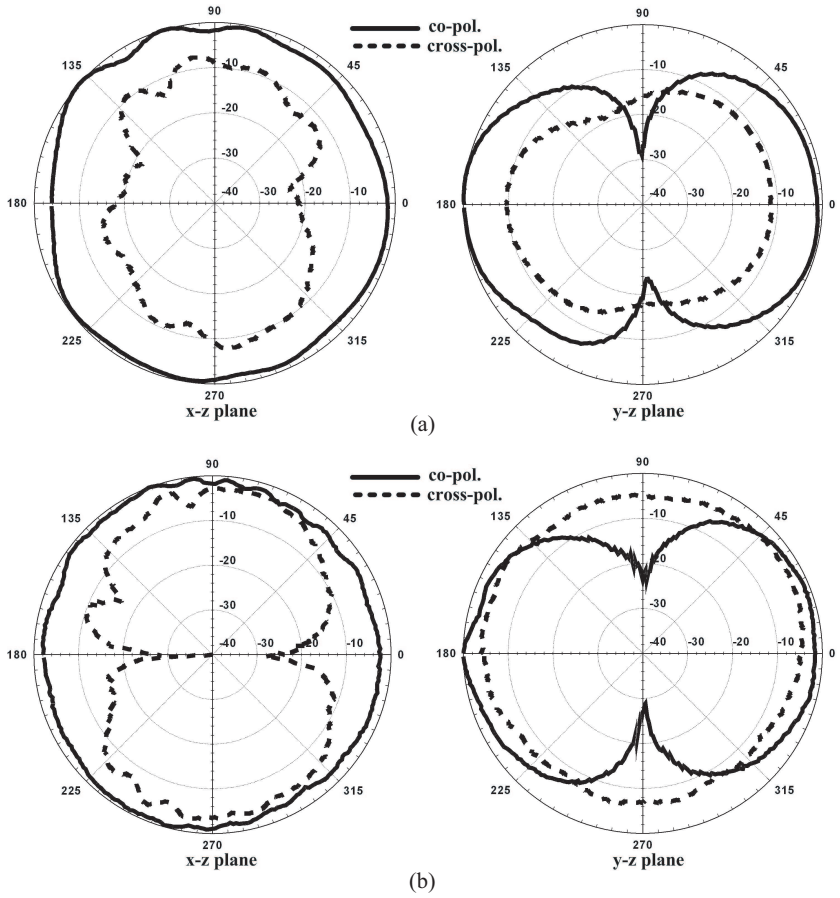

Figure 3: Radiation patterns of the proposed antenna (a) at 2.45 GHz, (b) at 5.2 GHz.

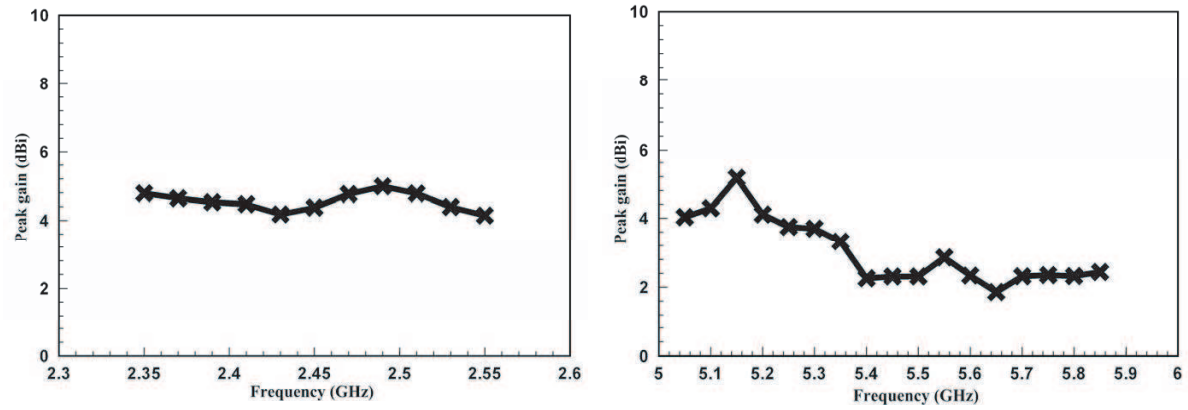

Figure 4: Peak gains of the proposed antenna (a) at lower band, (b) at upper band.

4. CONCLUSIONS

New printed compact slot antenna has been developed and could achieve the dual-band wireless communication operations by using the loop-slot structure. The experimental results of the slot on the metal plane in the printed compact antenna make a strong effect on the antenna's operating resonance modes and impedance bandwidths, so the characteristics of compact antenna with the slot configuration are improved and verified. Experimental results show that by using proposed design and tuning their dimensions, operating bandwidth, measured gain and radiation patterns can be obtained for 2.4- and 5-GHz WLAN applications.

REFERENCES

1. Hwang, S. H., J. I. Moon, W. I. Kwak, and S. O. Park, "Printed compact dual band antenna for 2.4 and 5 GHz ISM band applications," *IET Electronics Letters*, Vol. 40, No. 25, 1568–1569, 2004.
2. Cho, Y. J., S. H. Hwang, and S. O. Park, "Printed antenna with folded non-uniform meander line for 2.4/5 GHz WLAN bands," *IET Electronics Letters*, Vol. 41, No. 14, 786–788, 2005.
3. Janapsatya, J., K. P. Esselle, and T. S. Bird, "A dual-band and wideband planar inverted-F antenna for WLAN applications," *Microwave and Optical Technology Letters*, Vol. 50, No. 1, 138–141, 2008.

Power Feeding to RFID Tags Within Specific Distance and Transponder Control Signal

Kengo Ueyama, **Akitoshi Ito**, **Yukio Iida**, **and Noriaki Muranaka**
FSC, and Dept. of Electric and Electronic Eng., Faculty of Engineering Science
Kansai University, Japan

Abstract— We are proposing the method of supplying driving power of the RFID tag containing transponder control signal by the electro-magnetic field besides the communication signal. From this viewpoint, we are also proposing power supplying method to RF tags within specific distance using two antennas. In the method, we use two properties: (1) The intensity of the electromagnetic field from two loop antennas sharply decreases depending on the distance, and (2) the supplied-signal phase difference sharply changes at a position $1/(2\pi)$ of the wavelength. We used transmitting resonance-type antennas composed of capacitor of 1 pF and the five turns coil of 30 cm in diameter, and receiving antennas composed of variable capacitor from 10 pF to 120 pF and the card-type coil with five turns. The amplitude is 10 V at the transmitting side, and the resonance-frequency is about 17.6 MHz. Under this condition, we were able to drive an IC-encoder-chip of 2 V and 0.3 mA within the distance up to 70 cm. Next, we proposed the ball-type antenna to induce only magnetic fields mainly.

1. INTRODUCTION

The RFID (Radio Frequency Identification) technology [1] has been rapidly attracted attention in recent years, and its applications for various purposes have been considered. In these circumstances, we have thought that the applicability of the RFID technology would be highly improved by supplying power to RFID tags using a method different from a signal communication [2]. Meanwhile, new method of wireless energy transfer has been reported [3]. We proposed the new system to supply power to RFID tags within a restricted transmission distance using two small loop antennas before [4]. In this paper, we now report the problem on using this system and the solution.

2. DEMONSTRATION

We report methods and results of the demonstration.

- We used a loop antenna for the power transmitting antenna and card type antenna. Each parameter of these antennas is shown in Table 1.
- Figure 3 shows the card-type antenna with DC rectification circuit and the resistance 7 kΩ that in equivalent circuit of IC chip.
- We measured the rectified Voltage of IC chip (7 kΩ) on the card.
- Variations in DC voltage versus the distance are shown in Figure 4.

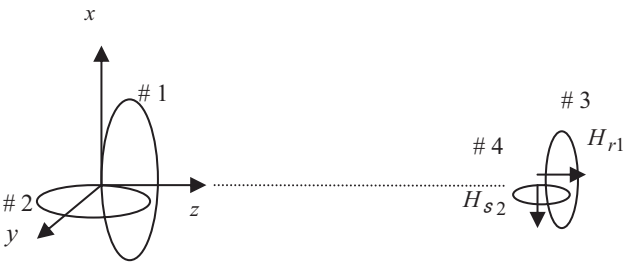

Figure 1: Power-transmitting antenna and a power-receiving antenna.

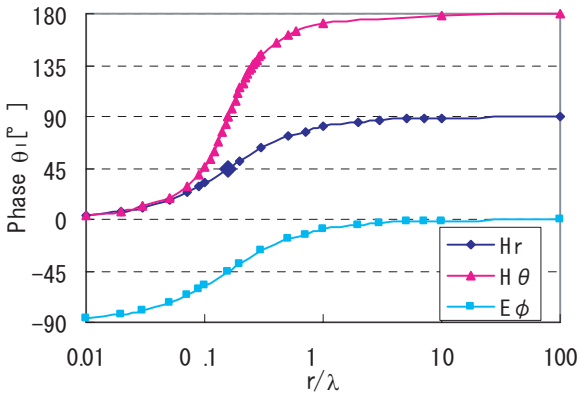

Figure 2: Distance characteristics of the phases of $Hr1$, $H\theta 2$ and $E\phi 2$ fields.

Figure 3: Card-type antenna.

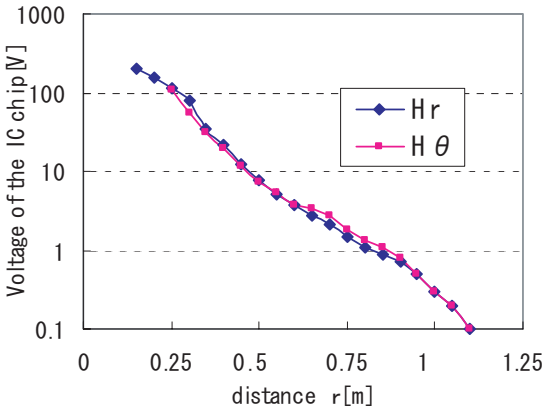

Figure 4: DC Rectified voltage for distance r.

Table 1: Parameters of the transmitting and receiving antennas.

	Capacitor [pF]	Resonance-freq. [MHz]	Size [cm]	Turn [times]
Loop antenna	1	17.6	30 (diameter)	5
Card-type antenna	10 ∼ 120	17.6	6 (length) 5.5 (width)	5

(20 Vp-p at the Oscillator)

As a result, we were able to drive an IC-encoder-chip of 2 V and 0.3 mA within the distance up to 70 cm. And we could also achieve power feeding of 0.3 V to same one within the distance up to 100 cm.

3. BALL ANTENNA

We need the antennas which emit stronger magnetic fields to various directions. So we propose a ball antenna to induce only magnetic fields mainly. We explain the ball antenna shown in Figures 5 and 6.

- We select the sphere of C-60 structure. We fix four loop antennas to the surface of the ball. These loop antennas are connected serially.
- We put excitation loop on the xy plane around the ball.

We perform the experiments to compare a ball antenna with a loop antenna.

- Each parameter of these antennas is shown in Table 2.
- The results are shown in Figure 7.

We can emit both magnetic field Hr and $H\theta$ to various direction except upper side of the ball. There is room for correction in the way to excite the ball antenna.

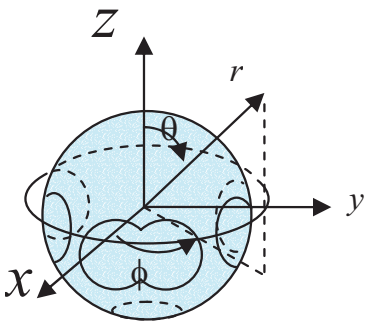

Figure 5: The ball antenna.

Figure 6: Structure of the ball antenna.

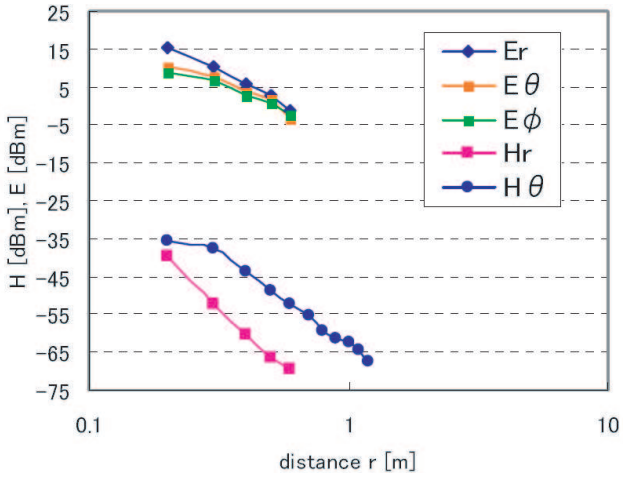

Figure 7: The field intensity characteristics of the ball antenna at distance r.

Table 2: Parameters of the transmitting antenna.

	Capacitor [pF]	Resonance-freq. [MHz]	Size [cm]	Turn [times]
Ball antenna	$10 \sim 70$	21.5	30 (diameter)	5

(20 Vp-p at the Oscillator)

4. CONCLUSIONS

We proposed the ball antenna could emit magnetic field elements Hr and $H\theta$ to various directions. Based on the results, we can develop the ball antenna and the new power supply system in which the maximum distance from the transmitting unit to RFID tags can be restricted effectively.

ACKNOWLEDGMENT

This work was supported by "Academic Frontier" Project for Private Universities: Matching Fund Subsidy from MEXT, 2007-2011. The computations for this research were performed by the Large-Scale Computer System at the Osaka University Cyber media Center.

REFERENCES

1. Finkenzeller, G. K., *RFID Handbook, Radio-Frequency Identification Fundamentals and Applications*, Chichester, John Wiley & Son., 1999.
2. Iida, Y., "Proposal of RF recognition system prepared for demand expansion and use of super-regenerative circuit," *Proceedings of 2007 IEICE Society Conference*, B-5-88, Japan, Sept. 2007.
3. Karalis, A., J. D. Joannopoulos, and M. Soljacic, "Efficient wireless non-radiative mid-range energy transfer, Physics," http://arxiv.org/ftp/physics/papers/0611/0611063.pdf.
4. Ueyama, K., Y. Iida, A. Ito, and N. Muranaka, "Feeding power method to RFID tags in specific distance, -basic study by using two loop antennas-," *Proc. 3-rd International Laser, Light-Wave and Microwave Conference*, PS-9, Yokohama, Japan, Apr. 2008.
5. Ito, A., Y. Iida, K. Ueyama, and N. Muranaka, "Power supplying method to RFID tags in specific distance by using the small loop and small dipole antennas," *Proc. 3-rd International Laser, Light-Wave and Microwave Conference*, PS-10, Yokohama, Japan, Apr. 2008.

Coupling of Transmitting/Receiving Antennas and Super Regenerative Transponder (SRGT) for RFID Tags

Akitoshi Ito, **Kengo Ueyama**, **and Yukio Iida**
FSC, Department of Electric and Electronic Eng., Faculty of Engineering Science
Kansai University, Japan

Abstract— We propose the system of wireless IC tag that is fed with electromagnetic wave power and communicates with very weak radio wave. In this paper, we study the coupling the transmitting/receiving antennas with Super Regenerative circuit. Receiver sensitivity and transmitting electromagnetic field strength are clarified.

1. INTRODUCTION

Recently, RFID technology [1] to discriminate individuals with radio wave has fast been noticed and studied at full length in many fields. RFID has a great many possible applications. However, it is worried whether demands necessary hereafter can be satisfied or not because frequency bands allotted for RFID are not so broad. Thus, we are considering utilization of faint radio wave. For, very broad frequency band can be used as well as its use requires no license. In a common sense, it may be considered that reading probability from the tag must be near 100%. In this time, sufficient role can be played even though reading probability is 70% or 50%. In the case of stray pet, for instance, it is considered that finding probability can get fairly higher than with past methods by installing sensors from place to place. Application range becomes very broad when including such ways of use. Thus, we are proposing utilization of faint radio wave and the super-regenerative receiver [2] as transponder for demand expansion RFID system [3]. The roles of SRGT are reception from reader/writer, amplification of faint radio wave and transmitting. The transmitting radio wave strength must be faint. Therefore, voltage must be controlled by SRGT. In this paper, first, describe about the transmitting/receiving antennas. Next, describe about super regenerative circuit, describe the coupling, finally, receiving sensitivity.

2. TRNSMITTING/RECEIVING ANTENNAS

Figure 1 shows the loop antennas which are 4.5 cm, 3 cm, 2 cm in length. Figure 2 shows the resonance-frequency characteristics for the capacitance. Figure 3 shows the Q value characteristics. We selected the #2 antenna ($C = 5\,\mathrm{pF}$, $Freq = 238.2\,\mathrm{MHz}$, $Q = 183$), combined the antenna and SRGT. Parameters are $R = 24\,\mathrm{k\Omega}$, $L = 89.29\,\mathrm{nH}$, $C = 5\,\mathrm{pF}$ for #2.

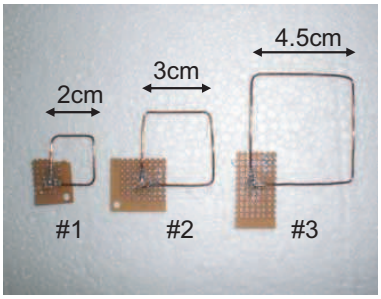

Figure 1: Loop antennas.

3. SUPER REGENERATIVE CIRCUIT

Figure 4 shows the super-regenerative circuit. We decided $C1 = 3\,\mathrm{pF}$, $C2 = 5\,\mathrm{pF}$, $C3 = 1\,\mathrm{pF}$. In the resonance circuit of Figure 4, the parameters ($R = 24\,\mathrm{k\Omega}$, $L = 89.29\,\mathrm{nH}$, $C = 5\,\mathrm{pF}$) are used. Figure 5 shows the waveform of resonance circuit voltage V_{rs} without input signal. We can see the quenching behavior of oscillation.

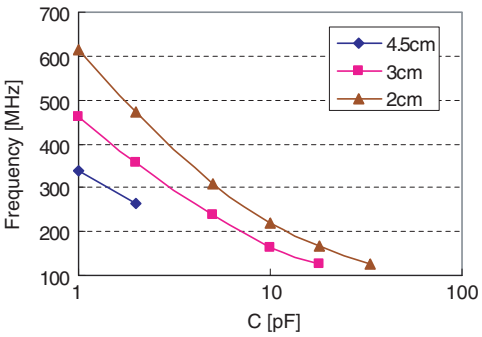

Figure 2: The resonance-frequency characteristics for capacitance.

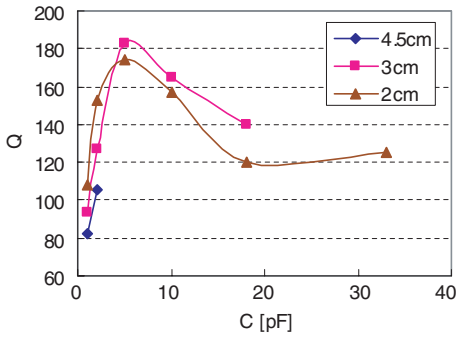

Figure 3: The Q characteristics for capacitance.

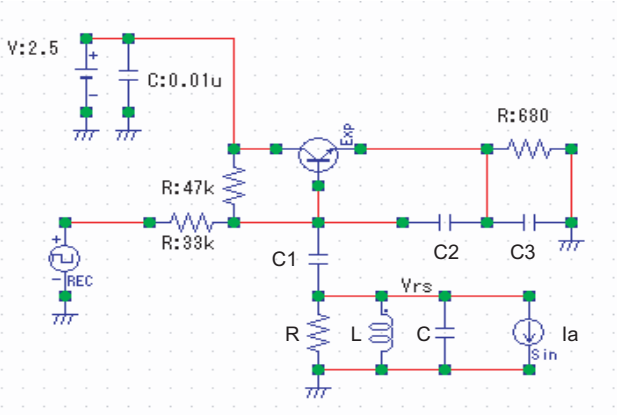

Figure 4: Super-regenerative circuit.

4. COUPLING OF ANTENNAS AND SUPER REGENERATIVE CIRCUIT

Figure 6 shows the variation of the maximum amplitude of oscillation for input signal current I_a. As input signal increasing, $v_{rs\,\max}$ increasing. This behavior suggests the operation of the super-regenerative receiver. Next, we describe about transmitting electromagnetic field strength. When 20% of the loss in resistance $R = 24\,\text{kohm}$ is radiation resistance of the antenna, the radiation power is below 37.5 nW ($v_{r\,\max} = -21\,\text{dB}$) shown in Fig. 6 with a line corresponding to faint radio wave.

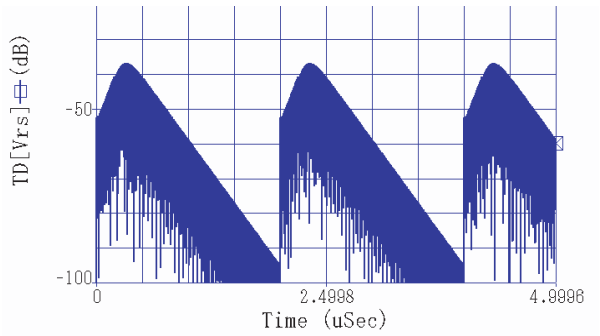

Figure 5: Waveform of resonant circuit voltage v_{rs} when $I_a = 0$. Vertical axis is $20 \log v_{rs}$.

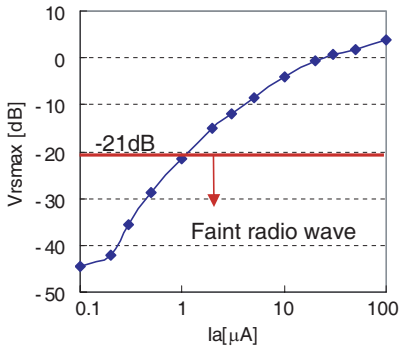

Figure 6: V_{rs} characteristics for I_a.

5. RECIVINRG SENSITIVITY

Figure 7 shows variation of peak values of v_{rs} for input power. We can see that the super-regenerative circuit has sensitivity over 0.1 nW (= −70 dBm) of the input power. When transmitting power is 37.5 nW, the receiving power by isotropic antenna at distance 1.3 m is −63 dBm. When radiation efficiency of receiving antenna is 20%, the receiving power is −70 dBm. If transmitting distance is 1.3 m, this system is used without license. Thus, we can see relationship among the voltage, radiation power and receiving sensitivity of super-regenerative circuit.

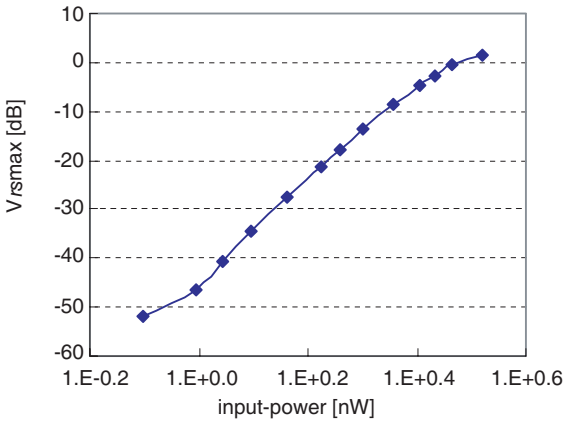

Figure 7: The voltage v_{rs} versus the input power.

6. CONCLUSION

We studied the coupling the transmitting/receiving antennas with super-regenerative circuit. We could clarify receiver sensitivity and transmitting electromagnetic field strength.

ACKNOWLEDGMENT

This work was supported by "Academic Frontier" Project for Private University: Matching Fund Subsidy from MEXT, 2007-2011. The computations for this research were performed by the Large-Scale Computer System at the Osaka University Cyber media Center.

REFERENCES

1. Finkenzeller, G. K., *RFID Handbook, Radio-frequency Identification Fundamentals and Applications*, Chichester, John Wiley & Son., 1999.
2. Hall, G. O., *Superregenerative Receivers, Microwave Receivers*, S. N. Van Voorhis ed., MIT radiation Lab. Series 23, Chap. 20, Mc-Graw-Hill, New York, 1948.
3. Iida, Y., "Proposal of RF recognition system prepared for demand expansion and use of super-regenerative circuit," *Proceedings of 2007 IEICE Society Conference*, B-5-88, Japan, Sept. 2007.

Calculation of Electromagnetic Wave Attenuation Due to Rain for Various Percentages of Time

M. Zilinskas[1,2], **M. Tamosiunaite**[2,3],
S. Tamosiunas[2,3], **and M. Tamosiuniene**[4]

[1]Department of Radio Communication
Communications Regulatory Authority of the Republic of Lithuania
Algirdo 27, Vilnius LT-03219, Lithuania
[2]Faculty of Physics, Vilnius University, Sauletekio 9, Vilnius LT-10222, Lithuania
[3]Institute of Materials Science and Applied Research, Vilnius University
Sauletekio 9, Vilnius LT-10222, Lithuania
[4]Semiconductor Physics Institute, A. Gostauto 11, Vilnius LT-01108, Lithuania

Abstract— The attenuation due to rain for various percentages of time has been analyzed. By using the rainfall amounts data measured in Lithuanian Weather Stations with 10-minutes integration time, the rain rates for different percentages of time have been determined. The rain rate-values obtained in Seacoast were compared with one obtained in Continental Regions of Lithuania. One-minute rain rate-values were determined according to the known model. Using measured rainfall data the relationships between rain rates and percentages of time suitable for use under Lithuanian climate conditions were derived. The suitability of the model, which was proposed in previous papers, was proven using the measured rainfall data of longer period. The specific rain attenuation was determined by using the rain rate-value obtained here.

1. INTRODUCTION

The conditions of electromagnetic wave propagation in atmosphere and quality of wireless communication depend strongly on the rain rate R. Therefore, rain rate data and rain attenuation prediction models are being required for establishing any microwave communication systems [1]. The values of R differ for various percentages of time. In [2], the maps of rain regions and the values of the rain rates for various percentages of time are presented. According to [2], Lithuania is in the Rain Zone E. The values of R for various percentages of time are presented in Table 1. In [3], it was mentioned, that the R-value ascribed to rain Zone E, is too low for use in Latvia. The analysis of the rainfall data collected in Lithuanian Weather Stations shows that the values of R, presented in [1], are too low to be used in territory of Lithuania also. The data presented in [3] and in our previous papers [4, 5] confirm this fact.

Table 1: Rain rates for various percentages of time in Rain Zone E [1].

Percentage of time, %	0.01	0.003	0.001
R, mm/h	22.0	41.0	70.0

Lithuania is in the geographical center of Europe in the Southeast Coast of Baltic Sea. The territory of Lithuania extends by 373 km starting from the East up to Seacoast in the West and by 276 km starting from the North up to the South. Though the territory of Lithuania is no large, the differences in the climatic conditions of various localities are observed. The climate of Continental part of Lithuania is typical climate of the middle part of the East Europe. The climate of the west part of Lithuania (for example, of Klaipeda) is specified as the moderate warm climate. The average temperature of the coldest month is more than -3°C. Such type of the climate is dominating in the West Europe [6]. This is the reason to compare the attenuation due to rain of the electromagnetic waves propagating over Seacoast and Continental parts of Lithuania.

The main goals of this paper are to analyze the rainfall data in the localities of Lithuania, to determine the rain rates-values for various percentages of time in Seacoast and Continental parts of Lithuania, to compare the R-values obtained here with the values presented in [2] and with ones obtained by using model (1) and to determine values of the specific rain attenuation.

2. DETERMINATION OF RAIN ATTENUATION

One of the most accepted rain attenuation prediction methods is an empirical relationship between the specific rain attenuation α and the rain rate R [2]:

$$\alpha = aR^b \tag{1}$$

where a and b are functions of frequency f and rain temperature t; the value of R is the value for an exceedance of 0.01% of the time for point rainfall rates with an integration time of one minute.

Evaluation of the rain rate value R is the first step in the determination of rain attenuation. Presented in [6], model for determination of $R_{(1\,\mathrm{min})}$ for 0.01% of time using rainfall amount data and considering the Lithuanian climate peculiarities can be written as

$$R_{(1\,\mathrm{min})} = \frac{\ln(0.0163 \cdot M_w)}{0.03} \tag{2}$$

where M_w is amount of rainfall, which falls during the months starting from May up to September.

2.1. The Rainfalll Data

The rainfall data set, used here, consists the rainfall amounts data of measurements performed in latter five years in Klaipeda (Seacoast), Kaunas (Continental part), and Birzai (Continental part in North of Lithuania); and the data of measurements performed in Vilnius (Continental part in Southeast of Lithuania; the distance from Baltic Sea is 312 km) starting from the year 1967 up to the year 2007. The rainfall data were collected in Lithuanian Weather Stations. It is worth to mention, that R-values were determined by using the rainfall amount data measured with integration time $\tau = 10\,\mathrm{min}$ in most cases. The highest values of R were selected in such a way that the sum of intervals of time would be equal 0.001, 0.002, 0.003, 0.004, 0.005, 0.006, 0.007, 0.008, 0.009, and 0.01% of time. However, 10 min integration time is too long for communications purposes and the known rain rate conversion model [7] was used in determination of one-minute values of $R_{0.01\%}$. In this method, the relationship between one-minute rain rate for 0.01% of time $R_{m0.01\%}$, and τ-minutes rain rate for 0.01% of time $R\,(\tau\,\mathrm{min})_{0.01\%}$ is expressed as:

$$R_{m0.01\%} = \left(R\,(\tau\,\mathrm{min})_{0.01\%}\right)^d, \tag{3}$$

where $d = 0.987\,(\tau\,\mathrm{min})^{0.061}$ and $R\,(\tau\,\mathrm{min})_{0.01\%}$ is R-value, which may be exceeded during 0.01 percent of time, for τ-minute integration time.

2.2. Variation of Rain Rates Values Both in the Location and Time

In order to emphasize the differences of rain rates in time, in Table 2 we present the rain rates values in Birzai (in northernmost location of Lithuania) in five latter years. This data shows that the differences in rain rates-values from year to year are obvious even for the same percentage of time. For example, the value of rain rate for 0.01% of time of the year $R_{0.01\%} = 73.0\,\mathrm{mm/h}$ (in the year 2004) is more than by three times higher than the value $R_{0.01\%} = 23.6\,\mathrm{mm/h}$ (in the year 2003) and by 1.6 times higher than the average value $R_{0.01\%} = 45\,\mathrm{mm/h}$ obtained by averaging over the period of five latter years.

The analysis of 10-min rain rates data presented in Table 2 shows that under Lithuanian climate conditions, a use of averaged R-values can to hide the probable rainfall peaks. It is worth to mention, that during the rainfall peaks, the highest outages take place [8].

The dependences of 10-minutes R-values percentages of time in the year 2004 in the localities of Lithuania are presented in Fig. 1. There are clearly seen the differences in rain rate-values in Vilnius, Klaipeda, Birzai, and Kaunas. The value $R_{0.01\%} = 73.0\,\mathrm{mm/h}$ obtained for Birzai is by 3.4 times higher than one obtained for Klaipeda (in Seacoast). The R-value for 0.001% of time $R_{0.001\%} = 128.4\,\mathrm{mm/h}$ obtained for Birzai in the year 2004 is approximately by 1.8 times higher than the value $R_{0.01\%} = 73.0\,\mathrm{mm/h}$ obtained for 0.01% of time. However, The R-value for 0.001% of time $R_{0.001\%} = 22.8\,\mathrm{mm/h}$ obtained for Klaipeda in the year 2004 is approximately only by 1.1 times higher than the value $R_{0.01\%} = 21.2\,\mathrm{mm/h}$ obtained for 0.01% of time. In Klaipeda, the dependence of R-value on the percentage of time was low in the year 2004. It is obvious, that the R-values (see Table 2 and Fig. 1) strongly differ for various percentages of time in Birzai and Kaunas. The dependence of R-value on the percentage of time in Vilnius is lesser than one in Birzai and one in Klaipeda is the lowest.

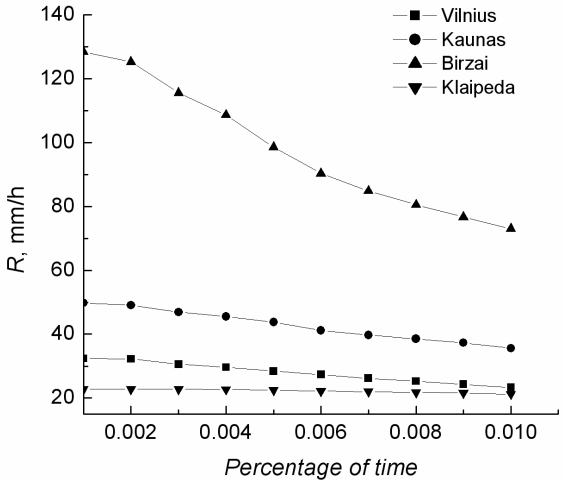

Figure 1: Dependences of rain rates values R on the percentages of time in the localities of Lithuania in the year 2004.

Table 2: The 10-minutes R-values for various percentages of time in Birzai.

Years / %	2003	2004	2005	2006	2007	Average
	R, mm/h	R, mm/h	R, mm/h	R, mm/h	R, mm/h	R, mm/h
0.001	94.8	128.4	128.4	47.9	77.8	69.8
0.002	55.1	125.3	127.6	40.4	72.0	84.1
0.003	44.2	115.6	106.1	37.9	66.8	74.1
0.004	38.1	108.7	94.8	35.3	64.0	68.2
0.005	33.8	98.6	82.2	33.1	62.3	62.2
0.006	30.4	90.3	71.3	30.5	60.1	56.5
0.007	28.4	84.9	65.3	28.8	58.1	53.1
0.008	26.4	80.5	60.7	27.5	55.7	50.2
0.009	25.0	76.7	56.8	26.1	53.1	47.5
0.01	23.6	73.0	53.2	24.7	50.5	45.0

Analysis of rainfall data shows, that the dependence of R (in mm/h) on percentage of time P in Vilnius could be described as relationship [9]

$$R = 45.236 + 65.828 \exp\left(-\frac{P}{0.00471}\right). \tag{4}$$

The dependence of R (in mm/h) on percentage of time P in Birzai (in North of Lithuania) could be described as relationship

$$R = 36.785 + 72.493 \exp\left(-\frac{P}{0.00468}\right) \tag{5}$$

and one in Klaipeda (in Seacoast of Baltic Sea) can be written as

$$R = 24.202 + 20.504 \exp\left(-\frac{P}{0.00424}\right). \tag{6}$$

It is worth to mention, that the relationships (5)–(6) were obtained by using the average 10-min R-values averaged over latter five years period. In [9], the relationship (4) was obtained by using

the average 10-min R-values averaged over decadal values starting from the year 1967 up to the year 2007.

The average value of ratios of $R_{0.001\%}$ and $R_{0.01\%}$-values in Vilnius is equal 2.17 and one presented in [2] (see Table 1) is 3.18. The average value of $R_{0.01\%}$ in Vilnius is equal 50.1 mm/h and it is near the one-minute-value $R_{0.01\%} = 50.2$ mm/h, which was obtained, using value $R_{0.01\%} = 22.0$ mm/h [1] and converting it by using relationship (3) into 1-min-value.

Using the data of rainfall amounts M, gathered during period of years 1997–2007 [9], and the model, proposed in [6], we determined the R-value for 0.01% of time in Vilnius. The value $R_{0.01\%} = 48.1$ mm/h was obtained. This value differs by 2.0 mm/h from the average value $R_{0.01\%} =$ 27 mm/h, obtained here by using ten-minutes rainfall data, measured at the Weather Station and converted to one-min value by using relationship (3). The average 10-min values $R_{0.01\%}$=26.4 mm/h (for Klaipeda) and $R_{0.01\%} = 45.0$ mm/h (for Birzai) were obtained. After conversion by using relationship (3) the values $R_{0.01\%} = 41.2$ mm/h (for Klaipeda) and $R_{0.01\%} = 75.5$ mm/h (for Birzai) were obtained. The marked difference in the values obtained in Seacoast (in Klaipeda) and in Continental Part of Lithuania (for example, in Birzai) has been observed.

Some regularity in the rain rates values was observed when analyzing the rain rates values in Vilnius Birzai and Klaipeda: the average 1-min $R_{0.01\%}$-values obtained by averaging over the period of the years 2003–2007 were near 10-minutes $R_{0.01\%}$-values obtained in the worst year in the localities named above.

The value of the specific rain attenuation α (in Vilnius), which was determined using the method presented in [2] and the average value $R_{0.01\%} = 50.1$ mm/h, obtained here is $\alpha = 1.5$ dB/km when frequency is $f = 10$ GHz, and $\alpha = 13.8$ dB/km when $f = 40$ GHz, temperature is $t = 20°$C, and the wave is horizontally polarized. In Klaipeda, $\alpha = 1.3$ dB/km when frequency is $f = 10$ GHz, and $\alpha = 11.5$ dB/km when $f = 40$ GHz and $R_{0.01\%} = 41.2$ mm/h. The value of the specific rain attenuation in Klaipeda is by 2.3 dB/km lower than one in Vilnius and by 8.8 dB/km lower than one in Birzai, when the wave is horizontally polarized and $f =$ 40 GHz.

3. CONCLUSIONS

There are clearly seen the differences in rain rate-values in Klaipeda (Seacoast) and in Continental parts of Lithuania. The dependences of R-value on the percentage of time in Vilnius and Kaunas are lesser than in Birzai and one in Klaipeda is the lowest. The E-Zone $R_{0.01\%}$-value, presented in [1] are near the one-hour-value obtained here for Vilnius. The model proposed in [6] may be used in calculation of the $R_{0.01\%}$-value under Lithuanian climatic conditions in cases, when only monthly rainfall amount data is available and the rainfall data measured with short integration time is unavailable. The relationships presented here may be revised when the rainfall data of longer period would be analyzed.

ACKNOWLEDGMENT

The authors are grateful to the Direction of the Lithuanian Weather-Station for possibility to use the data of the Archives of the Weather Stations.

REFERENCES

1. Choi, D. Y., "Rain attenuation prediction model by using the 1-hour rain rate without 1-minute rain rate conversion," *IJCSNS Int. J. Computer Science and Network Security*, Vol. 6, No.3A, 130–133, 2006.
2. Freeman, R. L., *Radio System Design for Telecommunications*, John Wiley & Sons, New York, 2007.
3. Ivanovs, G. and D. Serdega, "Rain intensity influence on to microwave line payback terms," *Electron. Electr. Eng.*, Vol. 6, No. 70, 60–64, 2006.
4. Tamosiunas S., M. Zilinskas, M. Sileika, and M. Tamosiuniene, "Revised model of attenuation of electromagnetic waves due to rain," *Lithuanian Journal of Physics*, Vol. 46, No. 4, 433–436, 2006.
5. Tamosiunas, S., M. Tamosiniene, and M. Zilinskas, "Calculation of electromagnetic wave attenuation due to rain using rainfall data of long and short duration," *Lith. J. Phys.*, Vol. 47, No. 2, 163–168, 2007.
6. Zilinskas, M., M. Tamosiunaite, S. Tamosiunas, and M. Tamosiuniene, "The influence of the climatic peculiarities on the electromagnetic waves attenuation in the baltic sea region," *PIERS Online*, Vol. 4, No. 3, 321–324, 2008.

7. Moupfouma, F. and L. Martin, "Modelling of the rainfall rate cumulative distribution for the design of satellite and terrestrial communication systems," *International J. of Satellite Comm.*, Vol. 13, No. 2, 105–115, 1995.
8. Ojo, J. S. and S. K. Sarkar, "Rainfall dynamics over two indian tropical stations for radio communication," *Int. J. Infrared Milli. Waves*, Vol. 29, No. 7, 649–656, 2008.
9. Tamosiunas, S., M. Tamosiunaite, M. Tamosiuniene, and M. Zilinskas, "Attenuation due to rain for various percentages of time," *Program and Materials of International Conference Radiation Interaction with Material and Its Use in Technologies 2008*, 242–245, Kaunas, Lithuania, September 2008.

A 2.4 GHz Low Phase Noise Voltage Controlled Oscillator

R. M. Weng and J. Y. Lin

Department of Electrical Engineering, National Dong Hwa University, Taiwan, R.O.C.

Abstract— A fully integrated voltage-controlled oscillator (VCO) fabricated with tsmc 0.18 µm 1P6M CMOS technology for Bluetooth specifications is presented. With the memory reduction tail current source and coupling capacitors, the proposed VCO achieves phase noise as low as −126.1 dBc/Hz at 1 MHz offset from 2.4 GHz carrier frequency. Figure-of-Merit (FOM) value at 2.4 GHz is around −188.8 dBc/Hz at 1 MHz offset. The power consumption is only 3.1 mW.

1. INTRODUCTION

Voltage-controlled oscillator (VCO) is an important part of wireless communication systems, especially in frequency synthesizer and Phase-Locked Loop (PLL). VCO is widely used to generate the local oscillation (LO) carrier frequency for up-conversion and down-conversion mixing of the input baseband and RF signal in a superheterodyne transceiver, respectively.

As a local oscillator in the transceiver, phase noise of VCO is one of the most important parameters for the quality and reliability. Phase noise in the oscillator can be determined by the VCO gain (K_{vco}) [1]. A large VCO gain will amplify the noise coupling to the control node and hence degrade the phase noise performance. It also makes VCO very susceptible to noise, because of AM to FM conversion. A VCO with a small K_{vco} is desirable because of its less susceptibility to noise. But when suffer from process and temperature variations, small K_{vco} may cause the central frequency of VCO drift away from the desired frequency. Tuning range and phase noise are the trade-off in optimization of VCO performance.

2. PHASE NOISE ANALYSES OF THE VCO

To minimize the flicker noise generated after up-conversion, all even harmonics must be suppressed, meaning the circuit must be symmetric [2]. The complementary differential structure can enhance the symmetry of the circuit and further minimize the flicker noise. By proper sizing of the transistors, the circuit can be optimized to have more symmetry in the output waveform, thus it can get lower $1/f^3$ noise corner frequency. To achieve low phase noise and low power consumption, complementary cross-coupled structure would be chosen in this design. Phase noise can be modeled by the modified Lesson's formula [3]:

$$L(f_m) = 10\log\left\{\left[1+\left(\frac{f_0}{2f_mQ}\right)^2\right]\left(1+\frac{f_c}{f_m}\right)\frac{FkT}{2P_{av}}+\frac{2kTRK_{vco}^2}{f_m^2}\right\}, \tag{1}$$

where

$L(f_m)$ phase noise in dBc/Hz;

f_m frequency offset from the carrier in Hz;

f_0 central frequency in Hz;

f_c flicker noise corner frequency in Hz;

Q the loaded quality factor (Q) of the tuned circuit;

F noise factor;

k Boltzmann's constant in J/K;

T temperature in K;

P_{av} average power at oscillator output;

R the equivalent noise resistance of the varactor;

K_{vco} oscillator voltage gain in Hz/V.

From (1), K_{vco} dominates the phase noise performance in the modified Lesson's formula, thus phase noise performance can be improved by reduction K_{vco}. K_{vco} can be written as:

$$K_{vco} = \frac{df}{dV} = \frac{df}{dC} \cdot \frac{dC}{dV} = \frac{-1}{4\pi} \cdot L^{-1/2} \cdot C^{-3/2} \cdot \frac{dC}{dV} = -2\pi^2 L f^3 \frac{dC}{dV}, \tag{2}$$

Thus for a given inductance L, K_{vco} is proportional to dC/dV of varactor within a small range of frequency.

3. PROPOSED LOW PHASE NOISE VCO

Figure 1 shows the proposed low phase noise VCO. The complementary structure has high transconductance compared to that of NMOS-only or PMOS-only architecture. Current reusing in double cross-coupled pairs (PMOS and NMOS) can be used to decrease the supply current so as to achieve low power design.

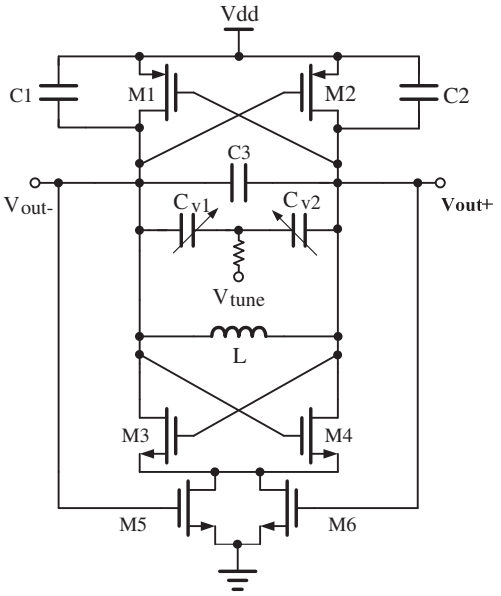

Figure 1: Proposed low phase noise VCO.

The cross-coupled pairs ($M1 \sim M4$) provide the negative resistances to compensate the parasitic resistance of an LC-resonator to have better quality factor. The negative resistance can be expressed as:

$$R_{negnative} = \frac{-2}{G_{Mn} + G_{Mp}}, \tag{3}$$

where G_{Mn} and G_{Mp} are the transconductances of NMOS and PMOS pair.

Table 1: Definition of four types of VCOs.

Type	Definition
VCO1	Traditional LC-tank VCO (Figure 1 without $C1 \sim C3$ and $M5$, $M6$)
VCO2	Proposed VCO with $C1 = C2 = 0.5$ pF without memory reduction tail current source ($M5$ and $M6$)
VCO3	Proposed VCO with $C1 = C2 = 1$ pF without memory reduction tail current source ($M5$ and $M6$)
VCO4	Proposed VCO with $C1 = C2 = 1$ pF and memory reduction tail current source ($M5$ and $M6$)

The oscillator frequency can be expressed as

$$f_{osc} = \frac{1}{2\pi\sqrt{LC}}, \tag{4}$$

where L is the inductance of LC-tank, C is mainly the capacity of C_{v1} and C_{v2} in parallel. The effect of $C3$ and coupling capacitors $C1$ and $C2$ are included in the total capacitance C.

In the previous section, K_{vco} is proportional to dC/dV. Coupling capacitors $C1$, $C2$, and fixed capacitor $C3$ are added to decrease dC/dV. The slope of CV curve is smoother than the traditional LC-tank VCO. When coupling capacitors become larger, the tuning range of VCO would be narrower. Thus a VCO with low phase noise can be achieved.

A small tuning range will result in central frequency drifting due to the process and temperature variations. In order to reduce phase noise while maintaining tuning range large enough to cover the process and temperature variation, $C1$ and $C2$ are designed with 1 pF.

Tail current source is usually added for two reasons. One is for the limiting of the VCO output amplitude, hence preventing devices from going into deep triode region which degrades phase noise performance [4]. The other is to provide large common-mode impedance to reject the noise coupling from ground. Unfortunately, the tail current source is one of the major contributor to the phase noise of VCO. Besides, traditional biasing circuit needs an extra biasing voltage, which increase the power consumption and also introduces noise to the VCO.

Hence, a memory reduction tail current source is formed with $M5$ and $M6$. $M5$ and $M6$ were used to force a trap and release its capture electron, rendering the transistors to be memory-less [5]. Since all the transistors in Figure 1 are switched biasing, it is expected to have lower flicker noise.

4. SIMULATION RESULTS

The VCOs are simulated with tsmc 0.18 µm CMOS process. Four types of VCOs are defined in Table 1 to demonstrate the performance of the proposed VCO.

When coupling capacitors $C1$ and $C2$ becomes larger, the tuning range of VCO would be narrow as shown in Figure 2. Thus low phase noise can be achieved by decreasing K_{vco}. Figure 3 shows a phase noise comparison with four types of VCOs. By adding the memory reduction tail current source ($M5$ and $M6$) with the same power consumption, phase noise of VCO4 at 1 MHz offset is about 1.5 dB lower than VCO3.

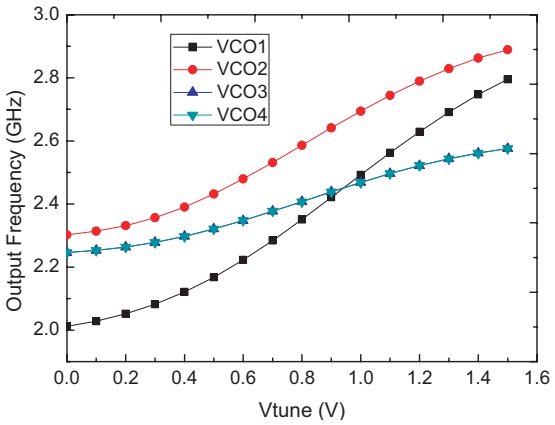

Figure 2: Tuning range performance.

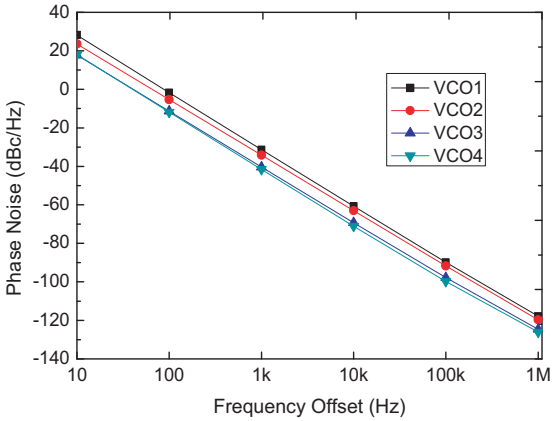

Figure 3: Phase noise performance.

Simulation results show that VCO4 has the lowest phase noise. The simulated phase noise of the proposed VCO4 is −126.1 dBc/Hz at 1 MHz offset frequency from the carrier frequency of 2.4 GHz. Figure 4 shows the output power 5 dBm at 2.4 GHz. The figure of merit (FOM) which used to depict the performance of VCO is defined as [6]:

$$FOM = L\{\Delta f\} - 20\log\left(\frac{f_0}{\Delta f}\right) + 10\log\left(\frac{P_{\mathrm{DC}}}{1\,\mathrm{mW}}\right), \tag{5}$$

where $L\{\Delta f\}$ is the phase noise at the offset frequency Δf from the carrier frequency of f_0 and P_{DC} is the power consumption in mW. The layout of the fabricated chip is shown in Figure 5. The whole chip area is $0.816 \times 0.976\,\mathrm{mm}^2$.

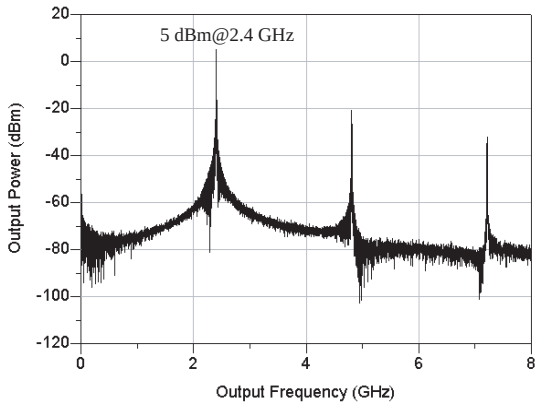

Figure 4: Output spectrum of the proposed VCO.

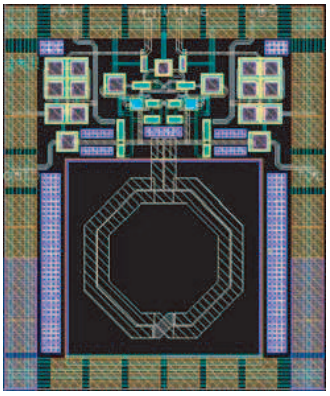

Figure 5: Layout of the proposed low phase noise VCO.

Table 2: Performance comparison of VCOs in 0.18 µm CMOS.

Ref	P_{DC} (mW)	Freq (GHz)	Tuning Range (MHz)	Phase Noise (dBc/Hz)	FOM (dBc/Hz)
Figure 1	3.1	2.4	330	−126.1@1 M	−188.8
[7]	2.77	1.95	341	−112.75@0.6 M	−178.6
[8]	1.5	2.55	131	−119.2@1 M	−185.6
[9]	2.7	2.6	560	−122.3@1 M	−186.3
[10]	3.06	1.57	240	−120@1 M	−179.1

5. CONCLUSIONS

Low phase noise and low power VCO in 0.18 µm CMOS technology is presented. With the memory reduction tail current source and coupling capacitors, the proposed VCO achieves phase noise as low as −126.1 dBc/Hz at 1 MHz offset from 2.4 GHz carrier frequency. The output oscillation frequency can be tuned from 2.25 GHz to 2.58 GHz with 14% tuning range. The performance comparison with the proposed VCO and some prior works are summarized in Table 2, a superior FOM of −188.8 dBc/Hz compared with other VCOs is proved. The proposed low phase noise VCO is suitable for 2.4 ∼ 2.4835 GHz ISM band of the Bluetooth standard.

ACKNOWLEDGMENT

The authors wish to thank the Chip Implementation Center (CIC) of the National Applied Research Laboratories, Taiwan, R.O.C., for supporting the tsmc CMOS process and further fabrication.

REFERENCES

1. Rogers, J. W. M., J. A. Macedo, and C. Plett, "The effect of varactor nonlinearity on the phase noise of completely integrated VCOs," *IEEE Journal of Solid-state Circuits*, Vol. 35, No. 9, 1360–1367, 2000.
2. Ramiah, H. and T. Z. A. Zulkifli, "A low-phase noise and high output swing RF LC-VCO in CMOS technology," *Proceedings of IEEE RF and Microwave Conference*, 197–200, Putrajaya, Malaysia, September 2006.
3. Rohde, U. L. and D. P. Newkirk, *RF/Microwave Circuit Design for Wireless Applications*, Wiley Interscience, 2000.
4. Aktas, A. and M. Ismail, *CMOS PLLs and VCOs for 4G Wireless*, Kluwer Academic Publishers, 2004.
5. Boon, C. C., M. A. Do, K. S. Yeo, J. G. Ma, and X. L. Zhang, "RF CMOS low-phase-noise LC oscillator through memory reduction tail transistor," *IEEE Transactions on Circuits and Systems*, Vol. 51, No. 2, 85–90, 2004.

6. Lee, S. H., Y. H. Chuang, S. L. Jang, and C. C. Chen, "Low-phase noise Hartley differential CMOS voltage controlled oscillator," *IEEE Microwaves and Wireless Components Letters*, Vol. 17, No. 2, 145–147, 2007.
7. Hsu, M. T., C. Y. Chiang, and T. Y. Chih, "Design of low power with low phase noise of VCO by CMOS process," *Proceedings of Asia-Pacific Microwave Conference*, Suzhou, China, December 2005.
8. Gil, J., S. S. Song, H. Y. Lee, and H. Shin, "A −119.2 dBc/Hz at 1 MHz, 1.5 mW, fully integrated, 2.5-GHz, CMOS VCO using helical inductors," *IEEE Microwaves and Wireless Components Letters*, Vol. 13, No. 11, 457–459, 2003.
9. Lee, S. Y. and J. Y. Hsieh, "Analysis and implementation of a 0.9-V voltage-controlled oscillator with low phase noise and low power dissipation," *IEEE Transactions on Circuits and Systems*, Vol. 55, No. 7, 624–627, 2008.
10. Park, K. G., C. Y. Jeong, J. W. Park, J. W. Lee, J. G. Jo, and C. Yoo, "Current reusing VCO and divide-by-two frequency divider for quadrature LO generation," *IEEE Microwaves and Wireless Components Letters*, Vol. 18, No. 6, 413–415, 2008.

Novel Super Regenerative Transponder (SRGT) for RFID Tags and ASK signals

Yukio Iida
FSC, and Dept. of Electric and Electronic Eng., Faculty of Engineering Science
Kansai University, Japan

Abstract— Recently, RFID technology to discriminate individuals with radio wave has fast been noticed and studied at full length in many fields. In this paper, we are proposing utilization of faint radio wave and super-regenerative transponder (SRGT) with power feeding by electromagnetic wave. We also study the SRGT circuit that transmits and receives the digital signals.

1. INTRODUCTION

RFID technology has fast been noticed and studied at full length in many fields [1]. RFID has a great many possible applications. However, it is worried whether demands necessary hereafter can be satisfied or not because frequency bands allotted for RFID are not so broad. Thus we are considering utilization of very weak radio wave. Very broad frequency band can be used as well as its use requires no license.

Solar power generation with satellites is a grand project [2]. Derived from this concept, there is an idea that unmanned airplane is kept flying by using energy transmitted with electromagnetic wave to use for wireless relay [3]. Regarding the wireless IC tag, we plan to use tag fed with electromagnetic wave instead of battery. We have considered that the tag fed with electromagnetic wave and communicating with very weak radio wave becomes an important element to support gigantic demand [4], and wrestled with research from this standpoint.

The roles of SRGT are reception from reader/writer, amplification of faint radio wave and transmitting. The transmitting radio wave strength must be faint.

Described first of all in this paper is the system of wireless IC tag that is fed with electromagnetic wave power and communicates with very weak radio wave. Next, we also study the SRGT circuit that transmits and receives the digital signals.

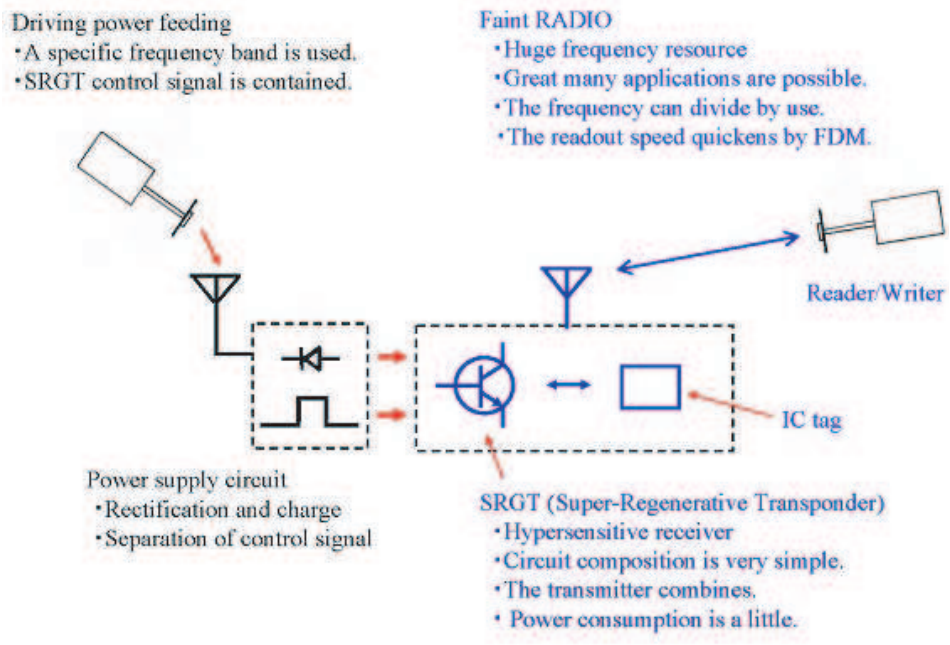

Figure 1: Concept of a system prepared for demand expansion.

2. A SYSTEM PREPARED FOR DEMAND EXPANSION

Very many applications of RFID are possible. It seems impossible to prepare for future demands only with frequency bands that have been allotted for RFID. Accordingly, very weak radio wave that requires no license is actively utilized though its definition will differ by country, too. As it can use a very broad frequency band, a large demand can be accommodated. In a common sense, it may be considered that reading probability from the tag must be near 100%. Sufficient role can be played even though reading probability is 70% or 50%. In the case of stray pet, for instance, it is considered that finding probability can get fairly higher than with past methods by installing sensors from place to place. Application range becomes very broad when including such ways of use.

Besides, use of battery for the tag is adverse from the viewpoint of management cost. Consequently, electromagnetic wave feeding is conducted by using frequency different from that for communication with the tag, as shown in Figure 1. As mentioned above, we have considered that the tag feeding with electromagnetic wave and communication with a very weak radio wave becomes an important element for supporting extravagant demand.

3. SRGT

The roles of SRGT are to receive, to amplify the faint wave from the reader/writer (R/W), and to reply to R/W. Basic operation of SRGT is shown in Figure 2. The SRGT circuit transmits and receives the digital signals as shown in Figure 3. Figure 4 shows an example of super-regenerative circuit. Figure 5 shows the simulation results of the SRGT response wave form for various input signal current levels injected into resonant circuit. It is understand the SRGT circuit is to be able to operate the digital signal as shown in Figure 3.

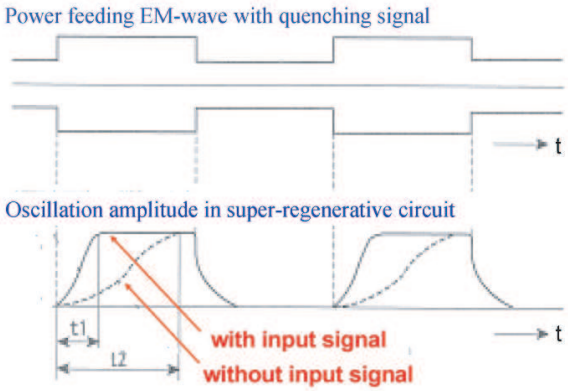

Figure 2: Basic operation of super-regenerative receiver.

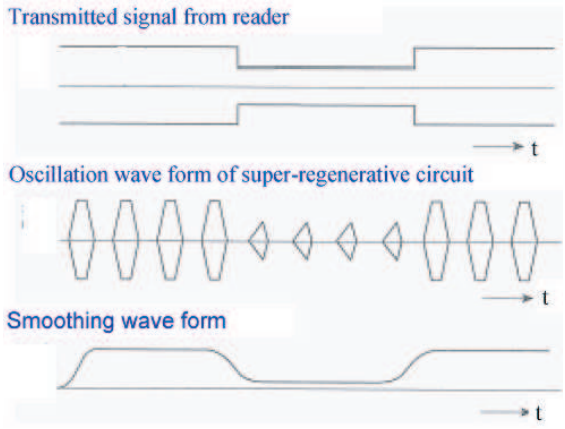

Figure 3: Operation of super-regenerative transponder.

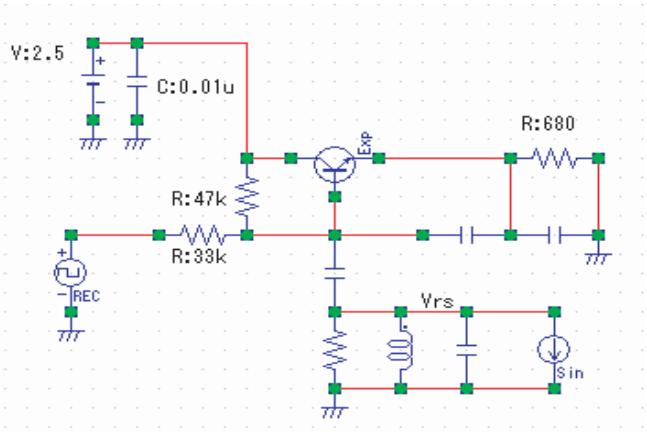

Figure 4: Super-regenerative circuit.

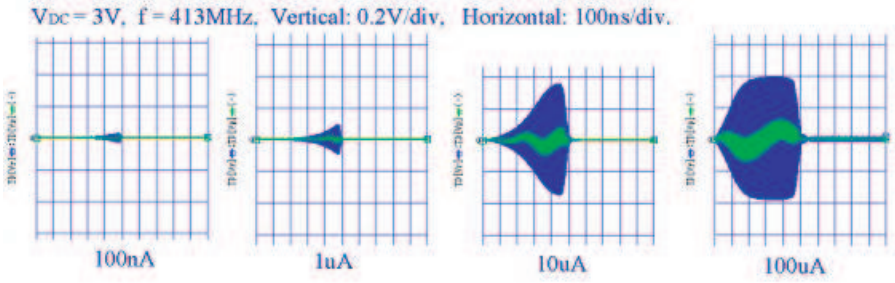

Figure 5: Oscillation amplitude construction.

4. SAFETY AND SAFE SOCIETY

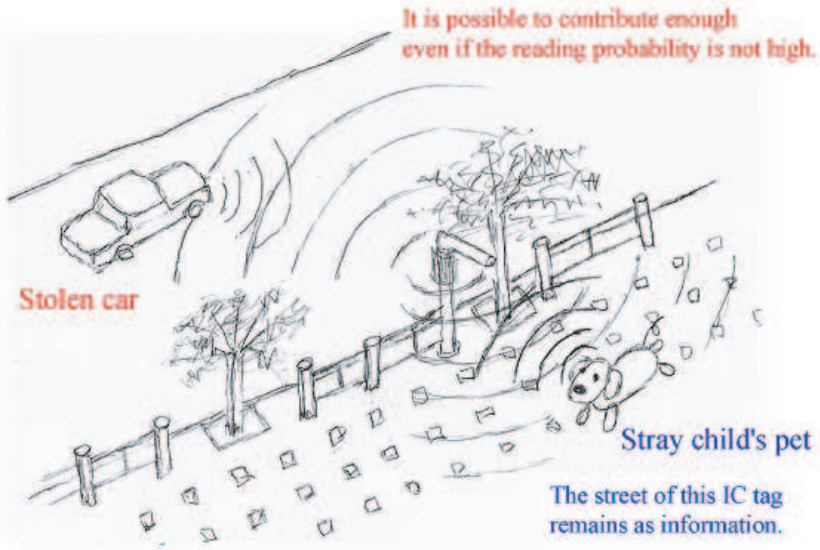

Figure 6: Support to safety and safe society.

5. CONCLUSIONS

Concept of a system of wireless IC tag that is fed with electromagnetic wave power and communicates with very weak radio wave was proposed.

ACKNOWLEDGMENT

This work was supported by "Academic Frontier" Project for Private Universities: Matching Fund Subsidy from MEXT, 2007-2011. The computations for this research were performed by the Large-Scale Computer System at the Osaka University Cyber media Center.

REFERENCES

1. Finkenzeller, G. K., *RFID Handbook, Radio-frequency Identification Fundamentals and Applications*, John Wiley & Son, Chichester, 1999.
2. Kraft, C. C. and R. O. Piland, "The solar power satellite concept — The past decade and the next decade," *Space Solar Power Review*, Vol. 1, 39–65, 1980.
3. Maruyama, M., M. Suzuki, Y. Hase, R. Miura, and W. Akinaga, "R&D of mobile communications systems using stratospheric platforms," *Pap. Am. Inst. of Aeronaut. and Astronaut.*, 8, 2002.
4. Iida, Y., "Proposal of RF recognition system prepared for demand expansion and use of super-regenerative circuit," *Proceedings of 2007 IEICE Society Conference*, Japan, Sept. 2007.
5. Hall, G. O., *Superregenerative Receivers, Microwave Receivers*, Chap. 20, S. N. Van Voorhis ed., MIT radiation Lab., Series 23, Mc-Graw Hill, New York, 1948.

A Low Cost 1 Watt Doherty Power Amplifier for WLAN and WiMAX Applications

Shilei Jin, Jianyi Zhou, Lei Zhang, and Wei Hong
State Key Lab. of Millimeter Waves, School of Information Science and Engineering
Southeast University, Nanjing 210096, China

Abstract— This paper presents the design and implementation of a low-cost 1 Watt Doherty Amplifier with high efficiency for the WLAN and WiMAX applications. Two 1 Watt Heterostructure FETs with SOT-89 surface-mount package are adopted as the final stage of the carrier amplifier and the peak amplifier. The proposed Doherty amplifier has the characteristic of both high power added efficiency (PAE) and acceptable linearity. The superior performance is achieved through selecting the best operation point of the peak amplifier. The sweet point of the developed Doherty amplifier is about 3.5 dB back-off from the saturated power. According to the experimental results, the output P1dB power is about 33.5 dBm. When the output power is 30 dBm, the tested PAE is about 31.5% and the IMD3 is about −34 dBc.

1. INTRODUCTION

It is well known that the power amplifier (PA) is one of the most important components in an RF transceiver. With the fast development and commercial applications of transmitters for the wireless local area network (WLAN) and worldwide interoperability for microwave access (WiMAX), the demand of medium output PA (about 1 Watt) is increasing rapidly [1].

Because of the high peak-to-average power ratio (PAPR) signals in the WLAN and WiMAX transceivers, the linearity of the transmitter becomes one of the most key factors in the system design. In fact, as the power amplifier operates close to the saturation region where both high efficiency and high output power are achieved, the degradation in linearity becomes significant. Consequently PA must operate at a large amount of back-off from the peak output power, thus efficiency is rather poor.

Power amplification architectures with inherently more power efficient are being considered to improve the power efficiency. Such techniques are included load modulation technique [2], envelope elimination and restoration (EER) [3], switching mode amplifiers [4], and envelope tracking [5]. These techniques can provide high PEA, however the architectures are complicated with other disadvantages. The Doherty Power Amplifier (DPA) is a promising candidate with advantages of high PAE, low cost and simple construction [6]. Doherty amplifier techniques have been extensively studied to improve efficiency, and could provide the advantage of improving the efficiency and linearity simultaneously using a simple circuit [7]. Some advanced techniques of DPA have been reported [8–10] such as envelop tracking technique, using defected ground structure (DGS) microstrip line and weighted polynomial digital predistortion technique. These methods improve performance of DPA however there are many drawbacks including complex circuit configuration, modest enhancement and high cost.

In this paper, two Heterostructure FETs (HFET) are adopted to construct a low-cost 1 Watt 2.4 GHz DPA for WLAN and WiMAX applications as shown in Figure 1. By selecting bias level of the peak amplifier, the PAE of the DPA is significantly improved with acceptable linearity at the 30 dBm output power. Additionally comparison between DPA and conventional Class-AB balanced power amplifiers (CPA) is discussed in terms of power gain, PAE and IMD3.

2. CIRCUIT CONFIGURATION OF DOHERTY AMPLIFIER

The Doherty amplifier was first proposed by W. H. Doherty in 1936 [11]. A DPA consists of a carrier amplifier and a peak amplifier. At low input levels the peak amplifier is cut off and carrier amplifier operates as a linear class-AB amplifier. For the input power above the transition point peak amplifier turns on. Carrier amplifier is still saturated to achieve high efficiency and peak amplifier provides additional power required. At peak output power both power amplifiers are saturated. The output load is connected to the carrier amplifier through an impedance inverter (a quarter-wave transmission line) and directly to the peaking amplifier. Key concept of DPA is obtaining maximum efficiency over 6 dB dynamic range using load modulation. The details of the discussion about the efficiency enhancement principles are in [12].

Figure 1 shows the schematic diagram of a DPA with off-set transmission lines at the output circuits which are used to fully match the two amplifiers and enhance efficiency of DPA [13].

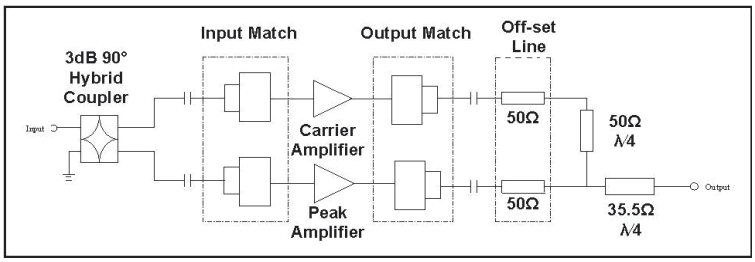

Figure 1: Schematic diagram of Doherty power amplifier.

3. EXPERIMENTAL RESULTS

3.1. Performance of Doherty Amplifier at Different Bias Level

The research on the performance of the Doherty amplifier focuses on different bias voltage of peak amplifier. P1dB of HFET used to construct the proposed Doherty amplifier is 30.8 dBm and the quiescent drain current is 250 mA operating at 2.4 GHz. At different bias level the peak amplifier works at different operation points. As the bias voltage decreases, drain current degrades and peak amplifier operates from class AB to class C. The carrier amplifier is biased at class AB when peak amplifier is cut-off to provide linear output power.

Figure 2(a) shows measured PAE of Doherty amplifier working at different bias level. Figure 2(b) shows the IMD3 character of two-tone signals measurement. The center of the two-tone signals is 2.4 GHz with space of 10 MHz. Table 1 shows values of quiescent drain current, IMD3, power gain and PAE at the average output power of 30 dBm.

When the peak amplifier is biased at class AB, both of quiescent drain current and power are higher. The peak amplifier starts working at low input power so the PAE cannot hold a high level

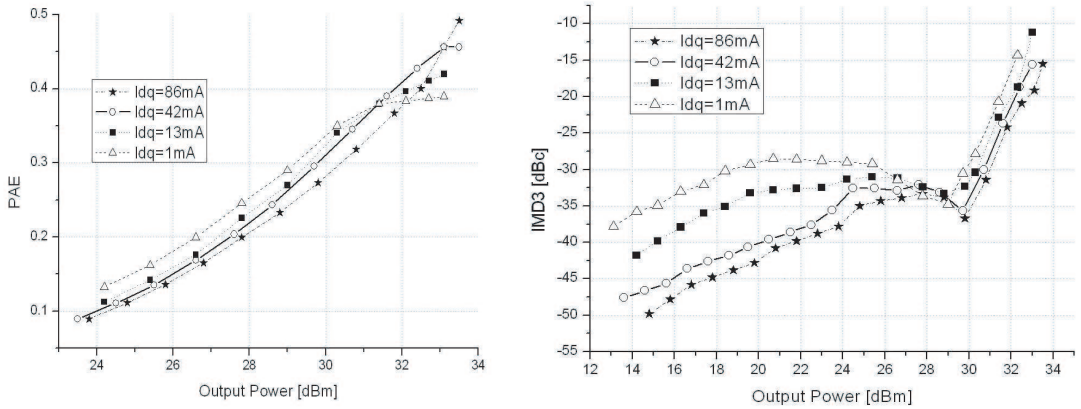

Figure 2: (a) Measured PAE performance of Doherty power amplifier at different operation points, (b) measured IMD3 performance of Doherty power amplifier at different operation points.

Table 1: Measure performance of Doherty amplifier at different bias point.

Drain Current [mA]	IMD3 [dBc]	Gain [dB]	PAE [%]
86	−36.2	14.1	28.6
42	−33.6	13.7	31.6
13	−32	13.3	33.1
1	−28.1	12.8	34.3

over a broad range at high input level. At class c level peak amplifier turns on hardly when carrier amplifier is saturated. Consequently PAE is improved. Because peak amplifier turns on later when biased at deeper class c, the peak PEA is lower than other biased level. Although PAE performance of deeper class c is best at output power of 30 dBm the IMD3 deteriorates greatly. We can draw the conclusion that DPA with the bias voltage of −2.2 V and quiescent drain current of 13 mA works better than other operation points because of high PAE and acceptable linearity.

3.2. Measured Performance of the Proposed Doherty Amplifier Biased at Perfect Point

Figure 3 shows a photograph of the implemented Doherty amplifier applying technique of off-set line. In order to validate the proposed DPA, we design a CPA. Both amplifiers use the same HFETs and work at 2.4 GHz. Peak amplifier of the Doherty amplifier is biased at the point we select above. The implemented Doherty amplifiers have been further optimized experimentally to achieve high efficiency and good linearity by modifying the off-set lines.

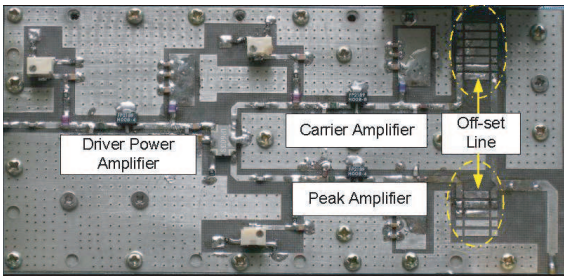

Figure 3: A photograph of the proposed Doherty amplifier with off-set lines.

Figure 4(a) shows the power gain characters and measured PAE performance of the two amplifiers at different output power levels. We can see that gain of DPA is degraded about 0.6–1.1 dB due to the lower bias voltage. The PAE of the Doherty amplifier is improved over a broad average output power levels and enhanced by 9.1% at the output power of 30 dBm. The enhancement of PAE is not significantly high because of consideration the linearity of Doherty amplifier. Two-tone measurements results of the two amplifiers are shown in Figure 4(b). Input signals are centered at 2.4 GHz with 10 MHz and 5 MHz spacing. Due to the different phase between carrier amplifier and peak amplifier third order harmonics tend to cancel out with each other. Through modifying the off-set lines we can change the phase to trade off between PAE and linearity. As shown in the figure, there is a trough around the output power of 30 dBm and the linearity is improved 2–4 dBc by harmonic cancellation.

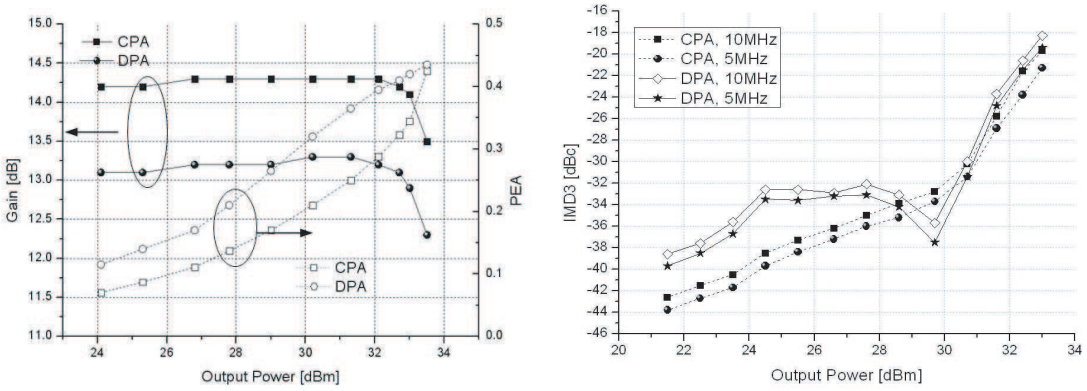

(a) (b)

Figure 4: (a) Measured gain and PAE performance of Doherty amplifier and balanced amplifier, (b) measured IMD3 performance of Doherty amplifier and balanced amplifier with the two-tone signal.

4. CONCLUSION

In this paper, we have constructed a low-cost 1 Watt average output power Doherty power amplifier using two 1 Watt HFETs. To select the suitable operation point we measured the performance of

the DPA with different bias level and chose the quiescent drain current of 13 mA as the perfect level. Additionally we optimized the Doherty amplifier by modifying the off-set line. Working at 2.4 GHz the proposed DPA has significantly improved the efficiency over a broad average output power compared to the conventional balanced amplifier. Moreover because of the harmonic cancellation of different IM3 phase the linearity of DPA is improved without any linearity enhancement techniques.

ACKNOWLEDGMENT

This work was supported in part by NSFC under Grant 60621002 and in part by the National High-Tech Project under Grant 2007AA01Z2B4.

REFERENCES

1. Ma, L. and D. Jia, "The competition and cooperation of WiMax, WLAN and 3G," *Mobile Technology, Applications and Systems 2nd International Conference*, 1–5, Nov. 2005.
2. Nam, J., J. H. Shin, and B. Kim, "A handset power amplifier with high efficiency at low level using load modulation technique," *IEEE Trans. Microw. Theory Tech.*, Vol. 53, No. 8, Aug. 2005.
3. Raab, F. H., B. E. Sigmon, R. G. Myers, and R. M. Jackson, "L-band transmitter using Kahn EER technique," *IEEE Trans. Microw. Theory Tech.*, Vol. 46, No. 12, 2220–2225, Dec. 1998.
4. Tsai Pi, H., A. G. Metzger, P. J. Zampardi, M. Iwamoto, and P. M. Asbeck, "Design of high efficiency current-mode class D amplifier for wireless handsets," *IEEE Trans. Microw. Theory Tech.*, Vol. 53, No. 1, Jan. 2005.
5. Kimball, D. F., J. Jeong, C. Hsia, P. Draxler, S. Lanfranco, W. Nagy, K. Linthicum, L. E. Larson, and P. M. Asbeck, "High-efficiency envelope tracking W-CDMA base-station amplifier using GaN HFETs," *IEEE Trans. Microw. Theory Tech.*, Vol. 54, No. 11, 3848–3856, Nov. 2006.
6. McMorrow, R. J., D. M. Upton, and P. R. Maloney, "The microwave Doherty amplifier," *IEEE MTT-S Int. Microwave Symp. Dig.*, 1653–1656, 1994.
7. Kenington, P. B., *High-linearity RF Amplifier Design*, Artech House, Norwood, MA, 1999.
8. Yang, Y., J. Cha, B. Shin, and B. Kim, "A microwave Doherty amplifier employing envelop tracking technique for high efficiency and linearity," *IEEE Microw. Wireless Compon. Lett.*, Vol. 13, No. 9, Sep. 2003.
9. Choi, H. J., J. S. Lim, and Y. C. Jeong, "A new design of Doherty amplifiers using defected ground structure," *IEEE Micro. Wireless Compon. Lett.*, Vol. 16, No. 12, Dec. 2006.
10. Hong, S., Y. Y. Woo, J. Kim, and J. Cha, "Weighted polynomial digital predistortion for low memory effect Doherty amplifier," *IEEE Trans. Microw. Theory Tech.*, Vol. 55, No. 5, May 2007.
11. Doherty, W. H., "A new high efficiency power amplifier for modulated waves," *Proc. IRE*, Vol. 24, No. 9, 1163–1182, 1936.
12. Raab, F. H., "Efficiency of Doherty RF power amplifier system," *IEEE Trans. Broadcast.*, Vol. BC-33, No. 3, 77–83, Sep. 1987.
13. Yang, Y., J. Yi, Y. Y. Woo, and B. Kim, "Optimum design for linearity and efficiency of microwave Doherty amplifier using a new load matching technique," *Microwave J.*, Vol. 44, No. 12, 20–36, Dec. 2001.

Planar Antennas for UMPC Integration

Cheng-Hung Lin[1], **Guan-Yu Chen**[2], **Jwo-Shiun Sun**[2], **Kwong-Kau Tiong**[1], **Yu-Hsiang Chen**[1], **Tsan-Hsuan Peng**[1], **and Y. D. Chen**[3]

[1]Department of Electrical Engineering, National Taiwan Ocean University, Taiwan
[2]Department of Electronic Engineering, National Taipei University of Technology, Taiwan
[3]Antenna and EMC Laboratory, HTC Corporation, Taiwan

Abstract— This UMPC will co-integration and co-design of the antennas for 2.5G/3G cellular, WLAN, BT, and GPS applications of 3G mobile handset (Figure 1), respectively. This 2.5G/3G antenna shows a wide operating bandwidth for low band and high band bandwidth, making it easy to cover the GSM, EDGE, CDMA, CDMA 2000, W-CDMA and UMTS band for wireless communication and dual mode operation of a mobile handset phone. Embedded Wi-Fi (2.4–2.5 GHz) and BT antenna in mobile handset for VoIP/IPTV and wireless connection. The resonance mode of a small PIFA antenna covers the GPS communication bandwidth of 1571.42–1579.42 MHz. The patch tuning expansion are introduced to confine the resonance mode region and to facilitate the frequency modes and impedance match expansion easily for antenna and wireless system integration design.

1. DESIGN AND RESULTS

Monopole planar antenna structure [1] have been implemented and developed to satisfy specific bandwidth specifications for modern wireless cellular communication systems like GSM (824–894 MHz), EGSM (880–960 MHz), DCS (1710–1880 MHz), PCS (1850–1990 MHz), CDMA Cellular (824–894 MHz), CDMA PCS (1750–1990 MHz) and W-CDMA/UMTS (1900–2200 MHz). Wi-Fi and BT antenna structure [2, 3] (PIFA) have been developed to satisfy specific bandwidth specifications for modern wireless LAN communication systems such as, IEEE 802.11b (2.4–2.485 GHz) and IEEE 802.11g (2.4–2.485 GHz). A GPS receiver can accurately determine its position worldwide to within a few meters. Signals for civil use are transmitted at a frequency of 1575.42 MHz and bands. Assisted GPS supports the mobile phone with assisted data in addition to the GPS data. The assisted data is transmitted over the cellular network. It contains information about the current position of the satellites and an error vector which is measured in the base station. With this information, the mobile phone is able to reduce the time to first fix, which is an advantage for travelers at the airport, and to increase the position accuracy. The general GPS functions of PDA support the assisted functionality in 2.5/3G wireless networks. In this paper, compact and low profile PIFA antenna for GPS function have been proposed and those antennas were designed and 3D measured [4, 5], as shown in Figure 2 to Figure 7 and Table 1 to Table 4.

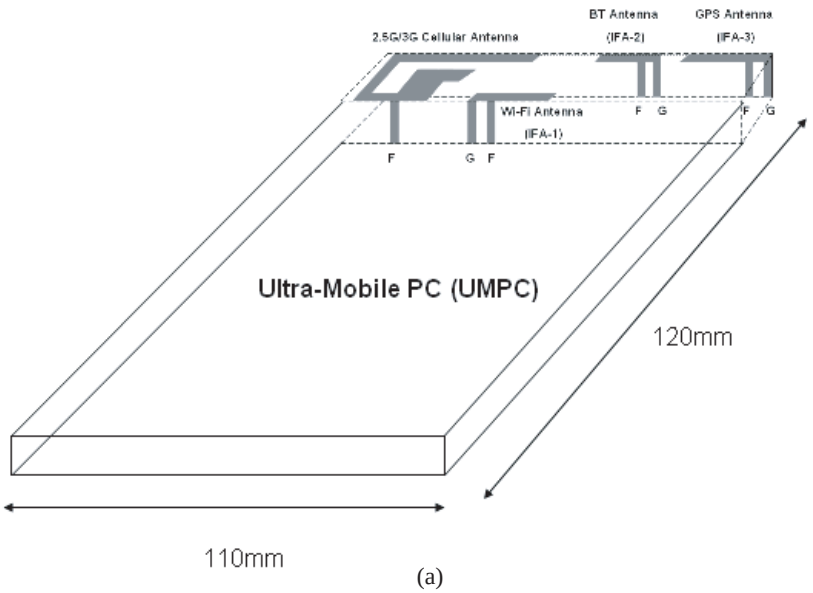

(a)

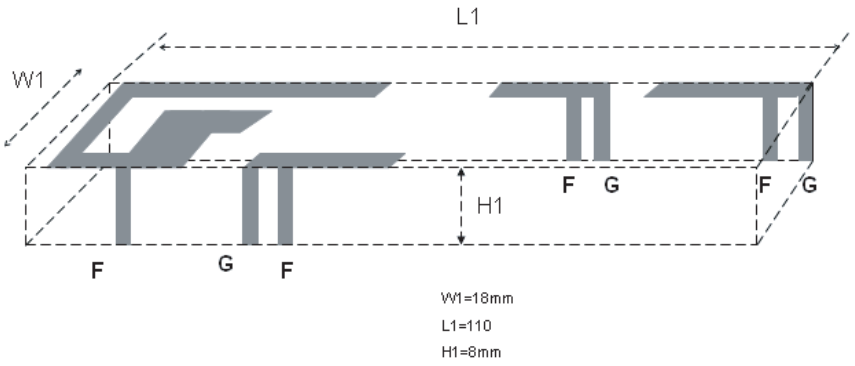

(b)

Figure 1: (a) The proposed antennas structure for UMPC application and integration (Dimension: 120 mm × 110 mm × 8 mm). (b) The proposed antennas structure for UMPC application and integration (Antennas dimension: L1 × W1 × H1 = 110 mm × 18 mm × 8 mm).

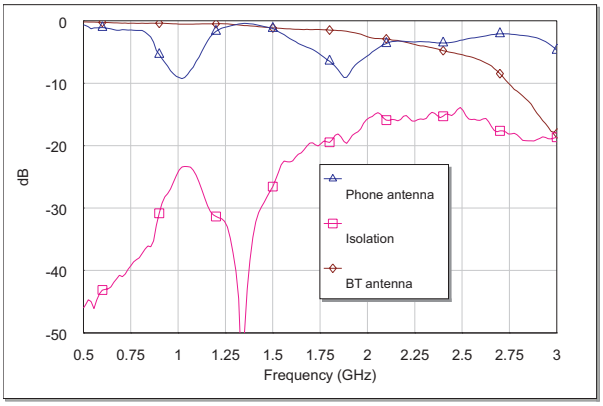

Figure 2: Measured data of phone & BT antenna.

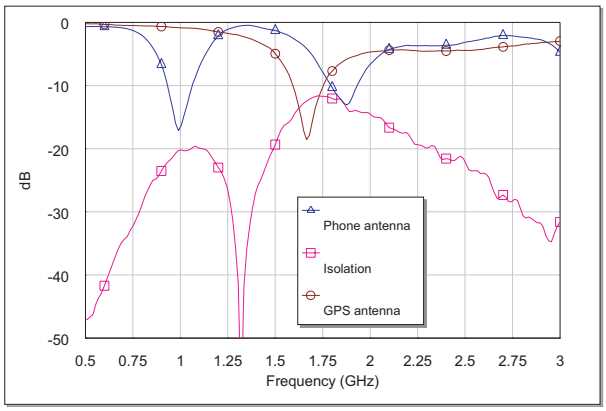

Figure 3: Measured data of phone and GPS antenna.

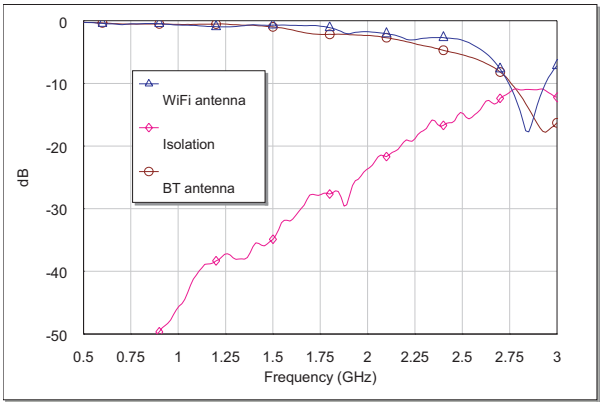

Figure 4: Measured data of WiFi and BT antenna.

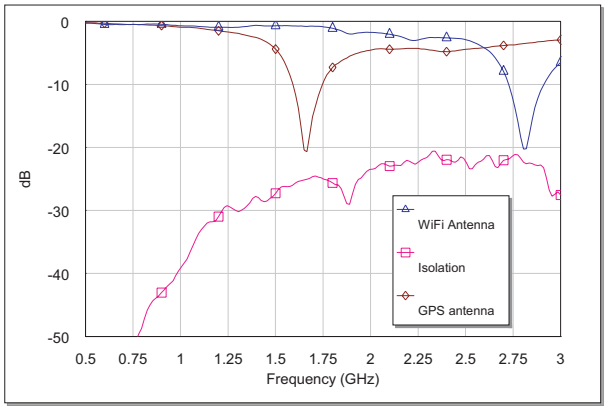

Figure 5: Measured data of WiFi and GPS antenna.

Table 1: Measured data of phone antenna.

Frequency (MHz)	800	850	900	950	1700
Efficiency (dB)	−4.2	−3.1	−1.2	−1.4	−3.2
Frequency (MHz)	1800	1900	2000	2100	2200
Efficiency (dB)	−3.5	−2.1	−2.4	−4.1	−3.8

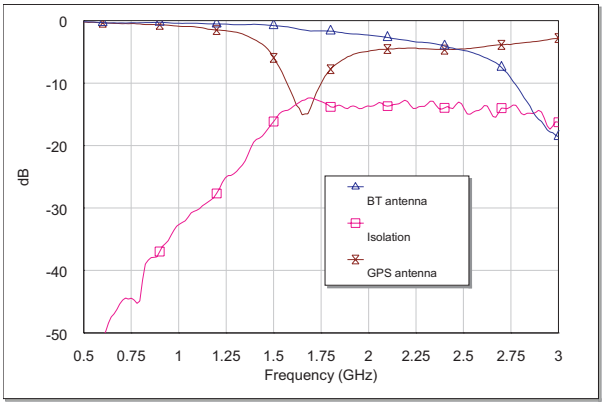

Figure 6: Measured data of BT and GPS antenna.

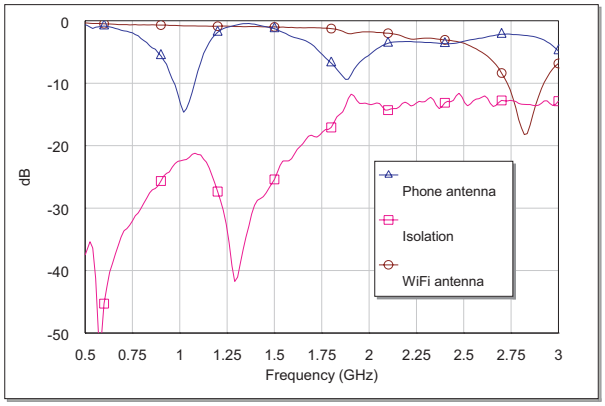

Figure 7: Measured data of phone and WiFi antenna.

Table 2: Measured data of WiFi antenna.

Frequency (MHz)	2400	2450	2500
Efficiency (dB)	−4.1	−4.3	−4.2

Table 3: Measured data of BT antenna.

Frequency (MHz)	2400	2450	2500
Efficiency (dB)	−3.3	−3.1	−3.5

Table 4: Measured data of GPS antenna.

Frequency (MHz)	1550	1575	1600
Efficiency (dB)	−1.5	−0.3	−0.52

2. CONCLUSION

In the UMPC antennas study, the author introduces several kinds of structures of cellular phone antenna, WLAN antenna, BT antenna, GPS antenna for multi-band applications.

ACKNOWLEDGMENT

The authors would like to thank the Antenna and EMC research laboratory, HTC Corporation, for their assistance in wireless and system integration measurements.

REFERENCES

1. Balanis, C. A., *Antenna Theory*, John Wiley & Sons, Inc, 1997
2. Kraus, J. D. and R. J. Marhefka, *Antennas for All Applications*, McGraw-Hill, 2002.
3. Wong, K. L., *Planar Antennas for Wireless Communication*, John Wiley & Sons, Inc, 2003.
4. Chen, G. Y., J. S. Sun, and Y. D. Chen, "The 3D far-field antenna measurement technology for radiation efficiency, mean effective gain and diversity antenna operation," *2006 The 7th International Symposium on Antennas, Propagation, and EM Theory (2006 ISAPE)*, 42–45, Guilin, China, Oct. 2006.
5. Chen, G. Y., J. S. Sun, C. H. Lin, K. K. Tiong, and Y. D. Chen, "Small antenna measurement facilities," *PIERS Proceedings*, 157–158, Hangzhou, China, March 24–28, 2008.

WLAN and Bluetooth Antenna Design

Kekun Chang[1], **Guan-Yu Chen**[1], **Jwo-Shiun Sun**[1], **and Y. D. Chen**[2]

[1]Department of Electronic Engineering, National Taipei University of Technology, Taiwan
[2]Antenna and EMC Laboratory, HTC Corporation, Taiwan

Abstract— A high performance monopole antenna fabricated using a folded planar line as radiator is presented. A prototype of the proposed monopole antenna with a compact area size of 20 mm × 9 mm is implemented, and the multi-band WLAN/Bluetooth antenna shows a wide operating bandwidth of about 200 MHz and 1000 MHz for low band and high band, bandwidth, making it easy to cover the IEEE 802.11a, IEEE 802.11b, IEEE 802.11g and IEEE 802.11n (MIMO) bands for wireless communication and future 4G wireless operation of a mobile VoIP/VoWLAN handset phone.

1. INFORMATION

Recently, antennas that can be easily integrated on the RF circuit board to satisfy the band specifications for wireless LAN applications such as IEEE802.11a (5.15–5.35 GHz and 5.47–5.825 GHz), IEEE802.11b (2.4–2.485 GHz), IEEE802.11g (2.4–2.485 GHz) and IEEE802.11n (2.4–2.485 GHz, 5.15–5.35 GHz and 5.47–5.825 GHz) have been reported [1–3]. The main study of this paper is to develop a compact and low profile antenna for WLAN applications on multi-media PDA and smart mobile phone. By utilizing the proposed planar antenna structure, it is easy to be embedded and co-integrated into a compact mobile handset. This proposed antenna is suitable for WLAN IEEE 802.11a/b/g/n and VoIP/WiFi applications. With the broadside radiations, the proposed dual wideband monopole antenna carries a stable gain variation in 2.4–2.5 GHz and 5–6 GHz bands, respectively.

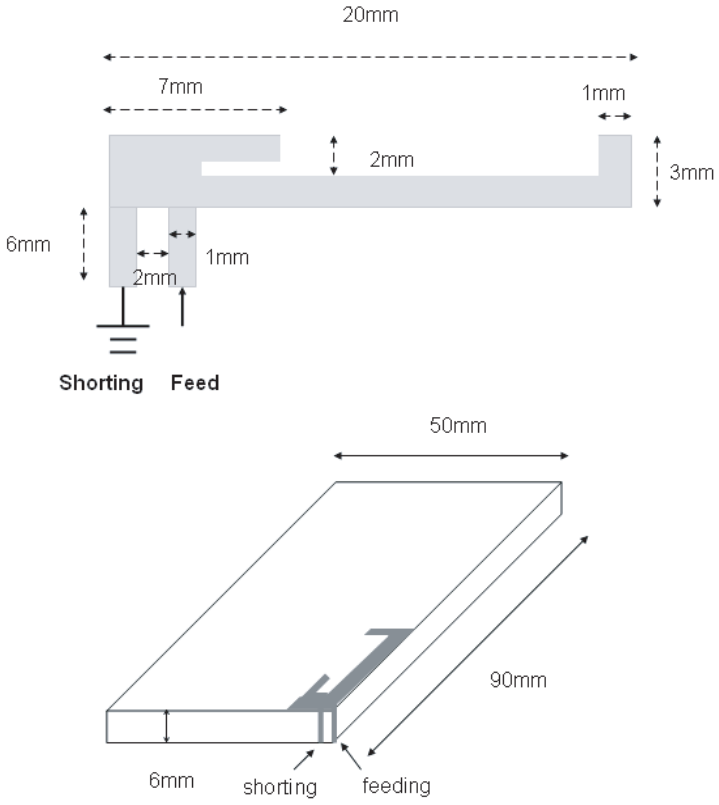

Figure 1: Dual-band shorting monopole antenna.

2. WLAN ANTENNA AND DESIGN

In this paper, the dual wideband monopole antenna has several advantages over conventional monopole-like antenna and planar antenna for mobile handsets. The co-design of folded metal patch antenna can overcome the problem of narrow band of the conventional antenna. By adding a low-Q resonator as a wideband radiator, the coupling between the lower band and higher band of the antenna can be improved. The design of a dual wideband monopole antenna with dual path of planar radiator for WLAN applications is shown in Figure 1. The proposed dual planar antenna is designed of compact size of 20 mm × 9 mm. This long folded wire radiator has a total length of about 29 mm, which excited lower band. The short metal patch radiator has a total length of about 12 mm, which excited higher band. The total length of the effective radiator wire path of the designed antenna is close to one quarter wavelength at free space of the center frequency about 2450 MHz of lower band and about 5700 MHz of higher band. By fine-tuning the length of the length of the long and short radiators, the antenna resonant frequencies can be effectively controlled.

3. RESULTS

An internal small antenna usually suffers from degradation in performance of narrow bandwidth and radiation efficiency. In this experiment, we design and fabricate a dual broadband interior type radiator and shorting monopole antenna with a high performance radiation pattern over a design operation band using dual path. It has a measured return loss bandwidth (referenced −10 dB) about 200 MHz with center frequency at 2.45 GHz (2.35–2.55 GHz) and 600 MHz with center frequency at 5.7 GHz (5.4–6 GHz), as shown in Table 1. The measured antenna gain is larger than 2 dBi. The compact shorting planar monopole dual-band antenna is easily to be applied on a practical mobile phone with VoIP/Wi-Fi applications.

Table 1: Measured gain data.

Frequency (MHz)	2400	2450	2500	5400	5600	6000
Gain (dBi)	3.3	3.1	3.5	3.6	3.5	4.2

4. CONCLUSIONS

A compact internal planar monopole antenna with folded radiator for WLAN applications on a practical multi-medium PDA phone has been implemented. The proposed antenna shows a wider operating bandwidth to cover the bands applied for IEEE 802.11a/b/g/n and VoIP/VoWLAN applications.

ACKNOWLEDGMENT

The authors would like to thank the Antenna and EMC research laboratory, HTC Corporation, for their assistance in wireless and system integration measurements.

REFERENCES

1. Wong, K. L., *Planar Antennas for Wireless Communication*, John Wiley & Sons, Inc, 2003.
2. Balanis, C. A., *Antenna Theory*, John Wiley & Sons, Inc, 1997.
3. Kraus, J. D. and R. J. Marhefka, *Antennas for All Applications*, McGraw-Hill, 2002.

UMTS and DVB-H Antenna Co-integration

Kekun Chang[1], **Guan-Yu Chen**[1], **Jwo-Shiun Sun**[1], **and Y. D. Chen**[2]

[1]Department of Electronic Engineering, National Taipei University of Technology, Taiwan
[2]Antenna and EMC Laboratory, HTC Corporation, Taiwan

Abstract— In mobile TV technology, 3 G UMTS and DVB-H antenna co-design for PDA phone in future. We have proposed a novel digital video broadcast for handheld (DVB-H) antenna for mobile handheld terminal using a meander monopole radiator and a simple matching circuit. The antenna impedance covers the DVB-H frequency band of 1452–1492 MHz. The proposed antenna was designed, fabricated, and measured. And the proposed 3 G antenna covers the entire UMTS/WCDMA (1900–2200 MHz) band for VSWR < 2. The simulated antenna gain varies from 1 to 3 dBi over the operating frequency range. The obtained radiation patterns are very close to those of a conventional omni-directional antenna. Details of the proposed antenna design and the simulated and measured results are presented and discussed.

1. INTRODUCTION

Digital video broadcasting handheld (DVB-H) is an adaptation of the digital terrestrial TV standard DVB-T to the requirements of mobile applications, particularly with battery-powered handheld equipment. DVB-H is one of three prevalent mobile TV formats. It is a technical specification for bringing broadcast services to mobile handsets. The addition of time slicing, forward error correction and a further modulation mode to DVB-T produces a transmission system that is just as good at meeting the requirements of battery-powered devices as it is at handling the reception conditions at high speed. DVB-H is the latest development within the set of DVB transmission standards. DVB-H technology adapts the successful DVB-T system for digital terrestrial television to the specific requirements of handheld, battery-powered receivers. DVB-H can offer a downstream channel at high data rates which can be used standalone or as an enhancement of mobile telecoms networks which many typical handheld terminals are able to access anywhere. Time slicing technology is employed to reduce power consumption for small handheld terminals. IP datagrams are transmitted as data bursts in small time slots. DVB-H is designed to work in VHF band (174–230 MHz), UHF band (470–830 MHz), and L band (1.452–1.492 GHz). It can coexist with DVB-T in the same multiplex. DVB-H is intended to provide digital transmission of multimedia for the fast moving handheld devices by allowing the reception of digital content through mobile phones, PDA phone, etc. To reduce the amount of power required to receive the content, DVB-H uses time slicing, which allows the handheld device to be switched on only at particular intervals. In addition, the error correction and mobility is improved. DVB-H can easily be implemented in DVB-T networks.

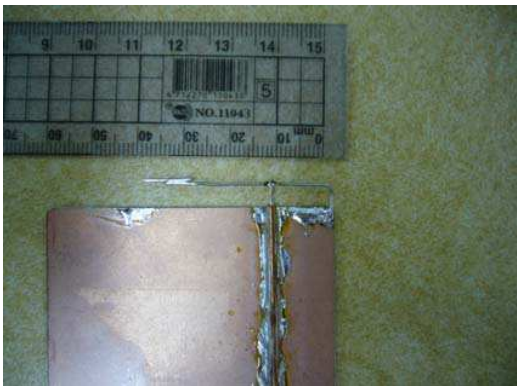

Figure 1: The proposed UMTS antenna (wire inverse-F type).

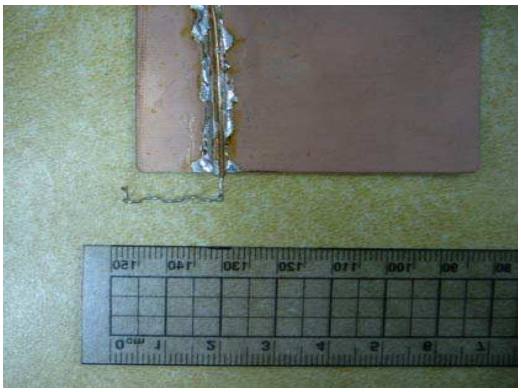

Figure 2: The proposed L-band DVB-H antenna (meander wire monopole type).

2. ANTENNA AND DESIGN

In this study, two simple structures of wire antennas with inverse-F and meander structure (Figure 1 and Figure 2) and bands for UMTS and DVB-H are investigated. Those antennas provide a wide input impedance bandwidth, and a small size for handset co-integration, as shown in Figure 3. The measured results show that the return loss, isolation (Figure 4), and wider antenna matching impedance of the shorting monopole and meander monopole type antenna provide a considerably large bandwidth even with a radiating area. The measured results are shown a simple monopole antenna performance. This design also reviews some mobile TV specifications, future progress and applications [1–3]. Simple monopole antennas for UMTS and DVB-H wireless mobile TV systems are presented. For some applications, it is required that a digital video broadcast-handheld (DVB-H) antenna be integrated into a PDA or smart phone to provide DVB-H signal reception. These compact designs and experimental results (Table 1) are described in detail in this study. This technique is suitable for creating wideband antenna with bandwidth improved and bandwidth and antenna impedance control.

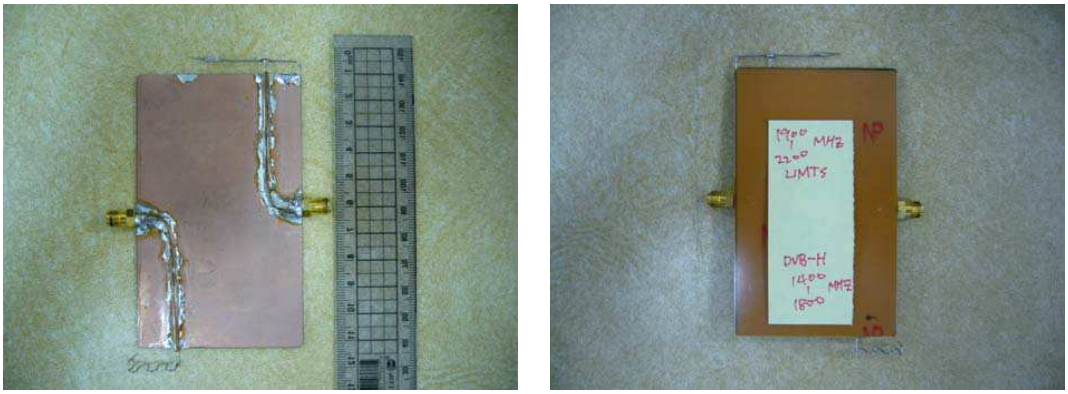

Figure 3: The practical antennas.

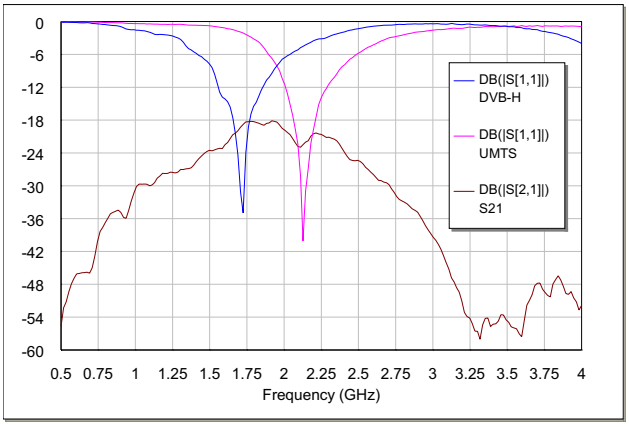

Figure 4: The measured data (return loss and antenna isolation).

Table 1: The measured antenna gain.

Band/Frequency				
UMTS	1900 MHz	2000 MHz	2100 MHz	2200 MHz
Gain	2.8	3.2	3.4	3.6
DVB-H	1425 MHz	1450 MHz	1475 MHz	1500 MHz
Gain	2.3	2.2	2.4	2.6

3. CONCLUSIONS

Two simple and very compact embedded low profile antennas for UMTS/WCDMA and DVB-H applications on a practical PDA phone have been successfully implemented. The designed antennas show the fairly good radiation characteristics. It demonstrates the coverage bandwidth for the lower band and higher band, respectively. Evidently, it is quite suitable to be implemented on a practical mobile PDA phone with 3 G mobile TV applications.

ACKNOWLEDGMENT

The authors would like to thank the Antenna and EMC research laboratory, HTC Corporation, for their assistance in wireless and system integration measurements.

REFERENCES

1. Balanis, C. A., *Antenna Theory*, John Wiley & Sons, Inc., 1997.
2. Kraus, J. D. and R. J. Marhefka, *Antennas for All Applications*, McGraw-Hill, 2002.
3. Wong, K. L., *Planar Antennas for Wireless Communication*, John Wiley & Sons, Inc., 2003.

Design of Trapezoidal Ring Antenna Using Conductor-backed CPW Structure

S. W. Lee[1], **N. Kim**[1], **S. W. Park**[1], **S. K. Jeon**[1], **and S. Y. Rhee**[2]

[1]Chungbuk National University, South Korea
[2]Chonnam National University, South Korea

Abstract— In this paper, the trapezoidal ring antenna using the conductor-backed CPW is designed and fabricated. The antenna has a broadband characteristic by the coupling effects through inserted the H-shaped parasitic patch. The conductor-backed CPW shows more stable characteristics than the CPW structure when there is occurred the variation between the feed-line and the ground plane in the front side. The bandwidth of the designed antenna is 2.2 GHz∼4.6 GHz below −10 dB.

1. INTRODUCTION

For the broadband or multiband characteristics of resonant antenna, there are some methods which are the use of higher order mode, the parasitic patch inserted in main radiation elements, slot structure, and CPW-fed structure. Especially, a more effective designing method of wideband antennas is by using coupled resonators. In particular, the patch antenna does not require being very special structure, but should be coupled to another patch or to resonant elements, which are near resonant slot in the ground plane, a resonant slot on the main patch, or a near resonant feed probe in general. If the resonant frequencies of two circuits are nearly the same, then a critical coupling coefficient can be found to match the dissimilar impedances [1].

Coplanar waveguide (CPW) structure is similar to the microstrip structure, but the ground plane located in the front side, which is beside to the feed line. Until now, the researched CPW fed slot antenna is the structure of the dipole slot shape, there are designed by various types for broadbanding and applying. In addition, the reason why the CPW fed slot antenna is interested is low radiation loss, low dispersion, and small impedance variation [2–4].

However, CPW structure is difficult to the impedance matching because of instability that is caused by the distance or the gap between the feed line and the ground plane. To solve this problem, the conductor-backed CPW structure is designed. The conductor-backed CPW structure is combined two types of the antenna, which are CPW and microstrip structure. So, even if the gap or the distance between the feed line and the ground plane is changed, they would not be significant effect to the impedance matching or the return loss. Moreover, it has small impedance and a large effective permittivity compared to CPW structure.

In this paper the proposed antenna has stable and broadband characteristics using CPWG fed. The basic structure is the trapezoidal antenna of the slot type, and H-shaped parasitic patch is inserted in the antenna. This antenna will be applicable to Wibro, WLAN, and UWB communications.

2. ANTENNA DESIGN

Figure 1 presents the layout of the proposed conductor-backed CPW-fed trapezoidal antenna. The antenna dimensions are 35 mm (W) × 70 mm (L) × 1 mm (T), and the substrate is used the FR-4 material having the permittivity 4.62. Generally, the patch antenna used the rectangular shape, but the trapezoidal shape makes that the current flows smoothly in the patch [4]. These types of the antenna are useful to UWB communication over 3 GHz band frequencies. From a long time, the circular ring (or the rectangular ring) antenna is used to make the broadband, and so the central parts of the plane type patch are removed to make the ring type, then this should appear the broadband characteristic [5].

Hence, in this research, the trapezoidal patch is removed as the antenna pattern design left only the base 3.5 mm, the upper side 3.5 mm, and both sides 3.2 mm. The resonant is occurred by adjust the antenna sizes at frequencies for the applications. Although the rectangular ring type of the antenna has the broadband frequencies, the beamwidth is the narrow. The other hand, the H-shaped patch has characteristics which are the narrow bandwidth and the wide beamwidth.

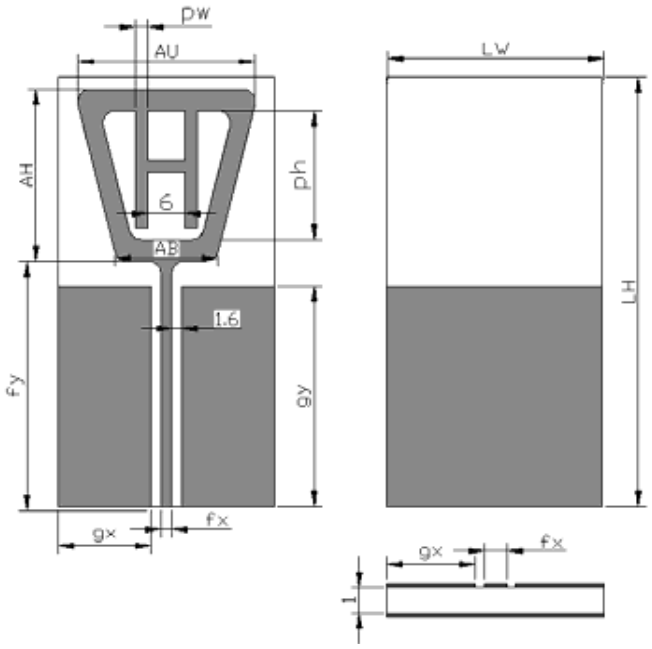

Figure 1: The structure of the proposed antenna.

Then, these types of the patches is coming the results, which are stable impedance matching and the resonant frequencies by using the coupling effect [6].

As mentioned, the reverse side ground plane is inserted to minimize the effect from the feed line or the front side ground plane. The impedance variation or the radiation loss is decreased by the stability of the structure. Also, the U-shape or n-shape patch is inserted instead of the H-shaped patch, but the results are not significantly different, just slightly shifted at the low frequency band.

3. SIMULATION AND MEASUREMENT RESULTS

Figure 2 presents the variation of the return loss according to the existence and nonexistence H-patch and patch types. The existence and nonexistence of the parasitic patch leads to very different results. In case of nonexistence parasitic patch, the resonant frequency band is very narrow, and the return loss is also small. The other case, the resonant frequency band and the return loss is obviously improved because of the coupling effect.

Table 1 presents the optimized parameters which are simulated by conditions that are the antenna and ground plane size, existence of the parasitic patch, etc. for using the 2.4 GHz frequency bands. The compared graphs between simulated results and measured results by using the optimized antenna parameters in Table 1 presents in Figure 3. For the VSWR $< 2:1$, the first resonance of simulated results is 1.4 GHz to 1.73 GHz bands, and the second resonance is 2.1 GHz to 4.85 GHz bands. Likewise the resonances of the measured results of the fabricated antenna are

Table 1: The optimized parameters of the designed antenna.

Parameters	Definition	values (mm)
AB	The base length of the trapezoid shape	16.6
AU	The upper length of the trapezoid shape	28.7
AH	The height of the trapezoid shape	28
pw	The width of the parasitic patch	2
ph	The height of the ground plane	18
gx	The width of the front ground plane	15
gy	The height of the ground plane	36

1.5 GHz to 1.7 GHz and 2.2 GHz to 4.6 GHz bands. They have very similar characteristics over 2 GHz bands, but the return loss decrease in 1.5 GHz band which is the center frequency. The error is not a big problem because the measurement of the return loss on the experimental environment is variable cause by the environmental effects, experimenter effects, etc. In addition, we do not use the 1.5 GHz band which is not adapted in our purpose, only use over the 2.2 GHz bands. As the measured results, the maximum gain is 3.4 dBi, and 2.3 GHz band for Wibro service is 1.3 dBi, 2.4 GHz band for WLAN service is 1.3 dBi.

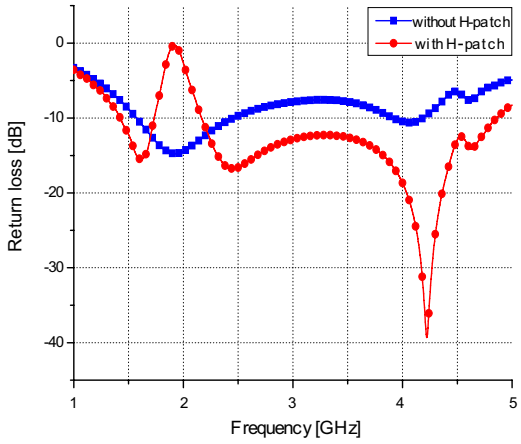

Figure 2: Variation of return loss by existence/nonexistence of the parasitic patch.

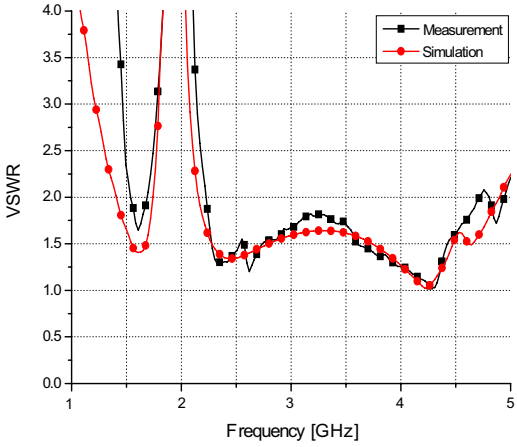

Figure 3: Comparison of VSWR of the antenna.

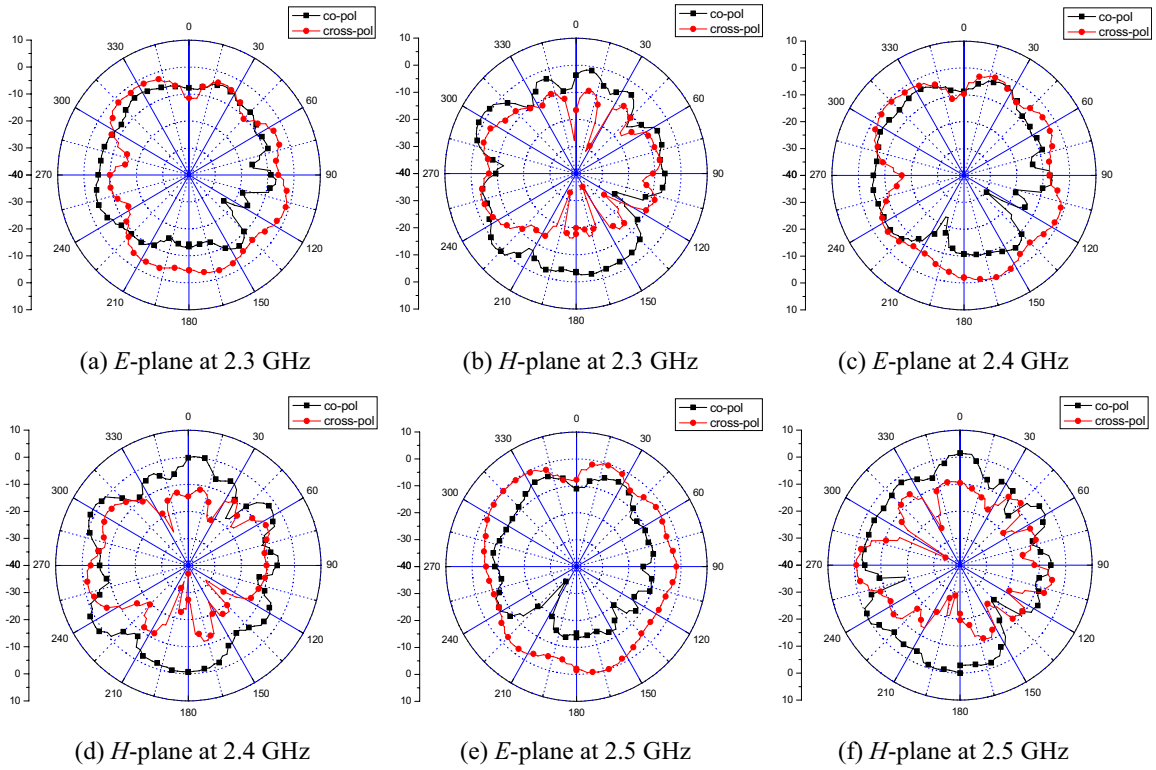

(a) *E*-plane at 2.3 GHz (b) *H*-plane at 2.3 GHz (c) *E*-plane at 2.4 GHz

(d) *H*-plane at 2.4 GHz (e) *E*-plane at 2.5 GHz (f) *H*-plane at 2.5 GHz

Figure 4: Radiation patterns of the antenna.

Figures 4(a)∼(f) presents the measured radiation patterns of the designed antenna. The radiation patterns measure at 2.3 GHz, 2.4 GHz and 2.5 GHz respectively, and show *E*- and *H*-plane. In case of the monopole antennas, they generally have omnidirectional radiation patterns in *H*-plane. The designed antenna has nearly omnidirectional patterns except 2.4 GHz, and *E*-plane also has similar radiation patterns at each frequencies.

4. CONCLUSION

We designed the CPWG antenna with trapezoidal slot antenna inserted to H-shaped patch for broadband characteristics in this paper. The original trapezoidal shaped antennas use UWB communications because it has broadband characteristics, but for Wibro and WLAN communications the slotted trapezoidal structure is used. Moreover H-shaped parasitic patch is inserted in the slotted trapezoidal shape for the product of the resonance at the wanted frequencies and 50-ohm impedance matching. CPWG structure reduced the error for reason by the distance between the front ground plane and the feed line. As the results, the antenna size is reduced by the CPWG structure, and the resonance or impedance matching is stabilized by the H-shaped parasitic patch. We confirmed the possibility by the simulations and experiments. The antenna is working in 1.5 GHz to 1.7 GHz and 2.2 GHz to 4.6 GHz by measurements, and they can be applicable to Wibro, WLAN, and UWB communications. Besides, the radiation pattern of the antenna is omnidirectional shape and the maximum gain is 3.4 dBi in the resonant bands, Wibro and WLAN services are 1.3 dBi respectively, and UWB communication has 1.7 dBi.

ACKNOWLEDGMENT

"This work was supported by the grant of the Korean Ministry of Education, Science and Technology" (The Regional Core Research Program/Chungbuk BIT Research-Oriented University Consortium).

"This research was supported by the MKE (Ministry of Knowledge Economy), Korea, under the ITRC (Information Technology Research Center) support program supervised by the IITA (Institute of Information Technology Advancement)" (IITA-2008-(C1090-0801-0034)).

REFERENCES

1. Hiraswa, K. and M. Haneishi, *Analysis, Design, and Measurement of Small and Low-profile Antennas*, Artech House, London, 1992.
2. Lee, J.-N., S.-H. Lee, and J.-K. Park, "A trapezoidal ultra-wideband antenna design," *Journal of KIEES*, Vol. 16, No. 3, 235–245, 2005.
3. Fortino, N., G. Kossiavas, J. Y. Dauvignac, and R. Staraj, "Novel antennas for ultra-wideband communications," *Microwave Opt. Tech. Lett.*, Vol. 41, No. 3, 166–169, 2004.
4. Kim, N., G.-B. Son, and S.-M. Park, "Sectorial form UWB antenna with a CPW-fed uniplanar," *Journal of KIEES*, Vol. 18, No. 3, 305–314, 2007.
5. Volakis, J. L., *Antenna Engineering Handbook*, (4th Edition), 16-5–16-6, McGraw Hill, 2007.
6. Palanisamy, V. and R. Garg, "Rectangular ring and H-shaped microstrip antennas-alternatives to rectangular patch antenna," *Electronics Letters*, Vol. 21, 874–876, 1985.

Design and Implementation of a Smart Antenna Using Butler Matrix for ISM-band

A. M. El-Tager and M. A. Eleiwa
Electronics Department, M. T. C., Cairo, Egypt

Abstract— In this paper, an ISM-band smart antenna system of 4-element microstrip linear array antenna with Butler matrix beamforming network is designed, analyzed and implemented using microstrip technology in completely planar structure without suffering from power losses or poor antenna pattern characteristics. The performance of this smart antenna system is analyzed and the beamforming features are monitored as function of geometrical antenna and Butler matrix parameters in the ISM-band at frequency from 2.4 to 2.48 GHz. Smart antenna efficiency and directivity are improved and its side lobe level is enhanced which make it very promising.

1. INTRODUCTION

Recently, switched beam smart antenna systems are investigated to improve the performance of wireless networks. Antenna arrays using microstrip fabrication technology are versatile in terms of their geometrical shapes and implementations. The popularity of Butler matrix as a beamformer in a switched multiple beam smart antenna is due to many advantages. First, it can be implemented easily using hybrids and phase shifters. Second, the generated beams are orthogonal of the Woodward-Lawson type and have narrow beamwidth and high directivity. Third, it has minimum path length and number of components compared to other uniform excitation beamforming networks. Fourth, it has a high and almost constant beam crossover level that does not change with frequency. This allows a good coverage pattern and full system gain at any point in the coverage area. It can achieve continuous beam scanning without any mechanical motion in the scanning process [1].

Several strategies for Butler matrix implementation are published. First, reflective Butler matrices are introduced in [2], but they need circulators, which add complexity to the circuit. Second, high-permittivity substrates are used to reduce the structure's size [3], but this creates difficulties in implementation and measurements. Third, hybrid [4] and multilayered implementations [5] are not easy as single layer structures. Therefore, planner implementation was very attractive for researchers [6–9].

This paper presents a planar design, simulation and implementation of a smart antenna system for wireless networks using microstrip antenna array with beamforming network in the ISM-band at 2.45 GHz. An antenna array is proposed in Section 2. A Butler matrix beamforming network is proposed in Section 3. The overall performance of both is presented in Section 4.

2. DESIGN AND ANALYSIS OF LINEAR MICROSTRIP ANTENNA ARRAY

The proposed 4×4 beamforming smart antenna (BFSA) consists of a linear antenna array and a beamforming network. The later consists of four directional couplers, two 0 dB cross over, and phase shifters. The objective is to design, optimize and implement this BFSA on a planar low loss teflon substrate. Rogers RT/Duroid 5880 ($\varepsilon_r = 2.2$, $\tan\delta = 0.0009$, and $h = 0.157$ cm) is chosen for best antenna performance.

Initially, a single rectangular patch with inset-fed stripline matching is designed and optimized using 3D modeling, namely HFSS, to be the antenna radiator element. The final patch size is $W = 48.4$ mm and $L = 40.025$ mm. The fabricated patch is shown in Figure 1(a). A very good agreement is achieved between measured and simulated S parameters as in Figure 1(b).

Then a 4-element linear array is designed with an initial inter-element spacing of 0.5λ and variable phase between elements based on the butler matrix outputs, using PCAAD software. The optimum inter-element spacing is found to be 0.45λ. The linear array is realized using microstrip technology and optimized using ADS/Momentum simulation, which is based on the method of moments. Table 1 summarizes the results obtained from the implemented single patch and the array compared to required specifications. Thus, it is clear from these results that the 4-element antenna array fulfills most of required specifications. Some other specifications such as beam steering in one of four directions and beam coverage will be achieved after the design of Butler matrix beamforming network.

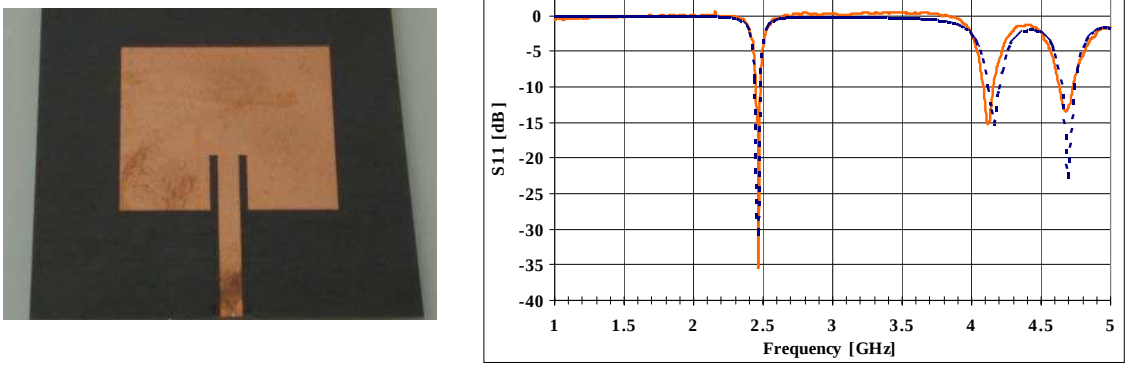

(a) (b)

Figure 1: (a) Fabricated antenna, (b) Measured S-parameters (continuous) versus simulated results (dotted).

Table 1: Achieved single patch and linear array parameters compared to required specifications.

	Bandwidth [GHz]	**Directivity [dB]**	**Efficiency [%]**	**Gain [dB]**	**Beam Width**
Required specs.	2.4 : 2.48	12	> 90	> 10 dB	30°
Achieved single patch specs.	2.443 : 2.475	7.5422	90	7.0244	99.1°
Achieved array specs.	2.35 : 2.55	11.389	92	11.0452	25.2°

3. DESIGN AND IMPLEMENTATION OF BUTLER BEAMFORMING

In this section, a multiple-beam forming network using Butler matrix is designed and realized with microstrip technology to feed the antenna array of the previous section at frequency 2.45 GHz. A 4×4 butler matrix creates a set of 4 orthogonal beams in space by processing the signal from the 4 antenna elements of an equi-spaced linear array. The Butler matrix is realized using four directional couplers, two 0 dB cross couplers, and phase shifters. Its components are designed and fabricated separately as shown in Figure 2. In addition, measured results are compared to simulated ones as shown in Table 2, achieving good agreement, which validates both design and simulation methodologies. The four-beam smart antenna generates four orthogonal beams to cover 120° area. Careful design and optimization procedure are performed to obtain accurate phase shift (β) results between ports as summarized in Table 3.

Table 2: Simulated versus measured results for both quadrature and cross couplers.

	Quadrature 3 dB Coupler		**0 dB Cross Coupler**	
	Simulated	Measured	Simulated	Measured
Return Loss (S_{11}) [dB]	−30.904	−19	−24.956	−10.7
Isolation (S_{41}) [dB]	−31.425	−18	−38.036	−23.7
S_{21}, S_{43} [dB]	−3.005	−3.5	−24.942	−28.9
S_{31}, S_{42} [dB]	−3.086	−3.8	−0.085	0.6

Table 3: Summery of phase shift results between different ports of the optimized Butler network.

	P5	**P6**	**P7**	**P8**	β
P1	62.718	16.935	−28.747	−72.850	45
P2	−28.478	107.768	−117.055	16.946	−135
P3	16.951	−117.045	107.760	−28.456	135
P4	−72.832	−28.739	16.925	62.717	−45

(a) (b)

Figure 2: (a) Fabricated directional microstrip coupler, (b) Fabricated cross coupler.

4. VERIFICATION OF THE ANTENNA ARRAY WITH ITS BEAMFORMING NETWORK

The final layout of the optimized antenna with its beamforming network is shown in Figure 3. Beamforming characteristics of the proposed smart antenna system are obtained for uniform amplitude distribution. 2-D polar far field patterns are obtained and plotted in Figure 4, which achieve the targeted specifications.

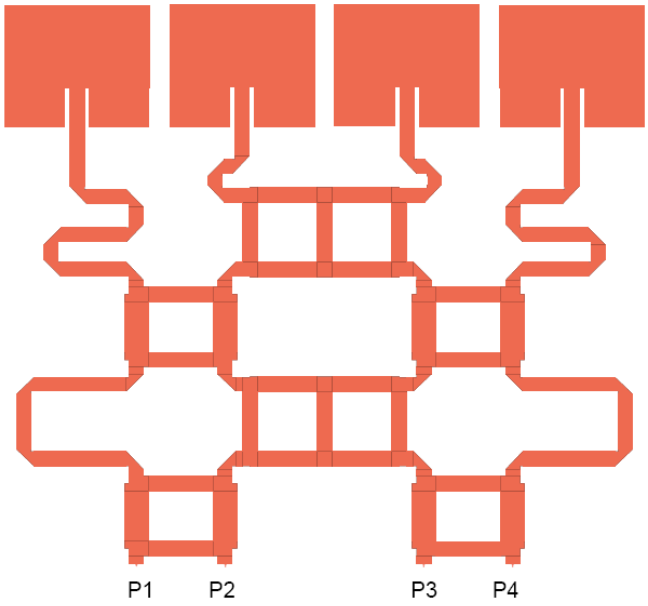

Figure 3: Final layout of the proposed antenna array with its beamforming network.

Furthermore, smart antenna efficiency and directivity are improved, while minimizing its size to cope with the required constraints. Finally, the implemented antenna is also compared to similar recent published implementation in Table 4. This comparison proves that this work enhances many parameters which shows an outstanding performance of the proposed antenna due to design and optimization efforts.

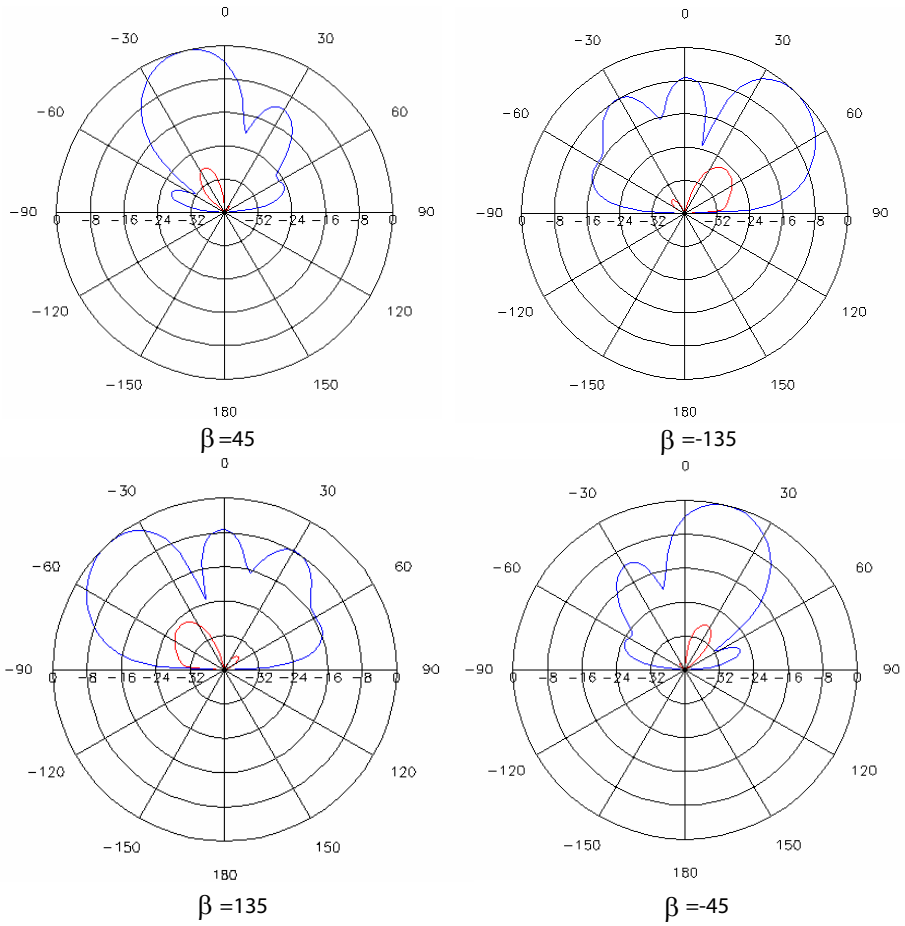

Figure 4: Simulated E-theta (in) and E-phi (out) beam patterns of the proposed BFSA at different β using ADS.

Table 4: Proposed BFSA versus other similar published ones.

Features	**Ref. [9]**	**Proposed Antenna**	**Enhancement**
Centre Frequency	2.4 GHz	2.45 GHz	----
Physical size cm × cm	24.2 × 18.5	21.3 × 18.6	11.5%
Microstrip substrate	$\varepsilon_r = 3.38$, $h = 0.51$ mm $\tan\delta = 0.0027$	$\varepsilon_r = 2.2$, $h = 1.57$ mm $\tan\delta = 0.0009$	----
Radiator Element	$S_{11} = -23$ dB @ f_o BW = 0.54%; (13 MHz)	$S_{11} = -33$ dB @ f_o BW = 1.31%; (32 MHz)	43.4% 146%
Amplitude taper	Uniform	Uniform	----
Antenna Gain	----	11.0452	----
Antenna Directivity	----	11.389	----
Spatial scan coverage	84°	97.4°	15.9%
Maximum scan angle **@ $\beta = \pm 45°$** **@ $\beta = \pm 135°$**	 ±12° ±42°	 ±14.3° ±47.8°	 19.2% 13.8%
SLL: **@ $\beta = \pm 45°$** **@ $\beta = \pm 135°$**	 −14 dB −8 dB	 −14 dB −8 dB	----

5. CONCLUSIONS

This paper presents a planar design, simulation and implementation of a smart antenna system using microstrip antenna array with Butler beamforming network for wireless applications in the ISM-band at 2.45 GHz. A linear antenna array is initially designed using PCAAD software. Then, realized and optimized using ADS Momentum simulation. The Beamforming/feeder network is designed using a 4×4 Butler matrix, and realized using 4 quadrature hybrids, 2 phase shifters and 2 crossover circuits. To verify modeling and simulation procedures, the main basic elements such as patch antenna, directional coupler, and cross coupler are fabricated and measured. Very good agreement between measurements and simulations is obtained which validates the design. Finally, the microstrip antenna array and the Butler matrix feed network are simulated and optimized to achieve the required parameters in the ISM-band. Smart antenna parameters such as efficiency, directivity and maximum scan angle are improved, while minimizing the physical size. This validates antenna parameters and shows that it has an outstanding performance compared to what is found in corresponding published literatures.

REFERENCES

1. Hansen, R. C., *Phased Array Antennas*, John Wiley and Sons, New York, 1997.
2. Shelton, J. P. and J. K. Hsiao, "Reflective Butler matrices," *IEEE Transactions on Antennas and Propagations*, Vol. 27, No. 5, 651–659, September 1979.
3. Corona, A. and M. J. Lancaster, "A high-temperature superconducting Butler matrix," *IEEE Transactions on Applied Superconductivity*, Vol. 13, No. 4, 3867–3872, December 2003.
4. Daneshmand, M., R. R. Mansour, P. Musavi, S. Choi, B. Yassini, A. Zybura, and M. Yu, "Integrated interconnect networks for RF switch matrix applications," *IEEE Transactions on Microwave Theory and Techniques*, Vol. 53, No. 1, 499–507, January 2006.
5. Bona, M., L. Manholm, J. P. Straski, and B. Svensson, "Low-loss compact Butler matrix," *IEEE Microwave Theory and Techniques*, Vol. 50, No. 9, 2069–2075, September 2002.
6. Hayashi, H., D. A. Hitko, and C. G. Sodini, "Four-element planar Butler matrix using half-wavelength open stubs," *IEEE Microwave and Wireless Component Letters*, Vol. 12, No. 3, 73–75, March 2002.
7. Néron, J. S. and G. Delisle, "Microstrip EHF Butler matrix design and realization," *ETRI Journal*, Vol. 27, No. 6, December 2005.
8. Nord, H., "Implementation of 8×8 — Butler matrix in microstrip," Diploma Thesis, Royal Institute of Technology, Stockholm, 1997.
9. Wu, L., "Planar multi-beam antenna for W-LAN," Duisburg, November 2007.

The Current Status of Automotive Electromagnetic Compatibility Research

Yi Sun and Chaoqun Jiao
Department of Electrical Engineering, Beijing Jiaotong University, China

Abstract— With the growing development of automobile market and increasing electronic and electrical appliances in vehicle, automotive EMC (electromagnetic compatibility) study has become a new hot spot of research. Automotive EMC, which comes into being in recent years as the automobile technical term, is still unfamiliar to many people, but it relates to the particular electronic systems, the surrounding electric and electronic system of auto, up to the security and stability of the whole car system. In this paper, through collection and analysis of related literature, technical information and research reports, it detailed described the current automotive EMC research from these three aspects: the electromagnetic environment of the auto, international organizations and standards for automotive EMC, experiment testing technologies. Furthermore, it pointed out the long-term developing trend of automotive EMC research and analyzed its influence on the development of related study in China.

1. INTRODUCTION

With the rapid development of the auto industry and the electronic technology, more and more new technology in modern cars has been widely used, especially micro-electronics technology, more effectively promoted the auto industry to the high value-added direction [2–4]. However, these new technologies also put forward higher requirements for the reliability of the entire vehicle system, that is, all electronic devices and electronic control systems must adapt to each other, automotive electronics applications will be related to a common problem — the automotive EMC [5–10].

2. AUTOMOTIVE ELECTROMAGNETIC COMPATIBILITY AND RESEARCH SIGNIFICANCE

EMC is that the electronic equipment in its electromagnetic environment does not interfere with the normal work of surrounding electrical equipments when it operating, and as well as has the capability of resisting to environmental EMI (electromagnetic interference) and working normally at meantime. Automotive EMC is to ensure the car's electrical and electronic equipments do not affect each other when the car is running, which can make them compatibly work [1].

The research of Automotive EMC has important significance. Although it is still unfamiliar to many people, which comes into being in recent years as the automobile technical term, it relates to the particular electronic systems, the surrounding electric and electronic system of auto, up to the security and stability of the whole car system. For example, Automotive electrical systems or electrical and electronic equipments would emit electromagnetic energy to the ambient during their working time, impacting the operation of the radio, television receivers and computer systems, causing electromagnetic pollution, meanwhile, auto radio generates the noise because of the interference. These interferences may be temporary and have the small influence, but it also may be fatal, such as the failure of the auto electronic ABS (anti-lock braking system) and the error trigger of the auto SRS (supplemental restraint system) due to the interference in the process of running, which may cause great harm to the person and a great loss of property [3–9].

3. ELECTROMAGNETIC ENVIRONMENT OF AUTO

For the unceasing change of the driving environment, the electromagnetic energy constitution in the work environment of the automotive electronics equipment would be very complex and changeable. Its electromagnetic disturbing source can be divided into three:

3.1. The Inner Electromagnetic Interference

EMI in the vehicle is because that the inside electronic products have many wire, coil and the electrical appliances with contacts, all with different inductors and capacitors, and any one of closed loop with the inductors and capacitors will form the oscillation circuit [6]. So the automotive electronic equipment at work would create the inner mutual interference. The most serious is the high-frequency radiation produced by the auto ignition system, which with the largest energy.

Secondly, it also would produce electromagnetic waves during the abrupt change and rectification of the load current in generator [2, 3]. Starters, generators, flash, contact electromagnetic vibration electric speakers, Wiper and instrument systems will also generate electromagnetic waves which could cause the smaller conducted and radiated interference.

Disturbing electromagnetic waves produced by auto electric implements can be divided into the conducted interference and the radiated interference [5–7]. The electromagnetic waves of conducted interference directly enter into radio and electronic equipments through the automotive wire. And the electromagnetic waves of radiated interference spread in space, coming into the inside of radio equipments through an antenna (such as the ignition system high-tension line is equivalent to the antenna) [11]. All these disturbing electromagnetic waves have the pulse characteristic and a wide frequency band, which the frequency is typically between 0.15 MHz and 1000 MHz [1–8].

The inner electromagnetic interference can be further divided into three:

(1) Frequency spectrum range from 10 kHz to 1000 MHz, a broadband interference generated by the high-voltage ignition devices;
(2) Frequency spectrum range from 10 kHz to 500 MHz, a broadband interference generated by DC motor and discrete output stage;
(3) Frequency spectrum range from the fundamental frequency to 4000 MHz, a narrowband interference generated by on-board digital computer (various electronic control units and on-board digital office equipments) [2].

If these EMI do not carry out any measures to be removed, the automotive receiving antenna could induct voltage up to 50 dBV.

3.2. The Body Static Interference

The body static interference is concerned with the car and the external environment. As the auto in motion has the high-speed friction with the air, it would form the uneven distributing static on the body. Then ESD (electrostatic discharge) would form the interference current and produce a high frequency radiation, causing EMI to the automotive electronic equipments [2–7].

3.3. The Outer Interference

The outer EMI is the interference to the traveling car when it has to go through a variety of external electromagnetic environment, which arises from the natural phenomenon, the social environment, etc. [4]. This type of interference consists in the particular space or the specific time: for example, the high-voltage transmission line, the place near the tramway, the broadcast and television equipment and the radio communication equipment. Other electronic devices closing to the car in environment also could cause interference, such as the close moving car [2].

To sum up, the auto outer EMI reduces with the increasing active distance, only if its energy is very large can it impact on the farther automotive electronic equipments. Years of research results show that large energy electromagnetic effect has harm to the human health [10]. At present, it has instituted various corresponding standards to limit these interferences, making automotive electronic equipments to reduce the influence. However, to the inner electromagnetic interference and the body static interference, because the interference distance is short and the disrupted time is long, their interfering intensity is relatively larger [3–9].

4. INTERNATIONAL ORGANIZATIONS AND STANDARDS FOR AUTOMOTIVE ELECTROMAGNETIC COMPATIBILITY

In order to ensure the EMC of vehicles, the EMI and EMS (electromagnetic susceptibility) technical parameters of automotive electrical systems, subsystems, electrical and electronic equipments must accord with the relevant international or national standards.

The automotive developed country in the world have been with a better automotive EMC testing standards and norms, with the effective institution for EMC test, management and certification of the complete car and vehicle component parts, with the high-precision automotive EMC testing system, and have developed a large-scale automotive EMC forecast, analysis and design software [5]. Third-party testing certification bodies, auto research institutions, and so on, have carried out the automotive EMC research, and successively set up their own EMC laboratory [6].

At present, in the field of EMC test for vehicles and on-board electronic equipments, the standards mainly have the following categories: international standards for automotive EMC, such as ISO, CISPR, etc.; European automotive EMC standards; American SAE (society of automotive

engineers) standards for EMC, etc. [3–7]. Of course, relatively well-developed large auto manufacturers, such as Volkswagen, BMW, Opel, Fiat, Ford, General Motors, Toyota, and other companies, all have their own EMC test standards and norms.

China automobile industry developed rapidly in recent years, but the development in automotive EMC testing standards and norms is lagging behind. However, these years the update of the standards and the release of the new standards in China all proved the rapid development in making standards. Subsequently, the Chinese auto test institutions and manufacturers began to buy measurement equipments and establish the EMC test sites.

For the complete vehicle test standards, there are ISO11451 and CISPR12. ISO11451 is divided into standard ISO11451-1-2000 "*Road vehicles — Electrical disturbances by narrow-band radiated electromagnetic energy; vehicle test methods — Part 1: General and definitions*" and standard ISO11451-2-2000 "*Road vehicles — Electrical disturbances by narrow-band radiated electromagnetic energy; vehicle test methods — Part 2: Off-vehicle radiation source*". CISPR12: 1997, is of the same use in China, the corresponding national standard is GB14023-2000 "*Limits and measurement methods of the radio disturbance characteristics of vehicles, motor boats and the devices driven by the spark ignition engine*".

For the vehicle component parts test standards, there are ISO11452 and CISPR25. ISO11452 is divided into standard ISO11452-1-2000 "*Road vehicles — Electrical disturbances by narrow-band radiated electromagnetic energy; component test methods — Part 1: General and definitions*", and standard ISO11452-2-2000 "*Road vehicles — Electrical disturbances by narrow-band radiated electromagnetic energy; component test methods — Part 2: Absorber lined chamber*". CISPR25: 1995, is of the same use in China, the corresponding national standard is GB18655-2002 "*Limits and measurement methods of the radio disturbance characteristics for the protection of on-board receivers*" [1–6].

5. EXPERIMENT TESTING TECHNOLOGIES AND THE CURRENT STATUS OF RESEARCH

EMC is not a kind of parameters which can be directly measured. Only through the test of EMI and EMS can its indicators in the technical evidence be provided. Automotive EMC research is basically limited to the test before. But with the inventions of the electric automobile and the hybrid driven car, the rapidly increasing automotive electrical systems and the rising signal frequency, the automotive EMC problems have become a heavy burden to auto manufacturers. In order to enhance problem-solving efficiency and reduce costs, applying the digital modeling and simulation technology to the automotive EMC research is becoming a hot spot.

It has carried out a lot of researches on the automotive EMC test mode abroad and the current methods which can be practically applied are various. The common EMC test methods are shown in Table 1.

Table 1: The common EMC test methods.

EMI Test	Conducted Interference Test	LISN Mode
		Current Clamp Mode
	Radiated Interference Test	GTEM Cell Mode
		Shielded Chamber Mode
		Absorb-wave Darkroom Mode
		Open Area Test Site Mode
EMS Test	Conducted Sensitivity Test	Simulating Interference Pulse Mode
	Radiated Sensitivity Test	Stripline Mode
		TEM Cell Mode
		GTEM Cell Mode
		High Current Injection Mode
		Reverberation Chamber Mode
		Absorb-wave Darkroom Mode

The "Auto EMC" working group which is composed of the two major European auto manufacturers (BMW and Renault), two European software providers (ESI and Analogy), the Fiat Technology Research Center and others is attending to develop a set of the computer analysis method for the automotive EMC simulation and prediction [1–3]. Research focused on the follows:

(1) CAD modeling;
(2) Ensure the scientificalness of computer simulation;
(3) Ensure the industrial effectiveness of computer simulation;
(4) Integrate different simulation tools;
(5) Determine the standards of EMC computer simulation.

In order to reduce the auto own weight and save material cost, now the materials of auto are using the composite materials to replace the previous steel. However, it brought a problem that the EMI shielding capability of vehicles had been reduced. In addition, it also increased the difficulty of automotive wiring, because there no longer exist in a common ground loop. At present, the "WHEELS" working group (the main members: the University of Warwick in Britain, the Volvo Group, Lucas Wiring Systems Company, etc.) is studying how to optimize the design and wiring of the light car to improve its electromagnetic compatibility [1–7].

China auto industry in this area has a late start. In 1994, China Automotive Technology Research Center firstly carried out the radio interference characteristic measure to the car and the thoroughly survey to the national various automobile (new). The results of the survey showed that the passing rate was 24%, a considerable amount of vehicles belonged to the serious failure of the standard. In 1998, Shanghai General Motors has proposed to establish China automotive EMC research system, and considered that the main task is composed of four aspects: the complete vehicle radiated emitting test, the complete vehicle radiated sensitivity test, the complete vehicle conducted emitting tests, the complete vehicle conducted sensitivity test. In the 1990s, China started to control the car radio interference [8]. The domestic auto test institutions and manufacturers have purchased the EMI receiver systems for research and testing the level of car radio interference, and control the limit-exceeding disturbance. Since then, China began to carry out the EMC technical research of the auto and parts and construct the large-scale EMC test facilities.

In March 2001, the China Automotive Technology Research Center EMC test laboratory was approved by the CNAL (China National Accreditation Board for laboratories), marking the new development of China automotive EMC test technology. The EMC test facilities in China Automotive Technology Research Center Laboratory include the wild open area test site, the anechoic chamber, the conductive shielded chamber, the amplifier room and the measuring control system. As the main body of EMC laboratory, the anechoic chamber can achieve the uniformity and decay of the indoor electromagnetic fields, simulate the electromagnetic distribution in the open area, and complete a variety of tests relating to the electromagnetic fields [1, 2]. The lab has passed the test of SIS test institution in the United States. Its performance indicators have met the technical requirements of international relative standards.

So far, the new EMC lab (including the anechoic chamber) in the auto industry is coming on stream in China. The current main test institutions are Shanghai-Volkswagen Co. Ltd., Tianjin China Automotive Technology Research Center, and Changchun Automobile National Center for Quality Supervision and Test. The other EMC laboratories also provide the corresponding tests.

6. THE LONG-TERM DEVELOPING TREND

On the whole, auto and automotive electronic market will strongly grow driven by the demands of the consumer, and lead to other electronic industry at the same time. The automotive safety system is one of the demands which have the strongest growth in the automotive electronic field, so automotive electronic EMC is an extremely important field, which can not be ignored. Whether on the market, economic or technical point of view, it is very attractive.

The current EMC study can not provide engineering to effectively solve the problems of automotive EMC, yet to be further developed [1]. The new issues, which would emerge along with the development of automobile technology, also need to be discovered and solved. Furthermore, the present domestic automotive EMC research, including standard regulations, testing technology, design forecast and so on, have a wide gap comparing with other automotive developed countries [2]. It believes that with the related standard regulations constantly improving, the domestic automotive EMC will become a research hot spot, and the study will also carry to a new and higher level.

REFERENCES

1. Xu, L., "The development of automotive electromagnetic compatibility technology in China," *Safety and EMC*, Vol. 49, No. 1, 35–37, Jan. 2003.
2. Rybak, T. and M. Steffka, *Automotive Electromagnetic Compatibility*, 1st ed., Kluwer Academic Publishers, Dec. 2003.
3. Liu, Q.-S., L.-X. Ding, X.-L. Xu, and B. Li, "Brief introduction on standard of automotive electromagnetic compatibility at home and abroad," *Communications Standardization*, Vol. 92, No. 2, 41–44, Mar. 2008.
4. Xu, L., *Automotive EMC Standards and Test*, 1st ed., Nation Technical Committee 79 on Radio Interference of Standardization Administration of China, Shanghai, 2007.
5. Yu, Z.-F. and M.-Q. Xu, "Automotive electromagnetic compatibility system approach," *Automobile Research and Development*, Vol. 77, No. 5, 54–57, Sep. 2002.
6. Chi, Q.-L., H. Liu, and Y.-Y. Zhao, "Technical analysis of automotive electromagnetic compatibility," *Journal of Heilongjiang Institute of Technology*, Vol. 20, No. 3, 38–40, Sep. 2006.
7. Dai, Z. and W. Zhou, "Electronic and magnetic disturbing source of automobile electronic system," *Journal of Wuhan Automotive Polytechnic University*, Vol. 21, No. 4, 4–7, Jul. 1999.
8. Guo, Z.-X., "EMC analysis in the application of automotive industry," *Electronic Test*, Vol. 174, No. 6, 35–38, Jun. 2008.
9. Rakouth, H., C. Cammin, L. Comstock, and J. Ruiz, "Automotive EMC: Key concepts for immunity testing," *2007 IEEE International Symposium on Electromagnetic Compatibility*, 1–7, Jul. 2007.
10. Sakthivel, K. N., S. K. Das, and K. R. Kini, "Comparison of civilian EMC immunity standards with automative EMC immunity standards," *Proceedings of the International Conference on Electromagnetic Interference and Compatibility*, 63–69, Feb. 2002.
11. Liu, G.-P., C.-C. Chen, Y.-H. Tu, and J. L. Drewniak, "Anticipating full vehicle radiated EMI from module-level testing in automobiles," *IEEE International Symposium on Electromagnetic Compatibility*, Vol. 2, 982–986, Aug. 2002.

A Novel Electromagnetic Bandgap (EBG) Structure for Electromagnetic Compatibility (EMC) Application

Cheng-Chi Yu, **Meng-Hsiang Haung**, **Yao-Tien Chang**,
Luen-Kang Lin, **and Tsung-Han Weng**
Department of Communications Engineering, Feng-Chia University, Taichung, Taiwan

Abstract— The EMC issues become possible critical problems for high speed, large scale or complex systems such as PCs, servers or automotive application, which cause significant time delay or extra developmental cost. A novel electromagnetic band-gap (EBG) structure is proposed in this paper. It can be easily fabricated on standard PCB material and can be used where space is at a premium. The cells of EBG structures are designed and developed to provide two stop bands at 2.8 GHz∼3.2 GHz and 4.3 GHz∼4.8 GHz. By properly arranging the unit cell dimension and location, the mutual coupling between transmission lines in multi-layers structure can be reduced. Several cases of different layout skill have been studied in this paper. The experimental results demonstrate that the mutual coupling between signal lines is effectively suppressed when the EBG structures are properly designed. They are suitable for EMC applications.

1. INTRODUCTION

When many devices switching at the same time cause voltage fluctuations or disturbances within the power distribution system (PDS), which is called simultaneous switching noise (SSN), it will influence the circuits performance. This problem of SSN has been investigated intensively in the recent year and different approaches have been taken to mitigate it. Typical technique can place decoupling capacitors between power and ground planes. Another method is to isolate the sensitive RF and analog circuits from the noisy digital circuits by separating the power plane and ground plane. The gap between the power plane and ground plane can partially block the propagation of electromagnetic wave.

Electromagnetic Band Gap (EBG) structures proposed in recent year have confirmed successfully for noise suppression at specific frequency. The EBG structures are increasingly considered as a viable solution to the problem of switching noise in high-speed power plane structures. The EBG structures are periodic structures that have some particular electromagnetic properties, such as negative permeability and permittivity [1], capable of blocking the surface electromagnetic wave propagation within a particular frequency band (stop band). For example, mushroom-like and folk-like EBG structure had shown agreement band-gap behavior in microwave frequency band. The concept was recently proposed in [2] and [3], and some applications had been reported in [4–6].

In this paper, a novel EBG structure on printed circuit board (PCB) is developed. It is used for multi-layer mutual coupling mitigation. The experimental result shows that the EBG exhibits a two-stopband characteristic. The two band-gap bandwidths of the EBG structure are 400 MHz (2.8 GHz∼3.2 GHz) and 500 MHz (4.3 GHz∼4.8 GHz), respectively.

2. THE EBG STRUCTURE MODEL AND DESIGN METHOD

Figure 1 shows a typical two-layer mushroom-like EBG structure. The EBG pattern put on top layer and the bottom layer is ground plane. The top layer metal pattern and bottom layer are connected by a via locating at the center of patch (EBG patch). The EBG-based circuit model for unit cell is shown in Figure 2. Capacitance C_1 is the equivalent capacitance of the gap between any two adjacent patches. Capacitance C_2 is the equivalent capacitance between patch and lower plane. Inductance L_1 is the equivalent inductance per metal patch for EBG pattern and L_2 is the equivalent inductance of the via connecting the patch to the lower plane.

The proposed unit cell of EBG structure consists of three elements: a square patch, slots and via, as shown in Figure 3. In this figure, the gray part is metallic pattern which is etched on top layer of dielectric substrate. The width (W_1) is 1 mm and the length (L_1) is 2.75 mm for large slot. The width (W_2) is 0.25 mm and the length (L_2) is 1.5 mm for small slot. The gap between any two unit cell patches is 1 mm. The patch is connected to the lower ground plane by a metal via. Photograph of proposed EBG array is shown in Figure 4. A 6×6 EBG array is built on a 0.8 mm thick FR4 substrate with relative permittivity of 4.4.

Table 1 shows the parameters of physical dimension relating to each EBG structure. The simulated and measured results of the EBG are illustrated in Figure 5. The two band-gap bandwidths of the EBG structure are 400 MHz (2.8 GHz∼3.2 GHz) and 500 MHz (4.3 GHz∼4.8 GHz). Figure 6 indicates simulated results under the conditions of various slot length. When the length of slot is increased, the band-gap position moves toward lower frequency. From the experimental demonstration, inserting slots to the EBG pattern can effectively turn band-gap position.

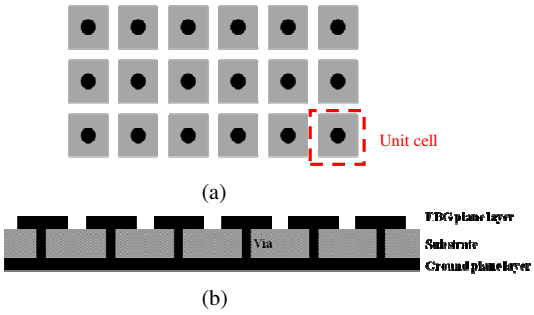

Figure 1: Mushroom-like EBG structure. (a) Top view of board. (b) Cross-section view of the EBG plane.

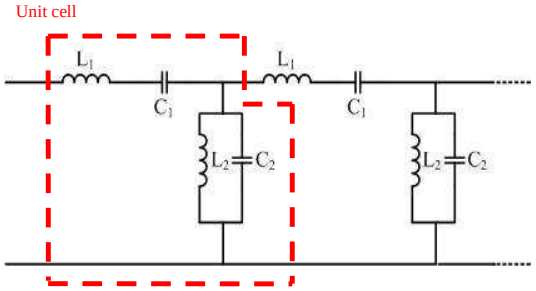

Figure 2: Mushroom-like EBG structure equivalent circuit for unit cell.

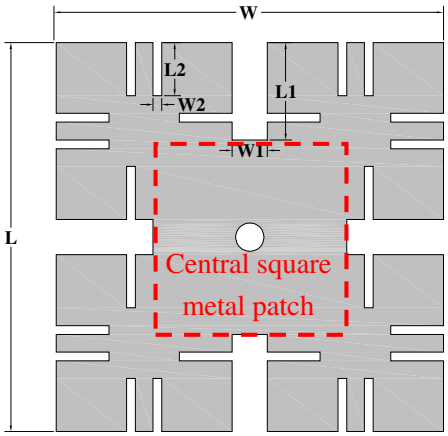

Figure 3: The schematic unit cell of EBG structure.

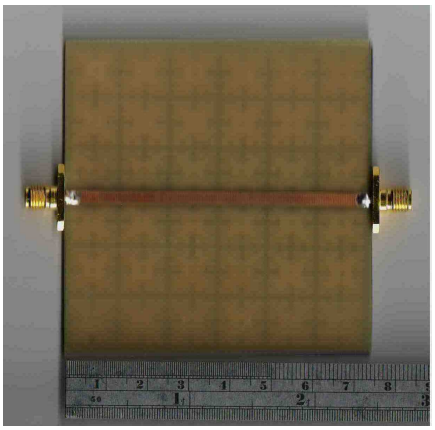

Figure 4: Photograph of proposed EBG array.

Parameter	Dimension
W	11 mm
W_1	1 mm
W_2	0.25 mm
L	11 mm
L_1	2.75 mm
L_2	1.5 mm
Radius of via	0.6 mm
ε_r (FR4)	4.4 mm
Substrate	0.8 mm

Table 1: Parameters of EBG structure.

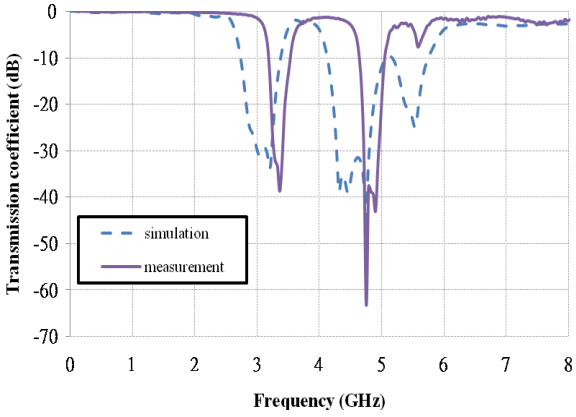

Figure 5: Simulated and measured results of proposed EBG structures.

Figure 7 depicts simulated results of different size of EBG central square metal patch. When the length of central square metal patch is 4 mm, the band-gap position varies from 7 GHz to 8.8 GHz. The two band-gap bandwidths of simulated result are 300 MHz (2.6 GHz∼2.9 GHz) and 1000 MHz (4.9 GHz∼5.9 GHz) when increases the length to 9 mm. A tunable stop-band of EBG structure is easily achieved by this way.

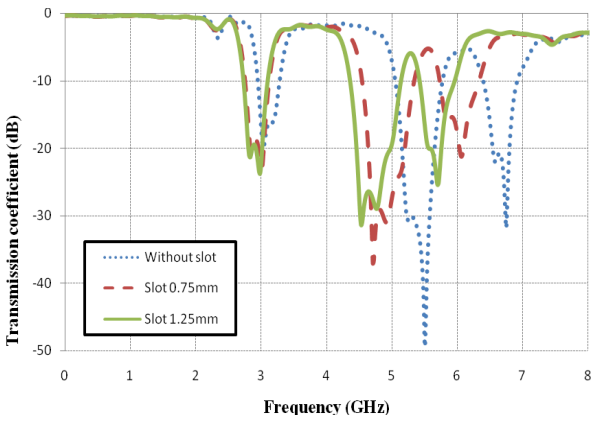

Figure 6: Comparison of simulated results of EBG structure with different slot length.

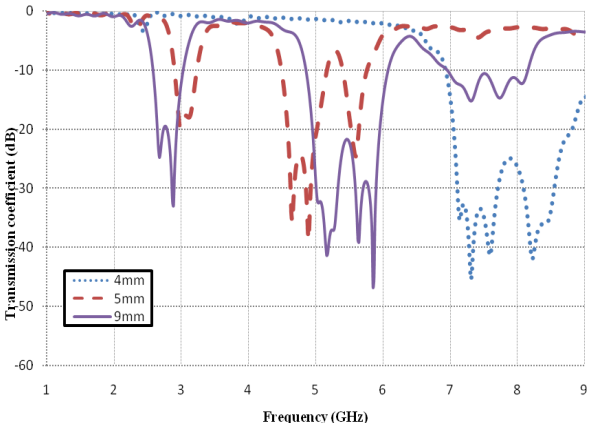

Figure 7: Simulated results of EBG structure with different size of central square metal patch.

3. EBG STRUCTURE FOR MUTUAL COUPLING REDUCTION

This section will discuss the impact of the proposed EBG structure on mutual coupling of multilayer layout design. Figure 8 illustrates measured results of with/without EBG for mutual coupling suppression of multilayer layout design. Photograph of proposed EBG array for multilayer layout design is shown in Figure 9. The layout skill is locating perpendicular transmission lines on different layer. In this case, the proposed EBG is embedded in the multilayer structure. The mutual coupling can be effectively suppressed within EBG stop-band range. The experimental result demonstrates that mutual coupling is reduced more than 20 dB when EBG structures are inserted.

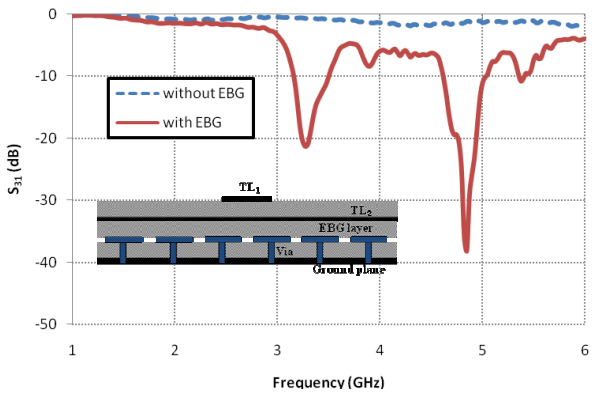

Figure 8: Measured result (S_{31}) of proposed EBG for mutual coupling suppression of multilayer layout design.

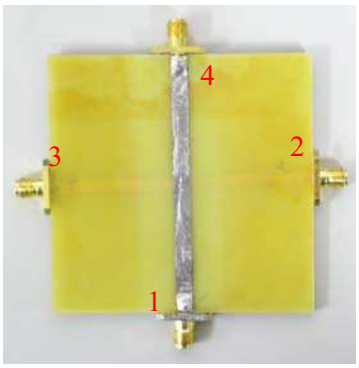

Figure 9: Photograph of proposed EBG array of multilayer layout design.

In the second case, we will discuss the influence when the metal traces are connected to the lower layer by means of shorting via, as shown in Figure 10. The signal trace starts from Port 1 pass through via to Port 2. The mutual coupling with/without EBG is compared. The coupling coefficient is around −20 dB in the normal condition. When the EBG structures are inserted, the mutual coupling effect is mitigated obviously.

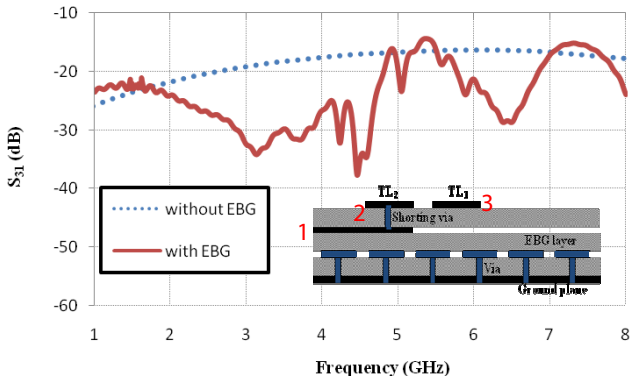

Figure 10: Comparison of simulated results that connecting different layer transmission line by via.

4. CONCLUSIONS

In this paper, a novel EBG structure is presented. The effects of proposed EBG structure on mutual coupling suppression of multilayer layout skill are discussed. Those cases include perpendicular transmission line and shorting via connect two transmission lines on different layers. More than 20 dB mutual coupling suppression of perpendicular transmission line is observed. The mutual coupling effect is mitigated when the EBG structures are inserted. This mutual coupling reduction technique can be used for multilayer layout applications.

ACKNOWLEDGMENT

The authors would like to thank the supports of the researcher in Electromagnetic Application Technology Lab, Feng-Chia University.

REFERENCES

1. Cheype, C., C. Serier, M. Thevenot, T. Monediere, A. Reineix, and B. Jecko, "An electromagnetic bandgap resonator antenna," *IEEE Trans. Antennas Propag.*, Vol. 50, No. 9, 1285–1290, Sep. 2002.
2. Sievenpiper, D., L. Zhang, R. F. J. Broas, N. G. Alexopolous, and E. Yablonovitch, "High-impedance electromagnetic surfaces with a forbidden frequency band," *IEEE Trans. Microwave Theory Tech.*, Vol. 47, 2059–2074, Nov. 1999.
3. Yang, L., M. Y. Fan, F. L. Chen, J. Z. She, and Z. H. Feng, "A novel compact Electromagnetic Bandgap structure and its applications for microwave circuits," *IEEE Trans. Microwave Theory Tech.*, Vol. 53, No. 1, 183–190, Jan. 2005.
4. Wu, T.-L., et al., "A novel power plane with super-wideband elimination of ground bounce noise on high speed circuits," *IEEE Microwave and Wireless Components Letters*, Vol. 15, No. 3, 174–176, 2005.
5. Ciccomancini Scogna, A., A. Orlandi, and V. Ricchiuti, "Signal integrity analysis of single-ended and differential signaling in PCBs with EBG structure," *IEEE International Symposium on Electromagnetic Compatibility, EMC 2008*, 2008.
6. Choi, J., V. Govind, and M. Swaminathan, "A novel electromagnetic bandgap (EBG) structure for mixed-signal system applications," *IEEE Radio and Wireless Conference*, 2004.

Antenna Effect Analysis of Laptop Platform Noise on WLAN Performance

Han-Nien Lin, Ching-Hsien Lin, Tai-Jung Cheng, and Min-Chih Liao
Department of Communications Engineering, Feng-Chia University
100 Wen-Hua Rd., Taichung 40724, Taiwan, R.O.C.

Abstract— Nowadays, due to increasingly high integration of multi-radios and high-speed digital system, serious platform noise is generated by ever higher speed digital clocking and signaling technologies. There are many sources of interference, such as EMI spectrum from CPU, LCD, and memory, which may be in the form of radiation or conduction emission and thus affect the quality of signal perceived at the transceiver. While encroaching upon the wireless communication band, those noises could result in a significant degradation to the throughput performance of wireless communications. It is very important to analyze the proximity effect on antenna performance due to different locations and types of antenna. An antenna was used to measure the noise floor of RF systems and examine its performance for different locations on a laptop. The laptop tested and analyzed in this paper has the following modules: CPU (Intel (R) T9400:2.53 GHz) and built-in 802.11a/b/g WLAN module. The measurement result demonstrates the impact of LCD noise on throughput for 802.11g. We also found the sensitivity of the receiver decreases (throughput decreases) as the LCD interference was injected to the communication link between the AP and NIC card. Furthermore, we will also use the different type of antennas for 2.4 G band to compare the communication performance, such as antenna efficiency, the radiation pattern, noise floor, for different locations. We will then show the increasing throughput of system by optimizing the design of antennas.

1. INTRODUCTION

With the advance of semi-conductor technology in recent years, the clocking speed and efficiency of the electronic parts are improving up progressively. In addition, the electronic product is made smaller but the function is more powerful. Products with collocated intented emission sources for compact size result in mutual interferences, and hence affect the wireless communication performances. There are many sources of interference on the system platform, such as EMI spectrum from CPU, LCD, and memory, which may be in the form of radiation or conduction emission and affect the quality of signal perceived at the transceiver [1]. Degradation of wireless performance could occur when platform noise encroaches in the wireless communication bands, to reduce the signal to noise ratio of the transceiver [2]. Since the antenna performance plays a key role in the complete link for reliable data assurance, it is very important to analyze the proximity effect on antenna performance for different locations and types of antenna.

In this paper we use the different types of antennas for WLAN band to compare the performance for free space and placement on laptop enclosure respectively. Three key parameters are investigated and discussed design and evaluation of laptop antenna design and evaluation: return loss (RL), average antenna gain, and pass-loss [3]. We also demonstrates the impact of LCD noise on throughput of 802.11g WLAN. The sensitivity of the receiver is found decreased (throughput decreases) as the LCD interference was coupled to the communication link between the AP and NIC card [4, 5]. Furthermore, the performance of the wireless communication could be improved by the antenna placement.

2. ANALYSIS OF THE LAPTOP STRUCTURE EFFECT ON ANTENNA

2.1. Characterization of Antennas Performance in the Free Space

The geometry of the simple dual-band monopole antenna for WLAN is depicted in Fig. 1. The proposed antenna consists of two monopoles and is printed on a FR4 substrate with a thickness of 1.6 mm (h) and relative permittivity of 4.4 (ε_r). The return loss of the antenna is calculated with CST EM simulator and measured with Agilent E5071B vector network analyzer (VNA). The simulated and measured return loss for both the proposed antenna and reference antenna are given and compared in Fig. 2. It shows good agreement between simulation and measurement results. Proposed design of microstrip-fed monopole antenna for dual-band operation has been proposed successfully implemented in laptop. In addition, we also use slot and chip antennas and measure

their performance in free space. Table 1 lists the center frequencies and bandwidths of antennas measured in the free space. Table 1 shows that the slot antenna has wider impedance bandwidths than monopole antenna and chip antenna. However, the size of slot antenna is larger than monopole antenna and chip antenna. Chip antenna with high dielectric loading could further reduce the antenna size, but its bandwidth would be unacceptably narrow. Those antennas investigated are very popular for laptop application because of easy design, overall performance and low cost.

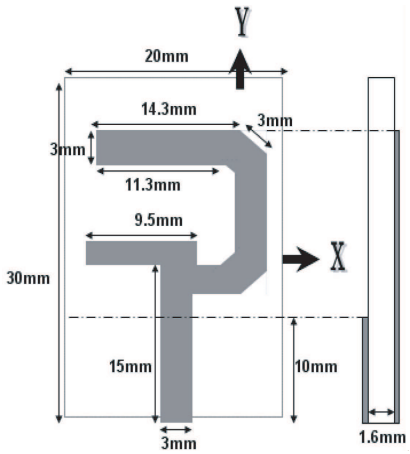

Figure 1: Geometry of dual-band monopole antenna.

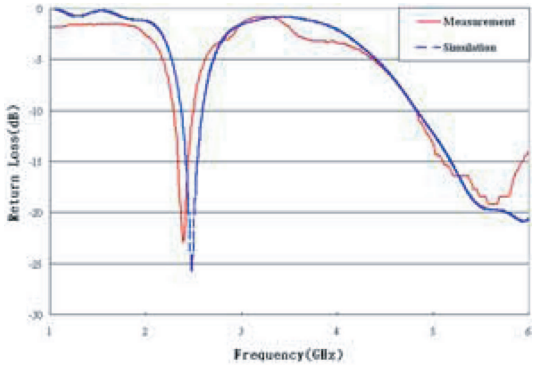

Figure 2: Return loss of monopole antenna.

Table 1: Measured characteristics of antennas in the free space.

Antenna type	Free space Frequency (MHz)			Bandwidth (MHz)
	f-c	f-min	f-max	
Chip antenna	2445	2375	2515	140
Slot antenna	2443	2395	2640	245
Monopole antenna	2400	2290	2500	210

Figure 3 shows the antenna has been integrated in a laptop prototype for WLAN applications. Because the proximity with attached dielectric material results in parasitic capacitive effect, the resonance frequency is slightly shifted to lower frequency as shown in Fig. 4. In order to compensate the frequency shift, the impedance bandwidth must be wide enough to cover both bands and antenna is reshaped as shown in Fig. 5. This bandwidth is therefore adjusted by reducing antenna area to minimized frequency deviation phenomenon. Photograph of the fabricated prototypes is shown in Fig. 6.

Figure 3: Monopole antenna placed in a laptop.

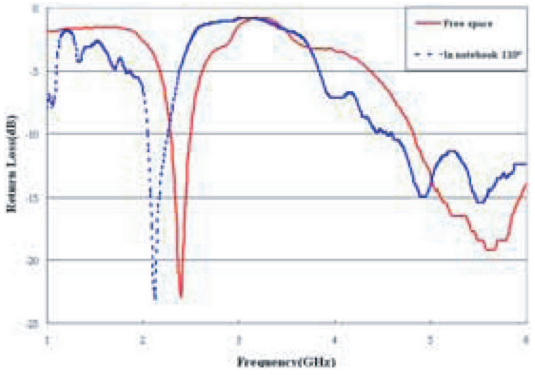

Figure 4: Measured return losses for monopole antenna in free space and a laptop.

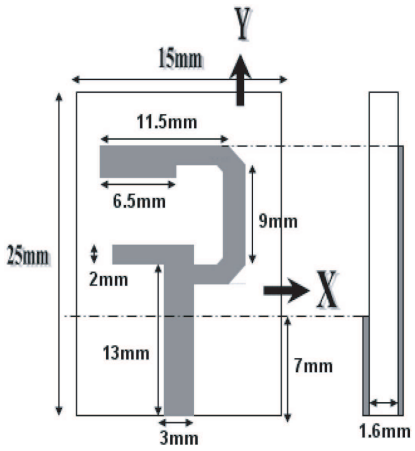

Figure 5: Size reduction for monopole antenna.

Figure 6: Photograph of the fabricated prototypes.

2.2. Characterization Antenna Performance vs. Location on the Laptop

Since the laptop case plays a significant role for the built-in antenna design, it is very important to determine the effects of antenna placement on laptops to antenna performance. The antenna performance strongly depends upon its location on the laptop, because an antenna detuned in a specific location may not have same effect for other locations. Hence, slight modification to the antenna is needed to an acceptable return loss (RL) requirement in each case. Table 2 compares the performance of different types of antennas for both 2.4 GHz and 5 GHz bands. The measured results clearly show that the monopole antenna has wider bandwidth than the chip antenna on the laptop, especially when antennas are placed on left-top and right-top positions for better WLAN performance. Radiation efficiency of chip antenna is lower than monopole antenna and slot antenna, because of its high dielectric constant effect. It may also be influenced by shielding aluminum foil on the laptop. Table 2 indicates that antenna placed on top position tends to yield maximum radiation, except for monopole and slot antennas placed on left-center location Fig. 7 shows the antenna locations under investigation. In addition, Fig. 8 shows the Pass-Loss measurement setup and test procedures as following:

(1) Put EUT into shielding box.
(2) Connect VNA port1 to Tx antenna and laptop antenna to port 2.
(3) Measure for specific frequencies antenna efficiency of Tx antenna and Rx antenna (laptop antenna).

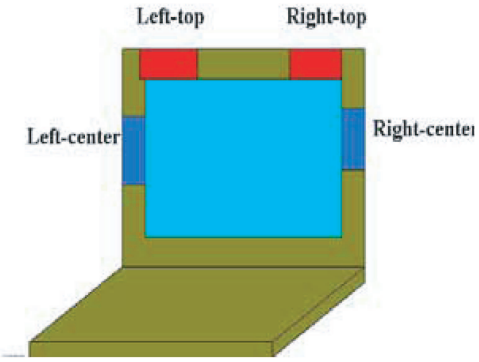

Figure 7: Antenna location on laptop display for comparison.

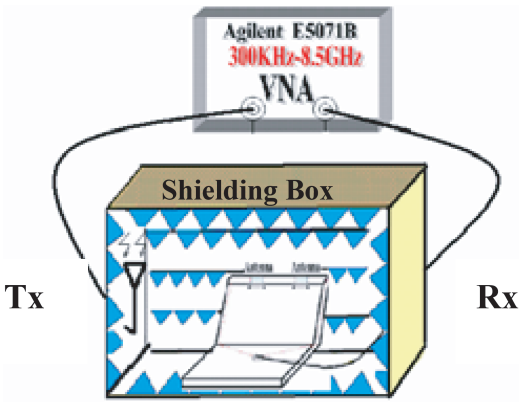

Figure 8: Test setup to measure Path-Loss.

3. IMPACT OF LCD EMI ANALYSIS ON 802.11G THROUGHPUT

In a laptop, there are many interference sources which can be in the form of radiation or conduction. LCD noise is the major interference to the wireless performance. Fig. 9 shows the frequency domain

Table 2: Performance of antennas on different laptop locations.

Monopole antenna

Antenna location on laptop	Frequency and Bandwidth (MHz)			Path Loss (dB)	Efficiency
	f-c	gain (dBi)	bandwidth		
Left-top	2445	0.10	175	−38.50	33.75%
Right-top	2480	−0.46	140	−36.67	22.19%
Left-center	2270	0.12	311	−39.38	35.75%
Right-center	2410	0.09	275	−32.49	27.39%
Antenna location on laptop	Frequency and Bandwidth (MHz)			Path Loss(dB)	
	f-c	f-min	bandwidth		
Left-top	5565	5280	1715	−39.85	
Right-top	5105	4870	2125	−37.23	
Left-center	5665	4775	2115	−48.50	
Right-center	5735	5280	1050	−33.00	

Slot antenna

Antenna location on laptop	Frequency and Bandwidth (MHz)			Path Loss (dB)	Efficiency
	f-c	gain (dBi)	bandwidth		
Left-top	2445	−1.22	105	−39.07	15.56%
Right-top	2445	−1.00	105	−33.18	21.80%
Left-center	2550	0.36	105	−40.29	28.08%
Right-center	2340	−2.36	70	−36.29	18.10%
Antenna location on laptop	Frequency and Bandwidth (MHz)			Path Loss(dB)	
	f-c	f-min	bandwidth		
Left-top	5565	5280	1785	−55.78	
Right-top	5805	5280	1765	−48.38	
Left-center	5560	5100	1755	−57.57	
Right-center	5805	5315	1575	−42.82	

Chip antenna

Antenna location on laptop	Frequency and Bandwidth (MHz)			Path Loss (dB)	Efficiency
	f-c	gain (dBi)	bandwidth		
Left-top	2585	−4.57	105	−37.48	8%
Right-top	2375	−6.54	175	−29.79	7.53%
Left-center	2375	−9.17	210	−37.39	3.46%
Right-center	2445	−8.70	210	−29.51	4.45%

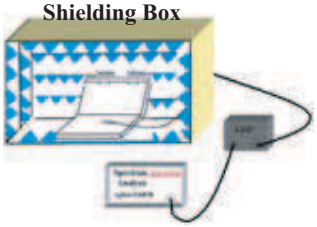

(a) Platform noise measurement setup.

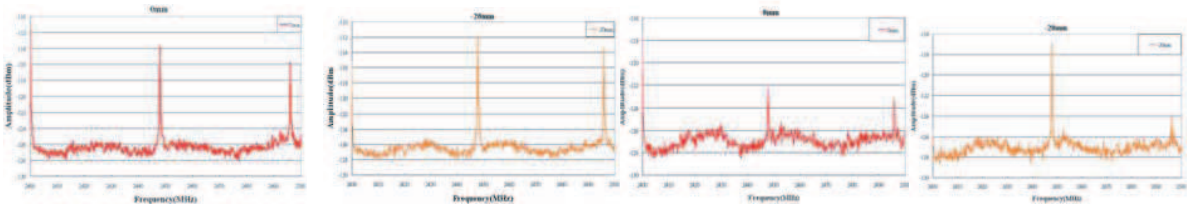

(b) Comparison of the different antennas measurement at different locations on the LCD panle.

Figure 9: LCD noise measured at antenna port in WLAN band.

measurement setup and measured results for platform noise from LCD. The measurement setup is shown in Fig. 9(a) and the test procedures are described as following:

(1) Put EUT into shielding box.
(2) Connect antenna cable to AMP/Spectrum analyzer via coaxial cable.
(3) Power on EUT.
(4) Measure noise level for the chosen target frequency.

Figure 9(b) shows the different antenna placements along the horizontal edge on top of a LCD panel. The measured results show that the noises at 2.400 GHz, 2.450 GHz, 2.490 GHz (harmonics of the pixel clock) are major interference sources that fall into WLAN band. We can obtain 2–5 dB noise suppression by simply moving the antenna several millimeters away from its initial location. The comparison for different antenna measurements at different locations shows that the LCD noise might have an significant impact on desensitization to 802.11g. The measurement of antenna positioned towards the left 20 mm serves as a reference to quantify the impact of antenna placement on the platform noise measurement. The noise picked up by antennas would desensitizes the receiver and reduced the throughput. Meanwhile, the throughput test procedure and test setup are as follows: the setup consists of an AP (access point), EUT (laptop) and Chariot console throughput software. The AP (access point) and EUT (laptop) are connected through path-loss attenuators to control RFI strength, and the communication traffic is controlled and monitored by a desktop using Ixia Chariot® software as shown in Fig. 4. The system path-loss includes cable loss, space loss and attenuators. The results in Fig. 10(b) the real line and dotted line, clearly show that the sensitivity and the throughput decrease as the LCD interference is injected to the communication link between the AP and NIC card. It is found that there is about 10dB desensitization between the

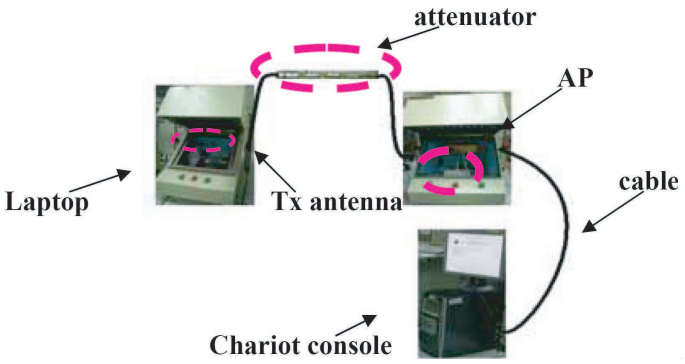

(a) Throughput measurement setup.

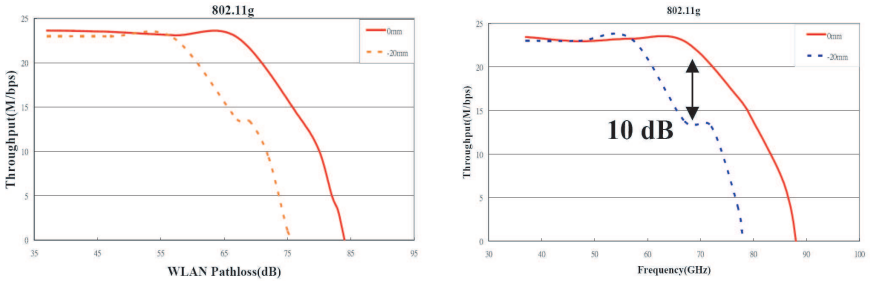

(b) Throughput comparison for in 802.11g antenna 2 and antenna 3 at two different positions.

(c) Photograph of the antenna integrate into a laptop.

Figure 10: Throughput comparison in 802.11g for different locations on the LCD panel.

two throughput measurements for different locations. It is show that when the LCD noise increases the sensitivity is reduced and performance is also degraded. Moreover, it is again shown that the location of antenna placement is significant to wireless communication performance. Fig. 10(c) shows the photograph of the antenna integrated into a laptop for investigation.

4. CONCLUSION

To maintain the characteristics of antenna performance, the antenna should be redesigned and size reduced to resolve the laptop parasitic capacitive effect. The measured results are used for WLAN performance analysis in laptop. Those antennas placed in different locations have different performances, and when antennas placed on left-top and right-top position will have better performance found in this study. This paper also demonstrates the impact of LCD noise on the wireless performance, and we found that there is about 10 dB desensitization between the two throughput measurements for different locations. Hence, optimization of the antenna placement location could help to mitigate the LCD platform noise, and improve the performance for WLAN applications.

REFERENCES

1. Shi, J., K. Slattery, and X. Dong, "A study of platform EMI from LCD panels," 626–631, 2006.
2. Schaffer, M., "Closed-Loop method to assess RF interference impact on wireless transceivers," Vol. 1, 178–181, Aug. 2006.
3. Liu, D., E. Flint, and B. Gaucher, "Integrated laptop antennas — Design and evaluation," *Antennas and Propagation Society International Symposium*, Vol. 4, 56–59, IEEE, June 16–21, 2002.
4. Liu, D., B. Gaucher, E. Flint, T. Studwell, and H. Usui, "Developing integrated antenna subsystems for laptop computers," *IBM Journal of Research and Development*, Vol. 47, 355–367, 2003.
5. Chen, Z. N., *Antennas for Portable Devices*, John Wiley & Sons, Ltd, 2007.

Optimized ARC Filters Using Goal-lossy GIC

J. Sedláček, Z. Szabó, and R. Kadlec
Brno University of Technology, Czech Republic

Abstract— The ARC filters based on RLC ladder prototypes realized using noncascade filter synthesis method exhibit some advantages-namely low sensitivity. On the other hand there are disadvantages which are coupled with ARC simulation of required ideal inductors of LC ladder prototypes what brings higher sensitivities to real parasitic properties of ARC simulation. Usage of new principle of goal-directed lossy RLC ladder prototypes enables to design ARC realizations with optimized parameters and minimized influence of real active elements. In paper are new possibilities of ARC filter optimization in some practical examples presented.

1. INTRODUCTION

By classical filter design there are usually single or double-sided termination RLC filter prototypes used. In many catalogues are these standard LC ladder prototypes which are using ideal lossless reactive L and C elements wide tabled. Here the terminal resistances are transformed to the internal structure and dumped the LC circuit to realize the required transfer function.

In [2] was described a new method how to optimize resulting active filter structures based on classical ladder prototypes using goal-lossy filter prototype design where the losses are dispersed to the whole ladder structure. It was shown that the performances of these filters designed with the lossy structures like sensitivities, components ratio etc, may be better than the synthesis based on the classical loss-less RLC ladder prototypes. Theoretically can be used goal-lossy ladder prototypes with losses dispersed to the all branches of network. In the practice, there are most often used two basic circuit LRC ladder configurations are to active filters used — with serial losses and parallel losses in parallel branches (Fig. 2).

In [2, 3], the design algorithm of these goal-lossy ladder prototypes with parallel lossy resistors was described and special software to goal-lossy filter synthesis was presented, for standard types of approximations in form of tables too. For many cases the width of approximation types or parameter ranges is not sufficient, requirement of special software is also some disadvantage for many designers. Therefore also a new method how to design the goal-lossy filter structures using usually accessible analysis software [4] was presented.

2. THE SYNTHESIS OF GOAL-DIRECTED LOSSY PROTOTYPES

2.1. Lossy Prototypes with Parallel Lossy Elements

The procedure of filter synthesis can be leaden to compute lossy ladder structure: a) to obtain the required quality factor of passive elements, b) to reach the transfer function with required resistor value. The accuracy of goal-lossy ladder prototype transfer response with comparison to ideal lossless can be in a case of 3rd order ladder RLC filter analysis demonstrated. Transfer function $H(s)$ of ideal LP filter from Fig. 1 and voltage transfer $H_L(s)$ of goal-lossy structure (with parallel

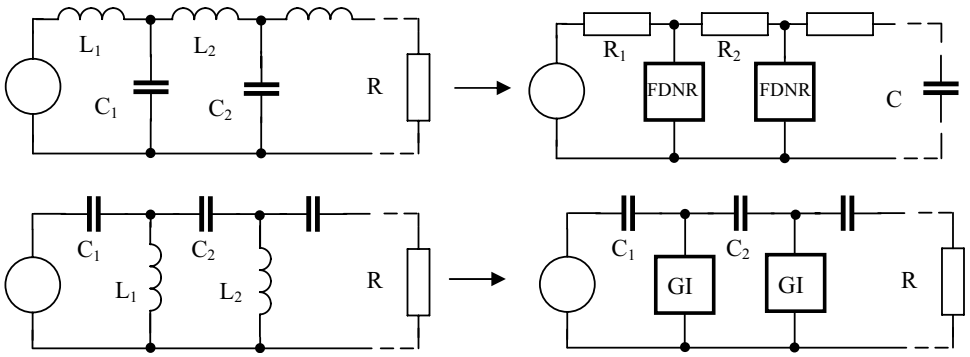

Figure 1: The transformation of LC ladder prototypes to active filters.

resistors R_p) from Fig. 2 can be written as:

$$H(s) = \frac{1}{a_0 + a_1 s^1 + a_2 s^2 + \ldots + a_n s^n} \tag{1}$$

$$H_L(s) = \frac{1}{a_0 + (a_1 + k_1)\, s^1 + (a_2 + k_2)\, s^2 + \ldots + a_n s^n} \tag{2}$$

where $a_0 - a_n$ are coefficients of denominator, s the complex frequency $j\omega$, and $k_{1,2}$ are the parts which are inserted due to losses. By comparison of this two equations, we can observe, that the exact solution of design (transfer function of goal-lossy prototypes with parallel dumped resistors which is equivalent with ideal transfer response) evidently can be (in limited range of parameters) found. As an example here are presented resulting normalized parameters of Tchebyshev and Butterworth LP filters from 5th to 9th order which has been ordered to the Table 1. The parameters have been calculated using developed programs based on iterative numerical methods.

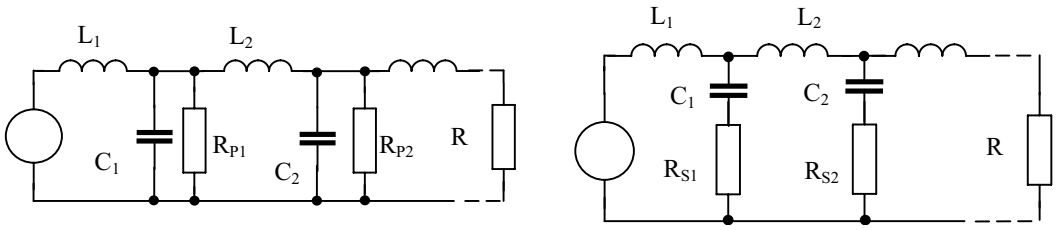

Figure 2: The RLC ladder prototype with parallel and serial losses.

Table 1: The prototypes of Tschebyschev and Butterworth single terminated RLC ladder filter (Fig. 2(a)), normalized to $\omega = 1$ with terminal resistor $r = 1\,\Omega$ — parallel losses.

Type	o	R_p	l_1	c_1	l_2	c_2	l_3	c_3	l_4	c_4	l_5
BUTTERWORTH	5	-	**1.5443**	**1.6936**	**1.3813**	**0.894**	**0.3089**	**-**	**-**	**-**	**-**
		6	1.1040	2.1440	1.2400	1.0290	0.3336	-	-	-	-
		4	0.9630	2.3700	1.1590	1.0980	0.3450	-	-	-	-
		2	0.6928	3.0570	0.9805	1.2820	0.3726	-	-	-	-
	7	-	**1.5571**	**1.7982**	**1.6583**	**1.3967**	**1.0546**	**0.6557**	**0.2224**	-	-
		6	0.9751	2.5700	1.2700	1.1800	0.9382	0.7628	0.2422	-	-
		4	0.8167	2.9500	1.1400	2.0100	0.8876	0.8132	0.2507	-	-
		2	0.5438	4.1200	0.8605	2.6100	0.7593	0.9585	0.2725	-	-
	9	-	**1.5624**	**1.8419**	**1.7767**	**1.6198**	**1.4034**	**1.1405**	**0.8411**	**0.5154**	**0.1736**
		6	0.8628	2.9200	1.2000	2.3500	1.0800	1.4800	0.7567	0.6009	0.1869
TSCHEBYSHEV	5	-	**2.1489**	**1.3016**	**2.6224**	**1.2502**	**1.7406**	**-**	**-**	**-**	**-**
		6	0.8225	2.0080	2.3880	1.5428	2.6329	-	-	-	-
		4	0.5053	2.8621	2.2035	1.6660	3.0700	-	-	-	-
	7	-	**2.1828**	**1.3281**	**2.7143**	**1.3613**	**2.6752**	**1.2665**	**1.7593**	**-**	**-**
		6	0.3768	3.5100	2.0600	2.0600	2.5300	1.4700	3.0600	-	-
		4	0.2207	5.7500	1.5700	2.3800	2.2200	1.5900	3.8100	-	-
	9	-	**2.197**	**1.338**	**2.7413**	**1.3827**	**2.7576**	**1.3733**	**2.6915**	**1.2762**	**1.767**
		6	0.1887	6.4000	1.6500	2.4900	1.8900	1.9000	2.6800	1.4300	3.7300
		4	0.0928	12.790	1.0600	3.1200	1.4600	2.3500	2.3900	1.6000	4.9300

2.2. Lossy Prototypes with Serial Lossy Elements

The synthesis of goal-lossy network with serial resistors R_S (see Fig. 2) brings more problems. Transfer function of 3rd order mentioned filter network with serial lossy resistors can be expressed as:

$$H_{(s)} = \frac{r_n + r_1 r_n c_1 s}{r_n + (r_1 r_n c_1 + l_1 + l_2)\, s + (r_1 l_1 + r_1 l_2 + r_n l_1)\, c_1 s^2 + l_2 c_1 l_1 s^3}. \tag{3}$$

However by comparison with Eq. (1), it is clear, that exact solution (equivalent transfer function by lossy structure) cannot be found. The nominator of transfer function (3) of goal-lossy RLC ladder prototype with serial dumped resistors exhibit inserted zero of transfer function. Therefore for this network structures, the range of possible filter solutions is limited. However, by proper optimized network value parameters can be successfully found solution with allowable difference of transfer function from ideal required transfer response.

As an example here are also presented derived resulting normalized parameters of Tchebyshev and Butterworth LP filters of 5th and 7th orders.

Table 2: The prototypes of Tschebyschev and Butterworth single terminated RLC ladder filter (Fig. 2(b)), normalized to $\omega = 1$ with terminal resistor $r = 1\,\Omega$ — serial losses.

Type	order	R_s	l_1	c_1	l_2	c_2	l_3	c_3	l_4
Butterworth	5	-	**1.5443**	**1.6936**	**1.3813**	**0.894**	**0.3089**	-	-
		0.05	1.3487	1.7132	1.4194	0.9068	0.3355	-	-
		0.1	1.1284	1.7808	1.4705	0.9247	0.3651	-	-
	7	-	**1.5571**	**1.7982**	**1.6583**	**1.3967**	**1.0546**	**0.6557**	**0.2224**
		0.05	1.2676	1.8322	1.6896	1.4187	1.0953	0.6709	0.2439
		0.1	0.8987	2.0297	1.76	1.4588	1.1472	0.6915	0.2685
Tschebyshev	5	-	**2.1489**	**1.3016**	**2.6224**	**1.2502**	**1.7406**	-	-
		0.025	1.898	1.2964	2.65	1.2908	1.8893	-	-
		0.05	1.5203	1.3316	2.7802	1.3656	2.0765	-	-
	7	-	**2.1828**	**1.3281**	**2.7143**	**1.3613**	**2.6752**	**1.2665**	**1.7593**
		0.025	1.7158	1.3066	2.7485	1.4008	2.7863	1.3409	1.9799
		0.035	1.1636	1.4291	2.9934	1.4907	2.922	1.4003	2.1028

3. SOME EXAMPLES OF OPTIMIZED ARC FILTER DESIGN

As the first example a low-pass Butterworth filter of 5th order with active building block — FDNR with parallel lossy and resulting magnitude response here is demonstrated (Fig. 3). As we can see from Fig. 3(b), the optimized version (with sufficient high GBW of operational amplifier) is very closely to ideal filter response.

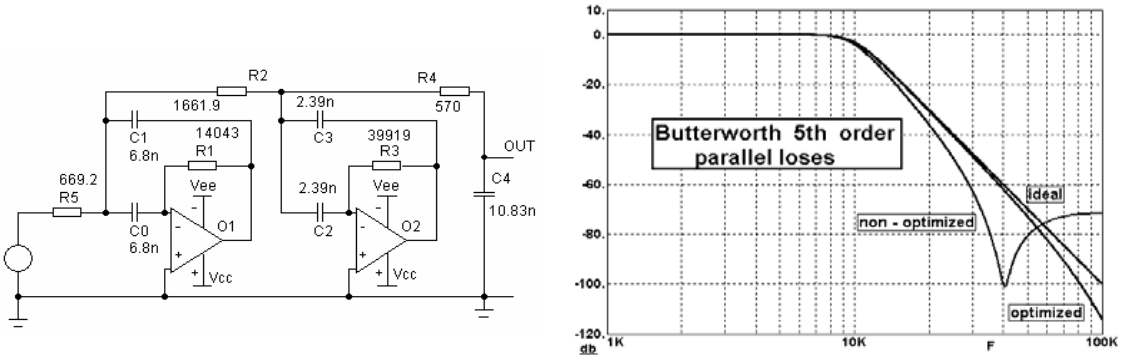

(a) (b)

Figure 3: (a) The active low-pass filter, (b) the resulting magnitude transfer response.

The next Fig. 4 is shown real measured magnitude response (Fig. 4(a)) and dynamic range (output-input) response (Fig. 4(b)) of ARC filter from Fig. 3(a), which has been designed using normalized RLC ladder prototype with parallel losses.

As the second example here is presented the low-pass Butterworth filter of 5th order designed using active — FDNR block with serial lossy based on serial lossy prototypes. From the comparison of ideal and real magnitude transfer responses (see Fig. 5(c)) is evidently seen the influence of parasitic pole for RLC lossy structure with serial resistors bringing effect of slope degradation in

the stop-band. The computed characteristic are agree with ideal approximately up to −80 dB what is in practice fully acceptable in more cases. Thus the active realization of serial lossy structures can be successfully used by synthesis with simple one op-amp synthetic elements with serial losses. This realization can exhibit in some cases an advantage as better properties in the stop-band (smaller effect of transfer response degradation due to absence of parasitic transfer zeros).

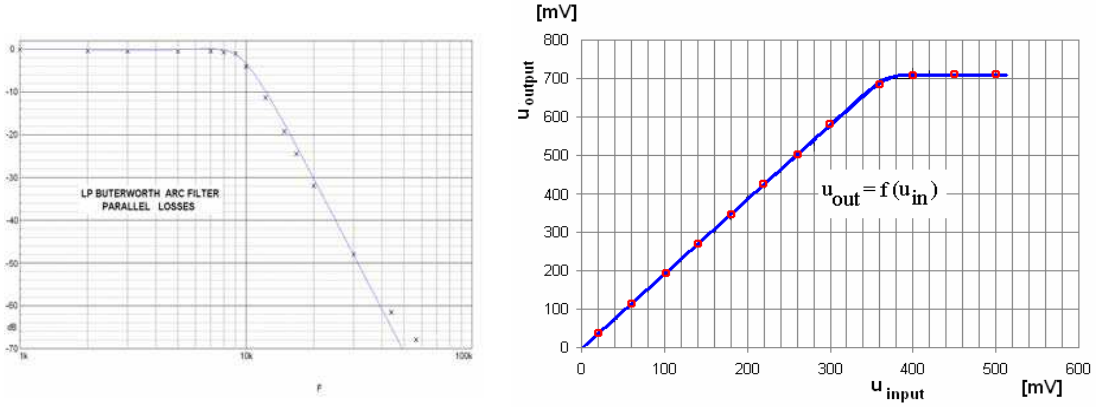

Figure 4: (a) The measured magnitude transfer response, (b) the resulting dynamic range (output-input) response of realized ARC filter.

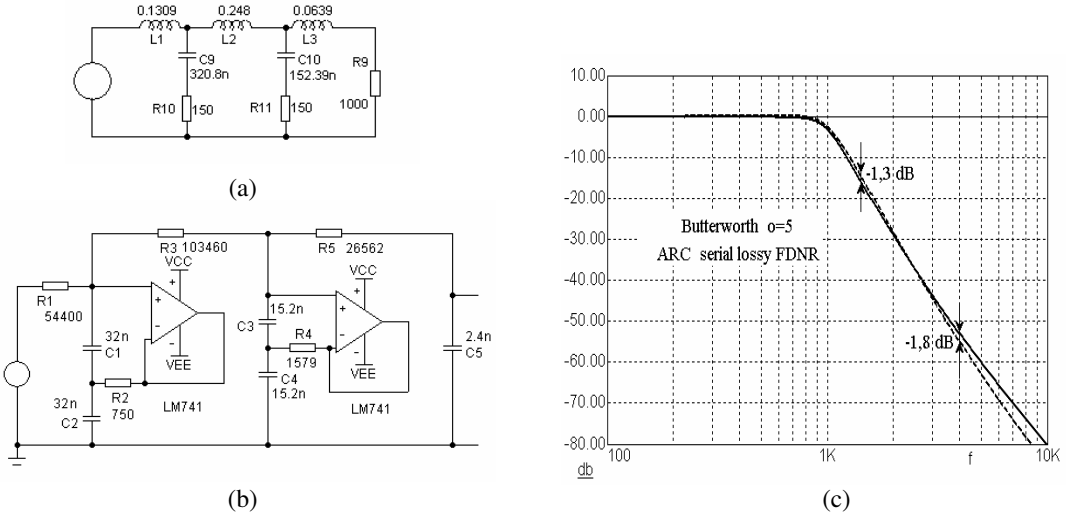

Figure 5: The ARC Butterworth LP filter: (a) RLC ladder prototype, (b) ARC filter circuit diagram, (c) magnitude transfer response.

The comparison between classically designed active filter of 7th order with active real building blocks (Fig. 6(b)) and active filter designed using goal-directed serial and parallel lossy prototype (Fig. 6(a)) we can see from next figures. How is very clearly seen from figures, optimized filter designed using serial goal-directed lossy synthesis method exhibit the magnitude response very near to filter with parallel losses, which is very nearly to ideal response. The classically designed low-pass filter starting from ideal LC ladder prototypes with real building active elements (with supposed $Q = 10$) exhibit significant degeneracy of magnitude response namely in area of corner frequency of filter, the similar degeneracy are visible also at higher frequencies of magnitude response. The resulting influences of real parameters of active block are also very significant by degeneracy of group delay (gd) curve.

In last year have been developed special programs for calculating goal-directed ladder prototypes with parallel lossy resistors [2], in present time is fully function also program for calculating of ladder prototypes with serial lossy resistors in parallel branches of filter. In [4] was published also a new

optimizing method, which can be used very easy to design of the goal–lossy filter structures using usually accessible analysis software. To easy design non-cascade active filter synthesis using goal–directed lossy prototypes a new short program ACTLOSS was developed. It enables to calculate all elements of low-pass and high-pass filters growing from goal–directed lossy LCR ladder prototypes. The main screens of designed program are for both types of filters shown in Fig. 7.

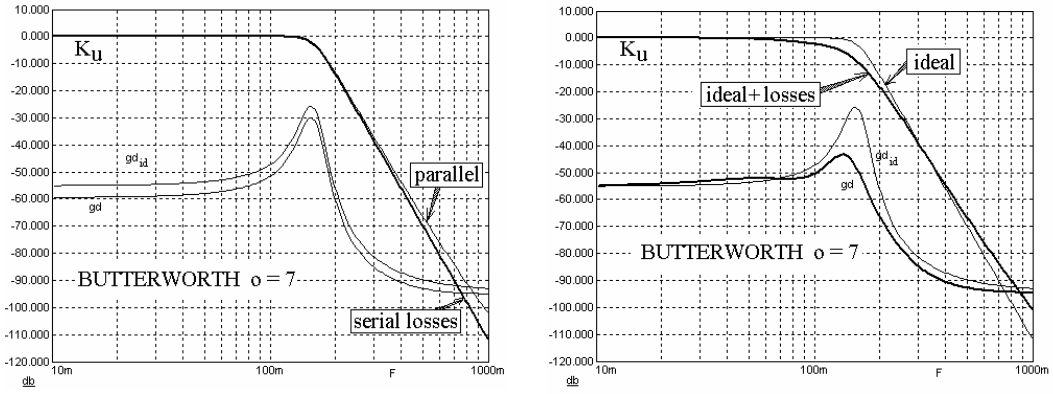

(a) (b)

Figure 6: The comparison of result of difference synthesis method (a) goal-directed lossy prototypes, (b) classical ideal prototypes.

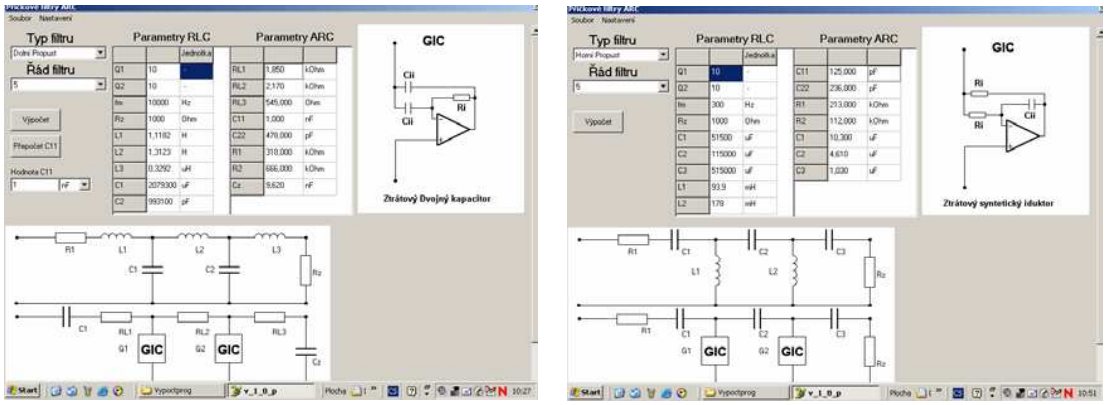

Figure 7: The main screen of ACTLOSS program.

4. CONCLUSION

In the paper, there is described the simple network synthesis method which brings further possibility to improve filter design and optimization in area of passive as well active filters. Here described method allows wider expansion of the filter synthesis based on goal-directed lossy filter RLC ladder prototypes. New presented filter synthesis method and programs developed to filter design and optimization enables to design and optimize above discussed group of ARC filters very easy. In some examples are here also presented the results, which declare many advantages of goal-directed lossy filter design as minimization of element value spread [5], optimization of sensitivities, minimization of OAs number and increasing of ARC filter dynamic range.

ACKNOWLEDGMENT

This work has been supported by the Research Project: MSM 0021630513 and Grant Agency of the Czech Republic under Grant 102/03/1181, 102/04/0442.

REFERENCES

1. Hájek, K. and J. Sedláček, "Kmitočtové filtry," Vydavatelství BEN, Praha, 2002.

2. Hájek, K. and J. Sedláček, "Lossy LC ladder prototypes and their use for ARC filter optimization," *Wseas Transactionson on Electronics*, Vol. 2, No. 3, 94–99, July 2005.
3. Martinek, P. and T. Daša, "Evolutionary algoritmes by ARC filter synthesis," *ECCTD 05*, 155–159, Cork, 2005.
4. Hájek, K., V. Michal, J. Sedláček, and M. Steinbauer, "A simple method of goal-directed lossy synthesis and network optimization," *Advances in Electrical and Electronic Engineering*, 249–253, Žilina, 2006.
5. Hájek, K., V. Michal, and J. Sedláček, "Modern operational amplifiers and their degeneracy effects on active filter performance," *IC-SPETO 2006*, 505–507, Gliwice-Ustroň, 2006.
6. Pavlovic, V. and M. Popovic, "An iterative method for lossy LC ladder filter synthesis," *Proc. 1987 CCTD*, Vol. 1, 185–190, Paris, France, September 1987.
7. Martinek, P. and D. Přívratský, "Elliptic filters with lossy FDNRs," *Radioelektronika'97*, 58–61, Slovak University of Technology, Bratislava, 1997.
8. Hájek, K., J. Sedláček, and B. Sviezeny, "Improving of the active RC and SC filters by use of goal-directed lossy LC ladder prototypes," *Proc. ECCTD-03*, I–381–384, Krakow, September 2003.

Investigation into New Type Piezomagnetic Materials and Acoustical Transducers Exhibiting Piezoelectricity and Piezomagnetic Effect

Quanlu Li[1], **Yuan Li**[2], **and Zhaohui Huang**[2]

[1]Institute of Applied Acoustics, School of Physics and Information Technology
Shaanxi Normal University, Xi'an 710062, China
[2]Department of Prevention Medicine, Fourth Military Medical University
♯17, Changlexi Street, Xi'an 710033, China

Abstract— The design, preparation, etc of newly multipurpose ferrites (i.e., a magnetoelectric ceramic materials) $Ba_{6-x}R_{2x}(Nb_{1-x}\ Fe_{2+x})O_3$, etc, which it exhibiting the piezoelectricity and the piezomagnetic effect (i.e., the ferrite is a multifunctional electroceramic) have been studied. The functional integrated devices including, with the magnetoelectric ceramic materials be made of a had piezoelectric vibration (electro-strctive type thickness extension vibration) and piezomagnetic vibration (magnetostriction type longitudinal extension vibration) both in the same vibrator (i.e., a functional integrated device of having two functions) which that is a composite acoustic transducer, and their applications have been investigated in acoustics etc, as may be noted.

1. MOTIVATION

Multifunctional electronic materials and integrated intelligent devices are needed in the development of advanced technologies, especially mechano-electronic integrative units. This work reports the preparation of new type piezomagnetic ferrite materialsacoustical transducers and their new applications in this study. These materials and devices will be of great significance for acoustics, information engineering, and other uses. However, Ferrites are magnetic ceramic materials. Piezomagnetic ferrite materials are the dielectric analog of piezoelectric ceramic materials. Their uses parallel those of piezoelectric materials in such applications as high permeability materials, electrostrictive transducer, delay lines, energy storage, memory devices etc. Piezomagnetic materials could be used as reversible electroacoustical or electromechanical transducing etc acoustical devices by piezomagnetic effect. This paper briefly reports on gave emphasis to the new type piezomagnetic ferrite materials, acoustical transducers, etc.

2. METHODS

In conventional ceramic processing techniques are modified and adapted to the fabrication of test specimens. Such as, parameters of chemical state and particle size of the reactants, method of mixing, forming process, and heat-treatment are must be considered.

Chemical, physical and structural measurements are made and correlated to the fabrication variables. X-ray diffraction, metallurgical microscopy and chemical analysis are employed in making these measurements. The fabrication and physicochemical parameters are studied in connection with structure-sensitive microwave properties such as Faraday rotation.

In this work, the formula for the new multifunctional piezomagnetic ferrite material.

FER_1 is expressed as:

$$Ba_{6-x}R_{2x}(Nb_{1-x}Fe_{2+x})O_3 \quad (x = 0.25 \sim 0.5) \tag{1}$$

in there R stands for the rare-earth elements.

FER_2 is expressed as:

$$Bi_{2-x}Fe_xO_2 \quad (x = 0.35 \sim 0.65) \tag{2}$$

In a word, the applications of piezomagnetic ferrite materials have (1) Magnetostrictor (including transverse length extension vibration mode, thickness- or width-flexure vibration mode, and twist magnetostriction vibration mode etc): Small change in the length of a piece of piezomagnetic material, which is accompanied the process of magnetization. Ferrite bar (rod), ferrite frequency meter, ferrite head, ferrite keeper, ferrite core, ferrite bead, ferrite-filled waveguide, ferrite-plate memory, ferrite-roe antenna, and ferrite-tuning devices, etc can also made of piezomagnetic ferrite

material. (2) More correctly, a magnetostrictive transducer is a device for converting electrical oscillations to mechanical oscillations by employing the property of magnetostriction. It consists in essence of a bar of piezomagnetic magnetic material, anchored at one point, and subjected to an oscillating magnetizing force, i.e., an oscillating current circulating in a coil carried by the magnetic member. The magnetostriction effect (change of length of ferrite with change of magnetization) results in oscillating movement of the free end or ends of the bar. In order to achieve maximum energy transmission, the system must be driven at or near its natural frequency. The oscillating magnetizing current can be derived from a dynamo-electric alternator or from a thermoionic generator. In the latter case the generator must either include an oscillating valve or receive an input consisting of an oscillating current induced in a pick-up coil incorporated in the transducer itself. The direction of the change of length is, in most material, independent of the direction of the applied magnetizing force, and the frequency of the mechanical oscillations is therefore twice the frequency of the field. However, by providing a magnetic bias by means of a superimposed unidirectional field produced by a direct current flowing in the main or in an auxiliary winging, the mechanical oscillation frequency can be made equal to the field frequency. The acoustical transducers are principally employed for producing pressure waves of ultrasonic frequency. This works were based on the principle theories and related techniques of materials, acoustics, chemistry, physics, electronics and mechanism etc, to pass the creation and the leap of the conception and technology, then to select is able to accomplishing methods and ways in our laboratory, starting from the formula, composition and testing of its properties of some new type piezomagnetic ferrite materials, and to improve on development techniques of the piezomagnetic community, to obtain better properties of the materials and their applications of new acoustic devices was made of the new multifunctional piezomagnetic ferrite materials.

3. RESULTS

Our investigation into piezomagnetic ferrite materials and their applications have shown good progress and results. However, in the development of new piezomagnetic ferrites and acoustical devices, there are many parts, which need precision processing techniques, electronics and thermal treatment techniques, and measurement of piezomagnetic properties, etc to be applied, also make the needs for physics, chemistry and engineering etc combining. To summarized:

Modern physics, chemistry and engineering etc combining make the needs for theory and technique ability etc of new type piezomagnetic ferrite materials. On the other hand, based upon present work, new multifunctional materials and acoustical devices of piezomagnetic ferrite materials exhibited piezomagnetic property and good piezoelectricity, which are investigated, such as $Ba_{6-x}R_{2x}(Nb_{1-x}Fe_{2+x})O_3$ (in there R stands for the rare-earth elements), $Bi_{2-x}Fe_xO_3$ and $Ga_{2-x}Fe_xO_3$, etc. In the properties, these multifunctional materials and acoustical devices will be

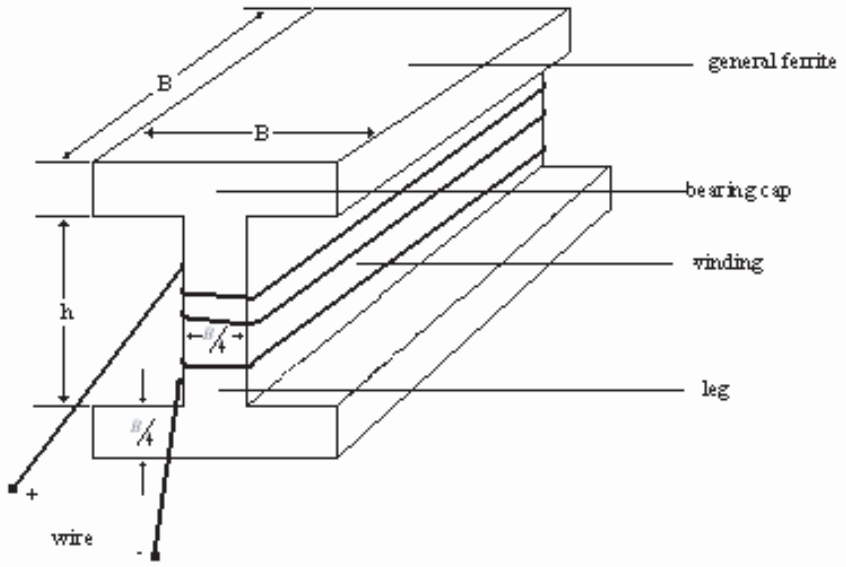

(a)

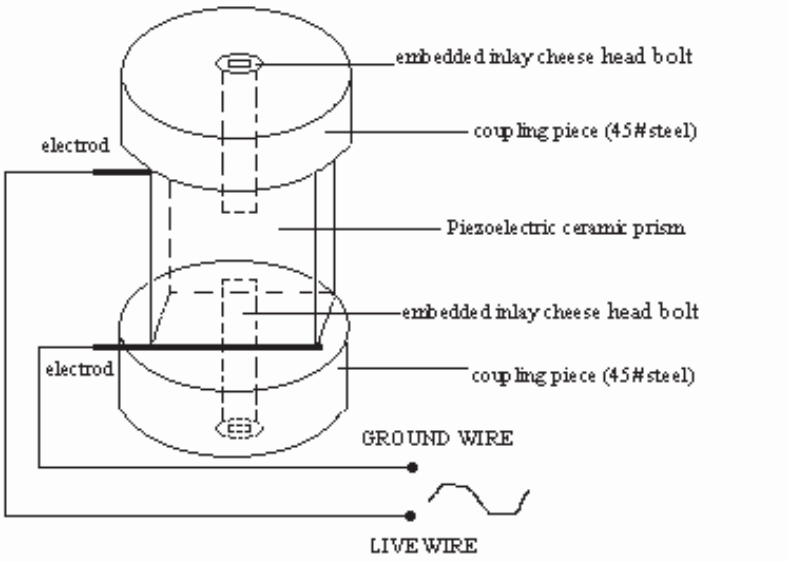

(b)

Figure 1: (a) Schematic diagram of the principle of the model of the had symmetrical bearing cap and single-leg magnetostrictiion ultrasonic transducer. (b) Schematic diagram of the principle of the model of the had symmetrical bearing cap and coupling piece (45♯ steel), and single-leg composite ultrasonic transducer exhibiting piezoelectricity and piezomagnetic effect.

exhibited the sum effect or product effect which they suit the needs of the rapid development of modern electronic industry and other technologies fields. For examples, the tests of the presumable new acoustic devices are given in Fig. 1(a) (Schematic diagram of the principle of the model of the had symmetrical bearing cap and single-leg magnetostriction ultrasonic transducer), Fig. 1(b) (Schematic diagram of the principle of the model of the had symmetrical coupling piece (45♯ steel) piezoelectric (ceramic prismatic) ultrasonic transducer) and Fig. 2 (Schematic diagram of the prin-

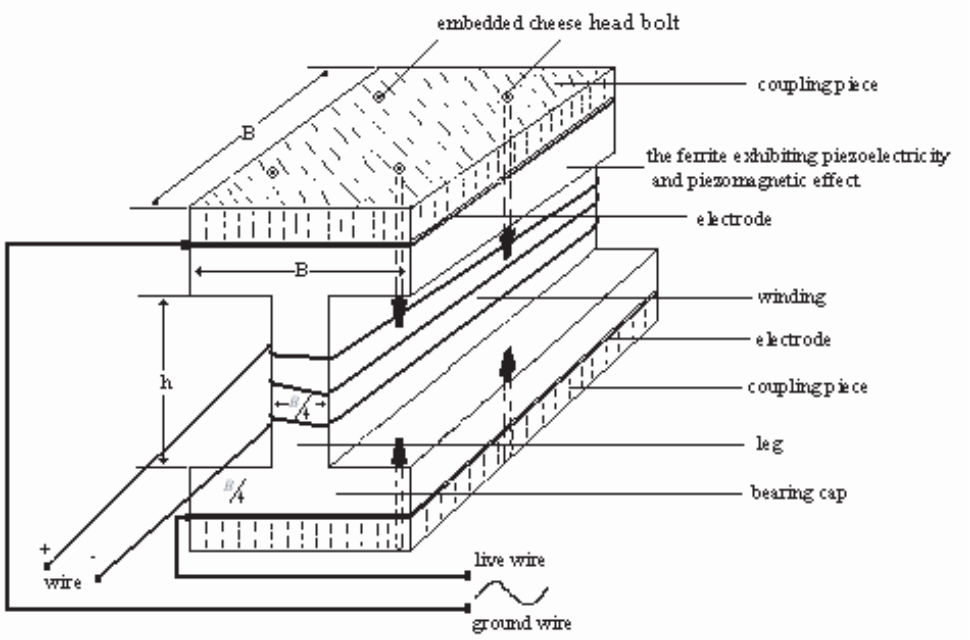

Figure 2: Schematic diagram of the principle of the model of the had symmetrical bearing cap and coupling piece (45♯ steel), and single-leg composite ultrasonic transducer exhibiting piezoelectricity and piezomagnetic effect.

ciple of the model of the had symmetrical bearing cap and coupling piece (45♯ steel), and single-leg composite ultrasonic transducer exhibiting piezoelectricity and piezomagnetic effect).

We make comparison between Fig. 1(a), Fig. 1(b) and Fig. 2, in the Fig. 1(a) the transducer is made from general ferrite which only could produce magnetostriction resonance, but in the Fig. 2 the composite ultrasonic transducer is made of the multifunctional ferrite (which is exhibiting piezoelectricity and piezomagnetic effect) integrated with the thickness extension vibration (piezoelectric resonator, frequency f_e) and longitudinal extension vibration (piezomagnetic resonator, frequency f_m) two kinds vibrations in the same transducer. When $f_e = f_m$, which both will be produce a summing strong vibration; $f_e \neq f_m$, both will be produce composite vibration in the same transducer. In reality, above two vibrations all have importantly practical values in the series power ultrasonics, etc. Specially, this multiprose ultrasonic transducer also provides possiblity for integrating acoustic levitation with magnetic levitation.

4. CONCLUSIONS

The research work of new type piezomagnetic materials and acoustical transducers which are exhibiting piezoelectricity and piezomagnetic effect shows that it is feasible in theory, and has certainly made some progress in experimental technique. But, there are other technologically difficult problems that require future research work and solutions to, such as the design and fabrication of the multiprose acoustical transducers, etc.

A. Mention in passing, there is pointed out that piezoelectric and piezomagnetic these two kinds of acoustoelectric transducing materials can't replace each other in some important applications and will be long-term coexistence, but also the both have better compatibility.
B. In addition, in chemical industry, piezomagnetic ferrite $Co_xFe_{3-x}O_4$ ($x = 0.1 \sim 0.5$) and ZrO_2 were combined, and prepared a magnetic solid acid catalyst which is possessed of very good catalytical activity and appropriate magnetic properties.
C. The present research work opens up and suggests further broad applied field for new type piezomagnetic ferrites and multiprose acoustical transducers.

Modal Analysis of an Antenna Feed System for a Multimode Monopulse Radar

A. M. El-Tager
Electronic Engineering Department, M. T. C., Kobry Elkoba, Cairo, Egypt

Abstract— A modal analysis of a rectangular waveguide antenna feed system for a multimode monopulse radar is presented. Design guidelines as well as 3D EM models are built for sum, azimuth and elevation channels. Simulations for each channel and for the complete assembled system are carried out. Measurements of each channel are performed for different target positions in the 9–10 GHz frequency range. Measurements showed excellent agreement with analytical results which verifies simulations and design concept.

1. INTRODUCTION

Monopulse refers to the ability to obtain complete angle error information on a single pulse. Monopulse technique is used in radars and communication systems for tracking targets or communicating partners because of its high angular accuracy [1]. The aim of monopulse radar is to generate the signals required for E and H plane error channels (azimuth, and elevation) [2]. This may be achieved by either multiple antennas or multi-mode waveguide propagation feed systems [2–4]. The last technique is found to be better in terms of size, complexity, and accuracy. A proposed structure assembly based on this technique is designed, simulated, implemented, and measured in X-band frequency range.

2. MODAL ANALYSIS AND DESIGN GUIDELINES

A dielectric loaded E-plane rectangular waveguide horn is designed to allow the propagation of the desired higher order modes [TE_{01}, TE_{10}, TE_{20}, TM_{11}, and TE_{11}]. The horn is extended by a non standard waveguide allowing the propagation of the previously mentioned modes. Waveguide dimensions and the dielectric constant of the partially filling dielectric material are chosen such that no other higher order modes are allowed to propagate. Figure 1 shows the E-field distribution for different propagating modes. Modes TM_{11} and TE_{11} are generated together due to offset in the incident waveform. These 2 modes are super imposed forming the field distribution shown in Figure 1(f).

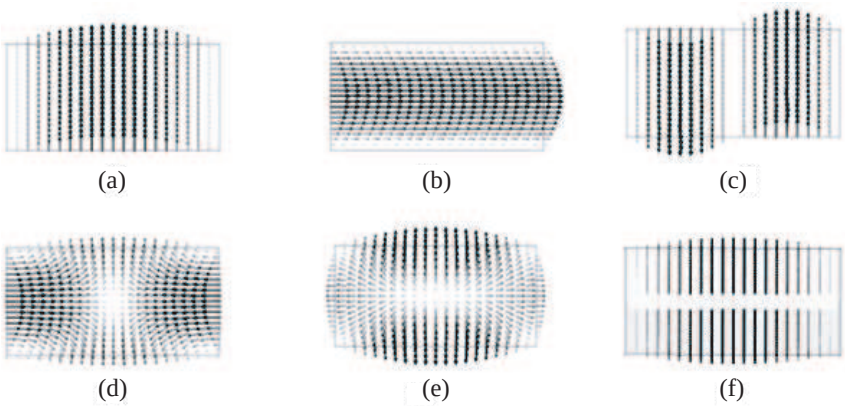

Figure 1: Different propagating waveguide modes; (a) TE_{10}, (b) TE_{01}, (c) TE_{20}, (d) TM_{11}, (e) TE_{11}, (f) $TM_{11} + TE_{11}$.

When the incident wave-front is on the antenna axis, the source is symmetrically excited, hence field distribution on the horn aperture is even. In this case, only TE_{10} mode is transmitted by the horn.

If the incident wave-front is offset in plane H of the horn, the diffraction pattern moves along X-axis of the horn aperture (Azimuth). The excitation becomes asymmetrical, such that higher order modes will propagate. The filtering action of the horn propagates only modes TE_{10} and

TE_{20}. Distribution of E-field amplitudes of both modes is given in Figure 2. On the otherhand, if the incident wave-front is offset in plane E of the horn aperture, the diffraction pattern moves along the Y-axis of the horn aperture (Elevation). This asymmetric excitation produces modes TE_{10}, TM_{11}, and TE_{11}. Distribution of each is given in Figure 3.

As a result of the diffraction patterns given in Figures 2 and 3, amplitude distribution of TE_{10} mode is even in both cases. Therefore, it is used for the sum channel. For any small movement of the diffraction pattern in front of the horn aperture, a corresponding variation occurs in the amplitude of TE_{10} mode.

On the other hand, for a certain movement of the diffraction pattern in front of the horn aperture, not all the amplitudes of the other higher order modes [TE_{20}, TM_{11}, and TE_{11}] vary considerably. However, the field distribution of these higher order modes is odd. Therefore, these modes are able to provide angular discrimination information concerning the wave-front, i.e., generation of error signals. Hence, TE_{20} is used for Azimuth channel and superposition of TM_{11}, and TE_{11} is used for Elevation channel.

3. 3D EM MODELING

A 3D model for the proposed monopulse feed system is carried out using Ansoft HFSS. Initially, each channel model is built up to check its propagating mode and finally all are assembled together to check isolation between each and simulate the overall performance of the multimode feed system.

3.1. Sum Channel

The sum channel signal is the amplitude of the TE_{10} mode which passes through the main non standard rectangular waveguide. The output port at which the sum signal is received should allow the propagation of TE_{10} mode only and isolate any higher order modes. Thus, the insertion loss between the output and the input of the sum channel for different propagating modes is simulated. The results show that the only propagating mode will be TE_{10}, which is the dominant mode, while

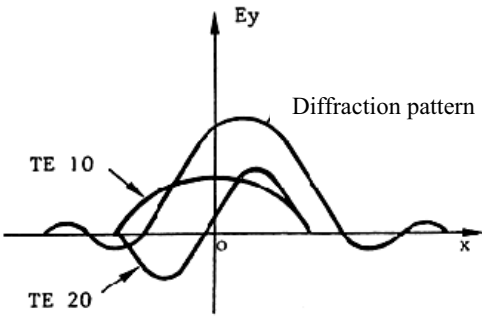

Figure 2: Diffraction pattern in X-plane.

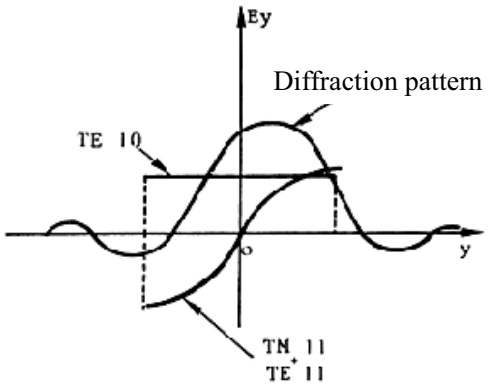

Figure 3: Diffraction pattern in Y-plane.

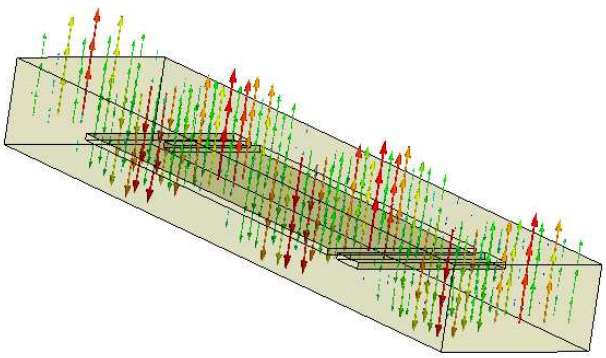

Figure 4: 3D EM model for the sum channel showing the propagation of TE_{10}.

all other modes will be suppressed. Figure 4 shows the 3D model of this channel as well as the propagation of TE_{10} mode through it.

3.2. Azimuth Channel

The Azimuth channel is formed by a slot machined in the side wall of the main guide. The slot is connected to a guide perpendicular to the main body. A 3D EM model is carried out as shown in Figure 5.

The sum signal, altogether with the difference signal at the input of the main guide create TE_{11} and TM_{11} modes. These 2 modes combine together forming the field distribution given in Figure 2(f).

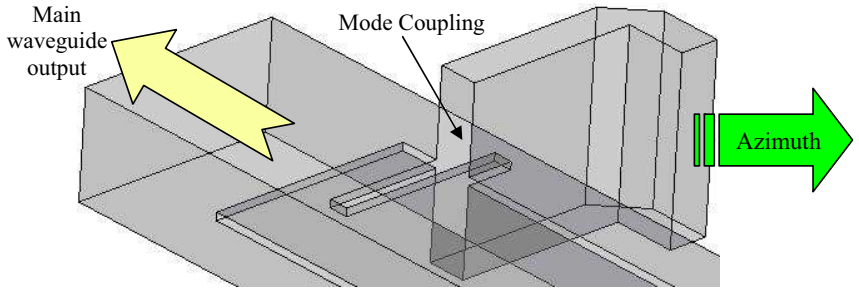

Figure 5: 3D EM model for the azimuth channel.

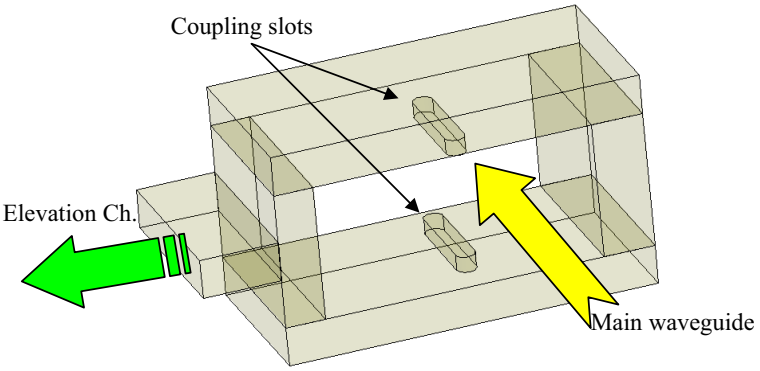

Figure 6: 3D EM model for the elevation channel.

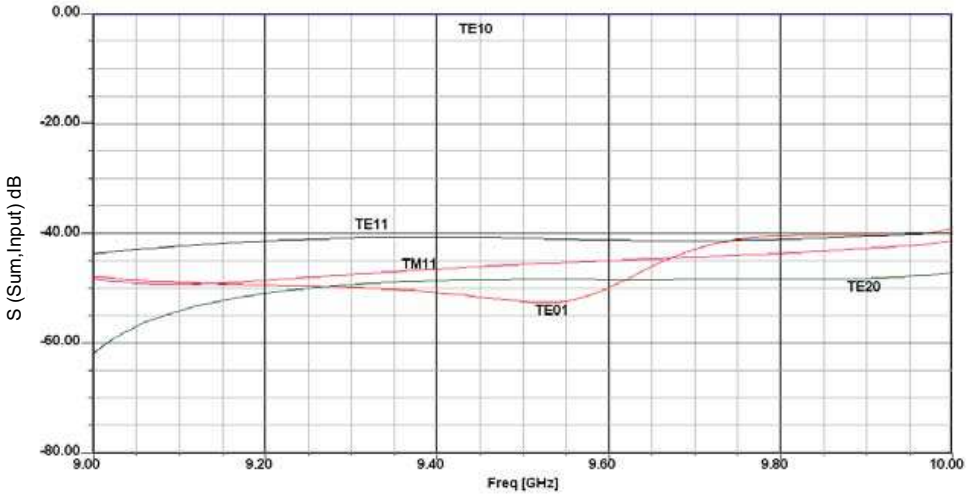

Figure 7: Insertion loss for different modes between input and sum channel.

3.3. Elevation Channel

The elevation channel is formed by two slots machined in the wider wall of the main guide. These 2 slots are connected to two guides placed against the source body. These two guides are combined by a folded magic-T. A 3D EM model is built for this channel as shown in Figure 6 to be coupled to the main waveguide of the sum channel. Considering reception, the incident TE_{20} signal excites the slots in phase-opposition and consequently the two lateral guides which produce the difference signal on the Elevation channel.

3.4. System Assembly

Finally, the three previous models are assembled together. System input is excited; at the horn side; with all modes of Figure 1 at frequency range 9 to 10 GHz. Insertion loss for each mode is simulated at every channel output. Figure 7 shows the insertion loss at sum channel port, which ensures that only TE_{10} mode dominants while other modes decay.

The insertion loss of all modes at the output of the azimuth channel with respect to the input is shown in Figure 8. Simulation results show that only TE_{20} mode propagates, while all other modes decay. On the other hand, insertion loss of all modes at the output of the elevation channel w.r.t. the input is shown in Figure 9. Simulation results show that only TE_{11} and TM_{11} modes will propagate, while all other modes will decay. Finally, the input and output matching are designed carefully and optimized for all modes as in Figure 10. This shows better performance than the monopulse feed system of [5].

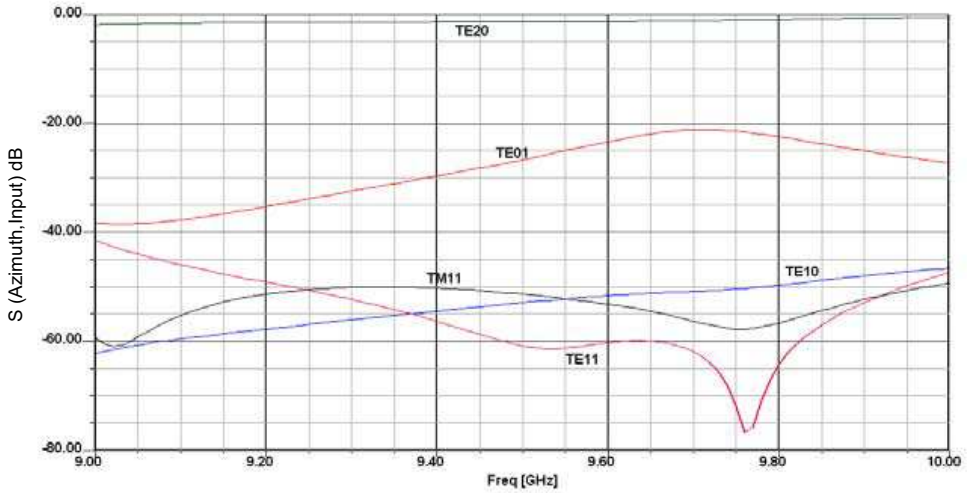

Figure 8: Insertion loss of all modes at the output of the azimuth channel.

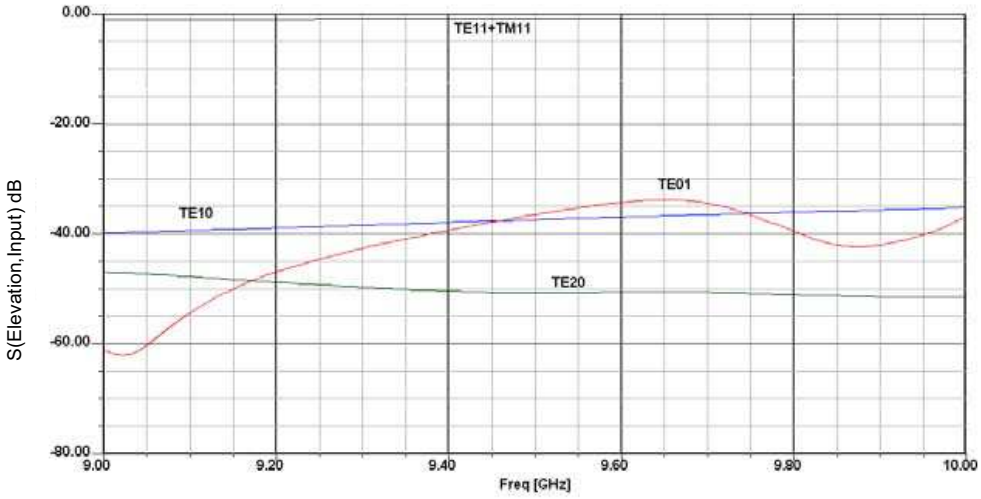

Figure 9: Insertion loss of all modes at the output of the elevation channel.

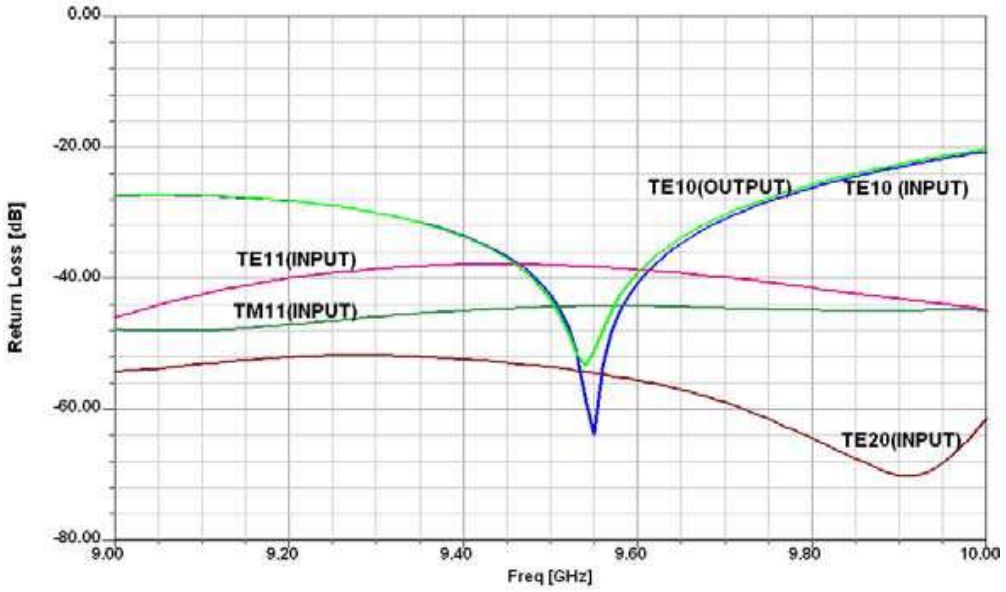

Figure 10: Return loss for different modes at input and sum (output) channel.

4. MEASUREMENTS

Measurements for the feed system are carried out to verify the modal analysis and simulation results. To carry out the measurements the monopulse feed system is mounted and a transmitting horn antenna is placed at different positions; bore sight, elevation and azimuth. The horn antenna and the monopulse feed system are connected to the two ports of a network analyzer. The transmitting horn is placed at different positions the output from each channel (sum, elevation, and azimuth) is measured with the other two ports matched.

Measurements are carried out in the 9–10 GHz frequency band [X-band]. The channels output are measured at five positions (bore sight, $+20^\circ$ elevation, -20° elevation, $+20^\circ$ azimuth, and -20° azimuth) in order to verify the multimode monopulse theory. Table 1 provides the results of the simulated and measured data for all channels at different target positions. It's clear that there is an excellent agreement between theoretical, simulated, and measured data which validates the 3D EM modeling of the proposed multi-mode monopulse feed system.

Table 1: Simulated vs. measured S-parameters for different modes [dB].

	TE_{10}		$TE_{11} + TM_{11}$		TE_{20}	
	Simulated	***Measured***	***Simulated***	***Measured***	***Simulated***	***Measured***
Sum	-0.2	-0.8	-42	-30	-50	-30
Azimuth	-40	-30	-2	-3	-50	-30
Elevation	-55	-30	-50	-30	-2	-3

5. CONCLUSIONS

This paper proposes an antenna feed system for an X-band multimode monopulse radar using rectangular waveguide. A modal analysis is performed following multimode design guidelines. A 3D EM model is built for sum, azimuth and elevation channels to obtain single mode propagation for each channel carrying its associated information. Finally, the three previous models are assembled together. Initial measurements are carried out for different target positions. Excellent agreement between simulations and measurements are found, which validates design and modeling strategies.

REFERENCES

1. Skolnik, M. I., *Introduction to Radar Systems*, Third Edition, McGraw-Hill J., New York, 2001.
2. Potter, P. D., "A new horn antenna with suppressed side lobes and equal beam widths," *Microwave Journal*, No. 6, 71–78, June 1963.
3. Clarricoats, P. J. B. and R. D. Elliot, "Multimode corrugated waveguide feed for monopulse radar," *IEE Proc.*, Vol. 128, Pt. H, No. 2, 102–110, April 1981.
4. Lee, K. M. and R. S. Chu, "Design and analysis of a multimode feed horn for a monopulse feed," *IEEE Trans. Antennas and Propagation*, Vol. 36, No. 2, 171–181, 1988.
5. Meyer, P., C. A. Vale, and W. Steyn, "On the design of waveguide devices using multiple propagating modes," *IEEE*, Vol. 9, No. 2, 2006.

Calculation of Electromagnetic Wave Logging Response by Using the Numerical Mode Matching Method

Yuan Zhao, **Yueqin Dun**, **and Jiansheng Yuan**
State Key Lab of Power Systems, Department of Electrical Engineering
Tsinghua University, Beijing 100084, China

Abstract— The Numerical Mode Matching (NMM) method as an efficient half-numerical and half-analytical algorithm has been successfully applied in the simulation of electromagnetic fields with multi-layer structure domains for both high and low frequency applications. In this paper, the response of the Logging While Drilling (LWD) problem with multiple-layer structure soil is simulated by using the NMM method. The simulated drill collar consists of one or two transmitting coils and two receivers. This device can be applied to detect physical property parameters of the soil or medium surrounding the borehole. According to the simulation results, the phase difference of signals received by the two receivers, but not the difference of the signal amplitude, is reflected by the parameters observably. In the numerical simulation, a model of LWD problem including drill collar is adopted. The drill collar is considered as specific layers of the earth to simplify the simulation.

1. INTRODUCTION

Well-logging is an important part of geophysical exploration. Among well-logging electric or electromagnetic tools which can measure conductivities, resistivities or dielectric constants are essential. The problem of electromagnetic wave propagation in cylindrical structures has been studied for a long time. Various numerical methods have been used. The Finite Element Method (FEM) is a most general-purpose method, but it encounters the difficulties of the large computer storage and high time complexity. Chew et al. propose the numerical mode matching (NMM) method to solve this problem [1–5], and it has been shown to be more efficient than a direct use of the FEM. The efficiency of the NMM method is based on the idea that a higher dimensional problem can be reduced to a series of lower dimensional problems. For example, a 2D problem is reduced to one-dimensional (1D) problems, and the field in all layers is obtained in a recursive scheme.

As an important part of electromagnetic well-logging, LWD becomes more popular. LWD tools usually consist of one or two transmitting antennas and two receiving antennas. This device can be applied to detect physical property parameters of the soil or medium surrounding the borehole.

2. EARTH MODEL WITH A DRILL COLLAR

To judge what layer or which depth of the earth is of petroleum or gas, a dill collar is put into a borehole and moved down to measure the physical characteristic of the soil.

The borehole and its surrounding layers are regarded as axisymmetrical structure with horizontal and vertical layers, as shown in Figure 1 where there are M horizontal layers.

The simulated drill collar consists of one or two transmitting coils and two receivers which can detect induction voltage. The transmitters operate at a frequency of 0.5∼2 MHz. The two receivers can be used to cancel the direct coupling effect by taking the ratio of two receiver signals.

3. INTRODUCTION OF NMM METHOD

The NMM method reduces a higher-dimensional problem to a lower-dimensional one in which the modes are found numerically. These modes are then propagated through the higher dimension analytically using mode propagators.

When the drill collar is centered in an axisymmetric formation, the problem is two-dimensional (2D), since the fields generated by these transmitters are independent of azimuthal angle. In the axisymmetrical field model, the field intensity E excited by the transmitter located at $(r',\ z')$ satisfies the Helmholtz equation

$$\nabla^2 \vec{E} + k^2 \vec{E} = i\omega\mu \vec{J}_T \tag{1}$$

where $\vec{J}_T$ is current density in the transmitter.

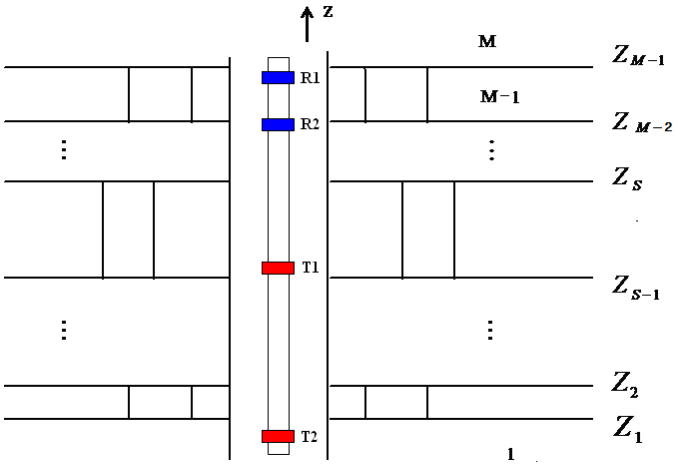

Figure 1: An axisymmetrical earth model with a drill collar.

In the circular cylindrical coordinate, the field intensity has nothing to do with φ. So function (1) can be written

$$\left[\frac{\partial}{\partial r}\left(\frac{1}{r}\frac{\partial}{\partial r}\right)+\frac{1}{r}\frac{\partial^2}{\partial z^2}+\frac{1}{r}k^2\right] rE_\varphi = i\omega\mu I_T\delta(r-r')\delta(z-z') \tag{2}$$

where k^2 is the complex wave number, μ is the permeability, and δ is the Dirac delta function.

The separation variable method is usually employed to solve such partial differential equations. By expressing the field intensity as $rE(r,z) = F(r)U(z)$, substituting it to the homogeneous form of (2), and dividing by $F(r)U(z)$ in both sides, we can have

$$\frac{r\frac{\partial}{\partial r}\frac{1}{r}\frac{\partial}{\partial r}F(r)+k^2F_m(r)}{F(r)} = -\frac{\frac{\partial^2}{\partial z^2}U(z)}{U(z)} \tag{3}$$

Since the left side of (3) only depends on variable z, while the right only on variable r, both sides must be equal to a constant, denoted by λ^2 that is called separation constant or mode constant. Consequently, the partial differential equation can be transformed to two ordinary differential equations as follows,

$$r\frac{d}{dr}\frac{1}{r}\frac{d}{dr}F(r)+k^2F(r) = \lambda^2F(r) \tag{4}$$

$$\frac{d^2}{dz^2}U(z) = -\lambda^2U(z) \tag{5}$$

Choosing N number of basis functions $[g_\alpha(r)] = [g_1, \ldots, g_N]$, the solution of (4) for λ^2 in layer m can be approximately described as

$$f_m(r) = \sum_{i=1}^{N} c_{mi}g_i(r) = [g(r)]^T C_m \tag{6}$$

where $[c_m] = [c_{m1}, \ldots, c_{mN}]^T$ are constants to be determined. Substituting (6) to (4), then choosing the basis functions as the weight functions, and evaluating the inner product of each weight function and (4), we can obtain a system of N equations, whose matrix form is shown below,

$$A_mC_m = BC_m\Lambda_m^2 \tag{7}$$

where A_m and B are the stiffness matrixes of the Galerkin FEM, and the basis functions are just the shape functions of FEM. $\Lambda_m^2 = \mathrm{diag}(\lambda_{m1}^2, \ldots, \lambda_{mN}^2)$ is a diagonal matrix, and C_m is an $N \times N$ matrix formed by combining N vectors $[c_{\alpha m}] = [c_{m1}, \ldots, c_{mN}]^T$ ($\alpha = 1, 2, 3, \ldots, N$). It is clear

that the number N is equal to the number of the finite element nodes in r direction. The solution of (7) is the complex number eigenvalue problem. The eigenvalue Λ_m^2 and the eigenmatrix C_m of each layer can be got by solved.

Function (5) has the analytic solution, that is

$$u_m^{\pm}(z) = e^{\mp\Lambda_m(z-z')}u_m^{\pm}(z') \tag{8}$$

Then the homogeneous Helmholtz function can be solved in each layer.

The determination of coefficients can be fulfilled by the boundary conditions on the interface of horizontal layers. Adding the source is that the horizontal layer where the source is located is divided into two. The boundary conditions at the interface between layer $m-1$ and m are

$$E_m = E_{m-1} \tag{9}$$

$$\frac{\partial E_m}{\partial z} - \frac{\partial E_{m-1}}{\partial z} = i\omega\mu r\xi(r) \tag{10}$$

If the interfaces without the current source, the right side in (10) is null.

When a discontinuity is present, the reflection, transmission, and conversion of modes are characterized by reflection and transmission operators. When many discontinuities are present, they can be treated as a concatenation of one-discontinuity problems. In this manner multiple reflections and transmissions are easily accounted for with generalized reflection and transmission operators using a recursive algorithm.

Suppose the receiver is at the point of $r = r_R$, $z = z_R$. After the electric field intensity $E(r_R, z_R)$ is solved, the induction voltage V can be got

$$V = 2\pi N_R r_R E(r_R, z_R) \tag{11}$$

where N_R is number of turns of the receiver.

4. RESULTS AND THE ANALYSIS

Based on the NMM method, a code for calculating the responses in layer structure soil has been developed. Tables 1 and 2 gives the comparison of induction voltages by NMM, FEM and analytic solutions in different structures. It shows very good agreement.

Table 1: Results of NMM, FEM and analytic solution (infinite media, with parameters as $\varepsilon_r = 1.0$, $\mu_r = 1.0$, $I_T = 2.5A$).

Resistivity (Ω / m)	Distance between R and T (mm)	NMM		FEM		Analytic Solution	
		Amplitude (mV)	Phase (degree)	Amplitude (mV)	Phase (degree)	Amplitude (mV)	Phase (degree)
1	660	3.3842	-136.5546	3.3810	-136.6381	3.4780	-136.1390
	840	1.3847	-154.4274	1.3839	-154.5172	1.4110	-154.1020
10	660	4.6433	-97.6209	4.6806	-97.6493	4.7500	-97.5200
	840	2.2436	-101.3622	2.4063	-100.9767	2.2760	-101.3230
100	660	4.7674	-90.9229	4.7634	-90.9781	4.8750	-90.9607
	840	2.3501	-91.4399	2.3488	-91.5043	2.3830	-91.4833

Table 2: Results of NMM and FEM (an axisymmetrical structure with 4 horizontal layers and 1∼3 vertical layers, $I_T = 1.0A$).

Distance between R and T (mm)	NMM		FEM	
	Amplitude (mV)	Phase (degree)	Amplitude (mV)	Phase (degree)
660	1.5203	-116.2704	1.5136	-116.3243
840	0.6500	-125.7910	0.6642	-125.5164

The Figure 2 shows when the electrical resistivity changes from 0.001∼3000 Ω/m, the amplitude attenuation and phase difference of induction voltages detected by two receivers. It is shown that the phase difference of signals received by the two receivers, but not the difference of the signal amplitude, is reflected by the parameters observably when the electrical resistivity varies.

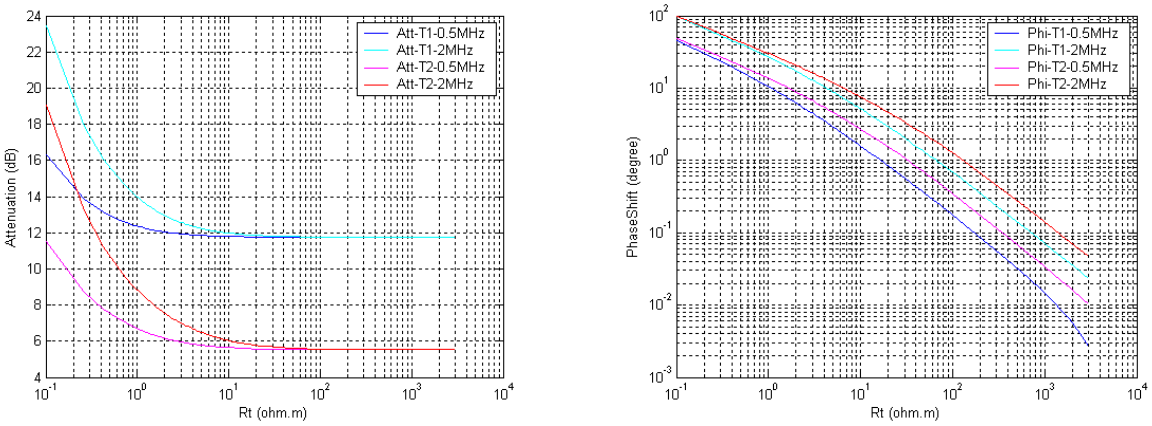

(a) The signal amplitude attenuation

(b) The phase difference

Figure 2: The drill collar model.

5. CONCLUSIONS

The NMM method is a very efficient method to solve the electric current problems with axisymmetrical multiple-layer structure domain. The numerical experiments show that the NMM method is more efficient and accurate than other traditional numerical methods.

According to the simulation results, the phase difference of signals received by the two receivers, but not the difference of the signal amplitude, is reflected by the parameters observably when the electrical resistivity varies.

REFERENCES

1. Chew, W. C., S. Barone, B. Anderson, and C. Hennessy, "Diffraction of axisymmetric waves in a borehole by bed boundary discontinuities," *Geophysics*, Vol. 49, No. 1, 1586–1595, 1984.
2. Chew, W. C., "Modeling of the dielectric logging tool at high frequencies theory," *IEEE Trans. Geoscience and Remote Sensing*, Vol. 26, No. 4, 382–387, 1988.
3. Chew, W. C., *Waves and Fields in Inhomogeneous Media*, Van Nost rand Reinhold, New York, 1990.
4. Liu, Q. H. and W. C. Chew, "Numerical model-matching method for multiregion, vertically stratified media," *IEEE Trans. Antennas Propagation*, Vol. 38, No. 4, 498–506, 1990.
5. Chew, W. C. and Z. P. Nie, "An efficient solution for the response of electrical well logging tool s in a complex environment," *IEEE Trans. Geoscience and Remote Sensing*, Vol. 29, No. 2, 308–313, 1991.

Analysis of Ridge Waveguide with Claddings of Metamaterials with Zero Index of Refraction

Wanzhao Cui[1], **Jia Chen**[2], **Tiancun Hu**[1], **Hongtai Zhang**[1], **and Enrang Zheng**[2]

[1]National Key Laboratory of Space Microwave Technology
Xi'an Institute of Space Radio Technology, Xi'an, Shannxi 710100, China
[2]Shannxi University of Science & Technology, Xi'an, Shannxi 710021, China

Abstract— In this paper, based on peculiar electromagnetic characteristics of metamaterials, peculiar properties of ridge waveguide with claddings of metamaterials with zero index of refraction are analyzed. These results provide some interested insights for potential applications.

1. INTRODUCTION

In 1968, lossless propagation of an electromagnetic wave in the metamaterials with negative permittivity (ε) and negative permeability (μ) was first investigated by V. G. Veselago [1], and was experimentally verified in 2001 based on split-ring resonators and rods [2]. V. G. Veselago speculated on the possible existence of metamaterials and anticipated their unique electromagnetic properties [1]. The unique properties of MTMs have allowed novel applications, concepts, and devices to be developed [3]. Science magazine even named metamaterials as one of the top ten scientific breakthroughs of 2003 [4].

Planar metamaterials that exhibit a zero index of refraction have been realized experimentally by several research groups [3]. Zero index of refraction metamaterials [5] have properties of a passive, dispersive metamaterial matched to free space, and here both the permittivity and permeability are zero at a specified frequency. However, few scientists have researched the peculiar characteristics of metamaterials in applications of radar, and peculiar radar cross section properties of metamaterials with zero index of refraction are not researched.

In this paper, based on peculiar electromagnetic characteristics of metamaterials, peculiar properties of ridge waveguide with claddings of metamaterials with zero index of refraction are analyzed. These results provide some interested insights for potential applications.

2. METAMATERIALS WITH ZERO INDEX OF REFRACTION

Metamaterial realizations of double negative metamaterials, i.e., metamaterials in which the permittivity and permeability are both less than zero, as well as double positive metamaterials, i.e., metamaterials in which the permittivity and permeability are both greater than zero, have been reported. Within these studies, there have been several demonstrations, both theoretically and experimentally, of metamaterials that exhibit a zero index of refraction within a specified frequency band [5]. There are three different metamaterials with zero index of refraction: zero-permeability metamaterials, zero-permittivity metamaterials, zero-permeability and zero-permittivity metamaterials.

Some researchers [6] have found that metamaterials and zero-permeability metamaterials share the same transmission band, and that the material's predominant refractive character strongly depends on the dielectric losses. The metamaterial converts from metamaterials with negative-permeability to zero-permeability metamaterial by increasing the dielectric loss. In some sense, the zero-permeability metamaterial is a special limiting case of a MTM for high dielectric losses and small refractive index. Metamaterials with zero permittivity [7] will create band gaps in a wide range of frequencies up to the visible, and will completely reflect electromagnetic waves in the limit of long wavelengths.

The electromagnetic matched metamaterials with zero-permeability and zero permittivity supports both transverse and longitudinal waves much like a cold plasma medium does [8], the dispersion relations for both types of waves are the same. Moreover, the zero-index transverse waves behave similarly to their longitudinal counterparts. Some researchers have shown that in both the source and scattering configurations the electromagnetic fields in a matched zero-index medium take on a static character in space, yet remain dynamic in time, in such a manner that the underlying physics remains associated with propagating fields. Zero phase variation at various points in the zero-index medium if steady-state conditions are satisfied. Many researches have found a

zero-index metamaterial, such as a zero-index electromagnetic band-gap structured medium, significantly narrows the far-field pattern associated with an antenna located within it, and a matched zero-index slab could be used to transform curved wave fronts into planar ones.

3. RIDGE WAVEGUIDE

Original publications on ridge waveguides date back to 1947 [9]. Since that time, ridge waveguides have been widely studied in conjunction with microwave and millimeter wave applications because of their unique characteristics, such as low cutoff frequency, wide bandwidth and low impedance characteristics [10]. Early investigations were focused on transmission characteristics of single and double rectangular-ridge waveguides [11]. Later, other structures were reported, such as two double rectangular-ridge waveguide [12] with a rich diversity of analytical techniques, such as transverse resonance techniques [11],magnetic field integral equations [13], mode-matching method [14] and finite-element method (FEM) [15]. The cross-sections of ridge waveguide is shown in Figure 1.

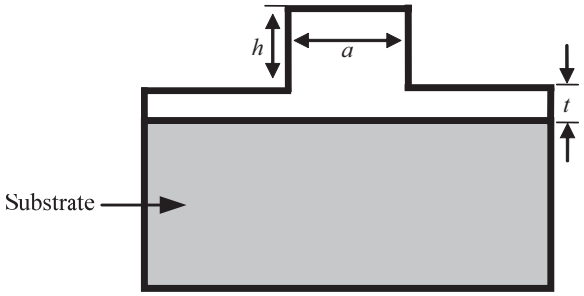

Figure 1: Cross-section of ridge waveguide.

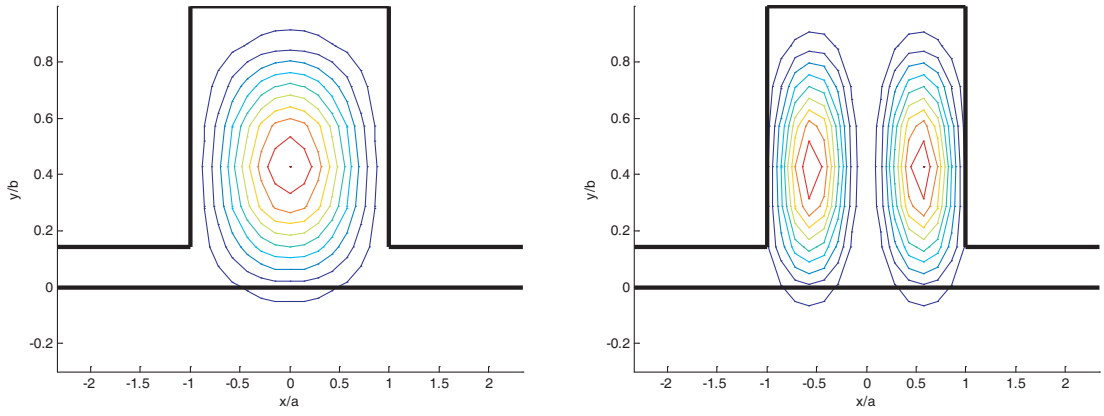

(a) b = 0.785711

(b) b = 0.643053

(c) b = 0.405345

(d) b = 0.296984

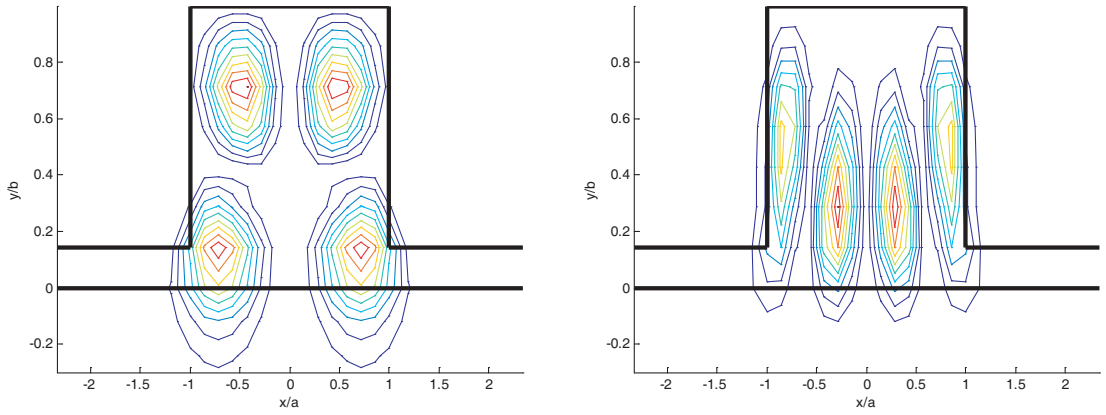

(e) b = 0.163469 (f) b = 0.076924

Figure 2: Simulation results of ridge waveguide with substrates of zero index of refraction metamaterials with different waveguide dimensions.

4. ANALYSIS

Peculiar properties of ridge waveguide with claddings of metamaterials with zero index of refraction with different waveguide dimensions are shown in Figure 2 by finite element method [16].

5. CONCLUSION

Based on peculiar electromagnetic characteristics of metamaterials, peculiar properties of ridge waveguide with claddings of metamaterials with zero index of refraction are analyzed. These results provide some interested insights for potential applications.

ACKNOWLEDGMENT

This work was supported by the National Key Laboratory Foundation of China (No. 9140C5304020704, 9140C5306010708, 9140C5304020804).

REFERENCES

1. Veselago, V. G., "The electrodynamics of substances with simultaneously negative values of ε and μ," *Sov. Phys.-Usp.*, Vol. 10, No. 4, 509–514, 1968.
2. Shelby, R. A., D. R. Smith, and S. Schultz, "Experimental verification of a negative index of refraction," *Science*, Vol. 292, No. 5514, 77–79, 2001.
3. Caloz, C. and T. Itoh, *Electromagnetic Metamaterials: Transmission Line Theory and Microwave Applications*, Wiley, New York, 2005.
4. "Breakthrough of the year: The runners-up," *Science*, Vol. 302, No. 5653, 2039–2045, 2003.
5. Engheta, N. and R. W. Ziolkowski, *Metamaterials: Physics and Engineering Explorations*, IEEE Press, 2006.
6. Monzon, C., P. Loschialpo, and D. W. Forester, "Zero-permeability materials: An artifact of losses in left-handed media," *IEE Proc. Microw. Antennas Propag.*, Vol. 152, No. 6, 2005.
7. Garcia, N., E. V. Ponizovskaya, and J. Q. Xiao, "Zero permittivity materials: Band gaps at the visible," *Appl. Phys. Lett.*, Vol. 80, 1120–1122, 2002.
8. Ziolkowski, R. W., "Propagation in and scattering from a matched metamaterial having a zero index of refraction," *Phy. Rev. E*, Vol. 70, 046608+12, 2004.
9. Cohn, S. B., "Properties of ridge waveguide," *Proc. IRE Trans. on Microwave Theory Tech.*, Vol. 35, 783–788, 1947.
10. Helszajn, J., *Ridge Waveguides and Passive Microwave Components*, IEE, UK, 2000.
11. Hopper, S., "The design of ridged waveguides," *IRE Trans. on Microwave Theory Tech.*, Vol. 3, 20–29, 1955.
12. Dasgupta, D., and P. K. Saha, "Rectangular waveguide with two double ridges," *IEEE Trans. on Microwave Theory Tech.*, Vol. 31, 938–941, 1983.
13. Sun, W. and C. A. Balanis, "Analysis and design of quadruple-ridged waveguides," *IEEE Trans. on Microwave Theory Tech.*, Vol. 42, 2201–2207, 1994.

14. Rong, Y. and K. A. Zaki, "Characteristics of generalized rectangular and circular ridge waveguides," *IEEE Trans. on Microwave Theory Tech.*, Vol. 48, 258–265, 2000.
15. Qiu, D., D. M. Klymyshyn, and P. Pramanick, "Ridged waveguide structures with improved fundamental mode cutoff wavelength and bandwidth characteristics," *Int. J. RF Microw. Comput. Aided Eng.*, Vol. 12, 190–197, 2002.
16. Volakis, J. L., A. Chatterjee, and L. C. Kempel, *Finite Element Method for Electromagnetics*, IEEE Press, Piscataway, NJ, 1998.

A Simple Method to Measure the Unloaded Q of a Transmission-type Resonator

Tiancun Hu and Wanzhao Cui
National Key Laboratory of Space Microwave Technology
Xi'an Institute of Space Radio Technology, Xi'an 710100, China

Abstract— A simple method to quickly obtain the unloaded Q of a transmission resonator is presented. Input and output coupling coefficients can be directly obtained by measuring the transmission and reflection coefficient using a network analyzer.

1. INTRODUCTION

Recently, a novel method to obtain the coupling coefficient has been developed. The special characteristics of resonators, capable of storing energy from a signal at a given frequency, make them important elements in circuits or as measuring cells. This characteristic has been responsible for a great volume of work [1].

There are many techniques used to characterise microwave resonators. They can be found as part of a circuit in various situations, operating in transmission modes. They also permit the measurement of the reflection or transmission coefficients as well as other related magnitudes. Different mathematical treatments may also be used to solve each situation.

2. THOERY ANALYSIS

Consider a resonator-coupling system (as shown schematically in Fig. 1) with input and output transmission lines of characteristic impedance Z_{01} and Z_{02}, respectively, and assume coupling structures that are essentially lossless and interact negligibly with each other. Assume further that a generator of internal resistance $R_g = Z_{01}$ is connected to the input line and a resistive load $R_L = Z_{02}$ to the output line. The equivalent circuit is shown in Fig. 2, with the resonator represented by a series resonator circuit and the coupling structures by ideal transformers of turns ratio n_1 and n_2. With input and output circuits transformed to the middle loop, the circuit appears as shown in Fig. 3. Therefore,

$$
\begin{aligned}
Q_0 &= \frac{\omega_0 L}{R} \\
\omega_0 &= \frac{1}{\sqrt{LC}} \\
Q_L &= \frac{\omega_0 L}{R + n_1^2 R_g + n_2^2 R_L} = \frac{\omega_0 L/R}{\left(1 + n_1^2 R_g/R + n_2^2 R_L/R\right)} = \frac{Q_0}{1 + \beta_1 + \beta_2}
\end{aligned}
$$

where $\beta_1 \equiv n_1^2 R_g/R$, and $\beta_2 \equiv n_2^2 R_L/R$, by definition.

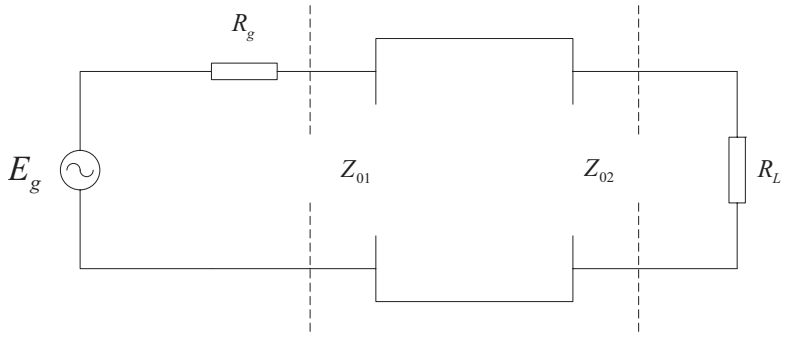

Figure 1: Transmission resonator with input and output lines ($R_g = Z_{01}$, $R_L = Z_{02}$).

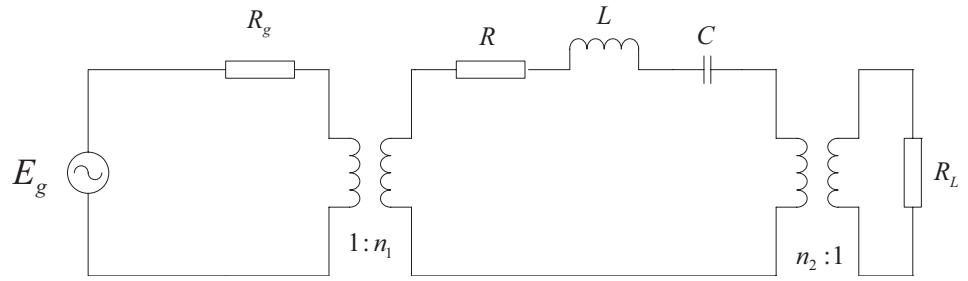

Figure 2: Equivalent Circuit representation.

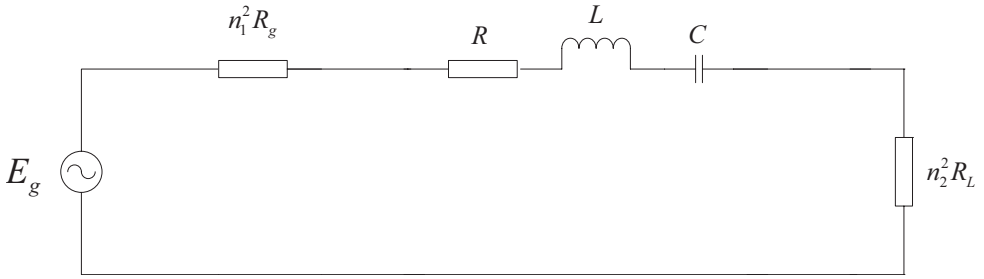

Figure 3: Equivalent Circuit of Transmission Cavity with Generator and Load Circuits Transformed.

We are interested in finding the power transmission through the resonator as a function of frequency. We may write for the impedance of the equivalent Circuit

$$Z = R\left[1 + \beta_1 + \beta_2 + jQ_0\left(\frac{\omega}{\omega_0} - \frac{\omega_0}{\omega}\right)\right]$$

The power delivered to load R_L is

$$\begin{aligned}
P_L &= |I|^2 n_2^2 R_L = n_1^2 E_g^2 n_2^2 R_L / |Z|^2 ; \\
P_L &= \frac{n_1^2 n_2^2 E_g^2 R_L}{R^2\left[(1+\beta_1+\beta_2)^2 + Q_0^2\left(\frac{\omega}{\omega_0} - \frac{\omega_0}{\omega}\right)^2\right]} \simeq \frac{n_1^2 n_2^2 E_g^2 R_L}{R^2\left[(1+\beta_1+\beta_2)^2 + 4Q_0^2\left(\frac{\delta_\omega}{\omega_0}\right)^2\right]} \\
P_L &\simeq \frac{n_1^2 n_2^2 E_g^2 R_L}{R^2(1+\beta_1+\beta_2)^2\left[1 + \left(\frac{2Q_0\delta_\omega/\omega_0}{1+\beta_1+\beta_2}\right)^2\right]} \simeq \frac{n_1^2 n_2^2 E_g^2 R_L}{R^2(1+\beta_1+\beta_2)^2\left[1 + 4Q_L^2(\delta_\omega/\omega_0)^2\right]}
\end{aligned}$$

At resonance

$$P_L = \frac{n_1^2 n_2^2 E_g^2 R_L}{R^2(1+\beta_1+\beta_2)^2}$$

The half power points are obtained when

$$\begin{aligned}
4Q_L^2(\delta_\omega/\omega_0)^2 &= 1 \\
Q_L = \frac{\omega_0}{2\delta_\omega} = \frac{\omega_0}{\Delta\omega} &= \frac{f_0}{\Delta f}\ [2]
\end{aligned}$$

where Δf is the "half power bandwidth".

Let the input and output coupling of a transmission resonator be into two lines of different characteristic impedance with a matched generator connected to the input line and a matched load to the output line.

$$T(\omega) = \frac{4\beta_1\beta_2}{(1+\beta_1+\beta_2)^2 + Q_0^2(\frac{\omega}{\omega_0} - \frac{\omega_0}{\omega})^2}$$

While at resonance ($\omega = \omega_0$), it is

$$T(\omega_0) = \frac{4\beta_1\beta_2}{(1+\beta_1+\beta_2)^2}$$

$\beta_1 =$ input coupling coefficient, $\beta_2 =$ output coupling coefficient.

The VSWR at resonance is given as S_0

$$S_0 = \frac{1+\beta_2}{\beta_1}$$

for the unloaded case, and

$$\frac{1}{S_0} = \frac{1+\beta_2}{\beta_1}$$

for the overcoupled case.

OVERCOUPLED CASE

$$\begin{aligned} \frac{1}{S_0} &= \frac{1+\beta_2}{\beta_1} \\ \beta_2 &= \frac{\beta_1 - S_0}{S_0} \\ T(\omega_0) &= \frac{4\beta_1\beta_2}{(1+\beta_1+\beta_2)^2} = \frac{4(\beta_1 - S_0)S_0}{\beta_1(S_0+1)^2} \end{aligned}$$

Solving for β_1 gives

$$\beta_1 = \frac{4S_0^2}{4S_0 - T(\omega_0)(S_0+1)^2}$$

While

$$\beta_2 = \frac{\beta_1 - S_0}{S_0} = \frac{T(\omega_0)(S_0+1)^2}{4S_0 - T(\omega_0)(S_0+1)^2}$$

UNDERCOUPLED CASE

$$\begin{aligned} S_0 &= \frac{1+\beta_2}{\beta_1} \\ \beta_2 &= \beta_1 S_0 - 1 \\ T(\omega_0) &= \frac{4\beta_1\beta_2}{(1+\beta_1+\beta_2)^2} = \frac{4(\beta_1 S_0 - 1)}{\beta_1(S_0+1)^2} \end{aligned}$$

Solving for β_1 gives

$$\beta_1 = \frac{4}{4S_0 - T(\omega_0)(S_0+1)^2}$$

While

$$\beta_2 = \beta_1 S_0 - 1 = \frac{T(\omega_0)(S_0+1)^2}{4S_0 - T(\omega_0)(S_0+1)^2}$$

3. CONCLUSIONS

A simple method to obtain the unloaded Q of a transmission resonator is presented. The loaded Q can be obtained by measuring the transmission coefficient. Input and output coupling coefficients can be directly obtained by measuring the transmission and reflection coefficient at resonance using a network analyzer.

ACKNOWLEDGMENT

This work was supported by the National Key Laboratory Foundation of China (No. 9140C5303020-704, 9140C-5306010708).

REFERENCES

1. Montgomery, C. G., *Technique of Microwave Measurements*, Constable, 1950.
2. Sucher, M. and J. Fox, *Handbook of Microwave Measurements*, Vol. 2, Polytechnic Press, Brooklyn, 1963.

Symmetric Unit Cell Models for Composite Right/Left-handed Transmission Lines (CRLH-TL) Metamaterials

Jia Chen[1], **Enrang Zheng**[1], **and Wanzhao Cui**[2]

[1]Shaanxi University of Science & Technology, Xi'an 710021, China
[2]National Key Laboratory of Space Microwave Technology
Xi'an Institute of Space Radio Technology, Xi'an 710100, China

Abstract— Based on the homogeneous composite right/left-handed transmissions lines (CRLH-TL) equivalent circuit model, an symmetric unit cell model for CRLH-TL metamaterials having left-handedness (LH), right-handedness (RH) at different frequencies presented. The CRLH TL unit model is a meta-structured TL composed of a series capacitance and a shunt inductance as well as a series inductance and a shunt capacitance. The series capacitance and the shunt inductance provide the LH nature at lower frequencies, whereas the series inductance and the shunt capacitance provide the RH nature at higher frequencies, an unique characteristic of CRLH-TL. We can obtain $|S_{21}| = 1$ at a desired center frequency and also make a desired phase shift over a unit cell possible. The unit cell model for CRLH-TL is analyzed using S-parameter formulations resulting in some useful closed-form expressions for design purposes. These results provide some useful references in facilitating the design of CRLH-TL.

In 1968, lossless propagation of an electromagnetic wave in the materials with negative permittivity (ε) and negative permeability (μ) was first investigated by V. G. Veselago [1], and was experimentally verified in 2001 based on split-ring resonators (SSR) and rods [2]. These materials were named "Left-Handed Metamaterials" (LHMs) because the vectors E, H, and $\boldsymbol{k}$ form a left-handed triplet. Many researchers have studied the characteristics and applications of SRR-based LHMs. However, since SRRs are lossy and narrow-banded, they are often difficult to implement for microwave applications [3, 4]. Several researchers soon realized that a transmission line (TL) approach towards LHMs was possible. By modeling a composite right/left-handed (CRLH) metamaterial as an equivalent TL unit model, TL theory can be used to analyze and design CRLH metamaterials for practical applications. Moreover, TL approach for LHM based on periodically loading a host microstrip transmission line with series capacitors and shunt inductors has been considered simultaneously.

The unit cell models for these left-handed transmission lines have been suggested in varied forms [5, 6]. In this paper, an symmetric unit cell model for composite right/left-handed transmissions lines metamaterials having left-handedness (LH), right-handedness (RH) and stop-bandedness is presented on the basis of the homogeneous CRLH-TL equivalent circuit model. The CRLH TL unit model is a meta-structured TL composed of a series capacitance and a shunt inductance as well as a series inductance and a shunt capacitance. The series capacitance and the shunt inductance provide the LH nature at lower frequencies, whereas the series inductance and the shunt capacitance provide the RH nature at higher frequencies, an unique characteristic of CRLH-TL. We can obtain $|S_{21}| = 1$ at a specified passband center frequency and also make a desired phase shift from $-150°$ to $50°$ over a unit cell possible at a specified frequency. The unit cell model for CRLH-TL is analyzed using S-parameter formulations resulting in some useful closed-form expressions for design purposes. These results provide some useful references in significantly facilitating the design of CRLH-TL for a given specification.

1. UNIT CELL MODELS FOR SYMMETRIC CRLH-TL

Figure 1 shows the symmetric CRLH-TL unit cell model. The total electrical length of the transmission line for CRLH is k_d. The characteristic impedance of the CRLH-TL is Z_O. The LH comes from the combination of the lumped series capacitor C_L and the shunt inductor L_L, whereas the RH comes from the combination of the series inductor L_R and the shunt capacitor C_R.

The input impedance Z_{in} at the reference plane t_1 is given by

$$Z_{in} = \frac{1}{j\omega C_L} + j\omega L_R + Z_O // \frac{1}{j\omega C_R} // j\omega L_L = \frac{1}{j\omega C_L} + j\omega L_R + \frac{j\omega Z_O L_L}{Z_O - \omega^2 L_L C_R Z_O + j\omega L_L} \quad (1)$$

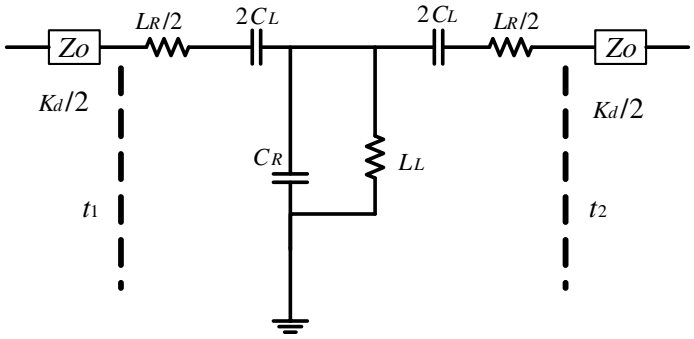

Figure 1: The CRLH-TL unit cell model.

The characteristic impedance of a CRLH-TL unit cell model is given by

$$Z_O = \sqrt{\frac{\omega L_R - \frac{1}{\omega C_L}}{\omega C_R - \frac{1}{\omega L_L}}} \tag{2}$$

Defined

$$Z = j\omega L_R - j\frac{1}{\omega C_L} \tag{3}$$

$$Y = \frac{1}{j\omega C_R} // j\omega L_L \tag{4}$$

the $[ABCD]$ matrix reads

$$\begin{bmatrix} A & B \\ C & D \end{bmatrix} = \begin{bmatrix} 1 & \frac{Z}{2} \\ 0 & 1 \end{bmatrix} \begin{bmatrix} 1 & 0 \\ Y & 1 \end{bmatrix} \begin{bmatrix} 1 & \frac{Z}{2} \\ 0 & 1 \end{bmatrix} = \begin{bmatrix} 1+\frac{Z}{2} & Z\left(1+\frac{ZY}{4}\right) \\ Y & 1+\frac{Z}{2} \end{bmatrix} \tag{5}$$

The input reflection coefficient

$$S_{11} = \frac{A + B/Z_O - CZ_O - 1}{A + B/Z_O + CZ_O + 1} \tag{6}$$

The transmission coefficient

$$S_{21} = S_{12} = \frac{2}{A + B/Z_O + CZ_O + 1}, \tag{7}$$

and the output reflection coefficient

$$S_{22} = \frac{-A + B/Z_O - CZ_O + 1}{A + B/Z_O + CZ_O + 1} \tag{8}$$

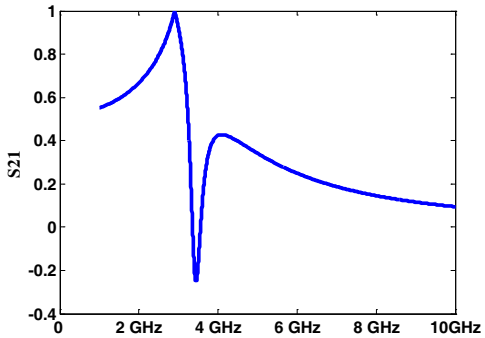

(a)

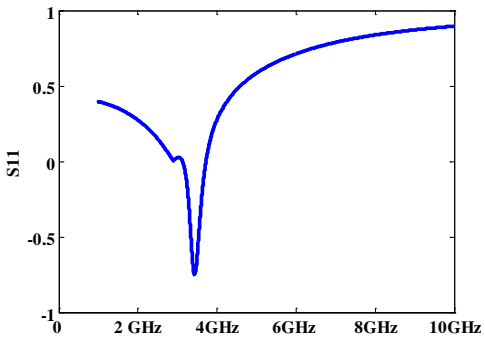

(b)

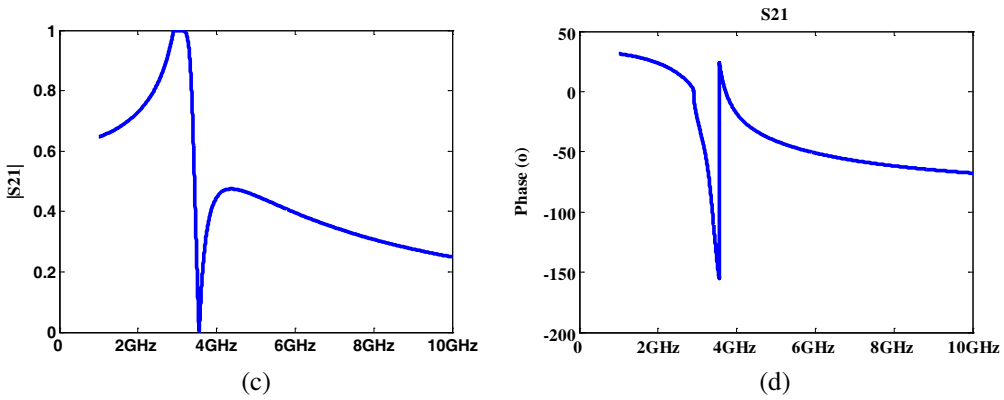

Figure 2.

2. RESULTS

The relationships between the frequencies f and S-parameters are shown in Fig. 2 for the proposed model with $L_R = 100\,\text{pH}$, $C_R = 100\,\text{pF}$, $L_L = 20\,\text{pH}$, $C_L = 30\,\text{pH}$ and $k_d = 0$, respcetively.

3. CONCLUSIONS

An symmetric unit cell model for composite right/left-handed transmissions lines metamaterials having left-handedness, right-handedness is presented based on the homogeneous CRLH-TL equivalent circuit model. The symmetrical unit cell models for CRLH-TL have been analyzed using S-parameter formulations resulting in some useful closed-form expressions for design purposes. The simple and essential expressions provided here facilitate the design of CRLH-TL.

ACKNOWLEDGMENT

This work was supported by the National Key Laboratory Foundation of China (No. 9140C5304020-804).

REFERENCES

1. Veselago, V. G., "The electrodynamics of substances with simultaneously negative values of ε and μ," *Sov. Phys.-Usp.*, Vol. 10, No. 4, 509–514, Jan.–Feb. 1968.
2. Shelby, R. A., D. R. Smith, and S. Schultz, "Experimental verification of a negative index of refraction," *Science*, Vol. 292, No. 5514, 77–79, 2001.
3. Lai, A., C. Caloz, and T. Itoh, "Composite right/left-handed transmission line metamaterials," *IEEE Microwave Magazine*, 34–50, 2004.
4. Caloz, C. and T. Itoh, *Electromagnetic Metamaterials, Transmission Line Theory and Microwave Applications*, Wiley, New York, 2005.
5. Caloz, C., A. Sanada, and T. Itoh, "A novel composite right-/left-handed coupled-line directional coupler with arbitrary coupling level and broad bandwidth," *IEEE Trans. Microwave Theory Tech.*, Vol. 52, No. 3, 980–992, Mar. 2004.
6. Kim, H.-M. and B. Lee, "Unit cell models for right/left-handed transmission lines (RLH-TL)," *APMC 2005*, 1–4, 2005.
7. Pozar, D. M., *Microwave Engineering*, John Wiley & Sons, New York, 2005.

Analysis and Simulation of Superresolution Image Restoration

Yi Zhang, **Quan Zhou**, **Minqi Li**, **and Wanzhao Cui**
National Key Laboratory of Space Microwave Technology
Xi'an Institute of Space Radio Technology, Xi'an 710100, China

Abstract— Superresolution image restoration reconstructs a frame of high-resolution (HR) image from low-resolution (LR) images. The resolution of the improved image is higher than any of the LR's. This kind of technique provides a novel method for obtaining HR image and reduces the cost, so it becomes one of the hotspots in the field of image processing, and has been widely used in the area of military affairs, weather, medicine and etc. Several aspects of superresolution restoration have been analyzed, and a frame of superresolution image has been reconstructed using a group of LR images in this paper.

1. INTRODUCTION

High-resolution images are obtained by two kinds of methods; one of these is improving capability of image-forming system, the other one is using super-resolution image restoration technology. Enlarging lens of the digital camera or reducing detector array area of the CCD is the usual way to enhancing performance of the image-forming system. The higher the image resolution is required the harder the first method is achieved, and the cost becomes higher. Obtaining high-resolution image by using super-resolution restoration technology becomes more and more popular in field of image processing. These were several restoration methods since 1980's, and obtaining high-resolution image by super-resolution restoration technology becomes one of the hotspots in the area of image processing.

The kind of novel technology was first presented by Harris [1] and Goodman since 1960's, but it didn't broadly used because the poor application effect. Super-resolution restoration developed rapidly until 1980's, so many approaches appeared, such as the projection onto convex sets (POCS) method [2] was suggested by H. Stark and P. Oskoui, maximum likelihood (ML) estimator by S. E. Meinel and maximum a posteriori probability estimator by B. R. Hunt and his co-workers. Iterated backprojection approach [3], improved POCS algorithm [4] and etc were contained in recent papers; the super-resolution reconstruction was more and more popular. POCS algorithm solves complicated imaging modal and makes full use of the information of the obtained images, so it is widely used and improved in the area of super-resolution restoration.

2. STATEMENT ON SUPER RESOLUTION RESTORATION

Super-resolution reconstruction is a technique for estimating one or more high-resolution images from a sequence of low-resolution images, and the same time eliminates the combating additive noise and blurring due to the finite detector size and optics. It's a branch of image fusion.

Super-resolution restoration contains methods in time and frequency domain. Approaches in frequency domain develops slowly for the disadvantages of it, such as it is limited to global translational motion, lacks relativity between the data in domain of frequency, difficult to take the information in time-domain to frequent-domain. The typical methods in time-domain are IBP algorithm, POCS approach and etc.

IBP method was presented by Michal Irani and Shmuel Peleg, in this approach super-resolution image is reconstructed by continuous simulations and updating the imaging modal, its process is described in Figure 1.

The simulation results aren't unique; the apriority knowledge can't be used in the restoration progress.

POCS algorithm was first proposed by H. Stark, P. Oskoui and their partners, and then Andrew J. Patti, M. Ibrahim and etc improved the original method and became one of the widely used algorithms. The simulation process is showed in Figure 2.

In this approach convex sets are defined according to the original images knowledge, the range of the estimated image is restricted by the sets. This reconstruction method makes full use of the information contained in the LR images; deals complex image degradation model. More and more researchers study and improve this method for its advantages.

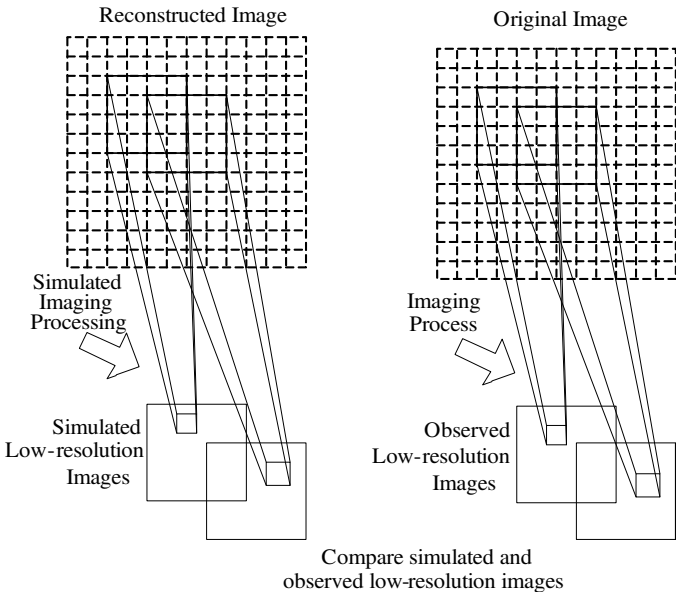

Figure 1: Schematic diagram of IBP algorithm.

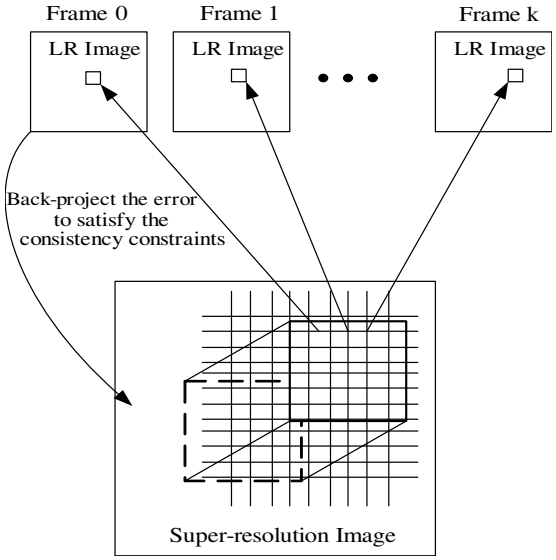

Figure 2: Reconstruction algorithm based on POCS method.

3. SOLUTION OF SUPER RESOLUTION RESTORATION

In order to analyzing super-resolution restoration, we researched the image resolution decrease procedure at first. According to reversing the decrease process, we can get the super-resolution restoration modal. The modal is showed in Figure 3.

Super-resolution reconstruction simulation process is introduced in this part. A sequence of LR images is obtained through high-resolution image degradation procedure at first. Then combining the POCS algorithm in [5] super-resolution image restoration is obtained by the LR images. The motion of the LR images is global translational motion; the sensor point spread function is Gaussian function; magnification times are four. The flow chart of super-resolution procedure is depicted in Figure 4.

The definite simulation steps are showed as follow:

Low-resolution images obtained through degradation are displayed in Figure 5.

Firstly, reference frame is selected among the LR image sequence. Secondly, SR grid is defined by the reference frame, and motion of the other images is estimated to it.

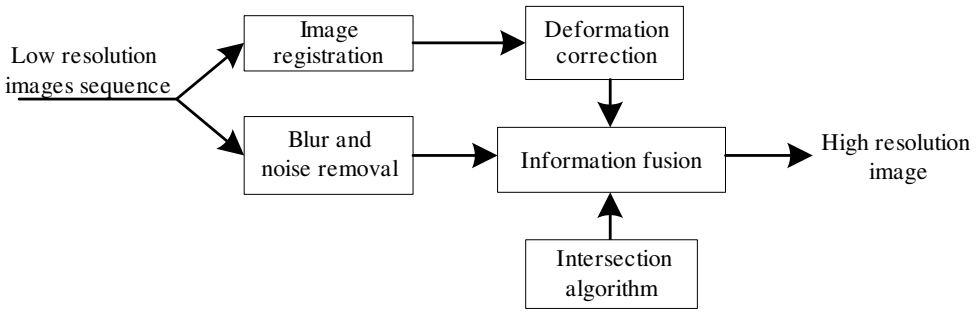

Figure 3: Schematic diagram of high-resolution image reconstruction system.

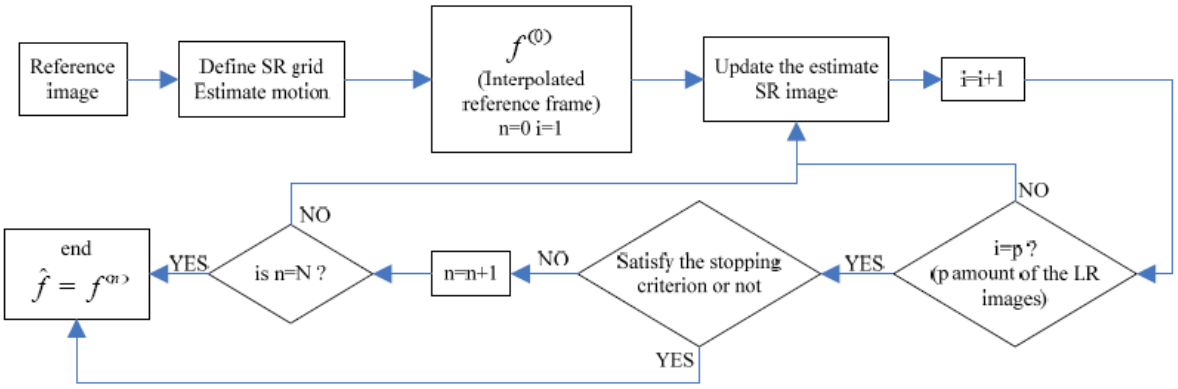

Figure 4: Flow chart of super resolution reconstruction.

Figure 5: Sequence of 8 synthetic low resolution images with controlled camera motion.

Interpolating the reference image and the enlargement factor is 4, the processed image is the initial estimate frame, and the interpolating image is given in Figure 7. Estimated image updating in Figure 4 can take the following sets (1∼3) into account.

Data consistency constrains sets:

$$C_i = \left\{ f : \delta_i^T f = y_i \right\}, \ 1 \le i \le M_1 M_2 \tag{1}$$

Image amplitude constrains set:

$$C_A = \{ f : \alpha \le f \le \beta, \ \alpha < \beta \} \tag{2}$$

If the estimated image is similar to one of the frame, then the set can be defined as (3).

$$C_R = \{ f : \| f - f_R \| \le \varepsilon_R \} \tag{3}$$

There are still more other constrains sets defined by the information of LR images.

According to measuring the changes between successive estimated images the intersections are terminated or not. If the changes can't satisfy the default value, the program will stop at the

maximum value of cycle index. The super-resolution image is the last estimated image of simulation; the result is displayed in Figure 8.

Compared with the low-resolution images and the original estimated super-resolution image the simulation result can identify the object clearly. Some of the words write on the right side of the super-resolution image are: "finer grid using interpolation, be obtained a single picture of higher spatial sampling rate."; The words in the original picture is: "finer grid using interpolation, he obtained a single *blurred* picture of higher spatial sampling rate." (the terms in italic type is not contained in the intercept image).

Figure 6: Reference frame.

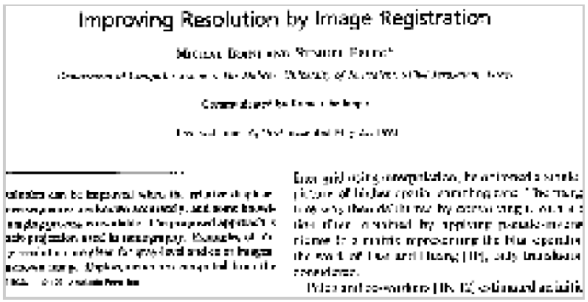

Figure 7: Initial estimate super-resolution image.

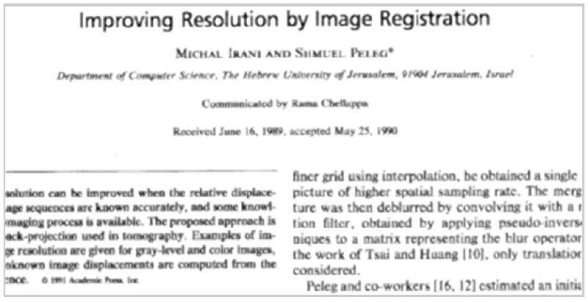

Figure 8: Super resolution image restoration result.

The simulation result is fault in single letters; it shows super-resolution restoration technique could improve the resolution of the processed LR images. This kind of approach can be used in target identification and expansion the range of super-resolution image.

4. CONCLUSION

In this paper, a sequence of low-resolution images was used to simulate super-resolution restoration technology, a frame of super-resolution image was reconstructed by the experiment. The resolution of the reconstructed image obviously improved, the targets in the super-resolution image were identified clearly.

With the development of super-resolution restoration technique this kind of technology provides novel method for obtaining high-resolution images. However, some problems exist in this technique still restrict the development of it. The development of reconstruction technology is on more exact image matching method, more practical image quality depress modal and improve original approaches with new technology in other area.

ACKNOWLEDGMENT

This work was supported by the National Key Laboratory Foundation of China (No. 9140C5305020-706).

REFERENCES

1. Harris, J. L., "Diffraction and resolving power [J]," *J. O. S. A.*, Vol. 54, No. 7, 931–936, 1964.
2. Stark, H. and P. Oskoui, "High-resolution image recovery from image-planear rays, using convex projections [J]," *J. O. S. A.*, Vol. 6, No. 11, 1715–1726, 1989.
3. Irani, M. and S. Peleg, "Improving resolution by image registration [J]," *CVGIP: Graph. Models Image Process*, Vol. 53, No. 3, 231–239, 1991.
4. Patti, A. J., M. I. Sezan, and A. M. Tekalp, "Superresolution video reconstruction with arbitrary sampling lattices and nonzero aperture time [J]," *IEEE Trans. IP*, Vol. 6, No. 8, 1064–1076, 1997.
5. Shah, N. R. and A. Zakhor, "Resolution enhancement of color video sequences [J]," *IEEE Trans. IP*, Vol. 8, No. 6, 879–885, 1999.
6. Xu, Q. and B. Tan, *Remote Sensing Image Fusion and Resolution Enhance Technology (the Front Page)*, Science Press, Beijing, 2007.

THz Rectangular Microstrip Patch Antenna on Multilayered Substrate for Advance Wireless Communication Systems

Aditi Sharma[1], **Vivek K. Dwivedi**[2], **and G. Singh**[1]

[1]Department of Electronics and Communication Engineering
Jaypee University of Information Technology, Solan 173 215, India
[2]Department of Electronics and Communication Engineering
Jaypee Institute of Information Technology University, Noida 201724, India

Abstract— In this paper, we have simulated a rectangular microstrip patch antenna using multilayered dielectric substrate materials at THz frequencies for advanced wireless communication systems. The 10 dB impedance bandwidth of the single-pin-shorted microstrip-line fed rectangular microstrip patch antenna on multilayered dielectric substrate is 33.67%. The electrical parameters of antenna depend on the structural parameters and feed positions. The simulation of this antenna has been performed by using CST Microwave Studio, which is a commercially available finite integral based electromagnetic simulator.

1. INTRODUCTION

Gigabit-data-rate for future wireless communication systems has opened the door to variety of applications demanding ultra-broad bandwidth. Among the applications that are already foreseen is the wireless extension of the next generation broadband access fiber-optic networks, which will support data rates tens of gigabits, and are expected to replace xDSL and cable-modem access network [1–4]. A multi-gigabit communication system could also be operated as wireless bridge between lower data rate WLANs/WPANs (wireless local area network/wireless personal area networks) and access network, and thus could enhance their interoperability by providing fixed multi-gigabit wireless access. Most of the present efforts towards higher data rates are aimed at enhancing the spectral efficiency of existing or currently developing microwave and millimeter wave wireless systems. However, the spectral bandwidth of such a system is limited, and they will not able to support data rates exceeding a few Gbps [4]. In communications several order of magnitude of increase in bandwidth as compared to current wireless technology is expected [1, 5]. Terahertz (THz) technique is considered as one of the method to solve this problem. Since it is commonly accepted that such high-data rates can not be achieved with IR systems, the THz range is a logical choice [1–10]. Using carrier frequencies above 300 GHz, oscillator and amplifier sources with ∼10% fractional bandwidths would enable very high data rate (> 10 GB/s) wireless communications with high security protection [3, 4]. THz band covers a wide rage, which is relatively free of spectrum users, offers many advantages for wireless communication and radar system such as broad bandwidth for high data rate information transmission, low transmission power (due to high antenna gain) and low probability of interference/interception (due to narrow antenna beam width) [1–8]. The microstrip antennas are most important component of several wireless communication applications with demand of multi-band and/or broadband frequency operation, high power gain and omnidirectional radiation patterns. The technology and propagation constants serve as boundary conditions for the determination of the required antenna gain to support ultra-broadband communication. They have the benefit of high data rate up to tens of Gbps, whereas in atmosphere the attenuation is very high. Therefore, the design of printed antennas suitable to meet the requirements of multiple operational services becomes a difficult task. The multi-band microstrip antennas have been developed in the past using multilayered substrate at lowered frequencies to obtain the multi-frequency operational characteristics [11–13].

In this paper, we have proposed a single-pin-shorted multilayered-dielectric (with different dielectric permittivity and thickness) substrate rectangular microstrip patch antenna at THz frequency for faster wireless communication systems. The design of this antenna is based on the philosophy of maximizing the current path for a given surface area to decrease the resonant frequency by shorting post [14] and use of multilayer substrate material to reduce the radiation losses by surface waves to enhance the efficiency [11–13]. The surface waves can be reduced by shorting post due to surface wave discontinuity used in the three dielectric layer structure. The organization of paper is as follows. The Section 2 concerns with the simulation model of THz microstrip antenna. The Section 3 discusses the simulated results and finally, Section 4 concludes the work.

2. SIMULATION MODEL OF THz MICROSTRIP ANTENNA

The proposed microstrip patch antenna consists of a rectangular patch on multilayer dielectric substrate materials with different dielectric permittivity and thickness. The geometrical configuration of the antenna is as shown in Fig. 1. The dimension of the ground plane and radiating rectangular patch of the antenna is $400 \times 400\,\mu m^2$ and $100 \times 150\,\mu m^2$, respectively. The substrate materials of the antenna are arranged as follows. The first substrate layer on ground plane is $50\,\mu m$ thick having $\varepsilon_1 = 2.42$ with $\tan\delta = 0.0009$. This layer is followed by $350\,\mu m$ thick substrate layer with $\varepsilon_2 = 2.2$ and last layer with $55\,\mu m$ thick having $\varepsilon_3 = 6.15$ with $\tan\delta = 0.0019$. The selection of the dielectric permittivity and dimension of the substrate will determine the surface wave losses. A thicker middle substrate layer has been used to achieve wide bandwidth [16]. The reason to take high dielectric constant (upper layer) is to reduce the radiation loss from the feed line and thin substrate material has been used for maximizing the bandwidth. The proper selection of the permittivity and dimensions of the substrate layers will reduce the surface wave loss and results in significant increase in impedance bandwidth and radiation efficiency. When the high relative permittivity substrate is over the low relative permittivity substrate, the suppression of the surface wave will takes place [15, 16]. The shorting post with a diameter of $5\,\mu m$ is loaded at the radiating end of rectangular patch. This loading position can ensure maximum reduction in the resonant frequency of the microstrip antenna that is maximum patch size reduction for the antenna can be obtained at a fixed frequency. Microstrip line feed has been used in the proposed antenna is one of the most commonly used feeding techniques. Since feeding technique influences the input impedance, it is often exploited for matching purpose. In this feeding technique, a conducting strip is connected directly to the edge of the rectangular patch microstrip antenna. The advantage of this technique is that both the feed and patch lie on the surface of the substrate and therefore is plane in construction and provide the right impedance match between the patch and feed line. The simulation of the proposed rectangular microstrip patch antenna is performed on CST Microwave Studio simulator, which is finite integral based solver.

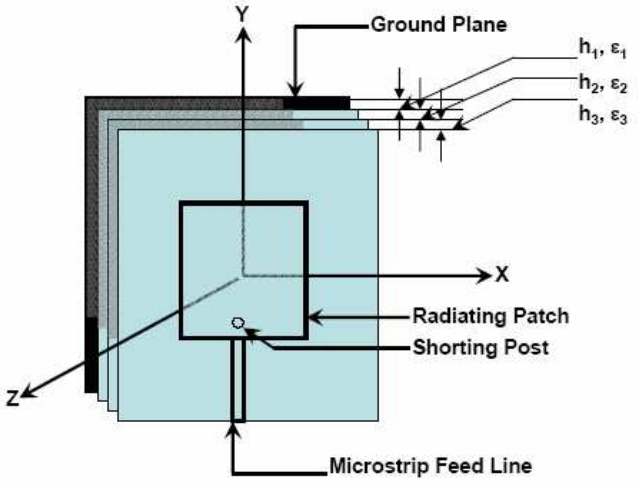

Figure 1: Geometrical configuration of the multilayer dielectric substrate single pin shorted microstrip line fed rectangular patch antenna.

3. SIMULATION RESULTS

The current and emerging systems use bandwidths between a few MHz to several GHz. Consequently, they cannot provide high enough data rates to satisfy the needs of the future wireless communication requirements. One can expect that wireless short-range communication networks will soon push towards the THz frequency range, which will provide several tens of Gb/sec to terabit data rates [1]. To compensate for the high free space losses one will need high gain emitter and receiver antennas. The return loss of the proposed rectangular microstrip patch antenna at the THz frequencies is shown in Fig. 2. The 10 dB bandwidth obtained from Fig. 2 is 33.67%. This simulated result shows two dip at which the return loss is minimum. This means, proposed antenna can operate efficiently at these two frequencies (796.95 and 916.65 GHz).

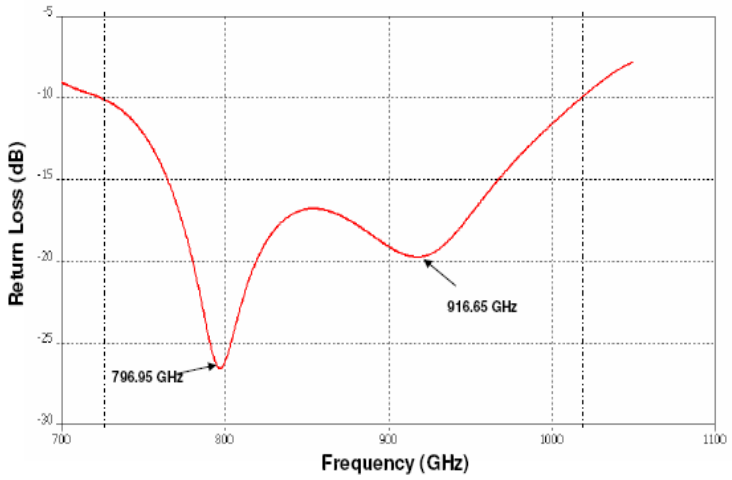

Figure 2: The return loss (dB) versus frequency (GHz) of the proposed rectangular microstrip patch antenna.

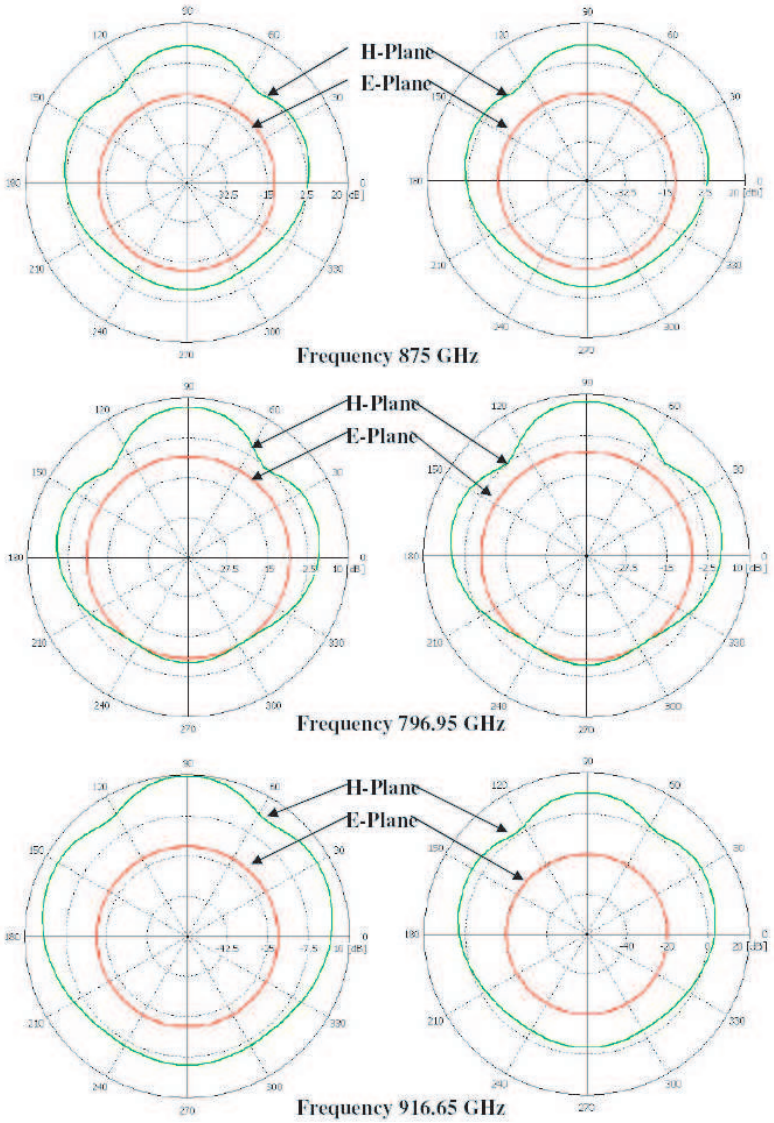

(a) (b)

Figure 3: Far-zone radiation patterns for (a) the gain and (b) directivity at the THz frequencies.

The far-zone radiation pattern of the gain (Fig. 3(a)) and directivity (Fig. 3(b)) of the proposed THz rectangular microstrip patch antenna is as shown in Fig. 3. The radiation efficiency and gain of the microstrip antenna are 90.69% and 10.05 dB, respectively at the center frequency of operation (875 GHz). At this frequency, the main lobe magnitude of gain is 10 dB with angular width 37.2° in H-plane configuration. The main lobe magnitude of the directivity and its angular width are 10.5 dBi and 37.2°, respectively in H-plane. The electrical parameters of the multilayer rectangular patch microstrip antenna at three THz frequencies are shown in Table 1.

Table 1: Electrical parameters of the rectangular microstrip patch antenna at THz frequencies.

Frequency/Electrical Parameters	875 GHz	796.95 GHz	916.65 GHz
Gain (dB)	10.05	7.291	9.708
Directivity (dBi)	10.47	7.928	10.45
Radiation Efficiency (%)	90.69	86.36	84.27

The radiation efficiency and gain of the microstrip antenna are 86.36% and 7.291 dB, respectively at frequency (796.95 GHz), which is first dip in Fig. 2. At this frequency the gain of main lobe magnitude is 7.3 dB and angular width is 90° in E-plane configuration. For directivity, the main lobe magnitude and angular width are 7.9 dBi and 90°, respectively in H-plane. The radiation efficiency and gain of the microstrip antenna are 84.27% and 9.708 dB, respectively at the frequency (916.65 GHz), which is second dip of Fig. 2. At this frequency for gain, the main lobe magnitude is 9.7 dB and angular width is 90° in H-plane configuration. For directivity, the main lobe magnitude and angular width are 10.5 dBi and 90°, respectively in H-plane.

The radiation efficiency and gain varies with distance of shorting post from the feed point as shown in Fig. 4. The radiation efficiency and gain of the rectangular microstrip patch antenna increases with increase in the distance of the shorting post from the feed point. The interesting point of simulation is highlighted in the Fig. 4. The radiation efficiency and gain at this point are 90.69% and 10.05 dB at 875 GHz, respectively. The distance of a shorting post from the feed point is 10 µm at this point. Here (at the marked point) the gain and efficiency are low as compare to other points but we get the dual frequency band of operation of the proposed antenna with broader bandwidth, that is the reason for considering this point.

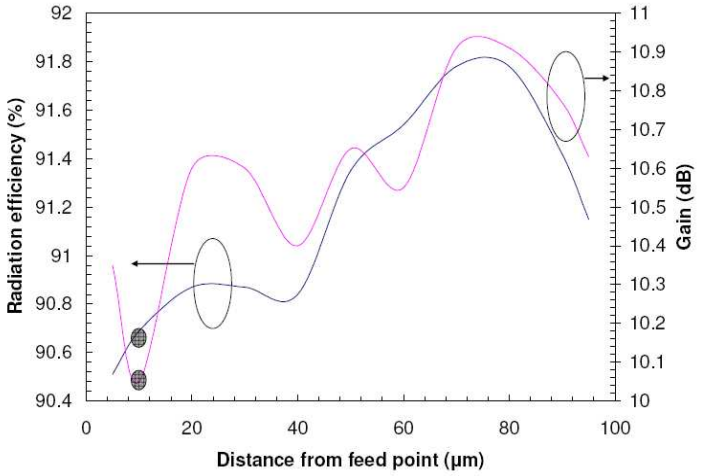

Figure 4: Variation of radiation efficiency and gain with distance of shorting post from the feed point.

4. CONCLUSIONS

Among the practical advantages of using THz region for satellite and indoor wireless communication system is the ability to employ robust and compact transmitting and receiving antennas. THz communication link is most likely secure communication for short-distance, point-to-point, and demanding high information data rate (Gb/s to Tb/s). The 10 dB impedance bandwidth of the

proposed antenna is 33.67%. The radiation efficiency and gain of the antenna are 90.69% and 10.05 dB at 875 GHz, respectively. Increased atmospheric absorption at the THz frequencies is unattractive in certain applications but the secure and ultrahigh bandwidth make attractive THz communication systems.

ACKNOWLEDGMENT

Authors are sincerely thankful to the Professor Dr. D. S. Chauhan (Vice-Chancellor, JUIT) for critical discussion and suggestions.

REFERENCES

1. Piesiewiez, R., T. Kleine-Ostmann, N. Krumbholz, D. Mittleman, M. Koch, J. Aschoebel, and T. Kürner, "Short-range ultra-broadband terahertz communications: Concepts and prospective," *IEEE Antenna and Prop. Magazine*, Vol. 49, No. 6, 24–39, 2007.
2. Zeadally, S. and L. Zhang, "Enabling gigabit network access to end users," *Proc. IEEE*, Vol. 92, No. 2, 340–353, 2004.
3. Driessen, P. F., "Gigabit/s indoor wireless systems with directional antennas," *IEEE Trans. Commun.*, Vol. 44, No. 8, 1034–1043, 1996.
4. Piesiewicz, R., J. Jemai, M. Koch, and T. Kürner, "THz channel characterization for future wireless gigabit indoor communication systems," *Proc. SPIE*, Vol. 5727, 166–176, 2005.
5. Woolard, D. L., E. R. Brown, M. Pepper, and M. Kemp, "Terahertz frequency sensing and imaging: A time domain of reckoning future applications?," *Proc. IEEE*, Vol. 93, No. 10, 1722–1743, 2005.
6. Mueller, E. and A. J. DeMaria, "Broad bandwidth communication/data links using terahertz sources and Schottky diode modulators/detectors," *Proc. SPIE*, Vol. 5727, 151–165, 2005.
7. Piesiewiez, R., T. Kleine-Ostmann, N. Krumbholz, D. Mittleman, M. Koch, J. Aschoebel, and T. Kürner, "Terahertz characteristics of building materials," *Electron. Lett.*, Vol. 41, No. 18, 1002–1004, Sept. 2005.
8. Sharma, A., V. K. Dwivedi, and G. Singh, "THz rectangular patch microstrip antenna design using photonic crystal as substrate," *PIERS Proceedings*, 161–165, Cambridge, USA, Jul. 2–6, 2008.
9. Lubecke, V., K. Mizuno, and G. Rebeiz, "Micromachining for THz applications," *IEEE Trans. Microwave Theory Tech.*, Vol. 46, No. 11, 1821–1831, 1998.
10. Kazemi, H., S. T. Wooton, N. J. Cronin, S. R. Davies, R. E. Miles, R. D. Pollard, J. M. Chamberlain, D. P. Steension, and J. W. Bowen, "Active micromachined integrated terahertz circuits," *Int. J. Infrared and Millimeter Waves*, Vol. 20, No. 5, 967–974, 1999.
11. Harokopus, W. P. and P. B. Katehi, "Characterization of microstrip discontinuities on multilayer dielectric substrate including radiation loss," *IEEE Trans. Microwave Theory Tech.*, Vol. 37, 2058–2066, 1989.
12. Tsai, M. J., F. D. Flaviis, O. Fordham, and N. G. Alexopoulos, "Modeling planar arbitrarily shaped microstrip elements in multilayered media," *IEEE Trans. Microwave Theory Tech.*, Vol. 45, 330–337, 1997.
13. Sharma, A. and G. Singh, "Design of single pin shorted three dielectric layered substrate rectangular patch microstrip antenna communication systems," *Progress In Electromagnetics Research Lett.*, Vol. 2, 157–165, 2008.
14. Waterhouse, R. B., S. D. Targonski, and D. M. Kokoto, "Design and performance of small printed antennas," *IEEE Trans. Ant. Prop.*, Vol. 46, 1629–1633, 1998.

Theoretically and Experimentally Investigation of Sparking of Metal Objects inside a Microwave Oven

Gholamreza Shayeganrad[1] **and Leila Mashhadi**[2]

[1]Islamic Azad University, Karaj Branch, Karaj, Iran
[2]Physics Department, Amirkabir University of Technology
P. O. Box: 15875-61390, Tehran, Iran

Abstract— Over the past years, some microwave oven experiments have been done by placing non-food objects such as metal objects, CDs, lightbulbs and etc. in the microwave oven cavity [1–4]. It is well understood, when a metal object is placed inside the oven cavity, sparking will result. Here, we have theoretically investigated the sparking of metal objects within the microwave oven, based on the electrostatic and alternating field. The resonant modes characteristics of both TE and TM electromagnetic fields in the oven cavity are determined. An approximate analysis for electric fields around the metal disks and sharp edges is carried out by solving Laplace equation in polar and elliptical coordinates. Some experiments are done for CD-ROMs and several types of metallic rings and wires. They have shown a good agreement with the theoretical predictions.

1. INTRODUCTION

A microwave oven is consist a conducting cavity resonator connected to a magnetron which emits non-ionization electromagnetic radiation, usually at a frequency of 2.45 GHz, or wavelength of 12.24 cm. The cooking cavity itself is a Faraday cage enclosure which prevents the microwaves from escaping into the environment. The oven door is usually a glass panel for easy viewing, but has a layer of conductive mesh which generally makes from aluminum and separated with 1–2 mm distance to maintain the shielding. Because the size of the perforations in the mesh is much less than the microwave wavelength, most of the microwave radiation cannot pass through the door, while visible light with a much shorter wavelength can [5, 6].

We have considered oven cavity as a volume enclosed by a conducting surface and within which an electromagnetic field can be excited. The electric and magnetic energies are stored in the volume of the cavity. The finite conductivity of walls gives rise to power loss and thus is equivalent to some effective resistance. Any metal or conductive object placed into the microwave will act as an antenna to some degree, resulting in an electric current. This causes the object to act as a heating element. This effect varies with the object's shape and the composition.

Over the past years, some microwave oven experiments have been done by placing non-food objects such as metal objects, CDs, lightbulbs and etc. in the microwave oven cavity [1–4]. It is well understood, when a metal object is placed inside the oven cavity, arcing will result. However, to our knowledge, there is no any exact analytical investigation to introduce this phenomenon.

Here, we have analytically introduced the physics of sparking of some non-food objects, such as CDs, metal rings and metal disks, within a microwave oven cavity. We have derived approximate experssions for electric fields around the metal disks and sharp edges by solving Laplace equation in polar and elliptical coordinates. Since the time lag of spark is very short, we have ignored of heat transfer to the space of cavity. Also, we have neglected from varying of electromagnetic fields in which caused by metals after inserting inside the oven cavity.

Finally, some experiments is made with CDs and some special shapes and types of metals within a compact Panasonic microwave oven NN-C2003S consists of a cooking chamber with dimensions of $(W \times H \times D)$ 412 mm×242 mm×426 mm and a magnetron of 1220 W output power. Experimental results show a good agreement with the obtained theoretical results in this work.

2. CHARACTERISTICS OF RESONANT MODES INSIDE THE OVEN CAVITY

Figure 1 illustrates a cavity of height b, width a, and length d. We have assumed a linear, isotropic, homogeneous, lossless interior medium with neglecting the charge and current inside the cavity. For this case, Maxwell's equations can be simplified to:

$$\nabla^2 \vec{E} + \omega^2 \varepsilon \mu \vec{E} = 0 \tag{1}$$

$$\nabla^2 \vec{H} + \omega^2 \varepsilon \mu \vec{H} = 0 \tag{2}$$

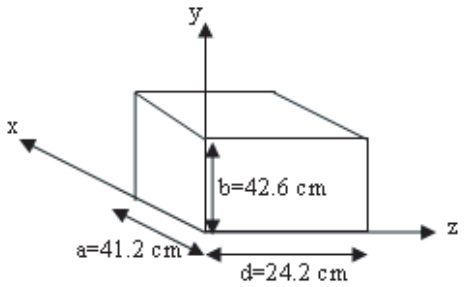

Figure 1: Cavity resonator of a microwave oven.

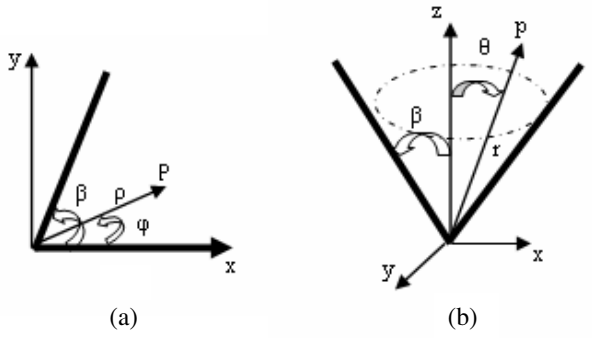

Figure 2: A corner in two dimensions with opening angle β (a), and a corner in three dimensions with opening angle β surrounded between two conducting plates (b).

These equations are called wave equations or Helmholtz equations. Each equation is composed of three scalar differential equations terms of the components of the vectors. By solving these equations, the components of TE and TM mode inside the cavity which fit the boundary conditions can be easily found. For TE_{mnp} modes [7]:

$$E_x = \frac{i\omega\mu}{\gamma^2}\frac{n\pi}{b}H_{mnp}\cos\left(\frac{m\pi x}{a}\right)\sin\left(\frac{n\pi y}{b}\right)\sin\left(\frac{p\pi z}{d}\right) \tag{3a}$$

$$E_y = \frac{-i\omega\mu}{\gamma^2}\frac{m\pi}{a}H_{mnp}\sin\left(\frac{m\pi x}{a}\right)\cos\left(\frac{n\pi y}{b}\right)\sin\left(\frac{p\pi z}{d}\right) \tag{3b}$$

$$E_z = 0 \tag{3c}$$

$$H_x = \frac{H_{mnp}}{\gamma^2}\frac{m\pi}{a}\frac{p\pi}{d}\sin\left(\frac{m\pi x}{a}\right)\cos\left(\frac{n\pi y}{b}\right)\cos\left(\frac{p\pi z}{d}\right) \tag{3d}$$

$$H_y = \frac{H_{mnp}}{\gamma^2}\frac{n\pi}{b}\frac{p\pi}{d}\cos\left(\frac{m\pi x}{a}\right)\sin\left(\frac{n\pi y}{b}\right)\cos\left(\frac{p\pi z}{d}\right) \tag{3e}$$

$$H_z = H_{mnp}\cos\left(\frac{m\pi x}{a}\right)\cos\left(\frac{n\pi y}{b}\right)\sin\left(\frac{p\pi z}{d}\right) \tag{3f}$$

and for TM_{mnp} modes [7]:

$$E_x = \frac{-E_{mnp}}{\gamma^2}\frac{m\pi}{a}\frac{p\pi}{d}\cos\left(\frac{m\pi x}{a}\right)\sin\left(\frac{n\pi y}{b}\right)\sin\left(\frac{p\pi z}{d}\right) \tag{4a}$$

$$E_y = \frac{-E_{mnp}}{\gamma^2}\frac{n\pi}{b}\frac{p\pi}{d}\sin\left(\frac{m\pi x}{a}\right)\cos\left(\frac{n\pi y}{b}\right)\sin\left(\frac{p\pi z}{d}\right) \tag{4b}$$

$$E_z = E_{mnp}\sin\left(\frac{m\pi x}{a}\right)\sin\left(\frac{n\pi y}{b}\right)\cos\left(\frac{p\pi z}{d}\right) \tag{4c}$$

$$H_x = \frac{i\omega\varepsilon}{\gamma^2}\frac{n\pi}{b}E_{mnp}\sin\left(\frac{m\pi x}{a}\right)\cos\left(\frac{n\pi y}{b}\right)\cos\left(\frac{p\pi z}{d}\right) \tag{4d}$$

$$H_y = \frac{-i\omega\varepsilon}{\gamma^2}\frac{m\pi}{a}E_{mnp}\cos\left(\frac{m\pi x}{a}\right)\sin\left(\frac{n\pi y}{b}\right)\cos\left(\frac{p\pi z}{d}\right) \tag{4e}$$

$$H_z = 0 \tag{4f}$$

In the above relations, for simplicity, $e^{j\omega t}$ is omitted. H_{mnp} and E_{mnp} are constant coefficients associated with the mnpth mode where m, n, and p are integer, often termed the order, and

$$\gamma^2 = \frac{m^2\pi^2}{a^2} + \frac{n^2\pi^2}{b^2} \tag{5}$$

For the mnpth mode the corresponding resonant frequency is given by:

$$\omega_{mnp} = c\pi\sqrt{\left(\frac{m}{a}\right)^2 + \left(\frac{n}{b}\right)^2 + \left(\frac{p}{d}\right)^2} \tag{6}$$

where $c = 3 \times 10^8$ m/s is the speed of light. They are analogous to the natural frequencies in other oscillation problems, for example, those of a plucked string or a vibrating drumhead.

The electric and magnetic energies are stored in the volume of the cavity. At resonance the time-averaged electric and magnetic energy stored in the cavity are equal. Using Eqs. (3) and (4), the time-average total electromagnetic energy stored in the oven cavity is given by:

$$W_{\mathrm{TE}} = \frac{\mu}{2}\frac{abd}{8}\left[1 + \frac{p^2\pi^2}{\gamma^2 d^2}\right] H_{mnp}^2 \tag{7a}$$

$$W_{\mathrm{TM}} = \frac{\varepsilon}{2}\frac{abd}{8}\left[1 + \frac{p^2\pi^2}{\gamma^2 d^2}\right] E_{mnp}^2 \tag{7b}$$

In the real cavities, the finite conductivity of walls give rise to power loss and thus are equivalent to some effective resistance. Therefore, the oscillation will damp gradually because of heating loss in the walls. The rapidity of this damping is characterized by a figure of merit called quality factor, Q. The quality factor is defined by

$$Q = \frac{\omega_0 W}{P_{loss}} \tag{8}$$

where W is time-averaged energy stored in the cavity and P_{loss} is energy losses per second in the walls. Q is also a measure of the sharpness of resonance and is given by

$$\frac{1}{Q} = \frac{\Delta\omega}{\omega_0} = \frac{\omega_0 \Delta\lambda}{2\pi c} \tag{9}$$

where ω_0 is the resonant frequency of the cavity and $\Delta\omega$ is the full width at half maximum (FWHM). Therefore, frequency selectivity and resonant modes in the oven cavity can be specified by cavity Q-factor.

In order to determine the cavity Q, the losses caused by the finite conductivity of the cavity walls must be evaluated. For small losses, the surface currents is given by $\vec{J}_s = \hat{n} \times \vec{H}$, where n is a unit normal to the surface and directed into the cavity. Hence the power loss in the walls is given by:

$$P_{loss} = \frac{R_m}{2}\int_{Walls} \vec{J}_s \cdot \vec{J}_s^* ds = \frac{R_m}{2}\int_{Walls} |H_{\tan}|^2 \, ds \tag{10}$$

where $R_m = 1/\sigma\delta$ is the resistive part of the surface impedance exhibited by the conductivity walls having a conductivity σ and for which the skin depth (or depth of penetration) is $\delta = (2/\omega\mu\sigma)^{1/2}$. In Eq. (10) $\vec{H}_{\tan}$ is the tangential magnetic field at the surface of the cavity walls which is essentially associated with the loss-free field solutions (3) and (4).

Depth of penetration is dependent on the metal composition and the frequency, with lower microwave frequencies penetrating better. For good conductors, the skin depth becomes extremely small as the frequency is increased and R_m will be increased. Typically, for aluminum walls with $\sigma = 3.64 \times 10^7/\Omega\mathrm{m}$, skin depth is about 1.6 µm at frequency of $\omega = 2\pi \times 2.45$ GHz and surface resistance $R_m = 58\,\Omega$. Therefore, the electromagnetic waves, and hence the induced currents to the surface of the conductor, are then effectively confined to a thin skin near the surface in order of magnitude of skin depth δ.

Substitution (3) and (4) into (10), the power losses for both TE and TM modes is obtained as:

$$P_{loss}^{\mathrm{TE}} = \frac{R_m}{4}\left[\frac{p^2\pi^2}{d\gamma^4}\left(\frac{m^2\pi^2}{a} + \frac{n^2\pi^2}{b}\right) + d\,(a+b) + \frac{p^2\pi^2}{d^2\gamma^2}ab\right] H_{mnp}^2 \tag{11a}$$

$$P_{loss}^{\mathrm{TM}} = \frac{\varepsilon}{\mu}\frac{R_m}{4}\left(\frac{p^2\pi^2}{d^2\gamma^2} + 1\right)\left[\frac{d}{\gamma^2}\left(\frac{m^2\pi^2}{a^2}b + \frac{n^2\pi^2}{b^2}a\right) + ab\right] E_{mnp}^2 \tag{11b}$$

Combining Eqs. (7), (8) and (11), the cavity Q for both TE and TM is approximately given by:

$$Q_{\mathrm{TE}} \approx \frac{3V}{S\delta} \tag{12a}$$

$$Q_{\mathrm{TM}} \approx \frac{V}{S\delta} \tag{12b}$$

where $V = abd$ is the volume of cavity, $S = 2(ab + ad + db)$ is the total interior surface area of cavity and δ is the skin depth of the walls. Typically, for the cavity with $a = 41.2\,\mathrm{cm}$, $b = 24.2\,\mathrm{cm}$, $d = 42.6\,\mathrm{cm}$ and aluminum walls, the Q_{TE} and Q_{TM} come out equal to $\sim 3 \times 10^4$ and 10^4, respectively. Substitution these values into (9), resonant half-width of wavelength for both TE and TM is obtained as:

$$\Delta\lambda_{\mathrm{TE}} \approx 0.4 \times 10^{-3}\ \mathrm{cm} \tag{13a}$$

$$\Delta\lambda_{\mathrm{TM}} \approx 10^{-3}\ \mathrm{cm} \tag{13b}$$

It can be seen that losses in the oven cavity causes a resonant bandwidth of $\Delta\lambda$ and it increases by increasing power losses in the cavity. It is noticeable that we have neglected from the dielectric losses inside the oven cavity and thus actual bandwidth may be greater than obtained values in Eq. (13).

Now, we can determine the resonant modes within the cavity by using Eqs. (6) and (13). Solutions for both TE and TM modes are summarized in Table 1.

Table 1: Several resonant modes inside microwave oven with dimension of $41.2 \times 24.2 \times 42.6\,\mathrm{cm}^3$.

m	**n**	**p**	**wavelength (cm)**
2	3	2	12.27
3	3	2	11.09
3	2	2	12.27
4	0	2	11.52
0	4	2	11.50
1	4	2	11.30
1	5	0	11.37

H_{mnp} and E_{mnp} in Eqs. (3) and (4) can be determined using Eq. (11) and considering the order of resonance modes in the cavity listed in Table 1. At threshold, the power of magnetron should be equal to power loss in the cavity surface, i.e., $P_{loss} = 1220\,\mathrm{W}$. Typically, considering $m = 3$, $n = 2$ and $p = 2$, the constant coefficients are found to be:

$$H_{322} \approx 700\ \mathrm{A/m} \tag{14a}$$

$$E_{322} \approx 2 \times 10^5\ \mathrm{V/m} \tag{14b}$$

Substitution (14a) and (14b) into (3) and (4), the electric field components of resonant modes are determined as:

$$E_x^{\mathrm{TE}} = \frac{\omega\mu}{\gamma^2}\frac{n\pi}{b}H_{322} \approx 4.6 \times 10^5\ \mathrm{V/m} \tag{15a}$$

$$E_y^{\mathrm{TE}} = \frac{\omega\mu}{\gamma^2}\frac{m\pi}{a}H_{322} \approx 12.3 \times 10^5\ \mathrm{V/m} \tag{15b}$$

$$E_x^{\mathrm{TM}} = \frac{(m\pi/a)\,(p\pi/d)}{\gamma^2}E_{322} \approx 5.3 \times 10^5\ \mathrm{V/m} \tag{15c}$$

$$E_y^{\mathrm{TM}} = \frac{(n\pi/b)\,(p\pi/d)}{\gamma^2}E_{322} \approx 2 \times 10^5\ \mathrm{V/m} \tag{15d}$$

$$E_z^{\mathrm{TM}} = E_{322} \approx 2 \times 10^5\ \mathrm{V/m} \tag{15e}$$

3. ELECTROSTATIC APPROXIMATION

According to the Drude's model, the electrical conductivity of a metal is given by [6]:

$$\sigma = \frac{f_0 N e^2}{m(\gamma_0 - i\omega)} \tag{16}$$

where $f_0 N$ is number of free electrons per unit volume in the metal and γ_0/f_0 denotes damping constant that can be determined empirically from experimental which is typically of the order of 10^{17} sec^{-1}. This means that, for frequencies beyond the microwave region ($\omega \leq 10^{11}\,\mathrm{s}^{-1}$), ω in the dominator of the Eq. (16) is negligible and σ is approximated by:

$$\sigma = \frac{f_0 N e^2}{m\gamma_0} \tag{17}$$

It indicates that conductivities of metals are essentially real and independent to frequency in microwave region. In the other word, electrostatic approximation is reasonable for conductors at microwave frequency. Hence, we have assumed the metal within the oven cavity is subjected into the electrostatic field.

The prior works have shown that probability of occurring spark in the vicinity of sharp points or edges of metals is much higher than other points. To investigate this phenomenon, for simplicity, we have obtained the electric field around a metal disk and a corner.

3.1. Spark around a Metal Sharp Point

Figure 2 shows a two and a three dimensional corner. Since the dimensions of sharp points and corners are too small compared to the microwave wavelength, therefore we can consider electric field uniformly in the vicinity of the sharp points and corners.

The electric field components around a two dimensional corner, Fig. 1(a), is obtained by solving Laplace equation in cylindrical coordinate system [6]:

$$E_\rho \approx \frac{-\pi A}{\beta}\rho^{\frac{\pi}{\beta}-1}\sin\frac{\pi\varphi}{\beta} \tag{18a}$$

$$E_\varphi \approx \frac{-\pi A}{\beta}\rho^{\frac{\pi}{\beta}-1}\cos\frac{\pi\varphi}{\beta} \tag{18b}$$

where A is a constant coefficient, ρ is distance from corner and β is the angle of corner which $\beta \to 2\pi$ for sharp corners. It can be seen by considering A equals to values determined in Eq. (15) and $\beta \to 2\pi$, electric filed around the corners, $\rho \to 0$, is sufficiently too large approximately equal to the dielectric strength of air ($3 \times 10^6\,\mathrm{V/m}$).

Similarly, the electric field components around the three dimensional corners can be obtained by solving Laplace equation in spherical coordinate system and standard calculus technique as [6]:

$$E_r \approx -\nu A' r^{\nu-1} P_\nu(\cos\theta) \tag{19a}$$

$$E_\theta \approx A' r^{\nu-1}\sin\theta\frac{\partial}{\partial\theta}P_\nu(\cos\theta) \tag{19b}$$

where $P_\nu(\cos\theta)$ is Logender function and A' is a constant coefficient. For sharp corners $\beta \to 2\pi$, therefore, $\nu \approx [2\ln(2/(\beta-\pi))]^{-1} < 0$ and by considering A' equals to values determined in Eq. (15), electric field around the corners, $r \to 0$, is too large approximately equal to the dielectric strength of air. Dielectric strength is the maximum electric-field magnitude that a material can withstand without the occurrence of breakdown. This quantity is affected significantly by temperature, trace impurities and others that are difficult to control.

3.2. Spark around a Metal Disk

We have assumed a metallic disk with radius a, is placed in xy-surface inside the uniform electric field $\vec{E} = E_0\hat{x}$. By solving Laplace equation in the elliptical coordinate system, the electric-potential around the metal disk can be derived as below:

$$\phi = \frac{-2aE_0}{\pi}\left[\tanh(u) + \cosh(u)\tan^{-1}(\sinh(u))\right]\cos(v)\cos(\varphi) \tag{20}$$

In order to evaluate the results, we have derived components of electric-field in the cylindrical coordinate system as:

$$E_\rho = \frac{2E_0}{\pi}\left[\frac{\left(\cosh^2(u)+\cos^2(v)\right)\sinh(u)}{\left(\cosh^2(u)-\cos^2(v)\right)\cosh^2(u)}+\tan^{-1}\left(\sinh(u)\right)\right]\cos\varphi \tag{21a}$$

$$E_\varphi = \frac{-2E_0}{\pi}\left[\frac{\sinh(u)}{\cosh^2(u)}+\tan^{-1}\left(\sinh(u)\right)\right]\sin\varphi \tag{21b}$$

$$E_z = \frac{2E_0}{\pi}\left[\frac{\sin(2v)\cos\varphi}{\cosh(u)\left(\cosh^2(u)-\cos^2(v)\right)}\right] \tag{21c}$$

where v, u and φ are components of elliptical coordinate which are related with the components of cylindrical coordinate as below:

$$\varphi=\varphi,\ z=a\sinh(u)\cos(v),\ \rho=a\cosh(u)\cos(v) \text{ where } 0\le u<\infty \text{ and } -\pi/2\le v\le\pi/2.$$

The charge density induced on the metal disk surface inside the electric field $\vec{E}$ is given by:

$$\sigma=\varepsilon_0 E_z\,|_{z=0} = \frac{4\varepsilon_0 E_0}{\pi}\frac{\rho}{\sqrt{a^2-\rho^2}}\cos\varphi \tag{22}$$

It can be seen that charge density at $\varphi=0$ and $\varphi=\pi$ and near edge of the disk, $\rho\to a$, is maximum.

According to Eq. (21), electric-field magnitude in some points around the edges of metal disk are calculated and summarized in Table 2. Substituting the calculated magnitude for E_0 ($\sim 10^5$ V/m) into the Eq. (21), we find that electric-field in the vicinity of the metal disk is higher than air strength for both TE and TM modes.

It is noticeable that the most charge density is distributed near the edge of the metal disk. Hence we can use this results for a metal ring with radius a, which is placed in xy-surface inside the uniform electric field $\vec{E}=E_0\hat{x}$.

Table 2: Electric-field for some points around a metal disk.

E	**z**	$\boldsymbol{\varphi}$	$\boldsymbol{\rho}$
239.64 E_0	0	0, π	$a+\frac{1}{10000}a$
0.0006 E_0	$\frac{1}{10000}a$	$\frac{\pi}{2}, \frac{3\pi}{2}$	$\frac{a}{2}$
319.46 E_0	$\frac{1}{100000}a$	0	a

4. ALTERNATING FIELD APPROXIMATION

4.1. A Metal Disk in an Alternative Field

Since the surface-charge-density is deposited at $\varphi=0$ and $\varphi=\pi$ in near edge of the disk, here, we have approximated a metal disk with radius a placed in the xy-surface to a square with length a. Therefore, according to Eq. (22), the charge on two parallel sides at a half period, $\tau/2=2.0\times10^{-10}$ s, is obtained as:

$$q=\frac{4\varepsilon_0 E_0}{\pi}\int_0^{\frac{\pi}{2}}\cos(\varphi)d\varphi\int_0^a d\rho\frac{\rho^2}{\sqrt{a^2-\rho^2}}=\varepsilon_0 E_0 a^2 \tag{23}$$

and the current density is approximately given by:

$$I=\frac{dq}{dt}\approx\frac{q}{\tau/2}=\frac{2\varepsilon_0 E_0 a^2}{\tau} \tag{24}$$

The current is sufficiently confined to a thin skin of order of magnitude penetration depth δ near the surface. Then, resistance of the metal disk can be determined as:

$$R\approx\frac{a}{(a\delta)\sigma}=\frac{1}{\sigma\delta} \tag{25}$$

where σ is the metal conductivity.

Power loss in the metal disk is introduced as:

$$P = I^2 R \approx \frac{1}{\sigma\delta\pi^2}\varepsilon_0^2 E_0^2 a^4 \omega^2 \tag{26}$$

Typically, for an aluminum disk with radius $a = 5\,\text{cm}$ and using values determined in Eq. (15), lost power for both TE and TM modes by the disk is obtained as:

$$P_{\text{TE}} \approx 41.9\,\text{J/s} \tag{27a}$$
$$P_{\text{TM}} \approx 15.3\,\text{J/s} \tag{27b}$$

Therefore, rate of increasing temperature of the aluminum disk, neglecting the heat transfer to the surrounding by convection and radiation because of the short time lag of breakdown, is given by:

$$\dot{\theta}_{\text{TE}} = \frac{P_{\text{TE}}}{mC} \approx 3997.7\,^\circ\text{C/s} \tag{28a}$$
$$\dot{\theta}_{\text{TM}} = \frac{P_{\text{TM}}}{mC} \approx 1429.8\,^\circ\text{C/s} \tag{28b}$$

where $m = \rho a^2 \delta = 0.0012\,\text{g}$ is mass of the surface layer of aluminum disk with δ thickness equal to skin depth and density of ρ.

Table 3: Some properties of several good conductors. ρ is volume density, c_p is specific heat at constant pressure, T_m is melting temperature, T_v is vaporization temperature.

metal	$\boldsymbol{\rho}$ **(g/cm^3)**	$\mathbf{c_p}$ **(J/g·K)**	$\mathbf{T_m}$ **(°C)**	$\mathbf{T_v}$ **(°C)**	$\boldsymbol{\sigma}$ **(Ω·m)$^{-1}$**
Al	2.70	0.90	660	2450	3.64×10^7
Ag	10.52	0.23	960.80	2212	6.17×10^7
Au	19.3	0.13	1063.00	2966	6.29×10^7
Cu	8.96	0.39	1083	2590	5.92×10^7
Fe	7.87	0.46	1537	2735	1.03×10^7
Sn	7.30	0.23	232	2270	3.25×10^7

It can be seen from Eq. (24) and Table 3, the change temperature of a thin disk with thickness of δ for both TE and TM modes are about melting and vaporization temperature of the metal. Therefore, a few second after inserting a thin thickness of metal inside an oven cavity, temperature of several points of its surface increases up to melting and vaporization point and therefore tracks are appeared on the surface at these points. Field within the tracks is increased dependently to the track width, smaller track width greater track field. Generally, when a track is making, its width is about micron. According to the Eq. (15), electric field in the track is increases up to dielectric strength of the air and therefore at this point arc is appeared.

In fact, both TE and TM modes are sufficiently affected to occurring spark in the metal surface. With neglecting heat transfer to the surrounding space before occurring spark, power loss in the thin surface layer causes a sufficiently increasing temperature.

4.2. A Metal Ring in an Alternative Field

Now, we consider a metal ring with radius a, which is placed in xy-plane in the presence of an alternative field. Free electrons in the ring are moved and therefore alternative current will induce. This current may be causing a sufficiently joule heat and therefore temperature of the ring at several points will be increased up to melting or vaporization point of the metal. Hence, at these points tracks are appeared along the ring. Field within the tracks is increased dependently to the track width, smaller track width greater track field.

Analogues circuit of this phenomenon is shown in Fig. 3. For a metal ring with conductivity σ, skin depth δ_s, radius a, and cross sectional radius r, effective resistant R and self-inductance L is determined as:

$$R = \frac{2\pi a}{\pi\sigma\left[r^2-(r-\delta)^2\right]} \approx \frac{a}{\sigma r\delta} \tag{29}$$

$$L = \pi\mu a/2 \tag{30}$$

Typically for an aluminum ring with $a = 5\,\text{cm}$ and $r = 1\,\text{mm}$, $R = 1.7\,\Omega$ and $L = 10^{-7}\,\text{H}$.

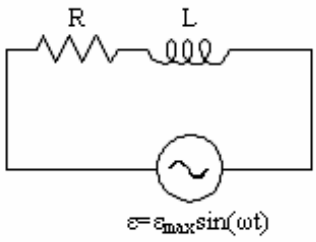

Figure 3: Analogy of a metal ring in an alternative electric field.

We have considered the electromagnetic waves inside the cavity as below:

$$\vec{E} = E_0\cos(\omega t)\,\vec{i} \tag{31a}$$

$$\vec{B} = \frac{E_0}{c}\cos(\omega t)\,\vec{k} \tag{31b}$$

So induced electromotive force, ε, in the ring which caused by changing the magnitude of $\vec{B}$ is given by:

$$\varepsilon = -\frac{d\phi_B}{dt} \approx \frac{E_0}{c}\pi a^2\omega\sin(\omega t) \tag{32}$$

The sign is specified by Lenz's law, which states that the induced current and accompanying magnetic flux is in such a direction as to oppose the change of flux through the circuit.

Maximum current, $I_{\max}$, and time averaged power dissipated in the metal ring, P_{loss}, are defined as:

$$I_{\max} = \frac{\varepsilon_{\max}}{\sqrt{R^2+(L\omega)^2}} \approx \frac{\varepsilon_{\max}}{L\omega} = 2.6\,\text{A} \tag{33}$$

$$P_{loss} = \frac{1}{2}RI_{\max}^2 = 5.75\,\text{J/s} \tag{34}$$

Neglecting heat transfer by conductivity to the surrounding space, the rate of increasing temperature of a skin aluminum ring is determined as:

$$\dot{\theta} = \frac{P_{loss}}{mC} = 2939\,^\circ\text{C/s} \tag{35}$$

where $m = \rho(2\pi r\delta)(2\pi a) = 4.3\times10^{-6}\,\text{kg}$ is the mass of skin depth layer.

Electric field in the appeared tracks along the ring is approximated as:

$$E_G \approx \frac{\varepsilon_{\max}}{d} = \frac{E_0\pi a^2\omega}{cd} \tag{36}$$

where d is width of track and c is velocity of light. It can be seen from Eq. (36), when d is very small, E_G increases much respect to E_0. For example, for $d = 1\,\text{mm}$ and $E_0 = 10^4\,\text{V/m}$, electric field in the track is $E_G \approx 4\times10^6\,\text{V/m}$ which is about strength of air. Consequently, first, power loss in the metal ring causes a tracked with small width and secondly, increasing electric field in the track about strength electric air causes an arc.

5. EXPERIMENTS AND RESOULTS

We have made several experiments CD-ROMs, glassware having an ornamental brass band, metal rings having a gap width $\sim 2\,\text{mm}$ and various cross-sections and types within a compact Panasonic microwave oven NN-C2003S which is tuned on 30 seconds. The experiment results are summarized in the following expressions.

Metals or conductive objects placed into the microwave oven cavity act as an antenna due to the induced electric current. The induced current leads to heat the objects that vary with the object's shape and composition. The local melting and vaporizing are caused to create some gapes or tracks on the metal. When a gap appears, a spark forms and ionizing the gas drastically reduces its electrical resistance. The air forms a conductive plasma, which is visible as a spark. The plasma and the metal may then form a conductive loop and produs a longer lived spark.

Some objects consisting a pice of metal such as CD-ROMs, metal foils, and etc., can create an electric arc or spark and will be very hot when microwaved. Spark forms faster around the sharp point than the other points of the metals. When a spark forms, a light with a sound appears. For objects, such as glassware and CD-ROMs, light and sound are faint but for tin band and iron wire, powerful light with a loud sound is created. For a thin tin ring with a thickness $\sim 0.1\,\text{mm}$, some points gradually become thin and at the moment of cutoff a spark is happened. While for a thin copper plate with thickness $\sim 0.1\,\text{mm}$, only at the edges spark is created. This is because the instantanius deposited surface-charge density at the edges becomes too large and then produce high voltage at the edges.

Figure 4 shows a recordable CD which is microwaved inside a cavity oven for a few seconds. The dark pictures show tracks on the CD. Writhing snake trails ranging from $\sim 1\,\text{mm}$ to $\sim 3\,\text{mm}$ in width and $\sim 7\,\text{mm}$ in height are appeared on the CD surface. This is because the induced current trough the thin aluminum layer of the CD resonates and consequently leads to vaporize the layer in some points due to the ohmic loss. It continues to vaporize trails on the CD until the tracks width become large ($\sim 3\,\text{mm}$). The electric field through the vapor forms visible plasma and hot spots from the spark at the tracks lead to burn the polycarbonate of the CD. Fig. 5 shows etched pattern on the CD-Rewritable inside the oven cavity. Comparing Figs. 4 and 5, it can be seen that width and shape of the tracks are depended on the type of metal layer of the CD.

Moreover, time of forming spark is dependent on the induced heat power loss and the type of metal object. When melting and vaporizing point of metal are lower, with the same cross-section, spark forms faster. For example, sparks are formed after $\sim 3--5\,\text{sec.}$ on CD-ROM, ~ 5 seconds in the brass ornamental band of the glass cap, $\sim 5\,\text{sec.}$ in the striped-iron ring with thickness $\sim 1\,\text{mm}$ and $\sim 2--3\,\text{sec.}$ on the thin cooper wire.

Generally microwaves cause currents to flow in metals. In a thick piece of metal, these currents won't cause problems for the metal. However, in thin pieces of metal, the currents may heat the metal hot enough to cause a track and subsequently a spark. Metallic decorations on fine porcelain tend to become hot enough to damage the porcelain. But even thick pieces of metal can cause problems because they tend to reflect the microwaves that may cause cooking problems for the food nearby. High electric field at sharp points, causes instantaneously spark and these sparks can cause fires. In general, smooth and thick metallic objects such as spoons are not a problem because of a large heat capacity, but sharp or thin metallic objects such as pins or metal twist-ties are.

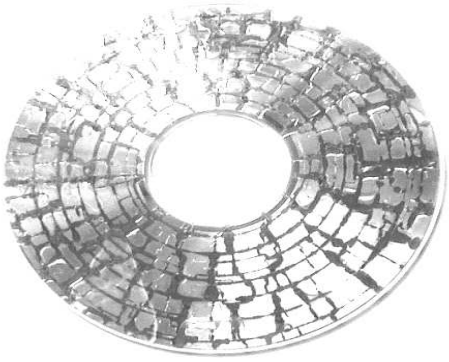

Figure 4: Etched pattern on the CD-ROM inside the microwave oven.

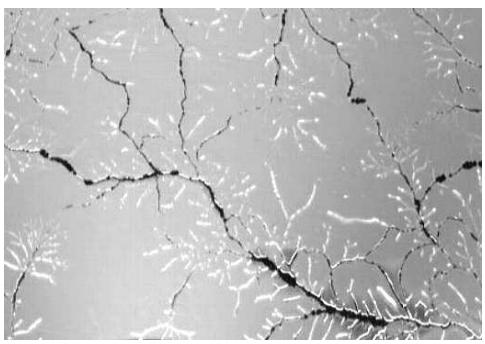

Figure 5: Etched pattern on the CD-ReWritable inside the microwave oven.

It is important to note that any time dielectric breakdown occurs in air, some ozone and nitrogen oxides are formed, both of which are toxic and the hot spots from the spark at the tracks lead to burn the polycarbonate.

6. CONCLUSION

The physical basis of sparking of metal objects within the microwave oven cavity has been theoretically and experimentally investigated. Using cavity Q-factor, the characteristics of both TE and TM electromagnetic resonant modes in the oven cavity are determined. Assuming electrostatic field approximation and solving Laplace equation in both cylindrical and elliptical coordinate systems, electric field components around the metal disks and sharp points are theoretically determined. It implies that the field strength around the sharp points or edges becomes approximately equal to the dielectric strength of air and charge deposits near the edges.

On the other hand, based on the alternating field approximation, it is shown that the induced temperature due to the absorption of both TE and TM modes inside the cavity leads to melting and vaporizing of the metal.

Practically is observed that objects with pointed metal can create an electric arc when microwaved. Metals or conductive objects are placed into the microwave will act as an antenna to some degree, resulting in an electric current. The induced current on the metal surface resonates with the microwave frequency and produce high voltage at the tips. Moreover, induced current heats metal and temperature of several points of its surface increases up to the melting or vaporizing point of the metal and some tracks on the surface at these points are appeared. Field within the tracks is increased dependently to the track width; smaller track width greater track field. This effect varies with the object's shape and the composition. If metal is not thin, or if there are sinke within the metal, discharge will not occure.

Moreover, the electricity field which passes through the vapor, forms visible plasma. The plasma and the metal may then form a conductive loop, which is visible as a spark. This effect can be seen clearly on aluminum foil, CD-ROM or DVD. Experimental results show a good agreement with the theoretical predictions.

ACKNOWLEDGMENT

Leila Mashhadi wishes to acknowledge Prof. Dr. Ahmad Shariati, for excellent scientific guidelines during doing M. S. theses.

REFERENCES

1. "Phenomena: The sparking of grapes in microwave ovens and cause thereof," WWW.geocities.com/ tohyo/temple/3717/greeks/eegrape.htm.
2. Chilton, J. E., "Temporal and aspects of microwave exitation of compact disk," 5370, Department of Physics, University of Wisconsin-Madison, Wisconsin.
3. Vollmer, M., et al., "Microwave oven experiments with metals and light source," WWW.iop/journals/physics.
4. Gallawa, J. C., "How does a microwave oven work? Basic theory of operation," *The Complete Microwave Oven Service Handbook*, http://www.gallawa.com/microtech/metal_arc.html, 2000.
5. "How a microwave oven works," (http://www.gallawa.com/microtech/how_work.html) Description with circuit diagrams.
6. Vollmer, M., et al., "Physics of the microwave oven," *Physics Education*, 2004.
7. Gandhi, O. M. P., *Microwave Engineering and Applications*, Maxwell MacMillan international editions, 1989.
8. Kraus, J. D. (Author) and R. C. Keith (Editor), *Electromagnetics with Applications*, 5th Edition, MaGraw-Hill Book Company, 1999.
9. Jacson, J. D., *Classical Electrodynamics*, 3rd Edition, Library of congress cataloging-in-pablication data, 1999.

A Congestion Control Algorithm Based on Onboard IP Switching

Yi Zhang, **Quan Zhou**, **Jun Li**, **Jie Li**, **and Wanzhao Cui**
National Key Laboratory of Space Microwave Technology
Xi'an Institute of Space Radio Technology, Xi'an 710100, China

Abstract— Onboard switching is a direction of satellite communication. Because of the limited satellite resources, the paper proposes an open-loop congestion control algorithm in onboard IP switches. We simply the RSVP in IP layer, in order to avoid the congestion in cache of onboard IP switches. The results of simulation show that the proposed algorithm can decrease the cell loss rate by sending path request message periodically.

1. INTRODUCTION

Onboard switching is a direction of satellite communication. The onboard IP switching primarily complete the switching of IP packets. Onboard switches can complete the switching among multi-beams and simplify the communication of many ground stations. Because the resources onboard are limited, it's important to control the congestion in satellite switching networks. To resolve this problem, onboard IP switching must adopt some strategies for congestion control, in order to guarantee the satellite networks are unblocked and supply quality of service. In this paper, we address the congestion control on IP layers with an iterative approach.

This paper is organized as follows. Section two presents the general principles of congestion control. The characteristics of onboard congestion control are described in section three. Section four proposes an algorithm of congestion control based on onboard switching for satellite IP. Simulation of the proposed algorithm is shown in section five. Section six concludes this paper.

2. GENERAL PRINCIPLES OF CONGESTION CONTROL

The presence of congestion means that the load is (temporarily) greater than the resource (in part of the system) can handle [1]. In satellite switching networks, the limited resource are shared by many users. For onboard IP switching, satellite networks can't restrict the number of users by the usable resources, because there is no call admission control algorithm. Without central control, the networks also can't compute the number of usable resources. Although congestion is caused by a shortage of buffer space, the congestion problem cannot be solved with a large buffer space. Cheaper memory has not helped the congestion problem. It has been found that networks with infinite-memory switched are as susceptible to congestion as networks with low-memory switches. In fact, too much memory is more harmful than too little memory since the packets have to be dropped after they have consumed precious network resources.

All solutions of congestion are divided into two groups [1, 2]: open loop and closed loop. Open loop solutions attempt to solve the problem by good design, in essence, to make sure it does not occur in the first place. Once the system is up and running, midcourse corrections are not made.

In contrast, closed loop solutions are based on the concept of a feedback loop. This method monitors the system to detect when and where congestion occurs, then pass this information to places where action can be taken. The obvious way is for the router detecting the congestion to send a packet to the traffic source or sources, announcing the problem. Of course, these extra packets increase the load at precisely the moment that more loads is not needed, namely, when the subnet is congested. Still another approach is to have hosts periodically send probe packets out to explicitly ask about congestion. In all feedback schemes, the hope is that knowledge of congestion will cause the hosts to take appropriate action to reduce the congestion.

The open loop algorithms are further divided into two classes [2]: ones that act at the source versus ones that act at the destination.

The source algorithm used broadly is the congestion-control with Transmission Control Protocol(TCP). The end-to-end congestion control mechanisms of TCP have been a critical factor in the robustness of the Internet. However, the Internet is no longer a small, closely knit user community, and it is no longer practical to rely on all end nodes to use end-to-end congestion control for best-effort traffic. In addition, owing to the particularity of satellite links, the control mechanisms of TCP can not play its role primely as in terrestrial links. Consequently, the Internet Protocol(IP) layer must participate in controlling its own resources utilization. Active Queue

Management (AQM) [3] is an effective link algorithm to enhance congestion control, and to achieve tradeoff between link utilization and delay. These policies attempt to estimate the congestion at a node and signal by dropping packet(s) before the buffer is full. And this Algorithm also depends on TCP.

3. CHARACTERISTICS OF ONBOARD CONGESTION CONTROL

Satellite link has the characteristics of long delay and poor quality of channel. It's difficult to enhance congestion control by the above methods. In this paper, we study congestion control based on IP layer, considering the characteristics of onboard IP switching.

Because of the long delay of satellite-ground link, it needs more time to notify for congestion, and this also increases the load of satellite-ground links. Consequently, this paper studies how to resolve the congestion problems based on onboard IP switching with open-loop solution, avoiding congestion by reserving resource before switching packets.

The Resource Reservation Protocol (RSVP) [1] is a proposal of the IEEE for setting up reservation state information for data flows along communication paths. It is intended to support real-time and multimedia applications, which require some Quality of Service (QoS) guarantees from the network.

RSVP is a signaling protocol developed to create and maintain reservation state information in Internet routers. A sequence of packets with a particular destination and transport layer is considered a session, so it may include several data flows. RSVP treats each session independently. A sender, which participates in a RSVP session, sends path messages periodically to the receiver(s). A path message creates and maintains path state information in each node along the communication path. Once a receiver receive the first path message, it may initiate sending Resv messages upstream to the senders. The Resv message creates and maintains reservation state information in each node along the route.

4. ALGORITHM OF CONGESTION CONTROL BASED ON ONBOARD IP SWITCHING

In this section, we present one congestion control method with RSVP in satellite IP switches. RSVP is complex, which is used in each node along the communication path. All the nodes need to maintain path state information. Consequently, in order to avoid congestion in cache of satellite IP switches, we need to simplify RSVP based on IP layer.

Considering the characteristics of satellite channel, we should reduce the number of interaction between satellite and ground, the types and the number of messages. Because our protocol is intended mainly to avoid the congestion of onboard switches cache, the protocol is used only in ground sending station and onboard switches.

4.1. Process of Congestion Control Based on Onboard IP Switching

The basic process of congestion control based on onboard IP switching is as follows: firstly, ground sending stations send path request message to onboard IP switches before sending IP packets. The onboard switches determines whether reserve resource for the data flows, according to the utilization of onboard switches cache. Then the switches send reserve or reject message to ground station. The ground station can send IP packets when it has received the reserve message from onboard switches, otherwise wait and send path request message periodically.

When the packet received is assort with which has been reserved, the resource information in cache need to be freshed. For overload data, if there are enough resource in onboard cache, this packet can be switched. But once the congestion appears onboard, this packet is discarded first.

If the ground sending stations send path request message for every IP packet, there are great path request and reserve messages, which will cause low transmission efficiency and long delay for shorter packets. Because approximately 40% of IP packet on the Internet is 40 bytes which are the TCP response message without data, the algorithm of congestion control in this paper doesn't conduct path request for shorter packets of 40 bytes and 44 bytes. This approach can reduce many path request and reserve messages.

4.2. Interactive Protocol in Onboard Congestion Control Algorithm

When we use RSVP to avoid congestion in onboard IP switches caches, the ground sending stations and onboard switches need to send or receive different messages in order to reserve resource and switch packets. If the message is lost or error, the station and switches must adopt some measures to ensure the normal switching.

(1) In most cases, the ground sending stations can send IP packets to satellite after receiving the accepting message for resource reserving from onboard IP switches.

(2) When the path request message from ground sending station to onboard IP switches is wrong or missing,in order to reduce the interactive number between satellite and ground, the ground stations retransmitted the message a prescribed number of times, and the onboard switches does not send the error message for instructing mistakes. The ground station can send IP packets until receive the accepting message from onboard IP switches.

(3) When the resource reserving message from onboard IP switches to ground sending station is wrong or missing, the ground stations also do not send the error message. The ground stations start a timer while sending path request message. If the time is ended, the answering message has not be received, or received error message, the ground station should send the path request message again. Then continue to start a timer and wait until receive the accepting message.

In this case, onboard switches has received resource for the IP packets, but the packets don't arrive. In order to release the resource, onboard switches also starts a timer. If the reserved data have not be received when the time is ended, onboard switches releases the resource reserved.

5. SIMULATION

In this section, the proposed algorithm is simulated in order to validate whether this approach can reduce the loss rate of onboard switches, achieving the object of congestion control. In this

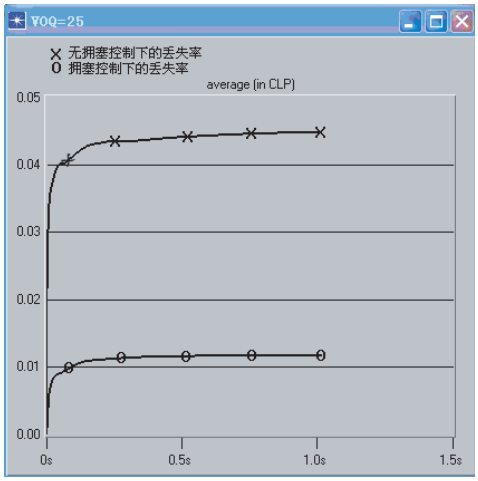

(a) VOQ = 25

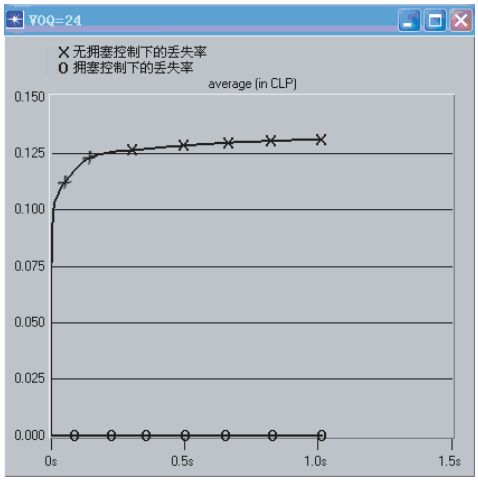

(b) VOQ = 24

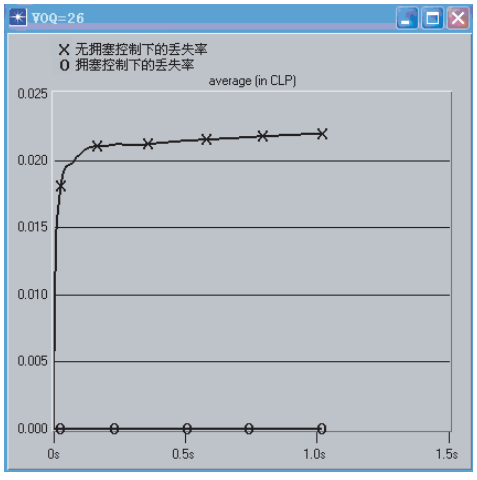

(c) VOQ = 26

Figure 1: The comparison of loss rate with or without congestion control.

simulation, the simplified RSVP is used in ground sending station and onboard switches. Because the congestion control algorithm is designed for the IP packets of Internet. The length of IP packets in our simulation is distributed as follows:

40 bytes — 34%, 44 bytes — 4%, 280 bytes — 42%, 576 bytes — 10%, 1500 bytes — 10%.

Figure 1(a) shows the comparison of loss rate with or without congestion control, and the length of the Virtual Output Queuing (VOQ) [5] in our switches is twenty-five. This is because the packets of 1500 bytes need to be divided into twenty-five cells in onboard switches. If we reserve resource for the packets of 1500 bytes, the shorter packets of 40 bytes and 44 bytes which have no extra resource will be dropped. In this case, the loss rate with congestion control is less than without congestion control obviously.

When the length of VOQ is twenty-four, comparison of loss rate with or without our algorithm is shown as Figure 1(b). In this case, the capacity of VOQ is not sufficiently great to buffer a packet of 1500 bytes, but is enough for shorter packets. All the path request messages of the long packet are rejected, and only the shorter packets are sent to onboard switches. As a result, there is no loss in onboard switches, but the packets of 1500 bytes can't be switched. According to this case, the length of VOQ should be sufficient to store one IP packet of 1500 bytes at least. By the way, the simulation result in Figure 1(b) shows that the loss rate is too high without congestion control, even is 10^{-1}.

As shown in Figure 1(c), the loss rate is compared when the length of VOQ is twenty-six. In this case, there are enough resources for the longest IP packet, and the shorter packets, which are divided into one cell, also can be stored. We can see from the result of simulation that with congestion control the loss rate is zero, less than without congestion control obviously.

The results of simulation show that the proposed algorithm can decrease the cell loss rate by sending path request message to onboard switches periodically. Meanwhile, this algorithm also has some issue. Because ground sending stations should send path request message to onboard IP switches before sending IP packets, the buffer are needed to store the IP packets in ground station. Then the ground stations should send path request message to satellite periodically. All the same, this algorithm can reduce the loss rate effectively, avoiding congestion of onboard IP switches.

6. CONCLUSIONS

In this paper, we studied the congestion control problem of onboard IP switches, and an open-loop method is proposed with simplified RSVP. The results of simulation showed that this congestion control approach, which sending path request message periodically, can reduce the loss rate of onboard IP switches. But the ground station should store the IP packets which need to be sent. Future work must consider how to use other function of RSVP in order to avoid congestion in onboard IP switches more efficient.

REFERENCES

1. Tanenbaum, A. S., *Computer Networks*, Fourth Edition, Prentice Hall, Mar. 2003.
2. Liu, H.-J., "Research of congestion control RED algorithms in IP network," *Journal of Huayin Teachers College*, Natural Science Edition, Vol. 1, No. 2, 2002.
3. Ostadabbas, S. and M. Haeri, "Adaptive congestion estimation and control in active queue management," *International Conference on Control, Automation and Systems 2007*, COEX, Seoul, Korea, Oct. 17–20, 2007.
4. Giannoulis, A., T. Salonidis, and E. Knightly, "Congestion control and channel assignment in multi-radio wireless mesh network," *IEEE*, 2008.
5. Zhang, Y., Q. Zhou, and J. Li, "An input-buffer scheduling algorithm in satellite switching system," *Seventh National Signal and Information Processing Joint Academic Conference*, Lan Zhou, China, Jul. 20–23, 2008.

A Broadband Two-stage MMIC Medium-power Amplifier

Yuanyuan Li and Long Jin
Research Institute of Electronic Science and Technology
University of Electronic Science and Technology of China, Chengdu, China

Abstract— A broadband two-stage MMIC medium-power amplifier operating from 6–20 GHz is developed for EW and communication applications using 0.15 μm low-noise PHEMT process. The amplifier use a single 3-volt DC power supply, each gain stage is self-biased for class-A operation for optimal power output with minimal distortion, the two-stage feedback power amplifier has 16.5 dB small signal gain with 2.0 typical noise figure and input and output VSWRs less than 1.7 over 6–20 GHz, the output power at 1 dB compression is 16.0 dBm at 20 GHz.

1. INTRODUCTION

The current trend in microwave technology is toward circuit miniaturization high-level integration, improved reliability, low power consumption, cost reduction, and high volume applications. Component size and performance are prime factors in the design of electronic systems for satellite communications, phased-array radar systems, electronic warfare, and other military applications, while small size and low cost drive the consumer electronics market. The broadband MMIC medium-power amplifiers based on PHEMT technology just agree with the above requirements. They play an increasing role in consumer electronics and military applications [1]. There are various techniques used to realize broadband power amplifiers: balanced circuit [2], feedback [3], active matching [4], resistive matching [5], distributed approach [6, 7]. The negative feedback topology has a drawback of the degradation of the gain. Generally, the chip size of the distributed and balanced amplifier is limited by the bandwidth of the transmission line and the coupler [8].

In this paper, a broadband two-stage MMIC medium-power amplifier from 6–20 GHz is developed for EW and communication applications using 0.15 μm low-noise PHEMT process. The first stage PHEMT with gate width of 6×30 μm was used to drive the second stage PHEMT with gate width of 6×70 μm. With a single 3-volt DC power supply, each gain stage is self-biased for class-A operation for optimal power output with minimal distortion, the two-stage feedback medium-power amplifier has 16.5 ± 0.5 dB small signal gain with 2.0 typical noise figure and input and output VSWRs are less than 1.7 over 6–20 GHz. The output power at 1 dB compression are 16.0 dBm at 20 GHz, the designing simulation results indicate that this method is simple and feasible.

2. PHEMT DEVICE

The MMIC was implemented using a commercial PHEMT MMIC foundry (UMS), which supports 0.15 μm gate length technology. Figure 1 shows the schematic diagram of the GaAs PHEMT structure. Figure 2 shows the small signal model for 0.15 μm PHEMT. The extraction of the parasitic parameters using cold-FET method and the intrinsic parameters using hot-FET method in small signal model for the 0.15 μm PHEMT is based on Ref. [9].

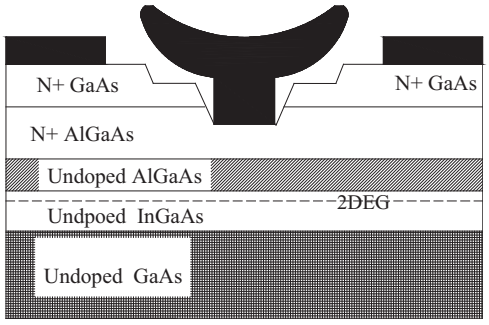

Figure 1: The Schematic diagram of the GaAs PHEME structure.

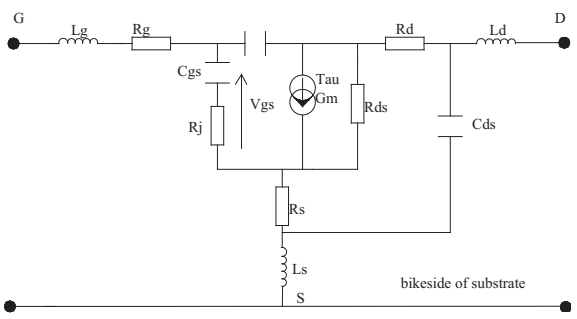

Figure 2: The Small-signal model of 0.15 μm PHEMT.

3. CIRCUIT DESIGN

Figure 3 shows the schematic drawing of the whole amplifier including the first drive stage and the second power stage. For single voltage purpose, the self bias circuit is used by adding resistor to the source port of each device. The first matching network for a power amplifier is the output matching network which is designed to transfer maximum output power from the FET to a 50 Ω system. Lossy matching techniques in the inter-stage network were used to provide additional gain slope compensation and to provide the optimum impedance level for power matching. Finally, the input network is designed to flatten the small signal gain and improve impedance match for better input return loss. Based on these essential matching networks, an optimization and EM simulation are performed to achieve the required circuit performance. One of the most important amplifier design criteria is unconditional stability at any frequency and at any source and load conditions. The requirements of characteristics of MMIC circuit designing are as follows: the circuit should be reasonable, simple, reliable; distributing every stage's power and gain target reasonably; reducing the stages of amplifier and using linearization technology cautiously in order to minimize the area of chip and increase the ration of eligibility. Based on the analysis above and the research about the designing of MMIC broadband power amplifier before, this paper has been given prominence to several points of consideration below, and adopt corresponding technology methods: (1) In order

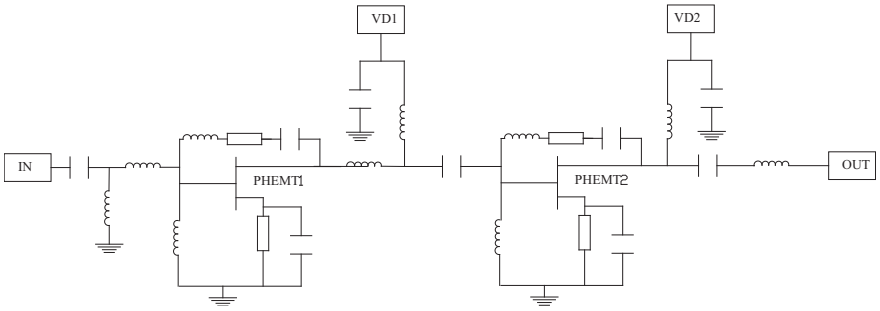

Figure 3: The topology of the medium-power amplifier.

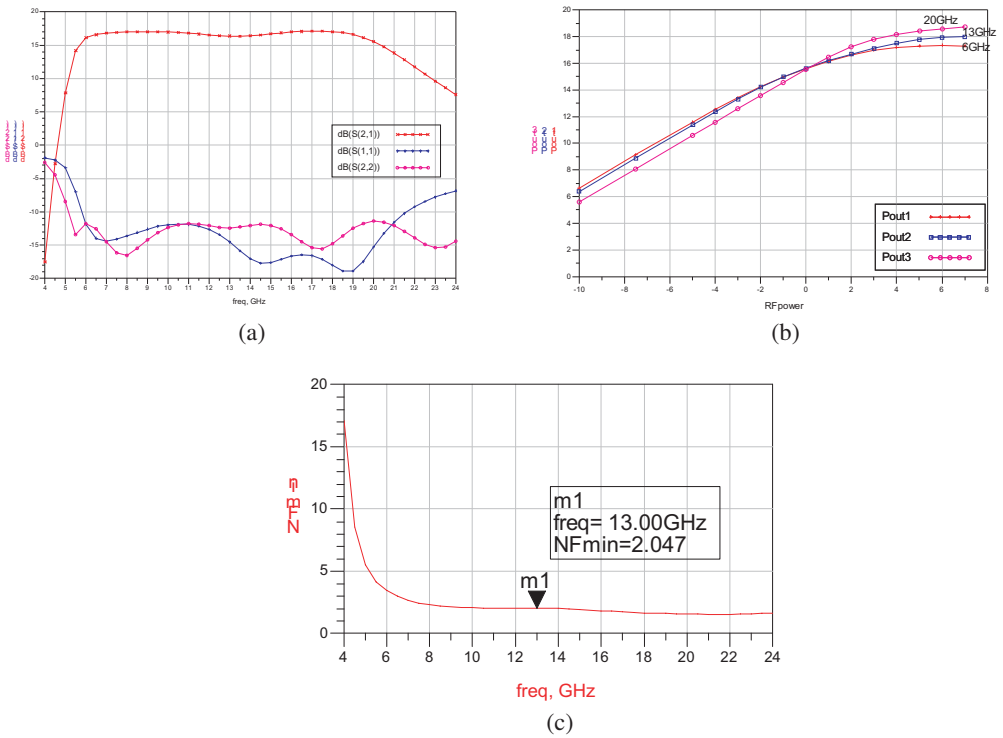

Figure 4: (a) Small-signal performance. (b) Output power vs. input power for various frequency. (c) Noise figure of amplifier.

to realize high gain, low noise figure, we try to use 0.15 µm low-noise PHEMT process to realize the design of this MMIC medium-power amplifier; (2) Considering practical use in engineering, the amplifier use a single 3.0-volt DC power supply, each gain stage is self-biased for class-A, thus simplify the matching and minimize the area of chip and costs; (3) Considering the target of designing in all, we use two-stage amplifier, based on the requirements of gain, output power, technical model, the first stage PHEMT with gate width of 6×30 µm was used to drive the second stage PHEMT with gate-width of 6×70 µm; (4) The two stages of amplifier employ negative feedback method, thus ensures that the amplifier has flat gain and unconditional stability over 6–20 GHz; (5) The output power's performance can be advanced through perfect inter-stage matches, simple but useful input and output matching networks make perfect input and output VSWRs.

4. PERFORMANCE

The gain and return-loss performance of the two-stage MMIC medium-power amplifier are shown in Figure 4(a). The amplifier has about 16.5 dB of small gain with good flatness over 6–20 GHz. The input return losses (S_{11}) and the output return losses (S_{22}) are less than -12 dB over 6–20 GHz. Figure 4(b) shows the output power as a function of input power. The amplifier has an advantage, the noise figure shown in Figure 4(c) is low.

5. CONCLUSION

This paper use 0.15 µm low-noise PHEMT process to realize the design of a 6–20 GHz broadband medium-power amplifier. Through load pull's analysis, optimal bias voltage is only 3-volt, lower than ordinarily power amplifier, and accord with currently low voltage application trend. The paper emphasize the design of feed-back networks, inter-stage matching network and bias circuits, to exert the power characteristics of active device under the condition of broadband. The combination of series-wound inductance feedback and shunt-wound negative feedback can obtain low noise figure, low input VSWR, high gain and perfect output power characteristic. The two-stage MMIC medium-power amplifier achieve a small-signal gain (S_{21}) of 16.5 dB, the average output power is around 16.0 dBm, both the input return loss and the output return loss are less than -12 dB over 6–20 GHz

REFERENCES

1. Bahl, I. and P. Bhartia, *Microwave Solid State Circuit Design*, Vol. 1, Second edition, John Wiley & Sons, New Jersey, Hoboken, 2003.
2. Lim, J. S., S. C. Kang, and S. Nam, "MMIC 1 watt wideband power amplifier chip set using PHEMT technology for 20/30 GHz communication systems," *Asia Pacific Microwave Conference*, Vol. 2, 425, 1999.
3. Kim, Y. G., S. J. Maeng, J. H. Lee, et al., "A PHEMT MMIC broad-band power amplifier for LMDS," *RAWCON Proceedings*, 121, 1998.
4. Peterson, W. C., et al., "A monolithic GaAs 0.1 to 10 GHz amplifier," *IEEE Int. Microwave Symp. Dig.*, 354, 1981.
5. Arell, T. and T. Hongsmatip, "A unique MMIC broadband power amplifier approach," *IEEE J. Solid-State Circuits*, Vol. 28, No. 10, 1005, 1993.
6. Platzker, A., K. T. Hetzler, and J. B. Cole, "Highly dense dual-channel C-X-Ku and 6–18 GHz MMIC power amplifier," *IEEE GaAs IC Symp. Digest*, 339, 1991.
7. Barnes, A. R., M. T. Moore, and M. B. Allenson, "A 6–18 GHz broad-band high power MMIC for EW application," *IEEE MMT-S Digest*, 1429, 1997.
8. Vendelin, G. D., A. M. Pavilo, U. L. Rohde, et al., *Microwave Circuit Design*, John Wiley & Son, 253, 1990.
9. Zang, S. J., R. Yang, X. Gao, et al., "The large signal modeling of GaAs HFET/PHEMT," *Chinese Journal of Semiconductors*, Vol. 28, No. 3, 439, 2007.

Implementation of a Radio over Fiber System in a Geographically-distributed Optical Network

S. Arismar Cerqueira, Jr.[1], **D. C. Valente e Silva**[2], **M. A. Q. R. Fortes**[1], **L. F. da Silva**[2], **O. C. Branquinho**[2], **and M. L. F. Abbade**[2]

[1]Optics and Photonics Research Center, UNICAMP, Brazil
[2]Faculdade de Engenharia Elétrica, Pontifícia Universidade Católica de Campinas, Brazil

Abstract— This work presents an implementation of a Radio over Fiber system based on IEEE 802.15.4 standard, in a geographically-distributed optical network, called KyaTera. The input signal was launched into hundreds of kilometers from KyaTera Network under real conditions of temperature, pressure, humidity and wind. Experimental results show no performance degradation of the transmitted radio frequency signal.

1. INTRODUCTION

The next generation of access networks is rushing the needs for the convergence of wired and wireless services to offer end users greater choice, convenience and variety in an efficient way [1]. This scenario will require the simultaneous delivery of voice, data and video services with mobility feature to serve the fixed and mobile users in a unified networking platform. In other words, new telecom systems require high-transmission bandwidths and reliable mobility. The Radio over Fiber (RoF) technology [2] represents a key solution for satisfying these requirements, since it jointly takes advantage of the huge bandwidth offered by optical communications systems with the mobility and flexibility provided by wireless systems. RoF systems consist of heterogeneous networks formed by wireless and optical links. Unlike traditional optical communications networks, in which a baseband signal in transmitted into the optical fibers, in RoF systems one or multiple analogous carriers are transported into the fibers. The transmission is performed by directly or externally modulating lasers by the analogous radio frequency signal. On the receiver side, the transmitted signal is recovered by using a photodiode. Compared to traditional optical systems, RoF technology provides the advantage of eliminating the gateways, since there is no need for analogous-digital or digital-analogous conversions. This simplifies the system complexity and reduces the operational costs.

RoF technology has been investigated by many Research Groups in the last years. However, the great majority of works published in literature are based on simulations and/or experiments carried out in laboratories. This work presents an implementation of a Radio over Fiber system based on IEEE 802.15.4 standard, in a geographically-distributed optical network called KyaTera [3], under real conditions of temperature, pressure, humidity and wind.

2. EXPERIMENTAL SETUP

The system performance of the RoF system based on IEEE 802.15.4 standard with Thin architecture has been analyzed in a real geographically distributed optical network, called KyaTera, which is a Brazilian optical network exclusively dedicated to research purposes. The optical links from this network are formed by aerial and underground cables. This means experiments carried out in it permits to evaluate the performance under practical conditions that may lead, for instance, severe changes in the signal polarization [4].

Two different RoF systems have been investigated in the KyaTera network: a wired RoF system and a RoF system with a wireless link. The experimental setup of first case, Setup 1, is shown in Fig. 1. A laser operating at 1550 nm is directly modulated by a 3.0 dBm RF signal at 2.48 GHz with Quadrature Phase Shift Keying (QPSK) modulation. This optical signal with 6.4 dBm of output power is then launched into KyaTera Network. The optical signal is received by a fast photodiode and converted back to an electrical signal.

The Setup 2 corresponds to the RoF system with a wireless link as presented in Fig. 2. The main difference compared to Setup 1 is that the electrical signal recovered by the photo-diode is retransmitted by using an antenna with gain $G = 12$ dBi. The wireless signal is finally received by a receiver antenna. Power monitors have been used in both setups to measure the optical power.

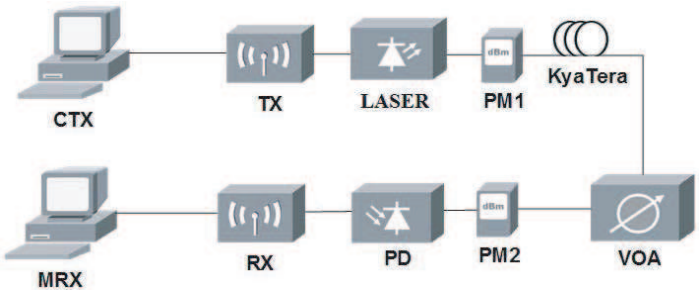

Figure 1: Experimental Setup 1: CTX — Transmitter controller; Tx — Transmitter; PM1 and PM2 — Power meters; VOA — Variable optical attenuator; PD — Photo-detector; RX — Receiver; CRX — Receiver notebook.

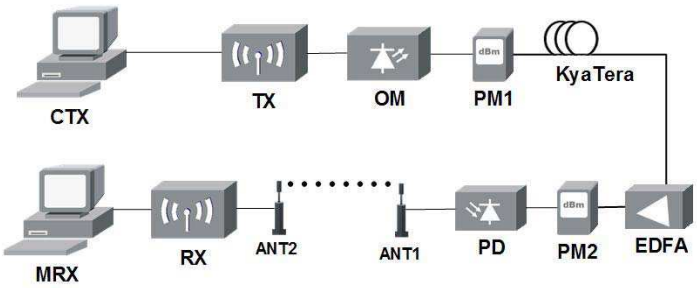

Figure 2: Experimental Setup 2: ANT1 — Transmission antenna; ANT2 — Reception antenna.

In both cases, TX and RX radios have been configured as Full Function Device (FFD) and Reduced Function Device (RFD), respectively. By using laptops we could configure TX radio with the following parameters: 25,000 frames; Frame size of 131 Bytes; 125 Bytes Payload size; Frame interleaving of 50 ms. The RF output power was 3.0 dBm.

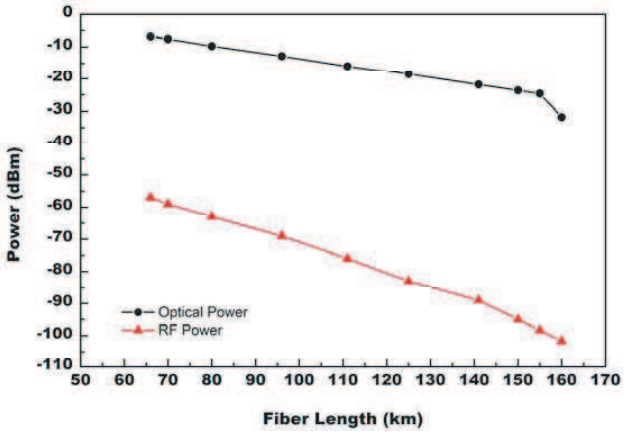

Figure 3: Power analysis as a function of fiber length in KyaTera network.

3. EXPERIMENTAL RESULTS

The performance parameters evaluated in the experiments were the RF power, the optical power and the Frame Error Rate (FER). We have firstly used the Setup 1 to analyze the optical and electrical powers as a function of the optical link length. As expected, for systems operating at 2.48 GHz and working at distances lower than 600 km the dependence between the optical and RF powers is linear, evidencing there are no fading effects and, consequently, no power performance degradation due to the dispersion influence.

By using the tunable optical attenuator from Setup 1 we have changed the optical power at the photo-diode input and measured the system Frame Error Rate. Fig. 4(a) reports that for power levels lower than −23.5 dBm, FER increases exponentially. Besides the noise from TX radio, it

happens due to the noise generated by the photo-detection process. On the other hand FER is below 10-3 for input powers higher than −23.5 dBm, achieving 1.10-4 in the best case. Systems at FER levels around 10-3 are extremely interesting for Wireless Sensor Network applications, which have a typical FER of about 10-1.

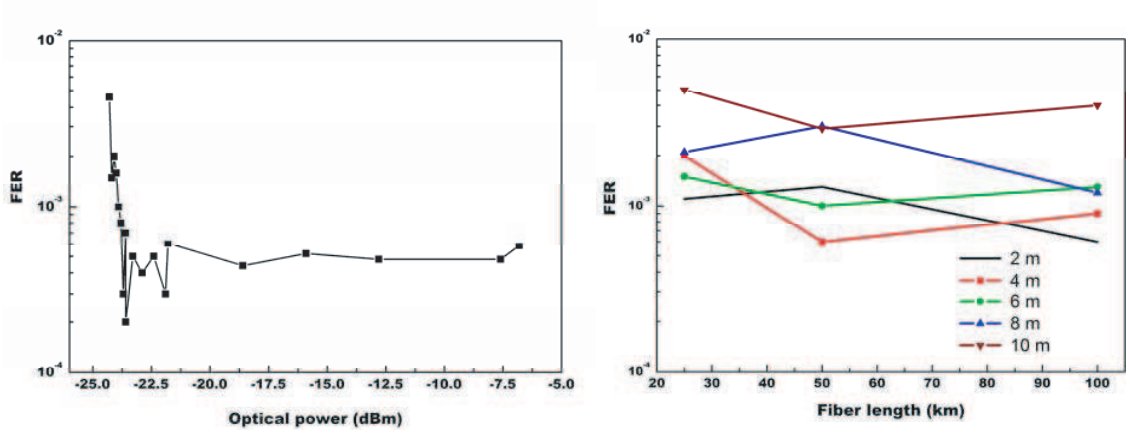

(a) Setup 1 (b) Setup 2

Figure 4: FER as a function of the optical input power for Setups 1 and 2.

Since the typical optical fiber attenuation is 0.2 dB/km and the typical output power from Telecom external cavity lasers is around 10 dBm, it is quite feasible to think about RoF systems operating over 160 km without using optical amplifiers. In case an optical amplifier is used the system reach will be limited by the first fading node around 600 km.

Setup 2 has been used to illustrate WSN applications based on Radio over Fiber technology. Fig. 4(b) presents a FER measurement as a function of fiber length for different distances between transmission and reception antennas. FER is worse in this experiment due to the multipath interference, but it continues to be very interesting for WSNs, where FERs up to 10^{-1} are acceptable. It is important to highlight this performance can be a lot improved by optimizing the wireless link and pieces of equipment, as for example, the RoF transceiver. However, this is not the focus of the current work.

4. CONCLUSIONS

It has been reported an implementation of a Radio over Fiber system based on IEEE 802.15.4 standard operating 2.48 GHz and using Thin architecture in a geographically-distributed optical network. The system performance was analyzed under real environmental conditions. Experimental results have shown no signal degradation and demonstrated RoF technology can be extremely interesting as a backhaul of Wireless Sensor Networks with reach of up to 160 km. These networks can be efficiently applied to the control and monitoring of different physical properties, such as temperature, pressure, humidity, toxic gases, and others.

ACKNOWLEDGMENT

Authors acknowledge FAPESP (Fundação de Amparo à Pesquisa e ao Ensino do Estado de São Paulo) for the financial support.

REFERENCES

1. Jia, Z., J. Yu, G. Ellinas, and C. Gee-Kung, "Key enabling technologies for optical wireless networks optical millimeter wave generation wavelength reuse and architecture," *J. of Light. Tech.*, Vol. 25, 3452–3471, 2007.
2. Chang, S. C. W., *RF Photonic Technology in Optical Fiber Links*, Cambridge University Press, 2002.
3. www.kyatera.fapesp.br.
4. Marconi, J. D., F. A. Callegari, M. L. F. Abbade, and H. L. Fragnito, "Field trial evaluation of the Q-factor penalty introduced by fiber four-wave mixing wavelength converters," *Opt. Communications*, In Press, 2008.

60 GHz Radio over Fiber Transmission System Based on Integrative Cascade MZM

Cheng Hong, **Siyu Liu**, **Cheng Zhang**, **Zhangyuan Chen**, **and Weiwei Hu**
State Key Laboratory on Advanced Optical Communication Systems & Networks
Peking University, Beijing, China

Abstract— We experimentally demonstrated a Radio over fiber transmission system which works in 60 GHz band with 2.5 Gbps bit Rate over 22 km SMF, using an integrative cascade MZM modulator.

1. INTRODUCTION

Radio over fiber technology is considered to be a potential solution to the broadband access networks [1–4]. Making use of convergence of mobility of wireless and good transmission channel property of optical fiber, Radio over fiber technology can easy transmit several Gigabit per second. 60 GHz frequency range would be a attractive band for Radio over fiber application. Because 1) 60 GHz band is a free license band in most countries and areas such as North America, Europe, Australia, Korea, Japan and China [5]. This property can reduce expensive using fee for the service applications in this frequency range and also avoid fierce competition in the use of radio frequency band among traditional wireless services such as WiFi, WiMax, which is in the frequency range of 2–5 GHz. 2) 60 GHz band is near the absorbing peak of oxygen. This performance allows radio signal base station to allocate much dense than traditional wireless application and we need not worry about frequency intervene among different base stations. Pico-cell distribution coming from dense base station allocating can support large number of subscriber per unit area and large bandwidth for each subscriber.

It would be much cheaper to share the high frequency equipments especially the 60 GHz oscillation for a couple of base stations than setting an oscillation for each base station. So just sending the modulated Radio signals over fiber and amplifying and broadcasting them through base station is a good way for radio over fiber network. The Up-conversion process which is put the data signal to radio carrier must be done in the center office to satisfy the sharing oscillation scheme. There are several ways to modulate data signals to radio carrier and put them over the optical fiber. The traditional way to modulate data to radio carrier is using electrical mix, but 60 GHz band up-conversion electrical mix is usually very expensive for its rigorous performance demand. The most significant drawback of using electrical mix is that it will lead to too much chromatic dispersion in the process of optical fiber transmission even through a few kilometers. The convenient method to overcome the drawback is to transfer two coherence optical wavelengths with data signal and beat them in the photo detector put in base station to generate radio signal for broadcasting. This method not only avoid to much chromatic dispersion coming from optical fiber and need not electrical up-conversion mix but also share the oscillation among base stations. Usually we low frequency oscillation to generation two coherence wavelengths apart 60 GHz according to optical suppress carrier modulation in the central office and reduce the system cost further.

Here we experimentally demonstrated the transmission system for 2.5 Gps on 60 GHz microwave over 22 km SMF. Cascade MZM modulation method is a simple way to generate two coherence optical modes to beat in photo detector for producing microwave signal.

2. PRINCIPLE

The block diagram depicted in Fig. 1 presents the prinple setup of the mm-wave link include the dual frequency optical carriers separated by the desired mm-wave frequency.

The out put signal of a laser diode emitting at a frequency v_0 is modulated by a CW-signal with an amplitude V_m and with a frequency f_m using a lithium niobate Mach-Zehnder modulator(MZM) biased at V_b, therefore, the output signal of the modulator (the previous one) result to

$$E(t) = \cos\left[\beta\frac{\pi}{2} + \alpha\frac{\pi}{2}\cos(\omega_m t)\right] \cdot \cos(\omega_0 t) \tag{1}$$

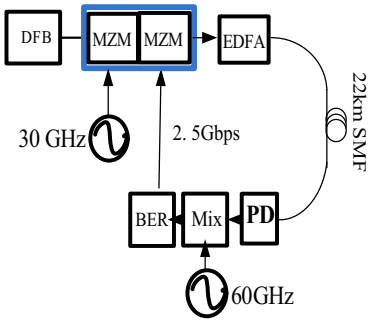

Figure 1: Experiment setup.

where $\beta = \frac{V_b}{V_\pi}$ is the normalized bias point of the modulator, $\alpha = \frac{V}{V_\pi}$ is the normalized amplitude of the diver signal, $\omega_m = 2\pi f_m$ is modulation anguler frequency, and $\omega_0 = 2\pi f_0$ is the angular frequency to the optical carrier. Using Bessel functions the equation can be expand to

$$\begin{aligned} E(t) \;=\; & J_0\left(\alpha\frac{\pi}{2}\right)\cdot\cos\left(\beta\frac{\pi}{2}\right)\cdot\cos(\omega_0 t) \\ & -J_1\left(\alpha\frac{\pi}{2}\right)\cdot\sin\left(\beta\frac{\pi}{2}\right)\cdot\cos(\omega_0 t)\cdot\{\cos[(\omega_0-\omega_m)t]+\cos[(\omega_0+\omega_m)t]\} \\ & -J_2\left(\alpha\frac{\pi}{2}\right)\cdot\cos\left(\beta\frac{\pi}{2}\right)\cdot\cos(\omega_0 t)\cdot\{\cos[(\omega_0-2\omega_m)t]+\cos[(\omega_0+2\omega_m)t]\}+\ldots \end{aligned} \tag{2}$$

For $\beta = 1$ all even terms vanish. The optical carrier suppress modulation achieved [6].

For the second MZM (the following one) set $\beta = 0.5$ for linear modulation and replace $\cos(\omega_m t)$ in Eq. (1) to $f(t)$ which stands for the data signal. Here we use OOK for data modulation so $f(t) = 1$ or 0.

3. EXPERIMENTAL RESULT AND DISCUSSION

For the imperfect of the MZM we use an optical interleaver to filter out the residual optical carrier [7] and a bassband filter to get rid on the ASE noise coming from the EDFA. The optical spectrum is show in Fig. 2. From these picture we can see that optical interleaver which plays the role of notch filter to take out the residue optical carrier is important, because this measure can make almost all the transferring optical power to be used to for data sending, since residue optical carrier is of no use in this kind of transmission.

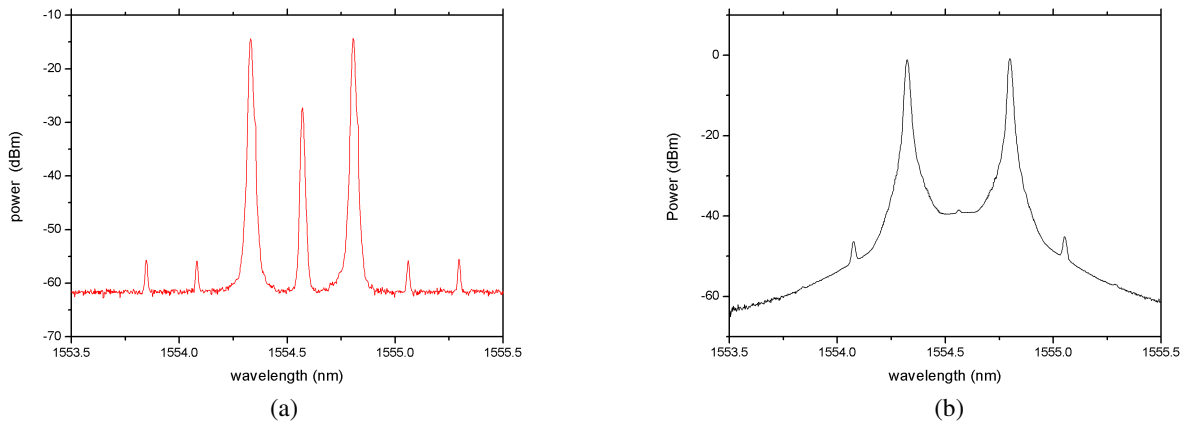

Figure 2: Optical spectrum, (a) with residual optical carrier, (b) filter out optical carrier.

Figure 3 shows the eye-diagram of the 2.5 Gbps signal after the Mix down conversion with the situation of back-to-back and 22 km single mode fiber transmission. The distorting eye-diagram of the 22 km SMF transmission comes from chromatic dispersion in optical fiber. The chromatic

dispersion penalty is much bigger than traditional baseband optical transmission for the chromatic dispersion comes not only from the data bite rate but also radio carrier frequency [8].

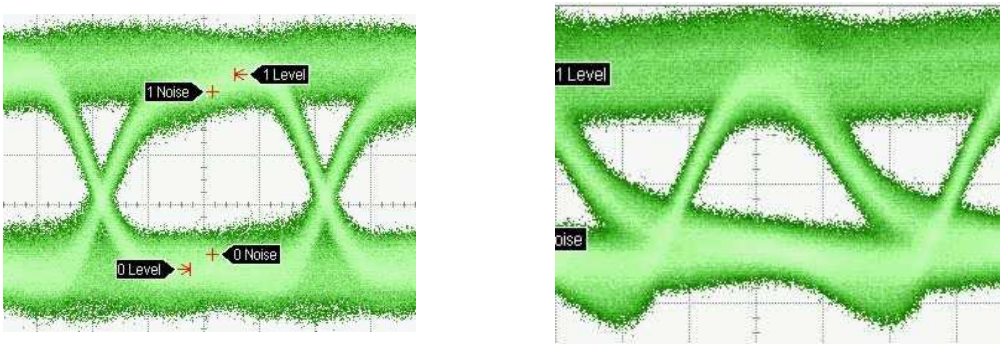

(a) (b)

Figure 3: Received eye-diagram, (a) back-to-back eye-diagram, (b) eye-diagram after 22 km SMF.

4. CONCLUSIONS

A primary demonstration of downlink Radio over system is realized by an integrative cascade MZM as modulator and coherent demodulation receiver.

ACKNOWLEDGMENT

This work is supported by The National High Technology Research and Development Program of China (863Program) under Grant 2006AA01Z261 and The National Natural Science Foundation of China (NSFC) under Grant 60736003.

REFERENCES

1. Koonen, T., "Fiber to the home/fiber to the premises: What, where, and when?," *Proc. IEEE*, Vol. 94, No. 5, 911–934, May 2006.
2. Seed, A. J., "Microwave photonics," *IEEE Transactions on Microwave Theory and Techniques*, 2002.
3. Noel, L., D. Wake, and D. G. Moodie, "Novel techniques for high capacity 60-GHz fiber-radio transmission system," *IEEE Transactions on Microwave Theory and Techniques*, 1997.
4. Ogawa, H., "Millimeter-wave wireless access systems," *Proc. APMC*, 2001.
5. http://www.windowsil.org
6. Wang, T., "Millimeter-wave singal generation using two cascaded optical modulator and fwm effect in semiconductor optical amplifier," *Photonics Technology Letter, IEEE*, Vol. 19, No. 16, 1191–1193, Aug. 2007.
7. Noguchi, K., O. Mitomi, and H. Miyazawa, "Millimeter-wave Ti:LiNbO3 optical modulators," *J. Lightwave Technol.*, Vol. 16, 615–619, Apr. 1998.
8. Hofstetter, R., et al., "Dispersion effects in optical millimeter-wave systems using self-heterodyne method for transport and generation," *IEEE Transactions on Microwave Theory and Techniques*, Vol. 43, No. 9, Sept. 1995.

Single-mode Modulation Using Injection-locked Fabry-Perot Laser in Radio-over-Fiber System

Cheng Zhang, **Mingjin Li**, **Siyu Liu**, **Cheng Hong**, **Weiwei Hu**, **and Zhangyuan Chen**
State Key Laboratory on Advanced Optical Communication Systems & Networks
Peking University, Beijing, China

Abstract— A scheme of single-mode modulation using injection-locked Fabry-Perot laser is proposed and investigated, which can be used in radio-over-Fiber (RoF) communication system. Good chromatic dispersion toleration performance is experimentally demonstrated.

1. INTRODUCTION

Radio-over-Fiber (RoF) system has been considered a promising technology for future broadband wireless communication. Recently, many schemes have been proposed to realize a low-cost and high-performance RoF system [1]. The commonly used method to generate millimeter wave (MMW) in these systems is optical heterodyning technique which use two correlated optical modes to beat a high-quality MMW. And usually the data is uploaded to the MMW by just modulating these two modes. However, standard modulation of two correlated modes will suffer from chromatic dispersion which results in a radio frequency (RF) fading and limits the transmission distance. Single-mode modulation is proposed to overcome this problem. But the former method using a Mach-Zehnder (MZ) interferometer filter is too complex to be practical [2]. Recently, we have demonstrated a new approach of single-mode modulation using injection-locked distributed feedback laser. And it has been proved much more chromatic dispersion tolerant than dual-mode modulation [3]. In this paper, we propose another approach to realize single-mode modulation using injection-locked Fabry-Perot laser dioxide (FPLD) which is much cheaper and can be used in a wide wavelength range.

2. EXPERIMENT SETUP

The configuration of the experiment is shown Fig. 1. A DFB laser's output is coupled into an intensity modulator which is driven by the reference frequency at 15 GHz from a signal generator. The modulator output is sent to an optical notch filter to select the first-order sidebands whose mode-spacing is 30 GHz. An EFDA and an attenuator are used to get the proper injection power and its output is connected with a 60 GHz mode-spacing FPLD through a three-port optical circulator (OC) for single-mode injection-locking. A polarization controller (PC) is used to control the input state of polarization to the FP laser diode. The intermediate frequency (IF) signal is uploaded by modulating the current of FPLD. Finally, the single locked mode and the other reflected mode are transmitted for 44.4 Km and sent to a 70 GHz photo detector (PD) for 30 GHz MMW generation. The electrical signal sidebands on both sides of 30 GHz carrier are measured for different IF. Another experiment using standard dual-mode modulation has also been done to for comparing data.

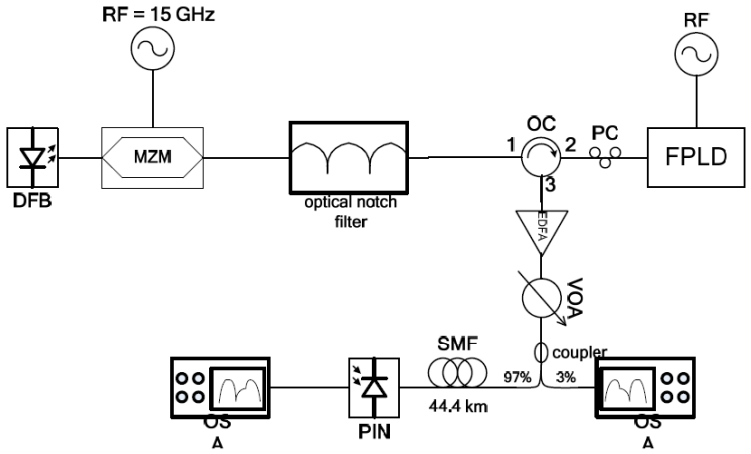

Figure 1: The experiment setup of the single-mode modulation injection-locked Fabry-Perot laser.

3. RESULTS AND DISCUISSION

The optical spectrum of single-mode modulation and dual-mode modulation before PD are shown in Fig. 2 and Fig. 3 respectively. For the single-mode modulation, in Fig. 2, the injection-locked mode (1550.83 nm) is effectively modulated, while the sideband of the unlocked mode (1551.07 nm) is lower than that of injection-locked mode by more than 10 dB. On the other hand, for the dual-mode modulation, the two modes are modulated equally.

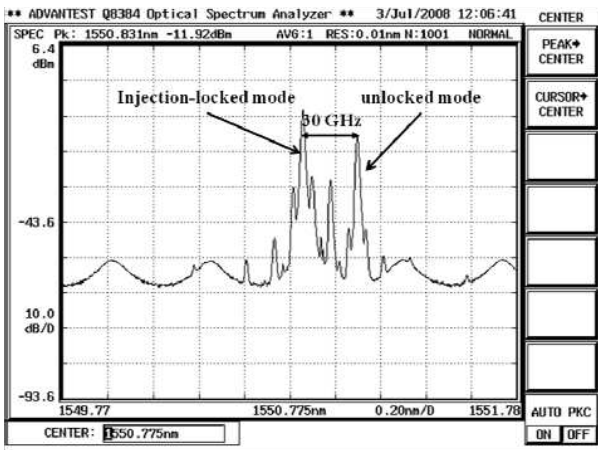

Figure 2: Optical spectrum for single-mode modulation.

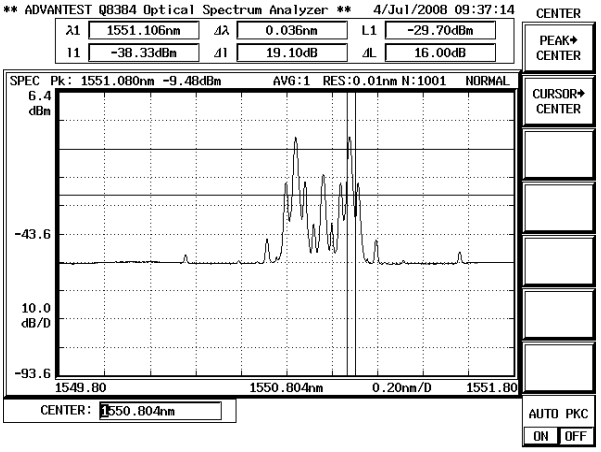

Figure 3: Optical spectrum for dual-mode modulation.

Figure 4 compares the sideband power after 44.4 Km SMF transmission for both single-mode modulation and dual-mode modulation whose wavelength is around 1550 nm. Different RF powers for single-mode modulation are also test in our experiment. It can be found that the proposed single-mode modulation is immune to RF signal fading due to chromatic dispersion, while in the dual-mode modulation the sideband electrical power suffers power degradation at about 3 GHz due to the chromatic dispersion of 44.4 Km SMF.

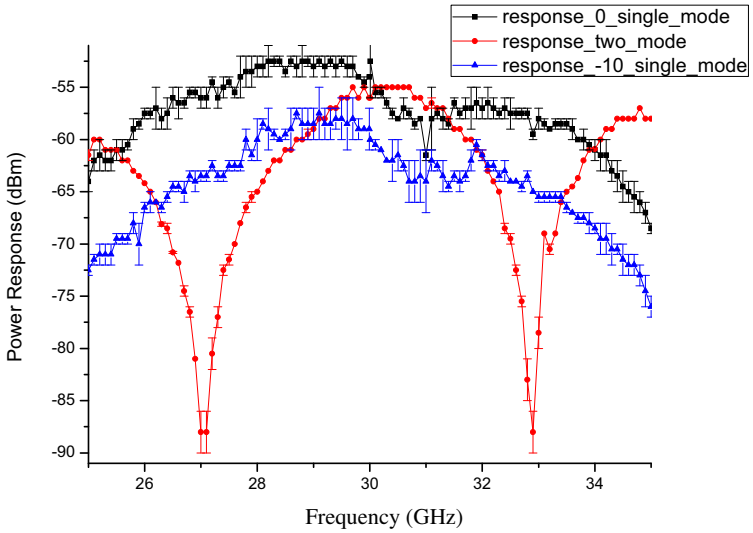

Figure 4: Received electrical power for different modulation frequency after 44.4 Km SMF transmission at 1550 nm.

Since the FPLD is multi-longitudinal mode laser which has a wide wavelength range for single-mode injection-locking, more experiments at other wavelength (such as 1540 nm and 1545 nm) have also been done to test the single-mode modulation validity. Fig. 5 and Fig. 6 show the comparisons between single-mode modulation and dual-mode modulation at different wavelength. And it proves that the single-mode modulation using injection-locked FPLD is suitable for a wide wavelength range.

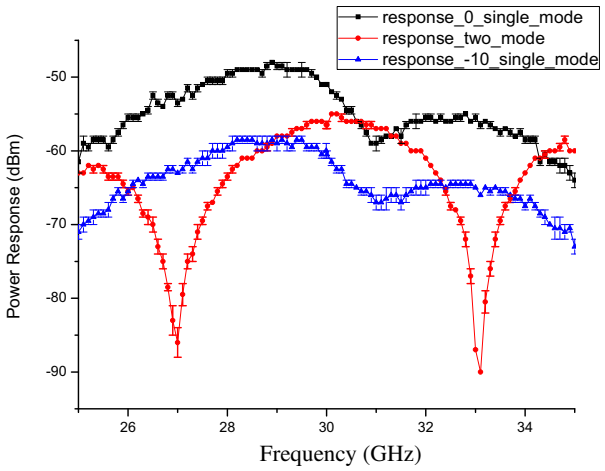

Figure 5: Received electrical power comparisons at 1540 nm.

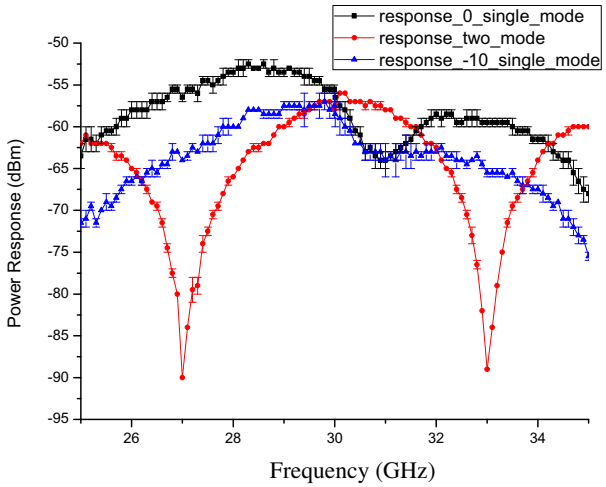

Figure 6: Received electrical power comparisons at 1545 nm.

4. CONCLUSIONS

A scheme of single-mode modulation using injection-locked Fabry-Perot laser in RoF communication system is proposed experimental investigated. The injection-locked mode is modulated effectively while the unlocked mode's sideband is lower than 10 dB. The experiment results show that the kind scheme is more tolerant to chromatic dispersion of single mode fiber than the dual-mode modulation and it can be also used in wide wavelength range.

ACKNOWLEDGMENT

This work is supported by The National Natural Science Foundation of China (NSFC) under Grant 60736003.

REFERENCES

1. Jia, Z., J. Yu, G. Ellinas, and G. K. Chang, "Key enabling technologies for optical-wireless networks: Optical millimeter-wave generation, wavelength reuse, and architecture," *Journal of Lightwave Technology*, Vol. 25, No. 11, 3452–3471, 2007.
2. Hofstetter, R., H. Schmuck, and R. Heidemann, "Dispersion effects in optical millimeter-wave systems using self-heterodyne method for transport and generation," *IEEE Transactions on Microwave Theory and Techniques*, Vol. 43, No. 9, 2263–2269, 1995.
3. Hong, C., M. Li, C. Zhang, C. Peng, W. Hu, A. Xu, and Z. Chen, "Single mode modulation using injection locked DFB lasers for millimetre wave radio over fibre system," *Proceedings of International Nano-Optoelectronics Workshop*, 129–130, Tokyo, Japan, August 2008.

A Scheme of Photonic Notch Filter Using DGD Method for Radio-over-Fiber Communication Systems

Hanhong Gao, Jinxuan Wu, Zhao Tu, Cheng Zhang, Dandan Wu, Weiwei Hu, and Zhangyuan Chen
State Key Laboratory of Advanced Optical Communication Systems & Networks
Peking University, Beijing, China

Abstract— We demonstrate a scheme of photonic notch filter using differential group delay (DGD) method for radio-over-fiber (RoF) communication systems. It is continuously tunable through adjustment of the central frequency of laser source, capable of achieving lowpass, bandpass or highpass filter. It can be operated in a wide range of optical carrier wavelength. Experimental results show a good notch rejection higher than 20 dB. This scheme could be used in RoF communication systems to reject the channel noise and achieve a better filter performance.

1. INTRODUCTION

Due to the advantageous features offered by optics, photonic filters can provide a large tunability and a high Q factor besides advantages such as low loss, light weight, and immunity to electromagnetic interference. A number of photonic microwave filters have been reported in the literature [1–9]. For coherent type, the optical phase can be used to perform negative weights, thus leading to a higher flexibility in the design of the system-transfer function. But the drawbacks of this type are that the whole system needs to be isolated from the outer environment in order to avoid phase fluctuation of the optical beam. Most of the recent work in this field is implementing incoherent processing approach based on intensity modulation of the optical signal which is difficult to realize negative coefficient. Many configurations with negative coefficients have been realized; however, their systems are always complex. A photonic filter with non-uniform spaced taps with an arbitrary bandpass response is realized recently [10]; however, its free spectral range (FSR) cannot be tuned continuously.

In this paper, we propose a scheme of tunable photonic notch filter, which implements a DGD element. The adjustment of the frequency of the laser source can be used to achieve great tenability. What's more, if a tunable optical delay is added to one PM fiber route, its FSR can be adjusted more flexibly. Its notch rejection higher than 20 dB can be used in RoF communication systems to reject channel noise.

2. PRINCIPLES AND SETUP

Figure 1 shows a block diagram of the DGD optical filter [11]. Laser output, after launched into a polarization controller (PC), is split into two orthogonally polarized beams by polarization beam splitter (PBS). Then they pass through two polarization maintaining optical fibers (PM-Fiber) with difference length of ΔL. These two beams are adjusted by two PCs to make sure their polarizations are in the same direction. Finally they are coupled by a polarization-maintaining coupler (PM-coupler). The interference of these beams will lead to the result that the intensity of output is related to ΔL and the central frequency of the laser ν. If the optical intensities of the two beams are the same and their polarizations are aligned to the same direction, the optical intensity of coupler's output is given by

$$I_0 = 2I\left(1 + \cos 2\pi \frac{n\Delta l}{\lambda}\right) \tag{1}$$

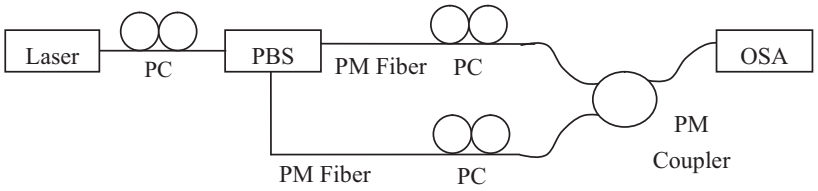

Figure 1: Block diagram of the DGD element. OSA: Optical spectrum analyzer.

where I is the intensity of two split lasers, n is index of refraction, λ is the wavelength of the laser. The FSR of this filter is given by

$$\mathrm{FSR} = \frac{c}{n\Delta L} \tag{2}$$

where c is light velocity.

By introducing the element of DGD optical filter, a tunable photonic filter can be realized. The principle of this filter is illustrated in Figures 2 and 3 [12].

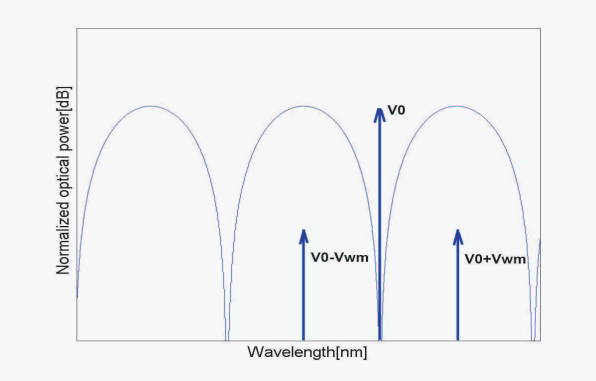

Figure 2: The relationship between modulated signal and optical filter.

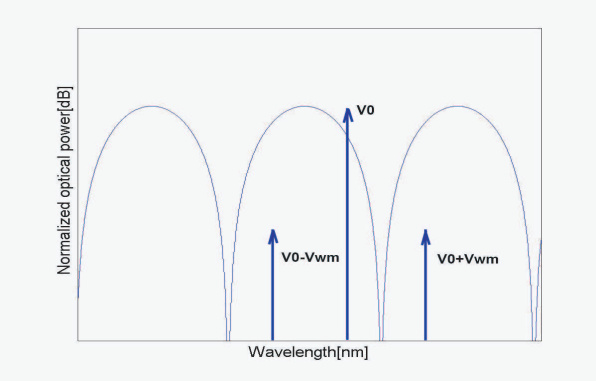

Figure 3: The relationship between modulated signal and optical filter in another frequency.

After intensity modulated by electro-optical modulator (EOM), the optical signal consists of the fundamental optical carrier ν and two first-order sideband component $\nu_0 \pm \nu_{mw}$, where ν_{mw} is the frequency of the microwave modulating signal. Considering ν_0 to be a constant, when ν_{mw} changes, the relative intensity of the demodulated signal alters and is proportion to the two first-order sideband. The period of this change is equal to the FSR of the optical filter, so the FSR of microwave photonic filter has the same FSR as the optical filter.

If ν_{mw} is unchanged, through the adjustment of the wavelength of the optical carrier ν_0 in the range of about 0.1 nm, the relative intensity of the demodulated signal alters. From (2) we can see that the FSR of the optical filter has no relationship with the wavelength, and is the same as that of the microwave photonic filter. So the amplitude-frequency response moves with the alternation of ν_0, while remaining the FSR unchanged.

Figure 4 shows a block diagram of the proposed photonic filter.

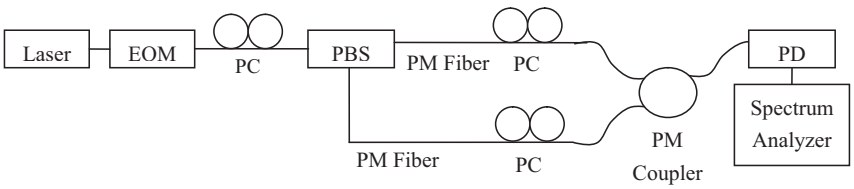

Figure 4: Block diagram of the proposed photonic filter.

3. EXPERIMENTAL RESULTS AND DISCUSSIONS

The experimental setup of optical filter is illustrated in Figure 1. The PM fibers difference is 4.0 cm, which is 5.1 GHz in frequency. The results of optical filter are demonstrated in Figure 5. The calculated curve is in solid line while the measured results are in discrete points.

The wavelength difference of one FSR is approximately 0.042 nm, which corresponding to 5.2 GHz. The notch rejection of the filter is about 10 dB. The experiment results match well with the theoretical deduction.

Based on this optical filter, photonic filter is experimentally demonstrated as in Figure 4. The results are shown in Figure 6 with solid line being the calculated results and discrete points being the measured ones. The match between the calculated response and the measured response is good. The FSR for wavelength of 1550.00 nm is 4.6 GHz, matching that of optical filter in previous paragraph. The right one of Figure 6 is the result when central wavelength of source is 1549.99 nm. The FSR is

4.6 GHz but the amplitude-frequency period has shifted to the right by 1.0 GHz. In calculation, the difference of 0.01 nm of laser source corresponds to a right shift of 1.2 GHz in frequency. They are approximately the same. Thus, by adjusting the frequency of laser source, different kinds of filters can be realized including lowpass, bandpass and highpass filters. A notch rejection over 20 dB can perform very good filter effects for rejecting channel noises in RoF communication system.

Further more, FSR can be changed if a tunable optical delay line is added into either of two PM-fiber routes. By varying the delay, a wide range of FSR can be achieved, which will provide more flexibility to this scheme.

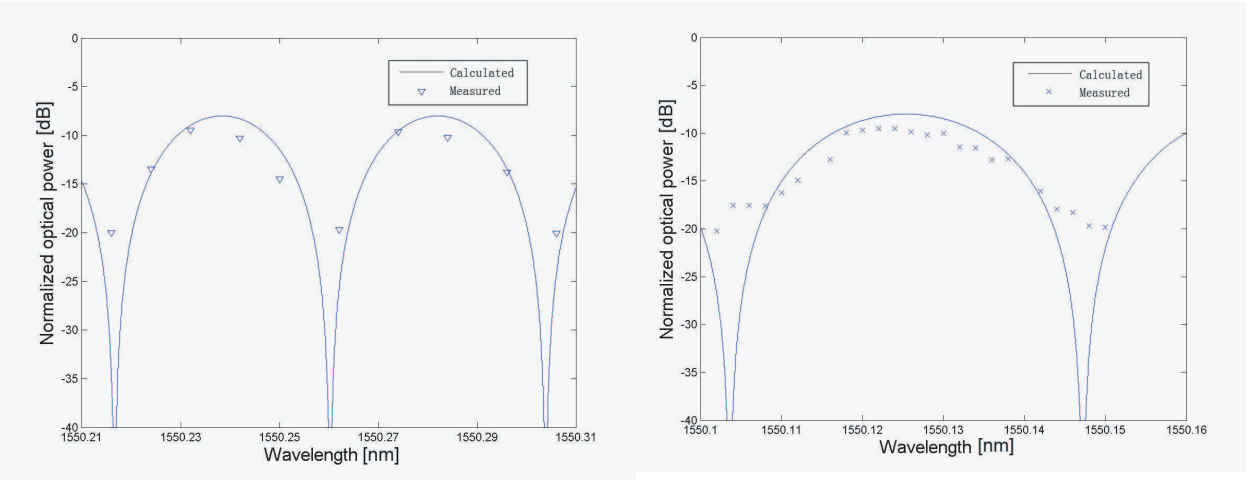

Figure 5: Frequency response of the optical filter with rough measurements (a) and detailed measurements of a period (b).

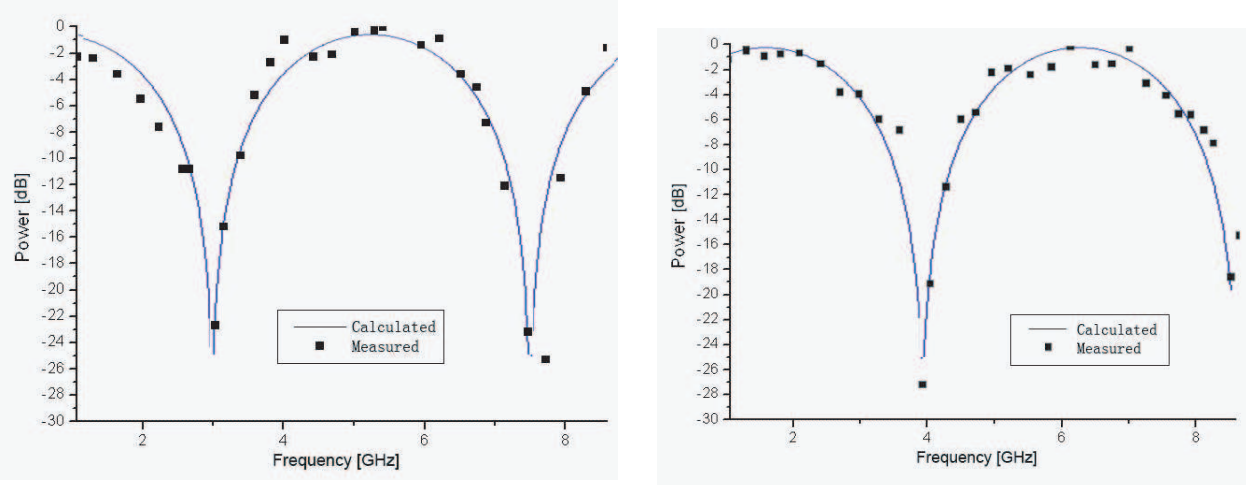

Figure 6: Frequency response for photonic filter for central wavelength of 1550.00 nm (a) and 1549.99 nm (b).

4. CONCLUSIONS

In this paper, a continuously tunable photonic notch filter is theoretically and experimentally demonstrated. First, an optical filter with FSR of 0.042 nm is implemented. Then a photonic filter is realized based it with FSR of 4.6 GHz and notch rejection over 20 dB. Varieties of filter types can be achieved by adjust the central frequency of laser source. The FSR can be modified if using an adjustable optical delay line. This scheme of photonic filters can be widely used in RoF communication systems to bring about better filter performance.

ACKNOWLEDGMENT

This work is supported by the National Undergraduate Innovative Test Program, the National Natural Science Foundation of China (NSFC) under Grant No. 60736003 and the National High Technology Research and Development Program of China (863 Program) under Grant 2006AA01Z261.

REFERENCES

1. Gweon, S., et al., "Wide-band fiber optic signal processor," *IEEE Photonics Technol. Lett.*, Vol. 1, No. 12, 467–468, 1989.
2. Moslehi, B. and J. W. Goodman, "Novel amplified fiber-optic recircularing delay line processor," *J. Lightwave Technol.*, Vol. 10, 1142–1146, 1992.
3. Norton, D., S. Johns, C. Keefer, and R. Soref, "Tunable microwave filter using high dispersion fiber time delays," *IEEE Photon. Technol. Lett.*, Vol. 6, 831–832, 1994.
4. Copmany, J., D. Pastor, and B. Ortega, "New and flexible fiber-optic delay-line filters using chirped fiber Bragg gratings and laser arrays," *IEEE Trans. Microwave Theory Tech.*, Vol. 47, 1321–1326, 1999.
5. Minasian, R. A. and D. B. Hunter, "Photonic signal processing of microwave signals using fiber Bragg gratings," *Proc. Optical Fiber Conf.*, Paper ThH3, 339-340, 1997.
6. Polo, V., J. Marti, F. Ramos, D. G. Moodie, and D. B. Hunter, "Synthesis of photonic microwave filters based on electro-absorption modulators and wide-band chirped fiber gratings," *J. Lightware Technol.*, Vol. 18, 213–220, 2000.
7. Frankel, M. Y. and R. D. Esman, "Fiber optic tunable microwave transversal filter," *IEEE Photon. Technol. Lett.*, Vol. 7, 191–193, 1995.
8. Coppinger, F., S. Yegnanarayanan, P. D. Trinh, and B. Jalali, "Continuously tunable photonic radio-frequency notch filter," *IEEE Photon. Technol. Lett.*, Vol. 9, 339–341, 1997.
9. Zeng, F. and J. Yao, "All-optical bandpass microwave filter based on an electro-optic modulator," *Opt. Express*, Vol. 12, 3814–3819, 2004.
10. Dai, Y. and J. Yao, "Nonuniformly-spaced photonic microwave delay line," *Opt. Lett.*, 2008.
11. Ning, G., P. Shum, S. Aditya, H. Dong, and M. Tang, "Novel tunable photonic microwave filters using adjustable DGD elements," *Proceedings of International Conference on Communications, Circuits and Systems*, Vol. 1, 643–646, 2005.
12. Kim, G.-D. and S.-S. Lee, "Photonic microwave reconfigurable filter based on a tunable polymeric ring resonator," *Opt. Comm.*, Vol. 278, 303–306, 2007.

A Scheme of Microwave Photonic Filter Based on Hi-Bi Fiber

Dandan Wu, **Weiwei Hu**, **and Zhangyuan Chen**
State Key Laboratory of Advanced Optical Communication Systems & Networks
Peking University, Beijing, China

Abstract— A scheme of microwave optical filter is proposed and demonstrated. The architecture is based on Hi-Bi Fiber which has a large refractive index difference between its fast and slow axis. The advantages of this kind of MPF compared with previous schemes are more stable and simpler due to using only one fiber delay line, which can implement a wide range of FSR.

1. INTRODUCTION

Over the past several decades Microwave photonic filter (MPFs) has attracted a lot of interest due to the processing of radio-frequency (RF) signals in the optical domain, saving bulky OE and EO conversion parts, and with the advantages of wide bandwidth, immunity to electromagnetic interference, low loss, tunability and reconfigurability [1], therefore they are widely applied to phased-array beamforming, radar, mobile communications, and radio-over-fiber (ROF) systems.

The MPFs can be operated in incoherent or coherent regime [2]. Incoherent filters are more stable against environmental conditions. Therefore, until now many kinds of incoherent MPFs have been reported in literatures. The conventional incoherent MPFs have been proposed using different optical delay lines [3] or electrically summing configurations, then the intensity of the modulated light outputs from different taps are added. However, the former limited the free spectrum range (FSR) of the MPFs, and the later lost the advantages of optical domain signal processing. Recently, polarization synthesizing method has been reported to realize incoherent operation, which is based on differential group delay (DGD) element with two fiber delay lines [4]. In this paper, we propose a structure of microwave photonic filter.

2. SYSTEM CONFIGURATION AND DISCUSSION

In this paper, we propose a novel structure of microwave photonic filter shown in Fig. 1.

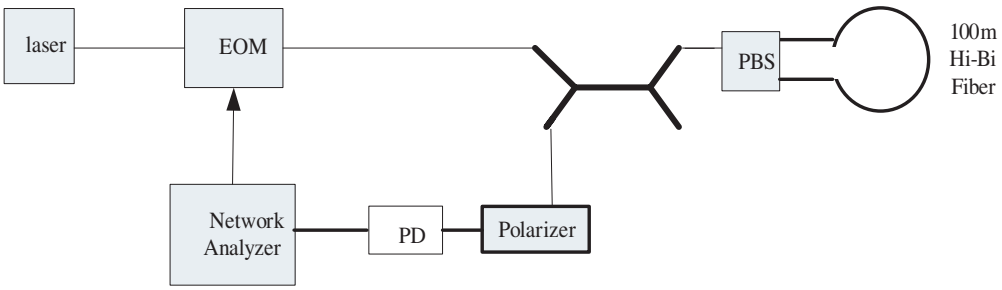

Figure 1: The system configuration of microwave photonic notch filter.

The radio frequency (RF) signal of a network analyzer drives an electrooptic modulator that modulates the output of a tunable laser source. The modulated optical signal transmits along a coupler and a three-port polarization beam splitter (PBS). One of the optical beams transmits clockwise along fast-axis of the Hi-Bi fiber, and the other transmits anti-clockwise along slow-axis of the Hi-Bi fiber. Because the Hi-Bi fiber has a large refractive index difference between its fast and slow axis, the time delay difference will be induced. The two orthogonal optical signals, which are differently delayed, are combined without interference and directed to the output of the coupler. In order to convert the combined signals which is circularly or elliptically polarized light into linearly polarized light, polarizer is used after the coupler to implement linear superposition of two MPF's taps.

The two orthogonal modulated signals translated in the 100 m Hi-Bi fiber. When the fast-axis polarization signal enters the Hi-Bi LCFBG from one of PBS ports, it will experience time delay t_1, however, the slow-axis polarization signal will have time delay t_2. The time delay difference Δt ($\Delta t = t_2 - t_1$) is induced the differential group delay (DGD) by the Hi-Bi Fiber between the two

polarization axes. If the PBS split the two orthogonal modulated signals equally, we can obtain a high performance optical notch filter. The normalized transfer function of the two-taps transversal filter is described by $H(f) = |\cos(\pi f \Delta t)|$, where f is the RF frequency. The FSR of the filter is equal to FSR $= \frac{1}{\Delta t}$. But if the PBS split two beams of optical signal unequally, or the polarizer which is used to produce a linear polarization with an varied azimuth, the normalized transfer function is described as $H(f) = 1 + \sqrt{a}e^{-j2\pi f \Delta t}$, where a is the normalized optical divide ratio of the two orthogonal modulated signals.

When the beat length of Hi-Bi fiber is 5 mm, the normalized frequency response of the microwave filter is given in Figure 2 as a solid line. The time delay of the two orthogonal modulated signals is 103 ps after 100 m Hi-Bi fiber, and the FSR of this kind of MPF is about 10 GHz. If the beat length of Hi-Bi fiber is 3 mm, the normalized frequency response is shown in Figure 2 as a dotted line, and the FSR is changed from 10 GHz to 5.8 GHz. Figure 3 shows the change of MPF's normalized frequency response with the different optical divide ratio of PBS, where the notch rejection ratio of the MPF is larger than 40 dB with the 0 dB optical divide ratio. Moreover, when the PBS split two beams of optical signal unequally, such as the optical divide ratio is converted to 1 dB, the notch rejection ratio of the MPF decrease to about 25 dB. But if the power difference of the two orthogonal modulated signals is increased to 3 dB, the notch rejection ratio is about 15 dB. Therefore, the MPF's notch rejection ratio is up to the optical divide ratio of the two orthogonal lights.

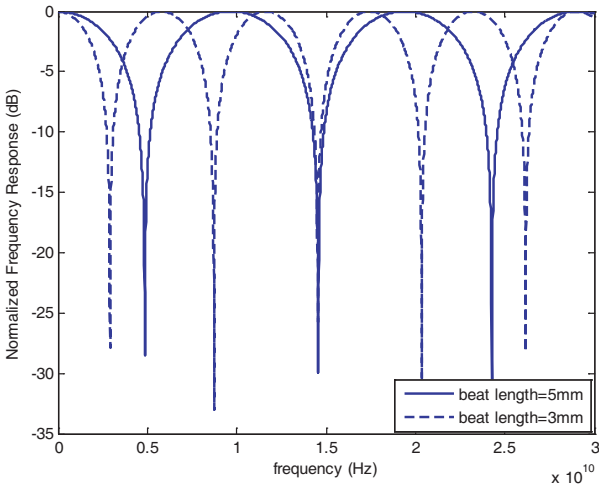

Figure 2: Simulated results of MPF's normalized frequency response. Solid line: Frequency response when Hi-Bi Fiber's beat length is 5 mm. Dotted line: Frequency response when Hi-Bi Fiber's beat length is 3 mm.

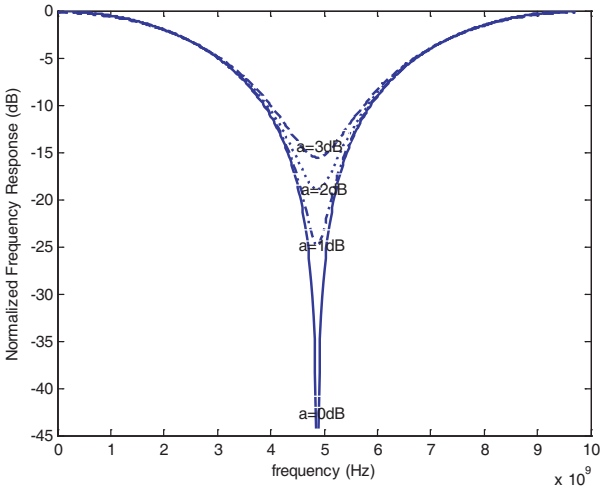

Figure 3: Simulated results of MPF's normalized frequency response with the different optical divide ratio of PBS.

3. CONCLUSIONS

Theoretical calculation show that the MPF structure can provide approximately 10 GHz FSR corresponding to the 100 ps time delay, and the FST depends on the Hi-Bi fiber's beat length. The notch rejection ratio is up to the optical divide ratio of the two orthogonal modulated signals. When the optical divide ratio is less than 2 dB, the notch rejection is larger than 20 dB. This MPF has several advantages comparing with previous schemes. First, it's more stable and simpler due to using only one fiber delay line, which can implement a wide range of FSR. Second, through the employment of temperature controller or PZT to adjust the length of the Hi-Bi fiber, the MPF will be tunable and reconfigurable.

ACKNOWLEDGMENT

This work is supported by The National Natural Science Foundation of China (NSFC) under Grant 60736003.

REFERENCES

1. Minasina, R. A., "Photonic singal processing of microwave signals," *IEEE Trnas. on Micrwave Theory and Techniques*, Vol. 54, No. 2, 832–846, 2006.
2. Capmany, J., B. Ortega, and D. Pastor, "A tutorial of microwave photonic filters," *J. Lightvwave Technol.*, Vol. 24, No. l, 201–229, 2006.
3. Wilner, K. and A. P. Van Den Heunel, "Filter_optic delay lines for microwave signal processing," *Proc. IEEE*, Vol. 64, No. 5, 805–807, 1976.
4. Ning, G., P. Shum, S. Aditya, H. Dong, and M. Tang, "Novel tunable photonic microwave filters using adjustable DGD elements," *IEEE*, Vol. 1, 643–646, 2005.

The Trend of Designing Rotation Sensors Based on Highly Dispersive Resonating Structures

Zinan Wang, **Xiaomu Wu**, **Chao Peng**, **Rui Hui**,
Xuefeng Luo, **Zhengbin Li**, **and Anshi Xu**
State Key Laboratory on Advanced Optical Communication Systems & Networks
School of Electronics Engineering and Computer Science, Peking University, 100871, China

Abstract— Optical rotation sensors based on some highly dispersive resonating structures are expected to be highly sensitive. An example is the coupled-resonator-induced transparency based rotation sensor, which is analyzed to be highly sensitive and promising to be made in a compact size. We also propose an idea of combining highly dispersive medium and resonator structure together to further increase the sensing sensitivity. Electrodynamics for modeling the Sagnac effect is discussed. Its application in the Finite-Difference Time-Domain algorithm can be used to analyze, design and optimize rotation sensors. A spatial frequency spectrum analyzing method is suggested for macrocavity designing.

1. INTRODUCTION

Optical rotation sensors, which are also known as gyroscopes, are widely used for industrial and military purpose. They are key components in many applications such as aircrafts, satellites, and remote control devices. Improvements in designing rotation sensors are always important to achieve high sensitivity, compact size, and low power consumption. Over the past few decades, gyroscope designing based on different structures have been intensively studied [1–11], and highly dispersive structures are mostly considered [4–11].

The basic idea of a rotation sensor is to detect the phase shift induced by the Sagnac effect in a closed loop [1]. It is recognized that dispersion cannot influence the magnitude of the Sagnac effect [2, 12]. But there are different manifestations in highly dispersive medium and resonator structure. For rotation sensors based on highly dispersive medium, as Doppler effect is proposed to be the intrinsic reason to enhance their sensitivity, they suit only situations when relative motion exists between the interferometer and the medium [10]. But it's different for sensors based on highly dispersive resonating structures, such as coupled-resonator slow-light waveguide structures [9] and various photonic crystal geometries. These structures may possess huge Q-factor and they are extremely susceptible to the phase perturbation in the light path. The Sagnac effect will induce additional phase shift in the light path when such a structure is rotating, and then influence its response. The total phase shift will be enlarged as a result [10]. An example is the CRIT (coupled-resonator-induced transparency) structure, which has highly dispersive property with low absorption at its resonant frequency [13]. The gyroscope based on this structure is proved to be highly sensitive, and it has the potential to be made in a compact size [11]. The active CRIT structure, where the dispersion can be optically tailored, can further increase the performance of the CRIT based gyroscope [14].

As the Sagnac effect in a highly dispersive resonating structure is enhanced because the structure's response is extremely susceptible to the phase perturbation, an idea of combining highly dispersive medium and coupled resonator structure together is promising to further improve the enhancement.

Electrodynamics in rotating optical elements is quite useful in designing rotation sensors. This is widely used in modeling the Sagnac effect [8, 15–18]. One way of using it is the application in the Finite-Difference Time-Domain (FDTD) algorithm [18]. This FDTD method is a promising tool to accurately analyze, design and optimize rotation sensors.

The photonic crystal is a good medium for miniature gyroscopes [6, 8]. With carefully designing, photonic crystal microcavities may possess ultrahigh Q-Factor [27–29], which is beneficial to the sensitivity of rotation sensing. We suggest a new tool for designing microcavities utilizing spatial frequency spectrum analysis, which is promising to be effective.

The structure of the paper is as follows. In Section 2, we discuss different manifestations of the Sagnac effect in highly dispersive medium and resonator structure, and confirm that some highly dispersive resonating structure will enhance the sensibility of rotation sensors. In Section 3, we study the CRIT structure based rotation sensor. In Section 4, an idea of combining coupled

resonator structure with highly dispersive medium is proposed. In Section 5, we talk about electrodynamics in rotating frames for modeling the Sagnac effect, especially an FDTD method for device designing. In Section 6, we discuss a promising method for analyzing photonic microcavities. Finally, we provide our conclusion.

2. THE SAGNAC EFFECT IN HIGHLY DISPERSIVE STRUCTURES

The Sagnac-effect-induced phase shift in an arbitrary closed light path is given by [1]

$$\Delta\phi = \frac{4\omega A}{c^2}\Omega, \tag{1}$$

where ω is the optical (angular) frequency, c is the speed of light in vacuum, and A is the area enclosed by the light path. The phase shift does not depend on the shape of the area, the location of the center of rotation, and the presence of refracting corotating medium in the waveguide.

There had been a historical dispute on the interplay between the Sagnac effect and the Fresnel drag effect [19] since the first demonstration of an operating fiber optic gyroscope was reported by Vali and Shorthill in the 1970's [20]. It is finally recognized that dispersion can in no way influence the magnitude of the Sagnac effect [2, 12]. Leonhardt and Piwnicki analyzed the Sagnac effect in a highly dispersive medium on the premise of Doppler detuning [5]. Since the Sagnac effect in its pure form is in no way related to the Doppler effect [21], as Peng et al. pointed out [10], the dispersive medium cannot be utilized to enhance the absolute rotation induced Sagnac phase shift.

But the situation is different for highly dispersive resonating structures. This kind of structure may possess huge Q-factor and it is extremely susceptible to the phase perturbation in the light path. It makes light circulate in the closed loop cavity for many times, and every circulation contributes an additional phase shift because of the Sagnac effect. The structure's response should be influenced by this phase perturbation, as it's highly dispersive. Thus the Sagnac effect can be enhanced [10].

We can describe the response of a resonating structure in the form of transfer function [22]

$$H(\omega) = A(\omega)\exp[j\Phi(\omega)], \tag{2}$$

where $A(\omega)$ is the response of the amplitude, and $\Phi(\omega)$ is the response of the phase. For a lossless structure, $\mathrm{A}(\omega) \equiv 1$. Then the phase response can be expressed as

$$\Phi(\omega) = \tan^{-1}\left\{\frac{\mathrm{Im}[H(\omega)]}{\mathrm{Re}[H(\omega)]}\right\}. \tag{3}$$

The resonator is always structured by a series of basic elements, and then $H(\omega)$ can be written in the form of every basic element's transfer function. We can rewrite Eq. (3) as [10]

$$\Phi(\phi(\omega)) = \tan^{-1}\left\{\frac{\mathrm{Im}[H(\phi(\omega))]}{\mathrm{Re}[H(\phi(\omega))]}\right\}, \tag{4}$$

where $\phi(\omega)$ is the phase response for a single element. Further, we assume the resonator has reciprocity, and the input and output ports are symmetric. In any medium the absolute rotation related phase shift of single segment $d\vec{r}$ is given by [1]

$$\mathrm{d}(\Delta\phi) = \frac{\omega n^2}{c^2}(1-\alpha)\vec{V}\cdot\mathrm{d}\vec{r}, \tag{5}$$

where α is the Fresnel-Fizeau drag coefficient given by $\alpha = 1 - n^{-2}$, and $\vec{V}$ is the linear velocity of the segment. Here the phase shift is induced by the pure Sagnac effect of an absolute rotation. For a closed light path, the phase shift is given by Eq. (1).

The Sagnac phase shift can be treated as a perturbation to the structure's response, and then the phase shift of two counterdirection beams in a resonating structure can be calculated as [10]

$$\Delta\Phi = \Phi_+(\phi(\omega)+\Delta\phi) - \Phi_-(\phi(\omega)) = \frac{\partial\Phi}{\partial\phi}\Delta\phi = \frac{\partial\Phi/\partial\omega}{\partial\phi/\partial\omega}\Delta\phi, \tag{6}$$

where $\Delta\phi$ is the phase difference of the counterdirections in a single element induced by the Sagnac effect. The premise of this is the direction requirement [10], which allows every element to contribute the same sign of phase shift.

The total phase shift for a single element is

$$\phi(\omega) = \omega n_0 L/c + 2\omega\Omega A/c^2. \tag{7}$$

Two terms stand for the phase shift from propagating and the Sagnac effect respectively. For small Ω, $\Omega R \ll c$, the second term can be neglected. Then Eq. (6) becomes

$$\Delta\Phi = \frac{\partial\Phi/\partial\omega}{n_0 L/c}\Delta\phi = \frac{c/n_0}{L/(\partial\Phi/\partial\omega)}\Delta\phi. \tag{8}$$

As $\tau(\omega) = -(\partial\Phi/\partial\omega)$ is the group delay of the system, $v_g = L/\tau(\omega)$ is the group velocity, and $n_g = c/v_g$ is the group index, the phase shift for $\Delta\phi = (4\omega A/c^2)\Omega$ can be derived [10]:

$$|\Delta\Phi| = \frac{4\omega A}{c^2}\Omega\frac{n_g}{n_0}. \tag{9}$$

We can see the total phase shift is proportional to n_g, which represents the dispersion property of the whole system. The sensitivity of the rotation sensor can be enhanced notably utilizing resonating structure with high dispersion. The reason for the enhancement is not the Doppler effect, but the structure's response is susceptible with the Sagnac effect induced phase perturbation. For this perspective, highly dispersive resonation structures are good candidates in designing rotation sensors. A key limitation to the linear resonator systems comes from the delay-bandwidth product [23]. Therefore a trade-off between group index and bandwidth should be considered.

3. ROTATION SENSOR BASED ON THE CRIT STRUCTURE

One can only analyze the Sagnac effect following Eq. (9) when every basic element of the resonating structure contributes the same sign of perturbation to its response. That is the direction requirement [10]. But we can still calculate the phase response numerically without this requirement. Scheuer and Yariv [9] show qualitatively that a highly dispersive slow light structure enhances the Sagnac effect for a general case.

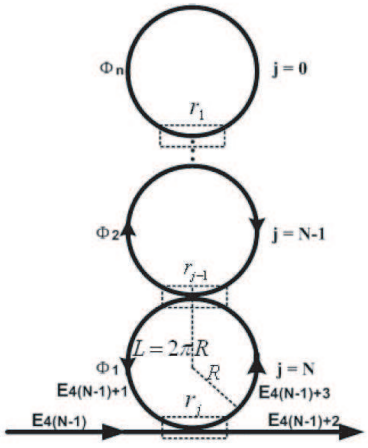

Figure 1: The CRIT configuration with N coupled optical resonator.

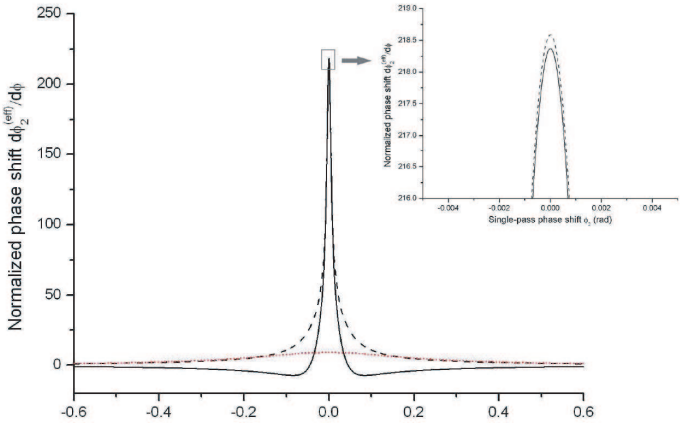

Figure 2: The Sagnac effect induced Normalized phase shift versus single-pass phase shift for the two rings configuration.

Another example of highly dispersive resonating structure is the coupled resonator waveguide based on the CRIT effect [13]. This structure exhibits similar behavior with an EIT medium, which has highly dispersive property with low absorption at resonant frequency. The perturbation of optical parameters induced by the Sagnac effect is equivalent to the perturbation of atomic parameters, and the structure is expected to achieve high sensitivity of rotation sensing as its highly dispersive property is considered [11]. The basic configuration of the CRIT structure is illustrated in Fig. 1.

The response of the CRIT structure can be described by the transfer function [13]

$$\tilde{\tau}_j(\phi_j,\, \phi_{j-1},\, \ldots,\, \phi_1) = \frac{r_j - a_j\tilde{\tau}_j e^{i\phi_j}}{1 - r_j a_j \tilde{\tau}_j e^{i\phi_j}}, \quad \tilde{\tau}_0 = 1, \quad \phi_0 = 0, \tag{10}$$

where r_j is the reflection coefficient of the coupler, ϕ_j is the single-pass phase shift, and a_j is the attenuation factor for the jth ring. When the device is mounted in a rotating frame, the most straightforward way to evaluate the relative phase shift induced by the Sagnac effect is to follow the effective phase shift $\tilde{\phi}_j^{(eff)} \equiv \arg(\tilde{\tau}_j)$, as [11]

$$\begin{aligned} \Delta\tilde{\phi}_j^{(eff)} \;=\; & \tilde{\phi}_{j,+}^{(eff)}(\phi_j + \Delta\phi_j,\, \phi_{j-1} + \Delta\phi_{j-1},\, \ldots,\, \phi_1 + \Delta\phi_1) \\ & -\tilde{\phi}_{j,-}^{(eff)}(\phi_j - \Delta\phi_j,\, \phi_{j-1} - \Delta\phi_{j-1},\, \ldots,\, \phi_1 - \Delta\phi_1), \end{aligned} \tag{11}$$

where $\Delta\phi_j$ is the phase perturbation induced by the Sagnac effect in the jth resonator, and two directions are notated as subscript "$\pm$". As for the N-rings configuration in sign, in which the rings are of the same size, $\Delta\phi_j$ is of the same value in quantity but different in sign, because the beams propagate in different directions according to the respective number of resonator, odd or even. Under the "direction requirement", the phase shift can be "summed up" as [11]

$$\Delta\tilde{\phi}_j^{(eff)} = \frac{\partial\tilde{\phi}_j^{(eff)}}{\partial\phi}\Delta\phi \tag{12}$$

The normalized phase shift is defined as the ratio of the effective Sagnac phase shift between input and output ports and the Sagnac-effect-induced phase shift in the single resonator. It represents the enhancement of the Sagnac effect contributed by the CRIT structure. For two rings configuration, the result is plotted in Fig. 2 [11]. The result following the dispersion relation (black dashed curve) and straightforward numerical calculation from transfer function (solid curve) are in similar curve shape, especially near the resonance. Comparing the performance of the CRIT structure with a usual passive single resonator (red dot curve), under the condition that the linear geometrical size and the minimal optical attenuation are identical, we can find that the Sagnac effect is notably enhanced.

Dumeige et al. demonstrated experimentally coupled active-resonator-induced transparency in a fiber system [14]. The active CRIT structure, where the dispersion can be optically tailored, can further increase the performance of the CRIT based gyroscope.

4. COUPLED RESONATOR STRUCTURE COMBINED WITH HIGHLY DISPERSIVE MEDIUM

As we discussed in Section 2, the high dispersion property of medium cannot enhance the absolute rotation induced Sagnac phase shift. But the effect can be enhanced notably in a resonating structure with high dispersion, because its response is susceptible with the phase perturbation. If several basic elements of a resonating structure are filled with highly dispersive medium, it is promising to further improve this enhancement.

The transfer function of a coupled resonator structure is expressed by Eq. (10), where $\phi_j = \omega n_0 L/c$ is the phase shift for a single loop. n_0 is refractive index, which is calculated as a constant in our discussions in Eq. (7). When some basic element is filled with highly dispersive medium, n_0 should be replaced by $n(\omega)$. The result of $\partial\phi/\partial\omega$ in Eq. (6) will no more simply be $n_0 L/c$, and the final $|\Delta\Phi|$ will change. From this perspective, an appropriate design of this kind of structure may further enlarge the magnitude of $|\Delta\Phi|$. This combination of coupled resonator structure with highly dispersive medium is another promising way to enhance the sensitivity of rotation sensing.

This idea has not been explicitly proved yet. And there are several practical problems to deal with. For example, a large dispersion is usually accompanied by strong absorption, which will limit the performance of a device. So it is necessary to carry on studying on this to make it practical.

5. ELECTRODYNAMICS FOR MODELING OPTICAL GYROSCOPES

Electrodynamics in rotating optical elements is widely used in modeling the Sagnac effect [8, 15–18], and several methods have been proposed. These are important tools when designing a rotation sensor.

In conventional waveguide, the Sagnac phase shift can be calculated by using an integral over the light path [10]. The response of a structure in rotation frame can be analyzed following the transfer function, while taking into account the Sagnac phase shift along each light path [9–11]. Another analytic model for analyzing the Sagnac effect in micro-cavity structures was proposed [6, 8, 24, 25]. For single resonant cavity, a wave-dynamical approach can be applied, and a tight-binding approximation assuming weak-coupling between micro-cavities can be used to deal with the case of multiple resonant cavities. Furthermore, the two-dimensional Green's function theory was proposed for electrodynamics of a rotating medium [26], which represents the response to a point source. It provides a systematic tool for the general study of the spectral properties of rotating systems.

Each of these methods can solve some specific problems but still has limitations [18]. For example, the transfer function method provides a phenomenological way to model the device. However, some parameters such as reflection coefficient and attenuation factor are difficult to determine when designing a device. Numerical algorithms can thus provide a vital tool to accurately analyze, design and optimize a rotation sensitive optical device.

The FDTD method is one of numerical algorithms to solve the problem talked above. It is proposed to simulate the Sagnac effect from the real physical parameters, such as dielectric property and geometry size [18]. The basic idea is to modify Maxwell equations with adding the terms describing the Sagnac effect. Up to the first order in velocity the constitutive relations in the rotating frame take on the form [15–17]:

$$\begin{aligned} \vec{D} &= \varepsilon\vec{E} - c^{-2}\Omega \times \vec{r} \times \vec{H} \\ \vec{B} &= \mu\vec{H} + c^{-2}\Omega \times \vec{r} \times \vec{E} \end{aligned} \tag{13}$$

Maxwell equations in rotation frame keep their basic forms as:

$$\begin{aligned} \frac{\partial \vec{D}}{\partial t} &= \nabla \times \vec{H} - \vec{J} & \vec{J} &= \overrightarrow{J_S} + \sigma\vec{E} \\ \frac{\partial \vec{B}}{\partial t} &= -\nabla \times \vec{E} - \vec{M} & \vec{M} &= \overrightarrow{M_S} + \sigma_m\vec{H} \end{aligned} \tag{14}$$

The FDTD method can be derived by discretizing Maxwell equations Eq. (14) with the new constitutive relation Eq. (12), and it is proved to be effective [18].

6. SPATIAL FREQUENCY SPECTRUM ANALYSIS OF PHOTONIC MICROCAVITIES

The photonic crystal is a good medium for miniature gyroscopes [6, 8]. A photonic crystal microcavity possessing an ultrahigh Q-Factor is beneficial to the sensitivity of rotation sensing. A cavity mode field with a Gaussian envelope is the key requirement for realizing a high-Q photonic microcavity, and a concept of "photonic multiheterostructures" has been proposed as a method to tune the envelope function of a cavity [27]. Past progress in achieving high Q-factor is based on variation of the lattice constant [27–29]. But it is still not easy to derive a proper lattice constant for a practical cavity, without varying the lattice constant continuously. We need a more reasonable method to analyze a photonic cavity structure.

The substantial problem to analyze is the relationship between electronic mode field and the distribution of dielectric constant of a cavity $\varepsilon(\vec{r})$. We can describe a plane structure using its spatial frequency spectrum instead of parameter distributions in real space. It could be a more comprehensive tool to analyze the relationship clearly. For example, we can use the Fourier transform (FT)

$$\hat{\varepsilon}(\omega_S) = F[\varepsilon(\vec{r})], \tag{15}$$

where ω_S is the spatial frequency of the structure. The spectrum $\hat{\varepsilon}(\omega_S)$ will conclude all the information of the distribution of dielectric constant in a 2-dimentional space (a plane). $\hat{\varepsilon}(\omega_S)$ can be used to analyze the structure's influence on light of different wavelengths instead of $\varepsilon(\vec{r})$, and it is much more easier. Then we may explain more reasonably how electronic mode fields vary with parameters of a cavity, such as the lattice constant.

More generally, we can use the wavelet transform instead of the Fourier transform for the analysis. Wavelets are functions generated from one single function by dilations and translations

$$\psi_{a,\,b}(t) = |a|^{-1/2}\psi\left(\frac{t-b}{a}\right), \tag{16}$$

where $\psi(t)$ is the *mother wavelet*, a represents a time dilation, and b represents a time translation. The Fourier transform of $\psi_{a,b}(t)$ is $\hat{\psi}_{a,b}(\omega)$, and the basic form of the continuous wavelet transform (CWT) in time domain goes as

$$Wf(a,b) = |a|^{-1/2} \int_{-\infty}^{+\infty} f(t)\psi^* \left(\frac{t-b}{a}\right) dt. \tag{17}$$

Its definition form in frequency domain is

$$Wf(a,b) = \frac{1}{2\pi} \int_{-\infty}^{+\infty} \hat{f}(\omega)\hat{\psi}_{a,b}(\omega) d\omega. \tag{18}$$

The use of an appropriate *mother wavelet* to decode the spatial frequency of the cavity structure may make this analysis easy and clear.

This method is a novel idea we are still working on.

7. CONCLUSIONS

The Sagnac effect can be enhanced in some highly dispersive resonating structures, and it is also different from its classical form in some other novel photonic structures. It reveals the potential improvement of rotation sensors' performance. Further study on designing rotation sensors is still attractive and necessary. With carefully designing, new rotation sensors may have all-solid configuration, compact size and high sensitivity.

REFERENCES

1. Post, E. J., "Sagnac effect," *Rev. Mod. Phys.*, Vol. 39, 475–493, 1967.
2. Arditty, H. J. and H. C. Lefevre, "Sagnac effect in fiber gyroscopes," *Opt. Lett.*, Vol. 6, 401–403, 1981.
3. Bergh, R. A., H. C. Lefevre, and H. J. Shaw, "An overview of fiber-optic gyroscopes," *J. Lightwave Technol.*, Vol. 2, 91–107, 1984.
4. Lefevre, H. C., *The Fiber-Optic Gyroscope*, Artech House Publishers, 1993.
5. Leonhardt, U. and P. Piwnitski, "Ultrahigh sensitivity of slow-light gyroscope," *Phys. Rev. A*, Vol. 62, 055801, 2000.
6. Steinberg, B. Z., "Rotating photonic crystals: A medium for compact optical gyroscopes," *Phys. Rev. E*, Vol. 71, 056621, 2005.
7. Matsko, B., A. A. Savchenkov, V. S. Ilchenko, and L. Maleki, "Optical gyroscope with whispering gallery mode optical cavities," *Opt. Commun.*, Vol. 233, 107–112, 2004.
8. Steinberg, B. Z. and A. Boag, "Splitting of microcavity degenerate modes in rotating photonic crystals — the miniature optical gyroscopes," *J. Opt. Soc. Am. B*, Vol. 24, 142–151, 2006.
9. Scheuer, J. and A. Yariv, "Sagnac effect in coupled-resonator slow-light waveguide structures," *Phys. Rev. Lett.*, Vol. 96, 053901, 2006.
10. Peng, C., Z. Li, and A. Xu, "Rotation sensing based on a slow light resonating structure with high group dispersion," *Appl. Opt.*, Vol. 19, 4125–4131, 2007.
11. Peng, C., Z. Li, and A. Xu, "Optical gyroscope based on a coupled resonator with the all-optical analogous property of electromagnetically induced transparency," *Appl. Opt.*, Vol. 15, 3864–3875, 2007.
12. Leeb, W. R., G. Schiffner, and E. Scheiterer, "Optical fiber gyroscopes: Sagnac or Fizeau effect," *Appl. Opt.*, Vol. 18, 1293–1295, 1979.
13. Smith, D., H. Chang, K. A. Fuller, A. T. Rosenberger, and R. W. Boyd, "Coupled-resonator-induced transparency," *Phys. Rev. A*, Vol. 69, 063804, 2004.
14. Dumeige, Y., T. Nguyên, L. Ghişa, S. Trebaol, and P. Féron, "Measurement of the dispersion induced by a slow-light system based on coupled active-resonator-induced transparency," *Phys. Rev. A*, Vol. 78, 013818, 2008.
15. Shiozawa, T., "Phenomenological and electron-theoretical study of the electrodynamics of rotating systems," *Proc. IEEE*, Vol. 61, 1694–1702, 1973.

16. Anderson, J. L. and J. W. Ryon, "Electromagnetic radiation in accelerated systems," *Phys. Rev.*, Vol. 181, 1765–1775, 1969.
17. Van Bladel, J., *Relativity and Engineering*, Springer, Berlin, 1984.
18. Peng, C., R. Hui, X. Luo, Z. Li, and A. Xu, "Finite-difference time-domain algorithm for modeling Sagnac effect in rotating optical elements," *Appl. Opt.*, Vol. 8, 5277–5290, 2008.
19. Vali, V., R. W. Shorthill, and M. F. Berg, "Fresnel-Fizeau effect in a rotating optical fiber ring interferometer," *Appl. Opt.*, Vol. 16, 2605–2607, 1977.
20. Vali, V. and R. W. Shorthill, "Fiber ring interferometer," *Appl. Opt.*, Vol. 15, 1099–1100, 1976.
21. Malykin, G. B., "The Sagnac effect: Correct and incorrect explanations," *Physics-Uspekhi*, Vol. 43, 1229–1252, 2000.
22. Madsen, C. K. and G. Lenz, "Optical all-pass filters for phase response design with applications for dispersion compensation," *IEEE Photon. Technol. Lett.*, Vol. 10, 994–996, 1998.
23. Lenz, G., B. J. Eggleton, C. K. Madsen, and R. E. Slusher, "Optical delay lines based on optical filters," *IEEE J. Quantum Electron.*, Vol. 37, 525–532, 2001.
24. Sunada, S. and T. Harayama, "Sagnac effect in resonant microcavities," *Phys. Rev. A*, Vol. 74, 021801, 2006.
25. Sunada, S. and T. Harayama, "Design of resonant microcavities: Application to optical gyroscopes," *Opt. Express*, Vol. 15, 16245–16254, 2007.
26. Steinberg, B. Z., A. Shamir, and A. Boag, "Two-dimensional Green's function theory for the electrodynamics of a rotating medium," *Phys. Rev. E*, Vol. 74, 016608, 2006.
27. Asano, T., B. Song, Y. Akahane, and S. Noda, "Ultrahigh-Q nanocavities in two-dimensional photonic crystal slabs," *IEEE J. Quantum Electron.*, Vol. 12, 1123–1134, 2006.
28. Song, B., T. Asano, and S. Noda, "Heterostructures in two-dimensional photonic-crystal slabs and their application to nanocavities," *J. Phys. D*, Vol. 40, 2629–2634, 2007.
29. Tanaka, Y., T. Asano, and S. Noda, "Design of photonic crystal nanocavity with Q-factor of 109," *J. Lightwave Technology*, Vol. 26, 1532–1539, 2008.

Theoretical and Numerical Study of Surface Waves in a Grounded Slab Waveguide of Biaxially Anisotropic Metamaterial

Salma Mirhadi and Manoochehr Kamyab Hessari
Department of Electrical Engineering, K. N. Toosi University of Technology, Tehran, Iran

Abstract— In this paper, first, we theoretically demonstrate a grounded slab of biaxially anisotropic metamaterial can support surface waves. Specific conditions for the existence of surface waves at the interface of the slab are investigated using graphical method, and it is shown that these conditions are greatly dependent on the tensor components of the constitutive parameters. Then, the finite-difference time-domain (FDTD) method based on the piecewise linear recursive convolution algorithm (PLRC) in conjunction with the convolutional perfectly matched layered (CPML) is employed to verify theoretical results. Furthermore, the FDTD method provides a means for visualizing propagation of surface waves at the interface of slab.

1. INTRODUCTION

Recent years have seen a remarkable attention in properties and applications of metamaterials, consisting of the periodic arrangement of metallic rods and split-rings [1–6]. Since the realization of 3D isotropic metamaterial structures may be difficult, considerable researches have been done to find out the exotic electromagnetic properties in anisotropic metamaterials [3, 4]. So far, a lot of attention has been drown to investigate unusual electromagnetic behaviors in an anisotropic metamaterial slab such as excitation of surface waves with imaginary transverse wavenumbers [5]. The energy of surface waves is concentrated at the interface of the left handed slab and the conventional right handed media (RHM); therefore, they can have useful applications in communication systems provided that these structures can be realized [6].

In this paper, we have investigated the possibility of supporting the surface waves in a grounded slab of biaxially anisotropic metamaterial excited by a line source. On the basis of the simple graphical method, sufficient conditions for existing of surface waves will be presented. Moreover, the finite difference time domain (FDTD) method is used to analyze the electromagnetic behavior of surface waves at the interface of metamaterial grounded slab and RHM.

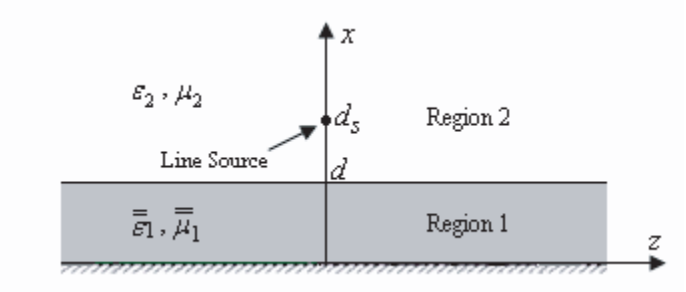

Figure 1: Geometry of an anisotropic grounded slab waveguide.

2. THEORY

The geometry under study is shown in Fig. 1. Region 1 ($0 < x < d$) is assumed to be a biaxially anisotropic slab placed on a perfectly conducting ground plane with the permittivity as $\bar{\bar{\varepsilon}}_1 = \varepsilon_{1x}\hat{x}\hat{x} + \varepsilon_{1y}\hat{y}\hat{y} + \varepsilon_{1z}\hat{z}\hat{z}$ and permeability as $\bar{\bar{\mu}}_1 = \mu_{1x}\hat{x}\hat{x} + \mu_{1y}\hat{y}\hat{y} + \mu_{1z}\hat{z}\hat{z}$, while region 2 ($x > d$) is considered to be a semi-infinite RHM with the permittivity ε_2 and permeability μ_2. An electric line source I, which excites transverse electric (TE) modes, is located at the ($x = d_s,\ z = 0$) in the right handed region. It is easily shown that the electric field can be expressed as an integral sum

of planar waves given by the following expression:

$$E_{2y}(x,\,z) \;=\; -\frac{\omega\mu I}{4\pi}\int\limits_{-\infty}^{+\infty} e^{-jk_z z}\frac{1}{k_{2x}}\left(e^{-jk_{2x}|x-d_s|}+A_2 e^{-jk_{2x}x}\right)d_{k_z} \tag{1}$$

$$E_{1y}(x,\,z) \;=\; -\frac{\omega\mu I}{4\pi}\int\limits_{-\infty}^{+\infty} e^{-jk_z z}\frac{1}{k_{2x}}\left(A_1 e^{-jk_{1x}x}+B_1 e^{jk_{1x}x}\right)d_{k_z} \tag{2}$$

where k_{1x} and k_{2x} are the transverse wavenumbers along the x direction in region 1 and 2 respectively, and k_z is the longitudinal wavenumber along the z direction. A_1 and B_1 represent coefficients of forward and backward waves in region 1, and A_2 represents coefficient of forward waves in region 2. The first term in Eq. (1), which describes the field emitted by the line source, can be evaluated as $-(\omega\mu I/4)H_0^{(2)}(k_2 R)$, where $R=\sqrt{(x-d_s)^2+z^2}$, $k_2=\omega\sqrt{\mu_2\varepsilon_2}$, and $H_0^{(2)}(k_2R)$ is the Hankel function of the second kind [7]. The dispersion relations for the two regions are separately:

$$k_{2x}^2+k_z^2 \;=\; \omega^2\mu_2\varepsilon_2 \tag{3}$$

$$k_{1x}^2+\frac{\mu_{1z}}{\mu_{1x}}k_z^2 \;=\; \omega^2\mu_{1z}\varepsilon_{1y} \tag{4}$$

For the surface waves with evanescent fields on both sides of the interface, both k_{1x} and k_{2x} become imaginary. Therefore, we consider $k_{1x}=-j\alpha_{1x}$ and $k_{2x}=-j\alpha_{2x}$, where $\alpha_{1x}>0$ and $\alpha_{2x}>0$. Using boundary conditions on the perfectly conducting surface at $x=0$ and the slab interface at $x=d$, we can obtain the equation of the guidance of surface waves as:

$$-\frac{\alpha_{1x}}{\mu_{1z}}\coth(\alpha_{1x}d)=\frac{\alpha_{2x}}{\mu_2} \tag{5}$$

where

$$\alpha_{2x} \;=\; \sqrt{k_z^2-\omega^2\mu_2\varepsilon_2} \tag{6}$$

$$\alpha_{1x} \;=\; \sqrt{\frac{\mu_{1z}}{\mu_{1x}}k_z^2-\omega^2\mu_{1z}\varepsilon_{1y}} \tag{7}$$

α_{1x}, α_{2x}, μ_2 and hyperbolic cotangent function in Eq. (5) always are positive, so there is no real solution for Eq. (5) unless $\mu_{1z}<0$. We conclude that surface waves can be supported only by the anisotropic metamaterial grounded slab. After determination of the sign of the μ_{1z}, we will discuss the problem based on the four possible cases for the sign of the other components of the permittivity and permeability. We are interested in the sign of the μ_{1x} and ε_{1y} here because the dispersion relation in Eq. (7) is only dependent upon those parameters for TE modes.

Case I: $\varepsilon_{1y}>0$ and $\mu_{1x}>0$

In such a case, for certain choice of the frequency and the slab thickness, the α_{1x} and α_{2x} versus k_z are plotted in Fig. 2(a) in the dashed-dotted and solid line respectively. α_{2x} in Eq. (6) is defined for $k_z>k_2=\omega\sqrt{\varepsilon_2\mu_2}$ and describes hyperbola with the horizontal axis which intersects transverse axis k_z at k_2, while α_{1x} in Eq. (7) is defined for $k_z<\omega\sqrt{\mu_{1x}\varepsilon_{1y}}$ and represents ellipse, as we can see in Fig. 2(a). Two conditions for supporting surface waves must be satisfied. 1) Both α_{1x} and α_{2x} must be positive, so $\sqrt{\mu_2\varepsilon_2}<\sqrt{\mu_{1x}\varepsilon_{1y}}$. 2) A solution to Eq. (5) for k_z satisfies inequality $\omega\sqrt{\mu_2\varepsilon_2}<k_z<\omega\sqrt{\mu_{1x}\varepsilon_{1y}}$.

Case II: $\varepsilon_{1y}<0$ and $\mu_{1x}>0$

In this case, the expression $\mu_{1z}/\mu_{1x}k_z^2-\omega^2\mu_{1z}\varepsilon_{1y}$ is always negative; therefore, α_{1x} is undetermined for every value of k_z in Eq. (7). In fact, such a structure cannot support guided modes with imaginary transverse wavenumbers.

Case I: $\varepsilon_{1y}>0$ and $\mu_{1x}<0$

In such a case, the curve of α_{1x} versus k_z that Eq. (7) stands for is hyperbola with vertical axis, as shown in Fig. 2(b) in the dash-dotted line. However, the curve of α_{2x} remains the same as Case I. α_{1x} is positive for every value of k_z, but α_{2x} is defined for $k_z>k_2$. When Eq. (5) has a solution for k_z that satisfies $k_z>k_2$, the surface waves can exist.

Case IV: $\varepsilon_{1y} < 0$ and $\mu_{1x} < 0$

Both α_{1x} and α_{2x} represent hyperbola with horizontal axis in this case, as illustrated in Fig. 2(c). α_{1x} is defined for $k_z > \omega\sqrt{\mu_{1x}\varepsilon_{1y}}$, and α_{2x} is defined for $k_z > k_2$. A solution to Eq. (5) for k_z must be satisfied $k_z > \max(\omega\sqrt{\varepsilon_{1y}\mu_{1x}},\ \omega\sqrt{\varepsilon_2\mu_2})$, which ensures the existence of the surface waves.

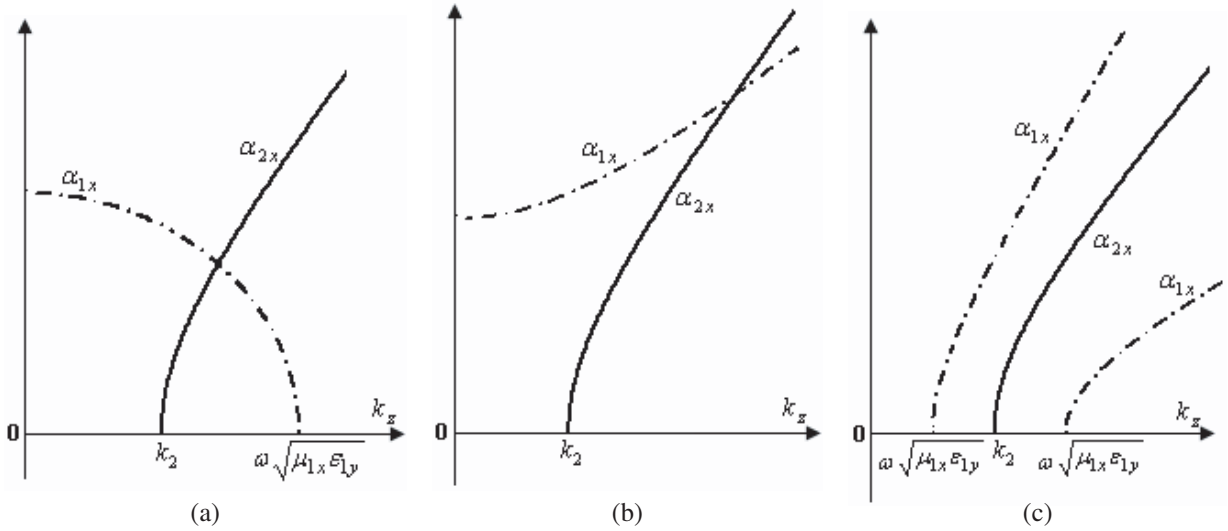

Figure 2: Graphical representation of the α_{1x} versus k_z in Eq. (7) (dash-dotted line) and the α_{2x} versus k_z in Eq. (6) (solid Line). (a) Case I, (b) Case III, (c) Case IV.

3. EXAMPLES AND NUMERICAL RESULTS

The FDTD method has been widely used for modeling of transient wave propagation in the metamaterial with anisotropic and dispersive constitutive parameters. In this section, we have employed 2D FDTD based on the piecewise linear recursive convolution (PLRC) algorithm to confirm validity of theoretical analysis in the pervious section [8]. The FDTD grid unit cells have a square side length of $\Delta = \lambda_0/30$ where λ_0 is the free space wavelength at the frequency of $f_0 = 10\,\text{GHz}$. We have considered 210 cells in z-direction, which translated to a FDTD grid of $7\lambda_0$, and 40 cells in x-direction. The convolutional perfectly matched layered, which is derived from the complex frequency-shifted formulation [9], with ten layers thickness is used to terminate computational domain at z-direction and $+x$-direction and is designed to have reflection of less than $-60\,\text{dB}$. The electric line source is located five cells above the slab interface in the RHM region, and sinusoidal excitation at the frequency of $f_0 = 10\,\text{GHz}$ is used. Negative permittivity and permeability for FDTD simulation can be realized with the Lorentz dispersion relation as:

$$\varepsilon(\omega) = \varepsilon_o\left(1 - k_e^2\frac{\omega^2}{\omega^2 - \omega_e^2 - j2\delta_e\omega}\right) \tag{8}$$

$$\mu(\omega) = \mu_o\left(1 - k_h^2\frac{\omega^2}{\omega^2 - \omega_h^2 - j2\delta_h\omega}\right) \tag{9}$$

The parameters $k_{e,h}$ and $\omega_{e,h}$ have been chosen such that the desired negative values of permittivity and permeability at $f_0 = 10\,\text{GHz}$ are provided. In the previous analysis, we have assumed that the anisotropic metamaterials are lossless. However, all realistic metamaterial structures are lossy; therefore, we have considered the slab is slightly lossy in FDTD simulation and chosen $\delta_{e,h} = 0.001\omega_{e,h}$. It can be shown that the slight loss will not affect the results significantly.

In the first example, we have simulated the structure as discussed in Case I to confirm our theoretical analysis. We assume $d = 1\,\text{cm}$, $\varepsilon_{1y} = 2\varepsilon_o$, $\mu_{1x} = 2\mu_o$, $\mu_{1z} = (-1 - j0.0138)\mu_o$, $\varepsilon_2 = \varepsilon_o$ and $\mu_2 = \mu_o$. It can be shown that one solution to Eq. (5) for k_z is $k_z = (1.4292 - j0.0038)k_2$. With these chosen parameters, the conditions of Case I are satisfied; consequently, surface waves must exist. From Fig. 3, we see that the electric field cannot penetrate into the grounded slab and concentrate at the interface as theory predicts.

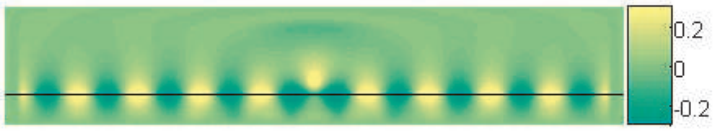

Figure 3: Electric filed distribution of surface waves at the interface of slab in Case I. Slab boundaries are indicated by dark line in figure. $d = 1\,\text{cm}$, $\varepsilon_{1y} = 2\varepsilon_o$, $\mu_{1x} = 2\mu_o$, $\mu_{1z} = (-1 - j0.0138)\mu_o$, $\varepsilon_2 = \varepsilon_o$, $\mu_2 = \mu_o$.

In the second example, to confirm validity of theoretical result in Case II, we have considered $\varepsilon_{1y} = (-0.5 - j0.0074)\varepsilon_o$ and $\mu_{1x} = \mu_o$. Other parameters are the same as the first example. The numerical result as well as the theoretical result shows that the grounded slab cannot support surface waves (see Fig. 4). Electromagnetic fields are transmitted along the grounded slab as guided modes.

Figure 4: Surface wave cannot be supported by anisotropic grounded slab in Case II. $d = 1\,\text{cm}$, $\varepsilon_{1y} = (-0.5 - j0.0074)\varepsilon_o$, $\mu_{1x} = \mu_o$, $\mu_{1z} = (-1 - j0.0138)\mu_o$, $\varepsilon_2 = \varepsilon_o$, $\mu_2 = \mu_o$.

In the third example, propagation of surface waves at the interface of slab and RHM region has been illustrated in Fig. 5, as we have discussed in Case III. Here, we have chosen $\mu_{1x} = (-2 - j0.035)\mu_o$ and the other parameters are the same as the first example. One solution to Eq. (5) equals to $k_z = (2.448 - j0.0428)k_2$ which satisfies the condition of Case III.

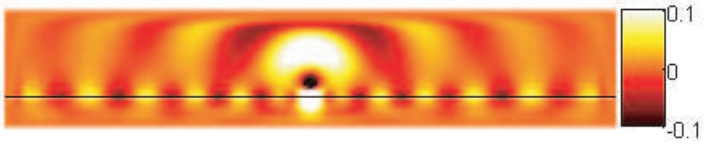

Figure 5: Electric filed distribution of surface waves at the interface of slab in Case III as theory predicts. $d = 1\,\text{cm}$, $\varepsilon_{1y} = 2\varepsilon_o$, $\mu_{1x} = (-2 - j0.0329)\mu_o$, $\mu_{1z} = (-1 - j0.0138)\mu_o$, $\varepsilon_2 = \varepsilon_o$, $\mu_2 = \mu_o$.

For last simulation, the waveguide has been simulated as discussed in Case IV. We have selected $\mu_{1x} = (-1.5 - j0.022)\mu_o$ and $\varepsilon_{1y} = (-0.5 - j0.0074)\varepsilon_o$, and the other parameters are the same as those in the first example. It can be easily shown that one solution to Eq. (5) is $k_z = (1.33 - j0.0322)k_2$ satisfying the condition of Case IV. Therefore, surface waves must exist. The excitation of surface waves has been clearly demonstrated in Fig. 6.

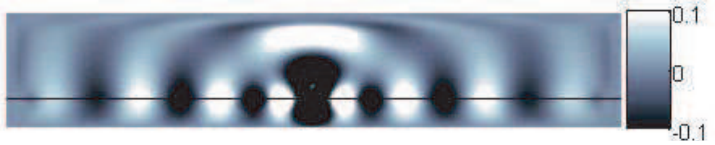

Figure 6: Electric field distribution of surface waves in Case IV. $d = 1\,\text{cm}$, $\varepsilon_{1y} = (-0.5 - j0.0074)\varepsilon_o$, $\mu_{1x} = (-1.5 - j0.022)\mu_o$, $\mu_{1z} = (-1 - j0.0138)\mu_o$, $\varepsilon_2 = \varepsilon_o$, $\mu_2 = \mu_o$.

4. CONCLUSION

Surface waves propagation in the biaxially anisotropic grounded slab waveguide has been studied theoretically and numerically. We have investigated three possible conditions for supporting TE surface waves, which localizes the field at the interface of the waveguide. Dispersive FDTD simulations based on the PLRC algorithm are in accordance with theoretical results.

ACKNOWLEDGMENT

This work is supported by the Iran Telecommunication Research Center (ITRC), and we would like to thank them for their helps.

REFERENCES

1. Pendry, J. B, A. J. Holden, D. J. Robbins, and W. J. Stewart, "Magnetism from conductors and enhanced nonlinear phenomena," *IEEE Trans. Microwave Theory Tech.*, Vol. 47, No. 11, 2075–2084, Nov. 1999.
2. Shebly, R. A., D. R. Smith, and S. Schultz, "Experimental verification of a negative index of refraction," *Science*, Vol. 292, 77–79, Apr. 2001.
3. Lindell, I. V. and S. Ilvonen, "Waves in a slab of uniaxial BW medium," *Journal of Electromagnetic Waves and Applications*, Vol. 16, No. 3, 303–318, 2002.
4. Liu, S. H., C. H. Liang, W. Ding, L. Chen, and W. T. Pan, "Electromagnetic wave propagation through a slab waveguide of uniaxially anisotropic dispersive metamaterial," *Progress In Electromagnetic Research*, PIER 76, 467–475, 2007.
5. Cheng, Q. and T. J. Cui, "Infinite guided modes in a planar waveguide with a biaxially anisotropic metamaterial," *J. Opt. Soc. Am. A*, Vol. 23, No. 8, 1989–93, 2006.
6. Ishimaru, A., S. Jaruwatanadilok, and Y. Kuga, "Generalized surface Plasmon resonance sensors using metamaterials and negative index materials," *Progress In Electromagnetic Research*, PIER 51, 139–152, 2005.
7. Uzunoglu, N. K. and J. Fikioris, "Scattering from an inhomogenity inside a dielectric-slab waveguide," *J. Opt. Soc. Am.*, Vol. 72, 628–637, 1982.
8. Mosallaei, H., "FDTD-PLRC technique for modeling of anisotropic-dispersive media and metamaterial devices," *IEEE Trnas. Electromagn. Compat.*, Vol. 49, No. 3, 649–60, 2007.
9. Toflove, A. and S. C. Hagness, *Computational Electrodynamics: The Finite-Difference Time-Domain Method*, 3rd ed., Artech House, Norwood, MA, 2005.

A New Method for Imaging Avian Based on Frequency-stepped Chirp Signal

Feng Zhu[1], **Yong Wu**[2], **You-Qian Feng**[1], **You-Qing Bai**[1], **and Qun Zhang**[3, 4]

[1]Institute of Science, AFEU, Xi'an 710051, China
[2]Shaanxi Institute of Metrology Science, Xi'an 710048, China
[3]Institute of Telecommunication Engineering, AFEU, Xi'an 710077, China
[4]Key Laboratory of Wave Scattering and Remote Sensing Information (Ministry of Education)
Fudan University, Shanghai 200433, China

Abstract— It is very important for the security and development of human's aviation as well as the development of avian ecology and the prevention from avian influenza that avian could be imaged by ISAR (Inverse Synthesis Aperture Radar) with frequency-stepped chirp high-resolution radar. In the paper, a new imaging method for avian targets is proposed, by which ISAR image quality can be improved obviously. In the method, the different parts of bird's gliding spectrogram are connected and the minimum waveform entropy criterion is employed for phase compensation. The feasibility and effectiveness of the methods are proved by simulation results.

1. INTRODUCTION

Nowadays, it is quite significant for security and development of human's aviation that avian can be detected and monitored at real time. Radar is an important tool for observing birds' activities availably [1–3], which is all-weather and round-the-clock effective for observing birds within air fields widely. However, with the development of modern signal processing and high-speed computer technology, it becomes a novel and important approach for the development of avian ecology and the prevention from avian influenza that avian can be imaged and identified accurately and successfully based on high-resolution ISAR imaging technology. Because of small size of birds, it needs that signals transmitted by radar with several GHz bandwidths for achieving their enough high range-resolution during their imaging. Frequency-stepped chirp signal is a kind of high-resolution range signal with some special advantages such as little instantaneous bandwidth and the virtue in synthesizing large bandwidth, and is considered as the major signal format to image for birds [4, 5].

The bird's moving status contains gliding and flapping status [6]. Because its moving velocity is generally comparatively slow, it must fly determinate distances which are required for imaging to achieve necessary cross-range resolution during ISAR imaging. During this process, alternating changes between gliding status and flapping status would take place usually. However, the ISAR images with traditional RD algorithm [6, 7] could be contaminated due to serious micro-Doppler effects [8–10] generated by birds' flapping wings. Thus, a new method of imaging for birds is proposed in the paper, on the basis of identifying bird's moving status accurately. In the method, the different parts of bird's gliding spectrogram [6, 7] are connected without the flapping spectrogram and the minimum waveform entropy criterion is employed for phase compensation to reach focusing level optimality of ISAR image. Finally, a comparatively clear ISAR image can be achieved.

2. ISAR IMAGING BY FREQUENCY-STEPPED CHIRP TECHNOLOGY

Frequency-stepped chirp signal transmitted by radar is made up of a series of bursts [4, 5]. Each burst consists of a series of periodical chirp sub-pulses. The sub-pulses in a burst are all chirps with stepped carrier frequency. Suppose each burst consists of N sub-pulses, frequency-stepped size is Δf, sub-pulse duration is T_1, and pulse repetition interval is T_r. The ith sub-pulse of a burst transmitted by the radar is

$$s_i(t) = \text{rect}\left(\frac{t}{T_1}\right) \cdot \exp\left(j2\pi\left(\left(f_c + i\Delta f\right)t + \frac{\mu}{2}t^2\right)\right), \quad i = 1, 2, \ldots, N \tag{1}$$

where $\text{rect}(t) = 1$, when $-1/2 \le t \le 1/2$. And $f_c + i\Delta f$ is the carrier frequency of ith sub-pulse, μ is chirp slope of sub-pulse. The returned signal is

$$s_r(t, i) = \sigma \cdot \text{rect}\left(\frac{t - 2R/c - iT_r}{T_1}\right) \cdot \exp\left(j\pi\mu\left(t - \frac{2R}{c}\right)^2\right) \cdot \exp\left(j2\pi(f_c + i\Delta f)\left(t - \frac{2R}{c}\right)\right) \tag{2}$$

where R is the distance between scatterer and radar, c is velocity of light and σ is reflection coefficient of scatterer. Suppose the reference signal is

$$s_{ref}(t,\, i) = \text{rect}\left(\frac{t - 2R_0/c - iT_r}{T_{ref}}\right) \cdot \exp\left(j\pi\mu\left(t - \frac{2R_0}{c}\right)^2\right) \cdot \exp\left(j2\pi(f_c + i\Delta f)\left(t - \frac{2R_0}{c}\right)\right) \quad (3)$$

where R_0 is the distance between reference point and radar, and T_{ref} is the width of the pulse of reference signal. Returned signal is processed with stretching as

$$\begin{aligned} s_c(t,\, i) = s_r(t,\, i) \cdot s_{ref}^*(t,\, i) \;=\; & \sigma \cdot \text{rect}\left(\frac{t - 2R/c - iT_r}{T_1}\right) \cdot \exp\left(-j\frac{4\pi}{c}\mu\left(t - \frac{2R_0}{c}\right)R_\Delta\right) \\ & \exp\left(-j\frac{4\pi}{c}(f_c + i\Delta f)R_\Delta\right) \exp\left(-j\frac{4\pi\mu}{c^2}R_\Delta^2\right) \end{aligned} \quad (4)$$

where $R_\Delta = R - R_0$. Taking Fourier Transform of Eq. (4) in terms of t and eliminating Residual Video Phase (RVP) [6, 7], the coarse-resolution range profile (CRRP) can be obtained as

$$S_f(\omega,\, i) = T_1\sigma \sin c\left(T_1\left(\omega + \frac{4\pi\mu}{c}R_\Delta\right)\right) \cdot \exp\left(-j\frac{4\pi}{c}(f_c + i\Delta f)R_\Delta\right) \quad (5)$$

Let $\omega = -4\pi\mu R_\Delta/c$, sample for each CRRP and take Fourier transform of them, thus we can get high-resolution range profile (HRRP) as

$$S(X) = \sigma T_1 \cdot \sin c\,(X + 2\Delta f R_\Delta/c) \cdot \exp\,(-j4\pi f_c R_\Delta/c) \quad (6)$$

Hence, each one HRRP can be obtained within each one burst transmitted by radar. Suppose imaging time is T, we can obtain $T/(T_r \cdot N)$ HRRPs. Where, the mth HRRP can be written as

$$S(X,\, m) = \sigma T_1 \cdot \sin c\,(X + 2\Delta f R_{\Delta m}/c) \cdot \exp(-j4\pi f_c R_{\Delta m}/c) \quad (7)$$

where

$$R_{\Delta m} = \sqrt{(X_c + x)^2 + (mNT_r v + y)^2} - \sqrt{X_c^2 + (mNT_r v)^2} \approx \frac{X_c x + mNT_r vy}{X_c} \quad (8)$$

where $(x,\, y)$ is the coordinate of scatterer relatively to reference point and v is the velocity of target along with cross range. $|S(X,\, m)|,\ m = 1,\, 2,\, \ldots,\, T/(T_r \cdot N)$ is called spectrogram. Take Fourier transform of Eq. (7) to m, and it yields,

$$S(X,\, Y) \approx \sigma T_1 \cdot \sin c\left(X + \frac{2}{c}x\Delta f\right) \cdot \sin c\left(Y + \frac{2y}{cX_c}f_c NT_r v\right) \cdot \exp(-j4\pi f_c x/c) \quad (9)$$

The peak of Eq. (9) is presented as $(-2x\Delta f/c,\, -2yf_c NT_r v/cX_c)$, and it is directly proportional to $(x,\, y)$. Hence, we can achieve ISAR image by simple conversion.

3. ISAR IMAGING FOR BIRDS BASED ON MINIMUM WAVEFORM ENTROPY CRITERION

In the following, we introduce a new imaging method for avian. The flapping spectrogram is eliminated and the latter gliding spectrogram is connected following ahead gliding spectrogram directly, on the basis of identifying bird's moving status accurately, but the steep phase change could happen. It is because the phase function corresponding to each high-resolution range cell is a continuous function in terms of slow time in the spectrogram, which can be seen from Eq. (7) and Eq. (8). Hence, the phase compensation must be executed to reach the best focus effect of ISAR image. The minimum waveform entropy criterion can be employed for phase compensation. Suppose a waveform of a discrete signal is $f(n)$, $n = 0,\, 1,\, 2,\, \ldots,\, M - 1$, the waveform entropy is defined [11] as

$$E = -\sum_{n=0}^{M-1} p_n \cdot \log_{10} p_n \quad (10)$$

where $p_n = \frac{|f(n)|}{\|F\|}$ and $\|F\| = \sum_{n=0}^{M-1} |f(n)|$.

If phase compensation is best, the value of waveform entropy of cross range signal is the minimum and focus effect of ISAR image is the best. The imaging method proposed in this paper can be carried out as follows.

Step (1) Obtain range-slow time spectrogram of bird's echoes and eliminate flapping spectrogram, on the basis of identifying bird's moving status accurately, and connect with the latter gliding spectrogram.

Step (2) From the spectrogram after connected, for each high-resolution range cell, compensate different phases θ_i, $i = 1, 2, \ldots, N$, where N is the total number of high-resolution range cell, namely, sub-pulse number in every burst.

Step (3) Take Fourier Transform of each high-resolution range cell in terms of slow time, and calculate all values of the waveform entropies of results.

Step (4) Search the phases θ_i^* which are compensated to achieve the minimum of waveform entropy. We consider them as the best compensating phases, and $\exp(j\theta_i^*)$ as the best compensating genes.

Step (5) For each high-resolution range cell, the corresponding best compensating gene is multiplied, and take Fourier Transform of compensated spectrogram in terms of slow time. The final ISAR image can be achieved.

4. COMPUTER SIMULATIONS

Suppose initial carrier frequency of millimeter wave radar is 94 GHz [5], frequency-stepped size $\Delta f = 46.875$ MHz, and each burst consists of $N = 64$ sub-pulses, thus synthesized bandwidth $N\Delta f = 3$ GHz can be obtained, and high range resolution $\Delta_R = 0.05$ m. Burst repetition interval $BRI = 1/400$ s. Assume a bird model shown in Fig. 1, its moving velocity $v = 20$ m/s [2], and flapping rate is 2 Hz. The distance between the target and the radar is 2 km, and the pitching angle is 60 degrees. Imaging time is 4.1489 s, where assumed that it is gliding in first 1.8 s, flapping in following 0.9 s, and gliding again in last 1.4489 s. If micro-Doppler effects generated by flapping wings are not considered, we obtain high cross range resolution $\Delta_C = 0.05$ m. The spectrogram of bird's echoes is shown in Fig. 2.

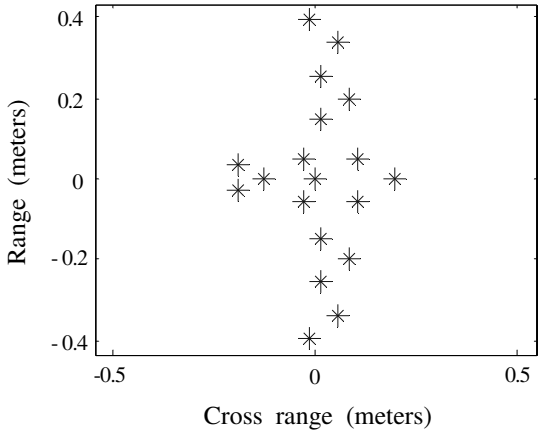

Figure 1: Bird model.

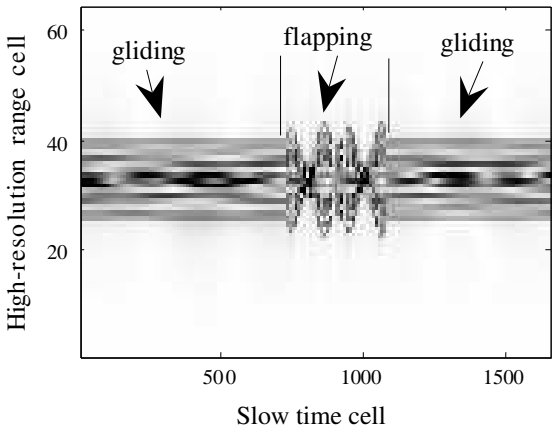

Figure 2: Spectrogram of bird model.

Bird can be imaged by RD algorithm directly as shown in Fig. 3. On the basis of identifying bird's moving status accurately, after eliminating flapping spectrogram from the whole spectrogram, we can connect the latter gliding spectrogram directly, as shown in Fig. 4. Take Fourier Transform of the connected spectrogram to slow time without any phase compensation, we can obtain the ISAR image as shown in Fig. 5. From Fig. 5, we can see that the image quality is better than that in Fig. 3, but it is still comparatively poor and not satisfied. Next, we can search the best compensating phases θ_i^* in $[0, 2\pi]$. And the best compensating phases responding to each high-resolution range cell can be obtained, which is shown in Fig. 6. For the connected spectrogram, after phase compensation to relative high-resolution range cell, we can achieve the final ISAR image, which is shown in Fig. 7. For the sake of comparing ISAR image quality more clearly and

conveniently, the ISAR image of bird gliding all the time during the whole imaging process is shown in Fig. 8.

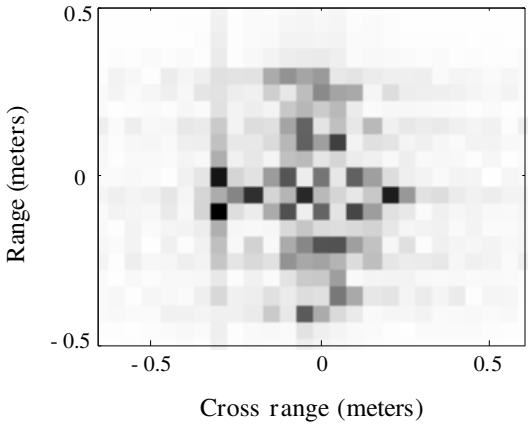

Figure 3: Image with micro-Doppler effect.

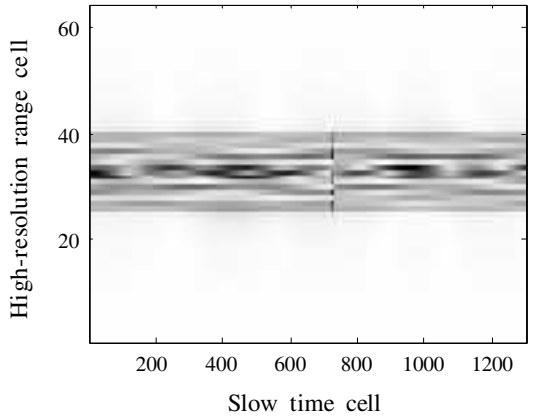

Figure 4: Spectrogram connected directly.

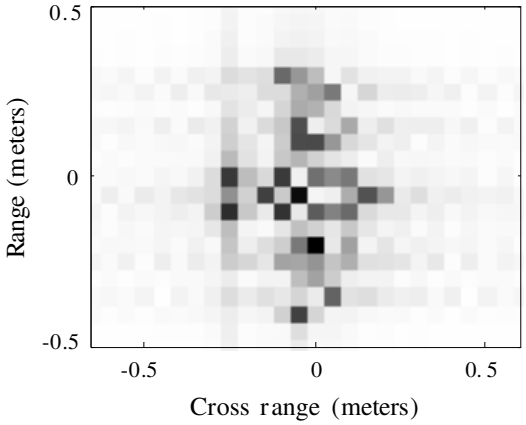

Figure 5: Image without compensating phases.

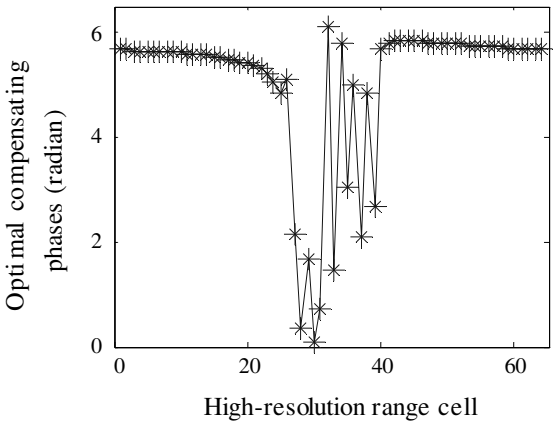

Figure 6: The best compensating phases.

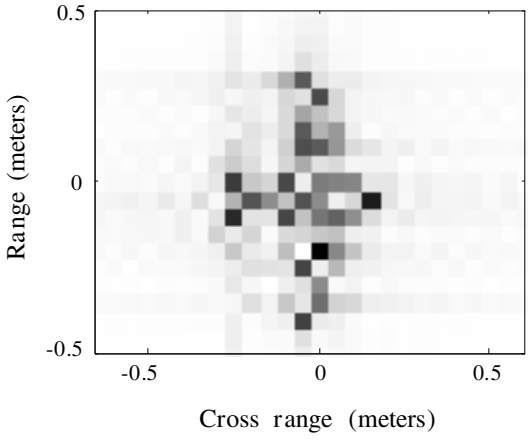

Figure 7: Image with compensating phases.

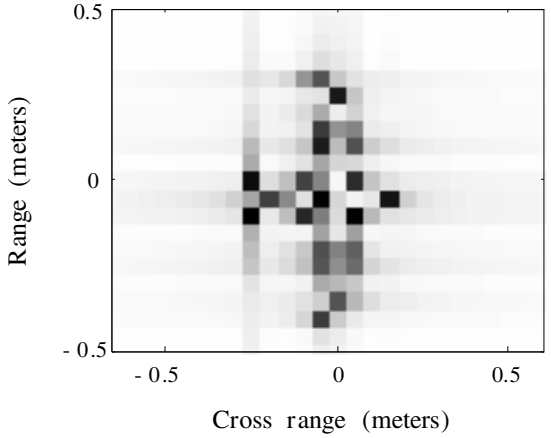

Figure 8: Image during bird's gliding status.

Compared with Fig. 3, it can be seen obviously that the image in Fig. 7 is much improved. And it is also suggests that the proposed method is feasible and valid.

5. CONCLUSIONS

It is quite important that avian can be detected, imaged and identified by ISAR with frequency-stepped chirp signals. A new imaging method for avian targets is proposed in the paper, based on

the continuity of slow time in range-slow time spectrogram, on the basis of identifying their moving status accurately. In the method, the different parts of bird's gliding spectrogram are connected and the minimum waveform entropy criterion is executed for phase compensation. By using this method, we can achieve a comparatively clear bird's ISAR image. The simulation results suggest that the proposed method is valid and feasible.

ACKNOWLEDGMENT

This work is supported by the National Natural Science Foundation of China (60672032) and the Natural Science Foundation Research Program of Shaanxi Province (2007F28).

REFERENCES

1. Nebuloni, R., C. Capsoni, and V. Vigorita, "Quantifying bird migration by a high-resolution weather radar," *IEEE Transactions on Geoscience and Remote Sensing*, Vol. 46, No. 6, 1867–1875, 2008.
2. Gauthreaux, Jr., S. A. and C. G. Belser, "Radar ornithology and the conservation of migratory birds," *USDA Forest Service Gen. Tech. Rep.*, PSW-GTR-191, 871–875, 2005.
3. Ning, H. S., W. M. Liu, J. Li, et al., "Research on radar avian detection for aviation," *Acta Electronica Sinica*, Vol. 34, No. 12, 2332–2335, 2006.
4. Zhang, Q. and Y. Q. Jin, "Aspects of radar imaging using frequency-stepped chirp signals," *EURASIP Journal on Applied Signal Processing*, Vol. 2006, Article ID 85823, 1–8, 2006.
5. Long, T., E. K. Mao, and P. K. He, "Analysis and processing of modulated frequency stepped radar signal," *Acta Electronica Sinica*, Vol. 26, No. 12, 84–88, 1998.
6. Zhu, F., Y. Q. Feng, and Y. Luo, "A novel method of identifying moving status of bird based on waveform entropy variance," *IEEE International Conference on Communications, Circuits and Systems*, 1035–1039, Xiamen, China, May 2008.
7. Zhang, Q., T. S. Yeo, H. S. Tan, et al., "Imaging of a moving target with rotating parts based on the hough transform," *IEEE Transactions on Geoscience and Remote Sensing*, Vol. 46, No. 1, 291–299, 2008.
8. Chen, V. C., F. Y. Li, S. S. Ho, et al., "Micro-Doppler effect in radar: Phenomenon, model and simulation study," *IEEE Trans. on AES*, Vol. 42, No. 1, 2–21, 2006.
9. Thayaparan, T., S. Abrol, and E. Riseborough, "Micro-Doppler feature extraction of experimental helicopter data using wavelet and time-frequency analysis," *RADAR 2004, Proc. of the International Conference on Radar Systems Journal Title Abbreviation*, 2004.
10. Sparr, T. and P. Krane, "Micro-Doppler analysis of vibrating targets in SAR," *IEE Proc. Radar Sonar Navig.*, Vol. 150, No. 4, 277–283, 2003.
11. Zheng, L. and S. H. Zhang, "A novel method of translational motion compensation for hopped-frequency ISAR imaging," *IEEE International Radar Conference*, 255–260, 2000.

Wind Direction Extraction from Coastal SAR Images Using Cross-spectral Method

Hiroyuki Saito and Yoshiharu Yamamoto
Hirosaki University, Japan

Abstract— A sensitive processing method for extracting the wind direction from SAR (synthetic aperture radar) images is presented. We transfer SAR images to the image spectra using two-dimensional FFT (fast Fourier transform) and take the integral of the image spectra between the wave length 400 m and 800 m, which is high end containing wind direction signatures in L-band SAR. From this and a reference signal (half or full wave rectified sinusoidal wave) we obtain the wind direction by using cross-spectral analysis. To examine the potential of our method, a set of simulated images with various SNR (signal to noise ratio) are used. It is shown that, even if the SNR is −30 dB, the agreement is to within ±3°. Therefore the processing technique we present allows us the precise estimation of wind direction. We also use 23 JERS-1/SAR scenes from the Tsugaru Strait located between Aomori and Hokkaido prefectures of Japan for the extraction of wind direction. The wind directions retrieved from these images have been compared with in situ wind data from the Kikonai, the Tappi and the Ooma lighthouse. Although the lighthouse estimates are lacking in directional resolution (16 direction, 22.5° interval), the SAR estimates obtained from spectra of 6.4-km-square images are shown to agree with the lighthouse estimates to within a mean absolute error of 21°. The estimates difference may be related to the directional resolution of in situ wind data, the SNR of JERS-1/SAR images, the effect of terrain around the lighthouse, and the ocean current.

1. INTRODUCTION

The wind power energy has the features that it is plentiful, widely distributed, renewable, and clean etc. However, there are some problems in the wind farm construction and operation, which are cost of land acquisition, noise and vibration of windmill, and visual impact [1]. In European nations, they tend to move their wind farm locations from land to coastal and off-shore areas to solve these problems [2]. In Japan, it has been assumed that the windmill installation in the coastal and off-shore areas is difficult because the sea depth around Japan becomes abruptly deep when leaving shore. However, the first wind turbine on coastal area in Japan was installed and started its operation in 2004, which is located in Setana Town of Hokkaido [3].

It is important to investigate wind patterns to determine the possibility of wind turbine as a viable sustainable energy source. To investigate the wind pattern in the coastal and off-shore areas, the use of satellite images is one of the promising methods. In particular, because the synthetic aperture radar (SAR) installed on satellites can obtain the image of large area with high-resolution, many researchers have been trying the extraction of the wind pattern from off-shore SAR images (for example, [4–6]).

In this research, we are focusing on the extraction of wind direction from coastal SAR images. The different approach is necessary for the coastal SAR images because of the coastal current and undulation which do not depend on the wind direction. First, we show the method that extracts wind direction from the synthetic aperture radar image for the wind by using the cross-spectral method. Then the feasibility of the proposed method is examined by applying to the pseudo SAR images and the coastal JERS-1/SAR images.

2. EXTRACTION METHOD FOR WIND DIRECTION

First, the Fourier coefficient of the subscene of the coastal SAR image is calculated by using two-dimensional Fourier transform. The Fourier coefficient in discrete type is expressed as

$$F(u, v) = \frac{1}{MN} \sum_{x=0}^{M-1} \sum_{y=0}^{N-1} f(x, y) W_M^{-ux} W_N^{-vy} \tag{1}$$

$$W_M = e^{i2\pi/M}, \quad W_N = e^{i2\pi/N} \tag{2}$$

where, $f(x, y)$ is the digital value of a pixel located at (x, y) within the subscene of M by N pixels, u is wavenumber in the x direction, and v is wavenumber in the y direction.

The 2-D power Spectrum is calculated from the 2-D Fourier coefficient, and converted into the polar coordinate system of wavelength and the direction. Then, 1-D directional power spectrum can be derived by integrating the 2-D power spectrum in the wavelength including contribution of wind. In case that the contribution of wind exists from the wavelengths of l_1 to l_2, the 1-D directional power spectrum is

$$p(\theta) = \int_{l_1}^{l_2} F(l, \theta)\, dl \tag{3}$$

where, l is wavelength, and $F(l, \theta)$ is 2-D power spectrum in the polar coordinate system of wavelength and the direction.

The contribution of the wind appears on the 1-D directional power spectrum as peaks at intervals of π. By using this characteristic, the wind direction is extracted by the cross-spectral analysis with a reference function of cycle π. The cross spectrum of the 1-D directional power spectrum $p(\theta)$ and the reference function $q(\theta)$ is defined as [7]

$$S_{pq}(\Theta) = K_{pq}(\Theta) - iQ_{pq}(\Theta) \tag{4}$$

where, Θ is reciprocal of the direction angle, $K_{pq}(\Theta)$ and $Q_{pq}(\Theta)$ are the cospectrum and the quadrature spectrum of $p(\theta)$ and $q(\theta)$, respectively. The wind direction can be calculated from the phase of $S_{pq}(\Theta)$. The phase is defined as

$$\Psi_{pq}(\Theta) = \tan^{-1}\left(K_{pq}(\Theta)/Q_{pq}(\Theta)\right) \tag{5}$$

and the coherence magnitude spectrum using the cross spectrum and the auto spectra as

$$coh(\Theta)^2 = \frac{\left|S_{pq}(\Theta)^2\right|}{S_{pp}(\Theta)\ S_{qq}(\Theta)} \tag{6}$$

The coherence magnitude spectrum ranges from 0 to 1 and is an estimator of the similarity of $p(\theta)$ and $q(\theta)$ around a given Θ. That is, the phase is calculated by using the Θ that the coherency becomes the maximum.

3. VERIFICATION WITH PSEUDO SAR IMAGE

The extraction method for the wind direction shown in the foregoing section was applied to pseudo SAR images, and the extraction ability was examined. In the off-shore images of SEASAT/SAR and ERS-1/SAR, the striped structures caused by wind are often visible. In such SAR images, they are aligned in the direction where the peaks of the power spectrum are roughly orthogonal to the wind direction; so that it can be extracted by using the direction of the peak row that wavelength is in 600 m or more [4, 5]. The striped structure was indistinct in the most of the JERS-1/SAR images used in this research. These did not relate for the wind direction though the peaks of the power spectrum concentrated on the long wave length part, and may be originated in the current and undulation of the Tsugaru Strait. Consequently, the wavelength of sea wave and the wind direction in the pseudo SAR images was fixed to 500 m and 249° (the north is 0°) respectively, and the integral of $F(l, \theta)$ was taken between 400 m and 800 m of the wavelength. In addition, the random noise at various levels was added to the pseudo SAR images because the various levels of SNR in actual SAR images were expected.

Figure 1 shows an example of the extraction results for the wind direction. The SNR is −30 dB. The full wave rectified sinusoidal wave of cycle $\pi/2$ was used as a reference function for the cross spectral analysis. On the sample of the pseudo SAR image, the striped pattern cannot be recognized due to low SNR. But it is possible to extract the wind direction with 3° in the error margin by integration in the wavelength of the power spectrum and the cross-spectral analysis. From this result, the presented method can be expected to be the steady extraction result for wind direction even for the actual SAR images of low SNR.

4. APPLICATION TO COASTAL SAR IMAGE

The study site is the coastal part in the Tsugaru Strait located between Aomori and Hokkaido prefectures in Japan. We used 23 scenes of JERS-1/SAR from 1992 to 1998 for the analysis, that

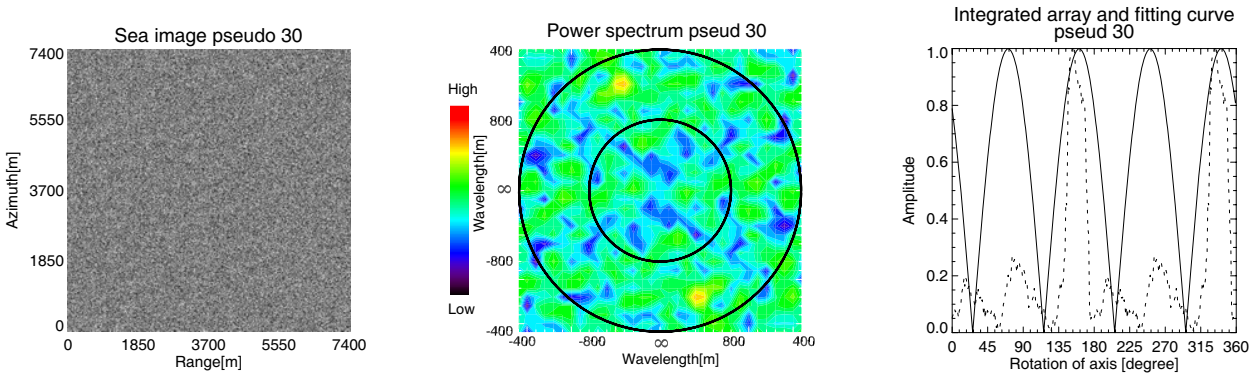

(a) (b) (c)

Figure 1: An example of the extraction results for the wind direction. (a) Pseudo-SAR image with SNR −30 dB. (b) Power spectrum of pseudo-SAR image. (c) Result of cross-spectral analysis.

the pass-low is 65–231. The coastal region in Ooma, Tappi and Kikonai were selected as the object areas, and the subscenes in the size of 6.4 km squares were cut out from the full scenes. There are lighthouses in the vicinity of these object areas, so that we can compare the extracted wind direction from SAR images with in the wind direction estimates of the lighthouses. Figure 2 shows the locations of the subscenes and the lighthouses.

Figure 3 shows the estimated error of the SAR wind directions extracted by the cross-spectral method. Because the wind direction extracted from the SAR images by the 2-D FFT has the arbitrariness of π, the each value in the figure, a closer value to the estimates of the lighthouses was selected. The SAR estimates obtained from spectra of 6.4-km-square images are shown to agree with the lighthouses' estimates to within a standard deviation of 25° and a mean absolute error of 21°.

The error of wind direction extracted from offshore SEASAT/SAR and ERS-1/SAR images are within a standard deviation of 20° [4, 5]. As to the main causes of the large error, the limits of integration in wavelength and the quality of the lighthouses' estimates used for the comparison can be

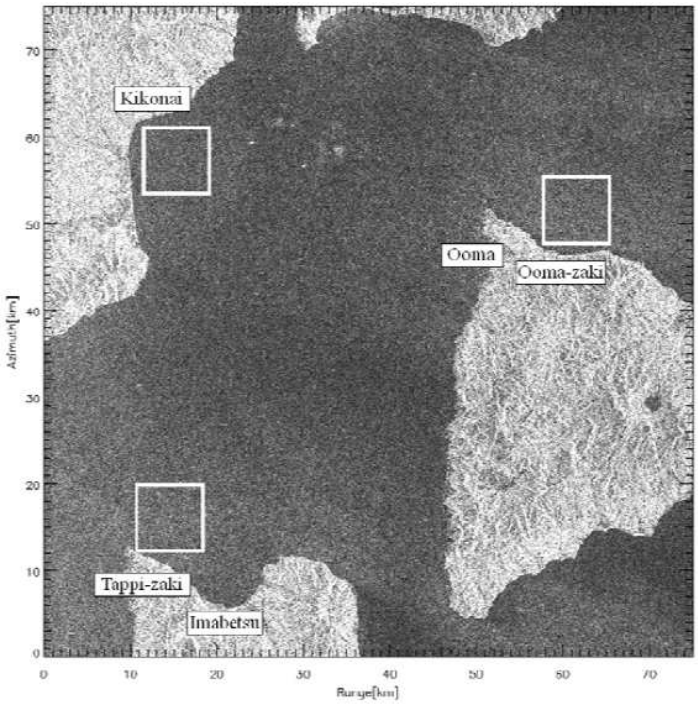

Figure 2: Locations of the subscenes and the lighthouses. Open squares show the subscenes. Solid squares filled with characters show the location of lighthouses.

examined. Concerning the limits of integration in wavelength, there are some estimates appearing the influence of the peaks in long wavelength area because the integral section may be made by setting the optimum limits of integration from 400 m to 800 m for all subscenes. The improvement of the error may be expected by setting the optimum integral section for each subscenes and using a weighting function for suppressing the peaks in long wavelength area. Concerning the lighthouses' estimates, the wind direction is provided in the 16-direction method, namely, the resolution of wind direction is 22.5°. That is, the resolution of wind direction is necessary as the reference data when comparing with the SAR estimates.

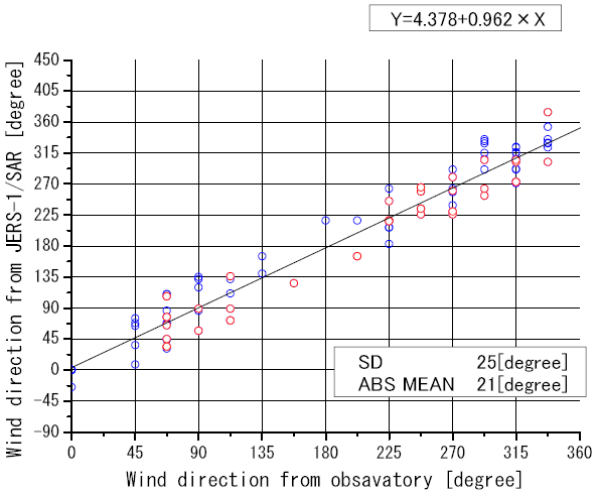

Figure 3: Estimated error of the SAR wind direction extracted by the cross-spectral method. The standard deviation is 25° and the mean absolute error is 21°.

5. CONCLUSIONS

In this research, the method to extract wind direction from SAR image using the cross-spectral method has been shown. As the result of having applied the method to pseudo SAR images, it has been clarified that the presented method can extract the wind direction precisely from the images on which large random error was superimposed. The estimated error is less than 3° even at −30 dB of the SNR. As the result of having applied to coastal JERS-1/SAR images, the SAR estimates of wind direction have been shown to agree with the lighthouse estimates to within a standard deviation of 25° and a mean absolute error of 21°. The improvement of accuracy may be expected by setting the optimum limits of integration in wavelength and using in situ wind direction as the reference data.

REFERENCES

1. Ushiyama, I., *Fundamentals of Wind Power*, Ohmsha, Tokyo, 2005 (in Japanese).
2. Birgitte, R. F. and H. A. Espedal, "Wind energy mapping using synthetic aperture radar," *Can. J. Remote Sensing*, Vol. 28, No. 2, 196–204, 2002.
3. Terakado, K., *Science Web*, Science Web, Tokyo, 2006 (in Japanese).
4. Gerling, T. W., "Structure of the surface wind field from the SEASAT SAR," *J. Geophys. Res.*, Vol. 91, No. C2, 2308–2320, 1986.
5. Vachon, P. W. and F. W. Dobson, "Validation of wind vector retrieval from ERS-1 SAR images over the ocean," *Atmosphere-Ocean*, Vol. 5, 177–187, 1996.
6. Shimada, T., H. Kawamura, and M. Shimada, "An L-band geophysical model function for SAR scatterometry using JERS-1 SAR," *IEEE Trans. Geosci. Remote Sensing*, Vol. 41, 518–531, 2002.
7. Walkerman, C. C., C. L. Rufenach, R. Schuchman, J. A. Johanssen, and K. Davidson, "Wind vector retrieval using ERS-1 synthetic aperture radar imagery," *IEEE Trans. Geosci. Remote Sensing*, Vol. 34, No. 6, 1343–1352, 1996.

Investigation on Volume Scattering for Vegetation Parameter Estimation of Polarimetric SAR Interferometry

Y. S. Zhou[1, 2, 3], **W. Hong**[1, 2], **and F. Cao**[1, 2]

[1]National Key Laboratory of Microwave Imaging Technology, China
[2]Institute of Electronics, Chinese Academy of Sciences, China
[3]Graduate University of Chinese Academy of Sciences, China

Abstract—The objective of this paper is to investigate the volume scattering for the vegetation parameter estimation of Polarimetric Interferometric Synthetic Aperture Radar (Pol-InSAR). Firstly the models for describing the volume scattering are derived from the Pol-InSAR imaging geometry and volume scattering characteristics. The interferometric properties of volume scattering as well as the polarimetric properties of volume scattering are analyzed based on the model. Then the effects of volume height, extinction coefficient, ground to volume ratio, ground phase, incidence angle, and perpendicular baseline, on the volume scattering coherence are analyzed based on the Random Volume over Ground model. Furthermore, with simulated Pol-InSAR data, the effects of these parameters on the estimation accuracy of vegetation height are presented and the radar parameters for better estimating vegetation height are discussed.

1. INTRODUCTION

Polarimetric Interferometric Synthetic Aperture Radar (Pol-InSAR) is an emerging technique that combines SAR interferometry and SAR polarimetry and has already shown its effectiveness and sensitivity to volumetric structures [1]. It has been applied to parameter estimation of volume scatterers (e.g., forest height, extinction coefficient) based on the coherence diversity of the volume scattering with polarization [2, 3]. In order to improve the performance of vegetation parameter estimation and help the design of Pol-InSAR system, this paper investigates the volume scattering systematically within the scope of Pol-InSAR.

Section 2 presents the models (Random Volume, Oriented Volume, Random Volume over Ground and Oriented Volume over Ground model) for describing the volume scattering and analyzes the interferometric and polarimetric properties of volume scattering. The effects of volume height, extinction coefficient, ground to volume ratio, ground phase, incidence angle, and perpendicular baseline, on the volume scattering coherence are analyzed in Section 3. Section 4 further analyzes the effects of these parameters on the vegetation height estimation. The conclusion and future work are given in the end.

2. COHERENT MODELS OF VOLUME SCATTERING IN POL-INSAR

Figure 1 shows an illumination of Pol-InSAR imaging geometry. Ignoring the thermal noises and temporal decorrelation effects, the time-domain representations of SAR images u_1 and u_2 can be expressed in the form of volume scattering integral as [4, 5]

$$\begin{aligned} u_1(x_1, R_1) &= e^{-i2k_1R_1} \int \tilde{a}_1(\vec{r}') \mathrm{e}^{-i2\vec{\kappa}_1\vec{r}'} h(x_1 - x_1', R_1 - R_1')\, dV' \\ u_2(x_2, R_2) &= e^{-i2k_2R_2} \int \tilde{a}_2(\vec{r}') \mathrm{e}^{-i2\vec{\kappa}_2\vec{r}'} h(x_2 - x_2', R_2 - R_2')\, dV' \end{aligned} \tag{1}$$

with the azimuth coordinate x, the range coordinate R, the wave vector $\vec{\kappa} = \kappa[0, \sin\theta, -\cos\theta]^T$, ($T$ is transpose), the wavenumber $\kappa = |\vec{\kappa}|$, the position vector of the scatterer $\vec{r} = [x', y', z']^T$, the system transfer function $h(\cdot)$ and the complex reflectivity function $\tilde{a}$.

Since the reflectivity functions $\tilde{a}_1$ and $\tilde{a}_2$ are considered as uncorrelated, denote the auto- and cross- correlation of them as

$$\begin{aligned} \left\langle \tilde{a}_i(\vec{r})\, \tilde{a}_i^*(\vec{r}') \right\rangle &= \sigma_{vi}\delta(\vec{r} - \vec{r}') \quad i = 1, 2 \\ \left\langle \tilde{a}_1(\vec{r})\, \tilde{a}_2^*(\vec{r}') \right\rangle &= \sigma_{ve}\delta(\vec{r} - \vec{r}') \end{aligned} \tag{2}$$

where σ_{ve} is the effective volume correlation coefficient.

The complex interferometric coherence is defined as

$$\tilde{\gamma} = \frac{\langle u_1 u_2^* \rangle}{\sqrt{\langle u_1 u_1^* \rangle \langle u_2 u_2^* \rangle}}. \tag{3}$$

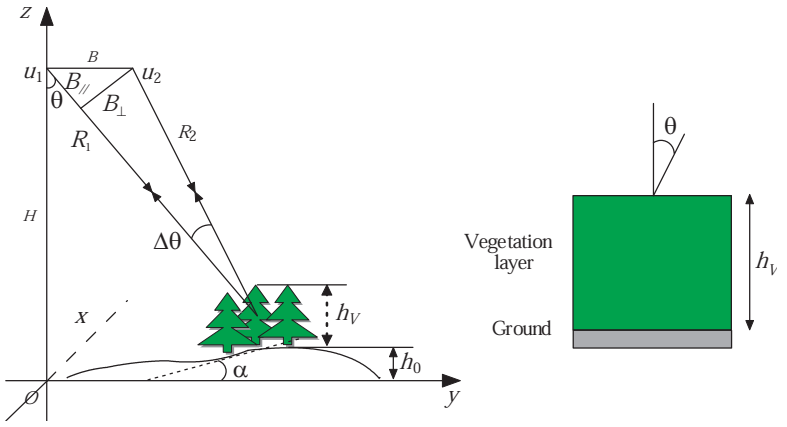

Figure 1: Pol-InSAR imaging geometry and RVoG model.

Assuming $\sigma_{v1}=\sigma_{v2}=\sigma_v$ and substituting (1) into (3) using (2), one can have the baseline decorrelation as

$$\tilde{\gamma} = e^{i\phi_0} \cdot \frac{\int \sigma_{ve}(\vec{r}') \exp\left\{2i\left(\vec{\kappa}_2 - \vec{\kappa}_1\right) \cdot \vec{r}'\right\} h_1(\cdot)\, h_2^*(\cdot)\, dV'}{\int \sigma_v(\vec{r}') h_1(\cdot)\, h_2^*(\cdot)\, dV'} \tag{4}$$

where $\phi_0 = 2\left(\kappa_2 R_2 - \kappa_1 R_1\right)$ is interferometric phase. The baseline decorrelation can be further divided into two contributions by using

$$\begin{aligned} \kappa_y &= \kappa \Delta\theta \cos\theta - \Delta\kappa \sin\theta \\ \kappa_z &= \kappa \Delta\theta \sin\theta + \Delta\kappa \cos\theta \end{aligned} \tag{5}$$

where κ_y and κ_z are horizontal and vertical wavenumbers, $\Delta\theta = \theta_2 - \theta_1 \approx \sin\Delta\theta$ is the look angle difference of two SAR images, $\theta = (\theta_2 + \theta_1)/2$ is average incidence angle. Thus wise, (4) becomes

$$\tilde{\gamma} = e^{i\phi_0} \frac{\int \exp(i2\kappa_y y') |h(\cdot)|^2 dx' dy'}{\int |h(\cdot)|^2 dx' dy'} \cdot \frac{\int \sigma_{ve}(z') \exp(i2\kappa_z z') dz'}{\int \sigma_{ve}(z') dz'} = e^{i\phi} \cdot \tilde{\gamma}_S \cdot \tilde{\gamma}_V \tag{6}$$

where $\tilde{\gamma}_S$ is the signal decorrelation due to the look angle difference of the two SAR images (namely surface decorrelation), $\tilde{\gamma}_V$ is the decorrelation caused by the height distribution of volume correlation coefficient $\sigma_{ve}(z)$ (namely volume decorrelation). From the expression of surface decorrelation, $\tilde{\gamma}_S$ can be eliminated, e.g., by performing range spectral filtering with the spectral shift $\Delta\kappa = \kappa\Delta\theta/\tan\theta$.

a) Random Volume (RV) model: Equation (6) shows that complex volume decorrelation is the Fourier transform of $\sigma_{ve}(z)$, which contains the physical information about the vertical structure of the volume scatterer. A modeled volume scattering description, which includes wave extinction σ through the random orientation homogeneous volume medium, is given by [6]

$$\sigma_{ve}(z) = \exp\left[-\frac{2\sigma}{\cos\theta}(h_V - z)\right], \quad 0 \le z \le h_V \tag{7}$$

with the volume height h_V. Then the complex volume decorrelation becomes

$$\tilde{\gamma}_V = \frac{\int_0^{h_V} e^{i\kappa_z z'} \exp\left(\frac{2\sigma z'}{\cos\theta}\right) dz'}{\int_0^{h_V} \exp\left(\frac{2\sigma z'}{\cos\theta}\right) dz'} = \frac{2\sigma}{\cos\theta\left(e^{\frac{2\sigma h_V}{\cos\theta}} - 1\right)} \cdot \frac{e^{\left(\frac{2\sigma}{\cos\theta} + i\kappa_z\right)h_V} - 1}{\frac{2\sigma}{\cos\theta} + i\kappa_z} \tag{8}$$

b) Oriented Volume (OV) model: If the volume is oriented, only the wave in eigenpolarization does not change its polarization as it travels in the volume. The eigenpolarizations are generally two orthogonal polarizations (for agricultural plants, H and V polarizations) that correspond to the maximum and minimum values of the extinction coefficients [7]. The expression in

(7) is correct for the eigenpolarizations, while extinction coefficients are dependent on the different eigenpolarizations

$$\sigma_{ve}\left(z,\vec{w}\right)=\exp\left[-\frac{2\sigma(\vec{w})}{\cos\theta}\left(h_V-z\right)\right],\quad 0\le z\le h_V \tag{9}$$

with the volume height h_V. Then the complex volume decorrelation becomes

$$\tilde{\gamma}_V(\vec{w})=\frac{\int_0^{h_V}e^{i\kappa_z z'}\exp\left(\frac{2\sigma(\vec{w})z'}{\cos\theta}\right)dz'}{\int_0^{h_V}\exp\left(\frac{2\sigma(\vec{w})z'}{\cos\theta}\right)dz'}=\frac{2\sigma(\vec{w})}{\cos\theta\left(e^{\frac{2\sigma(\vec{w})h_V}{\cos\theta}}-1\right)}\cdot\frac{e^{\left(\frac{2\sigma(\vec{w})}{\cos\theta}+i\kappa_z\right)h_V}-1}{\frac{2\sigma(\vec{w})}{\cos\theta}+i\kappa_z} \tag{10}$$

c) Random Volume over Ground (RVoG) model: For volume scattering at lower frequencies, it needs to further consider the ground contribution, which is polarization dependent [2, 8]

$$\tilde{\gamma}\left(\vec{w}\right)=e^{i\phi_0}\frac{\tilde{\gamma}_V+\mu\left(\vec{w}\right)}{1+\mu\left(\vec{w}\right)},\quad \mu\left(\vec{w}\right)=\frac{\mu_G\left(\vec{w}\right)}{\mu_V\left(\vec{w}\right)}\exp\left(-\frac{2\sigma h_V}{\cos\theta}\right) \tag{11}$$

where $\mu\left(\vec{w}\right)$ is the effective ground to volume ratio, μ_G is the scattered return from the ground seen through the volume and μ_V is the direct volume scattering return [2].

d) Oriented Volume over Ground (OVoG) model: Since the ground contribution is polarization dependent and wave propagation through an OV is completely described by the eigenpolarizations of the volume, the OVoG can be expressed by

$$\tilde{\gamma}\left(\vec{w}\right)=e^{i\phi_0}\frac{\tilde{\gamma}_V(\vec{w})+\mu\left(\vec{w}\right)}{1+\mu\left(\vec{w}\right)} \tag{12}$$

Figure 2 shows (a) geometrical interpretation of the RVoG model, (b) variation of coherence coefficient with polarization and (c) variation of interferometric phase with polarization. For small ground contribution (at $\mu=-20$ dB), the phase center is located at two thirds of the total volume height above the ground and the interferometric coherence is 0.7. With increasing ground contribution, the phase center moves monotonically towards ground. However, the interferometric coherence decreases with increasing ground contribution firstly and then increases with the increasing ground contribution. The former (decreasing) variation behavior is due to fact that the effective volume seen by the radar increases (increasing penetration depth), which in turn increases the volume decorrelation. The later (increasing) variation behavior is due to fact that ground contribution tends to become the dominant scatterer.

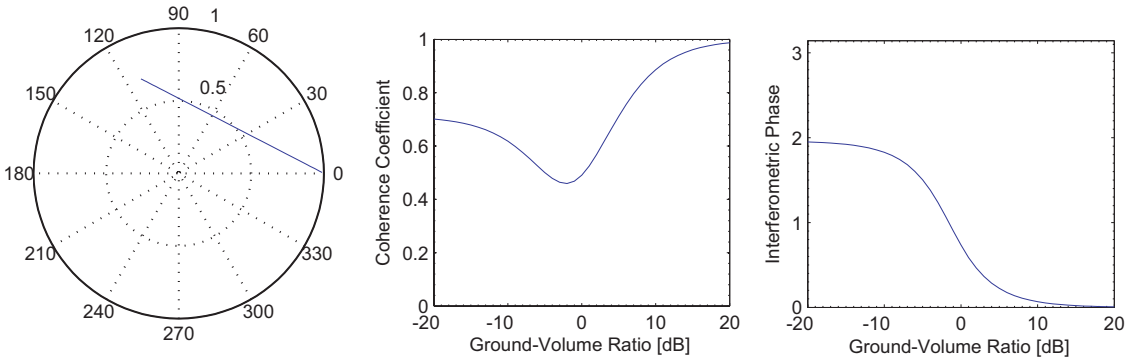

(a) (b) (c)

Figure 2: Coherence and interferometric phase characteristics of the RVoG model. Vegetation height $h_V=20$ m, extinction coefficient σ=0.3 dB/m and vertical wavenumber κ_z=0.15 rad/m.

3. RELATIONS BETWEEN VOLUME SCATTERING AND MODEL PARAMETERS

The variation of volume coherence with polarization is key to Pol-InSAR applications. The radar configurations should be designed to maximize the variation. There are five parameters in the RVoG model: vegetation height h_V, extinction coefficient σ, effective ground to volume ratio μ,

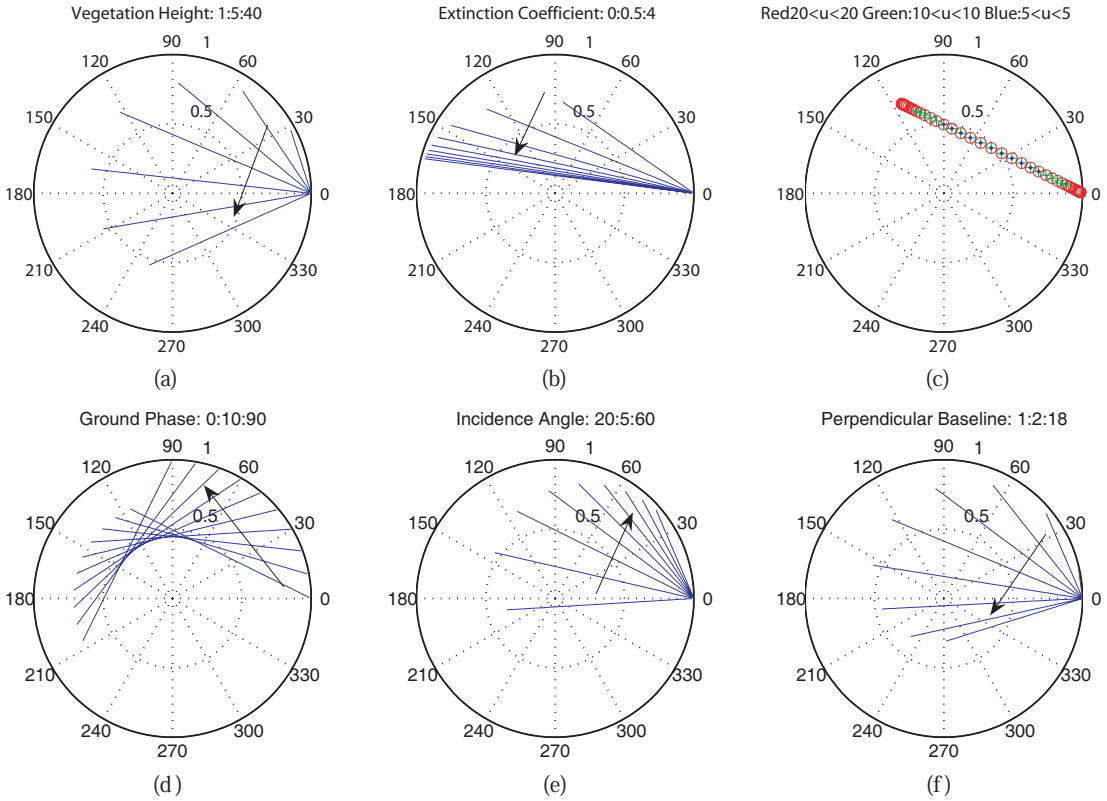

Figure 3: The effects of (a) vegetation height (b) extinction coefficient (c) ground to volume ratio (d) ground phase (e) incidence angle (f) perpendicular baseline on the variations of coherence with polarization. $\kappa_z = 0.15\,\mathrm{rad/m}$, $B_n = 5\,\mathrm{m}$, $\sigma = 0.3\,\mathrm{dB/m}$, $\theta = 45°$, $-20 < \mu < 20$, $\phi_0 = 0$, $\lambda = 0.236\,\mathrm{m}$, $H = 3\,\mathrm{km}$.

ground phase ϕ and vertical wavenumber κ_z, which is related to the radar operation frequency, platform height, perpendicular baseline and incidence angle: $\kappa_z = 4\pi B_n/\lambda H \tan(\theta)$.

Figure 3 shows the effects of model parameters on the variation of coherence with polarization. The vegetation height influences the length of the coherence line and variation range of interferometric phase. A maximum variation is achieved at $h_V = 26\,\mathrm{m}$ in this example case. The length of the coherence line increases monotonically with increasing extinction coefficient and tends to become 2. The range of ground to volume ratio, which is related to operation frequency, vegetation density and extinction, also determines the variation range of the coherence. The ground phase influences the intersection between coherence line and the complex plane. Furthermore the coherence line is also affected by the incidence angle and a maximum is achieved at 25°. Perpendicular baseline is also key to the coherence variation. Note that for Pol-InSAR vegetation estimation, the coherence variation should not be too large because longer coherence lines usually goes with lower coherence which is not good for the estimation of the coherence and phase from data [9].

4. EFFECTS OF MODEL PARAMETERS ON VEGETATION HEIGHT ESTIMATION

Pol-InSAR data are simulated based on the RVoG model (detailed description is given in [10]) and then inverted using the inversion procedures in [3]. Figure 4 shows the effects of model parameters on the estimation of vegetation height. We can see that vegetation height can be estimated well for various model parameters. Suitable radar parameters will provide better performance, for example, the best perpendicular baseline is 9 m, the incidence angle is between 25° and 45°.

5. CONCLUSION

This paper investigates the volume scattering for the vegetation parameter estimation by Pol-InSAR. The models for describing the volume scattering are derived and the effects of model parameters on the volume scattering coherence are analyzed. The effects of model parameters on the estimation accuracy of vegetation height are also presented based on simulated Pol-InSAR data. Further work will focus on the choosing of radar parameters for better vegetation parameter estimation based on the characteristics of volume scattering.

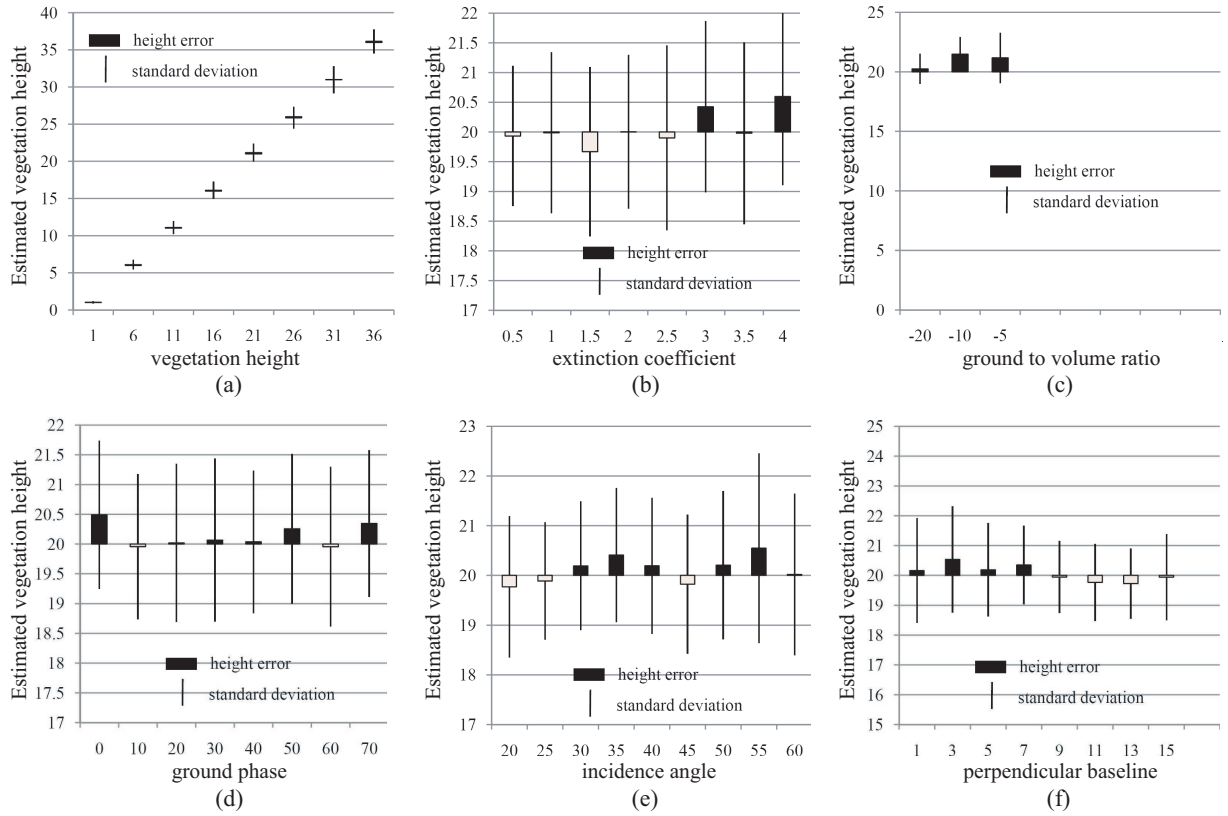

Figure 4: The effects of (a) vegetation height (b) extinction coefficient (c) ground to volume ratio (d) ground phase (e) incidence angle (f) perpendicular baseline on the estimation accuracy of vegetation height.

ACKNOWLEDGMENT

Thanks to the Project 2008DFA11690, CXJJ-257 and 07QNCX-1155 for funding.

REFERENCES

1. Cloude, S. R. and K. P. Papathanassiou, "Polarimetric SAR interferometry," *IEEE Trans. Geosci. Remote Sens.*, Vol. 36, No. 5, 1551–1565, 1998.
2. Papathanassiou, K. P. and S. R. Cloude, "Single-baseline polarimetric SAR interferometry," *IEEE Trans. Geosci. Remote Sens.*, Vol. 39, No. 11, 2352–2363, 2001.
3. Cloude, S. R. and K. P. Papathanassiou, "Three-stage inversion process for polarimetric SAR interferometry," *IEE Proc.-Radar Sonar Navig.*, Vol. 150, No. 3, 125–134, 2003.
4. Papathanassiou, K. P., "Polarimetric SAR interferometry," Ph. D. Thesis, Tech. Univ. Graz, 1999.
5. Bamler, R. and P. Hartl, "Synthetic aperture radar interferometry," *Inverse Problems*, Vol. 14, No. 4, R1-R54, 1998.
6. Treuhaft, R. N., S. N. Madsen, M. Moghaddam, and J. J. van Zyl, "Vegetation characteristics and underlying topography from interferometric radar," *Radio Science*, Vol. 31, No. 6, 1449–1485, 1996.
7. Treuhaft, R. N. and S. R. Cloude, "The structure of oriented vegetation from polarimetric interferometry," *IEEE Trans. Geosci. Remote Sens.*, Vol. 37, No. 5, 2620–2624, 1999.
8. Treuhaft, R. N. and P. R. Siqueira, "Vertical structure of vegetated land surfaces from interferometric and polarimetric radar," *Radio Science*, Vol. 35, No. 1, 141–177, 2000.
9. Lee, J.- S., K. W. Hoppel, S. A. Mango, and A. R. Miller, "Intensity and phase statistics of multilook polarimetric and interferometric SAR imagery," *IEEE Trans. Geosci. Remote Sens.*, Vol. 32, No. 5, 1017–1027, 1994.
10. Zhou, Y. S., W. Hong, and F. Cao, "An improvement of vegetation height estimation using multi-baseline polarimetric interferometric SAR data," in *Proceedings of PIERS 2009*, Beijing, China, March 2009.

An Improvement of Vegetation Height Estimation Using Multi-baseline Polarimetric Interferometric SAR Data

Y. S. Zhou[1,2,3], **W. Hong**[1,2], **and F. Cao**[1,2]

[1]National Key Laboratory of Microwave Imaging Technology, China
[2]Institute of Electronics, Chinese Academy of Sciences, China
[3]Graduate University of Chinese Academy of Sciences, China

Abstract— This paper proposes a method for improving the estimation accuracy of vegetation height using multi-baseline Polarimetric Interferometric Synthetic Aperture Radar (Pol-InSAR) data. Single-baseline Pol-InSAR technique has been applied to retrieve the vegetation parameters based on the random volume over ground (RVoG) model. There are two main error sources which might decrease the estimation accuracy. One is the non-volumetric decorrelation, such as thermal noise decorrelation, temporal decorrelation, etc. The other is the ground ambiguity and ideal assumption that volume-only coherence can be acquired in at least one polarization. This assumption may fail when vegetation is thick, dense, or the penetration of electromagnetic wave is weak. This paper proposes a method to solve both the abovementioned two problems at the same time based on the use of multi-baseline Pol-InSAR data. Firstly, the two main error sources are analyzed and an inversion model for representing them is constructed based on the RVoG model. With the constructed model, inversion procedure for estimating vegetation height using the multi-baseline Pol-InSAR data is presented. The performance of this new method is validated using simulated data, and the ratio between baselines and their effects on the estimation performance are also presented.

1. INTRODUCTION

Polarimetric Interferometric Synthetic Aperture Radar (Pol-InSAR) technique [1] is a combination of SAR polarimetry and SAR interferometry and has been demonstrated its success in the estimation of vegetation parameters (height, extinction, underlying terrain) based on the Random Volume over Ground (RVoG) model [2–4].

Pol-InSAR vegetation height estimation is based on the use of volume decorrelation. Any non-volumetric decorrelation, such as thermal noise decorrelation, temporal decorrelation, etc., might decrease the accuracy of the estimated height. Regarding temporal decorrelation, it has been introduced to compensate its effect on the inversion performance by fixing one of the model parameters (extinction coefficient) [5] or via a dual-baseline Pol-InSAR inversion procedure [6].

The inversion of RVoG model using single-baseline Pol-InSAR data, assumes that in at least one of the observed polarization channels (usually the cross-polarized HV channel), the effective ground to volume ratio is small. However, in some cases when vegetation is thick, dense, or the penetration of the electromagnetic wave is weak, the assumption fails. To solve this problem, an inversion procedure, which is based on the use of dual-baseline Pol-InSAR data, was proposed and validated [7, 8].

The two problems in the inversion of RVoG model were solved respectively. This paper discusses the feasibility to solve them at the same time based on the use of multi-baseline Pol-InSAR data. In Section 2, the error sources are analyzed and a revised inversion model for representing them is constructed based on the RVoG model. Section 3 describes the inversion procedure of the revised model. The performance of this new method is validated using simulated data, and the ratio between each baseline length and their effect on the estimation accuracy are also discussed in Section 4.

2. RVOG MODEL FOR VEGETATION HEIGHT ESTIMATION

2.1. RVoG Model

RVoG model is probably the most successful inversion model for the estimation of vegetation height using Pol-InSAR data. It is a two-layer model composed by a vegetation layer (trunks, branches, leaves or needles) and a ground layer. The vegetation layer is modeled as a layer of given thickness h_V and random orientation homogeneous volume medium with wave extinction σ and can be expressed by

$$\sigma_{ve}(z) = \exp\left[-\frac{2\sigma}{\cos\theta}(h_V - z)\right], \quad 0 \le z \le h_V. \tag{1}$$

The complex coherence of the random volume is related to the Fourier transform of σ_{ve} [4]

$$\tilde{\gamma}_V = \frac{\int_0^{h_V} e^{i\kappa_z z'} \exp\left(\frac{2\sigma z'}{\cos\theta}\right) dz'}{\int_0^{h_V} \exp\left(\frac{2\sigma z'}{\cos\theta}\right) dz'} = \frac{p}{p_1} \cdot \frac{\exp(p_1 h_V) - 1}{\exp(p h_V) - 1}, \text{ where } \begin{cases} p = 2\sigma/\cos\theta \\ p_1 = p + i\kappa_z \\ \kappa_z = \kappa\Delta\theta/\sin\theta \end{cases}. \quad (2)$$

θ is the incidence angle, κ_z is vertical wavenumber, $\kappa = 4\pi/\lambda$ for alternate-transmit mode ($\kappa = 2\pi/\lambda$ for single-transmit mode) and the look angle difference $\Delta\theta$ between the two antennas separated by the baseline. This random volume is located above a impenetrable ground scatterer. Considering both the volume and ground contribution, the total complex coherence can be expressed by

$$\tilde{\gamma}(\vec{w}) = e^{i\phi_0} \cdot \frac{\tilde{\gamma}_V + \mu(\vec{w})}{1 + \mu(\vec{w})}, \quad \mu(\vec{w}) = \frac{\mu_G(\vec{w})}{\mu_V(\vec{w})} \exp\left(-\frac{2\sigma h_V}{\cos\theta}\right). \quad (3)$$

where $\mu(\vec{w})$ is the effective ground to volume ratio, μ_G is the scattered return from the ground seen through the vegetation and μ_V is the direct volume scattering return [3].

2.2. Revised Model Accounting for the Errors and Its Inversion

Pol-InSAR vegetation height estimation is based on the use of volume decorrelation. Any non-volumetric decorrelation, such as thermal noise decorrelation, temporal decorrelation, quantization and coregistration decorrelation, etc., might affect the estimation accuracy of height. Figure 1(a) shows a geometric interpretation of this type of error. The volume-only coherence point is affected by decorrelation (γ_D) and shifts toward the origin along the radius. In order to improve the estimation accuracy, it has to shift the observed volume-only coherence point away from the origin. This type of error can be represented in the RVoG model by a decorrelation item (γ_D)

$$\tilde{\gamma} = e^{i\phi_0} \cdot \frac{\gamma_D \tilde{\gamma}_V + \mu}{1 + \mu} \quad (4)$$

The other error source is ground ambiguity and it is due to the ideal assumption that volume-only coherence can be acquired in at least one polarization. This assumption may fail when vegetation is thick, dense, or penetration of electromagnetic wave is weak. Figure 1(b) shows a geometric interpretation of this type of error. The volume-only coherence point lies outside of the observed area. In order to estimate accurate vegetation height, it has to shift the observed volume-only coherence point away from the ground coherence point and along the coherence line. In order to account for the error, it is necessary to insert one item ($\Delta\mu$) accounting for the coherence shifting.

$$\tilde{\gamma} = e^{i\phi_0} \cdot \frac{\tilde{\gamma}_V + [\mu + \Delta\mu]}{1 + [\mu + \Delta\mu]} \quad (5)$$

Now considering both the two types of errors, namely combining (4) and (5), it yields to the revised model which represents for both the abovementioned errors

$$\tilde{\gamma} = e^{i\phi_0} \cdot \frac{\gamma_D \tilde{\gamma}_V + [\mu + \Delta\mu]}{1 + [\mu + \Delta\mu]} \quad (6)$$

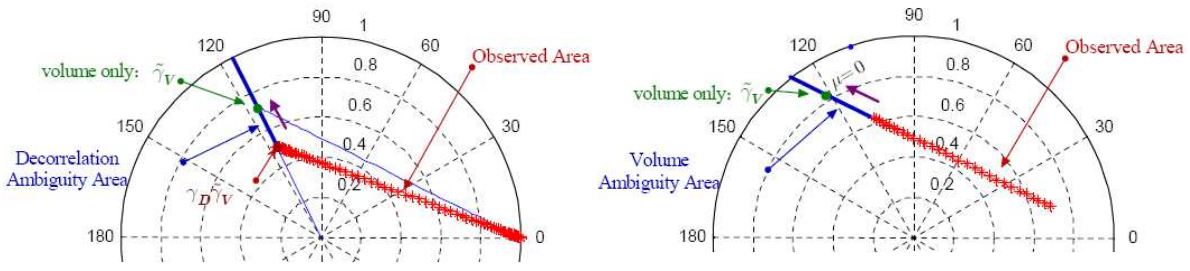

(a) along the radial line (b) along the coherence line

Figure 1: Geometric interpretation of two types of RVoG model inversion errors.

3. INVERSION PROCEDURE OF THE REVISED MODEL

The revised new model expressed in (6) consists of six parameters (ϕ_0, h_v, σ, μ, $\Delta\mu$, γ_D). Increasing one independent polarization channel will provide two more observables and one more model parameter (μ). Fully Pol-InSAR data provide six observables, but the number of unknowns becomes eight. Dual-baseline Pol-InSAR data provide six more observables, but the number of unknowns increases by six as well. Since the number of increased observables with increasing number of baselines is equal to that of increased unknowns, it is useless to increase the number of baselines except making some realistic assumptions.

In the case of single-pass Pol-InSAR operating mode and short revisit interval, the decorrelations during the two baseline acquisition could be assumed identical. Furthermore, by assuming the same $\Delta\mu$, the number of unknowns reduces to twelve, which is equal to the number of dual-baseline Pol-InSAR observables. Now the inversion of the revised model based on dual-baseline Pol-InSAR data could proceed. Figure 2 shows illustrations of the inversion procedure and the major steps are as follows

i. Find out the ground phase ϕ_{01}, ϕ_{02} for each baseline. It is the intersection between the coherence line and the unit cycle of the complex plane. This step is identical with that in the inversion of the RVoG model [4].

ii. Shift the phase of each observed coherence by $\exp(-\phi_{01})$, $\exp(-\phi_{02})$ so as to have the same zero ground phase.

iii. Stepping the non-volumetric decorrelation level γ_D from 1 to 0 using suitable hits and ground to volume ratio μ from -40 dB (relates to no ground ambiguity) to 0 dB using suitable hits, calculate volume-only coherence $\tilde{\gamma}_{V1}$ of the first baseline κ_{z1}.

iv. Based on the volume-only coherence $\tilde{\gamma}_{V1}$ of the first baseline, calculate the corresponding height h_V and extinction σ using LUT and then calculate volume-only coherence $\tilde{\gamma}_{V2}$ of the second baseline κ_{z2}.

v. Using the above the non-volumetric decorrelation level and ground to volume ratio, the observed coherence $\tilde{\gamma}$ of the second baseline is calculated using (3).

vi. If the calculated coherence is equal to the observed coherence of the second baseline, we then set the above vegetation height as the output.

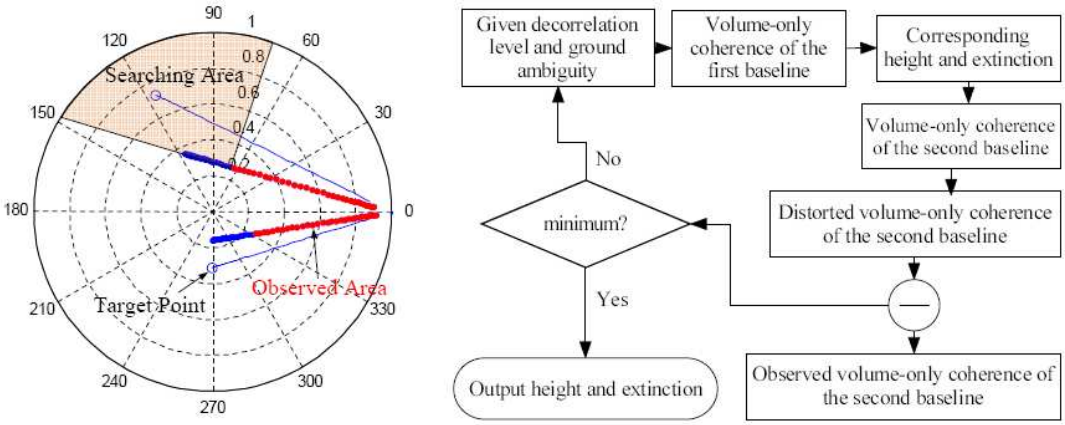

Figure 2: Illustrations of inversion procedure.

4. SIMULATION ANALYSIS OF THE INVERSION PROCEDURE

In order to evaluate validity of the aforementioned inversion procedure, dual baseline Pol-InSAR data are firstly simulated with both error sources described in Section 2.2 [9]. The main steps are as follows

a) Calculate the observable C_6 of a pixel using the RVoG statistical model with errors

$$C_6 = \begin{bmatrix} T_V + T_G & X \\ X^{*T} & T_V + T_G \end{bmatrix} \tag{7}$$

where $X = e^{i\phi}\left(\gamma_D \tilde{\gamma}_V T_V + T_G\right), [T_V] = \begin{bmatrix} 1 & 0 & 0 \\ 0 & \varepsilon & 0 \\ 0 & 0 & \varepsilon \end{bmatrix}, T_G = \begin{bmatrix} \mu_1 & 0 & 0 \\ 0 & \mu_2 & 0 \\ 0 & 0 & \mu_3 \end{bmatrix} T_V.$

b) Compute $C^{1/2}$, where $C^{1/2}(C^{1/2})^{*T} = C$.

c) Simulate a 6-component complex random vector v from the Gaussian distribution $\mathrm{G}(0, 0.5)$.

d) The simulated Pol-InSAR image is $g = C^{1/2}v$, where

$$g = \begin{bmatrix} h_1 \\ h_2 \end{bmatrix},\ h_i = \begin{bmatrix} S_{HH} \\ \sqrt{2}S_{HV} \\ S_{VV} \end{bmatrix},\ i = 1, 2$$

Table 1 shows the simulation parameters which are typical forest at L band. To simulate the non-volumetric decorrelation, γ_D is set to 0.8.

Table 1: Simulation parameters for dual-baseline Pol-InSAR data.

Parameter	Value	Parameter	Value
h_V	20 m	σ	0.3 dB
θ	45°	ε	0.2
μ_1	−10 dB	μ_2	−3 dB
μ_3	0 dB	γ_D	0.8

Table 2 shows the inversion results from simulated dual-baseline Pol-InSAR data using the procedure described in Section 3. In the case of single-baseline inversion, results of κ_{z2} and κ_{z3} are better than that of the others because they are much closer to the optimal baseline [10]. Vegetation heights estimated using dual-baseline data are much more accurate than those using single-baseline data. It should be noted that different combinations of baselines have different estimation accuracy, e.g., the combination of κ_{z2} and κ_{z3} provides the most accurate estimation results in this simulation analysis. Figure 3 shows the inversion results for different given heights and the advantages of using dual-baseline is obvious. Here we can also see that the combination of κ_{z2} and κ_{z4} provides better estimation results than that of κ_{z1} and κ_{z3}.

Table 2: Inversion results from simulated dual-baseline Pol-InSAR data.

Inversion Method	Estimated Mean Value	Standard Deviation
S.-B. $\kappa_{z1} = 0.1$	23.0552 m	3.1068
S.-B. $\kappa_{z2} = 0.15$	23.3332 m	1.8202
S.-B. $\kappa_{z3} = 0.2$	23.3840 m	1.8743
S.-B. $\kappa_{z4} = 0.3$	23.4660 m	6.0923
D.-B. $\kappa_{z1} + \kappa_{z2}$	20.7208 m	2.4365
D.-B. $\kappa_{z1} + \kappa_{z3}$	20.5084 m	2.3178
D.-B. $\kappa_{z1} + \kappa_{z4}$	19.7060 m	2.0423
D.-B. $\kappa_{z2} + \kappa_{z3}$	20.1076 m	1.9287
D.-B. $\kappa_{z2} + \kappa_{z4}$	19.7472 m	1.6903
D.-B. $\kappa_{z3} + \kappa_{z4}$	19.9372 m	1.6852

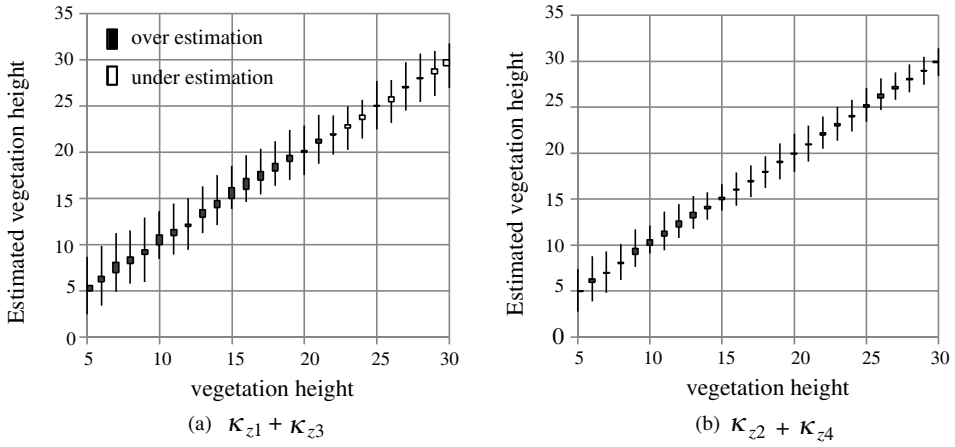

Figure 3: Estimated mean height and its standard deviation.

5. CONCLUSION

This paper proposes a method to compensate the errors in the single-baseline Pol-InSAR RVoG inversion by using the multi-baseline Pol-InSAR data. Two error sources are modeled into the RVoG model and the inversion problem using multi-baseline Pol-InSAR data is analyzed. Inversion procedure of the revised RVoG model is described and validated using simulated Pol-InSAR data. The estimated heights from dual-baseline data are more close to the ideal height than just from single-baseline data. Different combinations of baselines have different estimation performance and the choice of baseline combination will be analyzed in the further work.

ACKNOWLEDGMENT

Thanks to the Project 2008DFA11690 and 07QNCX-1155 for funding. Thank Dr. Shane Cloude for the advice and help on Pol-InSAR data simulation.

REFERENCES

1. Cloude, S. R. and K. P. Papathanassiou, "Polarimetric SAR interferometry," *IEEE Trans. Geosci. Remote Sens.*, Vol. 36, No. 5, 1551–1565, 1998.
2. Treuhaft, R. N. and P. R. Siqueira, "Vertical structure of vegetated land surfaces from interferometric and polarimetric radar," *Radio Science*, Vol. 35, No. 1, 141–177, 2000.
3. Papathanassiou, K. P. and S. R. Cloude, "Single-baseline polarimetric SAR interferometry," *IEEE Trans. Geosci. Remote Sens.*, Vol. 39, No. 11, 2352–2363, 2001.
4. Cloude, S. R. and K. P. Papathanassiou, "Three-stage inversion process for polarimetric SAR interferometry," *IEE Proc.-Radar Sonar Navig.*, Vol. 150, No. 3, 125–134, 2003.
5. Papathanassiou, K. P. and S. R. Cloude, "The effect of temporal decorrelation on the inversion of forest parameters from Pol-InSAR data," *Proceedings of IGARSS 2003*, 1429–1431, Toulouse, France, July 2003.
6. Zhou, Y. S., W. Hong, F. Cao, Y. P. Wang, and Y. R. Wu, "Analysis of temporal decorrelation in dual-baseline POLinSAR vegetation parameter estimation," *Proceedings of IGARSS 2008*, Boston, USA, July 2008.
7. Cloude, S. R., "Robust parameter estimation using dual baseline polarimetric SAR interferometry," *Proceedings of IGARSS 2002*, 838–840, Toronto, Canada, June 2002.
8. Koudogbo, F., T. Mette, K. P. Papathanassiou, and I. Hajnsek, "Dual-baseline approach for the retrieval of vegetation parameters," *Proceedings of EUSAR 2006*, Dresden, Germany, May 2006.
9. Lee, J.-S., S. R. Cloude, K. P. Papathanassiou, M. R. Grunes, and I. H. Woodhouse, "Speckle filtering and coherence estimation of polarimetric SAR interferometry data for forest applications," *IEEE Trans. Geosci. Remote Sens.*, Vol. 41, No. 10, 2254–2263, 2003.
10. Zhou, Y. S., W. Hong, Y. P. Wang, F. Cao, and Y. R. Wu, "Analysis of optimal baseline of polarimetric interferometric SAR based on RVoG model," *Acta Electronica Sinica*, Vol. 36, No. 12, 97–102, 2008.

On the Need of Developing Multi-Band Differential POLinSAR Theory and Algorithms for Remote Sensing and Monitoring of Natural Environments and Severe Environmental Stress Changes

Wolfgang-Martin Boerner[1] **and Kun-Shan Chen**[2]

[1]ECE/CSN Laboratory, University of Illinois at Chicago, USA
[2]Center for Space & Remote Sensing Research, National Central University, Taiwan

Abstract— Worldwide, medium- to short-term earthquake prediction is becoming ever more essential for safeguarding man due to an un-abating population increase, but hitherto there have been no verifiable methods of reliable earthquake prediction developed. This dilemma is a result of previous and still current approaches to earthquake prediction which are squarely based on the measurement of crustal movements, observable only after a tectonic stress-change discharge (earthquake) has occurred. During the past decades it was proved and shown that it is not possible to derive reliable models for earthquake predictions from crustal movement measurements alone, and that an entirely new approach must be taken and rigorously pursued over years and decades to come. In support of this conclusion, there have been reported throughout the history of man anecdotal historical up to scientifically verifiable earthquake precursor or "*seismo-genic*" signatures of various kind — biological, geological, geo-chemical and especially a rather large plethora of diverse electromagnetic ones on ground, in air and space, denoted as "*seismo-electromagnetic*" signatures. Taiwan is one of the few regions where those phenomena may best be observed. In this overview a systematic analysis of main historical records, a summary of pertinent "*seimo-genic*" as well as observed "*seismo-electromagnetic*" effects and modern ground-based to air- and space-borne metrological signature investigations are presented placing major emphasis on ongoing studies in Taiwan.

1. INTRODUCTION

In fact, we need to discover the true intrinsic forces including electrodynamic stress that cause the tectonic plates to move and to undergo continuous gradual as well as abrupt seismic changes, and which are active long to close before the tectonic stress-changes occur. Implementation of novel high-altitude drone (UAV) and space borne satellite RP-Diff-POL-In-SAR will add most essential tools for advancement as will be demonstrated. In support of this conclusion, there have been reported throughout the history of man anecdotal historical up to scientifically verifiable earthquake precursor or "*seismo-genic*" signatures of various kinds — first biological, geological, geo-chemical and then a rather large plethora of diverse electromagnetic ones — on ground, in air and space, denoted as "*seismo-electromagnetic*" signatures. This is necessary in order to provide an improved understanding on why and how such precursor signatures are generated, and how and where those may best be observed — either in the ground or on the surface through the atmosphere into the ionosphere — subject to the rather poor signal-to-noise ratio (SNR) — requiring much improved digital instrumentation. Again, the addition of implementing novel high-altitude drone (UAV) and space borne satellite RP-Diff-POL-In-SAR imaging technology will become most essential.

2. PREVIOUS AND ONGOING PILOT STUDIES

A number of pilot studies had been initiated in this direction during the past two decades, had been supported for a few years, and then aborted for several reasons. Those are the high operating costs involved, the poor SNR that makes signal detection very tedious if not impossible with the existing state of the art in instrumentation, and the fact that earthquakes just don't appear upon demand, requiring many years and decades until "*they*" happen. One needs to keep at all times in focus the ever persistent opposition of the scientific establishment against us "*radio-seismo-genic-alchemists*". Several major studies were initiated: the USGS/NSF NEHER Program of the early 1990's after the Loma Prieta M 7.1 Earthquake of 1989 October 19; in Japan, the ERSFP after the 1995 January 17 Hyogo-Ken Nanbu M 7.2 Earthquake near Hanshin, Awaki Island; in Greece, due to continuously reoccurring earthquakes of M 4.5–6.0, the ongoing electro-potential methods of Varatsov et al; in China, already before the devastating Yanshin M 8.1 Earthquake [1]; and now also in Taiwan as a result of the Chi-Chi M 7.4 & Chia-yi M 6.8 Earthquakes on 1999 September 21 & October 22/23 in Central-Southwest Taiwan [2]. These efforts have been initiated due to

the Spitak M 8.0 Earthquake of March/April 1989 which has been incorrectly considered as the first time that ground-based "*seismo-electromagnetic*" precursors had been observed. This honor goes to Professor Takeo Yoshino of UEC in Chofu-Shi, Tokyo, Japan who observed such "*seismo-electromagnetic*" precursors since the very late 1970-ies at ground and in space. Outranking among all previous multi-year assessment studies was the very productive international outreach oriented one in Japan after the Hanshin Awaji Earthquake of 1995 January 15. This study coordinated by Professor Masashi Hayakawa resulted in four books [1].

3. ADVANCEMENTS OF GROUND-BASED TO SPACE-BORNE SEISMO ELECTROMAGNETIC MEASUREMENTS

In order to obtain a much better insight into the worldwide appearance of "*seismo-electromagnetic precursors*", it would seem most essential to upgrade the existing INTER-MAG magnetometer network (only records up to frequencies of 0.1 MHz are collected and stored on venerable magnetic tapes) by adding 3-axis flux-gate magnetometers (able to operate up to several Hertz) at each of the INTER-MAG stations worldwide. This was already proposed more than twenty years ago by the late Dr. Arthur William (Bill) Green of USGS-GRF in Golden, CO. Such an upgrade is costly but highly desirable also for various other reasons, and now feasible with the highly improved ELF/ULF digital signal recording plus centralized telemetric collection, storage, analysis and processing systems, which did not exist only fifteen years ago, when Bill Green strongly recommended such studies. With it several sub-oceanic recording INTER-MAG recording stations require also to be upgraded. In order to assess any lithospheric to mesospheric to ionospheric precursor interaction effects such vital important continuous 3-axis magneto-metric records up to several Hertz must be obtained and the frequency bands of measurement and data storage must be extended to about 20 Hz. Note that Bill Green did not observe any seismo-electromagnetic signatures below 10 MHz but above 100 MHz, which appears to apply to all earthquakes. Prime emphasis must also be given to ionospheric precursor observations, which are summarized well in the various book-reports by Hayakawa et al. [1]. There exist a few pertinent newly discovered types of observations, which need to be further explored such as the flare-up of ionosphere-bound lightning discharges, the "*sprites (or Spritzer – according to Schumann)*", in addition to the observable earth-bound lightning- strokes "*Blitz*" located above highly ionized clouds generated during the early phases of final localized tectonic stress culmination close to epicenter regions. These phenomena require subtle additional studies and coordinated coincident ground to space recordings as proposed in several papers by Hayakawa, Yoshino in Japan, and others in China and Taiwan.

More so, remote sensing techniques — not yet conceived but in urgent need — are much sought for. An example is the remote sensing of the groundwater table with the tracking of sub-surface fluid flow [3]. The implementation of existing well established historical records collected by utilities worldwide is in desperate need. They are required for advancing our understanding of this highly interdisciplinary, complicated geophysical problem. Input is sought for highly expanded international collaboration and possible involvement for a major long-lasting global pilot study to be carried out simultaneously at several "*seismic hot spots.*" Entirely novel techniques for identifying and tracking the fluid flow at depths down to several hundreds of meters are desired. This remains to be a very essential research task of the twenty-first century, and of paramount relevance to these kinds of "*seismo-genic and seismo-electromagnetic precursor*" investigations. Closely related to the detection of sub-surface fluid-flow is the bulging and subsidence of surfaces before, during and after tectonic stress change events which need not necessarily be catastrophic. This can now be achieved with implementation of air/high-altitude/space-borne RP-Diff-POL-In-SAR imaging. As regards the acquisition of satellite SAR measurement data sets, the space-launched ALOS PALSAR, the forthcoming RADARSAT-II and TERRASAT-1&2 fully polarimetric sensors will play an essential role, and ought to be fully integrated in all of the forthcoming studies [4].

4. DEVELOPMENT OF MULTI-MODAL SYNTHETIC APERTURE RADAR (SAR) IMAGING TECHNOLOGY IN AIR AND SPACE

Decisive progress was made in advancing fundamental POL-IN-SAR theory and algorithm development during the past decade, which was based on the underlying accomplishments of fully polarimetric SAR and differential SAR interferometry and its current merger. This was accomplished with the aid of airborne & shuttle platforms supporting single-to-multi-band multi-modal POL-SAR and also some POL-IN-SAR sensor systems. Because the operation of airborne test-beds is extremely expensive, aircraft platforms are not suited for routine monitoring campaigns. These

are better accomplished with the use of drones (UAV). Such unmanned aerial vehicles (drones), hitherto developed mainly for defense applications, are currently lacking the sophistication for implementing advanced forefront POL-IN-SAR technology. High altitude drones are necessary for a great variance of applications beginning with flood, bush/forest-fire to tectonic-stress (earth-quake to volcanic eruptions) for real-short-time hazard mitigation. For routine global monitoring purposes of the terrestrial covers neither airborne sensor implementation — aircraft and/or drones — are sufficient; and therefore multi-modal and multi-band space-borne POL-IN-SAR space-shuttle and satellite sensor technology needs to be further advanced at a much more rapid pace. The existing ENVISAT and most recently launched ALOS-PALSAR will be compared with the forthcoming RADARSAT-2 and the TERRASAT-1&2, demonstrating that at this phase of development the fully polarimetric and polarimetric-interferometric SAR modes of operation must be treated as preliminary algorithm verification support, and not to be viewed as routine modes. The same considerations apply to the near future implementation of any satellite-cluster bi/multi-static space-borne tomographic imaging modes, which must however be developed concurrently in collaboration with all major national or joint continental efforts in order to reduce spending and the proliferation of space-platforms.

5. IMPLEMENTATION OF RP-DIFF-POL-IN-SAR ENVIRONMENTAL STRESS-CHANGE MONITORING FOR THE ANALYSES OF EARTHQUAKE EPISODES IN TAIWAN WITH SUBSEQUENT LAND-COVER SUBSISTENCE AND BULGING

Taiwan is an island located in the '*Circum-Pacific Seismic Belt*' subjected to the ongoing collision of the Philippine-Sea and the Eurasian Plates, and it experienced disastrous earthquakes in the past. The electromagnetically inter-related Chi-Chi (990921: M = 7.6) - Chia-Yi (991022/23: M = 6.8) earthquakes, which caused a total loss of more than 2500 lives, the collapse of more than 100,000 household dwelling-units, several bridges and major highways, hydro-electric dams and electric power-line distribution systems along the affected Chelungpu fault [1–3]. Taiwan and its environs to the East have, are, and will be experiencing seismic activity on a very wide scale from millions of small to several truly large earthquakes a year, Taiwan is ideally suited for embarking on a long-lasting major Earthquake Hazard investigation program. In comparison with other similar seismically active regions of the two major terrestrial seismic belts, Therefore, it was decided appropriate to initiate a National Taiwanese Program for Excellence in University Research on the subject of "Research on Seismo-Electromagnet Precursors of Earthquakes" entitled '*integrated Search for Taiwanese Earthquake Precursors — iSTEP*' at the National Central University (NCU) in Chung-Li, Tao-Yuan, Taiwan [3]. In support of the well developing iSTEP ground-based magneto-metric seismo-genic signature measurements [2], the SAR Image processing and analysis group of the NCU CSRSR have embarked on a rigorous program for producing a large set of RP-Diff-In-SAR overlay interferometric images that show the temporal stress-change history of up to six months in advance of the Chi-Chi (990921; M = 7.6), during the electromagnetically exceedingly active time-period until the two major aftershocks of the Chia-yi (991022/23; M = 6.8) earthquakes occurred, and thereafter for several months [3].

6. CONCLUSION

It was shown that several electromagnetic precursors associated with earthquakes provide essential information on tectonic stress change events which when correlated with high resolution RP-Diff-POL-IN-SAR imaging of crustal deformation will bring us closer to developing more reliable earthquake prediction methods. Specifically, the application of repeat-pass SAR interferometry proves to provide a useful high resolution tool for monitoring different types of crustal deformation in spite of the difficulties encountered from the dense subtropical vegetation in an area such as Taiwan. The results obtained come with unprecedented spatial density and compare favorably with other approaches including geodetic DEM variations derived from GPS networks [3, 4]. The knowledge gained from the Chi-Chi and Chia-Yi earthquake duplet has opened new approaches to combine electromagnetic and seismic earthquake analyses of the future.

ACKNOWLEDGMENT

The contributions by members of the National Central University (NCU), iSTEP (integrated Search for Taiwanese Electromagnetic Earthquake Precursors) team of Jhonli Taoyuan, Taiwan; and especially of Professors Kun-Shan Chen, Jann-Yenq (tiger), Chung-Pai Chan, and of Dipl. Ing.

Chie-Tien Wang is gratefully acknowledged. We are grateful for the continuing interest in our research of Professor Masashi Hayakawa of the University of Electro-Communications at Chofu-Shi, Tokyo, Japan and Professor Katsumi Hattori of Chiba University, Chiba, Japan.

REFERENCES

1. Hayakawa, M., (Ed.), *Proceedings of IWSE-05 (International Workshop on Seismo-Electromagnetics)*, University of Electro-Communications, UEC Chofu-Shi, Tokyo, Japan, March 15–17, 2005, TERRAPUB, Tokyo, (in final printing), 2006.
2. Tsai, Y.-B. and J.-Y. Liu, (Eds.), *Special Issue on Earthquake Precursors, TAO (Terrestrial, Atmospheric and Oceanic Sciences)*, Vol. 15, No. 3, 564, I-IV, published by Meteorol. Society of Taiwan (ROC), Taipei, 2004.
3. Chang, C.-P., K.-S. Chen, C.-T. Wang, J.-Y. Yen, T.-Y. Chang, and C.-W. Lin, "Application of space-borne radar interferometry to crustal deformations in Taiwan: A perspective from the nature of events," *TAO*, Vol. 15, No. 3, 523–543, Sept. 2004.
4. Boerner, W.-M., "Recent advances in extra-wide-band polarimetry, interferometry and polarimetric interferometry in synthetic aperture remote sensing, and its applications," *IEE Proc.-Radar Sonar Navigation, Special Issue of the EUSAR-02*, Vol. 150, No. 030603, 113–125, 2003.
5. Boerner, W.-M., H. Mott, E. Lüneburg, et al., "Polarimetry in radar remote sensing: Basic and applied concepts," *Principles and Applications of Imaging Radar*, F. M. Henderson & A. J. Lewis, (Eds.), Ch. 5, 271–357, *Manual of Remote Sensing*, R. A. Reyerson, (Ed.), 3rd Ed., Vol. 2, 940, John Willey & Sons, New York, 1998.
6. Massonet, D. and K. L. Feigl, "Radar interferometry and its application to displaying stress-changes in the earth's crust," *Review of Geophysics*, Vol. 36, No. 4, 441–500, Nov. 1998.
7. Cloude, S. and K. Papathanassiou, "Polarimetric SAR interferometry," *IEEE Trans. Geosci. Remote Sensing*, Vol. 36, No. 4, 1551–1565, 1998; (also see: Papathanassiou, K. P., "Polarimetric SAR interferometry," Ph.D Thesis, Tech. Univ. Graz (ISSN 1434-8485 ISRN DLR-FB-99-07), Graz, Austria, 1999).

BGP Security Configuration in ISP Networks

Hexing Wang[1], **Cuirong Wang**[1], **and Ge Yu**[2]

[1]Northeastern University at Qinhuangdao, Qinhuangdao 066004, China
[2]School of Information Science and Engineering, Northeastern University
Shenyang 110004, China

Abstract— The Border Gateway Protocol (BGP) is the de facto inter-domain routing protocol used to exchange network reachability information between ISP networks in the global Internet. The border gateway router of ISP network runs BGP protocol and maintains a table of prefixes designating IP networks that can be reached. However, as the Internet routing infrastructure, BGP is vulnerable to both accidental misconfigurations and malicious attacks because it trusts unverified control plane information received from its peers.

This paper considers the security risks of BGP system and surveys works relating to BGP security. While a number of enhanced protocols for BGP (such as S-BGP, SO-BGP, PGBGP, etc.) have been proposed to solve BGP security problem, these generally relay on a public key infrastructure or a central authority like ICANN, or require substantial changes to the protocol, hence none of them has been widely deployed. We present a security configuration framework based on currently available technologies to improve the security of BGP routers. The security configuration framework provides a set of guidelines to protect the BGP routers from misconfigurations and malicious attacks. We describe the countermeasures and security mechanisms of BGP system when it encounters potential attacks, such as BGP peer spoofing, BGP session hijacking, malicious or unallocated route injection, etc. Our proposition is easily deployable in ISP networks without additional cost and it can effectively improve the security of BGP system.

1. INTRODUCTION

The Internet is a vast global network which is made up of thousands of independently ISP networks. A network under the administrative control of a single organization is called an autonomous system (AS) [1]. An ISP often owns one or more AS number for administrative convenience, and provides the Internet Service to users. Within an AS, the intra-domain routing protocols such as RIP, OSPF, IS-IS are used to exchange routing information. And between ASes, the inter-domain routing protocol is introduced. The Border Gateway Protocol Version 4 (BGP-4) [2, 3] is the de facto inter-domain routing protocol used to exchange network reachability information between ISP networks in the global Internet; its simplicity and resilience have enabled it to play a fundamental role within the global Internet.

However, BGP has historically provided few security guarantees. The ISP network is vulnerable to attack though BGP. Misconfigured or deliberately malicious attack can disrupt overall Internet by injecting bogus routing information or hijacking network address space. On Apr 25, 1997 at 11:30 a.m. AS 7007 announced more specific routes (/24s) for practically the entire Internet [5, 6]. Routing was globally disrupted as the more specific prefixes took precedence over the aggregations routes. Many routers have been crashed and most Internet connectivity has been disrupted for over two hours. February 24, 2008, Pakistan Telecom hijacked a subnet address space for political reasons [7]. One of border router announced a very specific route (with prefix "/24") to Youtube. Because the more specific route to Youtube was announced, others routers took this route as the best route to Youtube. The effect was to take Youtube off the air globally for about two hours.

Such incidents shows that BGP is vulnerable and ISP should improve the routing security by some effective ways. There are a number of enhanced protocols for BGP (such as S-BGP [8], SO-BGP [9], PGBGP [10], etc.) have been proposed to solve BGP security problem, these generally relay on a public key infrastructure or a central authority like ICANN, or require substantial changes to the protocol, hence none of them has been widely deployed.

In this paper, we present a security configuration framework based on currently available technologies to improve the security of BGP routers. The security configuration framework provides a set of guidelines to protect the BGP routers from misconfigurations and malicious attacks. Our approach rely on existing technologies supported by router vendors, that is to say we can use carefully configure commands to protect BGP systems in ISP networks.

The paper is organized as following: Section 2 is related work. Section 3 analyzes the vulnerabilities of BGP systems in ISP networks. We propose the BGP security configuration framework to

improve the BGP system security in Section 4. And in Section 5, we give the BGP configuration guidelines in detail. Finally the conclusion is described in Section 6.

2. RELATED WORK AND

BGP security is an active area of research. Because this activity is relatively new, no solution has been universally deployed in the Internet. At present, most of research on BGP security has focused on the integrity, authentication, confidentiality, authorization, and validation of BGP data. PHAS [11] provides a web based service about possible prefix hijacks. The Listen and Wisper protocol [14] monitors TCP traffic flows and determines if hosts in remote prefixes are reachable, seeks to alert network administrators of potential routing inconsistencies. S-BGP [8] establishes a public-key infrastructure to stymie IP address spoofing. It enhances the security of BGP by verifying the authenticity and authorization of the BGP control traffic. It uses digital certificates to authenticate two pieces of data: which chunks of address space have been allocated to them and what autonomous system numbers have been allocated to them. SO-BGP [9] targets the need to verity the validity of an advertised prefix. It verifies a peer which is advertising a prefix has at least one valid path to the destination. PG-BGP [10] maintains a history of known origin ASes and prefixes. New origins and sub-prefix would be depreferenced for 24 hours and if they still exist in the RIB at that time, they would be added to the history. The delay period would provide monitoring ASes time to attend to events before they could cause widespread damage. This proposal is also facing difficulties to deploy, because of its need to change the BGP routing decision-making process.

These proposals generally relay on a public key infrastructure or a central authority like ICANN, hence none of them has been widely deployed. However, ISPs hope minimal changes to adapt to the BGP protocol for security needs. So there should be a solution for BGP security

3. BGP VULNERABILITIES ANALYSIS

As the de facto inter-domain routing protocol, BGP is widely used in interconnection of ISP networks. The vulnerabilities and risks in BGP systems will inevitably affect the ISP's network security and stability. RFC 4272 lists three primary limiting factors that lead to the vulnerabilities of BGP [4]: (1) BGP does not provide strong protection of the integrity, freshness, and peer entity authenticity of the messages. That's means the malicious attacks may tamper with, replay or fabricate BGP messages in peer-peer BGP communications. (2) BGP does not validate the authority of an AS to announce network layer reachability information. This is related to path subversion, as an AS can currently announce that it has the shortest path to a destination by forging the path vector, even if it is not part of the destination path at all. (3)BGP does not ensure the authenticity of the path attributes announced by an AS. A malicious AS can impair or manipulate the packets' routing path by changing the path attributes in BGP messages.

The following is a list of potential attacks on BGP. While not a complete list, the attacks discussed here are the most common that are likely to be a concern for BGP.

(1) BGP spoofing attacks. Peer IP addresses can often be found using the ICMP traceroute function. The attacker imitates the BGP peer with peculating the source address of peer's IP connection. The goal of the spoofing attack may be to insert false information into a BGP peer's routing tables.

(2) BGP session resets attack. Current IETF specifications do not require checking sequence numbers of received ICMP messages. It is easy for attacker to send spoofed ICMP error messges to peer with encapsulating the victim's IP address and port number, which cause TCP session reset. As a result, it causes loss of BGP peering sessions, forcing a need to rebuild routing tables and possibly causing route flapping.

(3) Malicious route injection attacks. There are three types of illegal route injection: DUSA (Documenting Special Use addresses) route injection, unauthorized route injection and unallocated route injection. Malicious route injection of DUSA addresses might cause disruptions in networks that use these addresses within their designated functions. Attacker use unauthorized or unallocated route injection can make serious DOS and DDOS attack.

(4) Hijacking attacks. Attacker hijackes netblock address by announcing a more specific route to target network, then packets to target network would be redirected to the attacker's machine. Youtube accident is an obvious example for netblock address hijacking attacks.

4. BGP SECURITY CONFIGURATION FRAMEWORK

In this section, we describe the BGP security configuration framework and the secure BGP configuration guideline in ISP networks.

As shown in Figure 1, the framework can be divided into three layers. The first layer is session security protection layer, which secures BGP session between peers by protecting the connection port and using authentication mechanism. BGP stability protection layer using soft reconfiguration and other technicals to reduce BGP instability because of IGP protocol failure and occasional interface or link failure. The third layer is very important to ISP security operations, it uses access control list, inbound and outbound filter to protect ISP networks avoid from network address hijacking. Details of each layer in the framework will be described in the next section (Section 5).

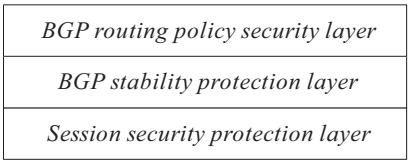

Figure 1: BGP security configuration framework.

5. BGP SECURITY CONFIGURATION GUIDELINES

This section describes the configuration guidelines of each layer, and then gives a BGP security template based Cisco IO. Most of guidelines can be found in the actual configuration corresponding to the configuration commands. So it can be easily deployed in ISP networks without additional costs.

5.1. Session Security Protection Layer

This layer protects session security. Since BGP runs on TCP/IP, any TCP/IP attack can be applied to BGP. These guidelines below will protect TCP session and BGP session from spoofing attacks and session hijacking attacks.

Guideline 1. Protect port 179 through access control lists. TCP port 179 is the standard port for receiving BGP peer's OPEN message, so attempts by peers to reach other ports are likely to indicate faulty configuration or potential malicious activity. Allow peers to connect to port 179 only and deny any other connections to or from this port.

Guideline 2. Use TTL security check feature in configuration. Most ISP peers are normally adjacent, so only one hop should be required for a packet sent in a BGP message, the TTL of IP packet is required to be 1. This feature can be used to protect the EBGP session between peers.

Guideline 3. Use TCP MD5 authentication. The MD5 hash algorithm (RFC 2385 [31]) can be used to protect BGP sessions by creating a hash key for TCP message authentication. Commercial routers offer MD5 as a configuration option, and it is relatively easy to set up, using one or two statements in configuration files. This option provides protection against TCP-based attacks such as spoofing and session hijacking, because the attacker must know the secret key used in the hash computation.

Guideline 4. Record peer changes. Logging whenever a peer enters or leaves established state provides useful records for debugging or audit trails for investigating possible security problems.

5.2. BGP Stability Protection Layer

Stability is an important aspect of BGP security. Instability in BGP system may have a wide range of routing oscillation, leading to large-scale routing failure, making the lost connection between communication hosts. Below is a detail list of guidelines that will help reducing BGP connection failure, controlling the scale of BGP routing table, and protecting connctions to DNS servers.

Guideline 5. Shut down synchronization with IBGP. BGP synchronization feature refers to a requirement that BGP wait until the IGP propagates a newly learned route within the AS before advertising the route to external peers. Shut down synchronization can avoid instability by IGP protocol failure.

Guideline 6. Turn off fast external failover feature. Turn off fast external failover to avoid major route changes due to transient failures of peers to send keepalives.

Guideline 7. Use soft reconfiguration. Normally a change in policy requires BGP sessions to be cleared before the new policy can be initiated, resulting in a need to rebuild sessions with

consequent impact on routing performance. Soft reconfiguration allows new policies to be initiated without resetting sessions. It can be set up for either or both inbound and outbound for updates from and to neighbors, respectively.

Guideline 8. Disable BGP version negotiation. This option provides BGP faster startup. Peers change infrequently in practice, so BGP versions for known peers can be established statically rather than renegotiated each time BGP restart.

Guideline 9. Use loopback interface for IBGP announcements. Using a loopback interface to define neighbors is common with iBGP, but not with eBGP. Normally the loopback interface is used to make sure the IP address of the neighbor stays up and is independent of hardware functioning properly.

Guideline 10. Shut down auto summarize announcements feature. Auto summarization causes the router to summarize network paths according to traditional Class A, B, C, and D boundaries. This behavior can be problematic if, for example, the AS does not own the complete classed network that is summarized.

Guideline 11. Use max prefix limits to avoid filling router tables. Routers should be configured to disable or terminate a session and issue warning messages to administrators when a neighbor sends in excess of a preset number of prefixes.

Guideline 12. Do not use route flap damping for netblocks that contain DNS root servers. DNS root servers are critical for Internet operations, so degraded access to them by damping netblocks could cause widespread disruption of network operations.

5.3. BGP Routing Policy security Layer

The complexity of BGP policy and AS relationship could lead to conflict configuration and human misconfiguration. Mahajan et al. [13] analyse the influence of BGP misconfiguration. Caesar and Rexford [14] discussed BGP routing policies in ISP networks. The list of guidelines belowing gives a basic principle when configuring BGP policies in ISP networks.

Guideline 13. Do not redistribute prefixes from an IGP protocol. Redistributing from an IGP is dangerous. AS 7007 incident is caused by misconfiguration which redistributing from IGP to EBGP. In practice, we should avoid unnecessary dynamic coupling of IGP and eBGP to prevent propagation of instability from IGP to EBGP (and vice versa).

Guideline 14. Set announce prefix list to allow announcing only designated netblocks. It will prevent the router from inadvertently providing transit to networks not listed by the AS.

Guideline 15. Filter all bogon prefixes. Bogon prefixes should not appear in routes. Filtering them reduces load and helps reduce the ability of attackers to use forged addresses idenial of service or other attacks.

Guideline 16. Block inbound announcements of bogon prefixes. Since these prefixes do not represent valid routes, they should not be announced or propagated.

Guideline 17. Deny over-specific prefix lengths. It can reduce the volume of update messages and BGP routing table. Outbound filter should deny all of the over-specific prefix, in addition to those can be confirmed.

Guideline 18. Deploy enhanced sinking hole to reduce the attack damage when DOS/DDOS attack occurs. DOS/DDOS attack cannot be removed but its hazards can be reduced as much as possible. Using enhanced black hole routing technology triggered by the BGP can protect the data center sever effectively.

6. CONCLUSIONS

In this paper we described the BGP security configuration framework based on currently available technologies to improve the security of BGP routers. The framework is made up of three layers. In each layer, specific guidelines according to configuration commands are described. The deployment of the framework doesn't rely on public key infrastructure or other central authority. So it can be easily deployed in ISP networks without additional costs.

ACKNOWLEDGMENT

This work was partially supported by the National natural science foundation, China, under Grant 06273078 and by the Doctor funds of science and technology bureau, Hebei, China, under Grant 55470130-3.

REFERENCES

1. Hawkinson, J. and T. Bates, "Guideline for creation, selection, and registration of an autonomous system (AS)," *RFC1930*, March 1996.
2. Rekhter, Y. and T. Li, "A border gateway protocol 4," *RFC1771*, March 1995.
3. Rekhter, Y., T. Li, and S. Hares, "A border gateway protocol 4 (BGP-4)," *RFC 4271*, January 2006.
4. Murphy, S., "BGP security vulnerabilities analysis," *RFC 4272*, January 2006.
5. Misel, S. A., "Wow, AS7007!" April 1997, http://www.merit.edu/mail.archives/nanog/1997-04/msg00340.html.
6. Bono, V. J., "7007 explanation and apology," April 1997, http://www.merit.edu/mail.archives/nanog/-199704/msg00444.html.
7. RIPE. YouTube Hijacking: A RIPE NCC RIS case study. http://www.ripe.net/news/study-youtube-hijacking.html.
8. Kent, S., C. Lynn, and K. Seo, "Secure border gateway protocol," *IEEE Journal on Selected Areas in Communications*, Vol. 18, No. 4, 582–592, 2000.
9. Ng, J., "Extensions to BGP to support secure origin BGP (soBGP)," *Internet Draft draft-ng-sobgp-bgp-extensions-02*, April 2004.
10. Wan, T., E. Kranakis, and P. van Oorschot, "Pretty secure BGP, psBGP," *Proceedings of network and distributed system security*, 2005.
11. Lad, M., D. Massey, D. Pei, Y. Wu, B. Zhang, and L. Zhang, "PHAS: A prefix hijack alert system," *USENIX Security*, 2006.
12. Subramanian, L., V. Roth, I. Stoica, S. Shenker, and R. Katz, "Listen andWhisper: Security mechanisms for BGP," *Proceedings of Networked Systems Design and Implementation*, March 2004.
13. Mahajan, R., D. Wetherall, and T. Anderson, "Understanding BGP misconfiguration," *Proceedings of ACM SIGCOMM*, 3–16, 2002.
14. Caesar, M. and J. Rexford, "BGP policies in ISP networks," *IEEE Network Magazine*, October 2005.
15. Wang, L., X. Zhao, D. Pei, R. Bush, D. Massey, and L. Zhang, "Protecting BGP routes to top level DNS servers," *IEEE transactions on parallel and distributed systems*, Vol. 14, No. 9, 851–860, 2003.
16. Gill, V., J. Heasley, and D. Meyer, "The generalized TTL security mechanism (GTSM)," RFC3682, February 2004.
17. CISCO, "BGP support for TTL security check," http://www.cisco.com/en/US/docs/ios/12_2-sx/feature/guide/fsxebtsh.html.

An Iterative QRD-M Detection Algorithm for MIMO Communication System

L. Liu, J. K. Wang, D. M. Yan, J. Gao, and Z. B. Xie
School of Information Science & Engineering, Northeastern University
Shenyang 110004, China

Abstract— Multiple input multiple output (MIMO) has been considered as a promising technique for its potential to significantly increase the spectral efficiency and system performance. Lots of detection algorithms have been proposed for MIMO systems in the literature. Among them, maximum likelihood detection (MLD) algorithm provides the best bit error rate (BER) performance. However, the complexity of MLD exponentially increases with the constellation size and the transmit antenna number. Therefore, it is impractical to use a full MLD without reducing its computational complexity, because it would be prohibitively large for implementation. Recently, several detection algorithms for MIMO systems achieving near-MLD performance have been proposed. The use of QR decomposition with an M-algorithm (QRD-M) and sphere decoding (SD) have been proposed to provide a tradeoff between the system performance and complexity in MIMO communications. However, with the exception of some special cases, their complexity still grows exponentially with increasing dimension of the transmitted signal. Moreover, the complexity of SD has big variations at different SNR values, which results in impractical to use in hardware implementation. To reduce these problems, a new detection scheme, named as iterative QRD-M (IQRD-M), is proposed in the paper. After performing QR decomposition of the channel matrix, the exhaustive search of the last layer is done, the accumulated metrics are calculated and sorted, which gives an ordered set of the last layer, then QRD-M algorithm are used to search the left layers with novel termination methods. The proposed algorithm provides the more near-ML performance and with low complexity.

1. INTRODUCTION

Multiple input multiple output (MIMO) wireless communication systems with spatial multiplexing has been considered as a promising technique for its potential to significantly increase the spectral efficiency and system performance in rich scattering multipath environments [1]. Efficient signal detection algorithms for spatial multiplexing MIMO systems have attracted much interest in recent years, and lots of detection algorithms have been proposed for MIMO systems in the literature [2–4]. In order to decode symbols corrupted by inter-antenna interference, maximum-likelihood (ML) detection is required at the receiver which achieves the minimum error probability for independent identically distributed (i.i.d) random symbols, which is a requirement that holds in many cases. However, the complexity of ML detector generally precludes its use in practical systems especially with many transmit antennas and large constellations. A lot of efforts have been put into the search for algorithms achieving ML or near-ML performance with lower complexity. Sphere detection (SD) [5–7] and The M-algorithm combined with QR decomposition (QRD-M) [8–10] are possibly the most promising algorithms. Both QRD-M and SD are tree search based algorithms. Specifically, QRD-M is a breadth-first and the SD is a depth-first tree search algorithm.

QRD-M algorithm is an implementation of the breadth-first tree traversal in MIMO signal detection which can provide very stable complexity. In the conventional QRD-M algorithm, the parameter M is used as the limitation of the number of maximum survived branches in its breadth-first tree traversal. By setting M equal to different values, it can provide different tradeoff solutions between the system performance and complexity. The larger M is set, the better performance is obtained and the more complexity is required.

In this paper, we propose a new detection scheme, which we will refer to as an iterative QRD-M (IQRD-M). After performing QR decomposition of the channel matrix, because of the upper triangular matrix property of R, the decision on the last layer does not depend on the others layers. So the exhaustive search of the last layer is done, the calculated metrics are sorted, which gives an order set of the last layer, then QRD-M algorithm are used to search the left layers with novel termination methods. The proposed scheme can reduce the performance gap between ML and QRD-M detection, gives more reliable estimates than QRD-M with slight complexity overhead.

2. SYSTEM MODEL, ML ALGORITHM AND QRD-M ALGORITHM

2.1. System Model

We consider a spatial multiplexing MIMO system with N_t transmit and N_r receive antennas ($N_r \geq N_t$). Assuming perfect timing and symbol-synchronous receiver, the complex baseband equivalent model of the received signal vector can be described as

$$y(t) = H(t)\,x(t) + n(t) \tag{1}$$

where $y(t) = \lceil y_1(t), \ldots, y_{N_r}(t) \rceil^T$ and $n(t) = \lceil n_1(t), \ldots, n_{N_r}(t) \rceil^T$ denote the N_r-size received signal vector and the additive white Gaussian noise (AWGN) vector; $x(t) = \lceil x_1(t), \ldots, x_{N_t}(t) \rceil^H$ denotes the N_t-size transmitted signal vector from M-ary phase-shift keying (M-PSK) or M-ary quadrature amplitude modulation (M-QAM). The symbols $x_m(t)$ and the noise $n_n(t)$ are mutually uncorrelated, zero-mean random processes with variances $E\{|x_m(t)|^2\} = 1$ and $E\{|n_n(t)|^2\} = N_0$. Throughout this paper, $(\cdot)^T$and $(\cdot)^H$ denote matrix transpose and conjugate transposition, respectively. $H(t)$ denotes the $N_r \times N_t$-size MIMO channel matrix between transmit and receive antennas at the discrete time t. The channel matrix contains uncorrelated Gaussian channel coefficients with unit variance. The channel is assumed to be flat fading and quasi-static, i.e., the channel matrix is constant within the frame and changes independently from one frame to another. We also assume the perfect knowledge about the channel state information in the receiver.

For brevity of notation the discrete time index t is abandoned in the subsequent consideration so (1) becomes

$$y = Hx + n \tag{2}$$

2.2. Maximum Likelihood Detector Algorithm (MLD)

In the sense of minimizing the error probability, MLD is the optimal. With perfect knowledge of the channel state information of H, the MLD performs signal detection based on

$$\hat{x} = \arg\min_x \left\{ \|y - Hx\|^2 \right\} \tag{3}$$

Since the whole alphabet size of vector x depends on the constellation size of each signal and the number of transmit antennas, an exhaustive searching over the whole alphabet has to be done when performing MLD, which is infeasible in practical if either the constellation size or the signal dimension size is very large. So the QR-decomposition of channel matrix is obtained first as $H = Q\tilde{R}$, where Q is a $N_r \times N_r$ unitary matrix,

$$\tilde{R} = \begin{bmatrix} R \\ 0_{(N_r - N_t) \times N_t} \end{bmatrix} \tag{4}$$

R is $N_t \times N_t$ upper triangular matrix, and $0_{(N_r - N_t) \times N_t}$ is zero matrix of size $(N_r - N_t) \times N_t$. Noting that $Q^H Q = I$, after left-multiplying received signal by Q^H, we can rewrite (2) as:

$$Q^H y = Q^H H x + Q^H n = Q^H Q \tilde{R} x + Q^H n = \tilde{R} x + Q^H n \tag{5}$$

And then ignoring the zero part at the bottom of $\tilde{R}$, (5) can be rewritten into

$$\tilde{y} = Rx + \tilde{n} \tag{6}$$

where $\tilde{y}$ is the first N_t rows of $Q^H y$ and $\tilde{n}$ is the first N_t rows of $Q^H n$, where the statistical properties of n and $\tilde{n}$ are equal.

Therefore, the ML detection problem (3) can be reformulated as

$$\hat{x} = \arg\min_x \left\{ \|\tilde{y} - Rx\|^2 \right\} = \arg\min_x \left\{ \sum_{i=1}^{N_t} \left| \tilde{y}_i - \sum_{j=i}^{N_t} R_{i,j} \hat{x}_j \right|^2 \right\} \tag{7}$$

$R_{i,j}$ is the (i,j)th component of R, and $|\cdot|$ denotes the absolute value. Let us assume

$$d(\hat{x}) = \sum_{i=1}^{N_t} \left| \tilde{y}_i - \sum_{j=i}^{N_t} R_{i,j} \hat{x}_j \right|^2 \tag{8}$$

where $\hat{x} = [\hat{x}_1, \hat{x}_2, \ldots, \hat{x}_{N_t}]$. To account for the case when the decision is made on symbols from x_{N_t} to x_k, $1 \le k \le N_t$, we generalize the metric in (8) as

$$d_k(x) = \sum_{i=k}^{N_t} \left| \tilde{y}_i - \sum_{j=i}^{N_t} R_{i,j} x_j \right|^2 \tag{9}$$

Here $x = [x_k, x_{k+1}, \ldots, x_{N_t}]$ of length $N_t - k + 1$.

2.3. QRD-M Algorithm

QRD-M algorithm achieves near-MLD performance while requiring comparatively low complexity [8]. It is a breadth-first tree traversal algorithm. At each detection layer, QRD-M algorithm keeps M reliable candidates instead of deciding the symbol. Decision is made after all detection layers processed. The concept of QRD-M is to apply the tree search to detect the symbols in a sequential manner. Starting from the last layer (first detection layer, $i = N_t$), the algorithm calculates the metrics for all possible values of $\hat{x}_i$ from the constellation using Euclidean distance given as (8). The metrics of these points or nodes are then ordered, and only M nodes with the smallest metrics are retained and the rest of the list is deleted. The same procedure is applied to the nodes of the next layer, and this process continues to the first layer (last detection layer, $i = 1$). To accomplish near-MLD performance for QRD-M algorithm, M should be large enough for the selected paths to include the correct one. However, in the subsequent layers, we have to repeatedly extend to qM (q is the modulation order) branches and calculate the corresponding Euclidean distances in order to select M survivor paths.

For easy understanding, an example of the conventional QRD-M algorithm is illustrated in Figure 1. We assume the transmitted signals are QPSK modulated and MIMO antenna configuration is 3×3, therefore the number of the stages in the signal tree is 3. The number of survived branches M is equal to 4, and the solid line and bold line denote the searched branch and the survived branch, respectively.

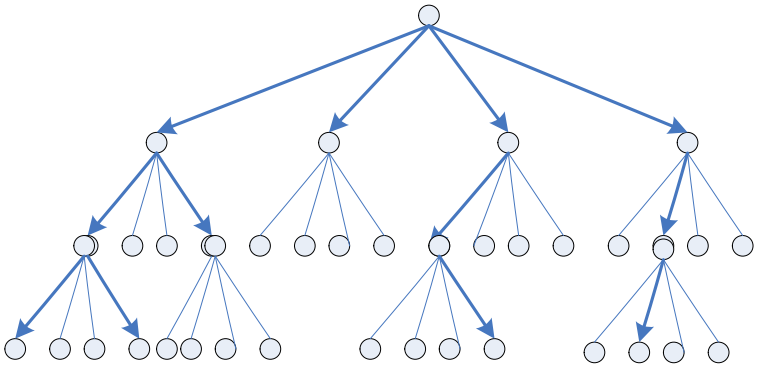

Figure 1: Tree structure of 3×3 MIMO system with QPSK and QRD-M ($M = 4$).

3. ITERATIVE QRD-M ALGORITHM

In this section, we propose a fresh detection scheme for MIMO system to improve the detection performance of conventional QRD-M algorithm with low computational complexity.

Because of the upper triangular property of R, the decision on the last layer x_{N_t} in x does not depend on x_j for $1 \le j \le N_t - 1$. So we perform the exhaustive search of x_{N_t}, the metric in (9) is evaluated for all q constellation points, $x_{N_t}^{(\lambda)}$, for $1 \le \lambda \le q$. Let us assume $d(\lambda) = d(x_{N_t}^{(\lambda)}) = |\tilde{y}_{N_t} - R_{N_t,N_t} x_{N_t}^{(\lambda)}|^2$, without loss of generality that the symbol with lower index has a smaller metric $d(1) \le d(2) \le \cdots \le d(q)$, which gives an ordered set $\{x_{N_t}^{(1)}, x_{N_t}^{(2)}, \ldots, x_{N_t}^{(q)}\}$ in terms of $d(\lambda)$. The smaller index in the superscript of $x_{N_t}^{(\lambda)}$ indicates the smaller metric.

We start searching for other symbols $\hat{x}_1 \sim \hat{x}_{N_t-1}$ using QRD-M algorithm assuming $x_{N_t} = x_{N_t}^{(1)}$. The result of the search is expressed as a vector, $x^{(1)} = [x_1^{(1)}, x_2^{(1)}, \ldots, x_{N_t}^{(1)}]$ with the metric

evaluated in (8), $d^{(1)} = \sum_{i=1}^{N_t} |\tilde{y}_i - \sum_{j=1}^{N_t} R_{i,j} x_j^{(1)}|^2$, where the superscripts in $x^{(1)}$ and $d^{(1)}$ indicate that x_{N_t} is assumed to be $x_{N_t}^{(1)}$. As the detection algorithm runs, λ^* in $x_{N_t}^{(\lambda^*)}$ indicates the assumption on x_{N_t}, which provides the smallest metric $d^{(\lambda^*)}$.

IQRD-M begins with $x_{N_t}^{(1)}$ sets λ^* to 1. We perform the next tree search assuming $x_{N_t} = x_{N_t}^{(2)}$ only if the second smallest metric $d(2) < d^{(1)}$ ($d^{(\lambda^*)} = d^{(1)}$ at the first step) since otherwise, the metric of the next tree search is already bigger than $d^{(\lambda^*)}$. The complexity of the tree search can be further reduced by comparing the partial metric with the smallest metric $d^{(\lambda^*)}$ in the IQRD-M. More specifically, when IQRD-M has decisions $[x_k^{(\lambda)}, x_{k+1}^{(\lambda)}, \ldots, x_{N_t}^{(\lambda)}]$ the λth tree search, we calculate its partial metric in (9) $d_k^{(\lambda)} = d_k(x^{(\lambda)}) = \sum_{i=k}^{N_t} |\tilde{y}_i - \sum_{j=i}^{N_t} R_{i,j} x_j|^2$, and compares it with $d^{(\lambda^*)}$. The tree search stops and restarts with the next assumption $x_{N_t}^{(\lambda+1)}$ if $d_k^{(\lambda)} \geq d^{(\lambda^*)}$. The proposed detection algorithm is stopped if $d^{(\lambda^*)} \leq d(\lambda)$, which significantly reduces the complexity in the tree search.

4. CONCLUSIONS

A new detection scheme is proposed in this paper for MIMO system on Rayleigh fading channel. The proposed detection algorithm, named as iterative QRD-M (IQRD-M), improves the conventional QRD-M through the exhaustive search of the last layer. And then the accumulated metrics are calculated and sorted, which gives an order set of the last layer. The left layers are searched with novel termination methods. The proposed algorithm provides the more near-ML performance with low complexity.

REFERENCES

1. Foschini, G. J. and M. J. Gans, "On limits of wireless communications in a fading environment when using multiple antennas," *Wireless Personal Communications*, Vol. 6, 311–335, 1998.
2. Seethaler, D., G. Matz, and F. Hlawatsch, "Low-complexity MIMO data detection using Seysen's lattice reduction algorithm," *IEEE International Conference on Acoustics, Speech and Signal Processing*, Vol. 3, III-53–56, 2007.
3. Lee, K. and J. Chun, "ML symbol detection based on the shortest path algorithm for MIMO systems," *IEEE Transactions on Signal Processing*, Vol. 55, No. 11, 5477–5484, Nov. 2007.
4. Xie, Y., Q. Li, and C. N. Georghiades, "On some near optimal low complexity detectors for MIMO fading channels," *IEEE Transactions on Wireless Communications*, Vol. 6, No. 4, 1182–1186, Apr. 2007.
5. Choi, J., Y. Hong, and J. Yuan, "An approximate MAP-based iterative receiver for MIMO channels using modified sphere detection," *IEEE Transactions on Wireless Communications*, Vol. 5, No. 8, 2119–2126, 2006.
6. Wang, R. and G. B. Giannakis, "Approaching MIMO channel capacity with soft detection based on hard sphere decoding," *IEEE Transactions on Communications*, Vol. 54, No. 4, 587–590, 2006.
7. Kim, K. J., J. Yue, R. A. Iltis, and J. D. Gibson, "A QRD-M/Kalman filter-based detection and channel stimation algorithm for MIMOOFDM systems," *IEEE Transactions on Wireless Communications*, Vol. 49, No. 10, 2389–2402, 2005.
8. Chin, W. H., "QRD based tree search data detection for MIMO communication systems," *Proc. IEEE VTC*, Vol. 3, 1624–1627, June 2005.
9. Li, W., M. Chen, S. Cheng, and H. Wang, "An improved QRD-M algorithm in MIMO communications," *Global Telecommunications Conference*, 4380–4384, 2007.
10. Kim, B.-S. and K. Choi, "A very low complexity QRD-M algorithm based on limited tree search for MIMO systems," *Vehicular Technology Conference*, 1246–1250, 2008.

Reconstruction of Multi-component Signals Based on Quasi Fourier Transform

Gang Bi and Yu Zeng
School of Information & Electrical Engineering
City College, Zhejiang University, Hangzhou 310015, China

Abstract— A novel method of Quasi Fourier Transform for reconstruction of multi-component signals is presented, which the characteristics and properties of this method are investigated. By transforming the various aliasing signals in frequency domain into a quasi frequency domain, the multi-component signals can be easily separated. Some contrasts of Quasi Fourier Transform compared with fractional Fourier domain filtering can avoid some problems of aliasing distortion in time domain and frequency domain. The results by citing specific examples show that Quasi Fourier Transform will be an efficient tool to extract effectively useful signals from buried in the noise.

1. INTRODUCTION

Parameter estimation and reconstruction of multi-component linear or nonlinear frequency modulated signals have a variety of applications, including sonar, radar and other communications. These signals have time-varying spectral properties, and the time-frequency representation (TFR) has been proved to be a powerful tool in analysis of such time-varying signal. Although the Short Time Fourier Transform (STFT) [1] is the most common method used in TFR, its accuracy in parameter estimation is often reduced because of window effects. The Wigner-Ville Distribution (WVD) ([1–3]) is commonly used as a basic quadratic TFR, and it provides optimal energy concentration about the instantaneous frequency (IF) in the time-frequency domain (TFD); therefore it gives more accurate parameter estimation results than the STFT. However, in multi-component cases, WVD suffers the cross-terms which may impair some of the auto-terms. Although by improving the kernel of the WVD, we can reduce cross-terms without degrading auto-terms ([4–6]), its usefulness will be restricted by the heavy computational load. Recently the fractional Fourier transform (FRFT) is proposed in [7, 8] to deal with linear frequency modulated (LFM) signals and it performs better in reducing cross-terms than original TFR. However, this method has difficulties in case of nonlinear frequency modulated signals. On the other hand, if useful information is modulated both in frequency and amplitude, it is not enough to estimate the IF only. In order to recover the amplitude information, it is necessary to separate the original multi-component signals into components and reconstruct them separately. In this case, the method of optimal filtering in the fractional Fourier domain is proposed in [9]. But this method has a problem that if signals have aliasing in the fractional Fourier optimal domain as well, the reconstructed signals will be distorted. In this letter, a novel method of the quasi Fourier transform is proposed in order to solve the problem of multi-component signal reconstruction. With this method, signals with aliasing in the frequency domain are transformed to a new domain where no aliasing appears.

This letter is organized as follows: in Section 2, we define the Quasi Fourier Transform (QFT), and investigate some of its properties. In Section 3, we use this method to deal with general multi-component signals, and give the simulation results. Conclusions are given in Section 4.

2. DEFINITION AND PROPERTIES OF QFT

The STFT has been used as the most common method for non-stationary signal analysis. It is defined as:

$$S(t,\omega) = \frac{1}{\sqrt{2\pi}} \int s(\tau) h(\tau - t) e^{-j\omega\tau} d\tau \tag{1}$$

with $h(t)$ selected appropriately, $S(t,\omega)$ can be plotted as the spectrogram of signal $s(t)$.

Consider a multi-component signal $s(t)$ which contains two nonlinear FM components, Figure 1 shows its spectrogram where the dashed curve $\omega = \alpha(t)$ will be able to separate component A and B, actually, the two components have aliasing both of the time and frequency domains.

If we can establish a transform $\tilde{F}_\alpha$, which transforms a time domain signal to an $\tilde{\omega}$ frequency domain, where component A just located in the range $\tilde{\omega} > \tilde{\omega}_s$, component B in range $\tilde{\omega} < \tilde{\omega}_s$,

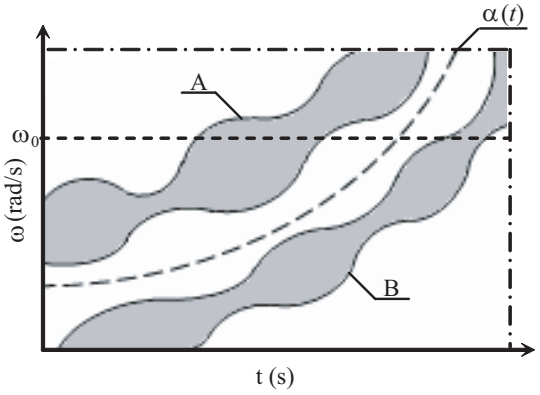

Figure 1: Spectra of a multi-component signal.

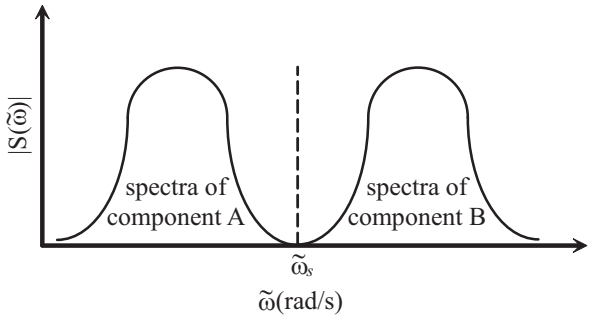

Figure 2: Distribution of a multi-component signal in $\tilde{\omega}$ frequency domain.

and let line $\tilde{\omega} = \tilde{\omega}_{\rm s}$ correspond to curve $\alpha(t)$ in the TFD, then we can separate easily those two components using a simple low-pass or high-pass filters. The spectra of the signal transformed by $\tilde{F}_\alpha$ are shown in Figure 2.

For this reason, we define $\tilde{F}_\alpha$ as follows:

$$\tilde{F}_\alpha[{\rm s}(t)] = \int_{-\infty}^{+\infty} {\rm s}(t) K(t,\tilde{\omega}) dt = S(\tilde{\omega}) \tag{2}$$

where curve $\alpha(t)$ in the TFD denotes the IF of time domain signal $s_0(t) = \frac{1}{2\pi}\exp(j\int_0^t \alpha(\tau)d\tau)$. In order to map $\alpha(t)$ to the point $\tilde{\omega}_{\rm s}$ in the $\tilde{\omega}$ frequency domain, signal $s_0(t)$ should be transformed into a Dirac function $\delta(\tilde{\omega} - \tilde{\omega}_{\rm s})$ in the $\tilde{\omega}$ frequency domain by $\tilde{F}_\alpha$. Then,

$$\int_{-\infty}^{+\infty} s_0(t) K(t,\tilde{\omega}) dt = \frac{1}{2\pi}\int_{-\infty}^{+\infty} e^{j\int_0^t \alpha(\tau)d\tau} K(t,\tilde{\omega}) dt = \delta(\tilde{\omega} - \tilde{\omega}_{\rm s}) \tag{3}$$

From Equation (3), we can derive the following formula,

$$K(t,\tilde{\omega}) = \alpha(t)\exp\left[-j(\tilde{\omega} - \tilde{\omega}_{\rm s} + 1)\int_0^t \alpha(\tau)d\tau\right] \tag{4}$$

Substituting (4) into (2), the QFT can be written as follows:

$$\tilde{F}_\alpha[{\rm s}(t)] \equiv \int_{-\infty}^{+\infty} {\rm s}(t)\alpha(t) e^{-j(\tilde{\omega}-\tilde{\omega}_{\rm s}+1)\int_0^t \alpha(\tau)d\tau} dt = S(\tilde{\omega}) \tag{5}$$

where $K(t,\tilde{\omega})$ is the kernel of the QFT.

Similarly, if $K^{-1}(t,\tilde{\omega})$ satisfies the following equation:

$$\int_{-\infty}^{+\infty} \delta(\tilde{\omega} - \tilde{\omega}_{\rm s}) K^{-1}(t,\tilde{\omega}) d\tilde{\omega} = \frac{1}{2\pi} e^{j\int_0^t \alpha(\tau)d\tau} \tag{6}$$

where $K^{-1}(t,\tilde{\omega})$ is the kernel of Inverse Quasi Fourier Transform (IQFT). From Equation (6), we can conclude that

$$K^{-1}(t,\tilde{\omega}) = \frac{1}{2\pi}\exp\left[j(\tilde{\omega} - \tilde{\omega}_{\rm s} + 1)\int_0^t \alpha(\tau)d\tau\right] \tag{7}$$

Conveniently, choose $\tilde{\omega}_{\rm s}$ to act as the unitary critical frequency, i.e., $\tilde{\omega}_{\rm s} = 1$. The IQFT is defined as follows:

$$\tilde{F}_\alpha^{-1}[S(\tilde{\omega})] \equiv \frac{1}{2\pi}\int_{-\infty}^{+\infty} S(\tilde{\omega}) e^{j\tilde{\omega}\int_0^t \alpha(\tau)d\tau} d\omega = s(t) \tag{8}$$

As $\alpha(t)$ used for QFT can be selected any function according to special needs, the QFT will be able be extend to reconstruction of most multi-component signals. Compare with the Fourier transform,

the frequency variable $\tilde{\omega}$ in the QFT transforms is not the classical frequency variable ω, but it is a function of time-varying. Finally, the QFT can be rewritten as follows:

$$\begin{cases} S(\tilde{\omega}) = \tilde{F}_\alpha[s(t)] = \int_{-\infty}^{+\infty} s(t)\alpha(t)e^{-j\tilde{\omega}\int_0^t \alpha(\tau)d\tau}dt \\ s(t) = \tilde{F}_\alpha^{-1}[S(\tilde{\omega})] = \frac{1}{2\pi}\int_{-\infty}^{+\infty} S(\tilde{\omega})e^{j\tilde{\omega}\int_0^t \alpha(\tau)d\tau}d\tilde{\omega} \end{cases} \tag{9}$$

Some properties of the QFT are investigated as follows:

(1) When $\alpha(t) = 1$, the QFT becomes the classical Fourier transform. From the definition of the QFT, we can obtain the following conclusion as

$$\frac{1}{2\pi}\int_{-\infty}^{+\infty} \delta(\tilde{\omega} - \tilde{\omega}'_{\rm s})e^{j\tilde{\omega}\int_0^t \alpha(\tau)d\tau}d\tilde{\omega} = \frac{1}{2\pi}e^{j\tilde{\omega}'\int_0^t \alpha(\tau)d\tau} \quad (\tilde{\omega}'_{\rm s} \neq \tilde{\omega}_{\rm s} = 1) \tag{10}$$

(2) Where $\frac{1}{2\pi}e^{j\tilde{\omega}'_{\rm s}\int_0^t \alpha(\tau)d\tau}$ $(\tilde{\omega}'_{\rm s} > 1)$ denotes signals located in the area above curve $\alpha(t)$ in TFD. Suppose that there are two component in the Time-Frequency Domain (TFD), as showed in Figure 1, by using QFT, these two signals can be separated by a reasonable curve $\alpha(t)$. In the context, $s_1(t)$ refers to signal and $s_2(t)$ to noise. The function $s_0(t) = \frac{1}{2\pi}\exp(j\int_0^t \alpha(\tau)d\tau)$ will be transformed to a Dirac function $\delta(\tilde{\omega} - \tilde{\omega}_{\rm s})$ in the $\tilde{\omega}$ frequency domain by QFT.

(3) The QFT is a process of TFD mapping based on $\alpha(t)$. Let $\omega = \alpha(t)$ in Equation (1). We can define the quasi STFT as follows:

$$S(t, \omega') = \frac{1}{\sqrt{2\pi}}\int s(\tau)h(\tau - t)e^{-j\alpha(t)\tau}d\tau \tag{11}$$

By selecting a reasonable $\alpha(t)$ and using Equation (11) to process the multi-component signal in Figure 1, we can get a spectrogram based on the quasi STFT is shown in Figure 3, in which the component A and B are separated in frequency domain. For any specific value of frequency (e.g., ω'_0), at most one of the two spectra is non-zero. However, in the TFD as shown in Figure 1, for some frequency values (e.g., ω_0), both signals' spectra are non-zero.

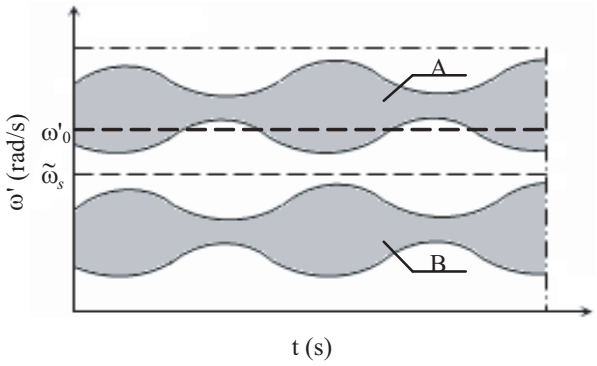

Figure 3: Spectrogram of multi-component signal based on quasi STFT.

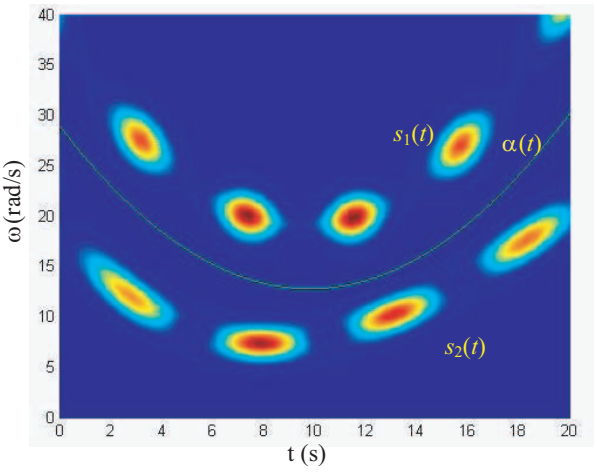

Figure 4: Spectrogram of signal $s(t)$.

3. SIMULATION RESULTS

Specifically, multi-component signals can be described as:

$$s(t) = \sum_{i=1}^{N} s_i(t) = \sum_{i=1}^{N} A_i(t)\exp(j\varphi_i(t)) \tag{12}$$

where $A_i(t)$ are amplitude modulated coefficients and $\omega_i(t) = d\varphi_i(t)/dt$ are the IF's. Consider a multi-component signal $s(t)$ which contains two nonlinear FM components $s_1(t)$ and $s_2(t)$ as

$$\begin{aligned} s(t) &= s_1(t) + s_2(t) \\ &= 3^{2-\cos(1.5t)} \exp(j(0.07t^3 - 2t^2 + 38t)) + 20\sin(0.6t)\exp(j(-100\exp(-0.2t) + 0.017t^3)) \end{aligned} \quad (13)$$

Figure 4 shows the spectrogram of this multi-component signal based on STFT, where the window function is $h(t) = \sqrt{2/\pi}e^{-t^2}$. The IF of $s_1(t)$ is $\omega(t) = 0.21t^2 - 4.0t + 38$, and the IF of $s_2(t)$ is $\omega(t) = 20\exp(-0.2t) + 0.051t^2$. Because signals are located along the IF's in the TFD, these two components are independent. In order to separate these two components, we can construct a filter whose cut-off frequency apply the time-varying function $\alpha(t)$. In this example, let $\alpha(t) = 0.168t^2 - 3.30t + 29$ (shown in Figure 4). According to Section 2, we use QFT to transform the time domain signal $s(t)$ to $\tilde{\omega}$ frequency domain. Figure 5 shows the distribution of $S(\tilde{\omega})$ in the $\tilde{\omega}$ frequency domain. Noted that $S(\tilde{\omega})$ is almost zero at the points $|\tilde{\omega}| = 1$. This is because the points $|\tilde{\omega}| = 1$ correspond to $\alpha(t)$. Component A is only located in the range $|\tilde{\omega}| > 1$ while component B in the range $|\tilde{\omega}| < 1$.

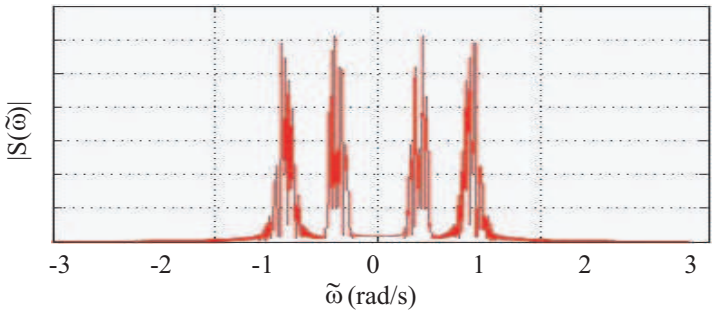

Figure 5: Distribution of $S(\tilde{\omega})$ in $\tilde{\omega}$ frequency.

The lowpass or highpass filter with time-varying cut-off frequency can be replaced by an ideal lowpass or highpass filter in the $\tilde{\omega}$ frequency domain. The frequency response $S_L(\tilde{\omega})$ of signal $S(\tilde{\omega})$ through an ideal lowpass filter can be written as follows:

$$S_L(\tilde{\omega}) = \begin{cases} S(\tilde{\omega}) & |\tilde{\omega}| \le 1 \\ 0 & |\tilde{\omega}| > 1 \end{cases} \quad (14)$$

By using the IQFT to transform $S_L(\tilde{\omega})$ to the time domain which yields the reconstructed signal $s_2'(t)$. Similarly, putting signal $S(\tilde{\omega})$ through an ideal highpass filter and using the IQFT to transform $S_H(\tilde{\omega})$ to the time domain yield the reconstructed signal $s_1'(t)$. Figure 6 shows the spectra of $S_L(\tilde{\omega})$ and $S_H(\tilde{\omega})$.

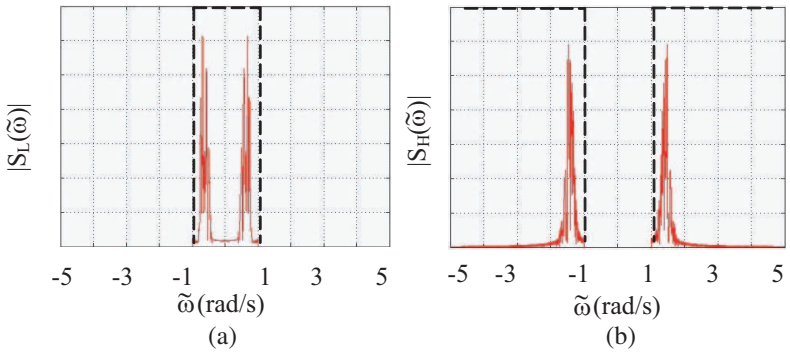

Figure 6: Spectra after going through lowpass and highpass filters in $\tilde{\omega}$ domain. (a) Output spectrum of the low pass filter; (b) Output spectrum of the high pass filter.

Figure 7 shows reconstruction results of the multi-component signal $s(t)$ in the time domain. Figure 7(a) shows the original multi-component signal $s(t)$, Figure 7(b) shows component $s_1(t)$

and Figure 7(c) shows component $s_2(t)$. Figure 7(d) shows the reconstructed component $s_1'(t)$ and Figure 7(e) shows the reconstructed component $s_2'(t)$. It can be observed that the reconstructed components are consistent with the original ones.

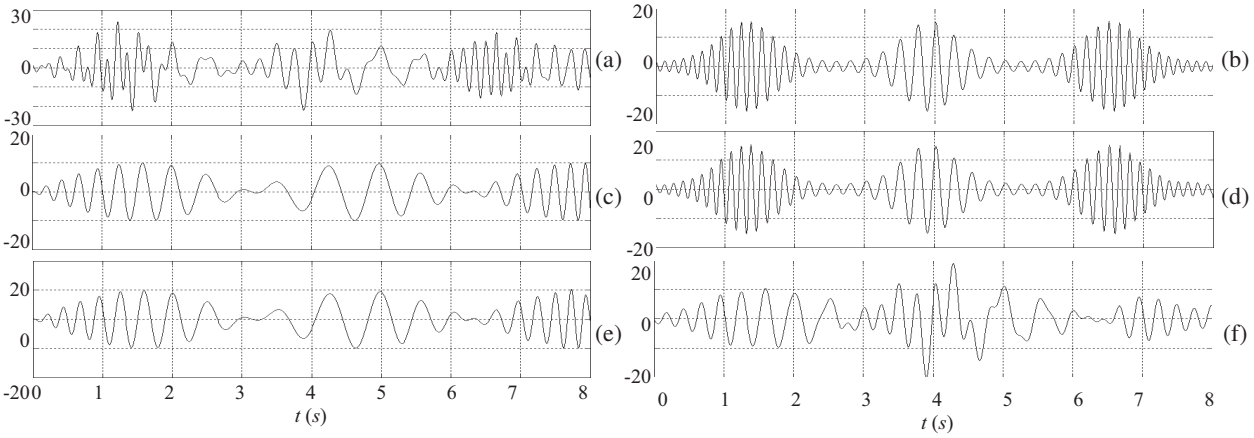

Figure 7: Comparison of the reconstructed signals and the original signals. (a) Multi-component signal; (b) Signal $s_1(t)$; (c) Signal $s_2(t)$, (d) Reconstructed signal $s_1'(t)$, (e) Reconstructed signal $s_2'(t)$; (f) Reconstructed Signal $s_2'(t)$ using optimal filtering based on FRFT.

Figure 7(f) gives the reconstruction results using the method of optimal filtering in the fractional Fourier domain. Obviously, the reconstructed component $s_2'(t)$ is not consistent with original component $s_2(t)$. In the fractional Fourier domain, when the multi-component signals have no aliasing, some components can be separated and reconstructed by the method of optimal filtering. As shown in Figure 8(a), for a multi-component signal, we can find a fractional Fourier optimal domain α, and suppose that component A and B have no aliasing in the α-fractional domain, with this context we can separate these two components and reconstruct them by using a bandpass filter. However, in other situation shown as in Figure 8(b), we can not find any Fourier optimal domain α to meet the separated condition. The two components can't be separated by a line, and there is aliasing existing in the α-fractional domain both components A and B. If using the bandpass filter shown via the dashed line, the component A is partly interfused into component B (as A1 shown in Figure 8(b)), and component B will also unavoidably lose information in both the low frequency region (as B1 shown in Figure 8(b)) and high frequency region (as B2 shown in Figure 8(b)). As a result the reconstructed components will be distorted. Figure 9 shows the spectrogram of the multi-component signal $s(t)$ based on the quasi STFT. It can be seen that component A and B are located at different sides of the line $\omega' = 1$. That is to say, the QFT is a process of TFD mapping based on $\alpha(t)$, and the two components can be separated by curve $\alpha(t)$ which are mapped to be a straight line, so the resulting components can be reconstructed easily.

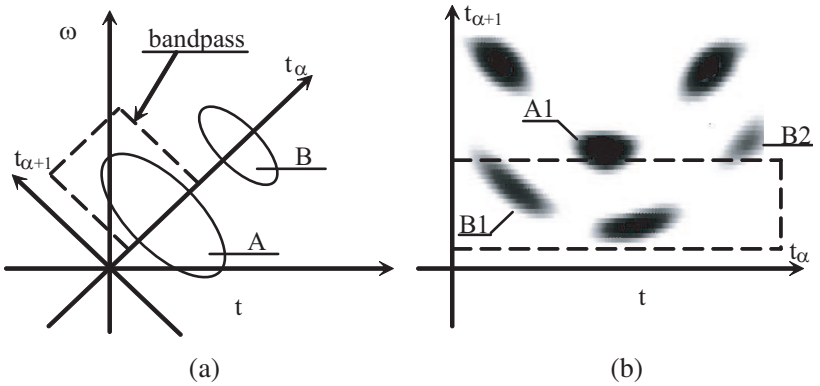

Figure 8: Signal reconstruction in α-domain. (a) No aliasing appears in α-domain; (b) Aliasing appears in α-domain.

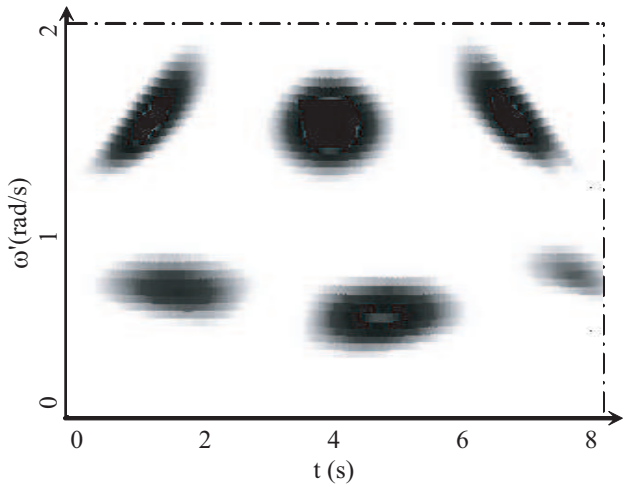

Figure 9: Spectrogram of signal $s(t)$ based on quasi STFT.

4. CONCLUSIONS

A quasi Fourier transform is proposed for the reconstruction of nonlinear frequency modulated and amplitude modulated multi-component signals. This method transforms signals which are aliased in the frequency domain, into the quasi frequency domain where the resulting spectra can be easily separated. The simulation results indicate that this method produces reliable reconstructed signals.

REFERENCES

1. Cohen, L., *Time-Frequency Analysis: Theory and Applications*, Prentice Hall, 77–111.
2. Özdemir, A. K. and O. Arikan, "Fast computation of the ambiguity function and the Wigner distribution on arbitrary line segments," *IEEE Trans. Signal Processing*, Vol. 49, No. 2, 381–393, 2001.
3. Wang, P., J. Yang, and Y. Du, "A fast algorithm for parameter estimation of multi-component LFM signal at low SNR," *2005 International Conference on Communications, Circuits and Systems, Proceedings*, Vol. 2, 765–768, May 27–30, 2005.
4. Nickel, R. M., T.-H. Sang, and W. J. Williams, "A new signal adaptive approach to positive time-frequency distributions with suppressed interference terms," *Proceedings of the 1998 IEEE International Conference on Acoustics, Speech, and Signal Processing, ICASSP '98*, Vol. 3, 1777–1780, May 12–15, 1998.
5. Özdemir, A. K. and O. Arikan, "A high resolution time frequency representation with significantly reduced cross-terms," *Proceedings of the 2000 IEEE International Conference on Acoustics, Speech, and Signal Processing, ICASSP '00*, Vol. 2, 11693–11696, 2000.
6. Khandan, F. and A. Ayatollahi, "A Performance region of center affine filter for eliminating of interference terms of discrete Wigner distribution," *Proceedings of the 3rd International Symposium on Image and Signal Processing and Analysis, ISPA 2003*, Vol. 2, 621–625, 2003.
7. Raveh, I. and D. Mendlovic, "New properties of the Radon transform of the cross Wigner/ambiguity distribution function," *IEEE Trans. Signal Processing*, Vol. 47, No. 7, 2077–2080, 1999.
8. Akay, O. and G. F. Boudreaux-Bartels, "Fractional autocorrelation and its application to detection and estimation of linear FM signal," *Time-Frequency and Time-Scale Analysis, Proceedings of the IEEE-SP International Symposium*, 213–216, 1998.
9. Kutay, M. A., H. M. Ozaktas, et al., "Optimal filtering in fractional Fourier domains," *IEEE Trans. Signal Processing*, Vol. 47, No. 5, 1129–1143, 1997.

Optimal Adaptive Waveform Selection for Target Tracking

B. Wang, J. K. Wang, X. Song, and F. L. Liu
Northeastern University, China

Abstract— In cognitive radar, the transmitter adjusts its illumination of the environment in an intelligent manner and selects the best waveform sequence according to different environment Waveform selection is an important problem in the research of cognitive radar. The problem of adaptive waveform selection can be viewed as a problem of stochastic dynamic programming. However, as a result of large state variable space and large decision variable space, the computational cost of solution of optimality equations is very high. To account for these shortcomings, we can use forward dynamic programming algorithm approximating the expectation. This method can reduce the computational cost compared to the traditional algorithm, especially in problems of high dimensions. The adaptive scheduling algorithm can minimize target tracking errors, too.

1. INTRODUCTION

Recently a new idea called cognitive radar is proposed by research team of Simon Haykin in 2006. There are three ingredients in the constitution of cognitive radar: intelligent signal processing, feedback from the receiver to the transmitter and preservation of the information content of radar returns. Cognitive radar can percept external environment real time, select optimal waveform and make transmitted waveform and target environment and information demand of radar working achieve optimum matching, and then multiple performance of searching, tracking, guidance and identification of friend or foe of multi-target can be realized. Related works are in [1–4].

There are many problems in the research of cognitive radar, among which optimal adaptive waveform selection is important. The aim of waveform selection is to select the optimal waveform sequence according to different environment and track targets with more accuracy. In [5], adaptive waveform selection schemes where selection is based on overall target tracking system performance are investigated. The problem of waveform selection can be thought of as a sensor selection problem, and various methods for solving such sensor selection problems have been examined in [6, 7]. In [8], different waveforms are combined to form transmitted waveforms, and then detecting and tracking performance of system is improved and the defect of single waveform is avoided. In [9], waveform design is treated as the major part of the whole tracking system design, and waveform selection scheme of one-step ahead. In [10], adaptive waveform scheduling problem for new target detection as a stochastic dynamic programming problem is posed and Incremental Pruning method is used to solve this problem.

However, suitable scheduling algorithms are lacked, and optimality equations are themselves computationally intractable as a result that state variable space and decision variable space are sometimes very large. To account for these shortcomings, we can use forward dynamic programming algorithm approximating the expectation, which is one method of approximate dynamic programming (ADP). ADP offers a powerful set of strategies for problems that are hard because they are large. In this paper, based on stochastic dynamic programming model, we will show how to use forward dynamic programming algorithm to approximate the expectation. The format of the reminder of this paper is as follows. In Section 2, stochastic dynamic programming model of adaptive waveform selection is set up. In Section 3, forward dynamic programming algorithm approximating the expectation is used to solve adaptive waveform scheduling problem. In Section 4, how to choose reward function is introduced. In Section 5, the whole paper is summarized.

2. MODEL

In heavy clutter environments, it is an acute problem that we can not obtain good Doppler and good range resolution in a waveform tailoring simultaneously. We should make a trade-off decision between them. The basic scheme for adaptive waveform selection is to define a cost function that describes the cost of observing a target in a particular location for each individual pulse and select the waveform that optimizes this function on a pulse by pulse basis.

The area covered by a particular radar beam can be divided into a grid in range-Doppler space. The cells in range are indexed by $\tau = 1, \ldots, P$ and those in Doppler are indexed by $\upsilon = 1, \ldots, Q$. So the number of possible scenes or hypotheses about the radar scene is 2^{PQ}, which is denoted by χ.

Now we will define state variable, measurement variable and control variable. The state variable is represented by X. The state of our model is $X_t = x$ where $x \in \chi$. The control variable is represented by u. Let u_t be the control variable that indicates which waveform is chosen at time t to generate measurement variable $Y_{t+1} = x'$, where $u_t \in U$ and $x' \in \chi$. Y represents the measurement variable. The probability of receiving a particular measurement $Y_{t+1} = x'$ will depend on both the true, underlying scene and on the choice of waveform used to generate the measurement. We define $m_{x'x}$ the measurement probability. $m_{x'x}$ is the probability of a detection in all the cells considered to have a scatter present under hypothesis x' given that the true scene is given by hypothesis x and is observed with waveform u. The definition of $m_{x'x}$ is

$$m_{x'x}(u_t) = P(Y_{t+1} = x' | X_t = x, u_t) \tag{1}$$

Define $\pi = \{u_0, u_1, \ldots, u_T\}$ where $T + 1$ is the maximum number of dwells that can be used to detect and confirm targets for a given beam. Then π is a sequence of waveforms that could be used for that decision process. Let

$$V_t(X_t) = E\left[\sum_{t=0}^{T} \gamma^t C(X_t, u_t)\right] \tag{2}$$

where $C(X_t, u_t)$ is the reward earned when the scene X_t is observed using waveform u_t and γ is discount factor. Then the aim of our problem is to find the sequence π^* that satisfies

$$V^*(X_t) = \max_{\pi} E\left[\sum_{t=0}^{T} \gamma^t C(X_t, u_t)\right] \tag{3}$$

π^* is our optimal waveform sequence.

If we can know the state variable X, the problem can be solved. Unfortunately, knowledge of the actual state is not available. We will consider replacing X with another variable that is known. Using the method of [11], we can obtain that the optimal control policy π^* that is the solution of (3) is also the solution of

$$V^*(\mathbf{p}(0)) = \max_{\pi} E\left[\sum_{t=0}^{T} \gamma^t C(\mathbf{p}_t, u_t)\right] \tag{4}$$

where $\mathbf{p}_t$ is the conditional density of the state given the measurements and the controls and $\mathbf{p}_0$ is the a priori probability density of the scene. So we need to solve the following problem

$$\max_{\pi} E\left[\sum_{t=0}^{T} \gamma^t C(\mathbf{p}_t, u_t)\right] \tag{5}$$

The refreshment formula of $\mathbf{p}_t$ is

$$\mathbf{p}_{t+1} = \frac{\mathbf{M}\mathbf{A}\mathbf{p}_t}{\mathbf{1}'\mathbf{M}\mathbf{A}\mathbf{p}_t} \tag{6}$$

where $\mathbf{M}$ is the diagonal matrix with the vector $(m_{x'x}(u_t))$ the non-zero elements and $\mathbf{1}$ is a column vector of ones. $\mathbf{A}$ is state transition matrix. $\mathbf{p}_t$ can be obtained in the model that all targets have a Swerling 1 distribution and the noise is additive, white and Gaussian with known power.

If we have a function U that determines u_t when $\mathbf{p}_t$ and π is known, then we can write

$$\max_{\pi} E\left[\sum_{t=0}^{T} \gamma^t C(\mathbf{p}_t, U_t^{\pi}(\mathbf{p}_t))\right] \tag{7}$$

3. SOLUTION METHOD

Using Bellman's equation, the solution of (7) can be written as

$$V_t(\mathbf{p}_t) = \max_{u_t}(C_t(\mathbf{p}_t, u_t) + \gamma E\{V_{t+1}(\mathbf{p}_{t+1}) | \mathbf{p}_t\}) \tag{8}$$

In probability form, it can be written as

$$V_t(\mathbf{p}_t) = \max_{u_t}\left(C_t(\mathbf{p}_t, u_t) + \gamma \sum_{\mathbf{p}' \in \mathbf{P}} P(\mathbf{p}' | \mathbf{p}_t, u_t) V_{t+1}(\mathbf{p}')\right) \tag{9}$$

We will use a forward dynamic programming algorithm approximating the expectation to solve this problem, which is an algorithm of ADP methods.

The foundation of approximate dynamic programming is based on an algorithmic strategy that steps forward through time. In order to simulate the process forward in time, we need to solve two problems. First, when we use exact dynamic programming, we stepped backward in time, exactly computing the value function which we then used to produce optimal decisions. When we step forward in time, we have not computed the value function, so we have to turn to an approximation in order to make decisions. Second, we need a way to randomly generate a sample of what might happen.

So there are four steps in our algorithm.

a. Making decisions: value function will be approximated.

b. Stepping forward through time: a sample realization of the information will be picked from the sample paths.

c. Approximating the expectation: a sample of outcomes of what information will be are randomly generated.

d. Updating the value function approximation: it depends largely on the specific form of the value function approximation.

Our algorithm is described in Figure 1.

Step1. Initialization:

Initialize $\bar{V}_t^0(\mathbf{p}_t)$ for all states $\mathbf{p}_t$, choose an initial state $\mathbf{p}_0^1$ and set $n=1$.

Step2. Choose a sample path so that we can get $P(\mathbf{p}'|\mathbf{p}_t^n, u_t)$, that is $p_{t+1}(\hat{\omega})$.

Step3. For $t=0,1,2,...,T$ do:

Step 3a. Choose a random sample of outcomes representing possible realizations of the information.

Step 3b. Solve

$$\hat{v}_t^n = \max_{u_t \in U_t^n}(C_t(\mathbf{p}_t^n, u_t) + \gamma \sum_{\hat{\omega}\in\Omega_{t+1}^n} p_{t+1}(\hat{\omega})\bar{V}_{t+1}^{n-1}(\mathbf{p}'))$$

Let u_t^n be the value of u_t that solves the maximization problem.

Step 3c. Update $\bar{V}_t^{n-1}(\mathbf{p}_t)$ using

$$\bar{V}_t^n(\mathbf{p}_t) = \begin{cases} (1-\alpha_{n-1})\bar{V}_t^{n-1}(\mathbf{p}_t^n) + \alpha_{n-1}\hat{v}_t^n, \mathbf{p}_t = \mathbf{p}_t^n \\ \bar{V}_t^{n-1}(\mathbf{p}_t), otherwise \end{cases}$$

Step 3d. Compute $\mathbf{p}_{t+1}^n = \mathbf{p}^M(\mathbf{p}_t^n, u_t^n, W_{t+1}(\omega^n))$, where $\mathbf{p}_{t+1} = \dfrac{\mathbf{MAp}_t}{\mathbf{1'MAp}_t}$.

Step4. Let $n=n+1$. If $n< N$, go to step 1.

Figure 1: A forward dynamic programming algorithm approximating the expectation.

In the algorithm, Ω represents the set of possible realizations of the information and ω represents a sample realization. $p_{t+1}(\hat{\omega})$ is probability of sampling ω and $\bar{V}$ is the approximation value of V. n represents the number of iteration and α is step length.

4. REWARD FUNCTION

Generally speaking, reward function can be different forms according to different problems. It represents the value that we stand in certain place and take some certain action. In the problem of adaptive waveform selection, two forms of reward function are usually used.

Linear reward function is usually used in the circumstance that $C(\mathbf{p}, u)$ is required to be a piecewise linear function. The form of this function is simple and easy to calculate. However, it can not reflect the whole value sometimes. The form of linear reward function is

$$C(\mathbf{p}, u) = \mathbf{p}'\mathbf{p} - 1 \tag{10}$$

Entropy reward function is usually used in the circumstance that $C(\mathbf{p})$ is not required to be a piecewise linear function. It comes from information theory. It can reflect the whole value accurately. But it is more complex than linear reward function. The form of entropy reward function is

$$C(\mathbf{p}, u) = \sum_{x \in \chi} p_x(k) \log(p_x(k)) \tag{11}$$

If $\mathbf{p}_t$ and reward function are determined, then we can solve adaptive waveform scheduling problem.

5. CONCLUSIONS

In this paper, based on stochastic dynamic programming model of adaptive waveform selection, ADP method is used to solve this problem. We use forward dynamic programming algorithm to approximate the expectation. This method can reduce the computational cost compared to the traditional algorithm, especially in the problems of high dimensions. The adaptive scheduling algorithm can also minimize target tracking errors.

REFERENCES

1. Haykin, S., T. Kirubarajan, and B. Currie, "Literature search on adaptive radar transmit waveforms," *ASL Report 02-01*, Adaptive Systems Laboratory, McMaster University, Canada, 2002.
2. Haykin, S., "Adaptive radar: Evolution to cognitive radar," *Proceedings of IEEE International Symposium on Phased Array Systems and Technology*, 613, Boston, USA, Oct. 2003.
3. Haykin, S., "Cognitive radar: A way of the future," *IEEE Signal Processing Magazine*, Vol. 23, No. 1, 30–40, 2006.
4. Haykin, S., T. Kirubarajan, and B. Currie, "Adaptive radar for improved small target detection in a maritime environment," *ASL Report 03-01*, Adaptive Systems Laboratory, McMaster University, Canada, 2003.
5. Kershaw, D. J. and R. J. Evans, "Optimal waveform selection for tracking systems," *IEEE Transactions on Information Theory*, Vol. 40, No. 5, 1536–1550, 1994.
6. Krishnamurthy, V., "Algorithms for optimal scheduling of hidden Markov model sensors," *IEEE Transactions on Signal Processing*, Vol. 50, No. 6, 1382–1397, 2002.
7. He, Y. and E. K. P. Chong, "Sensor scheduling for target tracking in sensor networks," *Proceedings of 43rd IEEE Conference on Decision and Control*, 743–748, Paradise, Island, Bahamas, 2004.
8. Rago, C., P. Willett, and Y. B. Shalom, "Detecting-tracking performance with combined waveforms," *IEEE Transactions on Aerospace and Electronic Systems*, Vol. 34, No. 2, 612–624, 1998.
9. Kershaw, D. J. and R. J. Evans, "Waveform selective probabilistic data association," *IEEE Transactions on Aerospace and Electronic Systems*, Vol. 33, No. 4, 1180–1188, 1997.
10. Scala, B. F., M. Rezaeian, and B. Moran, "Optimal adaptive waveform selection for target detection," *Proceedings of International Conference on Radar*, 492–496, Adelaide, Australia, Sept. 2003.
11. Bertsekas, D., *Dynamic Programming and Optimal Control*, Athena Scientific, Nashua, 2001.

Adaptive Cooperative Coding in Fast Rayleigh Fading Channel

Li Li[1], **Tinghuai Wang**[2], **Yang Du**[1], **and Honglin Hu**[3]

[1]The Electromagnetics Academy at Zhejiang University
Zhejiang University, Hangzhou 310027, China
[2]School of Engineering, University of Warwick, Coventry CV4 7AL, UK
[3]Shanghai Research Centre for Wireless Communication (SHRCWC), Shanghai, China

Abstract— The relay technique is an effective way to enlarge the cell coverage and enhance the spectral efficiency in wireless network. In this paper, we propose a novel cooperative transmission protocol based on the channel coding, named the adaptive cooperative coding (ACC), which is implemented by transmitting the rate-compatible punctured convolutional code (RCPC) sequence and its complementary punctured convolutional (CPC) sequence during the two-hop transmission. We discuss and evaluate the ACC protocol performance in fast Rayleigh fading channel by mathematical analysis. Through Monte Carlo simulation, the performance upper bound is proved to be tight with the simulation result, and the ACC protocol outperforms the traditional single hop (SH) transmission due to the considerable cooperative diversity, while maintaining the same transmit rate and power as that of the SH transmission.

1. INTRODUCTION

The cooperative transmission has been proposed recently in order to enhance coverage with high data rate and low equipment cost by placing the relay nodes (RN) between the source node (SN) and the destination node (DN) [1]. Mobile units or relays cooperate by sharing their antennas, so as to exploit diversity and reducing end-to-end path loss. However, the poor transmit efficiency is the greatest disadvantage for the multi-hop transmission, since the RN antenna cannot receive and transmit at the same time when RN works at a half-duplex model. In order to improve the spectrum efficiency, the coded cooperation is introduced by integrating cooperation transmission into channel coding, which has been studied in [2].

We have proposed a novel cooperative coding protocol in [3], in which different portions of the code sequence are sent to DN via two independent links while keeping the same transmit rate as the single hop (SH) transmission but with significant cooperative diversity improvement. We name it the adaptive cooperative coding (ACC), since the transmit rate for each hop is variable. In this paper, we discuss the performance of the ACC protocol in fast Rayleigh fading channel, and give a strict upper bound through the mathematical analysis. Meanwhile, in order to reduce the computational complexity, a simple but asymptotic bound is also introduced in this paper.

This paper is organized as follows: Section 2 introduces the ACC protocol concisely, and in Section 3 we give the strict performance bound in fast Rayleigh fading channel. The performance is evaluated through Monte Carlo simulation in Section 4, and Section 5 gives the conclusion.

2. SYSTEM MODEL

The information bit sequence $\mathbf{a}$ is processed into the coded bit sequence $\mathbf{s}$ before transmission. In this paper, the $R_c = 1/N$ rate convolutional coding (CC) is used for channel coding [5].

In the SH transmission, the BPSK modulated symbol sequence $\mathbf{x} = \mathbf{1} - \mathbf{2s}$ is transmitted from SN to DN directly, with transmit power E_s per symbol.

The ACC protocol is performed in two stages. During the first step, the lth RCPC [4] sequence $s^{(l)}$ with coding rate $R^{(l)} = \frac{P}{P+l}$ is broadcasted by SN, where P is the puncturing period and $l \in [1, (N-1)P]$. The received sequences at RN and DN during the first step are

$$\begin{aligned} \mathbf{y}_R &= \mathbf{h}_{S,R}\sqrt{E_s}\mathbf{x}^{(l)} + \mathbf{n}_R, \\ \mathbf{y}_{D,1} &= \mathbf{h}_{S,D}\sqrt{E_s}\mathbf{x}^{(l)} + \mathbf{n}_{D,1}. \end{aligned} \tag{1}$$

During the second step, if RN decodes $\mathbf{y}_R$ correctly, it forwards the regenerated CPC sequence $\bar{\mathbf{s}}^{(l)}$ to DN. ContrarilySN transmits $\bar{\mathbf{s}}^{(l)}$ to DN during the second step. The received sequence at DN becomes

$$\mathbf{y}_{D,2} = \begin{cases} \sqrt{G_{R,D}E_2}\bar{\mathbf{x}}^{(l)} + \mathbf{n}_{D,2}, & \text{if RN decodes correctly} \\ \sqrt{G_{S,D}E_2}\bar{\mathbf{x}}^{(l)} + \mathbf{n}_{D,2}, & \text{otherwise} \end{cases}. \tag{2}$$

The transmitted sequences $\mathbf{x}^{(l)} = 1 - 2\mathbf{s}^{(l)}$ and $\bar{\mathbf{x}}^{(l)} = 1 - 2\bar{\mathbf{s}}^{(l)}$ are the lth BPSK modulated RCPC and CPC symbols, with unit sample energy; the coefficient $\mathbf{h}_{i,\,j}$ captures the effects of the path loss and static fading on transmissions from node i to node j, where $\{i,\, j\} \in \{S,\, R,\, D\}$; E_s is the transmitted power per symbol; $\mathbf{n}_R$, $\mathbf{n}_{D,\,1}$ and $\mathbf{n}_{D,\,2}$ are zero-mean, mutually independent complex white Gaussian noises at RN and DN in those two steps, with variance $\frac{N_0}{2}$ per dimension.

Under the Rayleigh fading model, we define the SNR vector for each received symbol from node i to node j as $\boldsymbol{\gamma}_{i,\,j} = |\mathbf{h}_{i,\,j}|^2 E_s/N_0$, whose elements $\gamma_{i,\,j}(n)$ are independent exponential random variables with expected values $\Gamma_{i,\,j} \triangleq E[\gamma_{i,\,j}(n)] = G_{i,j}E_s/N_0$, where $G_{i,\,j}$ is the large scaled path loss.

At the end of the ACC transmission, DN depunctures the received sequences $\mathbf{y}_{D,\,1}$ and $\mathbf{y}_{D,\,2}$ separately, and combines these two streams into one CC sequence by performing the maximum-ratio combining (MRC) algorithm. Consequently DN decode the combined sequence with Viterbi algorithm.

Compared with the SH transmission, the ACC protocol maintains the same transmit rate and power consumption. Notice that $p_1 = \frac{P+l}{NP}$ and $p_2 = \frac{NP-P-l}{NP}$ parts of the mother sequence $\mathbf{s}$ are transmitted during two steps. The parameter p_2 is also defined as the level of cooperation (LoC) [2], which stands for the ratio of the period of cooperative transmission to that of overall transmission.

3. PERFORMANCE BOUND

In this section, we aim to find a packet error rate (PER) upper bound of the SH and ACC transmissions through the fast fading channel, the channel propagation for each symbol is an i.i.d. Rayleigh random variable.

3.1. SH Transmission

In the SH transmission, DN receives the sequence with SNR $\boldsymbol{\gamma}_{S,\,D}$, then the PER is upper bounded by

$$PER_{SH} \le I \sum_{d=d_f}^{\infty} a_d P_2(\Gamma_{S,\,D},\, d), \tag{3}$$

where $P_2(\Gamma_{S,\,D},\, d)$ is the ergodic pairwise-error probability (PEP) function of the BPSK modulated sequence at receiving SNR $\boldsymbol{\gamma}_{S,\,D}$ with distance d [5], which is derived by averaging the conditional PEP function $P_2(\Gamma_{S,\,D},\, d|\boldsymbol{\gamma}_{S,\,D}) = Q(\sqrt{2\sum_{n=1}^{d}\gamma_{S,\,D}(n)})$ over the distribution of $\boldsymbol{\gamma}_{S,\,D}$, yielding

$$\begin{aligned} P_2(\Gamma_{S,\,D},\, d) &= \int_0^{\infty} P_2(\Gamma_{S,\,D},\, d|\boldsymbol{\gamma}_{S,\,D}) p(\boldsymbol{\gamma}_{S,\,D}) d\boldsymbol{\gamma}_{S,\,D} \\ &= \left[\frac{1}{2}(1-u)\right]^d \sum_{k=0}^{d-1} \binom{d-1+k}{k} \left[\frac{1}{2}(1+u)\right]^k, \end{aligned} \tag{4}$$

where $u = \sqrt{\frac{\Gamma_{S,D}}{1+\Gamma_{S,\,D}}}$.

3.2. ACC Protocol

In the ACC transmission, the symbol sequence is transmitted stepwise. As discussed in [3], the overall PER performance of the ACC protocol is upper bounded as

$$PER_{ACC}(\gamma_s,\, l) \approx PER^{(1)}_{S,\,R} PER^{(2)}_{S,\,D;\,S,\,D} + PER^{(2)}_{S,\,D;\,R,\,D}, \tag{5}$$

where the superscripts $^{(1)}$ and $^{(2)}$ indicate the first and second steps respectively; the component $PER^{(1)}_{S,\,R}$ is the PER bound of the lth RCPC sequence at RN; $PER^{(2)}_{S,\,D;\,R,\,D}$ is the PER bound of the regenerated sequence combined from the SN-DN and RN-DN links at DN; and $PER^{(2)}_{S,\,D;\,S,\,D}$ is the PER bound of the whole sequence received from SN during the two steps.

During the first step, RN decodes the lth RCPC sequence received from SN with SNR $\boldsymbol{\gamma}_{S,R}$, thus the PER function at RN is upper bounded by

$$PER_{S,R}^{(1)} \leq I \sum_{d=d_f^{(l)}}^{\infty} a_d^{(l)} P_2(\Gamma_{S,R}, d). \tag{6}$$

With the same approach as that in the SH transmission, the ergodic PEP function of the RCPC sequence in fast Rayleigh fading channel is derived as

$$P_2(\Gamma_{S,R}, d) = \left[\frac{1}{2}(1-v)\right]^d \sum_{k=0}^{d-1} \begin{pmatrix} d-1+k \\ k \end{pmatrix} \left[\frac{1}{2}(1+v)\right]^k, \tag{7}$$

where $v = \sqrt{\frac{\Gamma_{S,R}}{1+\Gamma_{S,R}}}$.

However during the second step, the ACC protocol approaches into two ways:

If RN decodes the lth RCPC sequence correctly, it forwards the CPC sequence. Then the decoding sequence at DN is MRC combined of the RCPC sequence with SNR $\boldsymbol{\gamma}_{S,D}$ and the CPC sequence with SNR $\boldsymbol{\gamma}_{R,D}$. From the solution from [3], the conditional PEP of the combined sequence after VA decoding is derived as

$$P_2^{(l)}(\Gamma_{S,D}, \Gamma_{R,D}, d|\boldsymbol{\gamma}_{S,D}, \boldsymbol{\gamma}_{R,D}) = \frac{1}{Pa_d} \sum_{t=1}^{a_d} \sum_{s=1}^{P} Q\left(\sqrt{2 \sum_{n=1}^{\alpha_{t,s}^{(l)}(d)} \gamma_{S,D}(n) + 2 \sum_{n=1}^{d-\alpha_{t,s}^{(l)}(d)} \gamma_{R,D}(n)}\right), \tag{8}$$

where $\alpha_{t,s}^{(l)}(d)$ and $d - \alpha_{t,s}^{(l)}(d)$ indicate the numbers of the symbols with SNR $\boldsymbol{\gamma}_{S,D}$ and $\boldsymbol{\gamma}_{R,D}$ in the tth path with distance d at the sth start point. The ergodic PEP is generated by averaging the conditional PEP function (13) over the fading factor $\boldsymbol{\gamma}_{S,D}$ and $\boldsymbol{\gamma}_{R,D}$, i.e.,

$$\begin{aligned} P_2^{(l)}(\Gamma_{S,D}, \Gamma_{R,D}, d) &= \int_0^{\infty}\int_0^{\infty} P_2^{(l)}(\Gamma_{S,D}, \Gamma_{R,D}, d|\boldsymbol{\gamma}_{S,D}, \boldsymbol{\gamma}_{R,D}) p(\boldsymbol{\gamma}_{S,D}) p(\boldsymbol{\gamma}_{R,D}) d\boldsymbol{\gamma}_{S,D} d\boldsymbol{\gamma}_{R,D} \\ &\leq \frac{1}{2Pa_d} \sum_{t=1}^{a_d} \sum_{s=1}^{P} \left(\frac{1}{\Gamma_{S,D}+1}\right)^{\alpha_{t,s}^{(l)}(d)} \left(\frac{1}{\Gamma_{R,D}+1}\right)^{d-\alpha_{t,s}^{(l)}(d)}. \end{aligned} \tag{9}$$

Thus the PER function for the combined sequence after two steps is upper bounded by

$$PER_{S,D;R,D}^{(2)} \leq I \sum_{d=d_f}^{\infty} a_d P_2^{(l)}(\Gamma_{S,D}, \Gamma_{R,D}, d). \tag{10}$$

Correspondingly, if RN decodes the RCPC sequence incorrectly, SN transmits the CPC sequence in the second step. DN receives the whole packet from SN with SNR $\boldsymbol{\gamma}_{S,D}$. Then the PER bound is equal to that of the SH transmission, i.e.,

$$PER_{S,D;S,D}^{(2)} = PER_{SH}. \tag{11}$$

Ultimately, the strict ACC protocol bound under fast Rayleigh fading channel is given by Equations (6), (11), (15) and (16).

4. SYSTEM SIMULATION AND DISCUSSION

We follow the same simulation scenario as in [3]. We fix the SN and DN position, and glides RN along the line connecting SN and DN for simplicity. During transmission, all the links are assumed to be fast Rayleigh fading, and the large-scaled path fading between node i and j is modelled as $G_{i,j} = d_{i,j}^{-3}$, with the normalized distance $d_{S,D} = 1$, $d_{S,R} = dist$ and $d_{R,D} = 1 - dist$. A 1/2 rate CC with generator matrix $(15, 17)$ is utilized as the mother sequence, with a family of RCPC sequences rating between 8/16 and 8/10, by the puncturing period $P = 8$.

As illustrated in Figures 1–3, different *dist*s (0.3, 0.5 and 0.7) are sampled to evaluate the performance of the SH and ACC transmission in the fast Rayleigh fading channel. Compared with the SH transmission, the ACC protocol benefits from the cooperative diversity. At high SNR, the ACC protocol with higher *LoC* brings to the better performance gain, since the larger coding gain is achieved at high *LoC*. However at low SNR, either scenario at $dist = 0.3$ or $dist = 0.7$ performs not as well as that at $dist = 0.5$. When RN is close to SN ($dist = 0.3$), the higher *LoC* is preferred since the SN-RN link channel quality is 14dB higher than the direct link, thus more CPC bits could be sent by RN. However, slight cooperative diversity is achieved since RN is far from DN. Comparably, when RN is close to DN and far from SN ($dist = 0.7$), higher *LoC* impacts the detection reliability at low SNR for the first hop, which results in poor system performance. e.g., the ACC protocol with $LoC = 4/16$ even performs better than that with $LoC = 6/16$ at $dist = 0.7$, when SNR is less than 3 dB, as illustrated in Figure 3.

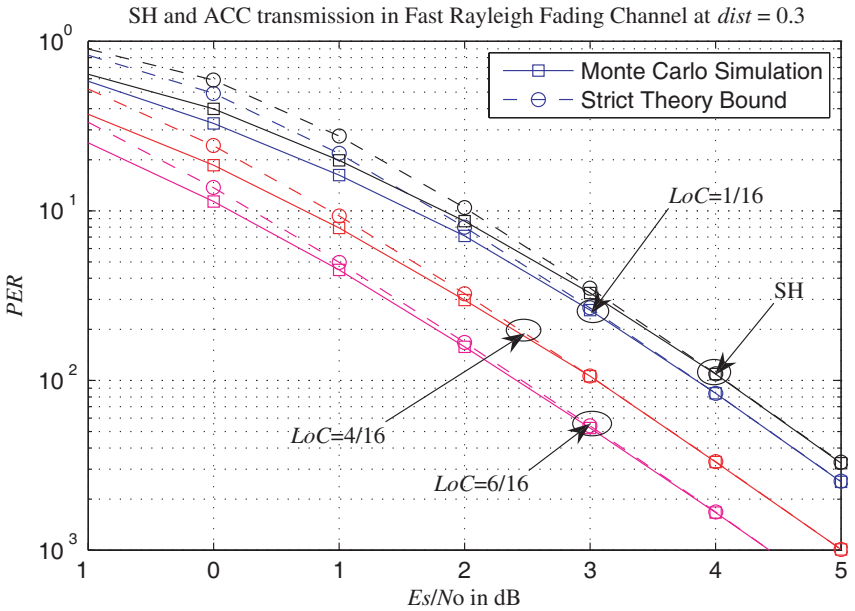

Figure 1: The SH and ACC performance in fading channel at $dist = 0.3$.

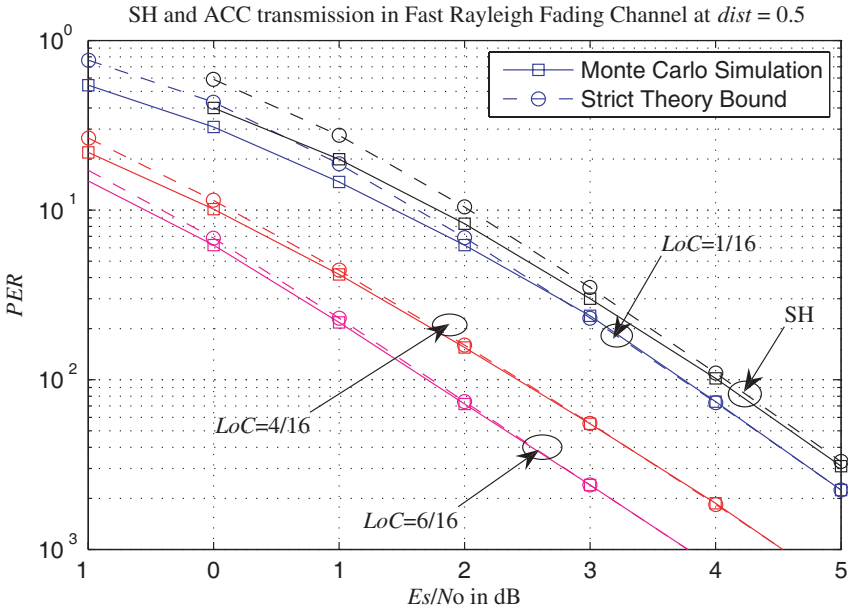

Figure 2: The SH and ACC performance in fading channel at $dist = 0.5$.

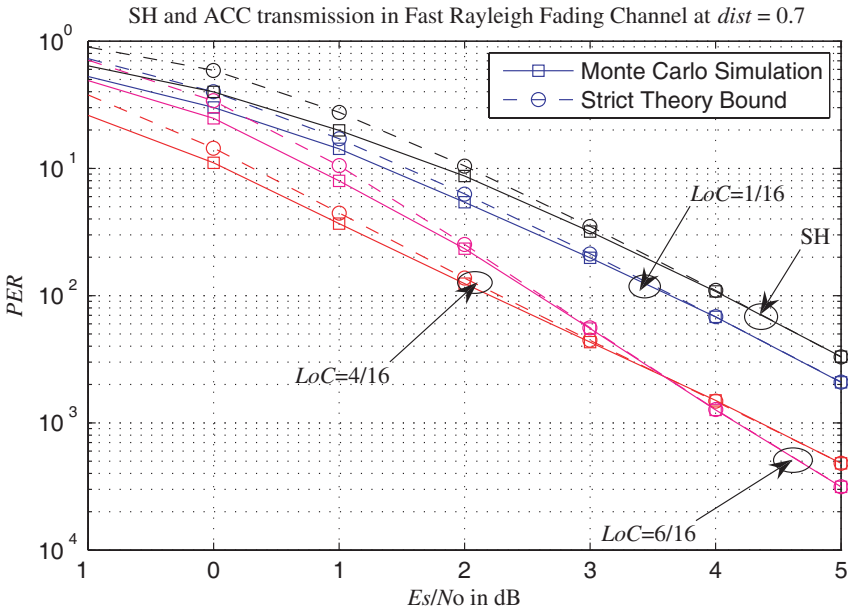

Figure 3: The SH and ACC performance in fading channel at $dist = 0.7$.

5. CONCLUSION

The cooperative transmission is a practical approach to enhance the wireless communication. However, it is impacted from the half duplexing characteristics of the relay antenna. We have proposed a novel relaying protocol, named the adaptive cooperative coding, which maintains the equivalent transmit rate and power as that of the SH transmission, but with great advantage that impressive cooperative diversity is achieved through channel coding. Further, we analysis the ACC protocol performance in the Rayleigh fading channel, and achieve a strict performance bound through mathematical analysis.

REFERENCES

1. Fitzek, F. H. P. and M. D. Katz, *Cooperative in Wireless Networks: Principles and Applications*, Springer, 2006.
2. Hunter, T. E. and A. Nosratinia, "Diversity through coded cooperation," *IEEE Trans. Wireless Commun.*, Vol. 5, No. 2, 283–289, 2006.
3. Li, L., L. Tang, S. Y. Jin, H. L. Hu, and H. F. Wang, "Adaptive cooperative coding in wireless networks," *Proc. IEEE VTC 2008 Spring*, 569–573, 2008.
4. Hagenauer, J., "Rate-compatible punctured convolutional codes and their applications," *IEEE Trans. Commun.*, Vol. 36, No. 4, 389–400, 1988.
5. Viterbi, A. J., "Convolutional codes and their performance in communication systems," *IEEE Trans. Commun.*, Vol. 19, No. 5, 751–772, 1971.

MAC Scheduling Schemes and Cross Layer Optimization for IEEE 802.15.3

G. D. Yang[1], **L. Rong**[2], **R. F. Lin**[1], **and Y. Du**[1]

[1]The Electromagnetics Academy at Zhejiang University
Zhejiang University, Hangzhou 310058, China
[2]Shanghai Research Center for Wireless Communications, Shanghai 200050, China

Abstract— In this paper, the performances of variety of HDR MAC scheduling schemes over IEEE 802.15.3 WPAN are examined. The scheduling schemes under investigation are 1) the shortest remaining processing time rule (SRPT); 2) the exponential rule (EXP); 3) the modified largest weighted delay first rule (M-LWDF); 4) the proportionally fair rule (PROP-FAIR); and 5) the maximum rate rule (MAX-RATE), most of which take advantage of wireless channel conditions to improve channel utilization. In addition, M-LWDF rule and EXP rule provide QoS guarantee to user traffic as well. The performances were studied under large number of simulation using ns-2, which take node mobility, channel fading and traffic characteristics into consideration in order to make the results more realistic.

We also studied the performances gain of scheduling schemes combined with some cross layer mechanisms, including frame-decodability aware (FDA) mechanism for MPEG traffic, adaptive MAC fragment size adjustment and hybrid automatic repeat request (H-ARQ).

The IEEE 802.15.3 standard [1] is designed to provide a high bandwidth, low power consuming solution for multimedia applications for wireless personal area networks (WPANs). It is based on a centralized and connection- oriented adhoc networking topology, with a master-slave hierarchy, where the master is the piconet coordinator (PNC). The PNC only has the roles of admission control, scheduling, and management, without the packet forwarding functionality. The 802.15.3 uses a hybrid medium access control (MAC) protocol; specifically, it uses a contention based protocol (carrier sense multiple access/collision avoidance, CSMA/CA) channel request and time-division multiple access (TDMA) based time slot allocations for data transmission.

Extensive work on scheduling schemes and cross-layer optimization with IEEE802.15.3 WPAN has been conducted over recent years. Kim et al. [2] proposed a rate adaptation mechanism according to the channel condition from the five different data rates supported by HDR WPAN. In [3], the performances of various channel aware scheduling schemes have been studied over IEEE802.15.3 WPAN. The results showed significant system gain when channel conditions were taken into account by resource scheduler. Choi et al. [4] presented a frame-size adaptive MAC protocol to improve the efficiency of the system by adjusting MAC frame size according to the channel conditions.

All the above designs are based on the optimization between the MAC and the physical layer. The application aware approach is also considered in this study, which includes optimization of multimedia application, one of the most important applications of the high data rate (HDR) WPANs. To support MPEG flows with quality of service (QoS) requirements in a HDR WPAN presents challenges to the link resource allocation management. This is due to the additional difficulties from the bursty nature of multimedia traffic and the hierarchical structure of MPEG stream which causes error propagation through its MPEG frame. There is already lots of work in the context of MPEG stream transmission over WPAN system ([5–9]). In [8], the inter-frame structure of MPEG-4 frames was studied and the FDA technique, which takes advantage of the structure information was proposed to reduce the channel resource wastage due to transmission of undecodable video frames.

The purpose of the current work is to provide insight of the system performances of IEEE802.15.3 WPAN designed with different channel aware scheduling schemes in cooperation with adaptive frame-size adjustment, H-ARQ and FDA technique.

The scheduling algorithms under consideration are 1) the shortest remaining processing time (SRPT) [10]; 2) the exponential rule (EXP) [11]; 3) the modified largest weighted delay first rule (M-LWDF) [12]; 4) the proportionally fair rule (PROP-FAIR) [13]; 5) the maximum rate rule (MAX-RATE).

Let us define
$\mu_i(t)$ to be rate corresponding to the state of the channel of user i at time t. It is the actual rate

supported by the channel and is assumed to be constant over one superframe;
$\bar{\mu}_i$ to be the rate corresponding to the mean fading level of user i;
$W_i(t)$ to be the amount of time the HOL packet of user i has spent at the local queue;
$Q_i(t)$ to be The queue size of the buffer of user i at time t.

The SRPT rule that had been proved to minimize the aggregate mean response of the system schedule the tasks based on their processing time. The rule is

$$j = \arg\max_i \frac{\mu_i(t)}{Q_i(t)} \tag{1}$$

The EXP rule tries to balance the weighted delays of all the queues when their differences are large. It renders the exponent term of a queue with large weighted delay to be very large and overrides channel considerations, while making the exponent term of a queue with small weighted delay close to unity. Shakkottai et al. [14] studied various scheduling algorithms for a mixture of real-time and non-real-time data over high data rate/code-division multiple access (HDR/CDMA). They found that the exponential rule performed well with regard to packet delays and average throughput. They stated that this rule is throughput-optimal, in the sense that it makes the queues stable if it is feasible to do so with any other scheduling rules. The rule is given by

$$j = \arg\max_i \gamma_i \mu_i(t) \exp\left(\frac{a_i W_i(t) - \bar{W}}{1 + \sqrt{\bar{W}}}\right), \tag{2}$$

where $\bar{W} = \frac{1}{N}\sum_i a_i W_i(t)$.

The M-LWDF rule is due to, where the authors have shown that this policy is throughput optimal in the sense that it has the largest stable admission region. The rule is

$$j = \arg\max_i \gamma_i \mu_i(t) W_i(t) \tag{3}$$

The PROP-FAIR rule tries to maximize the normalized instantaneous data rate with respect to the mean rate measured over a certain sliding window. It is given by

$$j = \arg\max_i \frac{\mu_i(t)}{\bar{\mu}_i} \tag{4}$$

The MAX-RATE rule schedules the flow whose channel can support the largest data rate over the next superframe, with no regard for other factors such as fairness or QoS. The rule is

$$j = \arg\max_i \mu_i(t) \tag{5}$$

In order to simplify our discussion, we divide these algorithms into three types. SRPT; the Qos group, including EXP and M-LWDF and the rate group, including MAX-RATE and PROP-FAIR.

The choice of parameters is the same as in [14]. γ_i is related to the weight a_i as $\gamma_i = \frac{a_i}{\bar{\mu}_i}$, and a_i is related to the QoS as $a_i = -\frac{\log(\delta_i)}{T_i}$, where δ_i and T_i are parameters pertaining to the QoS requirement of flow i as $P(W_i > T_i) \leq \delta_i$. The values of a_i are to balance reducing weighted delays with being proportionally fair when delay is small. This form of choice for a_i is suggested by a large deviation optimality study [14].

We run the simulation under ns-2.28. For simplicity, we do not consider the CAP duration, and beacon frame is assumed to be error-free since the size of which is much shorter than data frame and is always transmited by base rate. Some important parameters are listed in Table 1, other parameters such as guard time, mFirstCTAGap, minimum interframe space (MIFS), short interframe space (SIFS), frame check sequence (FCS), and base rate are chosen according to the IEEE 802.15.3 standard. The buffer size is assumed to be large enough.

We evaluate the performance with throughput over MPEG-4 traffic, which is generated using transform expand sample (TES) method [15]. The GOP structure is $(12, 3)$ and the data rate of each flow is chosen as 5 Mbps. There are up to 9 MPEG-4 flows Transmit over 9 pairs of nodes. All these flows start and terminate at the same time except for a small offset select randomly in a period of GOP to statistic different situations. One node runs as the PNC, it has no data to receive or to transmit. All these nodes distributed randomly in an area of 10 m × 10 m, of which

Table 1: Simulation parameters.

Max frame Length	1024 bytes
Superframe Size	4000 µs
PHY Header	9.4 µs
MAC Header	16 bytes
Retransmission Limit	4
ACK policy	Imm-ACK
Frequency	2.4 GHz
Transmit power	1 mw

the velocity are less than 0.5 m/s. For EXP and M-LWDF algorithm, as the same in [12], δ is set to 0.01 and T is set to the frame deadline of the flow.

The performance of each Algorithm is evaluated under a time-correlated fading channel. The fading gain is generated according to the modified Clarke and Gans fading model [16], in which the fading envelope is used to modulate a log-distance path loss model with the path loss exponent set to 2 according the measured result obtained form an office environment at 2.4 GHz [17]. Transmission rate is obtained according to the thresholds obtained by Karaoguz et al. in [18].

The of receiver is responsible for maintaining the mean channel rate as well. We use exponential moving average, as shown below, to calculate the mean channel rate and the parameter t_c is chosen to be 1000 as suggested in [19].

$$\bar{\mu}_i(t+1) = (1 - 1/t_c) \times \bar{\mu}_i(t) + 1/t_c \times \mu_i(t) \tag{6}$$

We assume that information is consistent between PNC and other nodes, which means PNC has perfect information of queue size, channel condition and head of line (HOL) packet delays. All simulation cases were performed 10 times for the duration of 120 seconds simulation time.

From the simulation results, we find that the FDA technique, without which the system throughput never reaches half of its capacity in any circumstance, is critical for MPEG-4 traffic. Thus, in the flowing discussions, we always assume that FDA technique is used.

The throughput performances of the QoS group constantly outperform those of other scheduling rules. The throughput gap between QoS group and other scheduling rules increases with network load and signal to noise ratio. When noise power is equal to −80 dbm and 9 MPEG-4 flows exist in the system, the condition which network load is beyond system capacity, the gap is approximately 3 Mbps. When taking into account the adaptive frame-size adjustment and H-ARQ, the throughput performance of each scheduling rules shows a gain around 5 Mbps.

The response time is treated to only apply to successfully transmitted frames. From simulation results, it is observed that in both case of high and low level of noise power, SRPT has the best response time, and the QoS group has the worst response time, with that of rate group lying in-between. Since SRPT is designed for minimizing response time and the scheduling rules in QoS group always give long waiting packets high priorities to save them form expiration, these results are understandable.

To sum up, the QoS group provides the best system performances in terms of system throughput. In addition with adaptive frame-size adjustment and H-ARQ, system throughput is dramatically increased. However, if one wants to balance between throughput and response time performance, a new scheduling algorithm, which considers both the waiting time and the processing time of packets, needs to be designed.

REFERENCES

1. IEEE Standard 802.15.3: Wireless Medium Access Control (MAC) and Physical Layer (PHY) Specifications for High Rate Wireless Personal Area Networks (WPANs), Sept. 2003.
2. Kim, B.-S., Y. Fang, and T. F. Wong, "Rate-adaptive MAC protocol in high-rate personal area networks," *Proc. of IEEE WCNC'04*, Vol. 3, 1394–1399, Mar. 2004.
3. Yang, G. D., L. Rong, D. Y. Tu, R. F. Lin, and Y. Du, "Numerical study of MAC scheduling schemes for IEEE 802.15.3," *Progress In Electromagnetcs Research Symposiun Abstracts*, Hangzhou, China, March 24–28, 2008.

4. Choi, E. C., J. D. Huh, K. S. Kim, and M. H. Cho, "Frame-size adaptive MAC protocol in high-rate wireless personal area networks," *ETRI Journal*, Vol. 28, No. 5, 660–663, Oct. 2006.
5. Rhee, S. H., K. Chung, Y. Kim, W. Yoon, and K. S. Chang, "An application-aware MAC scheme for IEEE 802.15.3 high-rate WPAN," *Proc. of IEEE WCNC'04*, Vol. 2, 1018–1023, Mar. 2004.
6. Wang, M. and G. S. Kuo, "Dynamic MAC scheduling scheme for MPEG-4 based multimedia services in 802.15.3 high-rate networks," *Proc. of IEEE VTC 2005*, Vol. 3, 1559–1663, Sept. 2005.
7. Kim, M. and Y. J. Cho, "Scheduling scheme for providing QoS to realtime multimedia traffics in high-rate wireless PANs," *IEEE Trans. on Consumer Electronics*, Vol. 51, No. 4, 1159–1168, Nov. 2005.
8. Moradi, S. and V. W. S. Wong, "Technique to improve MPEG-4 traffic schedulers in IEEE 802.15.3 WPANs," *Proc. of IEEE ICC'07*, 3782–3786, Jun. 2007.
9. Moradi, S., A. H. M. Rad, and V. W. S. Wong, "A novel scheduling algorithm for video traffic in high-rate WPANs," *Proc. of IEEE GLOBECOM'07*, 742–747, Nov. 2007.
10. Shao, Z. and U. Madhow, "A QoS framework for heavy-tailed traffic over the wireless Internet," *Proc. of MILCOM'02*, Vol. 2, 7–10, Oct. 2002.
11. Shakkottai, S. and A. Stolyar, "Scheduling for multiple flows sharing a time-varying channel: The exponential rule," Bell Laboratories Technical Report, Dec. 2000.
12. Andrews, M., K. Kumaran, K. Ramanan, A. Stolyar, R. Vijayakumar, and P. Whiting, "CDMA data QoS scheduling on the forward link with variable channel condition," Bell Laboratories Technical Report, Apr. 2000.
13. Tse, D., "Forward link multiuser diversity through proportional fair scheduling," presentation at Bell Labs, Aug. 1999.
14. Shakkottai, S. and A. Stolyar, "Scheduling algorithms for a mixture of real-time and non-real time data in HDR," *Proc. of 17th ITC*, 793–804, Salvador da Bahia, Brazil, Sept. 2001.
15. Matrawy, A., I. Lambadaris, and C. Huang, "MPEG4 traffic modeling using the transform expand sample methodology," *Proc. of 4th IEEE International Workshop on Networked Appliances*, 249–256, Jan. 2002.
16. Punnoose, R. J., P. V. Nikitin, and D. D. Stancil, "Efficient simulation of ricean fading within a packet simulator," *Proc. of IEEE VTC'00*, Vol. 2, 764–767, Sept. 2000.
17. Janssen, G. G. M. and R. Prasad, "Propagation measurements in indoor radio environments at 2.4 GHz, 4.75 GHz and 11.5 GHz," *Proc. of IEEE VTC'92*, 617–620, May 1992.
18. Karaoguz, J., "High-rate wireless personal area networks," *IEEE Commun. Mag.*, Vol. 39, No. 12, 96–102, Dec. 2001.
19. Jalali, A., R. Padovani, and R. Pankaj, "Data throughput of CDMA-HDR a high efficiency-high data rate personal communication wireless system," *Proc. of IEEE VTC'00*, Vol. 3, 1854–1858, May 2000.

An Optimal ADP Algorithm for Waveform Selection in Cognitive Radar Systems

Fulai Liu and Jinkuan Wang
Engineering Optimization & Smart Antenna Institute
Northeastern University at Qinhuangdao, China

Abstract— One of the major issues in cognitive radar is obtaining an adaptive transmitting waveform based on environmental measurements. Modern phased array radars, with flexible waveform generation and beam steering capability, are able to adaptively modify their performance to suit a variety of environments. This power has not yet been fully exploited, in part because of the lack of suitable scheduling algorithms. In this paper, we consider the problem of adaptive waveform selection for tracking a single target in clutter using a cognitive radar with a fixed set of waveforms. The aim is to select the best sequence of waveforms to track the target with the highest possible accuracy. The problem of adaptive waveform selection is considered as the multistage stochastic problems, in this paper. For target tracking in cognitive radar system, an optimal approximate dynamic programming algorithm is proposed, taking account that the probability distribution of the underlying stochastic process is not known and the state space is too large to be explored entirely. This presented method combines Monte Carlo simulation in a pure exploitation scheme, in order to construct concave piecewise linear functions approximations. The function slopes are updated through stochastic approximation integrated with a projection operation. The result is a scheduling algorithm that minimizes target tracking errors.

1. INTRODUCTION

Radar systems are an important component in military operations. It has established itself as an indispensable remote-sensing tool for the detection, parameter estimate, tracking, and imaging of targets of interest. Cognitive radar [1] techniques offer the promise of significantly improved performance of all radar systems. Radar signal processing enables the extraction of desired information while rejecting unwanted interference. In particular, a tracking radar, in addition to detection, adaptive diverse waveform selection is advanced technologies used to achieve substantial improvements. The simplest scheme for adaptive waveform selection define a cost function that describes the cost of observing a target in a particular location for each individual pulse and selects the waveform that optimizes this function on a pulse by pulse basis [2]. More improvement in the performance of tracking target, can be gained by solving the scheduling problem over a sequence of waveforms. In [3], different waveforms are combined to form transmitted waveform, and then detecting and tracking performance of system is improved and the defect of single waveform is avoided. In [4], waveform design is treated as the major part of the whole tracking system design, and waveform selection scheme of one-step ahead. The problem of waveform selection can be thought of as a sensor selection problem, as each possible waveform provides a different means of measuring the environment, and related works have been examined in [5, 6]. In [7], adaptive waveform scheduling problem for new target detection as a stochastic dynamic programming problem is posed and Incremental Pruning method is used to solve this problem. The problem of optimal adaptive waveform selection for target tracking is also presented in [8].

In this paper, we consider the problem of adaptive waveform selection for tracking a single target in clutter using a cognitive radar with a fixed set of waveforms. The problem of adaptive waveform selection is considered as the multistage stochastic problems.

2. BACKGROUND

We divide the area covered by a particular radar beam into a grid in range-Doppler space, with the cells in range indexed by $\tau = 1, \ldots, N$ and those in Doppler indexed by $v = 1, \ldots, M$. We assume that there is at most one target in the region, so the number of possible hypotheses about the location of the target is $NM + 1$. The extra hypothesis represents the "no target" is present case. Let H be set of hypothesis, then the state of our model is $x(k) = i$ where $i \in H$. Let u_t be the control variable that indicates which waveform is chosen at time t to generate measurement X_{t+1}, where $u_t \in U$. The probability of receiving a particular measurement $X_t = x$ will depend on

both the true, underlying scene and on the choice of waveform used to generate the measurement. We define $b_{x'x}$ is the measurement probability where

$$b_{x'x}(u_t) = P\left(X_{t+1} = x' | X_t = x, u_t\right) \tag{1}$$

Define $\pi = \{u_0, u_1, \ldots\}$, then π is a sequence of waveforms that can be used to track the target. Let

$$V(x) = E\left[\sum_{k=0}^{\infty} \gamma^k r(x(k), u(k))\right] \tag{2}$$

where $r(x, u)$ is the reward earned when a target at the location given by hypothesis x is observed using waveform u and $0 < \gamma < 1$ is a discount factor. Then the aim of our problem is to find the sequence π^* that satisfies

$$V^*(x) = \max_{\pi} E\left[\sum_{k=0}^{\infty} \gamma^k r(x(k), u(k))\right] \tag{3}$$

3. SOLUTION METHOD

With a little thought, we realize that we do not have to solve this entire problem (3) at once. According to Bellman's equations, the solution of the problem (3) can be found by proceeding backwards with the recursion

$$V_t(x_t) = \max_{u_t \in U} \{C_t(x_t, u_t) + \gamma V_{t+1}(x_{t+1})\} \tag{4}$$

where $V_{t+1}(x_{t+1})$ is the solution of (3) when u is used at dwell $t+1$. It is well known that Q-learning is oftern proposed for model-free applications, is even more difficult since the state space is enlarged with all possible actions. We propose an approximate dynamic programming

Table 1: The SPAR-mlutiperiod algorithm.

STEP0: Initialization:

STEP0a: Initialize $v_t^0(x_t)$ for all t and x_t to be monotone decreasing in H(which denotes the state space).

STEP0b: Initialize x_t^n for all $n \geq 0$.

STEP0c: Set $n = 1$.

STEP1: Sample the exogenous process $u_0^n, \cdots, u_T^n$.

STEP2: Do for $t = 0, 1, \cdots, T$;

STEP 2a: Find the optimal solution u_t^n of $\max_{u \in U} C_t(x_t^n, u) + \gamma V_{t+1}^{n-1}(x_{t+1})$

If $t < T$ then

STEP 2b: Find the post-decision state

$$(x_t^n, u_t^n) = (u_t^{x,n}, g(x_t^n) + Ax_t^n)$$

where g is a deterministic scalar function, A is a $1 \times l$ input-output vector.

STEP 2c: Find the next pre-decision state

$$(x_{t+1}^n, u_{t+1}^n) = \left(f_1(x_t^{x,n}, u_{t+1}^n), f_2(x_t^{x,n}, u_{t+1}^n)\right)$$

STEP 2d: Observe $v_{t+1}^n(x_t^{x,n})$ and $v_{t+1}^n(x_{t+1}^{x,n})$.

STEP 2e: For $u_t^x \in U_t$

$$z_t^n(u_t^x) = (1 - a_t^n(u_t^x))\, v_t^{n-1}(u_t^x) + a_t^n(u_t^x) v_{t+1}^n(u_t^x)$$

STEP 2f: $v_t^n = \prod(z_t^n)$

STEP 3: Increase n by one and go to step 1.

algorithm that exploits the structural properties of optimal value functions of this problem. It combines Monte Carlo simulation in a pure exploitation scheme, in order to construct concave piecewise linear functions approximations. The function slopes are updated through stochastic approximation integrated with a projection operation. The solution method [9] is given in Table 1.

From Table 1, we propose and implement an algorithm that only strores the state after the decision is made and samples all possible actions infinitely often in a uniform way. This implies that all states are sampled infinitely often as well. This algorithm should be at least as good as standard Q-learning, due to a smaller state space. However, a standard Q-learning algorithm stores all possible sate-action paris making this approach impossible to be implemented for our problem class.

4. CONCLUSIONS

In this paper, we propose an approximate dynamic programming algorithm for the waveform selection, which is considered as a multistage stochasitic control problems. The presented method is a combination of Monte Carlo simulation, stochastic approximation and a projection operation. It converges to an optimal policy and scales to high-dimensional problems. The result is a scheduling algorithm that minimizes target tracking errors.

REFERENCES

1. Haykin, S., "Cognitive radar: A way of the future," *IEEE Signal Processing Magazine*, Vol. 23, No. 1, 30–40, 2006.
2. Scala, B. L., M. Rezaeian, and B. Moran, "Optimal adaptive waveform selection for target tracking," *8th International Conference on Infromation Fusion*, Vol. 1, 25–28, 2005.
3. Rago, C., P. Willett, and Y. Bar-Shalom, "Detecting-tracking performance with combined Waveforms," *IEEE Transactions on Aerospace and Electronic Systems*, Vol. 34, No. 2, 612–624, 1998.
4. Kershaw, D. J. and R. J. Evans, "Waveform selective probabilistic data association," *IEEE Transactions on Aerospace and Electronic Systems*, Vol. 33, No. 4, 1180–1188, 1997.
5. He, Y. and E. K. P. Chong, "Sensor scheduling for target tracking in sensor networks," *43rd IEEE Conference on Decision and Control*, 743–748, Paradise, Island, Bahamas, 2004.
6. Krishnamurthy, V., "Algorithms for optimal scheduling of hidden Markov model sensors," *IEEE Trans. on Signal Processing*, Vol. 50, No. 6, 1382–1397, 2002.
7. La Scala, B. F. and R. J. Moran Wand Evans, "Optimal adaptive waveform selection for target detection," *The International Conference on Radar*, 492–496, Adelaide, SA, Australia, 2003.
8. La Scala, B. F., M. Rezaeian, and B. Moran, "Optimal adaptive waveform selection for target tracking," *International Conference on Information Fusion*, 552–557, 2005.
9. Nascimento, J. and W. Powell, "An optimal ADP algorithm for a high-dimensional stochastic control problem," *Proceeding or the 2007 IEEE Symposium on Approximate Dynamic Programming and Reinforcement Learning*, 52–59, 2007.

Reflection Cancellation from High Speed Transmission Line

Salahuddin Raju[1], **S. M. Salahuddin**[2], **and Ishfaqur Raza**[2]

[1]Department of Electrical and Electronic Engineering
American International University-Bangladesh, Bangladesh
[2]Department of Electrical and Electronic Engineering
East-West University, Bangladesh

Abstract— An IO driver architecture is presented here to compensate scattering in high speed transmission line circuits. In this methodology a system is calibrated initially to measure system response to a step or a lone pulse. The IO driver is then programmed to generate measured pulses at designated interval to compensate scattering responses due to impedance mismatch in the system transmission line. The compensation is done for every single bit or pulse transmitted from the driver end to eliminate sustained reflections and resonances. This methodology is demonstrated with high speed design tool. The architecture of the driver and calibration methodology is also outlined.

1. INTRODUCTION

Propagation of a signal with minimal changes to the original shape and phase is fundamental to signal and wave transmission in a high frequency system. Such a transmission system is also complex not only due to its topology but also on how the system is configured as a system setup is dynamic depending on transient requirements. With demand for superior and improved performance, system and associated interfaces are forced to operate at higher speeds. At these frequencies, the wavelengths are becoming comparable to and even less than the dimensions of the devices and components [1]. In these systems wires and waveguides are modelled as distributed element in the form of a transmission line. At these speeds systems are susceptible to signal degradation, which is compensated with equalization both at driver and receiver ends [2]. When devices of such diverse complexity are put together, energy propagation becomes very much dependent on the impedance distribution across all these devices. The nature of discontinuity of the impedance of these devices becomes a primary roadblock to optimum and efficient system performance. Matching of impedance of all these elements is not easy, particularly across frequencies due to reactive elements.

The impedance mismatch causes signal integrity degradation. A wide range of issues can cause these impedance disparities. In systems, these discontinuities can easily appear in the form of vias transitioning between signal layers in circuit board and a single source driving an antenna array [3]. System architectures use good design practices to avoid signal reflections, which includes series and parallel matching schemes. For example, CMOS gate drive impedance is different from the characteristic impedances of PCB lines. This is compensated with a resistor in series to the output of the driver — intending to match source impedance to the characteristic impedances of PCB line. In parallel matching scheme a resistor is placed in shunt with the load. There are major disadvantages to these matching schemes. The parasitic of the termination scheme contributes to the discontinuity which is a function of the frequency of operation. It is also function of the process of the devices. The terminations also consume power, adding to the power budget. At microwave frequencies, all these attributes are very significant [4]. In this paper, a programmable I/O driver architecture is proposed which will have programmable reflection compensation capabilities [5, 6]. The driver will first obtain the signature of the system observed at output of interest. The residual reflections observed at the output is then corrected with time delayed scaled pulses.

When a signal is propagated in a system, load or topology discontinuity will cause a part of the source driven signal back to the source driver. Impedance discontinuity at the driver will then result in a part of the load signal to be sent back again. To reduce these reflections, it is proposed that the driver will be programmed to either source or sink additional energy to cancel reflection from the source.

In this paper, the cancellation technique is discussed for high speed point-to-point interconnects and waveguides. The reflection back and forth within these transmission lines will translate into sustained resonances and introduce ISI, intersymbol interference. The ability to provide measured compensation for reflections at the source also empowers usage of incident wave reflection for greater received signal amplitude. In microwave systems, reflections signal can cause the efficiency to be significantly compromised.

2. MATHEMATICAL ANALYSIS

To introduce this concept, the high speed line shown in Fig. 1 is used. It is driven by a voltage source $V_s(t)$ with a series impedance Z_s. The characteristic impedance of the point to point interconnect line is Z_C which is terminated with load Z_L.

Impedance discontinuity at source and load ends will introduce reflections at both ends. As a result, a residual of the source signal will travel back and forth on the transmission line. From the voltage reflection diagram i.e., lattice diagram shown in Fig. 1 (right), the voltage distribution along the transmission line in time domain is calculated and shown.

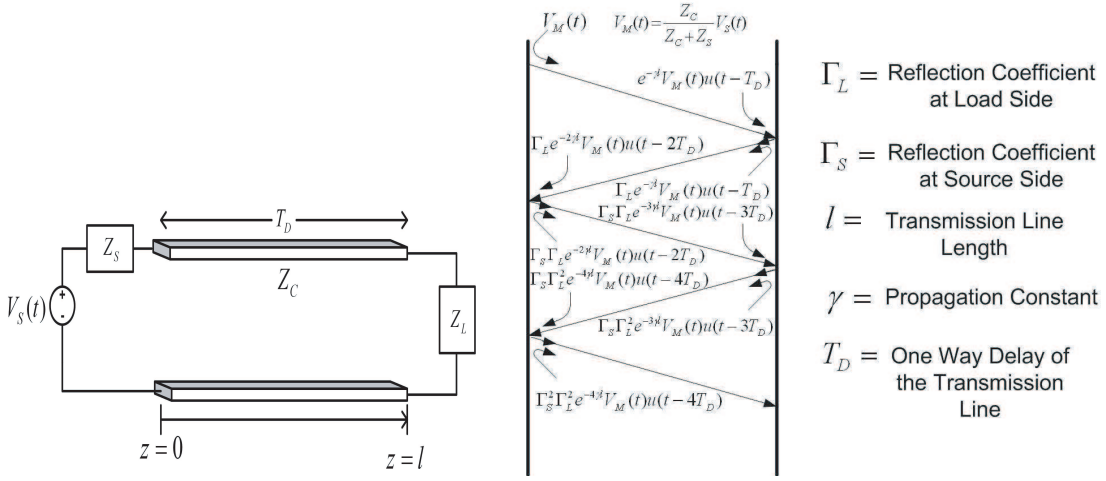

Figure 1: Transmission line terminated with load impedance Z_L (left) and Voltage Lattice Diagram (right).

The above diagram demonstrates the signal levels both at the source and load as time progresses [7]. To interpret this into time domain, consider both incident and reflected waves on the transmission line. The incident (first forward) wave propagating between source and load at any point on the line and the reflected wave from load to source (first reflection) is given by,

$$V_1^+ = \frac{Z_C V_S}{Z_S + Z_C} e^{-\gamma z} \quad \text{and} \quad V_1^- = \frac{Z_C V_S}{Z_S + Z_C} \Gamma_L e^{\gamma z} e^{-2\gamma l}, \quad \text{respectively.}$$

To eliminate reflections from the source end, a signal canceling the first reflection is added which is given by

$$x = -\Gamma_S \Gamma_L e^{-2\gamma l} e^{\gamma z} \frac{Z_C}{Z_S + Z_C} V_S(t) u(t - 2T_D) \tag{1}$$

The compensation signal x is delayed from the source by time $t = 2T_D$. After time $t = 2T_D$ only the original signal propagating from the source to load the first reflection from load to source will exist on the line. However, all other higher order reflections are cancelled due to the compensation signal x.

As indicated above, the definition of the amplitude and phase of the signal (x) depends on reflection coefficients at source and load, propagation constant and transmission line length.

3. PROGRAMMABLE I/O DRIVER

A circuit architecture is introduced here for the driver designed with the intent to compensate reflections. The schematic description is shown in Fig. 2. The circuit has programmable features designed to set the amplitude and delay of the driven compensation signal. The amplitude of x is programmed into constant multiplier circuit (CMn). The register MREG defines the magnitude of the compensation signal (x). Depending on when the reflection arrives to the source driver, the signal x is added by driver Dn after a programmed time delay. The time delay of x (measured from the source signal excitation time $t = 0$) is measured and is digitally stored into the register DREG. The value of this register is used to control the delay executed by the circuit Dn.

As the reflection on a transmission line can originate from multiple loads or impedance discontinuities, the source needs to be designed to compensate for more than one reflection. Therefore multiple compensation elements are designed in series. The registers CMn are programmed to add necessary compensation signal at the appropriate time defined by Dn, where n defines the nth compensation element. The reflected signal from the load or impedance discontinuity depends on the

magnitude of the load impedance (Z_L) compared with the line characteristic impedance (Z_C). If Z_L is greater than Z_C then the reflected component will be positive. In this case the compensation driver will generate a negative signal (equivalent to a sink). And vice versa when Z_L is less than Z_C. Hence, the polarity of signal (x) can be positive or negative depending upon the reflection coefficient and the driver will be either a source or sink. In the driver architecture the polarity pin (P) is to define the nature of source or sink of the compensation driver. If the polarity of (x) is negative, the polarity pin $P = 1$, on the other hand for positive polarity, $P = 0$. With DREG and MREG contents defining delay and multiplying factor, delayed and multiplied version of $V_S(t)$ i.e., reflection cancellation signal (x) will be generated using the programmable I/O driver. In this example the compensation driver strength is divided into seven levels. The multiplying factor is programmed by setting the 3 bit DSF register. To provide better accuracy larger DSF register to enable greater granularity in the multiplication factor is needed.

The 3 bit programmable constant multiplier for the compensation driver is designed with three sub-drivers with different drive strength factor, as shown in Fig. 2 (right). The drive strength of the three subdriver segments are scaled to 1, 2 and 4. These sub-drivers are enabled by bit0, bit1 and bit2 respectively, which are stored in magnitude register (MREG). Input voltage of constant multiplier is the source signal $V_S(t)u(t)$, where the amplitude is scaled and delayed by $2T_D$ to generate the compensation signal, which is $-\Gamma_S\Gamma_L e^{-2\gamma l}\frac{Z_C}{Z_S+Z_C}V_S(t)u(t-2T_D)$. The multiplying factor $-\Gamma_S\Gamma_L e^{-2\gamma l}\frac{Z_C}{Z_S+Z_C}$ is set by the contents of register MREG. By enabling combinations of multiple drivers, different amplitudes of drive strength for the compensation driver is defined.

4. CALIBRATION ROUTINE

The transfer function of a system (that defines the signature signal propagation and reflections within a system) will vary between configurations and working environment of the system. It is therefore necessary to calibrate a system prior to activation. During calibration, information regarding reflection compensation is measured and stored. At system initialization the recorded information is used to program the sub-drivers for reflection cancellation.

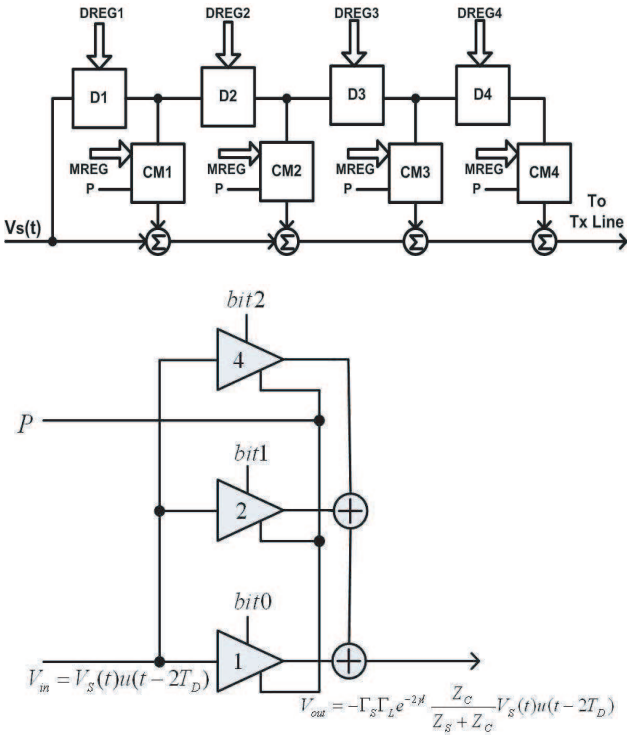

	P	Drive Strength Factor (DSF)			Multiplying Factor
		Bit 2	Bit 1	Bit 0	
	0	0	0	0	0
	0	0	0	1	0.1
	0	0	1	0	0.2
	0	0	1	1	0.3
	0	1	0	0	0.4
	0	1	0	1	0.5
	0	1	1	0	0.6
	0	1	1	1	0.7
	1	0	0	0	0
	1	0	0	1	-0.1
	1	0	1	0	-0.2
	1	0	1	1	-0.3
	1	1	0	0	-0.4
	1	1	0	1	-0.5
	1	1	1	0	-0.6
	1	1	1	1	-0.7

Figure 2: (left top) Programmable I/O driver, (left bottom) programmable const. multiplier, and (right) drive strength factor.

In the calibration routine, a unit pulse is transmitted by the source driver to measure the reflection being transmitted back to the driver. Both the reflection signal delay and magnitude is recorded. Measured delay and magnitude is stored into register to program I/O driver.

All active circuits of the system must be powered on as the state of the active circuits can vary

the impedances seen by the transmission line. Systems which allow hot remove and add, must implement this calibration procedures whenever the system configuration is modified specifically when hot add/remove device configuration are modified.

A flow chart on how to design the calibration and initialization sequence is presented here. Flow chart in Fig. 3 (left) describes this sequence. At first an initialization pulse is transmitted by the driver as soon as the system is powered on. The voltage at the driver is continuously stored (after certain delay to exclude the initial transmitted signal), which will include the reflected signal ($V_{reflected}$). The signal is stored into some sort of an analog storage device, such as a low leakage capacitor. The strength of $V_{reflected}$ is then measured and calibrated using the following sequence. In the beginning, registers DSF and a counter is initialized. Then the stored value is compared with incremental step values of the magnitude comparator circuit. Half of the difference between consecutive incremental values is considered to be the tolerance level. It should be noted that reflected signal is not registered as reflection if the strength of the reflected signal is less than the tolerance, which translates the reflection into noise. With continuous sampling of the voltage at the driver, the amplitude of the reflected signal is measured. The sampling rate depends on the harmonic content of signal. As soon as the circuit detects a reflected voltage greater than a defined threshold, the timer counter value is programmed into DREG which is used to define the compensation signal delay period. During the calibration of the reflected signal the magnitude of the reflected signal is also measured and incrementally compared. The binary equivalent of the final comparator value is stored in DSF, which is used to program the amplitude of the sub-drivers. The process will not stop with a single detection as the system may have multiple reflections which will result in the detection of several reflected signals. The amplitudes of each of the reflected component is recorded along with the delay time of each reflected pulse.

The polarity of the reflected signal is based on a simple comparator design. If $V_{reflected}$ is larger than tolerance it is assured that the signal polarity is positive, then P is set to '0'. Otherwise P is set to '1'.

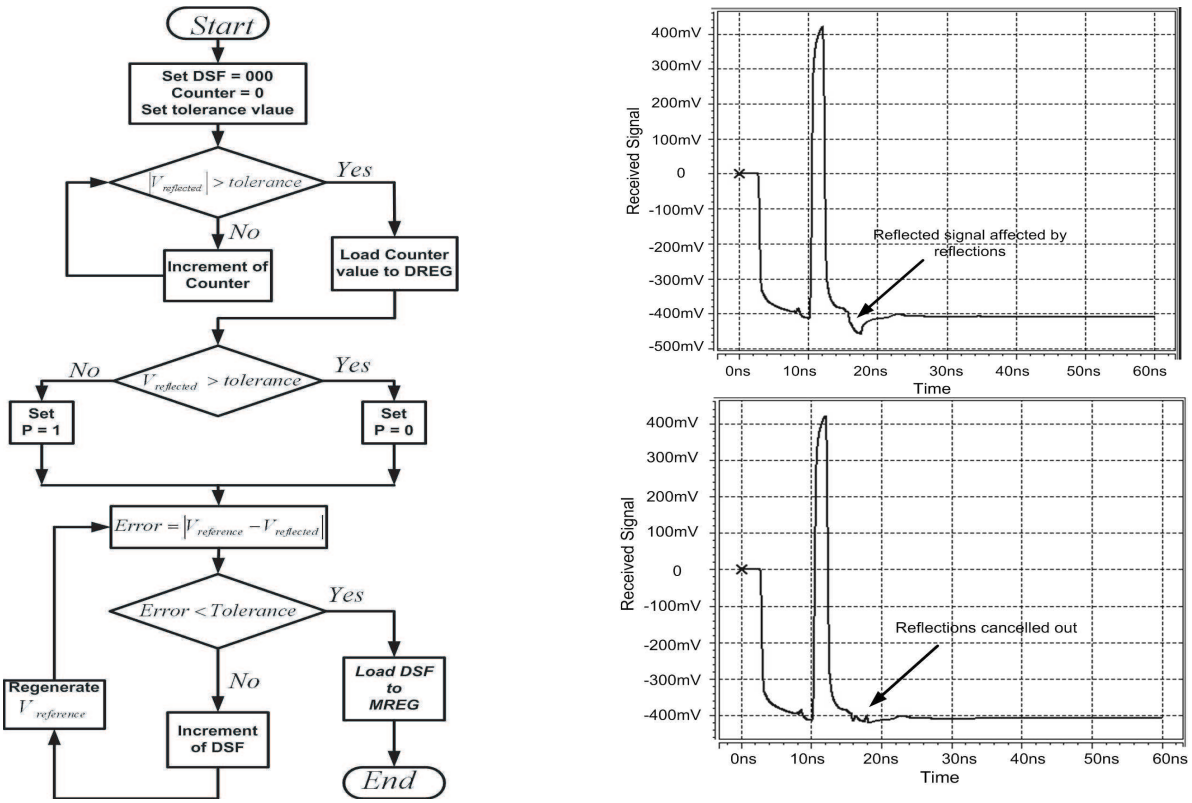

Figure 3: Calibration flow chart (left) and reflection compensation for a single pulse (right).

5. SIMULATION RESULTS

To demonstrate the proposed architecture, spice simulation was implemented. A netlist model of the driver configuration was constructed using behavioral transistors and tested on spice differential

transmission line system. Fig. 3 (right-top) shows a single received pulse. The signal is trailed by several reflections. The proposed compensation scheme was then implemented in spice. With the timely propagation of reflection cancellation signal using programmable I/O driver, reflections are significantly cancelled out (Fig. 3 (right-top)). Another simulation result, Fig. 4, shows the cancellation of reflection from source due to a series of pulses. Similarly, the reflections are greatly reduced using the proposed cancellation methods, shown in Fig. 4 (right). However, there are residuals which are not completely eliminated.

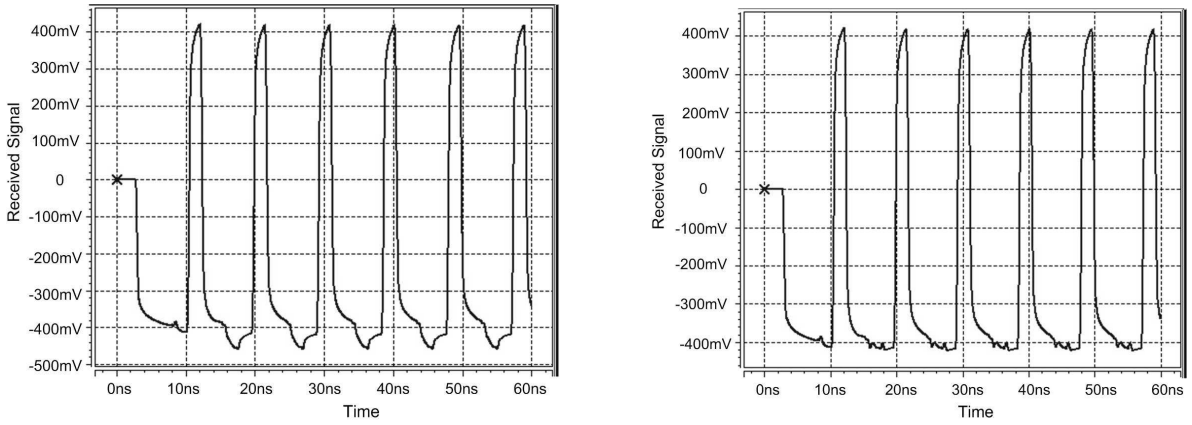

Figure 4: Simulation results for a pulse train.

6. DESIGN CONSIDERATIONS

If the transmission line length is l and velocity of propagation is v, then one way delay of the transmission line will be $T_D = l/v$, then the first reflection arrives at the source after $2T_D$ seconds. The delay units define delay as a multiple of the clock period T_{Clock}. The granularity of the time counter T_{Clock} will define the precision of the phase delay assignment to each reflection cancellation signal For more precise delay settings this interval has to be smaller Similarly, the number of sub-drivers dictate the granularity of the sub-driver strength. System simulation should be done to determine optimum increments.

7. CONCLUSION

This paper has presented a programmable I/O driver with programmable delay units and programmable constant multipliers to cancel reflections from high speed transmission line. Also presented is an efficient calibration routine to search magnitude and delay of the reflection cancellation signal. Simulation result shows that the programmable I/O driver successfully cancels reflections.

REFERENCES

1. Paul, C. R., *Introduction to Electromagnetic Compatibility*, 244–247, Second Edition, John Wiley & Sons, Inc. Publication, 2006.
2. Zerbe, J., et al., "Equalization and clock recover for a 2.5–10 Gb/s 2-PAM/4-PAM backplane transceiver cell," *IEEE Journal of Solid-State Circuits*, Vol. 38, No. 12, Dec. 2003.
3. Ikonen, P. M. T., et al., "Modeling and analysis of composite antenna supertrates consisting on grids of loaded wires," *IEEE Trans. Antennas Propag.*, Vol. 55, No. 10, Oct. 2007.
4. Pozar, D. M., *Microwave Engineering*, John Wiley and Sons Inc., 2nd ed., 1998.
5. Li, M., W. Huang, S. Wang, and T. Kwasneiwski, "0.18 µm CMOS backplane receiver with decision-feedback equalization embedded," *Electronic Letters*, Vol. 42, No. 13, Jun. 2006.
6. Jaussi, J. E., et al., "An 8 Gb/s source synchronous I/O link with adaptive receiver equalization, offset cancellation and clock De-skew," *IEEE International Solid-State Circuits Conference, ISSCC 2004*, Feb. 2004.
7. Cheng, D. K., *Field and Wave Electromagnetics*, 474–480, Second Edition, Pearson Education, 2004.

Special Approach for Estimation Ground Target Position in Passive Location

E. P. Voroshilina and V. I. Tislenko
Research Institute of Radiotechnical Systems, Tomsk, Russia

Abstract— Ground target tracking is difficult and actual problem. Because of the high target density and maneuverability, high clutter, low visibility due to terrain masking, etc, ground target tracking presents unique challenges not present in tracking other types of targets. But many tracking approaches have been developed for air targets and they may poorly when used to track ground targets.

This article includes results of the research work in estimation radar position in passive range-difference location. Radio source is not moving and perform circular scan. Signal from it is received in three points. But beside true measurements of time difference of arrival (TDOA) there are false measurements originated by clutter. Usually clutter measurements are modeled as independed identically distributed. But processing real experimental data shows that in cross-country it distribution may be multimodal. Therefore standard tracking algorithms are not efficient in this situation. Multimodal distribution is caused by re-reflected signal from underlying terrain. Some ground objects re-reflect signal and imitate additional (false) targets. We propose special approach to decide problem of position estimation in such high clutter environment and verify it on experimental data.

1. INTRODUCTION

Over the past four decades, multiple target tracking has developed into a fairly mature technology. Applications now include diverse areas such as air traffic control, air and missile defense, avionics, ocean surveillance, port monitoring, etc. Sensors that provide data include radar, infrared, acoustic, etc. However, until recently, there has not been much emphasis on tracking ground targets due to the lack of sensors [1]. But Ground target tracking is considerably more difficult than air target tracking because of higher target motion variability, higher target density, and possible miss-detection due to terrain masking. Thus, many tracking algorithms developed for air targets will not be suitable for ground targets.

Target tracking needs solving next tasks [2]:

- Track formation. Tracks are initiated from sequences of measurements.
- Prediction. When measurements are received, the current tracks are predicted to the time of the measurements.
- Association. When the origins of the measurements are uncertain, e.g., when clutter or multiple targets are present, the measurements have to be associated with other measurements or tracks before the target state estimates can be generated.
- Estimation (filtration). The associated measurements are used to update the state estimates of the each track.

Focus this article is estimation radar position in passive range-difference location when beside true measurements there are false measurements.

2. EXPERIMENTAL DATA PROCESSING

Our research institute workers conduct following experiment for signal analysis on surface trace (Fig. 1). Radio source was not moving and performed circular scan. Signal from it was received in three measuring points and its time of arrival was estimated.

Session duration of action measuring system was 120 sec. (two rotation of radio source antenna system). Time of arrival estimations are used for generation time difference of arrival (TDOA) and estimation target (radio source) position. Experiment was conduct on three traces with different degree of density natural obstacles. Trace extension was about 12 Km. Measurements of TDOA is shown in Fig. 2.

Natural obstacles weaken power direct signal and decrease its acceptance probability. Besides they re-reflect signal from radio-source and thereby generate stream of false measurements (signals with wrong time delay) in measuring points. It is impair accuracy of target position estimation.

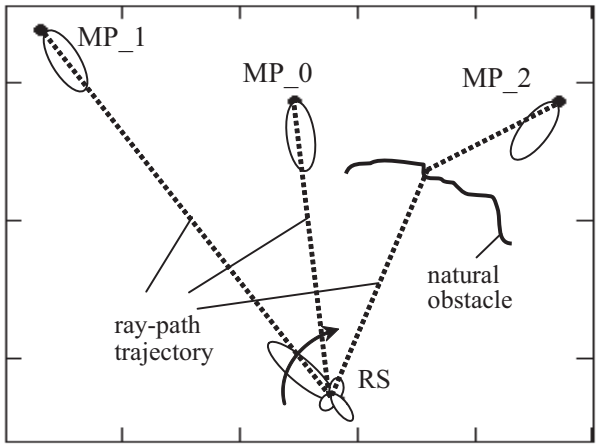

Figure 1: Location radio source (RS) and measuring points (MP) on the ground.

On Fig. 2 one can see that beside true measurements there are false measurements from re-reflected signals. Distribution bar chart for TDOA is multimodal. Main peak corresponds to the true value of target's TDOA (it is not always been). Multimodal distribution is caused by re-reflected signal from underlying terrain. Some ground objects re-reflect signal and imitate true target. We called them as secondary radio source.

Usually false measurements are modeled as independed identically distributed. Some algorithms

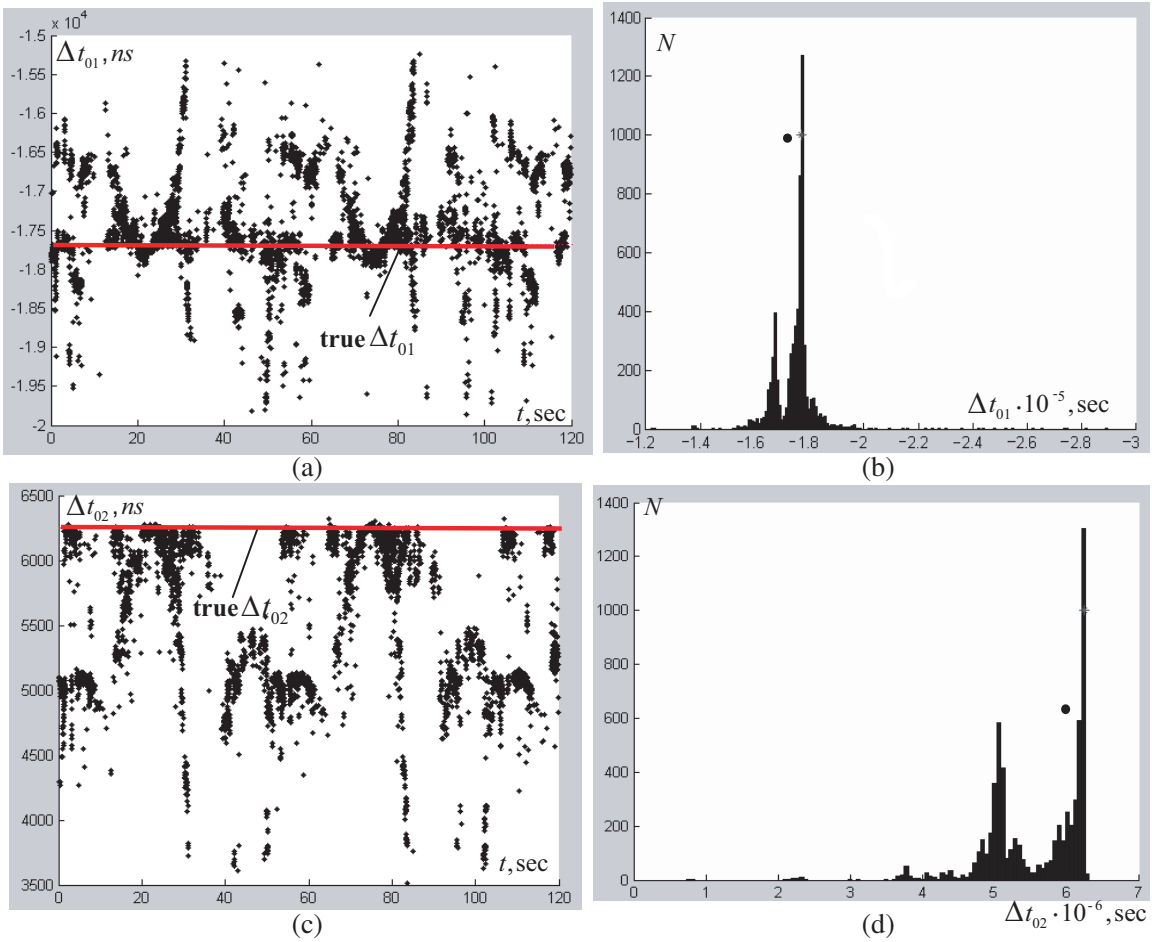

Figure 2: (a) TDOA between MP_1 and MP_0 (Δt_{01}) in the course of time; (b) Distribution bar chart for Δt_{01}; (c) TDOA between MP_0 and MP_2 (Δt_{02}) in the course of time; (d) Distribution bar chart for Δt_{02}.

don't require any model for its working [3–10]. Therefore standard tracking algorithms (Probabilistic Data Association, Nearest Neighbors, Probabilistic Multi-Hypothesis Tracker, Multi Hypothesis Tracking, etc) are not efficient in this situation. They generate several tracks (for target and secondary radio source) at the best. But it is unknown which of them is true. At worst measurements from different source are compounded and target position estimation is wrong.

We define multimodal distribution false measurements, originated from secondary radio sources, as:

$$w(\Delta t_{ar}) = \sum_{j=0}^{N} \frac{1}{\sigma_j \sqrt{2\pi}} P_j \cdot \exp\left(-\frac{(\Delta t_{ar} - \Delta t_j)^2}{2\sigma_j^2} \right)$$

where Δt_{ar} — estimation of TDOA; σ_j — RMSE of Δt_{ar}, N — number of natural obstacles (secondary radio sources); P_j — probability that Δt_{ar} is originated from jth natural obstacle; Δt_j — true value TDOA for jth natural obstacle.

Number of natural obstacles is unknown. N and P_j depends on specific trace realization, type of underlying terrain, radio source power, beam shape and receiver susceptibility, etc.

3. SPECIAL APPROACH FOR ESTIMATION GROUND TARGET TRACKING

The state of not moving radio source (primary or secondary) is assumed to evolve in time according to the equation:

$$\mathbf{x}(i) = \mathbf{x}(i-1),$$

and the corresponding measurement is given by

$$\mathbf{y}(i) = \mathbf{h}(\mathbf{x}(i)) + \mathbf{n}(i),$$

where i — discrete time, $\mathbf{x}(i) = \begin{pmatrix} x_i(i) \\ y_i(i) \end{pmatrix}$ — radio source position, $\mathbf{y}(i) = \begin{pmatrix} \Delta t_{01}(i) \\ \Delta t_{20}(i) \end{pmatrix}$ — TDOA; $n(i)$ — zero-men mutually independent white Gaussian noises with known covariance.

There are three possible events in measurements points at time k (k — number of time interval during which we collect measurements before processing. Interval size corresponds to the time of rotating target antenna system on insignificant angle):

A: all measuring points detect signal from target $y_t(i)$;

B: all measuring points detect signal from the same natural obstacle (reradiator) $y_{rerad}(i)$;

C: all measuring points detect signal originated from different types of radio source $y_{cl}(i)$ (for example, the first point detects signal from target, the second — from one natural obstacle, the third — from another natural obstacle).

Thereby we can write next model for measurements which enter the secondary treatment block on kth time interval:

$$\mathbf{Y}(k) = \mathbf{Y}_t(k) \cup \mathbf{Y}_{rerad}(k) \cup \mathbf{Y}_{cl}(k), \tag{1}$$

where $\mathbf{Y}_t(k)$ — set of measurements, originated by target and received on kth time interval; $\mathbf{Y}_{rerad}(k)$ — set of measurements, originated by secondary radio sources; $\mathbf{Y}_{cl}(k)$ — set of measurements, originated by different types of radio source.

Useful information about target position is kept in $\mathbf{Y}_t(k)$, but it is difficult separate it out mixture (1).

We suggest special heuristic approach to decide such problem of ground target position estimation. Its functional blocks are shown in Fig. 3.

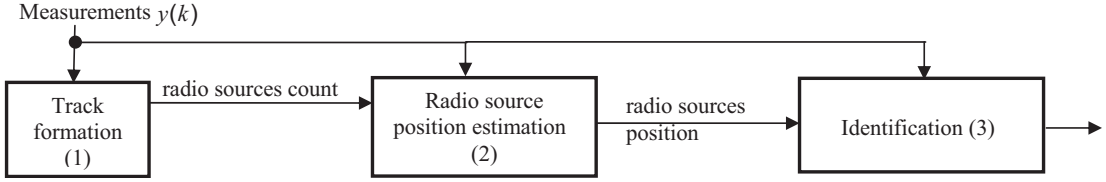

Figure 3: Functional blocks of ground target position estimation approach.

Track formation block estimates number of radio sources (target and reradiators) and generate preliminary information about its position. This block separates stream measurements. Therefore signals originated from different sources are processed individual in the sequel.

The second block performs measurements prediction, association and estimation position for each track. We choose probabilistic data association algorithm to implement this procedures [3–5].

Identification algorithm for each radio-source calculates probability that it is primary. And select that source as true target which has, for example, maximum value of probability.

Decision about it relies on next indications:

- RMSE measurements originated from target less RMSE measurements from reradiators;
- pulse magnitude of direct signal larger pulse magnitude of re-reflected signal;
- Usually signal from target is received more often than from each of reradiator.

4. ALGORITHM VERIFICATION ON EXPERIMENTAL DATA

Verification was provided on experimental data. We have 20 sessions of action measuring system. Duration of each session was 120 sec. True target position is (6254070.6 m; 15363520.3 m). On Fig. 4 is shown result of data processing showed on Fig. 2.

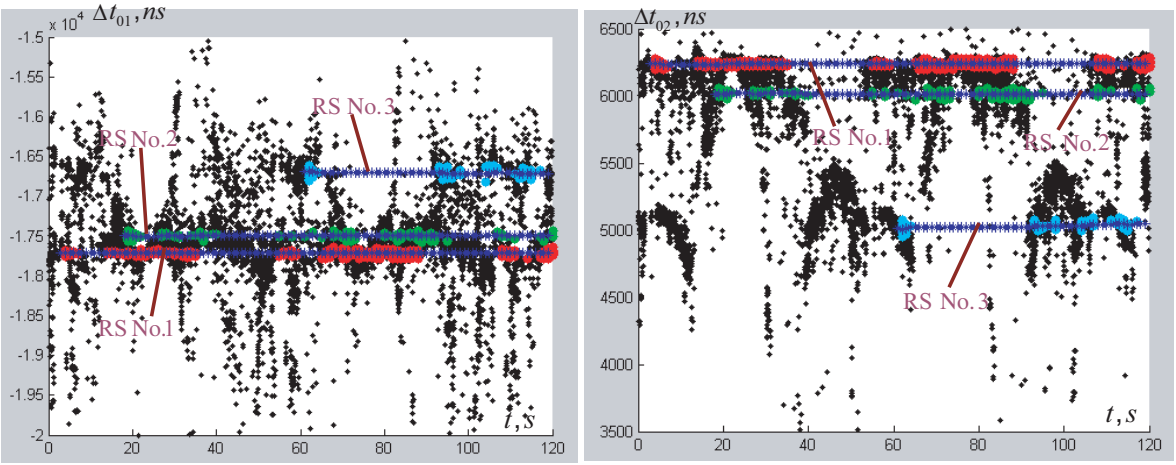

Figure 4: Result of data processing session s0017.

We can see that it was detected three radio sourced. One of them is primary. Others are originated from re-reflected objects — secondary. Measurements associated with each RS are marked by different colors (RS No. 1 is red, RS No. 2 — green, RS No. 3 — cyan). Blue stars mark predicted measurements for each track. Output information from identification block is:

- RS No. 1: $\widehat{x} = 6254082$ m, $\widehat{y} = 15363547$ m, $P_1 = 0.68$;

where $\widehat{x}$ and $\widehat{y}$ — estimates position RS No. 1, P_1 — probability that this radio source is primary, i.e., it is target.

- RS No. 2: $\widehat{x} = 6254091$ m, $\widehat{y} = 15363927$ m, $P_2 = 0.24$;
- RS No. 3: $\widehat{x} = 6254197$ m, $\widehat{y} = 15361160$ m, $P_3 = 0.07$;

Thus RS No. 1 has maximum value of probability. Algorithm define that it is target and absolute error of position estimation is 28 meters. Others radio source are false, they originated by re-reflected signal from natural obstacles.

5. CONCLUSIONS

Algorithm for estimation ground target position in high clutter environment is proposed in this article. It consists of three functional parts: track formation, filtration and identification. This algorithm separate measurements on individual streams originated from different radio-sources (target and reradiators). Then it define which of them is true, i.e., belongs to target. This algorithm was verified on 20 sessions of experimental data on three traces with different closure degree and density of natural obstacles. Mean value accuracy of target position was 35 meters on distance 12 Km. RMSE of position estimation was about 10 meters.

REFERENCES

1. Chong, C.-Y., D. Garren, and T. P. Grayson, "Ground target tracking — A historical perspective," *Aerospace Conference Proceedings IEEE*, Vol. 3, 433–448, San Francisco, 2000.
2. Farina, A. and F. A. Studer, "Radar data processing," *Introduction and Tracking*, Vol. 1, UK, 1986.
3. Kirubaraian, T. and Y. Bar-Shalom, "Probabilistic data association techniques for target tracking in clutter," *Proc. IEEE*, Vol. 92, No. 3, 536–557, 2004.
4. Bar-Shalom, Y., T. Kirubaraian, and X. Lin, "Probabilistic data association techniques for target tracking with application to sonar, radar and EO sensors," *IEEE System Magazine*, 2003.
5. Bar-Shalom, Y., "Tracking methods in a multitarget environment," *IEEE Trans. Automatic Control*, Vol. 23, No. 4, 618–626, 1978.
6. Musici, D., S. Suvorova, and S. Challa, "Multi target tracking of ground targets in clutter with LMIPDA-IMM," *The 7th International Conference on Information Fusion*, 1104–1110, Stockholm, 2004.
7. Lee, M. S. and Y. H. Kim, "New multi-target data association using OSJPDA algorithm for automotive radar," *Trans. Electron*, Vol. 84, No. 8, 1077–1082, 2001.
8. Lee, M.-S. and Y.-H. Kim, "New data association method for automotive radar tracking," *IEE Proc. Radar, Sonar and Navigation*, Vol. 148, No. 5, 297–301, 2001.
9. Smith, D. and S. Singh, "Approaches to multisensor data fusion in target tracking: A survey," *IEEE Trans. Knowledge and Data Engineering*, Vol. 18, No. 12, 1696–1710, 2006.
10. Pulford, G. W., "Taxonomy of multiple target tracking methods," *IEE Proc. Radar, Sonar and Navigation*, Vol. 152, No. 5, 291–303, 2005.

Studies on Effects of High Power Microwaves in Cell Cultures

M. Risling[1], **E. Malm**[1], **M. Angeria**[1], **and L. Malmgren**[2]

[1]Department of Neuroscience, Karolinska Institute, Stockholm, Sweden
[2]MaxLab, University of Lund, Sweden

Abstract— We have reported a decrease in the content of the cytoskeletal protein tubulin in endothelial cells exposed to multiple pulses of high power microwaves (HPM). In this study we have examined the gene expression for cytoskeletal genes and cell death regulators with aid of micro array analysis after HPM exposure. No evidence for an effect on these genes were found after HPM exposure. Therefore, we suggest that the previously observed cytoskeletal changes are induced by changes on the protein level rather the gene expression changes.

1. INTRODUCTION

In previous papers we have reported studies on possible biological effects after exposure to short pulsed fields of High Power Microwaves (HPM). In a study on adult rats it was we reported an absence of effects on the Blood Brain-Barrier or cell death. No structural changes in the hippocampus of the brain could be detected [4]. In order to use simpler but also more sensitive biological systems it was decided to use cell cultures for further experimentation. Changes in the shape of neuroblastoma cells exposed could be observed after exposure to long series of HPM pulses [5]. In endothelial cells exposed to multiple pulses of high power microwaves a decrease in the content of the cytoskeletal protein tubulin [6] (HPM). If a decrease of tubulin also occurred in more complex neuronal cells more severe changes could be expected. This hypothesis was addressed in a study on primary cultures of neurons from the hippocampus of rat embryos. The cells were exposed to 1.6 GHz HPM pulses with duration of 0.55 microseconds and field strength of 21.7 KV/m. The cultures were fixed and labeled with antibodies against tubulin and MAP2 (a microtubule associated protein) after 2, 6, 24 or 72 hours. The specimens were examined with a confocal microscope. The results showed extensive changes in dendrite structure in cultures exposed for more than 90000 pulses. This effect could be observed already 2 hours after exposure. Dendrite structure was gradually but not completely restored [7]. In this study, we describe an ongoing analysis the gene expression in the rat C6 glioma cell line based on micro arrays.

2. METHODS

Cultures of the rat C6 glia line were placed in an exposure chamber (wave guide) and exposed to 90000 pulses of HPM (from a source constructed a radar surveillance system) to at 1.6 GHz with duration of 0.55 microseconds and field strength of 21.7 KV/m. After 24 hours survival in the incubator, the cultures were prepared for high-density oligonucleotide arrays and hybridized at the Bioinformatics and expression analysis core facility (BEA) at Huddinge campus of the Karolinska institute (BEA is a member of the Affymetrix European Core Lab Program and appointed Center of Excellence for chIP-on-chip analysis by Affymetrix) to each GeneChip® Rat Gene 1.0 ST Arrays (Affymetrix). Following normalization [2], the change in gene expression between the three control cultures and three exposed cultures at each survival time was compared using an un-paired t-test.

3. RESULTS AND DISCUSSION

Low to moderate changes was observed in about 500 of the more than 27000 examined genes. This included changes in about 100 olfactory receptor genes. No significant changes in genes for cell death, cytoskeleton, inflammation or heat shock proteins were found, except for a moderate decrease in the expression for neurofilament, heavy polypeptide, prostaglandin E receptor 1, prostaglandin F receptor and prostaglandin I2 (prostacyclin) synthase (Ptgis), mRNA. Interestingly, we also observed a decrease in the expression for aquaporin 3, 4 and 6. Aquaporins are transport systems that control diffusion of water (by an energy-independent process) by passage through a transmembrane aqueous pore or channel [1]. Thus, effects on cytoskeletal gene expression seem to be small or absent. We therefore conclude that the observed effects on tubulin probably are related to changes at the protein level and not a decrease in the expression of the mRNA for tubulin.

One important question with regard to the possible mechanisms for the observed changes after this type of HPM exposure is whether this is related to thermal heating or not. Dose calculation computer programs are not specifically designed for this type of problems and it is difficult to predict if local heating can occur in the system. In future studies, it will also be important to reveal the threshold thermal effects in cells exposed to this type of fields cf [3].

REFERENCES

1. Agre, P., "Aquaporin water channels (Nobel Lecture)," *Angew. Chem. Int. Ed. Engl.*, Vol. 43, 4278–90, 2004.
2. Kirkegaard, M., N. Murai, M. Risling, A. Suneson, L. Jarlebark, and M. Ulfendahl, "Differential gene expression in the rat cochlea after exposure to impulse noise," *Neuroscience*, Vol. 142, 425–35, 2006.
3. Pakhomov, A. G., S. P. Mathur, J. Doyle, B. E. Stuck, J. L. Kiel, and M. R. Murphy, "Comparative effects of extremely high power microwave pulses and a brief CW irradiation on pacemaker function in isolated frog heart slices," *Bioelectromagnetics*, Vol. 21, 245–54, 2000.
4. Risling, M., A. Suneson, M. Meier, and L. Malmgren, "Studies on the possible effekts of high power microwaves on the central nervous system," *Non-lethal Weapons*, 10-1–10-9, Fraunhofer Institut Chemische Technologie, DWS Werbeagentur und Verlag GmbH, Karlsruhe, 2001.
5. Risling, M., A. Sondén, E. Malm, B. T. Kjellström, M. Meier, J. Bursell, J. Persson, I.-L. Larsson, A. Suneson, and L. Malmgren, "Further observations on biological effects of Non-thermalizing High Power microwave (HPM) pulses," *Non-lethal Capabilities Facing Emerging Threats, 2nd Symposium on Non-lethal Weapons*, 24-21–24-25, Fraunhofer Institut Chemische Technologie, DWS Werbeagentur und Verlag GmbH, Karlsruhe, 2003.
6. Risling, M., M. Sköld, E. Malm, A. Sondén, I.-L. Larsson, M. Angeria, and L. Malmgren, "Observations on changes in the content of tubulin and VEGF protein in cell cultures exposed to High Power Microwaves, in vitro," *Non-lethal Options Enhancing Security and Stability*, 18-1–18-11, Fraunhofer Institut Chemische Technologie, DWS Werbeagentur und Verlag GmbH, Karlsruhe, 2005.
7. Risling, M., E. Malm, M. Sköld, and L. Malmgren, "Observations on dendrite morphology in rat hippocampal neurons exposed to High Power Microwaves," *Non-lethal Weapons: Fufilling the Promise*, 17-1–17-9, Fraunhofer Institut Chemische Technologie, DWS Werbeagentur und Verlag GmbH, Karlsruhe, 2007.

Analysis of Scattering from a Finite Linear Array of Dielectric Cylinders Using the Method of Auxiliary Sources

Naamen Hichem and Taoufik Aguili
Ecole Nationale d'ingénieurs de Tunis
Département Technologie de l'information et de Communications, Tunisia

Abstract— The numerical analysis, in the order to approximate scattered fields by larger bodies, is limited by the allowed computational cost and memory needs. The method of auxiliary sources is exploited to model the scattering properties from a finite linear array of dielectric cylinders taking into account the coupling between the different cylinders [3].

According to the MAS and for each dielectric cylinder, two bases of auxiliary sources must be considered; the first one distributed outside the physical contour and acts inside, the second is inside and acts outside [1].

The coupling modeled by the mutual satisfaction of the boundary conditions involving the continuity of the tangential field components just on the collocation points of every cylinder [2].

In the aforementioned global coupling model, we implement the fact that every cylinder is coupled only to the neighbouring cylinders (partial coupling), the linear system matrix in fully simplified entraining a significant decrease in the computational cost and memory requirements.

According to the global and partial coupling, numerical results (RCS, pattern field) reveal good agreement with references.

1. INTRODUCTION

The MAS is applied to model coupling between different, infinitely, and parallel dielectric cylinders, illuminated by a TMz monochromatic plane wave. The global coupling is modelled by the mutual satisfaction of the boundary conditions just on the collocation points of every cylinder.

The method of auxiliary sources is a numerical technique used to solve boundary problems [1]. The EM fields within each domain are expressed as a linear combination of analytical solutions of Helmholz equation. These particular solutions constitute the base of auxiliary sources placed on the auxiliary contour surrounded by the physical one [2].

These boundary conditions lead to a linear system having as solution the amplitude and phase of scattered field [3].

In the general case, every constitutive part of an array interacts with the rest of the array in the purpose to model exact or global coupling between different parts witch lead to a completely filled matrix entraining a difficult computation.

In the order to decrease the computational cost, we suppose that every cylinder is coupled with only the adjacent or the two adjacent one. The mathematical calculus show that the global matrix is fully simplified and the implementation code realized with Mathematica justify the low computational cost achieved by this approximation.

Numerical results (RCS, pattern field) reveal good agreement with references [5, 8].

At the end, we have numerical results justifying the technique and the possibility to extend it to macro arrays (or for the other parts of the physical problems involving many mutual interactions...).

An $e^{j\omega t}$ time convention is assumed and suppressed throughout the paper.

2. FORMULATION

A TMz monochromatic plane wave illuminate under the φ_i incidence a linear array of K infinite, dielectric, circular cylinders positioned along the x-axis (Fig. 1).

The incident transverse magnetic wave has an electric field:

$$E_{inc}(x,\, y) = E_{oi}\vec{z}\exp[jk_0(x\cos(\varphi_i) + y\sin(\varphi_i))] \tag{1}$$

Here, z denote unit vector in the z direction, since the incident electric field is z directed and independent of z with uniform cylinders along z, then we deduce that the scattered field is z directed too, reducing the scattering problem to a bidirectional one.

For every cylinder, two bases of auxiliary sources are regularly distributed along the auxiliary contours situated inside and outside the boundary and surrounded by the physical one on which are positioned the collocation points.

An auxiliary source (x_n, y_n) produces an electric field expressed as:

$$E_{sn}(x, y) = A_n \vec{z} H_0^{(2)} \left[k_0 \sqrt{(x - x_n)^2 + (y - y_n)^2} \right] \tag{2}$$

where $H_0^{(2)}[.]$ is the Hankel function of the second kind of zero order and A_n the complex current.

According to the standard impedance boundary condition (SIBC), the tangential component of the total electric field must be continuous on the boundary, then for every cylinder [4]:

$$n_{DIEL} \wedge E_{inside} = n_{DIEL} \wedge E_{outside} \tag{3}$$

$$n_{DIEL} \wedge H_{inside} = n_{DIEL} \wedge H_{outside} \tag{4}$$

Let us consider the the collocation point m of the cylinder C_j, we obtain:

$$E^{inc}_{j(m)} + E^{I}_{j(m)} + \sum_{i \neq j}^{K} E^{I}_{ji(m)} = E^{II}_{j(m)} \tag{5}$$

$$n_{j(m)} \wedge \left(H^{inc}_{j(m)} + H^{I}_{j(m)} + \sum_{i \neq j}^{K} H^{I}_{ji(m)} \right) = n_{j(m)} \wedge H^{II}_{j(m)} \tag{6}$$

$E^{inc}_{j(m)}$ is the incident electric field just on the collocation point m of the cylinder C_j.

$E^{I}_{j(m)}$ is the total electric field radiated by the inside auxiliary base of C_j.

$E^{I}_{ji(m)}$ is the total electric field radiated by the auxliary base of C_i and evaluated on C_j.

$E^{II}_{j(m)}$ is the total electric field radiated by the outside auxiliary base and evaluated on C_j.

Supposing that for every cylinder, the number of auxiliary sources N is equal to the number of collocation points, the continuity Equations (3) and (4) apllied to the array gives us a linear system of $2.N.K$ equations:

$$\begin{pmatrix}
Z^{Ie}_{11} & Z^{Ie}_{12} & \cdots & Z^{Ie}_{1K} & Z^{IIe}_{11} & 0 & 0 & \cdots & 0 & 0 \\
Z^{Ie}_{21} & Z^{Ie}_{22} & \cdots & Z^{Ie}_{2k} & 0 & Z^{IIe}_{22} & 0 & \cdots & 0 & 0 \\
\vdots & \vdots & \cdots & 0 & 0 & \ddots & \ddots & \cdots & \vdots & \vdots \\
\vdots & \vdots & \cdots & \vdots & \ddots & 0 & \ddots & \ddots & \vdots & \vdots \\
\vdots & \vdots & \cdots & \vdots & \vdots & \ddots & \ddots & \ddots & 0 & 0 \\
\vdots & \vdots & \cdots & 0 & \ddots & \ddots & \ddots & \ddots & 0 & 0 \\
\vdots & \vdots & \cdots & 0 & 0 & \cdots & 0 & 0 & 0 & 0 \\
Z^{Ie}_{K1} & Z^{Ie}_{K2} & \cdots & Z^{Ie}_{kk} & 0 & 0 & 0 & \cdots & 0 & Z^{IIe}_{KK} \\
Z^{Ih}_{11} & Z^{Ih}_{12} & \cdots & Z^{Ih}_{1K} & Z^{IIh}_{11} & 0 & 0 & \cdots & 0 & 0 \\
Z^{Ih}_{21} & Z^{Ih}_{22} & \cdots & Z^{Ih}_{2K} & 0 & Z^{IIh}_{22} & 0 & \cdots & 0 & 0 \\
\vdots & \vdots & \cdots & 0 & 0 & \ddots & \ddots & \cdots & \vdots & \vdots \\
\vdots & \vdots & \cdots & \vdots & \ddots & 0 & \ddots & \ddots & \vdots & \vdots \\
\vdots & \vdots & \cdots & \vdots & \vdots & \ddots & \ddots & \ddots & 0 & 0 \\
\vdots & \vdots & \cdots & 0 & \ddots & \ddots & \ddots & \ddots & 0 & 0 \\
\vdots & \vdots & \cdots & 0 & 0 & \cdots & 0 & 0 & 0 & \square \\
Z^{Ih}_{K1} & Z^{Ih}_{K2} & \cdots & Z^{Ih}_{KK} & 0 & 0 & 0 & \cdots & 0 & Z^{IIh}_{KK}
\end{pmatrix}$$

3. NUMERICAL RESULTS

In order to validate our technique about coupling between cylinders, we apply the technique to two dielectric cylinders Fig. 4 taken as reference. Fig. 3 shows the MAS results.

We apply the MAS technique to three metamaterial cylinders Fig. 6 Ref. [6] and obtain results Fig. 5.

The obtained results agree with references

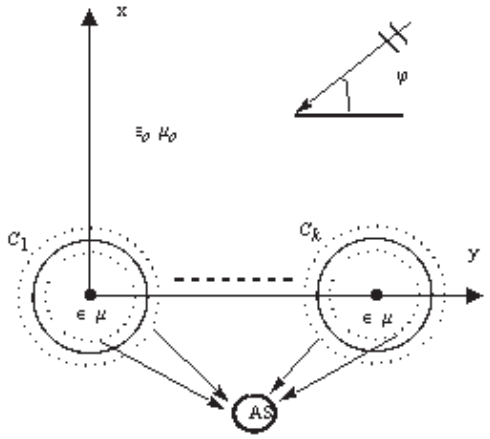

Figure 1: Array of K dielectric cylinders.

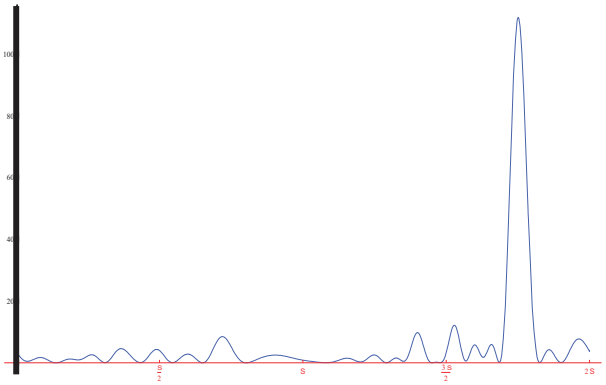

Figure 2: RCS given by the MAS for three dielectric cylinders Ref. [5].

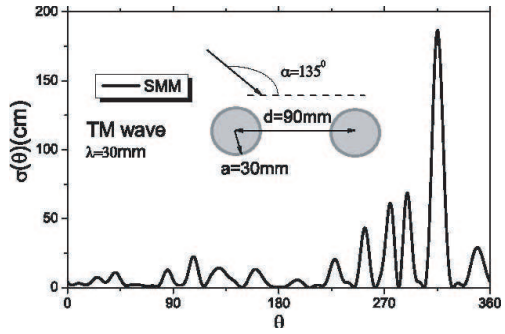

Figure 3: Bistatic scattering width of two dielectric rods ($\varepsilon_r = 2 : 25$).

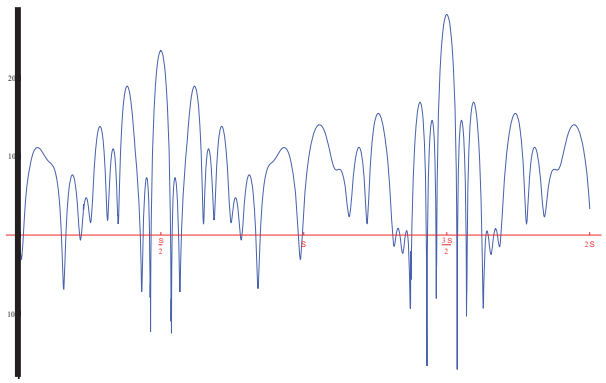

Figure 4: RCS according to MAS for three metamaterials as shown in Fig. 6 Ref. [6].

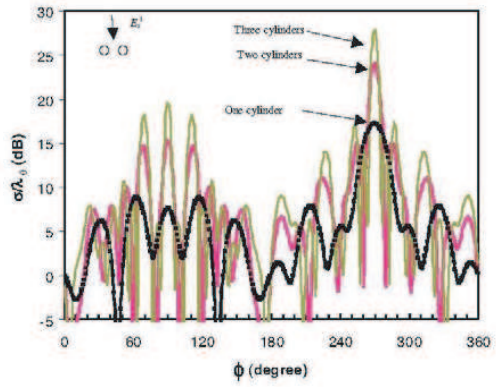

Figure 5: Scattering cross section of three different number: one, two, three metamaterial cylinders located on x-axis with $3\lambda_0$ center separation and $a = 1\lambda_0$ radius, metamaterial ($\varepsilon_r = -4,\ \mu_r = -1$). The angle of incidence is 90 degrees.

4. CONCLUSIONS

The MAS is applied is this paper to model coupling between dielectric and metamaterial cylinder-swith an acceptable accuracy.

We are working about the application of this technique to a dielectric array.

REFERENCES

1. Shubitidze, F., H. T. Anastassiu, and D. I. Kaklamani, "An improved accuracy version of the method of auxiliary sources for computational electromagnetics," *IEEE Transactions on Antennas and Propagation*, Vol. 52, No. 1, January 2004.
2. Anastassiu, H. T., et al., "Electromagnetic scattering analysis of coated conductors with edges using the method of auxiliary sources (MAS) in conjunction with the standard impedance boundary condition (SIBC)," *IEEE Transactions on Antennas and Propagation*, Vol. 50, No. 1, January 2002.
3. Kaklamani, D. I. and T. Hristos, "Aspects of the method of auxiliary sources (MAS) in computational electromagnetics," *IEEE Transactions on Antennas and Propagation*, Vol. 44, No. 3, June 2002.
4. Harrington, R. F., *Time Harmonic Electromagnetic Fields*, McGraw-Hill, New York, 1961.
5. Zhang, Y. J. and E. P. Li, "Fast multipole accelerated scattering matrix method for multiple scattering of a large number of cylinders," *Progress In Electromagnetics Research*, PIER 72, 105–126, 2007.
6. Shooshtari, A. and A. R. Sebak, "Electromagnetic scattering by parallel metamaterial cylinders," *Progress In Electromagnetics Research*, PIER 57, 165–177, 2006.

GL TM Dielectric Parameter Inversion

Ganquan Xie, **Jianhua Li**, **Lee Xie**, **and Feng Xie**
GL Geophysical Laboratory, USA

Abstract— A GL TM model inversion to detect the dielectric parameter is proposed in this paper. A nonlinear operator on the dielectric parameter is defined to present the transverse magnetic model inversion to detect the dielectric parameter. We derived the Frechet derivative operator of the nonlinear operator in integral equation. The singularity of the magnetic field excited by impulse on the boundary point is analyzed. We propose to construct a new TM model inversion method to detect the dielectric parameter. When impulse excitation is excited on the boundary point, our 1-D TM dielectric inversion is well posed. The GL TM inversions with non impulse source excitation are investigated and suitable regularized. Our inversion method can be extended to solve the 2.5D and 3D dimensional inverse problems. The 2D and 3D GL TM synthetic data inversion images are presented.

1. INTRODUCTION

There are several research works for the electromagnetic parameter inversion in frequency domain. Xie proposed a new iterative method for solving the coefficient inverse problem of wave equation in time domain [1]. Xie and Li proposed the 2D and 3D wave velocity inversion in the time domain and in frequency domain [2–9]. Lee and Xie proposed a virtual wave field tomography inversion in the q domain [10]. Habashy and Oristaglio proposed Born Approximation inversion for the conductivity and permittivity in frequency domain in [11]. Oristaglio and Habashy proposed the conductivity inversion based on reciprocity in wavefield inversion in [12]. Xie and Li proposed the GILD, AGILD and GL EM nonlinear inversion in [13–19]. According to [1, 3] and [6–8], in this paper, we propose a GL TM model inversion to detect the dielectric parameter in time domain [1, 20]. First of all, we define a suitable nonlinear operator on the dielectric parameter using convolution. The Frechet derivative operator of the nonlinear operator is derived. When the magnetic field is excited by the impulse on the boundary point, the magnetic field can be expanded by its singular and smooth components. The Frechet derivative operator can be presented as the second integral operator. We construct a new TM model inversion method to detect the dielectric parameter. When impulse excitation is excited on the boundary point, our 1-D TM dielectric inversion is well posed. The GL TM inversion with non impulse source excitation is investigated and suitable regularized. Our inversion method can be extended to solve the 2.5D and 3D dimensional inverse problem. The GL TM inversion method and theory in this paper are from GLGEO technology patent report [20]. The 2D and 3D GL TM synthetic data inversion images are presented.

The description arrangement of this paper is as follows. The introduction is described in Section 1. The 1-D TM forward and inverse problems are presented in Section 2. We propose 1-D TM inversion method for solving the dielectric inverse problem in Section 3. Nonlinear operator on dielectric inversion and its derivative operator are presented in Section 4. 2D and 3D TM inversion simulation and discussions are described in Section 5. We conclude this paper in Section 6.

2. THE 1-D TM FORWARD MODELING AND INVERSE PROBLEMS

2.1. The 1-D TM Forward Modeling Equation

We describe the one dimensional transversal magnetic (TM) forward modeling equation in this section.

Let $H_y(x,t)$ denote the nonzero y component of the magnetic field, the 1-D TM forward modeling is governed by the following wave equation,

$$\mu\frac{\partial^2 H_y}{\partial t^2}-\frac{\partial}{\partial x}\left(\frac{1}{\varepsilon_e(x)}\frac{\partial H_y}{\partial x}\right)=s(x,t),\ \ x>0,\ \ t>0, \tag{1}$$

where μ is basic permeability constant $\mu_0 = 10^{-7}\times 4\pi = 1.2566\times 10^{-6}\,\mathrm{m\,kg\,s^{-2}A^{-2}}$. The effective dielectric parameter $\varepsilon_e(x) = \varepsilon_r\varepsilon_0$. The ε_0 is the basic permittivity, $\varepsilon_0 = 8.85418\times 10^{-12}\,\mathrm{m^{-3}\,kg^{-1}\,s^4A^2}$. Let $H_y(x,t) = H(x,t)$, $x = cx'$, c is the light speed, the TM model wave

Equation (1) is translated to the following wave equation

$$\frac{\partial^2 H}{\partial t^2} - \frac{\partial}{\partial x'}\left(\frac{1}{\varepsilon_r(cx')}\frac{\partial H}{\partial x'}\right) = s\left(cx', t\right), \;\; x' > 0, \;\; t > 0, \tag{2}$$

Let $\frac{1}{\varepsilon_r(cx')} = \varepsilon^{-1}(x')$, $s(cx', t) = S(x', t)$, and remove the superscript of x' in the equation (2), we obtain

$$\frac{\partial^2 H}{\partial t^2} - \frac{\partial}{\partial x}\left(\varepsilon^{-1}(x)\frac{\partial H}{\partial x}\right) = S(x, t), \;\; x > 0, \;\; t > 0, \tag{3}$$

2.2. The 1-D TM Inverse Problem to Find the Dielectric Parameter

Suppose that the magnetic permeability $\mu = \mu_0$, let the source term in right hand of (1) $s(x, t) = 0$, the initial magnetic field and its time derivative are zero at the initial time $t = 0$. The y component of the transverse magnetic field H_y satisfies the following wave equation and initial and boundary conditions,

$$\begin{aligned} &\mu\frac{\partial^2 H_y}{\partial t^2} - \frac{\partial}{\partial x}\left(\frac{1}{\varepsilon_e(x)}\frac{\partial H_y}{\partial x}\right) = s(x, t), \;\; x > 0, \;\; t > 0, \\ &H_y(x, 0) = \frac{\partial}{\partial t}H_y(x, 0) = 0, \;\; x > 0, \\ &\frac{\partial H_y}{\partial x}(0, t) = h(t), \;\; t > 0. \end{aligned} \tag{4}$$

From the magnetic wave y component H_y measurement on the boundary point

$$H_y(0, t) = f(t), \;\; t > 0, \tag{5}$$

to find the effective dielectric parameter that is called the 1-D TM dielectric inverse problem. The inverse problem is translated the following TM inversion to find relative dielectric parameter $\varepsilon(x)$ from the following wave equation system:

$$\begin{aligned} &\frac{\partial^2 H}{\partial t^2} - \frac{\partial}{\partial x}\left(\varepsilon^{-1}(x)\frac{\partial H}{\partial x}\right) = s(x, t), \;\; x > 0, \;\; t > 0, \\ &H(x, 0) = \frac{\partial}{\partial t}H(x, 0) = 0, \;\; x > 0, \\ &\frac{\partial H}{\partial x}(0, t) = g(t), \;\; t > 0. \end{aligned} \tag{6}$$

and the measure data on the boundary

$$H(0, t) = f(t), \;\; t > 0, \tag{7}$$

to find the relative dielectric parameter $\varepsilon(x) \geq 1$.

3. GL TM INVERSION METHOD FOR SOLVING THE DIELECTRIC INVERSE PROBLEM

When the boundary excitation is exited by the impulse, $g(t) = \delta(t)$, let

$$H_1(x, t) = \frac{\partial a(x)}{\partial x}S(t - \phi(x)) + \frac{\partial}{\partial x}H_s(x, t), \tag{8}$$

$a(x)$ is amplitude in (20), $\phi(x)$ is wave front in (19), $H_s(x, t)$ is the scattering wave solution of the Equation (6) [1, 7, 20].

The TM inversion algorithm is proposed as following steps [20]:

(3.1) Let the start dielectric model be $\varepsilon_0(x) = \varepsilon(0)$, $\varepsilon(0)$ is known boundary value of the $\varepsilon(x)$.

(3.2) By induction, suppose that the $\varepsilon_{k-1}(x)$ is known, to calculate $\phi_{k-1}(x) = \int_0^x \varepsilon_{k-1}(\xi)d\xi$; to replace $\varepsilon(x)$ by $\varepsilon_{k-1}(x)$ in (6) and solve the Equation (6) and get $H_s(x, t)$ by GL method and to calculate $H_{1,k-1}(x, t) = H_1(x, t)$ in the (8).

(3.3) Solve the following well posed Second kind of integral equation

$$\varepsilon(0)^{-\frac{3}{4}}\frac{\varepsilon_{k-1}(x)^{-\frac{5}{4}}}{\sqrt{\varepsilon_{k-1}(x)}-\sqrt{\varepsilon(0)}}\delta\varepsilon_k(x)+\int_0^{x+\frac{\phi(x)}{\sqrt{\varepsilon(0)}}}\frac{\delta\varepsilon_k(\xi)}{\varepsilon_{k-1}^2(\xi)}H_1(\xi,\phi_{k-1}(x)+\sqrt{\varepsilon(0)}x-\sqrt{\varepsilon(0)}\xi)d\xi$$
$$=\varepsilon(0)^{-1}(H_{k-1}(0,t)-f(t)) \tag{9}$$

and get the increment dielectric $\delta\varepsilon_k(x)$.
(3.4) update

$$\varepsilon_k(x)=\varepsilon_{k-1}(x)+\delta\varepsilon_k(x). \tag{10}$$

4. NONLINEAR OPERATOR ON DIELECTRIC INVERSION AND ITS DERIVATIVE OPERATOR

The nonlinear operator on the dielectric parameter and its Frechet derivative operator are presented in this section. These contents, formulas and detailed theoretical proofs are proposed in the report [20].

4.1. Nonlinear Operator to Present the TM Dielectric Inversion

We define the nonlinear operator [1, 7, 20]

$$Q(\varepsilon(x),t)=\varepsilon^{-1}(0)\,(H(\varepsilon(x);0,t)-f(t))*_t g(t), \tag{11}$$

where

$$H(\varepsilon(x);0,t)=H(0,t), \tag{12}$$

is the boundary response of the magnetic component solution, $H(x,t)$, of the wave Equation (6) on the boundary point $x=0$, $H(x,t)$ is nonlinearly depended on the relative dielectric parameter $\varepsilon(x)$, therefore, we use Equation (7) to define nonlinear operator $Q(\varepsilon(x),t)$ respect with to dielectric parameter $\varepsilon(x)$.

The 1-D TM inverse problem to find the dielectric parameter is translated the following nonlinear operator equation with respect to the dielectric parameter $\varepsilon(x)$,

$$Q(\varepsilon(x),t)=\varepsilon^{-1}(0)\,(H(\varepsilon(x);0,t)-f(t))*_t g(t)=0. \tag{13}$$

4.2. Frechet Derivative Operator of the Nonlinear Operator

We derive the Frechet derivative operator of the nonlinear operator $Q(\varepsilon(x),t)$ in this section. The Frechet derivative operator is presented by a convolution differential integral form as follows:

$$Q'_\varepsilon\delta\varepsilon=\varepsilon^{-1}(0)\,(\delta H(0,t))*_t g(t)=\int_0^\infty\left(\left(\varepsilon^{-2}(x)\right)\delta\varepsilon(x)\frac{\partial H}{\partial x}*_t\frac{\partial}{\partial x}\left(G(x,t)\right)\right)dx' \tag{14}$$

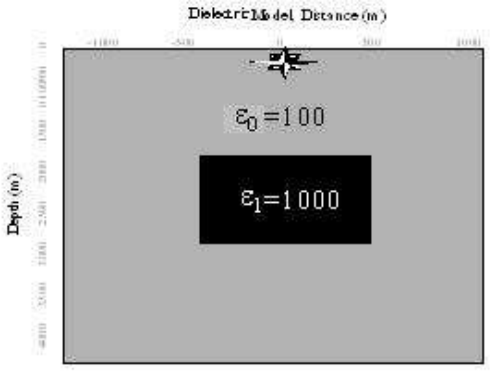

Figure 1: The dielectric bulk model, star is source.

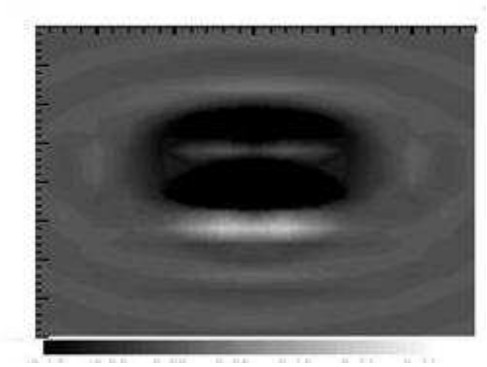

Figure 2: The dielectric image from the eighth iteration of the 2D GL TM inversion.

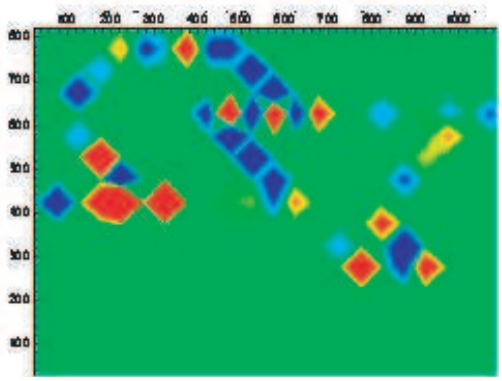

Figure 3: The dielectric imaging of quasi-PHC in section $z = 0$ by the 3D GL TM inversion.

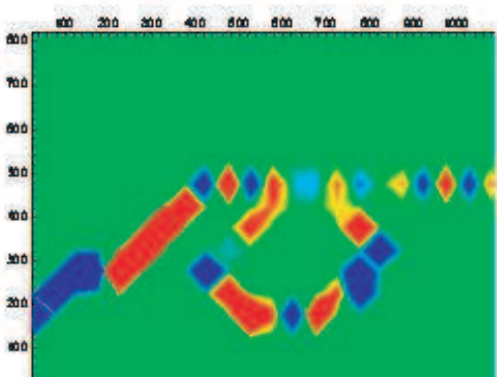

Figure 4: The dielectric imaging of quasi-PHC in section $z = 50\ Nm$ by the 3D GL TM inversion.

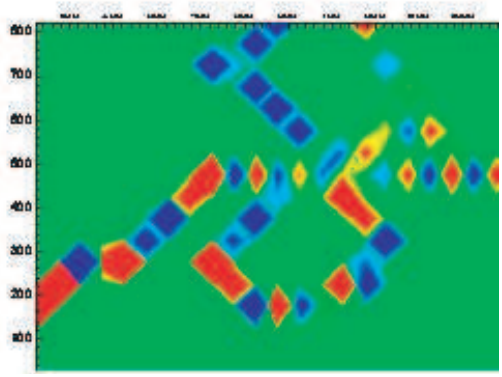

Figure 5: The dielectric imaging of quasi-PHC in section $z = 100\ Nm$ by the 3D GL TM inversion.

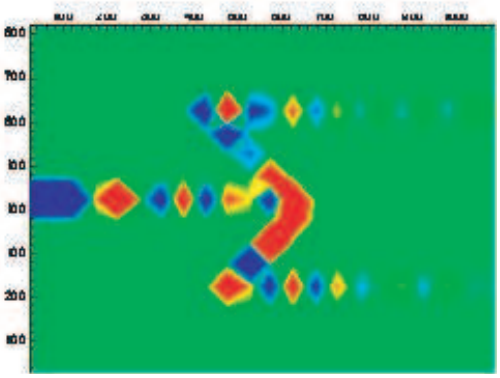

Figure 6: The dielectric imaging of quasi-PHC in section $z = 150\ Nm$ by the 3D GL TM inversion.

where $G(x,t)$ is Green function by boundary impulse excitation as following

$$\begin{aligned} &\frac{\partial^2 G(x,t)}{\partial t^2} - \frac{\partial}{\partial x}\left(\varepsilon^{-1}(0)\frac{\partial G(x,t)}{\partial x}\right) = 0, \ \ x > 0, \ \ t > 0, \\ &G(x,0) = \frac{\partial}{\partial t}G(x,0) = 0, \ \ x > 0, \\ &\frac{\partial G}{\partial x}(0,t) = g(t), \ \ t > 0. \end{aligned} \tag{15}$$

The integral Equation (14) is derived by the following equations

$$\varepsilon_b^{-1}(0)\frac{\partial G}{\partial x} *_t H(0,t) - \varepsilon^{-1}(0)\frac{\partial H}{\partial x} *_t G(0,t) = \int_0^\infty \left(\left(\varepsilon_b^{-1}(x) - \varepsilon^{-1}(x)\right)\frac{\partial H}{\partial x} *_t \frac{\partial}{\partial x}\left(G(x,t)\right)\right)dx' \tag{16}$$

and

$$\begin{aligned} Q'_\varepsilon \delta\varepsilon &= \varepsilon^{-1}(0)\left(\delta H(0,t)\right) *_t g(t) \\ &= \int_0^\infty \left(\delta\left(\varepsilon^{-1}(0) - \varepsilon^{-1}(x)\right)\frac{\partial H}{\partial x} *_t \frac{\partial}{\partial x}\left(G(x,t)\right)\right)dx \\ &= \int_0^\infty \left(\left(\varepsilon^{-2}(x)\right)\delta\varepsilon(x)\frac{\partial H}{\partial x} *_t \frac{\partial}{\partial x}\left(G(x,t)\right)\right)dx \end{aligned} \tag{17}$$

4.3. The Singular Expansion of the Magnetic Wave Field

In this section, when the boundary excitation is exited by the impulse, $g(t) = \delta(t)$, the singular expansion of the magnetic field is presented as following,

$$H(x,t) = a(x)S(t-\phi(x)) + H_s(x,t), \tag{18}$$

where $S(t-\phi(x))$ is the step function on the characteristic line $\phi(x)$,

$$\phi(x) = \int_0^x \sqrt{\varepsilon(\xi)}d\xi, \tag{19}$$

$a(x)$ is the amplitude,

$$a\,(x) = -\varepsilon(0)^{-\frac{3}{4}}\varepsilon(x)^{\frac{1}{4}}, \tag{20}$$

The scattering magnetic wave function $H_s(x,t)$ satisfies the following equations

$$\begin{aligned} \frac{\partial^2 H_s}{\partial t^2}(x,t) - \frac{\partial}{\partial x}\left(\varepsilon^{-1}(r)\frac{\partial H_s}{\partial x}(x,t)\right) &= \frac{\partial}{\partial x}\left(\varepsilon^{-1}(r)\frac{\partial a}{\partial x}\right)S(t-\phi(x)),\ \ x>0,\ \ t>0, \\ H_s(x,0) = 0,\ \ \frac{\partial H_s}{\partial t}(x,0) &= 0, \\ \frac{\partial H_s}{\partial x}(0,t) &= \frac{1}{4}\varepsilon^{-\frac{3}{2}}(0)S(t). \end{aligned} \tag{21}$$

When the boundary excitation is exited by the impulse, $g(t) = \delta(t)$, the Green magnetic solution of the wave Equation (15),

$$G(x,t) = -\frac{1}{\sqrt{\varepsilon_b}}H(t-\sqrt{\varepsilon_b}x). \tag{22}$$

5. 2D AND 3D DIELECTRIC IMAGING

We use GL TM dielectric inverion to make 2-D dielectric imaging. The dielectric model is embedded in to the background medium which is shown in the Figure 1. The magnetic moment dipole source "STAR" is located in $x = 0$, $z = 0$ on the surface boundary in the Figure 1. The Figure 2 shows that the dielectric image from the eighth iteration of the 2D GL TM inversion. The dielectric imaging of quasi-PHC in section $z = 0$ by the 3D GL TM inversion is presented in Figure 3. Figure 4 shows that the dielectric imaging of quasi-PHC in section $z = 50\ Nm$ by the 3D GL TM inversion. The dielectric imaging of quasi-PHC in section $z = 100\ Nm$ by the 3D GL TM inversion is shown in Figure 5. Figure 6 shows that the dielectric imaging of quasi-PHC in section $z = 150\ Nm$ by the 3D GL TM inversion. The frequency band is from 1 GHz to 50 GHz. The dispersion design in PHC by our 3D GL TE and GL TM inversion creates the light guide.

6. CONCLUSION

The synthetic data interpretations show that the proposed GL TM dielectric inversion is stable and is of high resolution. We use a small and suitable regularizing parameter to control the inversion process stable. The GL EM modeling is used for forward modeling in the inversion. The proposed GL TM inversion method has applications in the geophysical, earthquake, and oil explorations, materials, nanometer and metamaterial dispersion design. The GL modeling and the GL TM inversion are patented to GLGEO and all rights are reserved to GL Geophysical Laboratory.

ACKNOWLEDGMENT

We thank to GL Geophysical Laboratory for this paper is approved to be published. Authors thank to Professor Kong for his encouragements. Authors thank to Professor Jiang Qin for her help.

REFERENCES

1. Xie, G., "A new iterative method for solving the coefficient inverse problem of wave equation," *Comm. on Pure and Applied Math.*, Vol. 39, 307–322, 1986.
2. Xie, G. and Y. M. Chen, "A modified pulse spectrum technique for solving inverse problem of two-dimensional elastic wave equation," *Appl. Numer. Math.*, Vol. 1, No. 3, 217–237, 1985.

3. Xie, G., J. Li, and Y. M. Chen, "Gauss-Newton-Regularizing method for solving coefficient inverse problem of PD," *J. Comput. Math.*, Vol. 5, No. 1, 38–49, 1987.
4. Xie, G. and J. H. Li, "A characteristic iteration for solving inverse problems of a wave equation," *J. Comput. Math.*, Vol. 6, No. 3. 1990.
5. Xie, G. and Y. M. Chen, "Nonlinear integral equation of inverse scattering problems of wave equation and iteration," *J. Comput. Math.*, Vol. 9, No. 3, 1989.
6. Xie, G. and J. H. Li, "Nonlinear integral equation of coefficient inversion of acoustic wave equation and TCCR iteration," *Science in China*, Vol. 31, No. 12, 1989.
7. Xie, G. and J. H. Li, "3-D nonlinear inversion of the wave equation using integral equation," *Science in China*, Vol. 3, No. 12, 1988.
8. Xie, G. and J. H. Li, "New iterative method for solving inverse scattering problem of 3-D wave equation," *Science in China (Series A)*, Vol. 31, No. 10, 1988.
9. Xie, G. and Q. Zou, "A parallel numerical method for solving 3-D inverse scattering problem," *Computer Physics Communications*, Vol. 65, 320–326, 1991.
10. Lee, K. H. and G. Q. Xie, "A new approach to imaging with low-frequency electromagnetic fields," *Geophysics*, Vol. 58, No. 6, 780–796, 1993.
11. Habashy, T. M., M. Oristaglio, and de Hoop, "Deep simultaneous nonlinear reconstruction of the two dimensional permittivity and conductivity," *Radio Sci.*, Vol. 29, 1101–1118, 1994.
12. Oristaglio, M. L. and T. M. Habashy, "Some uses (and abuses) of reciprocity in wavefield inversion," Van den Berg, P. M., Blok, H., and Foklema, *Wavefield and Reciprocity*, 1–22, Delft University Press, 1996.
13. Li, J. H. and G. Xie, "A 3D cubic-hole element and its application in resistivity imaging, 3-D electromagnetic methods," *Proceedings of the International Symposium on Three-dimensional Electromagnetics in Schlumberger-Doll Research*, 415–419, 1995; *SEG book*, 591–599, 1999.
14. Xie, G., F. Xie, L. Xie, and J. Li, "New GL method and its advantages for resolving historical diffculties," *Progress In Electromagnetics Research*, PIER 63, 141–152, 2006.
15. Xie, G., J. Li, L. Xie, and F. Xie, "GL metro carlo EM inversion," *Journal of Electromagnetic Waves and Applications*, Vol. 20, No. 14, 1991–2000, 2006.
16. Xie, G., J. H. Li, L. Xie, and F. Xie, "GL method for solving equations in math-physics and engineering," *Acta Mathmatica Applicane*, Vol. 24, No. 3, 392–404, 2008.
17. Li, J. H., G. Xie, and L. Xie, "A new GL method for solving differential equation in electromagnetic and phys-chemical and financial mathematics," *PIERS Online*, Vol. 3, No. 8, 1151–1159, 2007.
18. Xie, G., J. H. Li, L. Xie, and F. Xie, "GL Method for solving equations in math-physics and engineering," *Acta Mathmatica Applicane*, Vol. 24, No. 3, 392–404, 2008.
19. Xie, G. and J. Li, "New parallel GILD-SOR modeling and inversion for E-O-A strategic simulation," *IMACS Series Book in Computational and Applied Math.*, Vol. 5, 123–138, 1999.
20. Xie, G., J. H. Li, F. Xie, and L. Xie, "New TE and TM model inversion methods to detect the conductivity, dielectric and permeability," *GL Geophysical Laboratory Technology Patent Report*, GLGEOTP0806, 2008.

Electromagnetic Modeling of Plasma Etch Chamber for Semiconductor Microchip Fabrication

Zhigang Chen, **Shahid Rauf**, **Kartik Ramaswamy**, **and Ken Collins**
Applied Materials, Inc., Sunnyvale, California 94085, USA

Abstract— In the plasma etch chamber used to fabricate semiconductor microchips, maintaining the symmetry and uniformity of the electric field in the plasma discharge region is critical. Very-high-frequency (VHF) RF sources are attractive for such applications as they improve the efficiency of plasma generation. Electromagnetic effects become important at these frequencies, and etch chamber design requires careful investigation of the electromagnetic field spatial structure in the chamber. In this paper, we apply the finite-difference time-domain (FDTD) method to examine various electromagnetic effects in the plasma etch chamber and investigate strategies for improved chamber design. These effects include the standing wave effects and asymmetric field distributions that can be caused by asymmetric RF power feed configurations. The FDTD method is formulated in both cylindrical and Cartesian coordinate systems to facilitate modeling of rotationally symmetric chamber and asymmetric RF feed structures. The electric field distribution generated by various RF feed configurations is studied at different VHF frequencies. Based on the FDTD simulations, we have been able to identify a variety of design approaches for ensuring electric field symmetry and uniformity.

1. INTRODUCTION

Radio frequency (RF) capacitively coupled plasma discharges are widely used in semiconductor microchip fabrication for plasma etching [1]. In such plasma etching reactors, the plasma is generated by applying a sinusoidal RF signal to two parallel circular electrodes spaced by a few centimeters. The RF power is guided to the electrodes via a coaxial line, and the whole system is enclosed by a cylindrical metal chamber. Initially, discrete frequencies between 2–30 MHz were used for plasma processing. To increase the power coupling efficiency to the plasma, VHF sources ranging from 30–162 MHz have since become popular. However, the excitation frequency cannot be increased indefinitely since major processing uniformity issues arise when electromagnetic effects are significant. That is, when the RF wavelength becomes comparable to the chamber dimension, which is ~ 500 mm for a semiconductor wafer size of 300 mm, and the plasma skin depth becomes comparable to the electrode size and spacing.

When the electromagnetic effects become significant, it is indispensable to fully understand the electrodynamic behavior of the RF fields in the etch chambers because any nonuniformity of the electric fields in the plasma region would directly have an impact on the etch uniformity and quality. In this paper, we apply the FDTD technique [2] to model the RF wave behavior in the chamber. We particularly pay attention to the electric field distribution at the wafer level and the corresponding electromagnetic effects at very high frequency. The FDTD method is formulated in both cylindrical and Cartesian coordinate systems to facilitate modeling of rotationally symmetric chamber and asymmetric RF feed structures. We couple the FDTD formulation with the CPML [2] absorbing boundary conditions to accurately simulate the RF power delivery via a coaxial line.

2. COMPUTATIONAL METHOD DESCRIPTION

To make the computational model conformal to the geometrical features in the cylindrical etching chamber, we formulate the FDTD method in the cylindrical coordinate system. In the cylindrical coordinate system, the Maxwell's curl equations for linear, isotropic, nondispersive materials can

be written as:

$$\frac{\partial E_r}{\partial t} = \frac{1}{\varepsilon}\left(\frac{1}{r}\frac{\partial H_z}{\partial \phi} - \frac{\partial H_\phi}{\partial z}\right) - \frac{\sigma}{\varepsilon}E_r \tag{1}$$

$$\frac{\partial E_\phi}{\partial t} = \frac{1}{\varepsilon}\left(\frac{\partial H_r}{\partial z} - \frac{\partial H_z}{\partial r}\right) - \frac{\sigma}{\varepsilon}E_\phi \tag{2}$$

$$\frac{\partial E_z}{\partial t} = \frac{1}{\varepsilon}\left[\frac{1}{r}\frac{\partial (rH_\phi)}{\partial r} - \frac{1}{r}\frac{\partial H_r}{\partial \phi}\right] - \frac{\sigma}{\varepsilon}E_z \tag{3}$$

$$\frac{\partial H_r}{\partial t} = \frac{1}{\mu}\left(\frac{\partial E_\phi}{\partial z} - \frac{1}{r}\frac{\partial E_z}{\partial \phi}\right) \tag{4}$$

$$\frac{\partial H_\phi}{\partial t} = \frac{1}{\mu}\left(\frac{\partial E_z}{\partial r} - \frac{\partial E_r}{\partial z}\right) \tag{5}$$

$$\frac{\partial H_z}{\partial t} = \frac{1}{\mu}\left[\frac{1}{r}\frac{\partial E_r}{\partial \phi} - \frac{1}{r}\frac{\partial (rE_\phi)}{\partial r}\right] \tag{6}$$

Discretizing Eqs. (1)–(6) using the conventional Yee lattice, we can obtain the corresponding finite-difference equations. For example, the finite-difference equation for E_z is given by

$$E_z|_{i,j,k+1/2}^{n+1} = \left(\frac{1-\frac{\sigma_{i,j,k+1/2}\Delta t}{2\varepsilon_{i,j,k+1/2}}}{1+\frac{\sigma_{i,j,k+1/2}\Delta t}{2\varepsilon_{i,j,k+1/2}}}\right)E_z|_{i,j,k+1/2}^{n} + \left(\frac{\frac{\Delta t}{\varepsilon_{i,j,k+1/2}}}{1+\frac{\sigma_{i,j,k+1/2}\Delta t}{2\varepsilon_{i,j,k+1/2}}}\right)\left[\begin{array}{l}\left(\frac{1}{2r_i}+\frac{1}{\Delta r}\right)H_\phi\Big|_{i+1/2,j,k+1/2}^{n+1/2} \\ +\left(\frac{1}{2r_i}-\frac{1}{\Delta r}\right)H_\phi\Big|_{i-1/2,j,k+1/2}^{n+1/2} \\ +\frac{H_r|_{i,j-1/2,k+1/2}^{n+1/2} - H_r|_{i,j+1/2,k+1/2}^{n+1/2}}{r_i\Delta\phi}\end{array}\right] \tag{7}$$

In cylindrical coordinate system, the time step required to ensure numerical stability is given by

$$\Delta t \le \frac{1}{c\sqrt{(1/\Delta r)^2 + \left[1/(r_{\min}\Delta\phi)\right]^2 + (1/\Delta z)^2}}, \tag{8}$$

where $r_{\min} = 0.5\Delta r$.

E_z is required to be evaluated along the z-axis where $r = 0$ and direct use of Eq. (7) would encounter singularities. To determine E_z along the z-axis, we start with the integral form of Ampere's law of Maxwell's equations:

$$\oint_C \mathbf{H}\cdot d\mathbf{l} = \int_S \left(\varepsilon\frac{\partial \mathbf{E}}{\partial t} + \sigma\mathbf{E}\right)\cdot d\mathbf{s}, \tag{9}$$

where C is a closed contour around the z-axis and S is the surface bounded by the contour C. Choosing the smallest contour around the z-axis that has a radius of $0.5\Delta r$, we obtain

$$E_z|_{0,j,k+1/2}^{n+1} = \left(\frac{1-\frac{\sigma_{0,j,k+1/2}\Delta t}{2\varepsilon_{0,j,k+1/2}}}{1+\frac{\sigma_{0,j,k+1/2}\Delta t}{2\varepsilon_{0,j,k+1/2}}}\right)E_z|_{0,j,k+1/2}^{n} + \left(\frac{\frac{2\Delta t\Delta\phi}{\varepsilon_{i,j,k+1/2}\pi\Delta r}}{1+\frac{\sigma_{i,j,k+1/2}\Delta t}{2\varepsilon_{i,j,k+1/2}}}\right)\sum_{j=0}^{N_\phi-1} H_\phi|_{1/2,j,k+1/2}^{n+1/2}, \tag{10}$$

where N_ϕ is the number of grid points along the azimuthal direction.

To accurately model the propagating TEM wave behavior in a coaxial line, we apply the CPML to truncate the coaxial line in the z-direction. The details of the CPML implementation can be found in [2].

The plasma etching chamber usually operates at discrete frequencies. Therefore, we excite the system using a monochromatic sinusoidal current source. The current source is designed to excite the TEM mode in the coaxial line. In a coaxial line, the TEM mode is defined by [3]

$$E_r = \frac{V(t)}{\ln(b/a)}\frac{1}{r}, \quad H_\phi = \frac{V(t)}{\eta\ln(b/a)}\frac{1}{r} \tag{11}$$

where $V(t)$ is the applied voltage, a and b are the radii of the inner and outer conductors, respectively, and η is the intrinsic impedance of the insulating material in the coaxial line. The

corresponding current sheet density on a $z = z_0$ plane based on the surface equivalence theorem is given by

$$J_r = -H_\phi = -\frac{V(t)}{\eta \ln(b/a)} \frac{1}{r} \tag{12}$$

This current sheet source is applied to a cross section of the coaxial line about 5 cells away from the PML.

To decrease the transient time in a single frequency simulation, we choose a new time function based on the Hanning window function to replace the stepped monochromatic excitation [4]:

$$V(t) = \begin{cases} 0.5 \sin(2\pi f t)[1 - \cos(\frac{\pi t}{T})], & 0 \le t \le T \\ \sin(2\pi f t), & t > T \end{cases} \tag{13}$$

where T is the rising time that can be taken to be several cycles of the excitation frequency.

3. RESULTS AND DISCUSSIONS

A simplified model for a plasma etch chamber is shown in Fig. 1. Fig. 1(a) shows the internal structures of the chamber whereas Fig. 1(b) presents a cross-sectional view. The RF power is delivered into the chamber via a coaxial line. The inner conductor of the coaxial line to which the RF voltage is applied is connected to the bottom electrode. Above the bottom electrode is the electrostatic "chuck" which makes use of the electrostatic force to hold a semiconductor wafer on it. The outer conductor of the coaxial line is connected to a grounded metal plate and chamber wall. The grounded metal plate and the RF "hot" electrode are separated by quartz. Between the electrostatic chuck and the top grounded electrode is the plasma region. A thin plasma sheath between 1 mm–1 cm is usually formed between plasma and wafer. The ions are accelerated by the electric field in the plasma sheath and will bombard the wafer with a significant energy to facilitate the etching process. The uniformity of the electric field distribution within the plasma sheath therefore would directly impact the etch rate uniformity. We investigate how the electric field distribution in the plasma sheath changes as we increase the RF frequency and as the plasma conductivity changes.

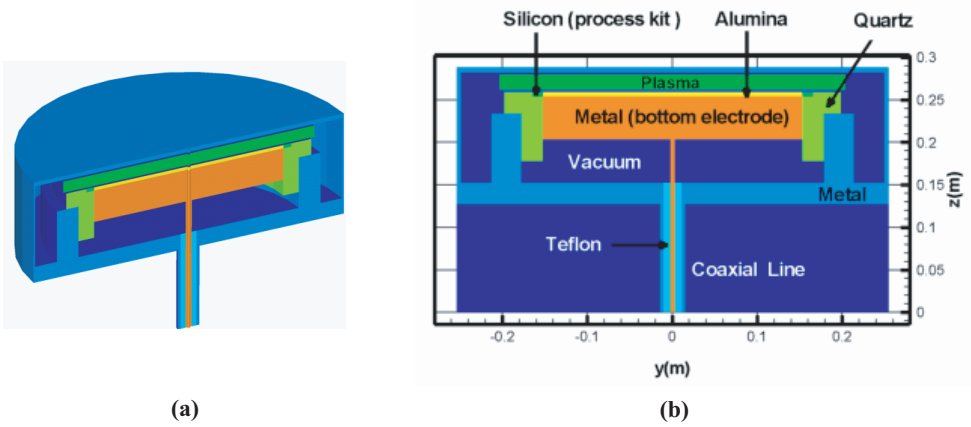

Figure 1: A simplified model for a plasma etching chamber. (a) The internal view of the chamber. (b) The cross-sectional view of the chamber.

We run the FDTD simulations for a mesh of $102 \times 36 \times 230$ cells for a number of periods until they reach steady state. Then we take discrete Fourier transform of the time-domain data to obtain the electric field at a given frequency. To facilitate the studies of the electromagnetic effects, we first treat plasma as a linear lossy medium with constant conductivity of 1 S/m and the plasma sheath as a vacuum gap of 2.5 mm. The chosen conductivity corresponds to a plasma density of about 1×10^{16} m^{-3}and collision frequency of about 3×10^8 s^{-1}. The discrete frequencies we have investigated are 13.56 MHz and 60 MHz. The electric field distributions at the wafer level (i.e., the electric field between plasma and electrostatic chuck) are shown on Fig. 2 where we have normalized the electric field by its maximum. Note that we have used different color scales for each frequency in order to amplify the nonuniformity within the boundary of a wafer (the black circle in the figure). Fig. 2(a) shows the electric field at 13.56 MHz. We see that the electric

field distribution at this frequency is uniform within the boundary of a wafer because the effective wavelength is large compared to the chamber dimensions. However, the electric field decays rapidly after passing the edge of the bottom electrode. Fig. 2(b) shows the electric field at 60 MHz. At this frequency, the effective wavelength is still large compared to the chamber dimensions. However, the skin depth of the plasma with 1 S/m conductivity is 6.5 cm and is comparable to the wafer radius. This skin effects lead to an edge-high and center-low pattern as shown in Fig. 2(b). We note that the nonuniformity caused by the skin effects is small ($< 1\%$). Fig. 2(c) shows the electric field at 60 MHz, but for 10 S/m plasma conductivity and 1.3 mm plasma sheath thickness. At such a high conductivity, the standing wave effects come into play even at 60 MHz and are dominant, leading to a center-high and edge-low pattern as shown in Fig. 2(c). We note that the lossy nature of the plasma can reduce the effective wavelength [3] and therefore make the standing wave effects more pronounced for high conductivity even at lower frequencies.

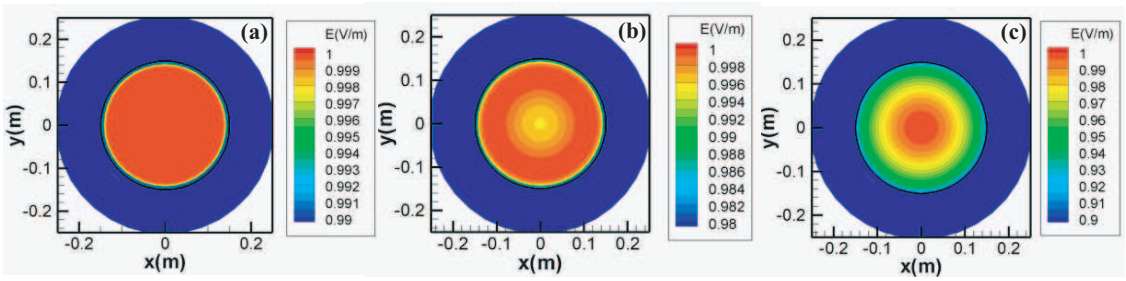

Figure 2: Electric field distribution 1 mm above the wafer level. The black circle denotes the boundary of a wafer. (a) 13.56 MHz (plasma conductivity = 1 S/m, plasma sheath thickness = 2.5 mm); (b) 60 MHz (plasma conductivity = 1 S/m, plasma sheath thickness = 2.5 mm); (c) 60 MHz (plasma conductivity = 10 S/m, plasma sheath thickness = 1.3 mm).

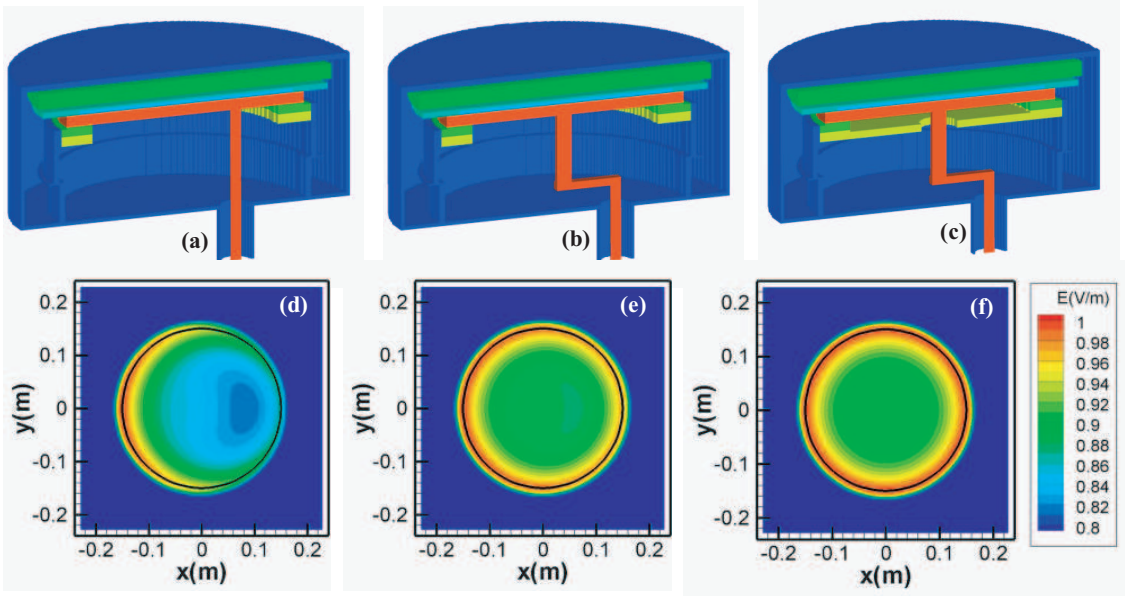

Figure 3: Three different RF feed configurations and the corresponding electric field distribution 1 mm above the wafer level at 60 MHz. Left: RF feed is about 7 cm off center; Middle: Center RF feed with off-center bend connected to power source; Right: Center RF feed with shielding grounded plate and off-center bend.

We also have studied the asymmetric field distributions that can be caused by asymmetric RF feed configurations in the chamber. Fig. 3 shows three different RF feed configurations and the corresponding electric field distribution 1 mm above the wafer level at 60 MHz. Here, we assume the plasma conductivity and sheath thickness are 0.1 S/m and 2.5 mm, respectively. These parameters correspond to a plasma density of about 1×10^{15} m^{-3}and collision frequency of about 3×10^{8} s^{-1}. The off-center RF feed in Fig. 3(a) causes significant asymmetric field distribution

shown in Fig. 3(d). Such asymmetric field distribution is not desired. One quick way to correct this problem is to use a bend structure to feed to the center of the bottom electrode, as shown in Fig. 3(b). Such a modification can significantly improve the field symmetry and uniformity as shown in Fig. 3(e). Further improvement can be achieved by adding a grounded metal plate (the yellow plate in Fig. 3(c)) above the RF bend. The grounded metal plate acts like a shield, and therefore minimizes the impact of the RF bend structure. The corresponding electric field distribution is quite uniform and symmetric, as shown in Fig. 3(f).

4. CONCLUSIONS

In summary, we have demonstrated electromagnetic modeling of plasma etching chamber based on FDTD method and evaluated the standing wave effects, the skin effects of the plasma and the asymmetric field distributions caused by asymmetric RF feed configurations in the chamber. Based on the FDTD simulations, we have been able to identify a variety of design approaches for ensuring electric field symmetry and uniformity. These design approaches are the foundation of new RF feed designs in our plasma etching chambers.

REFERENCES

1. Lieberman, M. A. and A. J. Lichtenberg, *Principles of Plasma Discharges and Materials Processing*, Wiley-Interscience, New Jersey, 2005.
2. Taflove, A. and S. C. Hagness, *Computational Electrodynamics: The Finite-Difference Time-Domain Method*, Artech House, Massachusetts, 2005.
3. Ramo, S., J. R. Whinnery, and T. V. Duzer, *Fields and Waves in Communication Electronics*, John Wiley & Sons, 1994.
4. Prescott, D. T. and N. V. Shuley, "Reducing solution time in monochromatic FDTD waveguide simulations," *IEEE Trans. Microw. Theory Tech.*, Vol. 42, No. 8, 1582–1584, 1994.

Analysis of Electric Field on Liquid Zoom Lens Based on Electrowetting

Shunan Shi
Department of Telecommunication, Xidian University, Shaanxi 710126, China

Abstract— The electro-wetting is a physical chemistry effect which can be used to control the micro droplets. In this paper, we mainly report the design and development of the liquid zoom lens based on the electro-wetting effect, the choose and manufacture of the cylinder transparent electrode, and calculated the relationship of the focus length and the electrical field and give the curves of the focus length and the biased voltage by simulation.

1. INTRODUCTION

In the optical system, the zoom lens plays an important role all the time. In recent years, along with the development of optical communication technology, there is an increasing demand for micro-zoom lens. The traditional optical lens system has been designed and optimized for centuries, the traditional mechanical lens group has been on the verge of development because of their complexity, cost, and cannot keep up with the requirement in the industry. To miniaturize the zoom lens and improve its performance and lifetime, many kinds of new micro-zoom lens technology has been raised recently [1], and liquid lensis the simplest one of them and has better image quality [2].

2. BASIC PRINCIPLES OF ELECTRO-WETTING EFFECT

In the mico-zoom lens system, the size of the components is from a dozens of microns to several hundreds of microns. In this scale, the liquid droplet is strongly controlled by surface tension, which is the leading force compared with the other forces.

If there is a thin insulation layer between the electrolyte and the electrode, the contact angle will change due to an applied potential difference between the electrode and the electrolyte, which is electro-wetting [3] effect. If we regard the droplet as a lens, the focus length will change with the change of the surface shape of the droplet due to electro-wetting effect. Figure 1 schematicly shows the electro-wetting effect setup. When voltage is zero, liquid surface was represented by the dotted line and the contact angle between liquid and insulation is θ_0. θ_0 can be calculated by Young's equation [4]:

$$\cos\theta_0 = \frac{\gamma_{sg} - \gamma_{sl}}{\gamma_{lg}} \tag{1}$$

γ_{sg} is the tension of the interface of solid (insulation layer) and gas, γ_{sl} is the tension of the interface of solid and liquid (electrolyte) and γ_{lg} is the tension of the interface of liquid and gas.

When the voltage is applied on the electrode and electrolyte, the hydrophobicity of insulation layer will change under the electrical field, therefore the tensions among liquid-gas-solid also changes. The surface shape of the droplet will reshape under the tension because the volume of the droplet is a constant. The contact angle change to θ, as shown in Figure 1.

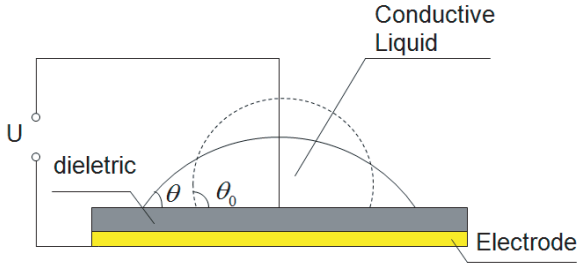

Figure 1: Schematic diagram of electro-wetting setup.

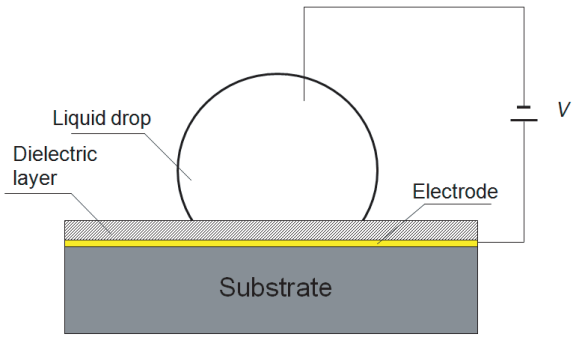

Figure 2: Structure of electro-wetting on dielectric.

3. PLANAR MICRO-ZOOM LENS

There are many kinds of methods used to control microfluid, including structured surface, capillary action, galvanic effect, electrophoresis, electro-wetting on dielectric (EWOD) and so on. Electro-wetting is paid close attention because of its merits, such as low power, high response speed, easy controllability and good repetitiveness. According to the electro-wetting theory, the basic structure of electro-wetting on dielectric is designed shown in Figure 2.

Electrolyte droplet (micro-litre) lies on the substrate with a plane electrode and a hydrophobic dielectric, and the voltage is applied on the droplet and the electrode. When the voltage is zero, the contact angle is blunt angle due to the hydrophobicity of dielectric. When the voltage is not zero, the inductive charge or polarization charge changed the free energy between the droplet and dielectric layer, which alter the wetting character and decreased the contract angle. The relation of contract angle and voltage is described by Lippmann-Young equation.

$$\cos\theta = \cos\theta_0 + \frac{\varepsilon_0\varepsilon_r}{2d\gamma_{LV}}V^2 \tag{2}$$

where, V is applied voltage, θ_0 the contract angle when the voltage is zero. γ_{LV} is the tension of the interface of the liquid and the dielectric. ε_r is relative dielectric constant, and ε_0 is the dielectric constant in vacuum. The thickness of dielectric is represented by d. In most cases, the contract angle cannot equal to that calculated by Equation (2) after equilibrium. The angle θ is between recedingcontact angle (θ_r) and advancing contact angle (θ_a) [5]. The difference of the two angles ($\Delta\theta = \theta_a - \theta_r$) is called the delay of contract. A most easy method is covered a layer oil as lubricant.

At present, the structure of the zoom lens made by electro-wetting on dielectric are same to that in Figure 2. Under the condition that the contract angle is unsaturation, the higher the voltage, the smaller the contact angle, the smaller the surface curvature, the biger the lens focal length. By this method, the focus length can be adjusted by changing the voltage. Recently, this kind of lens has been researched in many countries. Some kinds of products not only can change the focal length, also can control lens move on a plane. However, there are a lot of the structural defects, such as, there is no a stable optical axis. That is, the shake of the device will change the location of when a stable voltage is applied, which limits the application of this structure. In addition, the uneven structure of the electrodes under the droplets will also damage the image quality. Much work needs to do to improve the structure.

4. DOUBLE LIQUID LENS

We designed a double liquid lens, this special structure can stabilize the optical axis and guarantee image quality. There are varieties of structures of double liquid lens, but the basic principle is the same. That is, two kinds of transparent and non-infiltration liquid are permeated into a glass tube. They approximately have the same density through adjusting the ingredient of the two solutions. The conductive solution with the refractive index of n_1 is connected with power and the insulated non-polar liquid with the refractive index of n_2 is connected with dielectric. Because the two liquid has the same density and different refractive index, the interface can be used as a lens [6]. The structure of double liquid cylindrical lens is shown in Figure 3.

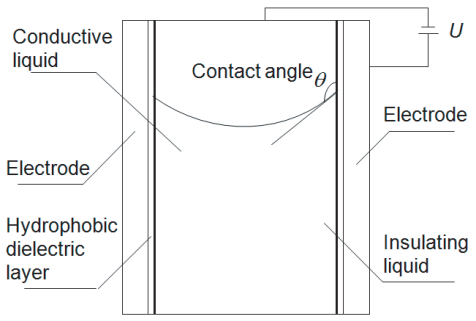

Figure 3: Double liquid cylindrical lens.

There are three key points in the preparing of double liquid lens. Firstly, the two liquid approximately has the same density to keep a spherical interface away from the effect of gravity; Secondly, the conductive liquid should always connect with the power. Lastly, the optical axis should be fixed on the center of the whole device, and is not affect by the voltage. This structure overcomes the defects of the plane electrode structure, in which the optical axis moves with voltage, the imaging quality is seriously damaged.

5. PREPARATION OF CYLINDRICAL TRANSPARENT ELECTRODE

The cylindrical electrical electrodes used to prepare the double liquid lens must have the following special characteristics, good transparence, providing even electrical field, small and thin. Based on the points, the transparent thin film was prepared on the glass tube with millimeter size by spray pyrolysis method. The thickness of the film is about 0.5 mm, the transparency is over 90%.

SnO_2 film has polycrystalline structure, and there are potential barriers among the crystal grains. By doping Sb or F, the conductivity of SnO_2 film can be enhanced by one order, and the conductivity of SnO_2: F is higher than SnO_2: Sb [7]. We prepared SnO_2: F film by using the ultrasonic spray pyrolysis. And the method has many advantages such as simplicity of facility, inexpensiveness of raw materials and shortness of production cycle; it is the most important that we can get high-quality film by this method [8]. In our experiment, the solution was compounded by adding $SnCl_4{\cdot}5H_2O$ and NH_4F into the mixed solvents of water and alcohol. The mass ratio of F to Sn is 0.03, and the volume ratio of water to alcohol is 5 [9]. Then the solution was put into the tank of ultrasonic atomizer with the frequency of 1.7 MHz. The substrate was a quartz tube, which was washed by ultrasonic cleaner. Put the substrate into a muffle furnace and heated until its temperature reached 430°C. Then we evenly sprayed the atomizing solution onto the substrate, took the tube out and cooled down in air. The electrodes were made by coating silver slurry on the ends of the tube. Then the tube was put into the muffle furnace at room temperature, slowly heated it to 600°C, and kept the temperature for 30 minutes. After that, turned off the muffle furnace, and did not open the door of the furnace. When the temperature receded to room temperature, the tube was taken out, and the SnO_2: F thin film heating tube was prepared.

SnO_2 film is multi-functional inorganic materials, it is has low-resistance, high transparency of visible light, excellent strength and chemical stability. The film has been widely used in the solar cells, liquid crystal display, anti-reflective coating, heating power and optoelectronic devices.

6. THE RELATIONSHIP OF THE FOCUS AND THE ELECTRIC FIELD

According to the Young's equation, the contact angle θ, as is shown in Figure 3, lies on the triphase interfacial tension:

$$\gamma_{12}\cos\theta = \gamma_{s1} - \gamma_{s2} \tag{3}$$

γ_{12} is the interfacial tension of the to kinds of liquid, γ_{s1} is the interfacial tension of the solid and insulating liquid, γ_{s2} is the interfacial tension of the solid and the conductive liquid. When the biased voltage V added on the conductive liquid and the transparent electrode, commensurable positive and negative charge will be gathered at the both sides of the lyophobic dielectric layer, the lyophobic dielectric layer can be regarded as a cylinder capacitor. γ_{12} and γ_{s1} can be approximatively considered as not be effected by the electrostatic field [8], only the γ_{s2} is the function of the electrostatic field. When the biased voltage is V, assume the interfacial tension of the solid and the liquid is $\gamma_{s2}(V)$, the interfacial tension without biased voltage is:

$$\gamma_{s2}(v) = \gamma_{s2}^0 + \Delta\gamma_{s2}(v) \tag{4}$$

The effect on the interfacial tension of the solid and liquid interface $\Delta\gamma_{s2}(v)$ is the change of Helmholtz free energy ΔF in unit area of the lyophobic dielectric layer, as is shown:

$$\Delta F = \Delta\gamma_{s2}(v) \tag{5}$$

In the constant temperature and the same chemical composition, the Helmholtz free energy of the solid and liquid interface changes as:

$$\Delta F = -\int_0^v \sigma dv \tag{6}$$

R is the surface charge density of the dielectric layer, V is the voltage of the electrode and the conductive liquid, the same as the voltage of the dielectric layer. The relationship is:

$$V = \frac{e\sigma}{\varepsilon_0 \varepsilon_r} \tag{7}$$

e is the thickness of the lyophobic dielectric layer, ε_0 and ε_r are the absolute specific inductive capacity of the lyophobic dielectric layer and the relative specific inductive capacity of the media. From the Equations (6) and (7), we can conclude that:

$$\Delta F = \Delta\gamma_{s2}(v) = -\frac{\varepsilon_0 \varepsilon_r}{2e} V^2 \tag{8}$$

From the Equations (3) and (8), we can conclude that:

$$\cos\theta = \frac{\gamma_{s1} - \gamma_{s2}^0}{\gamma_{12}} + \frac{\varepsilon_0 \varepsilon_r}{2\gamma_{12} e} V^2 = \cos\theta_0 + \frac{\varepsilon_0 \varepsilon_r}{2\gamma_{12} e} V^2 \tag{9}$$

θ_0 is the contact angle of the solid and liquid without the biased voltage.

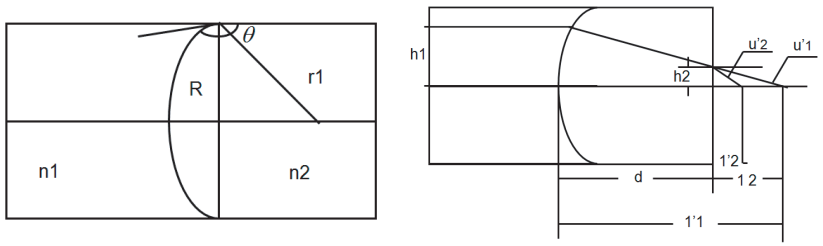

(a) (b)

Figure 4: (a) Parameter schematic diagram of double liquid lens and (b) schematic diagram of ray tracing.

As is shown in Figure 4, the index of refraction of the insulating liquid is n_2, the radius of the cylinder tube is R, the curvature radius of interface of the two liquids is r_1. Tracing a near axis ray and the project height is h_1, as is shown in Figure 3. The n_1, n_2 and r_1 has a relationship as follows:

$$\frac{n_2}{l_1'} - \frac{n_1}{\infty} = \frac{n_2 - n_1}{r_1} \tag{10}$$

So

$$l_1' = \frac{n_2 r_1}{n_2 - n_1} \tag{11}$$

For the paraxial ray,

$$l_1' \cdot u_1' = h_1 \tag{12}$$

So we can conclude that,

$$u_1' = \frac{h_1}{l_1'} = \frac{h_1(n_2 - n_1)}{n_2 r_1} \tag{13}$$

In the coaxial spherical optical system,

$$l_2 = l_1' - d = \frac{n_2 r_1}{n_2 - n_1} - d \tag{14}$$

$$h_2 = h_1 - d \cdot u_1' = h_1 - d \cdot \frac{h_1 (n_2 - n_1)}{n_2 r_1} \tag{15}$$

After the refraction,

$$l_2' = \frac{l_2}{n_2} = \frac{\left(\dfrac{n_2 r_1}{n_2 - n_1} - d\right)}{n_2} = \frac{r_1}{n_2 - n_1} - \frac{d}{n_2} \tag{16}$$

$$u_2' = \frac{h_2}{l_2'} = \frac{\left[h_1 - d \cdot \dfrac{h_1 (n_2 - n_1)}{n_2 r_1}\right]}{\dfrac{r_1}{n_2 - n_1} - \dfrac{d}{n_2}} = \frac{h_1 (n_2 - n_1)}{r_1} \tag{17}$$

From the Equation (17), the focus of the zoom lens is:

$$f' = \frac{h_1}{u_2'} = \frac{r_1}{n_2 - n_1} \tag{18}$$

Because of the relationship of R and r_1 as follows:

$$r_1 = \frac{R}{\sin(\theta - 90^\circ)} = \frac{-R}{\cos\theta} \tag{19}$$

The focus of the zoom lens is:

$$f' = \frac{1}{\dfrac{n_2 - n_1}{R}\cos\theta_0 + \dfrac{\varepsilon_0\varepsilon_r\left(n_1 - n_2\right)}{2eR\gamma_{12}}V^2} \tag{20}$$

7. CONCLUSIONS

Based on the model of plane liquid multifocal lens, we calculated the relationship of the double liquid multifocal lens focus and the biased voltage. The transparent conductive coating applied for the double liquid multifocal lens is fabricated. When the liquid lens based on the electrowetting effect is driven by a biased voltage, it has a fast zooming response, a good shake resistance, a stable image performance and low power dissipation. The transmission for the visible light has been up to 90%. The liquid lens is composed by two kinds of liquid with different index of refraction, like the doublet. We can put some additive into the liquid to adjust the optical character, and eliminate the aberration. In this way, the expensive and complex method to eliminate the aberration can be simplified. Meanwhile, by choosing appropriate liquid, we can ensure the lens work well in a large temperature range. The liquid lens can be applied in many areas, such as pocket digital camera, videos, cell phones, CCD camera inside of the computer, photoetching technology and so on, the liquid lens has a bright future.

REFERENCES

1. Chen, J., W. Wang, J. Fang, et al., *Journal of Micro-mechanics and Micro-engineering*, Vol. 14, No. 5, 675–680, 2004.
2. Kuiper, S., B. H. W. Hendriks, S. L. J. Huijbregt, et al., *Proceedings of SPIE, the International Society for Optical Engineering*, Vol. 5523, 100–109, 2004.
3. Froumkine, A., *Actualites Scientifiques et Indus-trielles*, Vol. 373, No. 1, 5–36, 1936.
4. Pollack, M. G., R. B. Fair, and A. D. Shenderov, *Applied Physics Letters*, Vol. 77, No. 11, 1725–1726, 2000.
5. De Gennes, P. G., *Rev. Mod. Phys.*, Vol. 57, 827, 1985.
6. Berge, B. and J. Peseux, *Eur. Phy. J. E*, Vol. 3, No. 2, 59–163, 2000.
7. Promier, R. and C. Cril, *Maruchi J. Thin Solid Films*, Vol. 77, 91–97, 1981.
8. Shiliu, F., *Chinese Journal of Materials Research*, Vol. 9, 434–437, 1995.
9. Wei, S. and H. Lei, *Journal of Functional Materials*, Vol. 35, 1162, 2004.

The Use of Ray-tracing and Genetic Algorithms to Optimize a Tapered Anechoic Chamber

S. M. J. Razavi and M. Khalaj-Amirhosseini
College of Electrical Engineering, Iran University of Science and Technology, Tehran, Iran

Abstract— Anechoic chambers are used for both emission and immunity testing. There are three major types of anechoic chamber including rectangular, tapered, and double horn. The tapered chamber is an established design concept used for antenna testing below 1 GHz but the ferrite tiles used to line the inside of the chamber are extremely expensive. This paper describes a method of reducing the number of tiles, whilst ensuring a reliable test environment.

In this paper, the ray-tracing method for wave's propagation is used for evaluation of the reflectivity level of a tapered anechoic chamber, and genetic algorithms are used to optimize the layout of ferrite tile absorber in a partially lined enclosure to produce a best performance.

The results show that it is possible to cover just 80% of the surface of the enclosure with ferrite absorber and obtain good agreement by fully lined enclosure with an error of less than 3 percent over the whole test points.

1. INTRODUCTION

Anechoic chambers are used for both emission and immunity testing. There are three major types of anechoic chamber including rectangular, tapered, and double horn. The illumination difference between the rectangular and tapered chambers is illustrated in Fig. 1. This is accomplished by forcing the wall image close together at the source end of the chamber. The tapered chamber is an established design concept used for antenna testing below 1 GHz.

The large demand for testing in the 30 to 1000 MHz frequency range has brought about the development of series of materials optimized for this application. The most common material is ferrite tile. The ferrite tiles are expensive and the room strength required to support the weight of the tiles (of the order of 30 kg/m) adds to the cost.

The need for decreasing the cost, led to develop some new optimized analytical and practical methods. Based On the experiments [1], with 80% of Fresnel zone absorbing coverage, the variation of the E-field is very uniform at all frequencies above 300 MHz and the maximum error is 1.4 dB. Some optimization methods by using additional absorbers and shifted them and new absorber lining of optimized material are proposed in [2].

The method offered in this paper, describe a new technique to reduce the need for full coverage of lining material and optimize the layout of absorbing material tiles to reach a good performance for the chamber and minimize the cost. The offered method has been simulated via computer programs and validated with CST MICROWAVE STUDIO.

2. RAY-TRACING METHOD

The waves from a transmitting antenna can be modeled as many ray tubes shooting from the location of the antenna [3]. In our ray-tracing program, every ray tube is composed of four rays defined by the increments of θ and φ ($\Delta\theta$ and $\Delta\varphi$) in local spherical coordinates centered at the antenna and the ray tubes have about the same solid angle to improve program efficiency.

The basic ray-tracing procedure is described below.

1) When a ray tube incidents on an interface, a reflected and a transmitted ray tube is generated according to Snell's law and the local plane wave approximation. The reflection and transmission coefficients derived for a plane wave illuminating a flat interface of two materials are employed [4].
2) The reflected ray is continuously traced, while transmitted ray tube is neglected in the chamber. However, those ray tubes will be terminated if their field values are less than a threshold or exits outdoor
3) When a ray tube enters the room containing the receiving antenna, as shown in Fig. 2, a test is then performed to determine whether or not. The E-field vector phasors of the tubes passing the receiving point are superposed to obtain the E-field at this field point [3]. Many field points may be checked and evaluated during this step to obtain the field distributions in the receiving room.

4) From the geometrical optics, the E-field of the ray tube at the receiving point, as shown in Fig. 2, can be determined from the following equation:

$$\vec{E} = \vec{E}_0 \cdot \left\{ \prod \overline{\overline{R_i}} \right\} \cdot \left\{ \prod \overline{\overline{T_i}} \right\} \cdot \left\{ \prod e^{-r_i l_i} \right\} \cdot SF \tag{1}$$

where E_0 is the E-field at a reference point r_0, R_i and T_i are, respectively, the reflection and transmission coefficient dyads, $\{\prod e^{-r_i l_i}\}$ is the product of the propagation phase variations and exponential losses for this ray contribution starting from r_0, and SF is the spreading factor. From the conservation of energy flux in a ray tube [5], SF can be obtained by using

$$SF = \sqrt{A_0}/\sqrt{A} \tag{2}$$

where A_0 and A are the cross-sectional areas of the ray tubes at the reference point r_0 and the field point r, respectively.

In this paper transmission ray tubes are attenuated and only reflection ray tubes are traced at each interface.

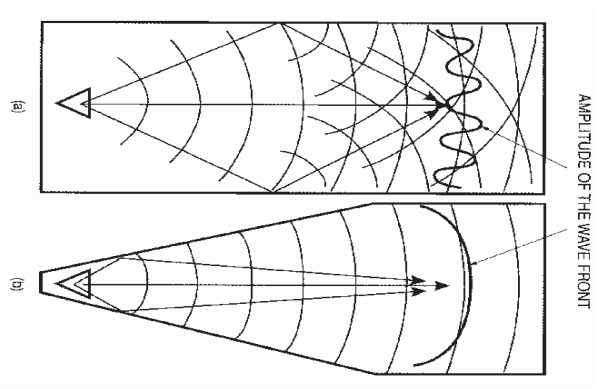

Figure 1: Test region illumination in (a)a rectangular chamber (b) a tapered chambers.

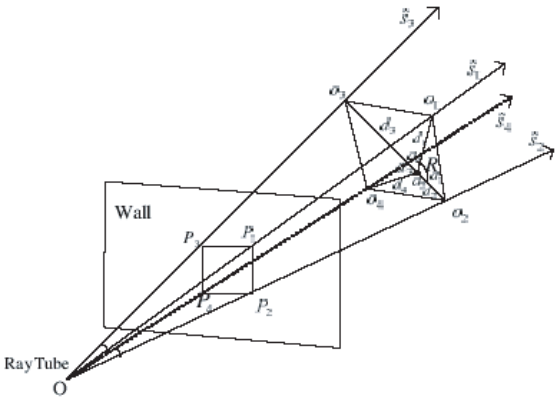

Figure 2: A ray tube passing a receiving antenna at R.

3. SETTING FOR OPTIMIZATION

Ferrite tiles are generally 10 cm squares. Thetapered anechoic chamber under investigation (8 m × 8 m × 24 m) here would need approximately 551810 tiles. (Cover just 80% of its no tapered walls). To search manually for the best performance in a problem of this size would be impossible. An automated system is necessary and the use of genetic algorithms is suited for this type of search.

Genetic algorithms are used to search for a solution to a problem which produces a global maximization (or minimization) of the function describing that problem. A set of possible solutions is expressed in a way (such as a binary string) which allows them to be subject to crossover and mutation to generate a new set of possible solutions [6, 7].

In the tapered anechoic chamber, excitation antenna is placed near the tapered walls (Fig. 3) therefore the strong rays incident these walls. For this reason in this work tapered walls lined completely by absorber materials and other five walls lined partially by these. This work optimized the position of absorber in the no tapered walls to produce a best performance.

To enable the work to be carried out within the time available, the problem space was reduced by dividing the surface area of the enclosure into 25-m squares, each one of which was either fully tiled or not tiled. The position of each square was then assigned to a point on the binary string with the 1/0 s indicating tiles/no tiles. The numbers of cells for this case (8 m × 8 m × 8 m no tapered surfaces of the anechoic chamber) are 1313 and equal by the size of string. This significantly reduced the number of possible permutations available and also simplified the problem when the tiles were installed in the enclosure.

Since the final aim of the work was to optimize the tile configuration with an automated computer program, a single figure of merit was required to represent the quality of each tile configuration.

The figure of merit chosen for this work was generated from the difference between the reflectivity level (RL) in the completely lined absorber anechoic chamber (RLCAC) and the RL in the partially

lined absorber anechoic chamber (RLPAC). The reflectivity level, RL, of an anechoic chamber is defined as

$$RL = \sum E_{Ri}/E_{Fs} \tag{3}$$

where E_{Ri} is the reflected field, at a receiving point R, due to the ith Reflected ray and E_{Fs} is the free space field at the point, R. the figure of merit is obtained by Equation (4).

$$\text{Cost} = \sum_{\text{frequency}} \sum_{\text{testpoints}} (\text{RLCAC} - \text{RLPAC})^2 \tag{4}$$

To keep the time taken for each model to a minimum, the grid size used was 50 cm. The waves from a transmitting antenna were modeled as 407 rays ray tubes shooting from the location of antenna.

4. RESULTS

The anechoic chamber dimensions used were 8 m × 8 m × 24 m. The position of excitation antenna was (4 m 4 m 2 m). The test points selected for optimization process is shown in Fig. 3. These points are numbered from 1 to 15 in result figures.

The first run was for a Hertzian dipole antenna at 100 MHz frequency. The optimization process was begun with 500 generations to reduce the cost factor. The final layout for tiles was obtained after nearly 30 iterations for optimization process. This layout is shown in Fig. 4.

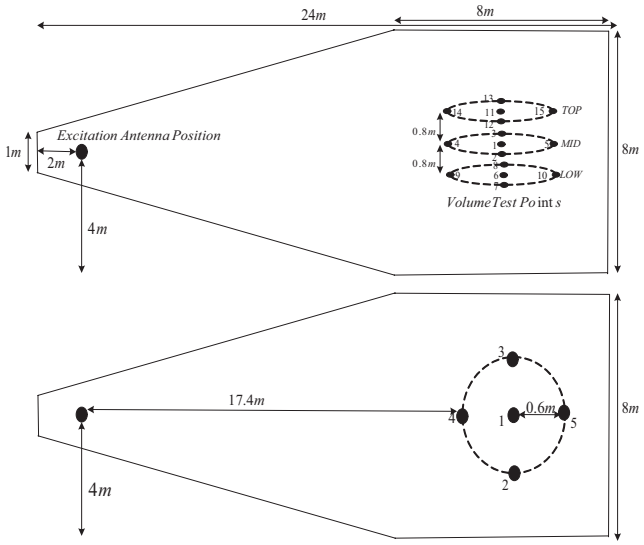

Figure 3: Positions of excitation antenna and 15 test point's volume.

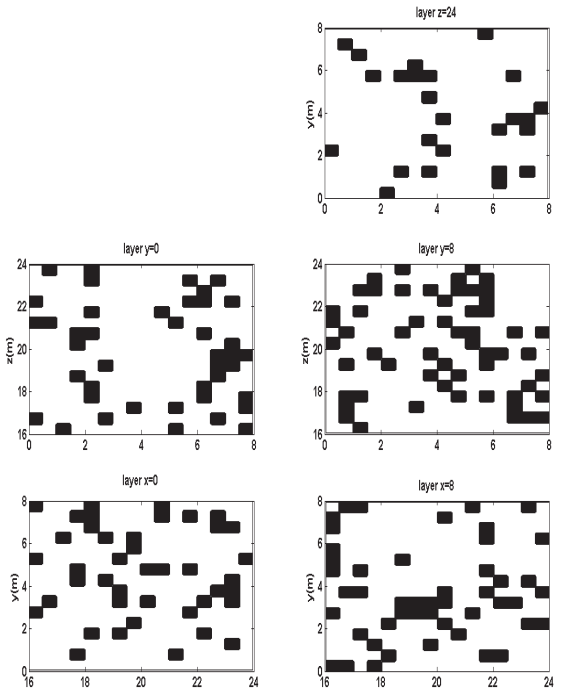

Figure 4: Optimized layout for Hertzian dipole excitation at 100 MHz (black = no tiles, white = tiles).

To validate this method, the predicted and simulated (with CST MICROWAVE STUDIO) results for a rectangular anechoic chamber were compared in [8].

In the test mode (for next results) the waves from a transmitting antenna were modeled as 12684 rays ($\Delta\theta = 0.0314R$, $\Delta\varphi = 0.0314R/\sin(\theta)$) ray tubes shooting from the location of antenna.

The Figures 5 and 6 show the reflectivity level of the fully and partially lined absorber enclosure. The maximum of reflectivity level of fully lined absorber enclosure and partially lined absorber enclosure are −11.5 dB and −10.5 dB respectively. Due to good optimization, the 20% reduction of the coverage of lining ferrite tile, led to an acceptable 1 dB increase of reflectivity level of tapered anechoic chamber

The final layout was optimized at the 100 MHz; however it is applicable for other frequency range of ferrite tile without any change. This is due to this fact that the ray tracing algorithm is

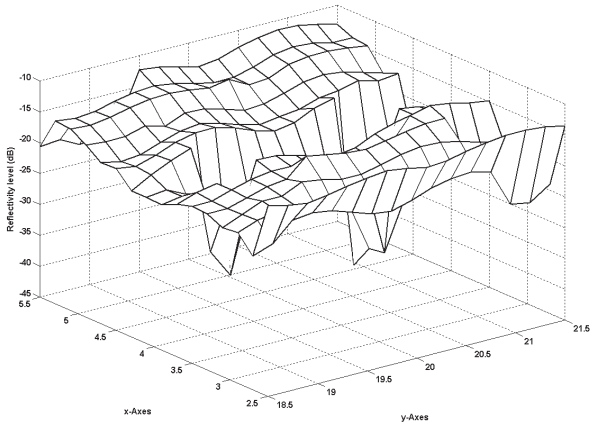

Figure 5: Reflectivity level of fully lined absorber enclosure at 100 MHz.

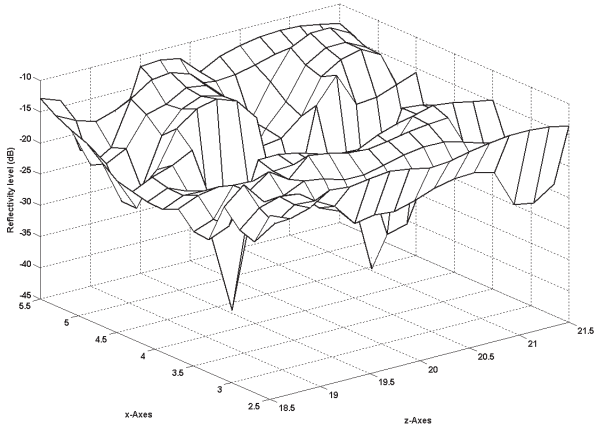

Figure 6: Reflectivity level of partially lined absorber enclosure at 100 MHz.

affiliated to space. The frequency range of reflectivity level of anechoic chamber is dependent on frequency of excitation antenna and frequency range of ferrite tile.

The obtained layout of ferrite tiles (Fig. 4) is not offered for very long frequency range because the ray tube in the ray tracing algorithm must be narrow and frequency range of ferrite tile is limited. The Figures 7 and 8 show the good result agreement between fully and partially lined absorber enclosure in the frequency range of 100–400 MHz at test point 1 and 6. The reflectivity level of tapered anechoic chamber at higher frequencies can be decreased by lining loaded carbon foam in free space between ferrite tile.

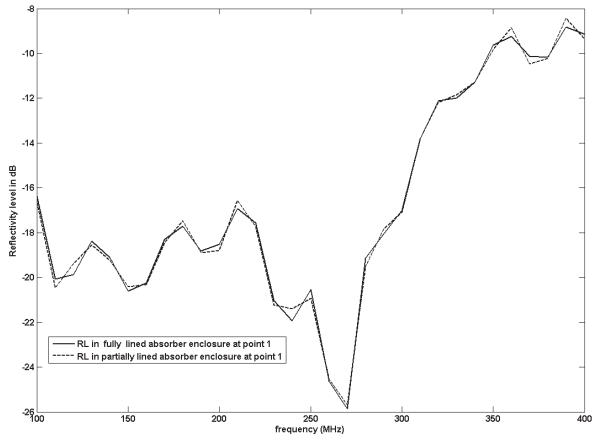

Figure 7: Compared reflectivity level of enclosure in the test point 1 at the wide frequency range.

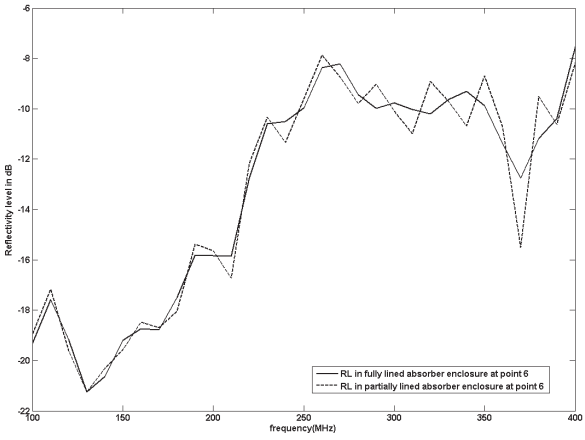

Figure 8: Compared reflectivity level of enclosure in the test point 6 at the wide frequency range.

5. CONCLUSIONS

This paper described a new method for optimization tapered anechoic chambers. It is based on reduction of the coverage of lining ferrite tile in the five no tapered walls of anechoic chamber to reduce the cost of an anechoic chamber and optimization of layout of absorbing material to produce a best performance. Due to good optimization, the 20% reduction of the coverage of lining ferrite tile, led to an acceptable 1 dB increase of reflectivity level of anechoic chamber. The final obtained layout has a good performance in the frequency range 100–400 MHz.

REFERENCES

1. Kineros, C. and V. Ungvichian, "A low cost conversion of semi-anechoic chamber to fully anechoic chamber for rf antenna measurements," *Electromagnetic Compatibility, 2003 IEEE International Symposium*, Vol. 2, 724–729, Aug. 2003.

2. Bornkessel, C. and W. Wiesbeck, "Numerical analysis and optimization of anechoic chambers for EMC testing," *IEEE Trans. Electromagn. Compat.*, Vol. 38, No. 3, 499–506, Aug. 1996.
3. Kim, H. and H. Ling, "Electromagnetic scattering from an inhomogeneous object by ray tracing," *IEEE Trans. Antennas Propagat.*, Vol. 40, 517–525, May 1992.
4. Chung, B.-K., C. H. Teh, and H.-T. Chuah, "Modeling of anechoic chamber using a beam-tracing technique," *Progress In Electromagnetics Research*, PIER 49, 23–38, 2004.
5. Balanis, C. A., *Advanced Engineering Electromagnetics*, Wiley, New York, 1989.
6. Johnson, J. M. and Y. Rahmat-Samii, "Genetic algorithms in engineering electromagnetic," *IEEE Antennas Propagat. Mag.*, Vol. 39, 7–21, Aug. 1997.
7. Meng, Z., "Autonomous genetic algorithm for functional optimization," *Progress In Electromagnetic Research*, PIER 72, 253–268, 2007.
8. Razavi, S. M. J. and M. Khalaj-Amirhosseini, "Optimization an anechoic chamber with ray-tracing and genetic algorithms," *Progress In Electromagnetics Research B*, Vol. 9, 53–68, 2008.

An Improved Method of Determining Permittivity and Permeability by S Parameters

Hao Zhou, **Guizhen Lu**, **Yanfei Li**, **Song Wang**, **and Yue Wang**
Communication University of China, Beijing 100024, China

Abstract— In the paper, a new method is presented for determining the complex permittivity and permeability of the linear materials by scattering coefficients. The coaxial line fixture is used to facilitate the measurement of the material's S Parameters. With the S Parameters, the complex permittivity and permeability of the linear materials as a function of frequency can be determined by the method. The phase ambiguity of the imaginary part of propagator can be resolved by the real part of S_{21}. Compared with former methods, the period of propagator can be got from a series of reflection and transmission S Parameters in the frequency domain, the results of the improved method can be more accurate in the wideband.

1. INTRODUCTION

The measurement of complex permeability and permittivity is required for a multitude of scientific and industrial applications. Due to its relative convenience and simplicity, the transmission/reflection (TR) method is widely used in broad-band measurement technique. The relevant literature in this area is copious. By placing a sample in a section of a coaxial line, the two-port complex scattering parameters can be measured with the TR method. A. M. Nicolson [1] introduced TR method in frequency domain. A. M. Nicolson and G. F. Ross [2] introduced TR method in time domain. William B. Weir [3] found the imaginary part of propagation coefficient of a complex quantity is equal to the angle of the complex value plus $2\pi n$, where n is equal to the integer of length of the sample divided by the transmission line guide wavelength. The phase ambiguity is resolved by finding a solution for permittivity and permeability from which a value of group delay is computed that corresponds to the value determined from measured data at two or more frequencies.

Jing Huixin [4] used a "phase jump" method to determine n, so the phase ambiguity can be resolved. Yang Guang [5] gave a new method to get the reflection coefficient more exactly when the reflection scattering coefficient (S_{11}) is too small. Abdel-Hakim Boughriet [6] used improved equations to make the complex permeability and permittivity have a great agreement with the sample.

S. S. Stuchly and M. Matuszewski [7] presented a slightly different derivation from Nicolson and Ross, their method is unstable for low-loss materials at multiples of one half integer wavelengths. L. L. Ligthardt [8] presented a method for shorted line measurements where the scattering equations for the permittivity were solved over a calculated uncertainty region and the results were then averaged. The equations are useful for high-loss materials, but for low-loss materials they have the same problem the method is unstable at multiples of one half integer wavelengths. There are many methods to improve the T/R method in the non-magnetic material, such as the method provided by Yang Buning, Yang Deshun [9] et al. James Baker-Jarvis [10] can solved the problem that the equations are unstable at multiples of one half integer wavelengths, but the equations are overdetermined. David A. Hill [11] had given analytical and numerical results for rectangular waveguides and coaxial transmission lines.

The goal of this paper is threefold: first, review A. M. Nicolson and G. F. Ross's method. Second, compared to these methods, the improved method is presented. The phase ambiguity is resolved by finding the frequency regions of the real part of S_{21}. Third, to present the results and the analysis of the procedure.

2. T/R THEORY

In the A. M. Nicolson's method, using coaxial line fixture, scattering coefficients can be got from the signal flow graph:

$$S_{21}(\omega) = \frac{V_B}{V_{inc}} = \frac{(1+\Gamma)(1-\Gamma)P}{1-\Gamma^2P^2} = \frac{(1-\Gamma^2)P}{1-\Gamma^2P^2} \tag{1}$$

$$S_{11}(\omega) = \frac{V_A}{V_{inc}} = \frac{(1-P^2)\Gamma}{1-\Gamma^2P^2} \tag{2}$$

The thickness of the sample is d, characteristic impedance $Z = \sqrt{\mu_R/\varepsilon_R}Z_0$, the reflection coefficient:

$$\Gamma = \frac{Z - Z_0}{Z + Z_0} = \frac{\sqrt{\mu_R/\varepsilon_R} - 1}{\sqrt{\mu_R/\varepsilon_R} + 1} \tag{3}$$

The propagation coefficient:

$$\begin{aligned} P &= \exp\left(-j\omega\sqrt{\mu\varepsilon}\cdot d\right) = \exp\left[-j\left(\omega/c\right)\sqrt{\mu_R\varepsilon_R}d\right] \\ V_1 &= S_{11} + S_{21}; \quad V_2 = S_{21} - S_{11}, \end{aligned} \tag{4}$$

if $X = \frac{1-V_1V_2}{V_1-V_2}$, then the reflection coefficient:

$$\Gamma = X \pm \sqrt{X^2 - 1} \tag{5}$$

The appropriate sign is chosen so that $|\Gamma| \leq 1$.
The propagation coefficient

$$P = \frac{V_1 - \Gamma}{1 - V_1\Gamma} \tag{6}$$

Define

$$\frac{\mu_R}{\varepsilon_R} = \left(\frac{1+\Gamma}{1-\Gamma}\right)^2 = c_1 \tag{7}$$

$$\mu_R\varepsilon_R = -\left[\frac{c}{\omega d}\ln\left(\frac{1}{P}\right)\right]^2 = c_2 \tag{8}$$

But, there are some problems:
Firstlywith Ruler formula, the Equation (4) can be showed as:

$$P = \cos[(w/c) * d * \sqrt{c2}] + j\sin[(w/c) * d * \sqrt{c2}] \tag{9}$$

If $P1$ is the real part of P, then:

$$\cos[(w/c) * d * \sqrt{c2}] = P1, \quad \text{also} \quad c_2 = \left[\frac{c}{\omega d}\left(\arccos P1\right)\right]^2$$

The problem is:
Since $\cos[(w/c) * d * \sqrt{c2} + 2\pi m] = P1$, m is an integer, then:

$$c_2 = \left[\frac{c}{\omega d}\left(\arccos P1 + 2\pi m\right)\right]^2 \tag{10}$$

So, different m will lead to different results of c_2. As a result, μ_R and ε_R are different.

Secondly, if the scattering coefficients are determined by μ_R and ε_R, when the method is used in the left hand materials, the scattering coefficients determined by μ_R and ε_R may be wrong. If μ_{R1} is a positive number, ε_{R1} is a positive number; then $\mu_{R1}/\varepsilon_{R1} = c_1$, $\mu_{R1}\varepsilon_{R1} = c_2$; if $\mu_{R2} = -\mu_{R1}$, $\varepsilon_{R2} = -\varepsilon_{R1}$, then $\mu_{R2}/\varepsilon_{R2} = c_1$, $\mu_{R2}\varepsilon_{R2} = c_2$, so we can find the results even if $\mu_{R2} = -\mu_{R1}$, $\varepsilon_{R2} = -\varepsilon_{R1}$, c_1 and c_2 will be the same, so the scattering coefficients will also be the same.

In fact, if $\mu_{R2} = -\mu_{R1}$, $\varepsilon_{R2} = -\varepsilon_{R1}$, the scattering coefficients will be different. So the method can not be used in the left hand material.

3. THE IMPROVED METHOD

Firstly, to find S_{21} and S_{11}'s period, with A. M. Nicolson's method, c_1 and c_2 can be found:

$$c_2 = \mu_R\varepsilon_R, \quad c_1 = \mu_R/\varepsilon_R \tag{11}$$

The propagation coefficient

$$P = \exp\left[-j\left(\frac{\omega}{c}\right)d\sqrt{c_2}\right] = \cos\left[\left(\frac{\omega}{c}\right)d\sqrt{c_2}\right] - j\sin\left[\left(\frac{\omega}{c}\right)d\sqrt{c_2}\right] \tag{12}$$

Then the period is $t = \frac{d}{c}\sqrt{c_2}$,

$$P = \cos\theta - j\sin\theta \tag{13}$$

where $\theta = \omega \cdot t$, ω is the phase velocity, the reflection coefficient:

$$\Gamma = \left(\sqrt{c_1} - 1\right) / \left(\sqrt{c_1} + 1\right) \tag{14}$$

The reflection coefficient is a constant, if the permittivity and permeability of the sample are fixed.

$$S_{21} = \frac{\left(1-\Gamma^2\right)P}{1-\Gamma^2 P^2} = \frac{1-\Gamma^2}{2\Gamma}\left(\frac{1}{1-\Gamma P} - \frac{1}{1+\Gamma P}\right) \tag{15}$$

The real part of S_{21}:

$$real\left(S_{21}\right) = \frac{1-\Gamma\cos\theta}{1-2\Gamma\cos\theta+\Gamma^2} - \frac{1+\Gamma\cos\theta}{1+2\Gamma\cos\theta+\Gamma^2} \tag{16}$$

The imaginary part of S_{21}

$$imag\left(S_{21}\right) = \frac{-j\Gamma\sin\theta}{1-2\Gamma\cos\theta+\Gamma^2} - \frac{j\Gamma\sin\theta}{1+2\Gamma\cos\theta+\Gamma^2} \tag{17}$$

Both of the real and imaginary parts of S_{21} have the same period of t.

Just as what Jing Huixin [4] said, $1/P$ can be determinedbut there is phase ambiguity in $\ln(1/P)$, the difference of the imaginary part of $\ln(1/P)$ is $2n\pi$. When computed, the results must be controlled in the ranges between $-\pi$ and $+\pi$; using computer simulation, if the imaginary part of $\ln(1/P)$ exceeds $\pm\pi$, the results will return to the ranges between $-\pi$ and $+\pi$. So there is the so-called phase ambiguity. And the imaginary part of $\ln(1/P)$ is $2\pi(df\sqrt{c_2}/c)$, it should be showed

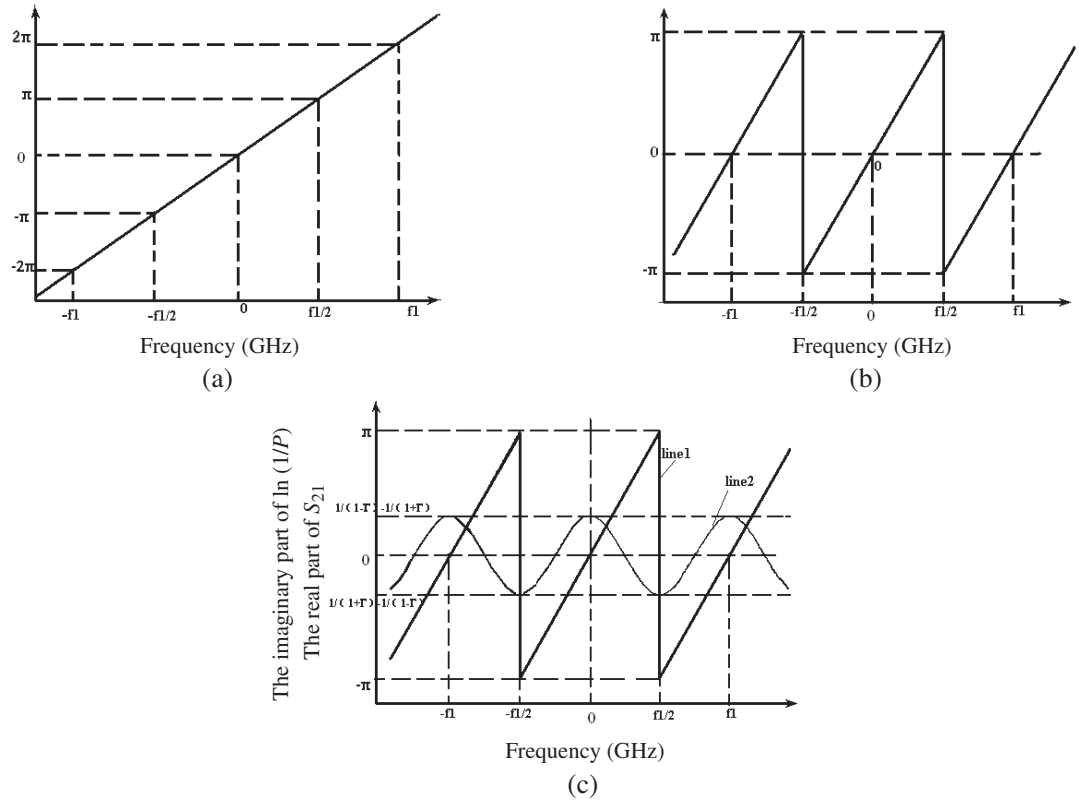

Figure 1: (a) The imaginary part of $\ln(1/P)$ as a function of frequency. (b) The imaginary part of $\ln(1/P)$ as a function of frequency using computer simulation. The real part of S_{21} and the imaginary part of $\ln(1/P)$ as a function of frequency using computer simulation. Line 1 is the imaginary part of $\ln(1/P)$, Line 2 is the real part of S_{21}.

as Figure 1(a), but it shows the imaginary part of $\ln(1/P)$ is periodic as Figure 1(b), the period is f_1: (where $f_1 = 1/t = c/d\sqrt{c_2}$).

It can be proved that the real part of S_{21} has its minimal record in the frequency of $(2n-1) \times f_1/2$, its maximal record in the frequency of $2n \times f_1/2$. The results are showed as Figure 1(c).

So the period of the imaginary part of $\ln(1/P)$ is f_1. If the frequency in the range between $-f_1/2$ and $f_1/2$, then m in the Equation (10) is 0; If the frequency in the range between $f_1/2$ and $3f_1/2$, then m in the Equation (10) is 1 . . .

It can be also defined like this: From beginning to the first minimal real part of S_{21}, the m in the Equation (10) is 0; From the first minimal real part of S_{21} to the second minimal real part of S_{21}, the m in the Equation (10) is 1 . . .

In addition, if the expression of the relative permittivity and permeability like these:

$$\varepsilon_R = n \times Z \tag{18}$$

$$\mu_R = n/Z \tag{19}$$

where Z which presented by Yang Guang et al. [4] is the characteristic impedance

$$n = \phi/(k_0 d) \tag{20}$$

where $k_0 = 2\pi f/c$, f stands for frequency, c stands for the velocity of light.

$$\phi = -i \cdot \log(p) + 2 \cdot \pi \cdot m \tag{21}$$

Then the method can be used in the left hand material too.

4. RESULTS

Conclusion paragraph should be here. . .

The results made by mathematics software are presented as below:

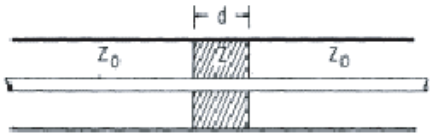

Figure 2: The sample in the coaxial line.

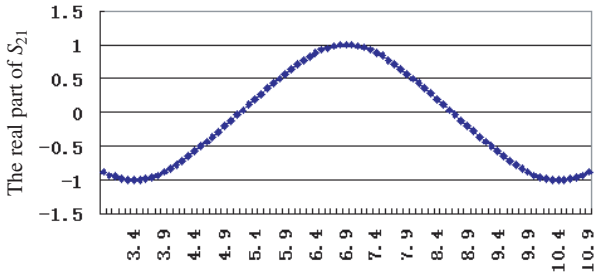

Figure 3: The real part of S_{21} as a function of frequency.

If the sample has relative permittivity and permeability, then the real part of S_{21} is measured as Figure 3.

$$(\varepsilon_R = 2.04 - j0.0005, \mu_R = 1, d = 3\,\text{cm})$$

The first minimal real part of S_{21} at the frequency of 3.5 GHz. So $f_1/2$ is equal to 3.5 GHz. f_1 is equal to 7 GHz. Assuming the relative permittivity and permeability of the sample are known, f_1 can be written as

$$f_1 = 1/t = \frac{c}{d\sqrt{c_2}} \approx 7\,\text{GHz} \tag{22}$$

It can be seen that f_1 determined by the minimal real part of S_{21} as a function of frequency is equal to Equation (22).

In the frequency range from 3 GHz to 11 GHz,the frequency between 3 GHz and 3.5 GHz is in the range between 0 and $f_1/2$, the m in the Equation (10) is 0, the frequency between 3.6 GHz and 10.5 GHz is in the range between $f_1/2$ and $3f_1/2$, the m in the Equation (10) is 1, the frequency between 10.6 GHz and 11 GHz is in the range between $3f_1/2$ and $5f_1/2$, the m in the Equation (10) is 2 . . .

Figure 4 to Figure 7 present the real and imaginary part of the relative permittivity and permeability as a function of frequency.

In conclusion, the relative permittivity and permeability determined by S_{21} (transmission scattering coefficient) have a great agreement with the sample, as they are presented by the Figure 4 to Figure 7.

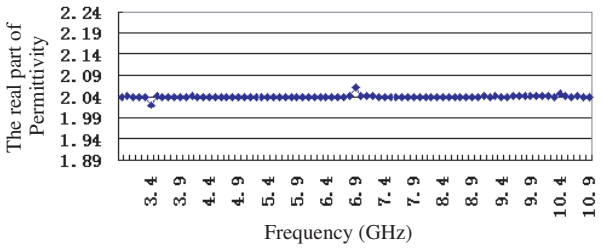

Figure 4: The real part of permittivity as a function of frequency.

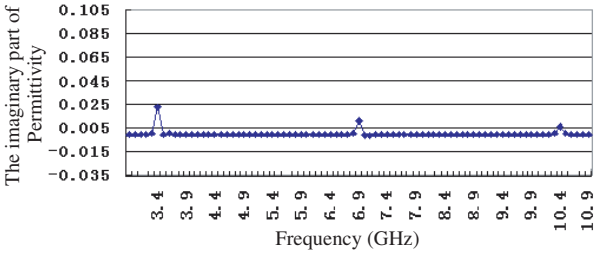

Figure 5: The imaginary part of permittivity as a function of frequency.

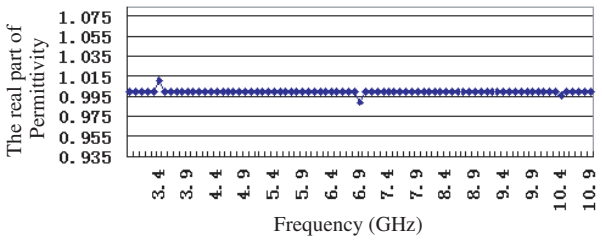

Figure 6: The real part of permeability as a function of frequency.

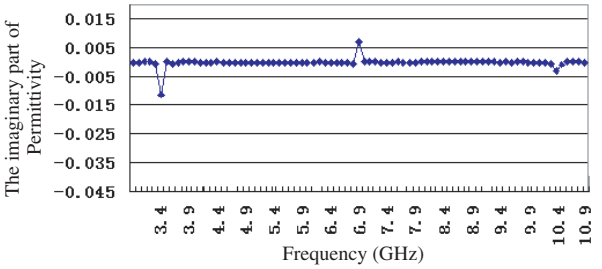

Figure 7: The imaginary part of permeability as a function of frequency.

5. CONCLUSION

The method provided by Tian Buning, Yang Deshun, et al. [12] and Yang Guang, Jiang Shan et al. [5] has improved stabilization for low-loss materials in multiples of one half integer period. Because S_{11} is too small in that regions, if $S_{11} \approx 0$, the reflection coefficient will be too small. It leads to the unstable problem.

Furthermore, the improved method has a significant advantage in industrial applications. Since the real part of S_{21} can be gotten from automatic network analyzer (ANA), the minimal and the period of S_{21}'s real parts can be easily seen from the results. Compared with the "phase jump" method provided by Jing Huixin and Jiang Quanxing [4], there is no need to draw the imaginary part of $\ln(1/P)$ as a function of frequency.

In conclusion, the improved method can be used in both right and left materials; it also can be widely used in the broad-band technique with a good stability in multiples of one half integer period. We can also use Ganquan Xie's [13] new global and local electromagnetic field (GL) modeling to rebuild the coaxial line model. Compared with other Finite Element Method (FEM), Ganquan Xie's [14] method has an outstanding superiority in resolving only small matrices rather than huge matrices of FEM. Given that the sample is difficult to made, and large FEM matrices are difficult to resolve, GL method is useful in inversion.

ACKNOWLEDGMENT

Thanks for Prof. Xie Ganquan. He gives me many useful suggestions in inversion.

REFERENCES

1. Nicolson, A. M., "Broad-band microwave transmission characteristics from a single measurement of the transient response," *IEEE Transactions on Instrumentation and Measurement*, Vol. 17, 395–402, Dec. 1968.
2. Nicolson, A. M. and G. F. Ross, "Measurement of the intrinsic properties of materials by time-domain techniques," *IEEE Transactions on Instrumentation and Measurement*, Vol. 19, No. 4. Nov. 1970.
3. Weir, W. B., "Automatic measurement of complex dielectric constant and permeability at microwave frequencies," *Proceedings of IEEE*, Vol. 62, No. 1, 33–36, Jan. 1974.
4. Jing, H. and Q. Jiang, "Transmission/Reflection method based on coaxialline for RF materials characterization measurement [J]," *Journal of Astronautics*, Vol. 26, No. 5, 2005.
5. Yang, G., S. Jiang, and G. Wang, "Modified algorithm on electromagnetic parameters test [J]," *Theory and Method*, Vol. 26, No. 8, 2007.

6. Boughriet, A.-H., "Noniterative stable transmission/reflection method for low-loss material complex permittivity determination," *IEEE Trans. Microwave Theory Tech.*, Vol. 45, No. 1, 343–349, Jan. 1997.
7. Stuchly, S. S. and M. Matuszewski, "A combined total reflection transmission method in application to dielectric spectroscopy," *IEEE Transactions on Instrumentation and Measurement*, Vol. 27, 285–288, Sept. 1978.
8. Ligthardt, L. L., "A fast computational technique for accurate permittivity determination using transmission line methods," *IEEE Trans. Microwave Theory Tech.*, Vol. 31, 249–254, Mar. 1983.
9. Tian, B., D. Yang, Q. Liu, et al. "Some problems of the transmission/reflection method for measuring complex permittivity of materials [J]," *Chinese Journal of Radio Science*, Vol. 17, No. 1, 10–15, 2002.
10. Baker-Jarvis, J., "Improved technique for determining complex permittivity with the transmission/reflection method," *IEEE Trans. Microwave Theory Tech.*, 1096–1103, Aug. 1990.
11. Hill, D. A., "Reflection coefficient of a waveguide with slightly uneven walls," *IEEE Trans. Microwave Theory Tech.*, Vol. 37, No. 1, Jan. 1989.
12. Tian, B., D. Yang, J. Tang, et al., "Analysis of transmission/reflection method for measuring electromagnetic parameters of materials [J]," *Chinese Journal of Radio Science*, Vol. 16, No. 1, 57–60, 2001.
13. Xie, G., J. Li, and F. Xie, "New global and local electromagnetic field (GL) modeling and inversion," *Progress In Electromagnetics Research Symposium*, Hangzhou, China, August 22–26, 2005.
14. Xie, G., F. Xie, L. Xie, and J. Li, "GL method and its advantages for resolving historical difficulties," *Progress In Electromagnetics Research*, PIER 63, 141–152, 2006.

Features and Mechanism of Satellite Infrared Anomaly before Ocean Earthquakes

Shanjun Liu[1,3], **Lixin Wu**[1,2], **Qunlong Chen**[3], **and Guoliang Li**[3]

[1]Institute for GIS/RS/GPS & Digital Mine Research, Northeastern University
Shenyang 110004, China
[2]Institute for GIS/RS/GPS & Subsidence Engineering Research,
China University of Mining and Technology, Beijing 100083, China
[3]College of Resources and Environment, Hebei Polytechnic University
Tangshan 063000, China

Abstract— The phenomenon of satellite thermal Infrared (TIR) anomaly before ocean earthquake has been reported since the early 1990s. The evolution pattern and the mechanism of TIR anomaly before ocean earthquake are of great importance. In this paper, taking Dec. 26, 2006 Hengchun Ms 7.2 earthquake in Taiwan and March 25, 2007 Noto Peninsula Ms 6.9 earthquake in Japan as the cases of ocean earthquakes, the features of satellite TIR anomaly before the ocean earthquakes are analyzed. To study the mechanisms of this phenomenon, a group of physical simulation experiments including the IR radiation detection experiment of rock fracturing and sliding process, and the heat conduction experiment of water are carried out. The mechanism of satellite Infrared anomaly before the earthquake in ocean region is discussed based on the experimental results.

1. INTRODUCTION

There are more than five million earthquakes occurring every years, and most of them occur in the ocean region. The satellite TIR anomaly phenomena before ocean earthquake has been reported for many times. Qiang [3], Kong [1], Xu [5], Lu [2] and Yurur [6] reported that there were large area of TIR anomalies in satellite remote sensing images before many ocean earthquakes. Usually, the anomaly appeared one month to several days before the earthquake, and the anomaly temperatures increment reached 2–4°C.

Taiwan and Japan region are located in the jointed position of Eurasia plate and Pacific Ocean plate. There are many earthquakes occurred every year due to the action of plate movements. For example, the Jiji Ms 7.6 earthquake in Taiwan, which happened in Sep 21, 1999, caused about 3000 people death and about 10000 people injured. The feature and the mechanism of TIR anomaly before ocean earthquake are of great importance

This paper takes Dec. 26/2006 Hengchun Ms 7.2 earthquake in Taiwan and March 25/2007 Noto Peninsula Ms 6.9 earthquake in Japan as examples of ocean earthquakes to analyze the spatial-temporal features of satellite TIR anomaly images. Then a group of simulation experiments are carried out to study the mechanisms of the infrared anomaly before the ocean earthquakes. Some views are also put forward to explain the TIR anomaly phenomenon before quake.

2. TWO OCEAN EARTHQUAKES WITH POSITIVE SATELLITE THERMAL IR ANOMALY

2.1. Hengchun Ms 7.2 Earthquake in Taiwan

A Ms 7.2 earthquake occurred in Hengchun of Taiwan at 12:26/Dec. 26, 2006 (UTC, same as the following), and the epicenter was at the position (21.9°N, 120.6°E). The earthquake caused 2 people death and about 50 people injured. The FY-2C satellite TIR images (10.3–11.3μm) showed positive thermal anomaly appearing before the earthquake. Fig. 1 showed that there was an isolated high temperature area on the east of Philippines 7 days before the earthquake. In the image at 16:00/Dec. 19 the anomaly area was restricted in the region (0–25°N, 125–145°E), and the west edge of the anomaly was about in Philippines, meanwhile the center of anomaly was about at the position (10°N, 135°E). After that the anomaly and its center moved gradually toward west. At 16:00/Dec. 21 the west end of the anomaly moved to Palawan island and its center moved to (10°N, 127°E). At 16:00 of Dec. 24 the center of anomaly had moved to Palawan island. The moving direction of the anomaly in the whole process was from east to west, which is consistent with the Pacific Plate' moving direction.

After Dec. 24, the anomaly changed the moving direction and moved toward the Taiwan island along manila ocean trench. The Fig. 1 shows following features: (1) 40 to half hours before the quake the bright temperature of anomaly increased continually. At 4:00/Dec. 25 the bright temperature of the epicenter was up to 24°C, which was about 5°C higher than that at same time of the previous day; (2) 40 to half hours before quake the anomaly area enlarged continually. At 20:00/Dec. 24 the anomaly was mainly seated in about Palawan island, and the area of anomaly was about 250000 km^2. However half hour before shocking the area of anomaly increased to about 1000000 km^2; (3) With the approaching of the earthquake, the anomaly moved gradually toward the epicenter. Before 4:00/Dec. 25 there was not thermal anomaly around epicenter. But the image at 4:00/Dec. 25 showed that there was a larger-scope anomaly appearing on surrounding of the epicenter. The area of anomaly was about 6000 km^2 and the temperature was 3°C higher than the surrounding area; (4) The anomaly distributed along the northeastern faults of South China Sea (see the image 16:00/Dec. 25), and the moving route of anomaly was coincident with the Manila trench, which indicated that the distribution and evolution of the anomaly were controlled by the geological structure of South China Sea.

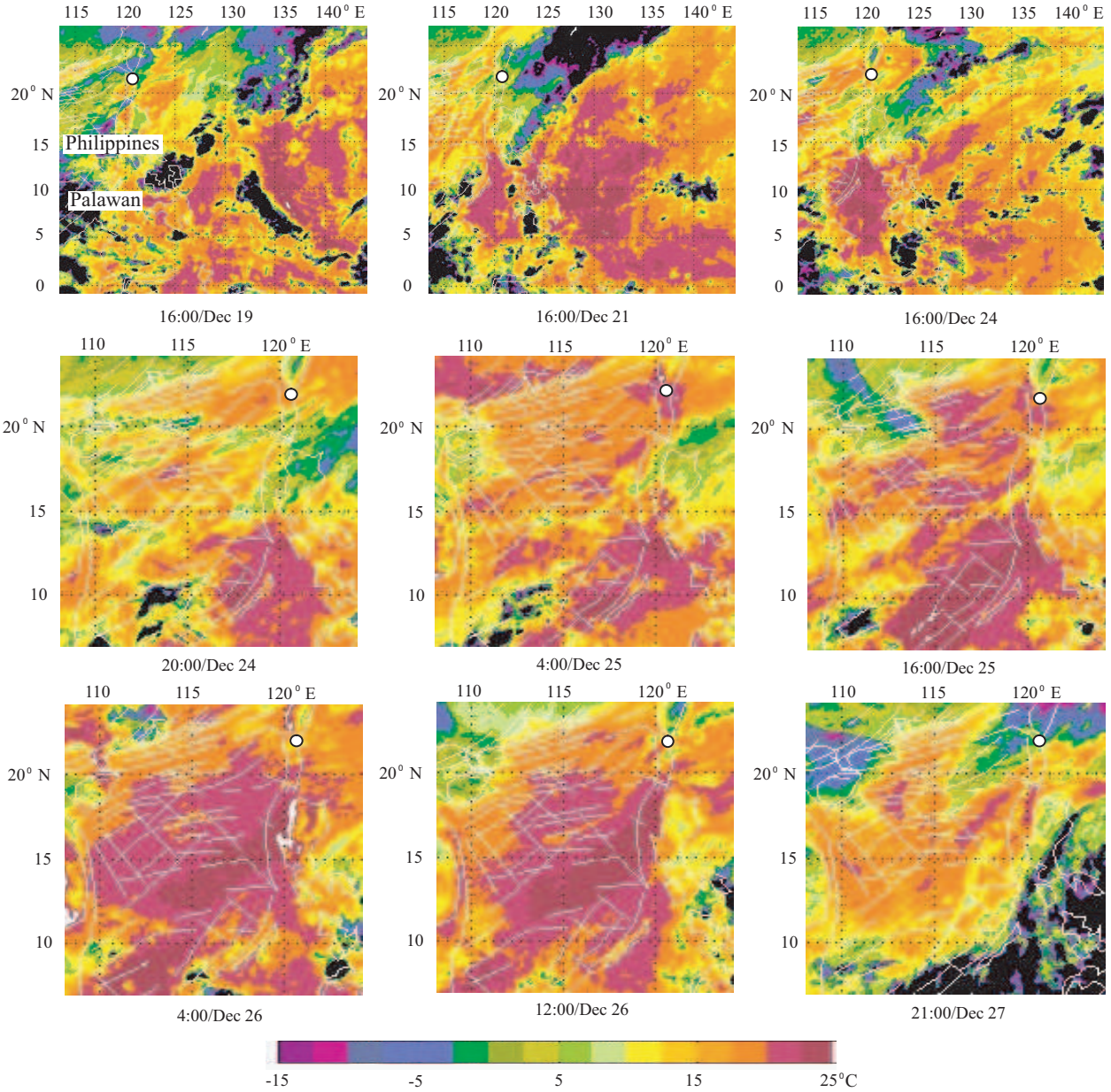

Figure 1: Evolution features of satellite TIR images before earthquake (the white circle represent the epicenter, and the white line represent faults).

2.2. Noto Ms 6.9 Earthquake in Japan

A powerful Ms 6.9 earthquake struck Noto of Japan at 0:42/March 25, 2007. The epicenter of the quake was at the position (37.3°N, 136.9°E). The FY-2C satellite TIR images appeared positive TIR anomaly before the quake. Fig. 2 showed that there was an isolated high temperature area on the west of the epicenter 7 days before the earthquake. From the Fig. 2, it can be seen that: (1) With approaching to the quake the anomaly area enlarged gradually. The Satellite IR image at 5:00/March 18 showed that a high temperature strip appearing on the southwest of Japan. After that the anomaly area enlarged gradually (see the yellow and green color region). The anomaly area enlarged up to the peak at 5:00/March 23; (2) The bright temperature of anomaly increased gradually with approaching to the quake. The highest bright temperature of the image at 5:00/March 23 was about 3°C higher than that at 5:00/March 18; (3) With the approaching of the quake, the anomaly moved gradually toward the epicenter. The Fig. 2 showed that at 5:00/March 18 the anomaly appeared like a strip, and the northeast end of the strip is far from the epicenter. However, at 5:00/March 23 the anomaly area enlarged obviously, and the northeast end of the anomaly had moved to the epicenter of impending quake.

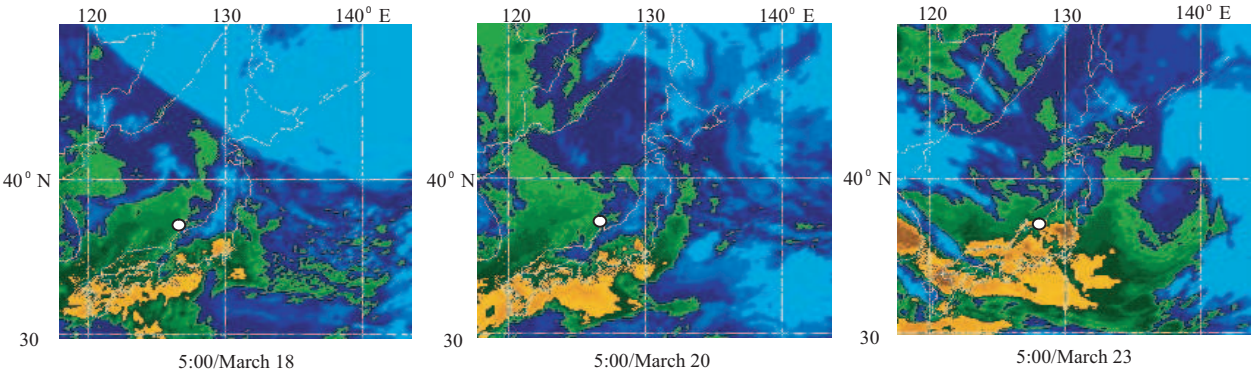

Figure 2: Evolution features of satellite TIR images before Noto earthquake (the white circle represent epicenter).

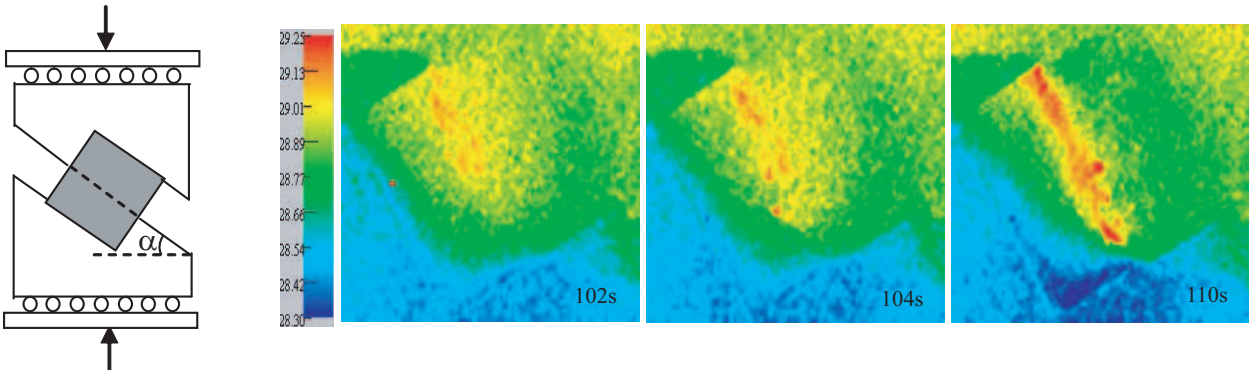

Figure 3: IR precursor of rock fracturing.

The moving route of the anomaly in the whole process was consistent with the conjunct zone of Pacific Plate and Eurasian Plate, which indicated that the IR anomaly was controlled by the geological structure of Plate structure.

3. EXPERIMENTAL RESEARCH ON MECHANISM OF EARTHQUAKE TIR ANOMALY

3.1. Experiments on the IR Radiation Variation of Rock in Fracturing and Friction Process

The earthquake is considered as the result of rock fracture or fraction. In order to study the mechanism of TIR anomaly before earthquake two physical simulated experiments on IR radiation of rock fracturing and friction process was carried out [4]. Fig. 3 and Fig. 4 show the diagrammatic sketches and the results of the experiments. The two simulating experiments exist following features:

(1) High-temperature IR radiation areas appear in the loading process, which distribute along the fault or future fracture and evolve from one end to the another end with the evolution of stress field; (2) With the coming of fracture the high-temperature radiation move gradually to the fracture position. (3) Before the fracturing the IR radiation temperature increases steeply and later decrease, which indicates the befalling of fracture.

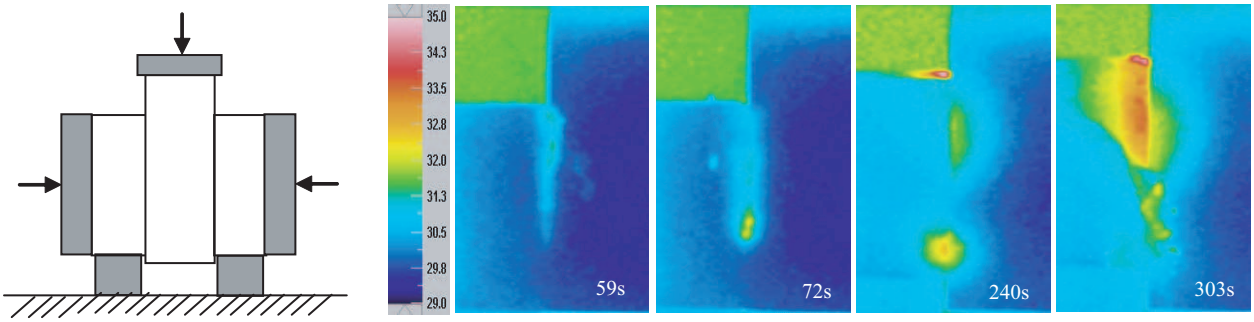

Figure 4: IR precursor of the rock friction.

Above experimental results is very consistent with the satellite IR anomaly phenomena before earthquake.

3.2. Heat Transfer Measurement of Water and Its Numerical Simulation

Above physical simulation experiments show that fracturing and friction of rock can produce heat. The result induces us to guess the thermal IR anomaly before earthquake is the result of stress-heat transfer from the deep crust toward surface of earth. In order to examine the guess a simple heat transfer measurement experiment is designed. In the experiment a basin, whose top caliber is 0.7 m, bottom caliber is 0.4 m and the height is 0.16 m, is applied. Some water is poured in the basin, and a electric heater is used below the basin to heat up the water. To measure the temperature of water in the heating process two thermometer are used to respectively measure the top and bottom temperature of water.

The experimental results showed that there is not variation in the top temperature of water before 100 seconds. But the bottom temperature of water changes immediately as the beginning of heating. During 20 minutes for heating the top temperature of water increases 5°C and the bottom temperature of water increases 11°C. When the heating stops the top temperature of water is still unceasingly increasing, but the bottom temperature of water stops increase immediately. Above experiment process can be numerical simulated by a software FLUENT.

To realize the heat conduction process of water in ocean another larger numerical simulation experiment was carried out. The size of numerical model was designed into 2 km high, 10 km wide and the width of heat resource is 1 km. The temperature of heat resource is assumed as 370 K, and the temperature of surrounding water is assumed as 300 K. The heating time is two days. The model is applied to simulate the fault-friction heat conduction process in water. Fig. 5 shows the numerical simulation results, which can be concluded that the heat conduction from 2 km-deep sea floor to the surface needs 413 days. The temperature rises about 2 K. The result indicates that the stress heat is not possible to transfer to the surface of ocean water in the shorter time. The phenomenon of TIR anomaly before earthquake can not be explained by the stress heat conduction mechanism.

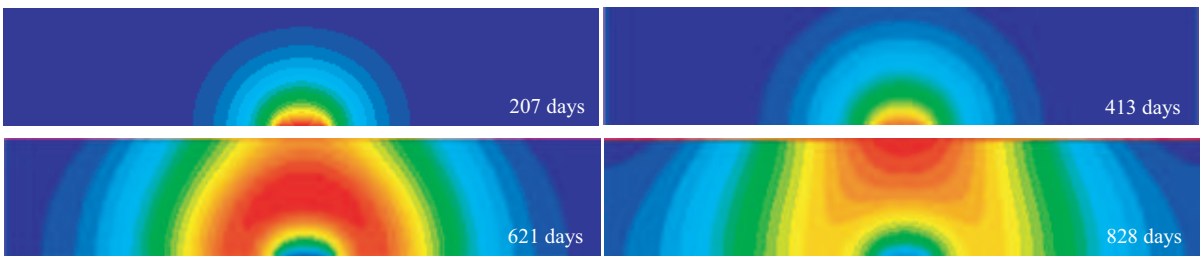

Figure 5: Numerical simulation results of water heat conduction.

4. CONCLUSION

From above earthquake examples and the experiment results, we can find that the space-time feature of TIR anomaly before quake is consistent with the space-time features of TIR anomaly of rock fracturing and sliding in the experiments. Earthquake is the result of crustal stress action, therefore all phenomena related to earthquake are the effects of crustal stress action, including the satellite TIR anomaly before quake. It can be inferred from the IR detection experiment of rock fracture and friction that the TIR anomaly before ocean earthquake originates from the stress-heat of crust rock. But the water conduction experimental result shows heat conduction in water is very slow and the TIR anomaly before ocean earthquake is impossible caused by the heat conduction of water. Whether the heat convection of water or gas play a main role in TIR anomaly needs further experiment to examine.

ACKNOWLEDGMENT

This work is supported by the National Natural Science Foundations of China (No. 50774017) and the National Outstanding Youth Fund (No. 50525414).

REFERENCES

1. Kong, L. and Z. Qiang, "Anomaly of thermal infrared increase temperature before Taiwan strait earthquake of Ms 7.3," *Journal of Seismology*, No. 3, 34–37, 1997.
2. Lu, Z., Z. Qiang, and B. Wu, "A tentative interpretation of the formation of high temperature anomaly in satellite based thermal infrared scanning images (STISI) of the South China Sea before earthquake," *Acta Geoscientia Sinica*, Vol. 23, No. 1, 42–46, 2002.
3. Qiang, Z., C. Dian, L. Li, et al., "Satellite thermal infrared anomaly and earthquake prediction in advance and in short-term," *Proceedings of the 30th International Geological Congress*, 186–194, Beijing, China, 1996.
4. Wu, L. X., S. J. Liu, et al., "Experimental study on infrared abnormity of tectonic earthquake," *Proceedings of the Society of Photo-Optical Instrumentation Engineers (SPIE)*, Vol. 5238, 376–387, 2003.
5. Xu, X., X. Xu, and Y. Wang, "Satellite infrared anomaly before Nantou Ms = 7.6 earthquake in Taiwan, China," *Acta Seismologica Sinica*, Vol. 22, No. 6, 666–669, 2000.
6. Yurur, M. T., "The positive temperature anomaly as detected by Landsat TM data in the eastern Marmara Sea (Turkey): Possible link with the 1999 Umit earthquake," *International Journal of Remote Sensing*, Vol. 27, No. 5–6, 1205–1218, 2006.

Sumudu Applications to Maxwell's Equations

Fethi Bin Muhammad Belgacem
Faculty of Information Technology, Arab Open University
P. O. Box 830, Al-Ardhia 92400, Kuwait

Abstract— A main attribute of the Sumudu transform lies in its units preserving property. Connected to Fourier, bilateral, two-sided, and ordinary Laplace transforms, the Sumudu is beginning to claim more fame through its unique advantages and pragmatic applications. Here, Maxwell's equations, pertaining to transient electromagnetic planar, (TEMP), waves propagation in lossy media, are shown to yield electric field solutions, through Sumudu transformation.

1. A HANDFUL OF INTEGRAL TRANSFORMS

The Laplace transform usage dates back to Euler's 1737 'De Constructione Aequationum'. Its use has been prevalent in solving ordinary differential, difference, and functional equations. Like Euler, a list of contributors to the Laplace transform theory, many of whom have other transforms attached to their names, include but is certainly not limited to Lagrange, Laplace, Fourier, Poisson, Cauchy, Abel, Liouville, Boole, Riemann, Pincherle, Amaldi, Tricomi, Picard, Mellin, Borel, Heaviside, Bateman, Titchmarsh, Bernstein, Doetsch, and Widder [1]. The bilateral Laplace transform is an integral transform closely related to the Fourier transform, the ordinary one-sided, and the two-sided or s-multiplied Laplace transform [5, 12]. For, $f(t)$, a real or complex valued function of the real variable t taking domain over all real numbers, the bilateral Laplace transform is defined by the integral,

$$\mathcal{B}[f(t)](s) = F(s) = \int_{-\infty}^{+\infty} f(t)e^{-st}dt. \tag{1}$$

Albeit less famed than its one sided counterpart, the bilateral transform can be encountered in all areas of scientific applications where the functions used may be defined, but not necessarily, over subsets of both sides of the real axis. For instance, the moment generating function of a continuous probability density function, $p(x)$, is defined, $\mathcal{B}[p(x)](-s)$.

Given any real number, a, and the shifted unit step function, $H_a(t)$, of the Heaviside function, $H(t) = H_0(t)$,

$$H_a(t) = \begin{cases} 1, & \text{for} \quad t \geq a, \\ 0, & \text{for} \quad t < a, \end{cases} \tag{2}$$

the one-sided ordinary Laplace transform, $\mathcal{L}$, may be defined in terms of the bilateral Laplace transform by,

$$\mathcal{L}[f(t)](s) = \int_0^{+\infty} f(t)e^{-st}dt = \mathcal{B}[f(t)H(t)](s), \ \text{Re}s > 0. \tag{3}$$

Clearly, either version of the Laplace transform can be defined in terms of the other, since we also have,

$$\mathcal{B}[f(t)](s) = \mathcal{L}[f(t)](s) + \mathcal{L}[f(-t)](-s). \tag{4}$$

The Fourier transform may also be defined in terms of the bilateral Laplace transform as follows,

$$\mathcal{F}[f(t)](w) = \mathcal{B}[f(t)](s = iw) = F(\omega) = \int_{-\infty}^{+\infty} f(t)e^{-i\omega t}dt. \tag{5}$$

According to this definition, the inverse Fourier transform is then given by,

$$\mathcal{F}^{-1}[F(\omega)](t) = f(t) = \frac{1}{2\pi}\int_{-\infty}^{+\infty} F(\omega)e^{i\omega t}d\omega. \tag{6}$$

Therefore,

$$f(t)e^{-\alpha t} = \frac{1}{2\pi}\int_{-\infty}^{+\infty} F(\alpha + i\omega)e^{i\omega t}d\omega, \tag{7}$$

provided,

$$\lim_{T\to\infty}\int_0^T |e^{-\alpha t}f(t)|dt < \infty. \tag{8}$$

In science, and engineering applications, the argument t often represents time (in seconds), while the function $f(t)$ represents a signal or waveform that varies with time. In these cases, $f(t)$ is called the time domain representation of the signal, while $F(s)$ is called the frequency domain representation. The inverse transformation then represents a synthesis of the signal as the sum of its frequency components taken over all frequencies, whereas the forward transformation represents the analysis of the signal into its frequency components [9].

The two-sided Laplace (different from bilateral) transform used by some authors, is defined by,

$$\mathcal{T}[f(t)](s) = s\mathcal{B}[f(t)] = sF(s) = s\int_{-\infty}^{+\infty} f(t)e^{-st}dt. \tag{9}$$

The two-sided Laplace transform is at times referred to as the s-multiplied Laplace transform as can be traced to Mclachlan 1948 book (see references in [5]). If, s, is real and we take, $u = 1/s$, then the two-sided Laplace transform [12], is what Watagula [13], defined as the Sumudu transform or simply the *Sumudu* as connoted in [2-, 3], given by,

$$\mathcal{S}[f(t)](u) = \mathcal{T}[f(t)](1/u) = \frac{1}{u}\int_{-\infty}^{+\infty} f(t)e^{-t/u}dt, \ \ -\tau_1 \le u \le \tau_2. \tag{10}$$

2. SUMUDU TRANSFORM PROPERTIES

While much more may be needed, extensive research has been carried out to date concerning the properties and applications of the Sumudu transform. It turns out that among other attributes, the Sumudu does preserve, average, scale, sign, and unit properties [2–5]. Provided the function, $f(t)$ satisfies,

$$|f(t)| < \begin{cases} Me^{-t/\tau_1} & \text{for} \quad t \le 0, \\ Me^{t/\tau_2} & \text{for} \quad t \ge 0, \end{cases} \tag{11}$$

after a change of variable, the sumudu of $f(t)$, can be rewritten as (see for instance [4, 5]),

$$\mathcal{S}[f(t)](u) = G(u) = \int_0^{\infty} f(ut)e^{-t}dt, \ \ -\tau_1 \le u \le \tau_2. \tag{12}$$

Hence, if, Γ, denotes the Gamma function, and, $\alpha \ge -1$, $\mathcal{S}[t^\alpha] = \Gamma(1+\alpha)u^\alpha$ [10]. In particular, for any nonegative integer, n, we have, $\mathcal{S}[t^n/n!] = u^n$, $\mathcal{S}[e^{at}] = \frac{1}{1-au}$, for $u \in (-1, 1)$, $\mathcal{S}[H_a(t)] = \mathcal{S}[H(t-a)] = e^{\frac{-a}{u}}$, with, $u \ge a$, and,

$$\mathcal{S}[f(t-a)](u) = \mathcal{S}[H_a(t)f(t)](u) = \mathcal{S}[H(t-a)f(t)](u) = e^{\frac{-a}{u}}\mathcal{S}[f(t)](u). \tag{13}$$

Clearly, for real s, we have a Laplace-Sumudu Duality (LSD [2–5] or Reciprocity Property [9]) in the sense that,

$$\mathcal{S}[f(t)](u) = \frac{\mathcal{B}[f(t)](1/u)}{u}, \text{ and, } \mathcal{B}[f(t)](s) = \frac{\mathcal{S}[f(t)](1/s)}{s}. \tag{14}$$

This relation extends in fact to when, $s = 1/u$, is complex, and to the ordinary one-sided Laplace transform,

$$\mathcal{L}[f(t)](s) = \mathcal{B}[f(t)H(t)](s) = \frac{\mathcal{S}[f(t)H(t)](1/s)}{s} = \frac{\mathcal{S}^+[f(t)](1/s)}{s}, \ \text{Re}s > 0. \tag{15}$$

Using the LSD, it is pragmatic to reproduce an inverse Sumudu, $\mathcal{S}^{-1}$, residue theorem [4].

Theorem 1. Let M(u) denote the Sumudu of the function, f(t), such that,

(i) the function, $sM(s)$, is meromorphic, with singularities having, $\text{Re}(s) < \beta$, and

(ii) there exist a circular region C with radius r, and positive constants, p and q, such that,

$$\mid sM(s) \mid < pr^q, \tag{16}$$

then, modulo null functions, $f(t)$, is uniquely given by,

$$f(t) = \mathcal{S}^{-1}[M(u)] = \frac{1}{2\pi i}\int_{\beta-i\infty}^{\beta+i\infty} e^{ut}\frac{M(1/u)}{u}du = \sum \text{Residues } [e^{ut}M(1/u)/u]. \tag{17}$$

Now, denoting by, $f^{(n)}(t)$, the n'th derivative for the function, $f(t)$, for integers $n \geq 0$, we have [5],

$$\mathcal{S}[f^{(n)}(t)](u) = \frac{G(u)}{u^n} - \frac{f(0)}{u^n} - \cdots - \frac{f^{(n-1)}(0)}{u}. \tag{18}$$

In particular,

$$\mathcal{S}[f'(t)](u) = \frac{\mathcal{S}[f(t)](u)}{u} - \frac{f(0)}{u}, \text{ and, } \mathcal{S}[f''(t)](u) = \frac{\mathcal{S}[f(t)](u)}{u^2} - \frac{f(0)}{u^2} - \frac{f'(0)}{u}. \tag{19}$$

Extensions of the Sumudu differentiation properties to fractional exponents were recently established in [10].

Now, we present various useful Sumudu convolution (and hence integration) results (see [3]).

Theorem 2. Let $M(u)$ and $N(u)$, be the sumudi for the functions, $f(t)$ and $g(t)$, respectively, then,

(i) The Sumudu of the convolution of f, and g,

$$\mathcal{S}[(f*g)(t)](u) = \mathcal{S}\left[\int_0^t f(\tau)g(t-\tau)d\tau\right] = uM(u)N(u). \tag{20}$$

(ii) The Sumudu of the derivative of the convolution of functions, f and g,

$$\mathcal{S}[(f*g)'(t)](u) = M(u)N(u). \tag{21}$$

(iii) The Sumudu of the derivative of the convolution of f with itself,

$$\mathcal{S}[(f*f')(t)](u) = M^2(u). \tag{22}$$

(iv) The Sumudu of the anti-diderivative of the function, $f(t)$,

$$\mathcal{S}\left[\int_0^t f(\tau)d\tau\right](u) = uM(u). \tag{23}$$

Proof: To prove (i), we note that,

$$uM\left(u\right)N\left(u\right) = u\int_0^\infty e^{-v}f\left(uv\right)dv\int_0^\infty e^{-w}g\left(uw\right)dw, \tag{24}$$

which upon making the variable change, $t = v + w$, becomes,

$$uM\left(u\right)N\left(u\right) = \int_0^\infty\int_0^\infty e^{-(v+w)}f(uv)g\left(uw\right)udvdw = \int_0^\infty e^{-t}\int_0^t f\left(uv\right)g(u(t-v))d(uv)dt. \tag{25}$$

Now, if we set, $\tau = uv$, then $d\tau = udv$, with uv in $[0, ut]$, when v is in $[0, t]$. Hence,

$$uM(u)N(u) = \int_0^\infty e^{-t}\int_0^{ut} f(\tau)g(ut-\tau)d\tau dt = \mathcal{S}[(f*g)(t)](u), \tag{26}$$

yielding the sumudu of the convolution of f and g. This is obviously consistent with the commutativity of the convolution, $f * g = g * f$. Since, $(f * g)' = (f' * g) = (f * g')$, and, $(f * g)(0) = 0$, using Equation (18), proves (ii),

$$\mathcal{S}[(f * g)'(t)](u) = [uM(u)N(u) - (f * g)(0)]/u = M(u)N(u). \tag{27}$$

To prove (iii) and (iv), set, $g = f$, and $g(t) \equiv 1$, respectively in Equation (26),

$$\mathcal{S}\left[\int_0^t f(\tau)d\tau\right](u) = \mathcal{S}[(f * 1)(t)](u) = uM(u). \tag{28}$$

For instance, this confirms that since,

$$\mathcal{S}[\sin(t)] = u\mathcal{S}[\cos(t)] = u/(1 + u^2), \tag{29}$$

then,

$$\mathcal{S}[\sin(t) * \cos(t)] = (\mathcal{S}[\sin(t)])^2 = u^2/(1 + u^2)^2. \tag{30}$$

3. SUMUDU BASED MAXWELL'S EQUATIONS TREATMENT

Based on transient excitation functions, the ordinary Laplace transform method has been the traditional tool used for solving Maxwell's equations. Here, we use the Sumudu to solve the problem of transverse electromagnetic planar, (TEMP), waves propagating in the z-direction in an unbounded lossy medium with constant permittivity ϵ, permeability μ, and positive conductivity, σ [6–8]. The development below follows closely the one in [9]. The electric field vector, E, and the magnetic field vector, H, interactions are generally described by Maxwell's equations [11],

$$\begin{cases} (i)\ \nabla \times \mathbf{E} = -\mu \frac{\partial \mathbf{H}}{\partial t}, \\ (ii)\ \nabla \times \mathbf{H} = \epsilon \frac{\partial \mathbf{E}}{\partial t} + \sigma \mathbf{E}. \end{cases} \tag{31}$$

Taking account of the transversality of the TEMP wave and the medium conditions, this equation expands to,

$$\begin{cases} (i)\ \frac{\partial E_x}{\partial z} + \mu \frac{\partial H_y}{\partial t} = 0, \\ (ii)\ \frac{\partial H_y}{\partial z} + \epsilon \frac{\partial E_x}{\partial t} + \sigma E_x = 0. \end{cases} \tag{32}$$

Setting, $F(z,u) = \mathcal{S}[E_x(z,t)]$, and, $G(z,u) = \mathcal{S}[H_y(z,t)]$, and resorting to the Sumudu differentiation property (19) above, the Sumudu transform of the previous system delivers the set of equations,

$$\begin{cases} (i)\ \frac{\partial F(z,u)}{\partial z} + \mu \frac{G(z,u)}{u} - \mu \frac{H(z,0)}{u} = 0, \\ (ii)\ \frac{\partial G(z,u)}{\partial z} + \epsilon \frac{F(z,u)}{u} + \sigma F(z,u) - \epsilon \frac{E(z,0)}{u} = 0. \end{cases} \tag{33}$$

Now taking the partial derivative of (i) with respect to z,

$$\frac{\partial^2 F(z,u)}{\partial z^2} + \frac{\mu}{u}\frac{\partial G(z,u)}{\partial z} - \frac{\mu}{u}\frac{\partial H(z,0)}{\partial z} = 0, \tag{34}$$

helps us eliminate $G(z,u)$ and obtain a differential equation for $F(z,u)$ only,

$$\frac{\partial^2 F(z,u)}{\partial z^2} - (\frac{\mu\epsilon}{u^2} + \frac{\mu\sigma}{u})F(z,u) = \frac{\mu}{u}\left[\frac{\partial H(z,t)}{\partial z}\right]_{t=0} - \frac{\mu\epsilon}{u^2}E(z,0). \tag{35}$$

Now inputting the consequent initial time values relation into the previous equation,

$$\left[\frac{\partial H(z,t)}{\partial z}\right]_{t=0} = -\epsilon\left[\frac{\partial E(z,t)}{\partial t}\right]_{t=0} - \sigma\left[E(z,t)\right]_{t=0}, \tag{36}$$

we get the resulting equation,

$$\frac{\partial^2 F(z,u)}{\partial z^2} - (\frac{\mu\epsilon}{u^2} + \frac{\mu\sigma}{u})F(z,u) = -\left(\frac{\mu\epsilon}{u^2} + \frac{\mu\sigma}{u}\right)E(z,0) - \frac{\mu\epsilon}{u}\left[\frac{\partial E(z,t)}{\partial t}\right]_{t=0} \tag{37}$$

If we assume the known initial conditions to satisfy, $E(z,t\to 0)=f_0(z)$, and, $\partial E(z,t\to 0)/\partial t = f_0'(z)$, and we set, $\rho=\frac{\mu\sigma}{u},\ \lambda=\frac{\mu\epsilon}{u}$, and, $\gamma^2=\frac{\mu\sigma}{u}+\frac{\mu\epsilon}{u^2}=\rho+\lambda/u$, we see that Equation (37) yields,

$$\frac{d^2F(z,u)}{dz^2}-\gamma^2F(z,u)=W(z,u), \tag{38}$$

where,

$$W(z,u)=-(\gamma^2f_0(z)+\lambda f_0'(z))=-(\rho f_0(z)+\lambda[f_0'(z)+f_0(z)/u]). \tag{39}$$

As expected, for unit consistency, both quantities, $f_0'(z)$, and, $(f_0(z)/u)$, must have the same exact units. We observe that the homogeneous solution of Equation (38), $F_h(z,u)$, and particular solution, $F_p(z,u)$, are given by,

$$\begin{cases} F_h(z,u)=A(u)e^{\gamma z}+B(u)e^{-\gamma z},\ \text{and,} \\ F_p(z,u)=\frac{e^{\gamma z}}{2\gamma}\int e^{-\gamma z}W(z,u)dz+\frac{e^{-\gamma z}}{2\gamma}\int e^{\gamma z}W(z,u)dz. \end{cases} \tag{40}$$

Next, considering the boundary conditions concerning the electric field, $E(z,t)$, we have,

$$\lim_{z\to 0}E(z,t)=E(0,t),=f(t),\quad t\geq 0, \tag{41}$$

along with the assumption that for, $z>0$, the wave, $f(t)$, is traveling in a lossy medium having positive conductivity. In this case, we get, the time coefficients A, and B in Equation (40), satisfy,

$$\begin{cases} A(u)=0,\ \text{and,} \\ B(u)=F(0,u)=F(u)=\mathcal{S}\left[f(t)\right]. \end{cases} \tag{42}$$

Therefore, since, $e^{-\gamma z}=e^{-\frac{b}{a}z}e^{-\frac{1}{au}z}-a\int_{z/a}^{\infty}e^{-b\tau}\frac{\partial}{\partial z}J_0\left(\frac{b}{a}\sqrt{z^2-a^2\tau^2}\right)e^{-\tau/u}d\tau$, we get, (see [9] for more details),

$$F(z,u)=F(z,u)=F(u)e^{-\gamma z}=F(u)e^{-\frac{b}{a}z}e^{-\frac{1}{au}z}-auF(u)\mathcal{S}\left[\Phi(z,\tau)\right] \tag{43}$$

where, with the substitutions $a=1/\sqrt{\mu\epsilon}$, $b=\sigma/2\epsilon$, and, J_0 denotes the Bessel function of order 0, we have,

$$\Phi(z,\tau)=\begin{cases} e^{-b\tau}\frac{\partial}{\partial z}J_0\left(\frac{b}{a}\sqrt{z^2-(a\tau)^2}\right),\ \text{for}\ \ \tau\geq z/a, \\ 0,\ \ \text{for}\ \ 0<\tau<z/a \end{cases} \tag{44}$$

Now, by the shift and convolution Sumudu properties, (13), and (20), and development in this section we have,

Theorem 3. Subject to lossy media conditions, the transient electric field, $E(z,t)$, in Equation (31) is given by,

$$E(z,t)=e^{-\frac{b}{a}z}f(t-z/a)-a\int_{z/a}^{\infty}f(t-\tau)e^{-b\tau}\frac{\partial}{\partial z}J_0\left(\frac{b}{a}\sqrt{z^2-(a\tau)^2}\right)e^{-\tau/u}d\tau. \tag{45}$$

Further details concerning TEMP waves electric field solutions can be found in [6–9].

ACKNOWLEDGMENT

The author wishes to thank the Arab Open University-Kuwait (AOUKWB) Admin, and the AOU Planning, Research, and Development Office at the AOU HQ, for their continuous support.

REFERENCES

1. Bäumer, B. and F. Neubrander, "Laplace transform mehods for evolution equations," *Proceedings of the Conferenze del Seminario di Matematica*, dell'Università di Bari, Vol. 259, 27–60, 1995.
2. Belgacem, F. B. M., "Applications of the Sumudu transform to indefinite periodic parabolic problems," *Proceedings of the 6th International Conference on Mathematical Problems & Aerospace Sciences, (ICNPAA 06)*, Chap. 6, 51–60, Budapest, Hungary, 2007.

3. Belgacem, F. B. M., "Introducing and analyzing deeper Sumudu properties," *Nonlinear Studies Journal (NSJ)*, Vol. 13, No. 1, 23–41, 2006.
4. Belgacem, F. B. M. and A. A. Karaballi, "Sumudu transform fundamental properties investigations and applications," *Journal of Applied Mathematics and Stochastic Analysis, (JAMSA)*, Article ID 91083, 1–23, 2006.
5. Belgacem, F. B. M., A. A. Karaballi, and L. S. Kalla, "Analytical investigations of the Sumudu transform, and applications to integral production equations," *Mathematical Problems in Engineering, (MPE)*, No. 3, 103–118, 2003.
6. El-Shandwily, M. E., "Solutions of Maxwell's equations for general nonperiodic waves in lossy media," *IEEE Trans. Electromagn. Compat.*, Vol. 30, No. 4, 577–582, 1988.
7. Harmuth, H. F. and M. G. M. Hussain, *Propagation of Electromagnetic Signals*, World Scientific, Singapore, 1994.
8. Hussain, M. G. M., "Mathematical model for the electromagnetic conductivity of lossy materials," *Journal of Electromagnetic Waves and Applications*, Vol. 19, No. 2, 271–279, 2005.
9. Hussain, M. G. M. and F. B. M. Belgacem, "Transient solutions of Maxwell's equations based on Sumudu transformation," *Progress In Electromagnetic Research*, PIER 74, 273–289, 2007.
10. Katatbeh, Q. D. and F. B. M. Belgacem, "Sumudu transform of fractional differential equations," *Nonlinear Studies Journal, (NSJ)*, 2009.
11. Kong, J. A., *Maxwell Equations*, EMW Publishing, Cambridge, MA, 2002.
12. Van der Pol, B. and H. Bremmer, *Operational Calculus Based on the Two-sided Laplace Integral*, 3rd ed., Chelsea Publication Company, New York, 1987.
13. Watugala, G. K., "Sumudu transform a new integral transform to solve differential equations and control engineering problems," *Mathematical Engineering in Industry, (MEI)*, Vol. 6, No. 4, 319–329, 1998.

Dyadic Electromagnetic Green's Function for a Graphene Bilayer

Norman J. Morgenstern Horing[1] **and S. Y. Liu**[2]

[1]Department of Physics and Engineering Physics, Stevens Institute of Technology
Hoboken, New Jersey 07030, USA
[2]Department of Physics, Shanghai Jiaotong University
1954 Huashan Road, Shanghai 20030, China

Abstract— The obvious promise of single and multiple Graphene sheets for new and improved electronic devices mandates a serious exploration of their electromagnetic properties. In this paper, we employ techniques that we recently used to develop an exact explicit analytical expression for the dyadic electromagnetic Green's function of a thin excitonic layer (in a study of inhomogeneous radiative exciton polariton modes corresponding to the complex poles of the matrix Green's function). Here, we further extend this technique to determine the structure of the dyadic electromagnetic Green's functions for a bilayer, and apply it to examine Graphene bilayer electromagnetics.

1. INTRODUCTION

Graphene, a single-atom-thick two-dimensional planar layer of Carbon atoms in a hexagonal honeycombed lattice composed of two superposed triangular sub-lattices, has been receiving a great deal of attention, both experimental and theoretical, since the first report in 2004 of its unusual device-friendly material properties [1, 2]. These properties include: high mobility at elevated temperature [3], reaching 200,000 cm^2/Vs (over two orders of magnitude higher than that of silicon-based materials, over twenty times that of GaAs, over twice that of InSb); high electron density, about $10^{13}\,\mathrm{cm}^{-2}$ in a single subband; long carrier mean-free-path, $L \sim 400$ nm at room temperature, opening the possibility of Graphene-based ballistic devices; stability to high temperatures, ~ 3000 K; quantum Hall effect occurs at room temperature in Graphene; the planar form of Graphene generally allows for highly-developed top-down CMOS compatible process flows, a substantial advantage over Carbon nanotubes that are difficult to integrate into electronic devices and are difficult to produce in consistent sizes and electronic properties. All of these properties make Graphene an extremely promising material for future nanoelectronic devices. Such applications of Graphene are already in progress, including: Graphene *sensors* [4] that can detect minute concentrations (1 part per billion) of various active gasses; a Graphene *spin valve* [5]; a Graphene *electromechanical resonator* [6] can actuate an electromechanical resonator by an rf-gate-voltage superposed on a dc-voltage applied to the Graphene sheet, or by optical actuation using a laser focused on the sheet; a Graphene *field effect transistor* [7, 8] has already been produced; a Graphene *quantum interference device* was built to manipulate electron wave interference effects.

Bilayers of Graphene are similarly of great interest at this time and their charge transport and electromagnetics are also under investigation. In this paper we determine the electromagnetic dyadic Green's function for such a bilayer taking the separation "a" of the constituent Graphene layers to be sufficiently large that tunneling between them can be neglected. In this analysis, we employ the same techniques used in our earlier derivation [9] of the exact, explicit analytic expression for the dyadic electromagnetic Green's function of a thin 2D planar excitonic layer. To start, we note that the Levine-Schwinger [10] dyadic Green's function for a spatially homogeneous and isotropic host medium of dielectric constant ϵ_h can be written as ($\hat{\mathbf{I}}$ is the 3×3 unit dyadic)

$$\begin{aligned}\hat{\mathbf{G}}_{3D}(z, z', \mathbf{k}_\parallel, \omega) \;=\; & \frac{1}{2\imath k_z} \\ & \times \left\{ \hat{\mathbf{I}} - \frac{c^2}{\omega^2 \epsilon_h} [\mathbf{k}_\parallel \mathbf{k}_\parallel + k_z sign(z - z')(\mathbf{k}_\parallel \mathbf{e}_z + \mathbf{e}_z \mathbf{k}_\parallel) + \mathbf{e}_z \mathbf{e}_z (k_z^2 - 2\imath k_z \delta(z - z'))] \right\} \\ & \times \exp(\imath k_z |z - z'|), \end{aligned} \tag{1}$$

Here, we have Fourier transformed in the x-y plane of spatial translational invariance, $(\mathbf{r}_\parallel - \mathbf{r}'_\parallel) = (x - x', y - y') \Rightarrow \mathbf{k}_\parallel$, and in time, $t - t' \Rightarrow \omega$, and

$$k_z = \sqrt{(\omega^2/c^2)\epsilon_h - k_\parallel^2}. \tag{2}$$

The sign before the radical has been chosen in such a way that the field in the host medium satisfies the radiation condition for $k_\parallel < \omega\epsilon_h^{1/2}/c$ and the evanescent field condition for $k_\parallel > \omega\epsilon_h^{1/2}/c$. When calculating $\hat{\mathbf{G}}_{3D}(0,0,\mathbf{k}_\parallel;\omega)$ in Eq. (1), we approximate the Dirac delta-function, $\delta(0)$, by the inverse of the excitonic layer thickness, $1/d$. Moreover, since $sign(0) = 0$, we have

$$\hat{\mathbf{G}}_{3D}(0,0,\mathbf{k}_\parallel;\omega) = \frac{1}{2\imath k_z}\left\{\hat{\mathbf{I}} - \frac{c^2}{\omega^2\epsilon_h}[\mathbf{k}_\parallel\mathbf{k}_\parallel + \mathbf{e}_z\mathbf{e}_z(k_z^2 - 2\imath k_z/d)]\right\}. \tag{3}$$

In general we will suppress the explicit appearance of $\mathbf{k}_\parallel$ and ω below.

2. BILAYER DYADIC EM GREEN'S FUNCTION

The integral equation for the electromagnetic Green's function for a medium with conductivity $\hat{\sigma}(\mathbf{r},\mathbf{r}') \to \hat{\sigma}_{2D}(\mathbf{r},\mathbf{r}')$ here is given by (take $\epsilon_h \to 1$)

$$\hat{\mathbf{G}}(\mathbf{r},\mathbf{r}') = \hat{\mathbf{G}}_{3D}(\mathbf{r},\mathbf{r}') - \frac{4\pi i\omega}{c^2}\int d^3\mathbf{r}''_\parallel \int d^3\mathbf{r}'''_\parallel \hat{\mathbf{G}}_{3D}(\mathbf{r},\mathbf{r}'')\hat{\sigma}_{2D}(\mathbf{r}'',\mathbf{r}''')\hat{\mathbf{G}}(\mathbf{r}''',\mathbf{r}'). \tag{4}$$

In the case at hand of a planar homogeneous bilayer, we have

$$\hat{\sigma}_{2D}(\mathbf{r}'',\mathbf{r}''') = \hat{\mathbf{I}}\sigma_{2D}(\omega)\delta^{(2)}(\mathbf{r}''_\parallel - \mathbf{r}'''_\parallel)[\delta(z''-a/2)\delta(z'''-a/2) + \delta(z''+a/2)\delta(z'''+a/2)], \tag{5}$$

where the two layers have conductivity $\sigma_{2D}(\omega)$ and they are situated at $z = \pm a/2$. Employing Eq. (5), the integral Eq. (4) reduces to (Fourier transform $\mathbf{r}_\parallel - \mathbf{r}'_\parallel \to \mathbf{k}_\parallel$ and suppress it)

$$\hat{\mathbf{G}}(z,z') = \hat{\mathbf{G}}_{3D}(z,z') - \frac{4\pi i\omega}{c^2}\sigma_{2D}(\omega)\hat{\mathbf{I}}\sum_{\pm}\hat{\mathbf{G}}_{3D}(z,\pm a/2)\hat{\mathbf{G}}(\pm a/2,z'). \tag{6}$$

To solve, we require $\hat{\mathbf{G}}(\pm a/2,z')$ on the right of Eq. (6), so we set $z = \pm' a/2$ throughout it:

$$\hat{\mathbf{G}}(\pm' a/2;z') = \hat{\mathbf{G}}_{3D}(\pm' a/2;z') - \frac{4\pi i\omega}{c^2}\sigma_{2D}(\omega)\hat{\mathbf{I}}\sum_{\pm}\hat{\mathbf{G}}_{3D}(\pm' a/2,\pm a/2)\hat{\mathbf{G}}(\pm a/2,z'). \tag{7}$$

This 2×2 matrix equation arising from the multiplicity of $(\pm',\pm)$ values is readily solved (carefully noting the order of dyadics) as: [since $\hat{\mathbf{G}}_{3D}(z,z') = \hat{\mathbf{G}}_{3D}(z-z')$, we write $\hat{\mathbf{G}}_{3D}(\pm a/2,\pm a/2) = \hat{\mathbf{G}}_{3D}(0)$ and $\hat{\mathbf{G}}_{3D}(\pm a/2,\mp a/2) = \hat{\mathbf{G}}_{3D}(\pm a)$; and also use the notation $\hat{\mathbf{G}}(\pm a/2,z') = \hat{\mathbf{G}}_{\pm}$, and $\hat{\mathbf{G}}_{3D}(\pm a/2,z') = \hat{\mathbf{G}}_{3D\pm}$, etc.].

$$\hat{\mathbf{G}}_{\pm} = \hat{\Delta}_{\pm}^{-1}\left\{\hat{\mathbf{G}}_{3D\pm} - \hat{C}\hat{\mathbf{G}}_{3D}(\pm a)(1+\hat{C}\hat{\mathbf{G}}_{3D}(0))^{-1}\hat{\mathbf{G}}_{3D\mp}\right\}. \tag{8}$$

Here, $\hat{C} = \frac{4\pi i\omega}{c^2}\sigma_{2D}(\omega)\hat{\mathbf{I}}$, and

$$\hat{\Delta}_{\pm} = \hat{\mathbf{I}} + \hat{C}\hat{\mathbf{G}}_{3D}(0) - \hat{C}\hat{\mathbf{G}}_{3D}(\pm a)(\hat{\mathbf{I}} + \hat{C}\hat{\mathbf{G}}_{3D}(0))^{-1}\hat{C}\hat{\mathbf{G}}_{3D}(\mp a). \tag{9}$$

Eqs. (6)–(10) provide all the information needed to determine the double-layer dyadic EM Green's function.

3. GRAPHENE BI-LAYER EM DISPERSION RELATION

We choose the coordinate system such that $\mathbf{k}_\parallel$ is along the x axis and $k_y \equiv 0$. From Eq. (3) it follows that $(\hat{\mathbf{I}} + \hat{C}\hat{\mathbf{G}}_{3D}(0))^{-1}$ is diagonal:

$$\left(\hat{\mathbf{I}} + \hat{C}\hat{\mathbf{G}}_{3D}(0)\right)^{-1} = \lambda_x\mathbf{e}_x\mathbf{e}_x + \lambda_y\mathbf{e}_y\mathbf{e}_y + \lambda_z\mathbf{e}_z\mathbf{e}_z, \tag{10}$$

with

$$\lambda_x = \left[1 + \frac{2\pi\omega\sigma_{2D}}{k_z c^2}\left(1 - \frac{k_\parallel^2 c^2}{\omega^2\varepsilon_h}\right)\right]^{-1},\ \lambda_y = \left(1 + \frac{2\pi\omega\sigma_{2D}}{k_z c^2}\right)^{-1},\ \lambda_z = \left[1 - \frac{2\pi\sigma_{2D}}{k_z\omega\varepsilon_h}(k_z^2 - 2ik_z/d)\right]^{-1}.$$

Furthermore, $\hat{\mathbf{G}}_{3D}(\pm a)$ can be written as

$$\hat{\mathbf{G}}_{3D}(\pm a) = \frac{1}{2ik_z}\left\{\hat{\mathbf{I}} - \frac{c^2}{\omega^2\varepsilon_h}\left[k_\parallel^2\mathbf{e}_x\mathbf{e}_x \pm k_\parallel k_z(\mathbf{e}_x\mathbf{e}_z + \mathbf{e}_z\mathbf{e}_x) + k_z^2\mathbf{e}_z\mathbf{e}_z\right]\right\}\exp(ik_z a). \tag{11}$$

Using Eqs. (10) and (3), $\hat{\Delta}_\pm$ can be written as

$$\hat{\Delta}_\pm = M_{xx}\mathbf{e}_x\mathbf{e}_x + M_{yy}\mathbf{e}_y\mathbf{e}_y + M_{zz}\mathbf{e}_z\mathbf{e}_z \pm M_{xz}\mathbf{e}_x\mathbf{e}_z \pm M_{zx}\mathbf{e}_z\mathbf{e}_x, \tag{12}$$

with

$$M_{xx,zz} = \lambda_{x,z}^{-1} + \left(\frac{i\omega\sigma_{2D}}{k_z^2c^2}\right)^2 \mathrm{e}^{2ik_z a}\left[\left(1 - \frac{k_{\parallel,z}^2c^2}{\omega^2\varepsilon_h}\right)^2\lambda_{x,z}^2 - \left(\frac{k_\parallel k_z c^2}{\omega^2\varepsilon_h}\right)^2\lambda_{z,x}\right],$$

$$M_{yy} = \lambda_y^{-1} + \left(\frac{i\omega\sigma_{2D}}{k_z^2c^2}\right)^2\lambda_y\mathrm{e}^{2ik_z a},$$

and

$$M_{xz,zx} = \frac{1}{\varepsilon_h}\left(\frac{i\sigma_{2D}}{k_z^2 c}\right)^2 k_\parallel k_z \mathrm{e}^{2ik_z a}\left[\left(1 - \frac{k_{z,\parallel}^2c^2}{\omega^2\varepsilon_h}\right)\lambda_{x,z} - \left(1 - \frac{k_{\parallel,z}^2c^2}{\omega^2\varepsilon_h}\right)\lambda_{z,x}\right].$$

Here, $M_{xx,zz}$ refers to M_{xx} or M_{zz}; and $M_{xz,zx}$ refers to M_{xz} or M_{zx}. The symbols $\lambda_{x,z}$ and $\lambda_{z,x}$ refers to λ_x or λ_z and λ_z or λ_x, respectively, in accordance with the first M subscript before or after the comma.

The electromagnetic dispersion relations for a bilayer are determined by the vanishing of $\det\hat{\Delta}_\pm$, or

$$M_{xx}M_{zz} - M_{zx}M_{xz} = 0 \quad \text{and} \quad M_{yy} = 0. \tag{13}$$

The significant differences between the electromagnetic modes of Graphene and those of more traditional two dimensional materials arise from its conductivity expressed in terms of the Graphene polarizability as given in Refs. [11–15]. Even the low wavenumber Graphene plasmon makes a distinctive contribution because of its unusual dependence on 2D density, $n_{2D}^{1/4}$, as opposed to the usual $n_{2D}^{1/2}$ for traditional materials.

ACKNOWLEDGMENT

SYL gratefully acknowledges support from the National Science Foundation of China (grant 10804073), and from the Program for New Century Excellent Talents in University.

REFERENCES

1. Novoselov, K. S., A. K. Geim, et al., "Electric field effect in atomically thin carbon films," *Science*, Vol. 306, No. 5696, 666–669, 2004.
2. Castro Neto, A. H., et al., "The electronic properties of graphene," arXiv:0709.1163v2 (unpublished), 2007.
3. Morozov, S. V., et al., "Giant intrinsic carrier mobilities in graphene and its bilayer," *Phys. Rev. Lett.*, Vol. 100, No. 1, 016602, 2008.
4. Schedin, F., K. S. Novoselov, et al., "Detection of individual gas molecules absorbed on graphene," arXiv.cond-mat/0610809 (unpublished), 2006.
5. Hill, E. W., A. K. Geim, K. S. Novoselov, et al., "Graphene spin valve devices," *IEEE Trans. Magn.*, Vol. 42, No. 10, 2694–1696, 2006.
6. Bunch, J. S., et al., "Electromechanical resonators from graphene sheets," *Science*, Vol. 315, No. 5811, 490–493, 2007.
7. Georgia Tech Research News — http://gtresearchnews.gatech.edu/newsrelease/graphene.html
8. Lemme, M. C., "A graphene field-effect device," *IEEE Electron Device Letters*, Vol. 28, No. 4, 282–284, 2007.
9. Horing, N. J. M., et al., "Excitation of radiative polaritons in a 2D excitonic layer by a light pulse," *J. Opt. Soc. Amer. B*, Vol. 24, 2428, 2007.
10. Levine, H. and J. Schwinger, "On the theory of diffraction by an aperture in an infinite plane screen," *Phys. Rev.*, Vol. 74, No. 8, 958–974, 1948; ibid, *Phys. Rev.*, Vol. 75, No. 9, 1423–1432, 1949; also see *Commun. Pure & Appl. Math.*, Vol. 3, 355–391, 1950.

11. Shung, K. W.-K., "Dielectric function and plasmon structure of stage-1 intercalated graphite," *Phys. Rev. B*, Vol. 34, No. 2, 979–993, 1986.
12. Shung, K. W.-K., "Lifetime effects in low-stage intercalated graphite systems," *Phys. Rev. B*, Vol. 34, No. 2, 1264–1272, 1986.
13. Ando, T., "Screening effect and impurity scattering in monolayer graphene," *J. Phys. Soc. Jpn.*, Vol. 75, No. 7, 074716, 2006.
14. Hwang, E. H. and S. Das Sarma, "Dielectric function, screening, and plasmons in two-dimensional graphene," *Phys. Rev. B*, Vol. 75, No. 20, 205418, 2007.
15. Wunsch, B., T. Stauber, F. Sols, and F. Guinea, "Dynamical polarization of graphene at finite doping," *New J. Phys.*, Vol. 8, No. 12, 318, 2006.

Open-ended MEMS Probes for Dielectric Spectroscopy of Biological Cells at Radio Frequencies

Hsin-Hung Li[1], **Jen-Yu Jao**[1], **Ming-Kun Chen**[1], **Ling-Sheng Jang**[1], **and Yi-Chu Hsu**[2]

[1]Department of Electrical Engineering and Center for Micro/Nano Science and Technology
National Cheng Kung University, Taiwan
[2]Department of Mechanical Engineering, Southern Taiwan University, Taiwan

Abstract— When an electrical current with a low frequency is applied to a cell, the current passes through the outside of the cell. Thus, impedance measurements at low frequencies cannot be used to determine the pathological change of the cellular organelle taking place inside the cell. However, increasing the frequency of the electrical current makes the capacitive impedance of the cell decrease, allowing the electrical current to flow through the cell. This study presents the design and fabrication of a microfluidic device integrated with a coplanar waveguide open-ended MEMS probe for the impedance measurement of the single HeLa cell at radio frequencies. The device includes a PDMS cover with a microchannel and microstructures to capture the single HeLa cell and a conductor-backed CPW fabricated using a silicon chip and two PCB boards. The effects of the substrate on the characteristic impedance of the CBCPW structure were investigated under three conditions by utilizing a Time-Domain Reflectometer (TDR) to obtain the characteristic impedance of the device (46.43 Ω). Finally, impedance measurements using the proposed device and a vector network analyzer (VNA) are demonstrated for sodium chloride solutions with different concentrations, DI water, alcohol, PBS, and a single HeLa cell.

1. INTRODUCTION

Biological cells can be analyzed at low frequencies or high frequencies. When an electrical current with a low frequency is applied to a cell, the current passes through the outside of the cell. However, the pathological change of a cellular organelle taking place inside the cell cannot be determined using low frequency measurements. Additionally, double layer capacitance acts like a traditional parallel plate capacitor, whereby the capacitance is roughly proportional to the surface area [1]. Therefore, this effect makes it impossible to express the cell status using quantitative analysis. To overcome the shortcomings of low frequency measurement, high frequency measurement has been used to reduce the electrical shielding effect and the double layer effect [2]. With an increase of the frequency of the electrical current, the capacitive impedance of the cell decreases and the electrical current flows through the cell; this can be used to obtain the impedance characteristics of the cell in different pathological statuses. This technique allows us to perform dielectric spectroscopy on a variety of biological samples — from cells to molecules — in solution [3].

In this study, planar-type probes are chosen as the open-ended probe structure. We present a microfluidic device consisting of an open-ended MEMS probe and a PDMS cover plate with a microfluidic channel and cell-trapping microstructures for the impedance measurement of single Hela cells at radio frequency using the vector network analyzer (VNA). Two kinds of substrate material (silicon and PCB board) are used to fabricate the open-ended MEMS probe as a compound CPW device. The effects of the substrate on the characteristic impedance of the CBCPW structure under three conditions are investigated using a Time-Domain Reflectometer. Additionally, the impedance measurements of various solutions and single HeLa cells are also performed.

2. DESIGN AND MATERIALS

Biological spectroscopy is usually performed on a metal interface, such as the platform of a microscope. Hence, a conductor attached to the back of the device is required to isolate unwanted noise. Wen's analysis for conventional CPW is extended to the CBCPW [4] on the assumption that a quasi-static transverse electromagnetic (TEM) mode is assumed to propagate on this structure. In this study, two structures are combined to achieve the biological analysis of a single cell. The first is a microfludic device with cell-trapping micropillars, which traps a single cell to be analyzed. The other is a CBCPW device that is used to perform an impedance measurement on the trapped single cell. The microfludic device is firmly bond onto the CBCPW.

Figure 1 shows the schematic of the CBCPW device, which comprises two parts: part 1 contains a PCB board with an FR4 substrate as an interface connecting to vector network analyzer (VNA)

through the SubMiniature Version A (SMA) adapter (Fig. 1(a)), and part 2 is the CPW open-ended probe working as an excited electrode to measure its reflected signal (Fig. 1(b)).

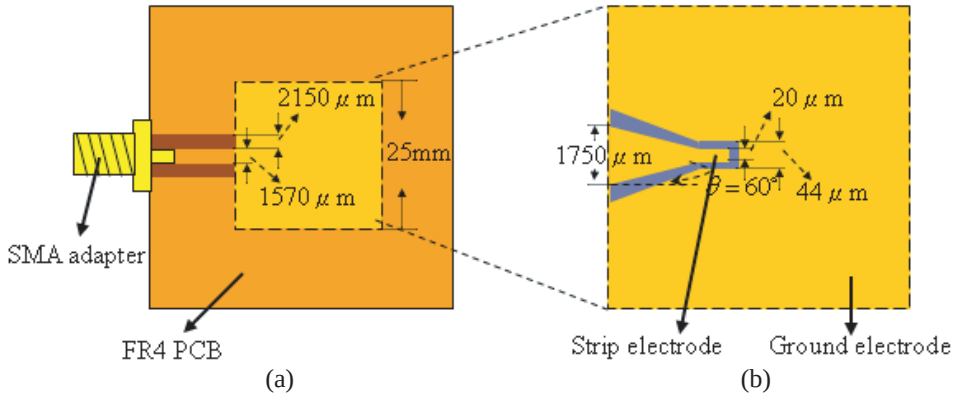

Figure 1: Schematic of the CBCPW device: (a) a PCB board with FR4 substrate and (b) the CPW open-ended probe working as an excited electrode.

According to the research of Bedair and Wolff [5], different substrates have different dielectric constants, which affect the electrode size. The electrode size must be designed depending on the adopted substrate. Silicon is a general material in semi-conductor fabrication. Due to its large dielectric constant ($\varepsilon_r = 11.8$), a silicon wafer used as the substrate facilitates a small-size electrode. Hence, silicon was used as the substrate of the CPW probe in this study. A narrow strip electrode (20 μm in width) was patterned on this substrate to perform the measurement for a single cell (with diameter of $10 \sim 20$ μm). The detailed CBCPW parameters were simulated by AppCad. A coplanar taper with an angle (θ) equal to 60° between the CPW on the PCB board and the narrow part of the electrode on silicon was designed to minimize impedance mismatch (Fig. 1(b)) [6]. Around the narrow strip electrode is the ground electrode, which provides shielding from unwanted noise.

The microfluidic device developed in this study consists of an inlet reservoir and an outlet reservoir connected by a microchannel containing a cell-trapping microstructure. This structure is made out of PDMS to form a cover plate that binds onto the CBCPW. The fluid enters and exits the microfluidic device via plastic tubes attached to the two reservoirs and is driven by a syringe pump. Fig. 2 shows a schematic showing the details of the inlet reservoir and cell-trapping structure within the microchannel. The basic components of the device, namely the reservoirs, the main microchannel, the front filter in the inlet reservoir, and the cell-trapping structure. The width and depth of the microchannel on the PDMS cover plate are 100 μm and 25 μm, respectively, while the micro-pillars in the cell-trapping structure have dimensions of 10 μm × 10 μm × 25 μm (width × length × height). The silicon substrate with the CPW probe was covered by the PDMS microfluidic channel and 3-mercaptopropyltrimethoxysilane was used to strengthen the bond between PDMS and the gold electrodes on the silicon substrate.

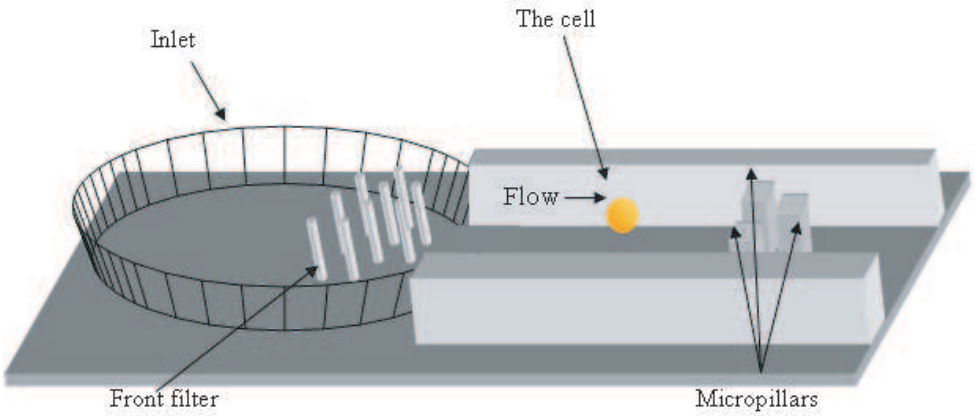

Figure 2: Schematic of the PDMS cover plate, including the inlet reservoir and the microchannel.

For the designed CPW fixture and the VNA used in this work, one port calibration is suitable.

A customized calibration kit was manufactured to improve the calibration accuracy by shifting the calibration reference plane located at the port of VNA to the CPW device plane. During one-port calibration, the calibration data were obtained by connecting an OPEN standard, a SHORT standard, and a LOAD standard to the desired test port. OPEN and SHORT standards are almost the same except that OPEN is not connected to ground. The LOAD standard used two 0402 SMD resistors (100 Ω) connected to ground to realize a 50 Ω LOAD standard. Two 100 Ω resistors were used instead of one 50 Ω resistor to reduce parasitic inductance. The performance of the impedance measurement system developed in this study was characterized using HeLa cells.

3. CAPACITANCE EFFECT OF THE SUBSTRATE

In the measurements at high frequency, the desired characteristic impedance of the central electrode is 50 Ω. However, the characteristic impedance of the central electrode of the proposed CBCPW structure is measured at around 10 Ω, which results in inaccuracy. According to theory [7], the characteristic impedance of the central electrode of the CBCPW structure is dominated by the capacitance effect of the substrate. In other words, regulating the capacitance of the substrate can result in the desirable characteristic impedance of the central electrode. Therefore, the effects of the substrate on the characteristic impedance of the CBCPW structure under three conditions were investigated. The three conditions of the substrate are shown in Fig. 3. First, the original design of the CBCPW contains a double-side PCB whose ground plane is 34.2 µm thick (Fig. 3(a)). Second, the ground plan of the double-side PCB is engraved (Fig. 3(b)). Engraving the ground plan changes the condition of the substrate and thus affects the capacitance of the substrate. Third, the additional single-side PCB is attached to the engraved ground plane of the double-side PCB (Fig. 3(c)). In this case, there is an air gap with a height of 34.2 µm between the double-side PCB and single-side PCB; this gap also influences the capacitance of the substrate. The characteristic impedances of the central electrode under three conditions of the substrate were measured using a Time-Domain Reflectometer (TDR). The characteristic impedance of the central electrode in the original design decreases to around 10 Ω. When the ground plan of the double-side PCB was engraved, the characteristic impedance of the central electrode on silicon increased to 92.65 Ω. In the third case, when an air gap was formed between two PCBs, the characteristic impedance of the central electrode decreased to 46.43 Ω, which is close to the desired impedance of 50 Ω.

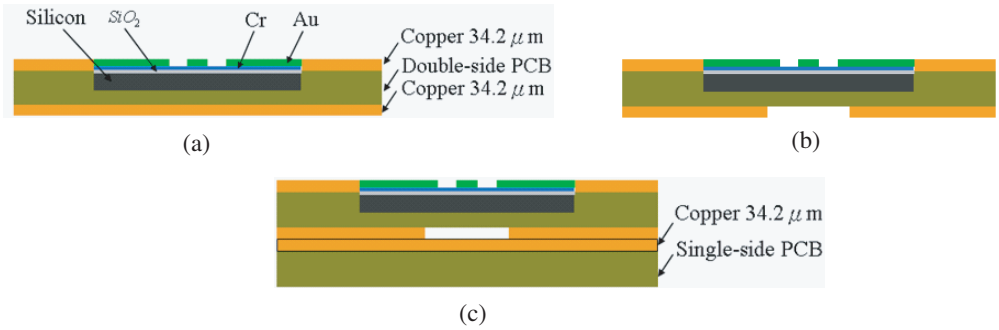

Figure 3: Schematic of the substrate under three conditions. (a) The original structure of CBCPW. (b) Engraving the ground plane on the double-side PCB bottom surface. (c) Attachment of an additional single-side PCB.

4. RESULTS AND DISCUSSION

The impedance measurements were performed for sodium chloride solutions with three concentrations, three kinds of solution, and solutions with/without the captured cell. The experiments for different solutions without the cell were conducted to demonstrate the changes of their impedance by utilizing the proposed open-ended probe. First, three concentrations of sodium chloride solutions (0.2 g/ml, 0.17 g/ml, and 0.14 g/ml) were used for the impedance measurements. Fig. 4(a) shows that the difference in impedances of sodium chloride solutions with different concentrations can be distinguished below 60 MHz. Below 60 MHz, the results show that the magnitude of impedance increases as the sodium chloride concentration decreases, which coincides with the fact that the conductivity is proportional to the electrolyte concentration. With a frequency of over 60 MHz, the difference in impedances of sodium chloride solutions with different concentrations becomes small

because the capacitance effect of the solution becomes lower at high frequencies. The open circuit magnitude is higher than that in sodium chloride solution because the air acts as an insulator. Impedance measurements of DI water, alcohol, and PBS were also conducted, with results shown in Fig. 4(b). The figure shows that each curve is distinct. The difference in impedance decreases as the frequency increases. Fig. 4(c) shows the measurement results of a single HeLa cell in PBS solution. Prior to the experiment, a calibration was conducted with the PBS solution to reduce the effect of the PBS. The results show that a single HeLa cell can be discriminated from the PBS solution using the proposed open-ended probe.

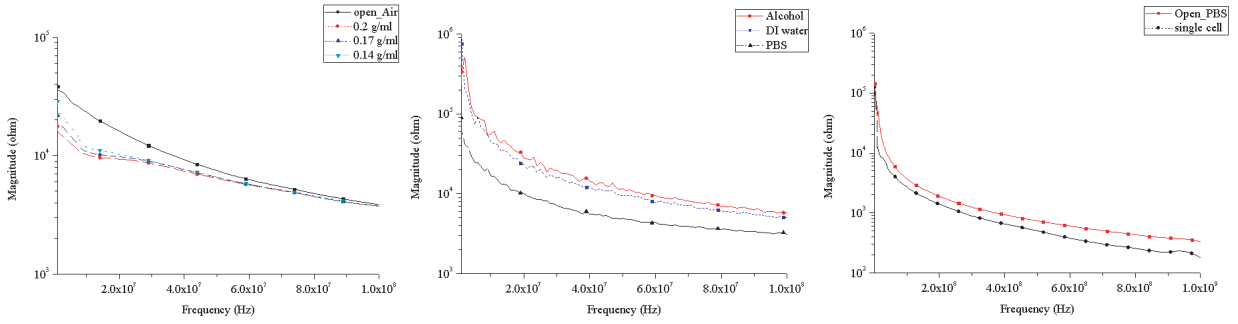

(a) (b) (c)

Figure 4: (a) The impedance magnitude of an open circuit and sodium chloride solution with three concentrations. (b) The impedance magnitude of alcohol, DI water, and PBS. (c) The impedance magnitude of cells and PBS.

5. CONCLUSIONS

A microfluidic device integrated with an open-ended MEMS probe that perform single-cell impedance measurements at radio frequencies using the vector network analyzer (VNA) was developed. The device includes a PDMS cover with a microchannel and microstructures to capture a single HeLa cell and a conductor-backed CPW fabricated using a silicon chip and two PCB boards. In order to achieve the desired characteristic impedance of the device (50 Ω), the effects of the substrate on the characteristic impedance of the CBCPW structure under three conditions were investigated by utilizing a Time-Domain Reflectometer. According to the results, regulating the capacitance of the substrate can produce the desirable characteristic impedance of the device. Therefore, the ground plan of the double-side PCB was engraved and a single-side PCB was attached to form an air gap for an acceptable characteristic impedance of 46.43 Ω.

The impedance measurements of sodium chloride solutions with three concentrations (0.2 g/ml, 0.17 g/ml, and 0.14 g/ml) and different solutions (DI water, alcohol, and PBS) were performed. The results show that the magnitude of impedance increases as the sodium chloride concentration decreases, which coincides with the fact that the conductivity is proportional to the electrolyte concentration. At frequencies over 60 MHz, the difference in impedances of sodium chloride solutions with different concentrations becomes small because the capacitance effect of the solution becomes lower at high frequencies. The difference in impedance of DI water, alcohol, and PBS decreases as the frequency increases. The measurement of a single HeLa cell in PBS solution was also carried out. The results show that the single HeLa cell can be discriminated from the PBS solution using the proposed device. The optimization and reliability of the proposed device will be studied in the future. The biological applications of the proposed device will also be explored.

ACKNOWLEDGMENT

This study was supported by the National Science Council, Taiwan, R.O.C., (NSC 96-2221-E-006-289), and made use of shared facilities provided under the Program of Top 100 Universities Advancement funded by the Ministry of Education in Taiwan. The authors would also like to thank the Center for Micro/Nano Science and Technology at National Cheng Kung University and the National Nano Device Laboratories for access granted to major equipment throughout the duration of this study and for their general technical support.

REFERENCES

1. Chmiola, J., G. Yushin, R. K. Dash, E. N. Hoffman, J. E. Fischer, M. W. Barsoum, and Y. Gogotsi, "Double-layer capacitance of carbide derived carbons in sulfuric acid," *Electrochemical and Solid-State Letters*, Vol. 8, A357–A360, 2005.
2. Lohndorf, M., U. Schlecht, T. M. A. Gronewold, A. Malave, and M. Tewes, "Microfabricated high-performance microwave impedance biosensors for detection of aptamer-protein interactions," *Applied Physics Letters*, Vol. 87, 243902, 2005.
3. Messina, T. C., L. N. Dunkleberger, G. A. Mensing, A. S. Kalmbach, R. Weiss, D. J. Beebe, and L. L. Sohn, "A novel high-frequency sensor for biological discrimination," *The 7th International Conference on Micro Total Analysis Systems*, 2003.
4. Wen, C. P., "Coplanar waveguide: A surface strip transmission line suitable for nonreciprocal gyromagnetic device applications," *IEEE Transactions on Microwave Theory and Techniques*, Vol. 17, 1087–1090, 1969.
5. Bedair, S. S. and I. Wolff, "Fast, accurate and simple approximate analytic formulas for calculating the parameters of supported coplanar waveguides for MMIC's," *IEEE Transactions on Microwave Theory and Techniques*, Vol. 40, 41–48, 1992.
6. Malherbe, J. A. G. and A. F. Steyn, "Compensation of step discontinuities in TEM-mode transmission lines," *IEEE Transactions on Microwave Theory and Techniques*, Vol. 26, No. 11, 883–885, 1978.
7. Simons, R. N., *Coplanar Waveguide Circuits, Components, and Systems, Wiley Series in Microwave and Optical Engineering*, New York, 2001.

SPECAN Azimuth Pre-processing for Bistatic Spotlight SAR Imaging

Lei Zhang[1], **Meng-Dao Xing**[1], **Cheng-Wei Qiu**[2], **Zheng Bao**[1], **and Wei Jing**[1]

[1]Key Lab for Radar Signal Processing, Xidian University, Xi'an 710071, China
[2]Radar and Signal Processing Lab, National University of Singapore
Singapore 117576, Singapore

Abstract— We expand the spectral analysis (SPECAN) convolution to support the generation of high resolution imagery over a large scene via bistatic spotlight synthetic aperture radar. An azimuth pre-processor overcoming the Doppler aliasing of the echoed signal is proposed. Since the spatial characteristics of the returns are preserved, the pre-processor is compatible with conventional focusing approaches. The proposed method is validated by simulated data.

1. INTRODUCTION

Modern synthetic aperture radar (SAR) is required to provide imagery with both high resolution and large processing scene. By illuminating the same scene during the data acquisition interval, the spotlight SAR provides high resolution with a considerable scene. The receiving instantaneous Doppler bandwidth depends on the width of the scene in azimuth, which should be lower than the pulse repetition frequency (PRF). In the mode, the azimuth bandwidth is generally much higher than PRF and azimuth spectral aliasing occurs. Straightforward application of the precise imagery formation, such as the chirp scaling algorithm (CSA) [1], is thus ill-suited.

The Two-Step focusing approach [2] is a novel method to overcome the limit and provide high precision in monostatic imagery. Its essence is to filter data with a SPECAN convolution in the azimuth time domain, and compensate the introduced phase term in the frequency domain. Using the long-track alignment and formatting system (ATAFS) to reformat the data support and apply proper interpolations to reconstruct the ideal support, in [3] three algorithms have been proposed to focus widefield spotlight SAR image. To our knowledge, a few approaches have been proposed to produce bistatic spotlight SAR imaging. The bistatic polar formation algorithm (BPFA) [4] is an effective one to provide fine resolution and overcome the aforementioned limitation. However, similar with the monostatic PFA, the imaging scene is limited due to the presence of the range curvature quadratic phase error (RCQPE). Another approach is the sub-aperture processing [5].

In this paper, we extend the monostatic wildfield spotlight SAR imaging algorithms and propose a pre-processor based on the bistatic SPECAN convolution. The essence of the pre-processor is utilizing SPECAN convolution to remove the Doppler aliasing caused by long synthetic aperture, along with preserving the spectral spatial characteristics. The chirp phase approximation in azimuth of the returns is the precondition of the pre-processor. The method is compatible with the current bistatic SAR focusing algorithms.

2. BISTATIC SIGNAL MODEL

The bistatic geometry is shown in Fig. 1, where the coordinate is built according to the transmitting trajectory with the scene center as the origin. The transmitter and receiver are with different velocity vectors of v_T and v_R. The receiving coordinates are constructed in Fig. 2. Define the centers of synthetic apertures as (x_{T0}, y_{T0}, z_{T0}) and (x_{R0}, y_{R0}, z_{R0}) respectively. We assume that a target scatterer P at (x_T, y_T, z_T) and (x_R, y_R, z_R) in transmit and receive coordinates is on the ground scene. Assuming that a linear frequency modulated signal with frequency rate γ is transmitted, the echoed signal from P in the range frequency domain is given as follows:

$$s(K_r,\, t) = A(K_r) \cdot \mathrm{rect}\left(\frac{t - t_b}{T}\right) \cdot \exp(-jK_r R) \tag{1}$$

where K_r is the range wavenumber, K_{rc} is the wavenumber center, $A(K_r) = \mathrm{rect}(\frac{K_r - K_{rc}}{bcT_p/2}) \cdot \exp(-j\frac{c^2}{16\pi\gamma}K_r^2)$, t is the azimuth time, and $\mathrm{rect}(\frac{t-t_b}{T})$ is the azimuth time window centered on

t_b, describing the time interval during which the point scatterers are within the beamwidth of the transmit and receiver antennas. Instantaneous range is

$$R = \frac{\sqrt{R_{bt}^2 - (v_t t - x_t)^2} + \sqrt{R_{br}^2 - (v_r t - x_r)^2}}{2} \tag{2}$$

and $x_t = x_T - x_{T0}$, $x_r = x_R - x_{R0}$. We can obtain the Doppler spectrum by using an azimuth Fourier transform (FT) as

$$s(K_r,\, f_d) = \int_T s(K_r,\, t) \exp(-j2\pi f_d t) dt \tag{3}$$

where T is the azimuth coherent processing interval. Several techniques [6, 7] are available to deduce the analytic formula for $s(K_r,\, f_d)$. These methods form the basis for the several focusing approaches [8, 9]. However, in the spotlight SAR mode, the synthetic aperture bandwidth (B_{sa}) is usually higher than PRF, and thereby the Doppler spectrum is aliasing. Fig. 3 shows the time-frequency characteristic of bistatic spotlight SAR returns.

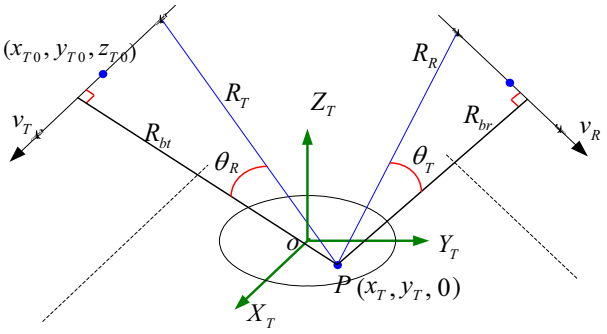

Figure 1: Bistatic SAR geometry.

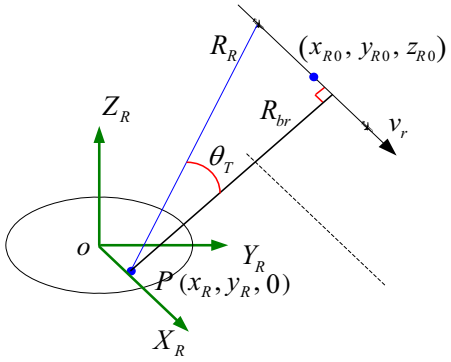

Figure 2: Receiving geometry.

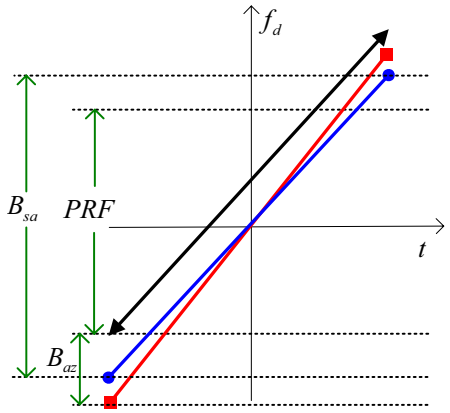

Figure 3: Aliasing spectrum.

3. SPECAN CONVOLUTION PRE-PROCESSING

SPECAN convolution is a n efficient algorithm for scan and spotlight SAR imaging. In the convolution, a quadratic phase azimuth deramping is used followed by a Fourier transform (FT) to focus the signal in azimuth. The azimuth deramping function is updated with range due to the azimuth focusing depth. One of its advantages is overcoming the azimuth spectral folding effect, as the quadratic phase of the returns is approximately compensated by the azimuth deramping operation. In what follows, we expand this to build a bistatic spotlight SAR pre-processing procedure.

We use the azimuth chirp rate of the signal of scene center to construct a reference phase function as follows:

$$H_q = \exp\left[j \cdot \left(\frac{K_{rc}v_t^2}{4R_{ct}} + \frac{K_{rc}v_r^2}{4R_{cr}}\right) \cdot t^2\right] = \exp\left(j2\pi\delta t^2\right) \tag{4}$$

where R_{ct} and R_{cr} represent the closest slant range from the center point to transmitting and receiving tracks respectively. For simplicity, we define the chirp rate as

$$\delta = \left(\frac{v_t^2}{2R_{ct}\lambda} + \frac{v_r^2}{2R_{cr}\lambda}\right) \tag{5}$$

Then the convolution between signal and the quadratic phase function is given by

$$\begin{aligned} s\left(K_r,\, t'\right) &= \int_T s\left(K_r,\, t\right) \exp\left[j2\pi\delta\left(t'-t\right)^2\right] dt \\ &= \exp\left(j2\pi\delta t'^2\right) \cdot \int_T s\left(K_r,\, t\right) \exp\left(j2\pi\delta t^2\right) \cdot \exp\left(-j4\pi\delta t' t\right) dt \end{aligned} \tag{6}$$

The convolution includes three steps: 1) the product between $s(K_r,\, t)$ and reference function approximately removes quadratic phase related to the center frequency; 2) taking a curve integration, which can be implemented by FT, and it approximately compresses the signal in azimuth, as the azimuth quadratic phase is approximately removed in former step; and 3) the residual quadratic phase $\exp(j2\pi\delta t'^2)$ is compensated, by which the spectrums in the $[K_r,\, f'_d]$ frequency domain is aligned. $f'_d(f_d)$ denotes the Doppler coordinate corresponding to $t'(t)$. The convolution is truly a time-frequency transform. Based on (6) and Fourier theory, we have

$$f'_d = 2\delta t \qquad\qquad f_d = 2\delta t' \tag{7}$$

The extent of f'_d is defined as $\Delta f'_d$, which equals to the bandwidth of $\exp(j2\pi\delta t^2)$ as $\delta \cdot T$. It is indicated that if we increase the signal length by padding zeros ΔT, the bandwidth of the reference function can be increased up to $\delta \cdot (\Delta T + T)$ while B_{sa} remains the same. In the following, we can find that the spectrum is transformed into the $(K_r,\, f'_d)$ domain without Doppler aliasing if $\delta(\Delta T + T) \geq B_{sa}$.

Use an azimuth FT to transform $s(K_r,\, t')$ into frequency domain as follows:

$$\begin{aligned} s\left(K_r,\, f'_d\right) &= \int_{T'} s\left(K_r,\, t'\right) \exp\left(-j2\pi f'_d t'\right) dt' \\ &= \int_{T'} \exp\left(j2\pi\delta t'^2\right) \cdot \left[\int_T s\left(K_r,\, t\right) \exp\left(j2\pi\delta t^2\right) \exp\left(-j4\pi\delta t' t\right) dt\right] \cdot \exp\left(-j2\pi f'_d t'\right) dt' \\ &= \exp\left(-j\pi\frac{f'^2_d}{2\delta}\right) \int_T s\left(K_r,\, t\right) \exp\left(-j2\pi f'_d t\right) dt \end{aligned} \tag{8}$$

By removing the residual phase term outside the integral, the spectrum becomes

$$s\left(K_r,\, f'_d\right) = \int_T s\left(K_r,\, t\right) \exp\left(-j2\pi f'_d t\right) dt \tag{9}$$

From (3) and (9), it can be found that the spectrum formula remains the same, while the frequency coordinate is scaled from f_d to f'_d. The azimuth coordinates have the relations:

$$T = N \cdot \frac{1}{PRF} \quad \Delta f_d = PRF, \quad \Delta f'_d = 2\delta \cdot T \quad T' = \frac{\Delta f_d}{2\delta} \tag{10}$$

where N is the azimuth sample number, Δf_d is the original Doppler domain span, $\Delta f'_d$ and T' are the frequency and time span after SPECAN convolution respectively. Based on (7) and (10), the

scaling factor of the frequency domain is given by

$$\varepsilon = \Delta f_d / \Delta f_d' = \frac{PRF^2}{2\delta \cdot N} \tag{11}$$

The scaling function of the convolution on the frequency spectrum is shown in Fig. 4. The improvement of the preprocessor by zero-padding is presented in Fig. 5. In Fig. 5, the three bold lines represent the time-frequency characteristics of returns from different directions. The broken lines in green represent the respective quadratic phase multiplied in the procedure above. T is the azimuth time interval with ΔT denoting the additional azimuth zeros padded. Based on (16), we respectively substitute f_d and t with t' and f_d' to obtain Fig. 5. By zero-padding ΔT, the azimuth frequency extension equivalently increases with Δ. Thus no spectral folding occurs in the scaled frequency domain. However, the time spectrum is aliasing in the t' domain, which is the same in the f_d domain. It indicates that the following imagery processing should be operated in the f_d' domain. The steps such as motion compensation and range walking from squint angle correction in the t_m domain before the SPECAN preprocessing.

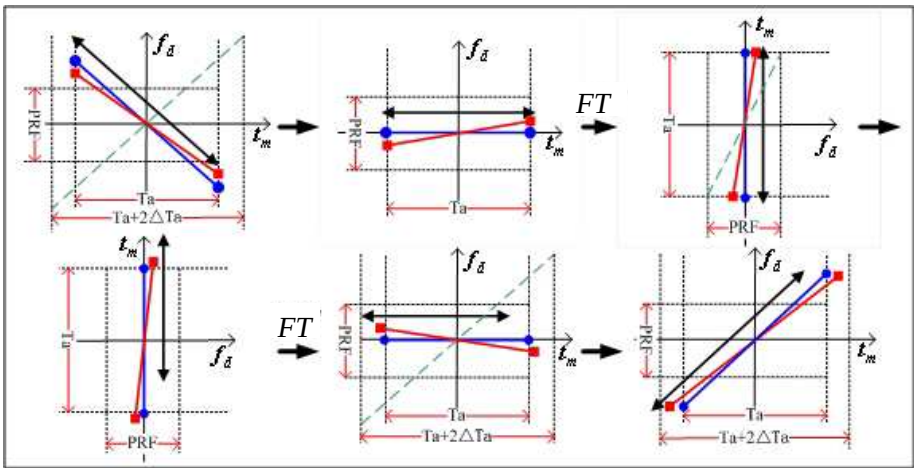

Figure 4: Procedure of SPECAN convolution pre-processing.

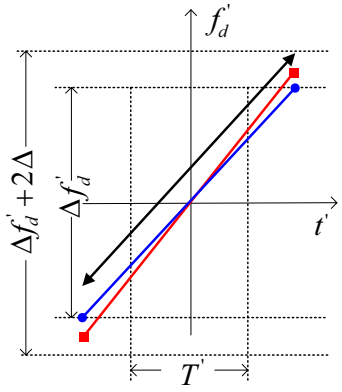

Figure 5: Output of the pre-processor.

4. SIMULATIOON

We use a general bistatic SAR configuration to generate simulation data in time domain. The data is utilized to validate the proposed pre-processor for Doppler aliasing suppression. The simulation parameters are listed in Table 1. The Doppler bandwidth is numerically calculated with the geometry parameters (approximately two times of the sampling rate), resulting in serious Doppler aliasing in the original spectrum as Fig. 6(a) shows. After the SPECAN pre-processing with 512 zeros padded, the spectrum in the scaled Doppler domain is shown in Fig. 6(b). The Loffeld's

bistatic format (LBF) [6] is utilized to derive the 2D spectrum analytic formula of (8). And the 2D spectrum matched filtering is carried out after SPECAN preprocessing to focus the data. The focal without being windowed is evaluated. As the LBF is validated to be precise, the validity of the SPECAN pre-processor is confirmed by the simulated results.

Table 1: Bistatic parameters.

Simulation parameters	transmitter	receiver
Velocity in x direction	150 m/s	118.20 m/s
Velocity in y direction	0	21.47 m/s
Velocity in z direction	0	0
Center frequency	5 GHz	
Range bandwidth	200 MHz	
Doppler bandwidth	327.8 Hz	
Pulse repetition frequency	150 Hz	
Altitude	3000 m	2000 m
Range to point target at t=0	15370 m	10247 m
Squint angle at t=0	5.64 degree	4.51 degree

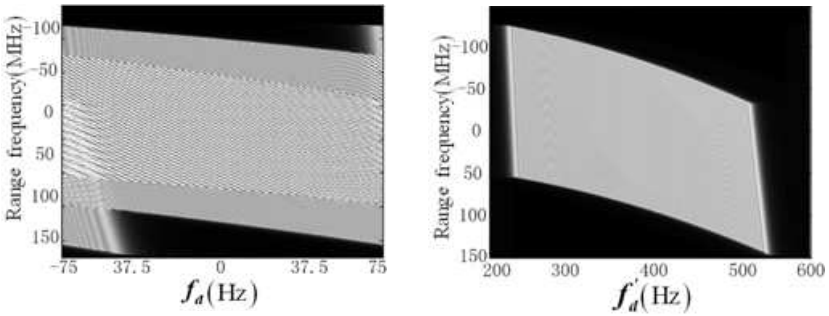

(a) Original spectra (b) Preprocessed spectra

Figure 6: Point spectra before and after pre-processing.

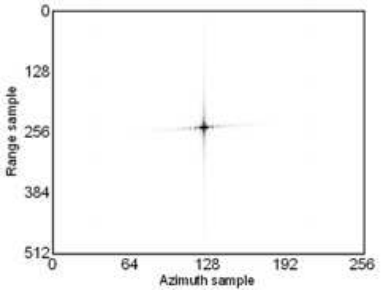

Figure 7: Point focal after LBF matched filtering.

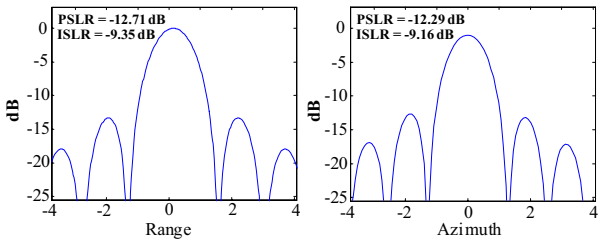

(a) Range compression (b) Azimuth compression

Figure 8: Measurement of focal.

5. CONCLUSION

A SPECAN convolution based pre-processor is proposed to overcome the Doppler aliasing for bistatic spotlight SAR imaging. Its essence is to employ SPECAN convolution to scale the frequency domain and suppress the Doppler folding. Because the pre-processor preserves the spatial characteristics and analytic form of the spectrum in the scaled frequency domain, it is compatible with available bistatic focusing approaches. By zero-padding, we can improve its performance with suppressing Doppler ambiguity. The method is capable of supporting generation of high resolution imagery over a large scene, which has been verified by simulated data of general bistatic configuration.

ACKNOWLEDGMENT

This work was supported by the National Natural Science Foundation of China under grant 60890072.

REFERENCES

1. Raney, R. K., H. Runge, R. Bamler, I. G. Cumming, and F. H. Wong, "Precision SAR processing using chirp scaling," *IEEE Trans. Geosci. Remote Sensing*, Vol. 32, No. 4, 786–799, July 1994.
2. Lanari, R., M. Tesauro, E. Sansosti, and G. Fornaro, "Spotlight SAR data focusing based on a two-step processing approach," *IEEE Trans. Geosci. Remote Sensing*, Vol. 39, No. 9, 1993–2003, Sept. 2001.
3. Carrara, W. G., R. S. Goodman, and M. A. Ricoy, "New algorithms for widefield SAR image formation [A]," *IEEE Radar Conference [C]*, 38–43, Philadelphia, PA, 2004.
4. Rigling, B. D. and R. L. Moses, "Polar format algorithm for bistatic SAR," *IEEE Trans. Aerospace Electronic Systems*, Vol. 40, No. 4, 1147–1159, Oct. 2004.
5. Mittermayer, J., A. Moreira, and O. Loffeld, "Spotlight SAR data processing using the frequency scaling algorithm," *IEEE Trans. Geosci. Remote Sensing*, Vol. 37, 2198–2214, Sept. 1999.
6. Loffeld, O., H. Nies, V. Peters, and S. Knedlik, "Models and useful relations for bistatic SAR processing," *IEEE Trans. Geosci. Remote Sensing*, Vol. 42, No. 10, 2031–2038, Oct. 2004.
7. Neo, Y. L., F. Wong, and I. G. Cumming, "A two-dimensional spectra for bistatic SAR processing using series reversion," *IEEE Geoscience Remote Sensing Letters*, Vol. 4, No. 1, 93–96, Jan. 2007.
8. Natroshvili, K., O. Loffeld, H. Nies, A. M. Ortiz, and S. Knedlik, "Focusing of general bistatic SAR configuration data with 2-D inverse scaled FFT," *IEEE Trans. Geosci. Remote Sensing*, Vol. 44, No. 10, 2718–2727, Oct. 2006.
9. Neo, Y. L., F. H. Wong, and I. G. Cumming, "Processing of azimuth-invariant bistatic SAR data using the range Doppler algorithm," *IEEE Trans. Geosci. Remote Sensing*, Vol. 46, No. 1, 14–21, Jan. 2007.

Developing Polarimetric GPR System

Xuan Feng[1], **Li-Li Li**[1], **Li-Min Liu**[2], **and Cai Liu**[1]
[1]College of Geo-Exploration Science and Technology, Jilin University
No. 6 Xi Minzhu Street, Changchun 130026, China
[2]College of Instrumentation and Electrical Engineering
No. 6 Xi Minzhu Street, Changchun 130026, China

Abstract— Most ground penetrating radar (GPR) transmits and receives radio waves with a single polarization. That is, they measure the reflected power returned from the radar's horizontal pulses or vertical pulses. Polarimetric GPR measure the reflected power returned from both horizontal and vertical pulses. By comparing these reflected power returns in different ways (ratios, correlations, etc.), we are possibly to enhance signal and obtain more information on the size, shape, and physical property, etc. We are developing a stepped-frequency (SF) polarimetric GPR system, which consists of two transmit antennas, two receive antennas, scanning platform, and vector network analyzer (VNA). VNA can generate ultra-wideband electromagnetic signal. Vivaldi antennas are employed in this system, because it is a kind of microstrip antenna, which possesses a wide bandwidth and a high cross-polarization ratio. Four antennas are oriented downwards to the ground and are organized into a tetrahedral square. The measurement method is to alternate between horizontal and vertical polarizations with each successive pulse. That is, first horizontal, then vertical, then horizontal, then vertical, etc. And, of course, after each transmitted pulse there is a short listening period during which the GPR receives both reflected horizontal and vertical polarization radio wave pulses. We test the polarimetric performance of the GPR system using both copper plate reflector and copper trihedral corner reflector. When the reflector is the copper plate, strong co-polarimetric (VV polarimetric and HH polarimetric) signals are detected and very weak cross-polarimetric (HV polarimetric and VH polarimetric) signals are detected. When the reflector is the copper trihedral corner reflector, strong cross-polarimetric signals are detected.

1. INTRODUCTION

Ground-penetrating Radar (GPR) is an effective shallow subsurface detection tool that detects the structure and characteristics of target by transmitting and receiving high-frequency electromagnetic pulse, and is an important non-destructive detection technique. Generally two parallel antennas are used in GPR detection and the Co-polarization model is chosen. So common GPR only acquire single ploarimetric data.

Now many radar systems are designed to transmit microwave radiation of orthogonal polarization pairs, for example, that is either horizontally polarized (H) or vertically polarized (V). A transmitted wave of either polarization can generate a backscattered wave with a variety of polarizations. It is the analysis of these pairs of orthogonal transmitting and receiving polarization combinations that constitutes the science of radar polarimetry. HH — for horizontal transmit and horizontal receive; VV — for vertical transmit and vertical receive; HV — for vertical transmit and horizontal receive, and VH — for horizontal transmit and vertical receive. The combination of HH HV VH VV also called fully polarization [1].

In this work, we are trying to import the fully polarization technique into the GPR system and developing a full polarimetric stepped-frequency GPR system. Also we test the polarimetric performance of the GPR system using both copper plate reflector and copper trihedral corner reflector.

2. POLARIMETRIC GPR SYSTEM

We are developing a vector network analyser-based GPR system, using the computer, adapted antipodal Vivaldi antenna and a vector network analyser for its flexibility in selection of frequencies. Figure 1 shows the stepped-frequency GPR system and the three-dimension scanning platform.

In this GPR system, we used four kinds of antenna sets, shown in Figure 2, including VV model, HH model, VH model and HV model. Depending on these antenna sets, the system possibly acquires full polarimetric GPR data. Vivaldi antennas are employed in this system. It is a kind of microstrip antenna, which possesses a wide bandwidth and a high cross-polarization ratio [2]. It has an advantage of being easy to be manufactured to make an antenna array for a

Figure 1: GPR system.

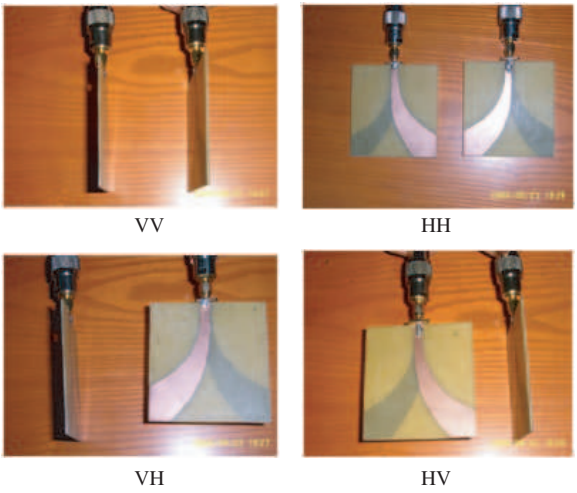

Figure 2: Antenna sets.

stand-off down-looking GPR since it can be made on a thin and light weight circuit board. Figure 3 shows the measured transmission between two antipodal Vivaldi antennae facing each other. In the figure, VV is for vertical transmit and vertical receive, and HV is for vertical transmit and horizontal receive, and VH — for horizontal transmit and vertical receive.

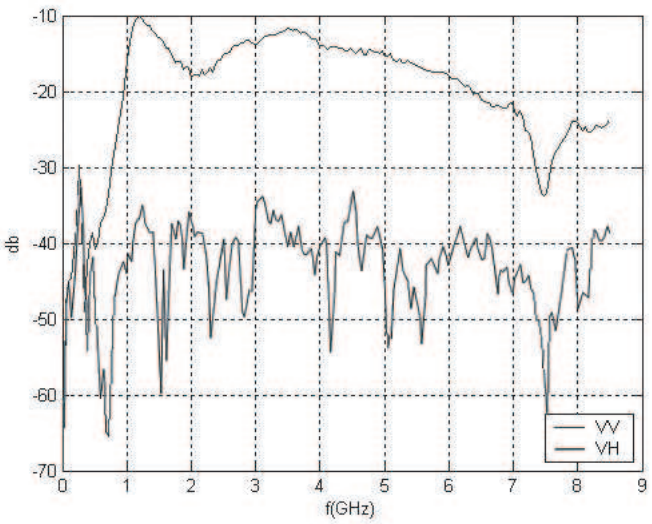

Figure 3: Measured transmission between two antipodal Vivaldi antennae facing each other.

3. EXPERIMENTS

We test the polarimetric performance of the GPR system using both copper plate reflector shown in Figure 4 and copper trihedral corner reflector shown in Figure 5. The parameters of the measurement are shown in Table 1. The frequency range is from 300 KHz to 8.5 GHz.

Table 1: The parameters of the experiments.

sample	bandwidth	Center frequency	average	power	IFBW
201	300 KHz–8.5 GHz	4.25 GHz	30	10 dB	30 KHz

Figure 6 and Figure 7 show the echo signals. In figures, dot lines show the echo signals from copper plate reflector and solid lines show the echo signals from copper trihedral corner reflector.

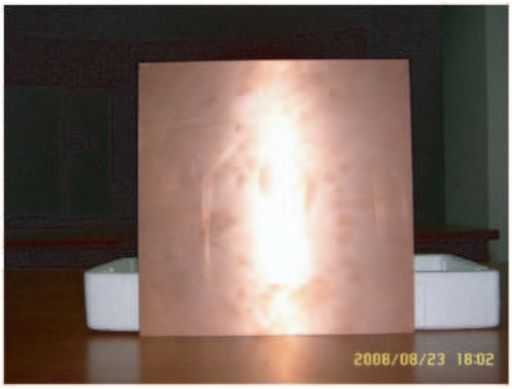

Figure 4: Copper plate reflector.

Figure 5: Copper trihedral corner reflector.

In the VV model, the echo signal from copper plate reflector is stronger than the echo signals from copper trihedral corner reflector. But in the VH model, the echo signal from copper plate reflector is weaker than the echo signals from copper trihedral corner reflector.

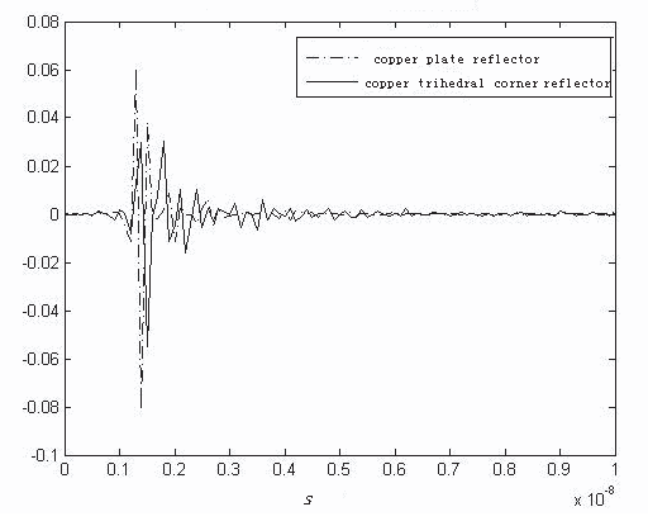

Figure 6: Echo signal in the VV model.

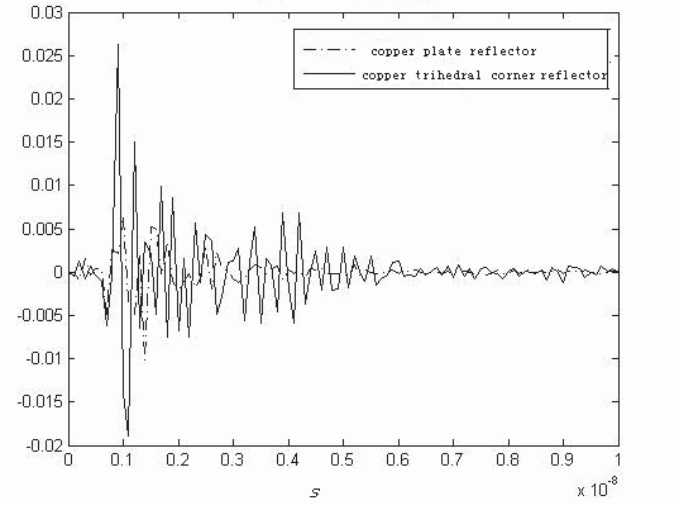

Figure 7: Echo signal in the VH model.

4. DISCUSSION AND CONCLUSION

We are developing a stepped-frequency polarimetric GPR system. Also we test the polarimetric performance of the GPR system using both copper plate reflector and copper trihedral corner reflector. When the reflector is the copper plate, strong co-polarimetric (VV polarimetric) signals are detected and very weak cross-polarimetric (HV polarimetric) signals are detected. When the reflector is the copper trihedral corner reflector, strong cross-polarimetric signals are detected. So depending on this feature, we possibly identify the target.

ACKNOWLEDGMENT

This work was supported in part by the National Natural Science Foundation of China under Grant 40704020, Jilin Provincial Science & Technology Department under Grant 20070123, Scientific Research Foundation for the Returned Overseas Chinese Scholars, State Education Ministry under Grant 2007-1108.

REFERENCES

1. Zhou, Z.-S., W.-M. Boerner, and M. Sato, "Development of a ground-based polarimetric broadband SAR system for noninvasive ground-truth validation in vegetation monitoring," *IEEE Transactions on Geoscience and Remote Sensing*, Vol. 42, No. 9, 1803–1810, 2004.
2. Guillanton, E., J. Y. Dauvignac, C. Pichot, and J. Cashman, "A new design tapered slot antenna for ultra-wideband applications," *Microwave Opt. Tech. Lett.*, Vol. 19, 286–289, 1998.

Review of GPR Rebar Detection

Xian-Qi He, **Zi-Qiang Zhu**, **Qun-Yi Liu**, **and Guang-Yin Lu**
Info-physics and Geomatics School of Central South University, China

Abstract— The background and current state of the art of ground penetrating radar testing of rebar in concrete is briefly reviewed. This encompasses developments of Polarization in rebar detection, diameter detection, corrosion detection,neural network and other automatic method in rebar detection.

1. INTRODUCTION

Radar uses an electromagnetic signal and was first applied by Huelsmeyer to detect metal objects in 1904 [1]. Applications of GPR to Structures started to grow in the 1980s [2]. Initial civil engineering applications included condition assessment of highway pavements and their foundations, with applications to structural concrete focusing on inspection of bridge decks. Cantor [3] reviewed early developments in these areas in 1984, and Clemena reviewed radar testing of concrete in 1991 [4]. Bungey [5] reviewed the recent development in equipment, materials characteristics, signal processing, numerical modeling and practical aspects of applications and interpretation in concrete survey, authorities guidance was published In the UK and in USA for the test of concrete [5–8].

Principle current and potential applications are summarized below:

Estimation of element thickness from one surface.

Location of reinforcing bars and metallic ducts, and estimation of the concrete cover depth.

Determination of major construction features.

Location of moisture variations.

Location of voids.

Localization and the dimensions of voids.

Estimation of bar size [5, 9–15].

Amongst these, location of reinforcing bars is an important and popular application that has received particular attention with emphasis on the effects of bar size, spacing and depth upon ability to detect individual bars and the problems caused by masking of deeper features [5–16].

In 1997, Concrete Society published the standard specification for the radar methodology [17], while in 2003 the Federation of Construction Material Industries of Japan proposed two drafts test standard (Method for locating of rebars in reinforced concrete by radar and Method for locating of rebars and determining the diameters of rebars in reinforced concrete by electromagnetic induction) [18].

Ground-penetrating-radar is an electromagnetic investigation method. Mostly it is used in reflection mode where a signal is emitted via an antenna into the structure under investigation. The arrival time and the ampleness of reflected signals caused by changes in material properties is recorded and analyzed. The result can be present in A-scan, B-scan and C-can. In civil engineering applications it is more conventional to present these same results by converting the magnitude of the signal into a grey-scale or color representation (B-scan) [5]. The vertical axis is a time axis. In order to obtain depths the signal velocities in the different materials under investigation have to be known and the time interval (wave propagation time), can be transformed to a space dimension (depth) [19, 20].

For the reinforcement concrete, concrete could be regarded as isotropy medium in reinforced concrete structure, but the rebar would be regarded as abnormal objects [21]. Radar wave would be shapely reflected at the interface between rebar and concrete because there exists strong abnormality between the two mediums. As a radar antenna is translated across the surface of the concrete a series of signals returning to the receiving antenna can then be presented as the raw results. Signal reflections from reinforcing bars displaying a hyperbolic image format (Figures 1 and 2).

Detection of reinforcing bars in concrete is one of the most widespread applications of GPR in Civil Engineering [20, 22, 23], but the results is very difficult to interpret and may require the skills of an experienced operator and the use of lengthy manual post-processing and subjective expertise to

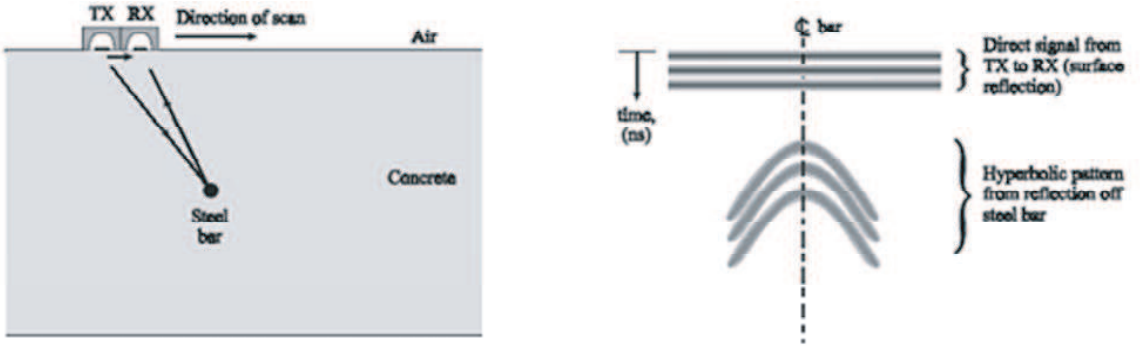

(a) Sub-surface reflection (b) Singal reflection image

Figure 1: Hyperbolic reflection image from steel bar concrete.

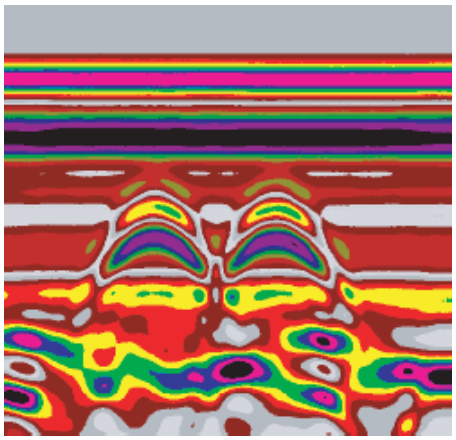

Figure 2: Radar image from sub-surface steel bars.

produce a reliable end result [10, 15]. Because the visual representation of this result can bear little resemblance to the shape or size of the sub-surface bar. Recent years many automatic algorithms have been developed for interpretation [5]. Neural networks potentially offer considerable scope for automatic interpretation of radar results [24, 25], however, success has so far been limited to straightforward cases such as reinforcing bar location. Bar sizing is more difficult and there is little evidence of industrial usage.

The potentially enhanced value of test combinations is widely recognized, for example by combining radar with infra-red thermography [26] or impact echo [27] according to the application whilst combination with both Impact Echo and radiography [28] has also been proposed.

Optimization of antenna orientation, to take advantage of signal polarization, is an important feature in successful location of reinforcing bars in time-depth slice [29].

2. POLARIZATION AND REBAR DETECTION

Polarization, the direction and amplitude of the electromagnetic field as a function of time and space, can have a significant impact on the GPR response, and is therefore important to consider during data acquisition, processing and interpretation [30–34]. Investigations have demonstrated the potential of using the polarization characteristics of GPR for defining the size, shape, orientation, and material properties of buried objects [35].

The scattering properties of rebar are strongly polarization dependent. The backscattered fields from rebar may be strongly depolarized depending on the orientation of the rebar relative to the antennas, and the radius of the rebar compared to the incident wavelength [36]. These polarization dependent scattering properties have important implications for rebar detection, survey design, and data interpretation. The radiation from rebar is linearly polarized, thus the reflections can be maximized by varying the antenna orientation [5].

Most commercial GPR antennas are dipole antennas that radiate linearly polarized energy with the majority of the radiated electric field oriented along the long axis of the dipole [37, 38]. A co-pole antenna configuration receives reflected and scattered energy that has the same polarization as the incident energy. Rebar yield strong reflections when oriented parallel to the long axis of a dipole transmit antenna in a co-pole antenna configuration, but yield weak reflections when oriented orthogonal to the transmit antenna.

A cross-pole configuration is less sensitive to smooth planer targets, and is more sensitive to targets that yield more depolarized energy [32]. It is important however to consider polarization when planning a GPR field survey, as the sensitivity of cross-pole and co-pole antenna arrangements are different depending on the type of target and subsurface conditions.

Crossed-dipole antennas can be used to reduce clutter and improve antenna isolation when stratigraphy is considered clutter and only rebar are of interest. Maximum amplitudes are observed over rebars when the crossed-dipoles are oriented at 45° to the rebars. Optimization of antenna orientation, to take advantage of signal polarization, is an important feature in successful location of reinforcing bars in the time-depth slice.

For the processing of GPR data, scalar migration algorithms developed for three-dimensional seismic data are commonly used. However, these algorithms do not account for the radiation characteristics of GPR source and receiver antennas or the vectorial nature of radar waves. A multi-component vector imaging algorithm that takes into account the polarization and vectorial radiation characteristics of GPR data has recently been developed or far-field [39, 40]. R. Streich and J. V. D. Kruk [41, 42] developed multi-component vector imaging scheme that jointly images co-polarized and cross-polarized data accounts for the far-, intermediate-, and near-field contributions to the radiation patterns. Polarization of the electric field can be used to reduced unwanted reflections [43, 44]. Polarimetric stepped-frequency GPR and fully-polarimetric processing technique have also be developed considering the polarization [45] for GPR detection.

Polarization can be used to improve S/N ratio, Co-pole and cross-pole antenna configurations can be combined with polarization dependent scattering characteristics of subsurface objects to recognize and reduce antenna ring-down for improved imaging and interpretation of rebars [46, 47], also can be used to detect the dual layer rebar mesh [48].

Detection algorithm searches a target response using neural networks and discriminates the target response of a buried pipe among clutters by analyzing the polarization characteristics. Polarization also can be used to discriminate rebar from other linear target such a dielectric cylinder [49].

3. MEASUREMENT OF REBAR DIAMETER

It is known that Ground Penetrating Radar (GPR) can be used to provide an indicative measurement of the size of reinforcement bars [50] despite it is difficult and little industrial application. Vincent Utsi [51] had used GPR to estimates of bar diameter based on the X/N amplitude ratios (the amplitudes ratios of the bar signals along and across the E-field) and the rebar sizing accuracy is about 20%. As the X/N ratio is easy to be distorted, so practical application is highly dependent on the specifies of the built environment.

M. R. Shaw developed a neural network approach [52] to automate estimation the diameter of reinforcing bars by analyzing the data taken with the transducer axis parallel and then orthogonal to the bar using a MLP neural network. It is estimated effectively, but not very accuracy and it is conditionally.

Rebar is one of the cylinder targets which is popular for GPR detection, for estimation of the diameter of rebar there also have two procedure as other cylinder such as pipe.

One is the mathematical model of the hyperbola another is hyperbola fitting.

The reflection signal present in radargram is a hyperbola as show in Figure 3, so we can establish some relation between the radius of rebar and the geometry of the hyperbola.

Stolte and Nick [53] investigate the relationship between cylinder radius and hyperbola eccentricity for the purpose of migration, while Olhoeft [54] attempts in to derive radius information from the curvature of the hyperbola apex with human intervention. Al-Nuaimy [55] et al., presented one model relates the two-way travel time t to the horizontal position x and the velocity of propagation v. But this model relies on the assumption that the hyperbolic signatures, result from point reflectors, and hence the radius is assumed to be zero. Using this model to characterize the signatures of such targets leads to erroneous information. S. Shihab and W. Al-Nuaimy [56, 57] develop a more generalized equation that takes into account the possibility of a finite radius R. This allows for cylinders of arbitrary radii to be detected and characterized uniquely from a single

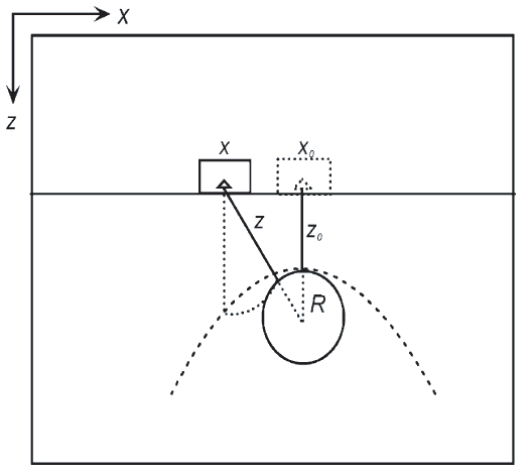

Figure 3: Effect of changing the value of R on the resulting hyperbola.

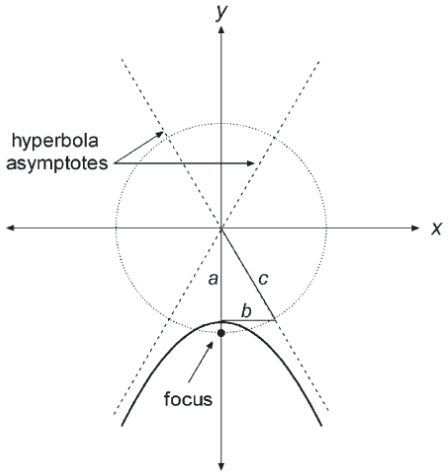

Figure 4: A general hyperbola with its asymptotes and related parameters indicated.

radargram. S. Shihab also establish the following relation between R and the general hyperbola centered around (x_0, y_0) Figure 4.

$$a = t_0 + \frac{2R}{v} \tag{1}$$

$$b = \frac{v}{2}\left(t_0 + \frac{2R}{v}\right) \tag{2}$$

The fitting of primitive models to image data is a basic task in pattern recognition,fitters specific to hyperbola is important as the hyperbolic signature is popular for GPR detection. Hough transform-based approaches develop by Al-Nuaimy [58] are simple, but are computationally expensive. Polynomial methods [5] develop by Olhoeft do not adequately characterize the hyperbola in terms of the parameters a and b, and hence fall short of providing the necessary information for target identification. S. Shihab and W. Al-Nuaimy [57] develop a fitter based on direct least-square method and was specifically adopted for a hyperbolic conic section, overcoming the above limitations. It can adequately deal with noisy data having missing points and is completely efficient. Both a, b and t_0 are obtained as a result of the fitting process and v and R can be calculate from a and b.

The fitting technique is applied on a variety of real hyperbolic signatures that are collected from a controlled test site, the results indicate this technique is fully capable of successfully estimating the depth and radius to within 10%, which validates the method and justify the assumptions used. In two-dimensional data [59] obtained from orthogonal sounding of cylinders are analyzed. It is shown that the generalized Hough method can be used to measure buried pipe diameters from radar measurements. An interactive technique of 3D-data processing is developed by B. A. Yufryakov and O. N. Linnikov [60] to estimate cylindrical objects radius directly and automatically.

A. Dolgiy and V. Zolotarev [61], considered some practical examples of pipes radius estimation on the basis of the technique presented in [56], and designated some problems appeared during this process. The pipe radius estimations in and were performed without taking into account, for example, random errors of measurement of delay time for the signal reflected from pipes [50, 52]. A. Dolgiy and V. Zolotarev [62] use the techniques based on the weighted least squares method, the recursive Kalman filter, the maximum likelihood method, the direct least-square fitting of hyperbola and the Nelder-Mead direct search method of optimization.

For a pipe with smaller radius, fast attenuation of the GPR signal was observed with distance increase between the antenna and pipe. Therefore small difference between maximum and minimum delay times of the signal reflected from pipe and also short azimuthal length of a hyperbola were acquired. As a result the error for estimation of pipe radius is increased.

4. CORROSION DETECTION

Corrosion of rebar in concrete structure causes subsurface cracks and is a major cause of structural degradation that necessitates repair or replacement. Early detection of corrosion effects can limit the location and extent of necessary repairs, while providing long-term information about the infrastructure status [63, 64].

There are many factor that induce the rebar corrosion, among the various influential factors, moisture and chloride contents of concrete are predominant in the initiation of rebar corrosion, and reversely the rebar corrosion resulting in cracking and saplling of concrete cover and allow more infiltration of water and chloride and also cause delamination around rebars, the change of the water and chloride content along with the delamination around rebar provide the basic condition for using of GPR to detection rebar corrosion. Different GPR signatures may be used for detecting internal corrosion of steel reinforcement within the concrete. Moisture and dissolved chlorides within the concrete attenuate the radar signals that are reflected from embedded rebar [65]. They also decrease their average velocity of the reflected signal resulting in increased arrival times. Generally, lower relative reflection magnitudes and greater travel times are indicative of greater corrosion or deterioration of rebar [66–68], seeing Figure 5. the amplitude of rebar reflection in sound section is strengthener the amplitude of the corrosion or deteriorated section.

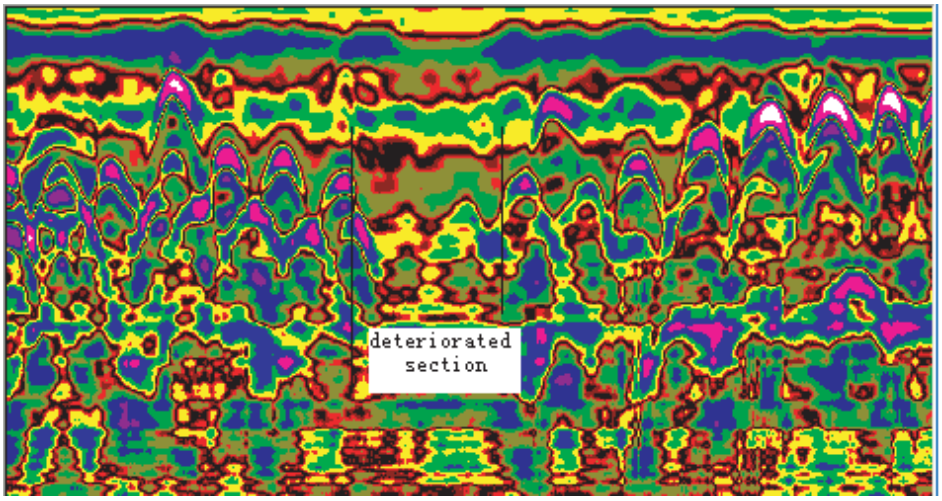

Figure 5: Example GPR data displaying from good rebars and carrion rebars.

Narayanan et al. [69] analyzed rebar reflection features to extract information regarding the corrosion state, a threshold level [70] was determined to differentiate between good and corroded rebars. The variance simulations helped to determine the reflectivity of the corroded rebar. Hubbard et al. [71] reported that the radar amplitude data of rebar reflection had the potential to indicate whether the corrosion had occurred. GPR method hold potential for direct and early detection of reinforcing bar corrosion, and that the combined use of GPR and electrical impedance techniques for assessing reinforcing bar corrosion state merits further study.

The location and cover depth of reinforcing steel in concrete structures has a great effect on the condition of that structure. A thin cover depth would result in rapid reinforcement corrosion, and therefore lead to early deterioration.

Rebar corrosion can result in cracking and spalling of the concrete cover and decreasing load-carrying capacity of concrete, so it is important to detection the corrosion at its early time, but for the most detection method used currently are destructive or time consuming, GPR is a potential method for direct and early detection of rebar corrosion, but most of this are carried out in laboratory, some are implement in site successfully combined with conventional method. The threshold of reflection amplitude used to discriminate the good and corroded rebar is different from on project to another and is influenced by many factors such as the water and chloride content of rebar cover and the type of the concrete in which the rebar are embedded. So there need further study before the GPR is used to detection rebar corrosion universally.

5. AUTOMATIC DETECTION

GPR displays are usually either manually scaled and interpreted, or stored and subsequently processed off-line. It require considerable operator skill, experience and time to produce a reliable end result. The processing aids that have been developed to aid in data interpretation are generally computationally expensive systems inadequate for on-site application. As GPR is becoming more and more popular as a shallow subsurface mapping tool, the volume of raw data that must be analyzed and interpreted is causing more of a challenge. There is thus a growing demand for automated subsurface mapping techniques that are both robust and rapid.

In the literature, there are still few published works dealing with the automatic detection of patterns associated with buried objects. In [72], the authors proposed also a method for extracting hyperbolic signatures of buried objects and hence estimating their position. In [73], the detection process is subdivided in three mainstages: 1) preprocessing step to reduce noise and undesired system effects; 2) image segmentation with an artificial neural network classifier to identify areas potentially containing object reflections; and 3) Hough transform to detect hyperbolic patterns. In [74], some preprocessing steps aiming at enhancing the signature of buried targets are implemented. Then, automatic image interpretation is carried out by a detector based on artificial neural networks. In [75], the authors applied a fuzzy clustering approach to identify hyperbolas from GPR images beforehand de-noised.

T. C. K. Molyneaux [76] examined the capability of three-layer, fully connected networks to detect the presence of a bar, the size of a bar, and the depth of a bar and demonstrated that the use of a neural network approach to interpret complex sub-surface radar results of embedded reinforcing bars is promising.

W. Al-Nuaimy and S. Shihab [77–81] has developed many automatic detection and interpretation method for GPR such as neural network techniques.

M. R. Shaw [52] used a neural network approach to automate and facilitate post-processing procedure and presented a novel technique for the estimation of the diameter of reinforcing bars. The results show that data taken with the transducer axis parallel and then orthogonal to the bar can be analysed by means of a MLP neural network to effectively estimate the diameter of embedded steel reinforcing bars.

M. R. Shaw [82] studied the use of a neural network approach to automate and facilitate the post-processing of ground penetrating radar results. The radar data is reduced to a simplified data set by using an edge detection routine. Signal reflections from reinforcing bars displaying a hyperbolic image format are detected using a multi-layer perceptron (MLP) network with a single hidden layer containing 8 nodes to recognize a simplified hyperbolic shape. The results showed that the use of a MLP neural network approach could be quite effective in automating the identification and location of embedded steel reinforcing bars from a radar investigation.

Francesco Soldovieri [83] exploit a linear inverse scattering algorithm in frequency domain based on the Born Approximation (BA); it allows to obtain satisfactory and reliable results in terms of localisation, sizing and shape of the buried objects and is computationally much more effective than nonlinear algorithms.

Edoardo Pasolli [84] proposed a novel system to identify and classify buried objects from GPR imagery using Genetic Algorithms and Support Vector Machines to detection and Classify Buried Objects.

ACKNOWLEDGMENT

Special thanks are due to Li Hua for his un-selfless help in the process of paper writing and willing exchange of information and ideas relevant to this topic.

REFERENCES

1. Ulricksen, C. P. F., "Application of impulse radar to civil engineering," 143, Doctoral Thesis, Department of Engineering Geology, Lund University of Technology, Sweden, 1982.
2. Forde, M. C., "Ground penetrating radar," *Introduction to Nondestructive Evaluation Technologies for Bridges, Transportation Research Board Pre-conference Workshop*, 2004.
3. Cantor, T. R., "Review of penetrating radar as applied to nondestructive testing of concrete," Malhotra, V. M., editor, ACI SP-82, 581–602, InsituyNondestructive Testing of Concrete, American Concrete Institute, 1984.
4. Clemena, G. G., "Short pulse radar methods," Malhotra, V. M., N. J. Carino, editors, *Handbook on Non-destructive Testing of Concrete*, Chapter 11, 253–74, CRC Press, Boston, 1991.

5. Bungey, J. H., "Sub-surface radar testing of concrete: A review," *Constr. Build Mater.*, Vol. 18, 1–8, 2004.
6. Concrete Society, "Guidance on radar testing of concrete structures," *Tech. Rep.*, Vol. 48, 88, 1997.
7. Matthews, S. L., "Applications of subsurface radar as an investigative technique," BRE Report BR340, CRC, London, 1998.
8. American Concrete Institute, "Non-destructive test methods fore valuation of concrete in structures," ACI 228.2R-98, 1998.
9. Barrile, V. and R. Pucinotti, "Application of radar technology to reinforce concrete structures: A case study," *NDT& E International*, Vol. 38, 596–604, 2005.
10. Maierhofer, C. and S. Leipold, "Radar investigation of masonry structures," *NDT& E International*, Vol. 34, 39–147, 2001.
11. Bungey, J. H., M. R. Shaw, S. G. Millard, and T. C. K. Molyneaux, "Location of steel reinforcement in concrete using ground penetrating radar and neural networks," Forde, M. C., editor, *Structural Faults and Repair*, 8, Engineering Technics Press, London, 2003.
12. Hamasaki, H., T. Uomoto, H. Ikenaga, K. Kishi, and A. Yoshimura, " Identification of reinforced in concrete by electro-magnetic methods," (http://www.ndt.net/article/ndtce03/papers/v006/v006.htm).
13. Binda, L., G. Lenzi, and A. Saisi, "NDE of masonry structures: Use of radar test for the characterisation of stone masonries," Forde, M. C., editor, *Proceedings of the Seventh International Conference on Structural Faults and Repair*, 505–14, ETC, Edinburgh, 1997.
14. Maierhofer, C., S. Leipold, D. Schaurich, L. Binda, and A. Saisi, " Determination of the moisture distribution in the outside walls of the S. Maria Rossa using radar," *Proceedings of the Seventh International Conference on GPR (2)*, 509–14, Radar Systems and Remote Sensing Laboratory, Kansas, USA, 1998.
15. Bungey, J. H. and S. G. Millard, "Radar inspection of structures," *Proceedings of the International in Civil Engineering Structures and Buildings*, 173–8, 1993.
16. Bungey, J. H., S. G. Millard, and M. R. Shaw, "The influence of reinforcing steel on radar surveys of concrete structures," *Constr. Build Mater.*, Vol. 8, No. 2, 119–26, 1994.
17. Concrete Society, "Concrete society; guidance on radar testing of concrete structures," *Tech. Rep.*, Vol. 48, 88, 1997.
18. Federation of Construction Material Industries of Japan, "Nondestructive evaluation of concrete properties," March 2003.
19. Halabe, U. B., "Condition assessment of reinforced concrete structures using electromagnetic waves," PhD Thesis, MIT, 1990.
20. Ulriksen, P., "Application of impulse radar to civil engineering," PhD Lund University of Technology, Lund, Coden, Lutvdg (TVTG-1001), Sweden, 1982.
21. Millard, S. G., M. R. Shaw, A. Giannopoulos, and M. N. Soutsos, "Modelling of sub-surface pulsed radar for non-destructive testing of structures," *J. Mater. Civ. Eng.*, Vol. 10, No. 3, 188–96, ACSE, 1998.
22. Pucinotti, R. and R. A. De Lorenzo, "Nondestructive in situ testing for the seismic damageability assessment of ancient r/c structures," *Book of Proceedings, Third International Conference on NDT*, 189–94, Chania, Crete, Greece.
23. Pucinotti, R. and V. Barrile, "L'utilizzo di tecniche radar per le indagini non distruttive sulle opere in c.a.," *Atti del 148 Congresso C.T.E.*, Vol. 1, 147–56, Mantova, 2002.
24. Newnham, L. and A. Goodier, "Using neural networks to interpret sub-surface radar imagery of reinforced concrete," *Proceedings of GPR 2000*, University of Queensland, Australia, 2000 wCD-ROMx.
25. Shaw, M. R., T. C. K. Molyneaux, S. G. Millard, J. H. Bungey, and M. J. Taylor, "Automatic analysis of GPR scans on concrete structures," *Proceedings of GPR 98*, 449–454, University of Kansas, USA, 1998.
26. Maierhofer, Ch., A. Brink, M. Rollig, and H. Wiggenhauser, "Detection of shallow voids in concrete structures with impulse thermography and radar," *Proceedings of Structural Faults and Repair*, London, Engineering Technics Press, Edinburgh, 2001 wCD-ROMx.
27. Colla, C., M. Krause, Ch. Maierhofer, H. J. Hohberger, and H. Sommer, "Combination of NDT techniques for site investigation of non-ballasted railway tracks," *NDT EInt 2002*, Vol. 35, No. 2, 95–105, 2002.

28. De'robert, X., Ch. Aubagnac, and O. Abraham, "Review of NDT methods on a post-tensioned beam before autopsy," *NDT EInt 2002*, Vol. 35, No. 8, 541–8, 2002.
29. Annan, A. P., S. W. Cosway, and T. De Souza, "Application of GPR to map concrete to delineate embedded structural elements and defects," *Proceedings of GPR 2002*, Vol. 4758, 359–364, SPIE, Santa Barbara, 2002.
30. Van der Kruk, J., "Multi-component imaging for different heights of source and receiver antennas," *2nd International Workshop on Advanced Ground Penetrating Radar, Delft*, The Netherlands, May 14–16, 2003.
31. Slob, E. C., "Toward true amplitude processing of GPR data," *Proceedings of the 2nd International Workshop on Advanced Ground Penetrating Radar*, 16–23, May 14–16, 2003.
32. Roberts, R. L. and J. J. Daniels, "Improved GPR interpretation from analysis of buried target polarization properties," *Transactions of the Symposium on the Application of Geophysics to Engineering and Environmental Problems: Soc. Eng. and Min. Expl. Geophys.*, 597–611, Oakbrook, Il, April 26–29, 1992.
33. Roberts, R., "Analysis and theoretical modeling of GPR Polarization data," *The Ohio State University Geological Sciences*, 1994.
34. Roberts, R. L. and J. J. Daniels, "Analysis of GPR polarization phenomena," *Journal of Environmental and Engineering Geophysics*, Vol. 1, No. 2, 139–157, 1996.
35. Roberts, R. L. and J. J. Daniels, "Modeling near field GPR in three dimensions using the FDTD method," *Geophysics*, Vol. 62, No. 4, 1114–1126, 1997.
36. Radzevicius, S. J. and J. J. Daniels, "Ground penetrating radar polarization and scattering from cylinders," *Journal of Applied Geophysics*, Vol. 45, 111–125, 2000.
37. Kraus, J. B., *Electromagnetics*, 775, McGraw-Hill, New York, 1984.
38. Guy, E. D., J. J. Daniels, S. J. Radzevicius, and M. A. Vendl, "Demonstration of using crossed dipole GPR antennae for site characterization," *Geophysical Research Letters*, Vol. 26, No. 22, 3421, 1999.
39. Van der Kruk, J., C. P. A. Wapenaar, J. T. Fokkema, and P. M. van den Berg, "Three-dimensional imaging of multicomponent ground-penetrating radar data," *Geophysics*, Vol. 68, 1241–1254, 2003.
40. Van der Kruk, J., "Multi-component imaging for different heights of source and receiver antennas," *Conference Proceedings, 2nd International Workshop on Advanced Ground Penetrating Radar*, 6, 2003.
41. STreich, R. and J. van der Kruk, "Accurate imaging of multicomponent GPR data based on exact radiation patterns," *IEEE Transactions on Geoscience and Remote Sensing*, Vol. 45, 93–103, 2007.
42. Streich, R., J. V. D. Kruk, and A. G. Green, "Vector-migration of standard copolarized 3D GPR data," *Geophysics*, Vol. 72, No. 5, 65–75, 2007.
43. Van der Kruk, J. and E. C. Slob, "The influence of the soil on reflections from above surface objects in GPR data," *Proceedings Eight International Conference on Ground-penetrating Radar*, 453–457, Queensland, Australia, May 23–26, 2000.
44. Van der Kruk, J. and E. C. Slob, "Reduction of reflections from above surface objects in GPR data," *Journal of Applied Geophysics*, Vol. 55, 271–278, 2004.
45. Narayanan, R., R. Becker, and M. Bashforth, "Detection of buried pipes using polarimetric stepped-frequency GPR images," *Pipes & Pipelines International (1965)*, Vol. 45, No. 6, 15–31, 2000.
46. Jensen, O. K. and O. G. Gregersen, "Stepped frequency GPR for utility line detection using polarization dependent scattering," *GPR 2000, Proceedings of the Eight International Conference on Ground Penetrating Radar*, Vol. 4084, 727–730, Gold Coast, Australia, May 2000.
47. Radzevicius, S. J., E. D. Guy, and J. J. Daniels, "Pitfalls in GPR data interpretarion: Differentiating stratigraphy and buried objects from periodic antenna and target effects," *Geophys. Res. Lett.*, Vol. 27, 3393–3396, 2000.
48. Zhang, W.-B., W.-B. Wei, J.-E. Jing, and Z.-Y. Jia, "Application of ground penetrating radar polarization in the concrete structure detection," *Journal of Jilin University (Earth Science Edition)*, Vol. 38, No. 1, 156–160, January 2008,
49. Youn, H.-S. and C.-C. Chen, "Neural detection for buried pipe using fully polarimetric ground penetrating radar system," *GPR 2004, Proceedings of the Tenth International Conference on Ground Penetrating Radar*, Vol. 1, 303–306, 2004.

50. Bnngey, J., "Geophysics in pavement engineering meeting of the EIGG," *Geol. Soc. HQ*, Burlington, London, October 14, 2003.
51. Utsi, V. and E. Utsi, "Measurement of reinforcement bar depths and diameters in concrete," *Proceedings of the Tenth International Conference on Ground Penetrating Radar*, 2004.
52. Shaw, M. R., T. C. K. Molyneaux, S. G. Millard, M. J. Taylor, and J. H. Bungey, "Assessing bar size of steel reinforcement in concrete using ground penetrating radar and neural networks," *Insight: Non-Destructive Testing and Condition Monitoring*, Vol. 45, No. 12, 813–816, 2003.
53. Stolte, C. and K. Nick, "Eccentricity-migration: A method to improve the imaging of pipes in radar reflection data," *Fifth International Conference on Ground Penetrating Radar, Expanded Abstracts, Proceedings*, Ontario, Canada, 723–733, 1994.
54. Olhoeft, G., "Maximizing the information return from ground penetrating radar," *J. Appl. Geophys.*, Vol. 43, 175–187, 2000.
55. Al-Nuaimy, W., Y. Huang, M. Nakhkash, M. Fang, V. Nguyen, and A. Eriksen, "Automatic detection of buried utilities and solid objects using neural networks and pattern recognition," *J. Appl. Geophys.*, Vol. 43, No. 2–4, 157–165, 2000.
56. Utsi, V. and E. Utsi, "Measurement of reinforcement bar depths and diameters in concrete," *Tenth Intemational Conference on Ground Penetrating Radar*, Delft, The Netherlands, June 21–24, 2004.
57. Shihab, S. and W. Al-Nuaimy, "Radius estimation for cylindrical objects detected by ground penetrating radar," *Subsurface Sensing Technologies and Applications*, Vol. 6, No. 2, 1–16, 2005.
58. Al-Nuaimy, W., Y. Huang, V. Nguyen, and A. Eriksen, "Automatic detection of hyperbolic signatures in ground-penetrating radar data," *SPIE International Conference on Subsurface and Surface Sensing Technologies and Applications III*, Vol. 4491, 327–335, Cam Nguyen, Editor, San Diego, 2001.
59. Windsor, C. G., L. Capineri, and P. Falorni, "The estimation of buried pipe diameters by generalized hough transform of radar data," *PIERS Online*, Vol. 1, No. 3, 345–349, 2005.
60. Yufryakov, B. A. and O. N. Linnikov, "Buried cylinders geometric parameters measurement by means of GPR," *PIERS Online*, Vol. 2, No. 2, 187–191, 2006.
61. Dolgiy, A. and V. Zolotarev, "GPR estimation for diameter of buried pipes," *11th European Meeting of Environmental and Engineering Geophysics, Expanded Abstract*, Session P023, Palermo, Italy, September 4–7, 2005.
62. Dolgiy, A. and V. Zolotarev, "Optimal radius estimation for subsurface pipes detected by ground penetrating radar," *11th International Conference on Ground Penetrating Radar*, Columbus Ohio, USA, June 19–22, 2006.
63. Huston, D., N. Pelczarski, and B. Esser, "Damage detection in roadways with ground penetrating radar," *Proc. Eighth International Conference on GPR*, Gold Coasts, Australia, 2000.
64. Hugenschmidt, J. and R. Loser, "Detection of chlorides and moisture in concrete structures with ground penetrating radar," *Materials and Structures*, Vol. 41, No. 4, 785–792, 2007.
65. Kim, W., A. M. Ismail, N. L. Anderson, E. A. Atekwana, and A. Buccellato, "Non-destructive testing (NDT) for corrosion in bridge decks using ground penetrating radar (GPR)," *Geophysics 2003, The 3rd International Conference on the Application of Geophysical Methodologies and NDT to Transportation Facilities and Infrastructure*, Orlando, Florida, USA, Dec. 8–12, 2003.
66. Barnes, C. L., J.-F. Trottier, and D. Forgeron, "Improved concrete bridge deck evaluation using GPR by accounting for signal depth-amplitude effects," *NDT & E International*, Vol. 41, No. 6, 427–433, 2008.
67. Laurens, S., J.-P. Balayssac, J. Rhazi, and G. Arliguie, "Influence of concrete moisture upon radar waveform," *RILEM Mater. Struct.*, Vol. 35, No. 248, 198–203, 2002.
68. Laurens, S., J. Rhazi, J.-P. Balayssac, and G. Arliguie, "Assessment of corrosion in reinforced concrete by ground penetrating radar and half-cell potential tests," *RILEM Workshop on Life Prediction and Aging Management of Concrete Structures*, Cannes, France, 2000.
69. Narayanan, R. M., S. G. Hudson, and C. J. Kumke, "Detection of rebar corrosion in bridge decks using statical variance of radar reflected plulses," *Proceedings of Seventh International Conference on Ground-penetrating Radar*, University of Kansas, Lawrence, Kansas, USA, 1998.

70. Narayanan, R. M., S. G. Hudson, C. J. Kumke, M. W. Beacham, and D. D. Hall, *Better Roads*, Vol. 73, No. 2, 70–73, Electrical Engineering Department, University of Nebraska, February, 2003.
71. Hubbard, S. S., J. Zhang, P. J. M. Monteiro, J. E. Petrson, and Y. Rubin, "Experimental detection of reinforcing bar corrosion using nondestructive geophysical techniques," *ACI Mater. J.*, Vol. 100, No. 6, 501–9, 2003.
72. Capineri, L., P. Grande, and J. A. G. Temple, "Advanced image-processing technique for real-time interpretation of ground-penetrating radar images," *International Journal of Imaging Systems and Technology*, Vol. 9, 51–59, 1998.
73. Al-Nuaimy, W., Y. Huang, M. Nakhkash, M. T. C. Fang, V. T. Nguyen, and A. Eriksen, "Automatic detection of buried utilities and solid objects with GPR using neural networks and pattern recognition," *Journal of Applied Geophysics*, Vol. 43, 157–165, 2000.
74. Gamba, P. and S. Lossani, "Neural detection of pipe signatures in ground penetrating radar images," *IEEE Trans. Geosci. and Remote Sens.*, Vol. 38, 790–797, 2000.
75. Delbò, S., P. Gamba, and D. Roccato, "A fuzzy shell clustering approach to recognize hyperbolic signatures in subsurface radar images," *IEEE Trans. Geosci. and Remote Sens.*, Vol. 38, 1447–1451, 2000.
76. Molyneaux, T. C. K., S. G. Millard, J. H. Bungey, and J. Q. Zhou, "Radar assessment of structural concrete using neural networks," *NDT & E International*, Vol. 28, No. 5, 281–288, 1995.
77. Al-Nuaimy, W., Y. Huang, M. Nakhkash, and M. T. C. Fang, "Neural network for the automatic detection of buried utilities and landmines," *PIERS Proceedings*, 141, Nantes, Frances, July 1998.
78. Shihab, S., W. Al-Nuaimy, Y. Huang, and A. Eriksen, "Automatic region-based shape discrimination of ground penetrating radar signatures," *Proceedings of the Symposium on the Application of Geophysics to Environmental and Engineering Problems SAGEEP 2003*, San Antonio, USA, 2003.
79. Al-Nuaimy, W., H. Lu, S. Shihab, and A.Eriksen, "Automatic mapping of linear structures in 3-dimensional space from ground-penetrating radar data," *Ninth International Conference on Ground Penetrating Radar, GPR 2002, Proceedings of SPIE*, 121–124, 2002.
80. Shihab, S., W. Al-Nuaimy, and A. Eriksen, "Image processing and neural network techniques for automatic detection and interpretation of ground penetrating radar data," *Proceedings of 6th WSEAS International Multi-conference on Circuits, Systems, Communications and Computers*, Crete, 2002.
81. Al-Nuaimy, W., Y. Huang, A. Eriksen, and V. T. Nguyen, "Automatic detection of hyperbolic signatures in ground-penetrating radar data," *Proceedings of SPIE: Subsurface and Surface Sensing Technologies and Applications III*, San Diego, Vol. 4491, 327–335, August 2001,
82. Shaw, M. R., S. G. Millard, T. C. K. Molyneaux, et al., "Location of steel reinforcement in concrete using ground penetrating radar and neural networks," *NDT & E International*, Vol. 38, No. 3, 203–212, 2005.
83. Soldovieri, F., R. Persico, E. Utsi, and V. Utsi, "The application of inverse scattering techniques to the problem of rebar location in concrete," *Non Destructive Sensing and Evaluation*, Vol. 39, No. 7, 602–607, 2006.
84. Pasolli, E., F. Melgani, M. Donelli, et al., "Automatic detection and classification of buried objects in GPR images using genetic algorithms and support vector machines," *IEEE Trans. Geosci. and Remote Sens.*, Vol. 46, 3374–3385, 2008.

The Application of FDTD Method to UHF Electromagnetic Wave Analysis in Gas Insulated Switchgear

Xianglong Zhang and Yi Wang
School of Electrical Engineering, Beijing Jiaotong University, China

Abstract— Gas Insulated Switchgear is an important equipment in a substation, and it's highly desirable to analyze a partial discharge occurring in GIS which is a symptom of an insulation breakdown. Ultra high frequency (UHF) electromagnetic wave can be radiated by partial discharge. In order to explore the relationship between UHF signal and partial discharge sources in GIS, this paper proposes a method of finite difference time domain (FDTD) to investigate the characteristics of UHF signal. With the resort to the XFDTD simulation of electromagnetic wave propagation in GIS, factors such as PD current pulse amplitude and pulse width are analyzed. The result shows that UHF signals have direct relation to the distance of PD source. And when the pulse width is constant, the square root of UHF signal energy is direct ratio to the amplitude of the real pulse.

1. INTRODUCTION

Gas Insulated Switchgears (GIS) have the advantage of covering the smaller area, running more safely and reliably, less constant-maintenance, overhauling in a longer period and so on, so it develops very quickly and gets more and more applications when it came out. Operation experience shows that intrinsic defects in GIS still cause accidents though its high reliability. Insulation breakdown is the primary reason for GIS electrical failures. A partial discharge (PD) phenomenon is the most common characteristic before insulation breakdown in GIS. The UHF-method, as its name suggests, works in the frequency range above 300 MHz called the UHF-range (300 MHz–3 GHz). The UHF electromagnetic waves, caused by PD are picked up by a UHF sensor inside the GIS. A lot of practical experience with the UHF-method has been reported in the past. But for the effective application of the UHF-method in practice and the correct interpretation of the measurement results, it is necessary for us to research the characteristics of UHF electromagnetic waves. This paper proposes the method of finite difference time domain to resolve it, and the results of simulation help us to find some useful and progressive conclusion.

2. FDTD METHOD AND NUMERICAL SIMULATION OF ELECTROMAGNETIC WAVE

To study the Ultra high frequency behavior of GIS, it can be modeled as a cylindrical coaxial waveguide. The electromagnetic waves radiated by PD propagate along the cavity of GIS and can be explored depending on the principle of wave propagation and current pulse radiating electromagnetic wave in waveguide.

Three different types of wave modes which can propagate in the GIS are established. They are TM_{mn} mode ($H_z = 0$), TE_{mn} mode ($E_z = 0$), and TEM_{mn} mode ($H_z = 0$, $E_z = 0$). Parameters m and n mark the different types of wave modes. But all of these three modes in waveguide meet helmholtz Equation (1)

$$\nabla^2 E + \omega^2 \mu\varepsilon E = 0; \quad \nabla^2 H + \omega^2 \mu\varepsilon H = 0 \tag{1}$$

Equation (2) defines the mode-characteristic cut-off frequency f_c (m, n), below which the corresponding wave mode cannot exist in GIS. μ and ε are the permeability and dielectric constant of the medium. The modal eigenvalue constant k_{mn} in (2) has to be determined by the evaluation of the boundary conditions of the electromagnetic waves in the GIS.

$$f_c(m, n) = \frac{k_{mn}}{2\pi\sqrt{\mu\varepsilon}} \tag{2}$$

For TEM mode, cut-off frequency does not exist. Therefore, all frequencies of TEM mode will propagate in GIS. According to the boundary conditions:

$$\begin{aligned} r &= a,\ \varphi = u_0 \\ r &= b,\ \varphi = 0 \end{aligned} \tag{3}$$

The field components along Z-axis are:

$$E_r = \frac{u_0}{r\ln(b/a)} e^{j(wt-kz)}, \quad H_\varphi = \frac{E_r}{\eta} \tag{4}$$

As to TM_{mn} mode ($H_z = 0$),

$$E_z = [CJ_n(k_c r) + DN_n(k_c r)] \left\{ \begin{array}{c} \cos n\varphi \\ \sin n\varphi \end{array} \right\} e^{j(\alpha x - \beta z)} \tag{5}$$

And for TE_{mn} mode ($E_z = 0$),

$$H_z = [AJ_n(k_c r) + BN_n(k_c r)] \left\{ \begin{array}{c} \cos n\varphi \\ \sin n\varphi \end{array} \right\} e^{j(\alpha x - \beta z)} \tag{6}$$

Among them, $J_n,\ D_n$ are the first and the second Bessel function, and $A,\ B,\ C,\ D$ are constants. So, when the frequency is high enough which results in $k > k_c$, β is the real number, and the factor of travelling wave is $e^{-j\beta z}$, that means the electromagnetic wave propagates along Z-axis. Otherwise, when $k < k_c$, energy will attenuate. If frequencies of TE and TM lower than cut-off frequency, the signals will attenuate rapidly. On the contrary, if frequency is above cut-off frequency, the loss of wave in the propagation would be small. Therefore, it turns out ot be that UHF electromagnetic wave can propagate with small loss.

The FDTD method first presented by Yee in 1966 and later improved upon by several researchers is a numerically exact technique to solve Maxwell's equations with given boundary conditions. It is based on the discretization of electric and magnetic fields over a rectangular grid with the second order central difference approximation for both spatial and temporal derivatives appearing in differential forms of Maxwell's equations. In solution procedure, the coupled Maxwell's equations in differential forms are solved for the scatter and its surroundings in a time-stepping manner. This procedure involves positioning the components of electromagnetic fields around the unit cells of the lattices, and calculating the electric and magnetic fields in alternative half-time steps. In Cartesian coordinate system, the Maxwell's time-dependent curl equation can be written in terms of a set of six scalar equations. Difference equations are derived from these six equations by applying central difference. Maxwell's Equations of rotation are:

$$\begin{aligned} \nabla \times \vec{E} &= -\frac{\partial B}{\partial t} - \sigma_m \vec{H} \\ \nabla \times \vec{H} &= \frac{\partial D}{\partial t} + \sigma \vec{E} \end{aligned} \tag{7}$$

Six scalar equations derived from Maxwell's Equations of rotation are:

$$\begin{aligned} \frac{\partial E_x}{\partial t} &= \frac{1}{\varepsilon}\left(\frac{\partial H_z}{\partial y} - \frac{\partial H_y}{\partial z} - \sigma E_x\right) \\ \frac{\partial E_y}{\partial t} &= \frac{1}{\varepsilon}\left(\frac{\partial H_x}{\partial z} - \frac{\partial H_z}{\partial x} - \sigma E_y\right) \\ \frac{\partial E_z}{\partial t} &= \frac{1}{\varepsilon}\left(\frac{\partial H_y}{\partial x} - \frac{\partial H_x}{\partial y} - \sigma E_z\right) \\ \frac{\partial H_x}{\partial t} &= \frac{1}{\mu}\left(\frac{\partial E_y}{\partial z} - \frac{\partial E_z}{\partial y} - \sigma_m H_x\right) \\ \frac{\partial H_y}{\partial t} &= \frac{1}{\mu}\left(\frac{\partial E_z}{\partial x} - \frac{\partial E_x}{\partial z} - \sigma_m H_y\right) \\ \frac{\partial H_z}{\partial t} &= \frac{1}{\mu}\left(\frac{\partial E_x}{\partial y} - \frac{\partial E_y}{\partial x} - \sigma_m H_z\right) \end{aligned} \tag{8}$$

According to the accuracy of design, divide the field domain into many grid units along three axis with $\Delta x,\ \Delta y,\ \Delta z$, which are the space step of grid, and Δt which is the time step. Then, any function can be expressed below:

$$F^n(i,\ j,\ k) = F(i\Delta x,\ j\Delta y,\ k\Delta z,\ n\Delta t) \tag{9}$$

Apply central difference in this function for time and space partial derivative, and FDTD equations can be obtained by using finite difference arithmetic expression in space. Following Yee's notation, the grid points in space are defined as (i, j, k) with coordinates$(i\delta_x, j\delta_y, k\delta_z)$, where δ_u $(u = x, y, z)$ is the cell size in each dimension and δ_t is the time increment. This space configuration not only allows difference calculation in space, but also meets the integral form of Maxwell equation, thus it is able to simulate the propagation of electromagnetic wave. For example, When $t = (n-1/2)\Delta t$, difference type of scalar equations at the point $(i+1/2, j, k)$ can be approximated to:

$$E_x^{n-\frac{1}{2}}\left(i+\frac{1}{2}, j, k\right) = \frac{1}{2}\left[E_x^{n-1}\left(i+\frac{1}{2}, j, k\right) + E_x^{n}\left(i+\frac{1}{2}, j, k\right)\right] \tag{10}$$

Further, we can get difference equation about E_x

$$\begin{aligned} E_x^n\left(i+\frac{1}{2}, j, k\right) \;=\; & \left[1-\frac{\sigma(i+\frac{1}{2}, j, k)\Delta t}{2\varepsilon(i+\frac{1}{2}, j, k)}\Big/1+\frac{\sigma(i+\frac{1}{2}, j, k)\Delta t}{2\varepsilon(i+\frac{1}{2}, j, k)}\right] \\ & \cdot E_x^{n-1}\left(i+\frac{1}{2}, j, k\right) + \frac{\Delta t}{\varepsilon(1+\frac{1}{2}, j, k)}\cdot\frac{1}{1+\frac{\sigma(i+\frac{1}{2}, j, k)\Delta t}{2\varepsilon(i+\frac{1}{2}, j, k)}} \\ & \cdot\left[\frac{H_z^{n-\frac{1}{2}}(i+\frac{1}{2}, j+\frac{1}{2}, k) - H_z^{n-\frac{1}{2}}(i+\frac{1}{2}, j-\frac{1}{2}, k)}{\Delta y}\right. \\ & \left. - \frac{H_y^{n-\frac{1}{2}}(i+\frac{1}{2}, j, k+\frac{1}{2}) - H_y^{n-\frac{1}{2}}(i+\frac{1}{2}, j, k-\frac{1}{2})}{\Delta z}\right] \end{aligned} \tag{11}$$

And the other five can also be obtained like this. Electric fields are assigned to half-integer $(n + 1/2)$ time steps and magnetic fields are assigned to integer (n) time steps for the temporal discretization of fields. The central difference ensures that the spatial and temporal discretizations are second-order accuracy, where errors are proportional to the square of the cell size and time increment. After the EM fields are obtained, the power density at any space point can be found by the Poynting Theory.

In numerical calculation, suppose components of electromagnetic fields are single-precision variables. Each variable takes up four bytes and the summery of FDTD domain cellular are N. If we use serial number of each medium instead of electromagnetic parameters, only a byte is needed to recognize all parameters. Suppose v stands for variables and sn stands for serial number, then

$$Memory = N \times (6v/cell \times 4B/v + 6sn/cell \times 1B/sn) \tag{12}$$

Without doubt, it will save a lot of space of computer memory. By means of calculation, we can get the needed memory of 3DFDTD showed as Figure 1:

Memory (M)	FDTD domain	Total domain
32	100×100×100	80×80×80
64	125×125×125	105×105×105
128	158×158×158	138×138×138
256	198×198×198	178×178×178
512	270×270×270	250×250×250

Figure 1: Computer memory needed for 3DFDTD.

In order to make full use of FDTD method and finish a reliable operation, software XFDTD is used to simulate the process of UHF electromagnetic wave propagating in waveguide.

Model structure setting: Figure 2 is the waveguide simulation. It is made up of three parts of coaxial waveguides. The inner part radius $a = 5$ cm, outer part radius $b = 25$ cm, and exine is 1 cm thick. The full length of waveguide cavity is 360 cm, involving two Epoxy Resin insulators. Point A is the PD source, others are receiving points. The distance between A and B is 75 cm, A and C is 110 cm, A and D is 140 cm. Four points are at one line.

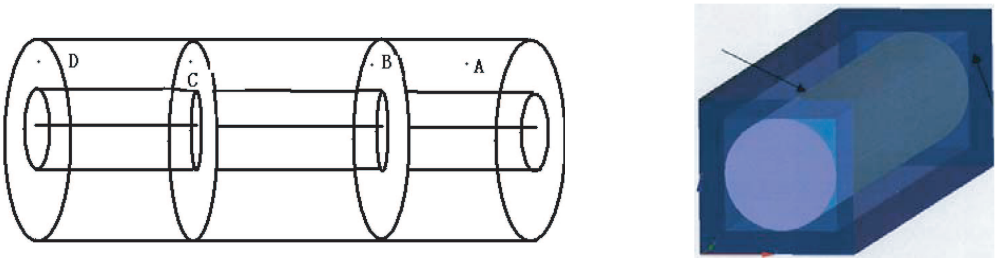

(a) (b)

Figure 2: Coaxial waveguide.

Meanwhile, superposition method is chosen to model current supply. Firstly, superimpose time function of discrete current supply on FDTD iteration expression of grid boundary. Secondly, choose proper time function waveform of current supply.

Here we choose the Gauss pulse source:

$$I(t) = I_0 \exp\left(-\frac{4\pi(t-t_0)^2}{\pi^2}\right) \tag{13}$$

Then, settle the time width of Gauss pulse. The pulse width was given in the form of the number of time step in XFDTD. However, it needs to multiply a step time in practice. In order to meet the limit of Courant stable condition, suppose Δx is the length of side of cellular, then, the upper limit of frequency in simulation is:

$$Frequency \leq \frac{1}{10\Delta t\sqrt{3}} = \frac{c}{10\Delta x} \tag{14}$$

In simulation, the waveform of Gauss current pulse which injects into PD source has been showed in Figure 3, and the upper limit of the pulse frequency is above 5 GHz, which has been showed in Figure 4.

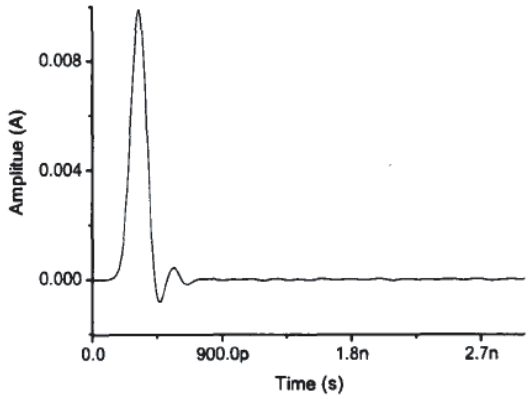

Figure 3: Gauss pulse.

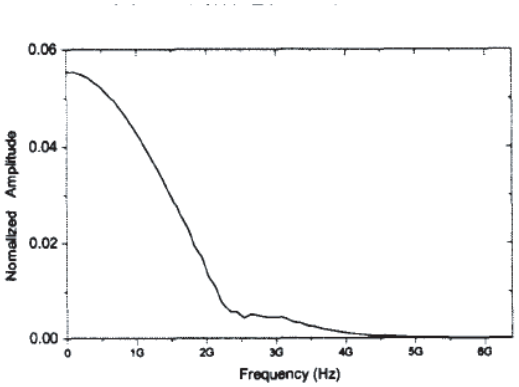

Figure 4: Frequency spectrum of Gauss pulse.

In addition, discharge magnitude of Gauss pulse can be calculated with integral formula (15), approximated to 1.3 pC.

$$Q = \int_{t_1}^{t_2} i(t)dt \tag{15}$$

On the other hand, subdivision setting means dividing the rectangle solution domain along X, Y, Z axis with the unit Δx, Δy, Δz. In order to simulate the electromagnetic process of open domain, we should set absorbing boundary condition in modal cut off boundary. The side length of cellular could be no more than tenth-wavelength of the highest frequency. But if the cellular

size was too small, excessive computer memory would be occupied. When Gauss current pulse was chosen, the smallest pulse width is 308 ps. Settle the upper limit frequency to 6 GHz, and the size of cellular could be obtained:

$$L_{\max} = \frac{c}{10 \times f} = \frac{3 \times 10^8}{10 \times 6 \times 10^9} = 0.5\,\text{cm/cell} \tag{16}$$

Thus, a completed cellular size is 0.5 cm × 0.5 cm × 0.5 cm, and space subdivision of model has been established. It is made up of free space domain, boundary, and the object. The general size is 96 cell × 688 cell × 96 cell, and the total memory needed is 232 M. Subdivision 3D image is made into Figure 2(b).

3. SIMULATION RESULTS

According to transient electromagnetic wave theory, while electromagnetic wave propagating in waveguide, its energy size and distribution relates to wave propagation characteristic, including structure size of waveguide, the distance between PD source and receiving point, current pulse's gradient and so on. Many factors that affect the UHF signal receipt have been analyzed. Moreover, the inner relationship and regularity have been found out from the simulation. UHF signal's energy calculation formula is :

$$e(t) = \frac{1}{Z_L} \int v(t)^2 dt \tag{17}$$

Several modes have been established below:

1) Distance between PD source and receiving points has been settled as 75 cm, 110 cm, and 140 cm separately.
2) PD pulse width has been settled as 2.4 ns, 1.2 ns, 0.6 ns, and 0.3 ns separately in simulation.
3) Amplitude of the Gauss pulse which is injected into PD source has been settled as 10 mA, 20 mA, and 30 mA separately.

Firstly, just as the Figure 2, four points are in one line. Point A is PD source, B, C, D are receiving points. In Y axial, the distance between PD source and each receipt is 75 cm, 110 cm, and 140 cm separately and a, b, c are corresponding receiving ponits waveform, showed as Figure 5. By means of calculation, each couple energy of a, b, c is 0.393E-15J, 0.627E-15J, 0.923E-15J. We can get that UHF singles have direct relation to the distance of PD source. The longer distance between two points, the weaker signal received.

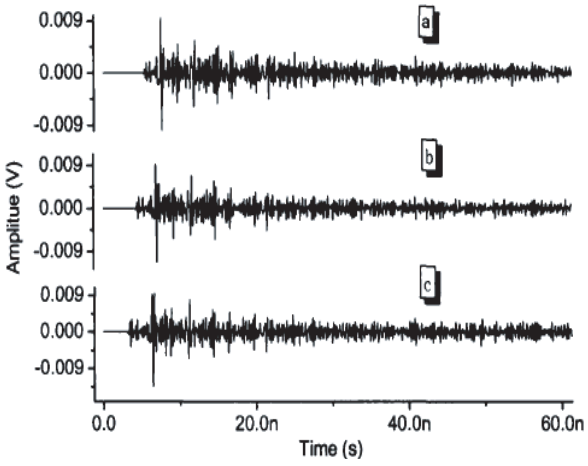

Figure 5: Compare of three waveforms with different receiving distance.

Secondly, as the Figure 6 shows, four different width pulses with the same amplitude (10 mA) are injected into the PD source.

a, b, c, d corresponding PD quantity are 1.26 pC, 2.52 pC, 5.05 pC, 10.10 pC, the distance between two points is 120 cm long. Four waveforms are showed in Figure 7. Obviously, the highest amplitude can be obtained with the pulse with 0.3 ns width. On the contrary, the lowest amplitude

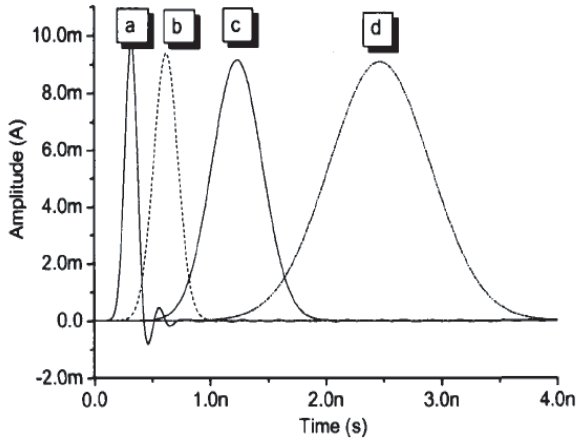

(a 0.3 ns, b 0.6 ns, c 1.2 ns, d 2.4 ns)

Figure 6: Four different width pulses with same amplitude.

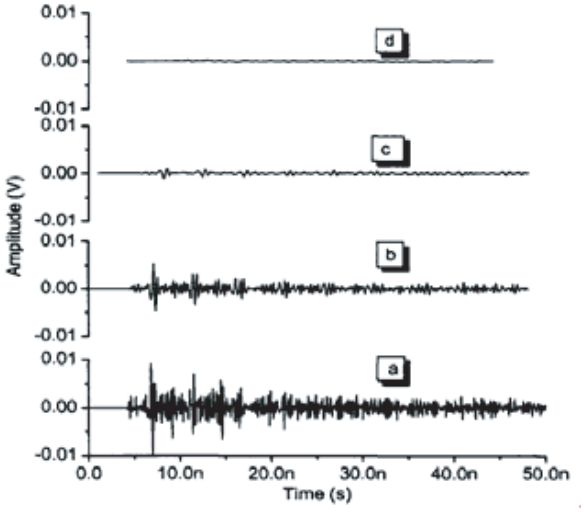

Figure 7: Compare of four waveforms.

is obtained with 2.4 ns one (the widest pulse of four). By means of calculation, each couple energy of a, b, c, d is 0.627E-15J, 0.147E-15J, 0.009E-15J and 1E-18J. Also, wave a can stimulate the most energy and wave d gets the least. The results indicate that pulse width play a crucial part in UHF signal receipt. The narrower pulse width is, the stronger UHF signal receives.

Thirdly, as the Figure 8 shows, four pulses of different amplitude with the same width (0.3 ns) are injected into the source.

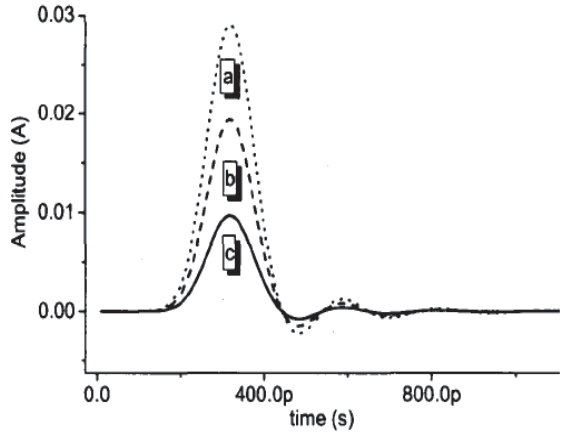

(a 30 mA, b 20 mA, c 10 mA)

Figure 8: Four different amplitude pulses with same width.

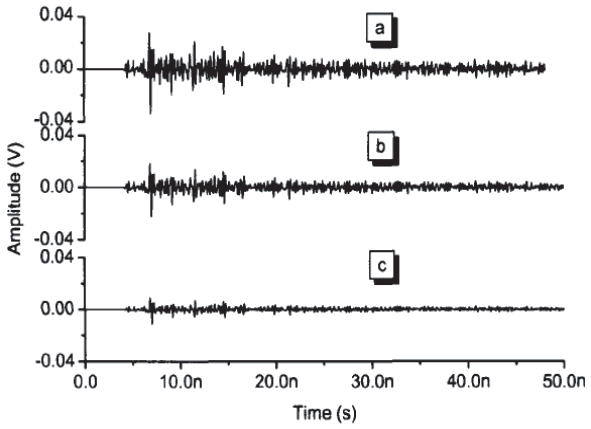

Figure 9: Compare of four waveforms.

By means of calculation, each couple energy of a, b, c is 5.645E-15J, 2.509E-15J, 0.627E-15J. As is showed in Figure 9, the square root of UHF single energy is direct ratio to the amplitude of the real pulse.

4. CONCLUSION

With the resort to FDTD method, several useful and progressive conclusions are reached:

1) UHF signals have direct relation to the distance of PD source. The longer distance between two points is, the weaker receiving points' signals are.
2) The energy of UHF signal has no direct relation to the real pulse's discharge magnitude. However, pulse width plays a very important part in it. If the electromagnetic wave pulse has narrow width and high amplitude, that is to say it has a large gradient, and then UHF signal received is strong.

3) Meanwhile, experiment shows that UHF single energy is direct ratio to the square of the amplitude of the real pulse.

REFERENCES

1. Judd, M. D., "Partial discharge diagnostics for Gas insulated substations," *IEEE Transactions on Dielectrics and Electrical Insulation*, Vol. 2, No. 5, Oct. 1995.
2. Kurrer, R., "The application of UHF partial discharge measurements to GIS," *IEEE Transactions on Power Delivery*, Vol. 13, No. 3, Jul. 1998.
3. Li, X., "Research on UHF detection for partial discharge in GIS," Doctor dissertation, North China Electric Power University, Jun. 2005.
4. Lan, W.-C., "Numerical studies of wave propagation through concrete walls using effective material property technique and FDTD method," *Antennas and Propagation Society International Symposium*, IEEE, Vol. 1, 1999.

Detection of Pseudo-singularities by Wavelet Technique for Extracting Leaky and Bulk Waves in Piezoelectric Material

D. Benatia[1], **T. Fortaki**[1], **and M. Benslama**[2]

[1]Département d'Electronique, Faculté des Sciences de l'Ingénieur
Université de Batna, Algeria
[2]Département d'Electronique, Faculté des Sciences de l'Ingénieur
Université de Constantine, Algeria

Abstract— In this paper, we propose a new numerical method for leaky and bulk wave detection of an acoustic microwave signal during the propagation of acoustic microwaves in a piezoelectric substrate. Moreover, we know that the Fourier transform presents a global spectral study of signal, this is not interesting if we want to study a signal locally and know its features in a more precise manner. By the use of wavelet transform, we can reduce this drawback. The originality of the wavelet transform consists of the local analysis of signal singularities (or signal pseudo-singularities) where abrupt events appear and hence access to hidden information by using the scale of this transform as up scaling parameters. These pseudo-singularities (correspond to abrupt variations) inform us of presence of leaky and bulk waves in piezoelectric materials.

Furthermore, this transform proved its efficiency in many applications, such as signal processing and the analysis of waves in microstrip structures. Hence, it can play an important role in the modeling of pseudo-singularities in acoustoelectronic.

1. INTRODUCTION

The investigation of bibliography in micro-acoustic area permits us to point the state of the art. Two major works can be mentioned, the first one is Greeb' paper [1], which explore the interaction using effective permittivity concept, another work of Lakin [2] which elaborate a perturbation theory to explain the interaction phenomena. Following the work of Greeb, Milson [3] in 1977 elaborates a relation based of the charge density, and develops a formalism based on the Fourier Transform. In spite of it, this method doesn't permit to distinguish easily the different modes of propagation by a numerical methods based on the inverse Fourier transform. These works were taken by Junjhunwalla [4] that granted a particular attention to the SSBW (Surface Skimming Bulk Waves). Yashiro and Goto [5] introduce the method of the stationary phase of Lightill [6] to calculate the pseudo-singularities that inform us on the presence of the pseudo- waves, particularly the leaky and bulk waves.

In our case, we propose another approach for the modelling of the acoustic microwaves with a complementary vision to the literature mentioned above. In this approach we interested especially in the detection of pseudo-singularities by the use of a wavelet transform as detection tool [7, 8] in order to mark the mode of a leaky waves and the mode of a bulk waves [9–12].

2. PHENOMENOLOGICAL TENSORIAL PIEZOELECTRIC EQUATIONS

The signal to be treated will be applied to the electrodes of the transducer that generate the compression and dilatation, so a piezoelectric wave is generated and propagated in the X direction (Figure. 1).

We consider the space coordinates: $X_1 = X$, $X_2 = Y$, $X_3 = Z$.

The mechanical state of the medium is defined by two magnitudes of tensorial type, the stress T_{ij} and the mechanical deformation (Strain) S_{ij} $(i, j = 1, 2, 3)$. The electric state of the medium is defined by two vectors, the electric field E_k and the electric induction D_i. The stress tensor and the electric induction are given by:

$$T_{ij} = C_{ijkl} \cdot S_{kl} - e_{kij} \cdot E_k \tag{1}$$

$$D_i = e_{ikl} \cdot S_{kl} + \varepsilon_{ik} \cdot E_k \tag{2}$$

with $i, j, k, l = 1, 2, 3$.

Where ε_{ik}: permittivity tensor (F/m), e_{jkl}: piezoelectric tensor (c/m), C_{ijkl}: elastic tensor (N/m^2)

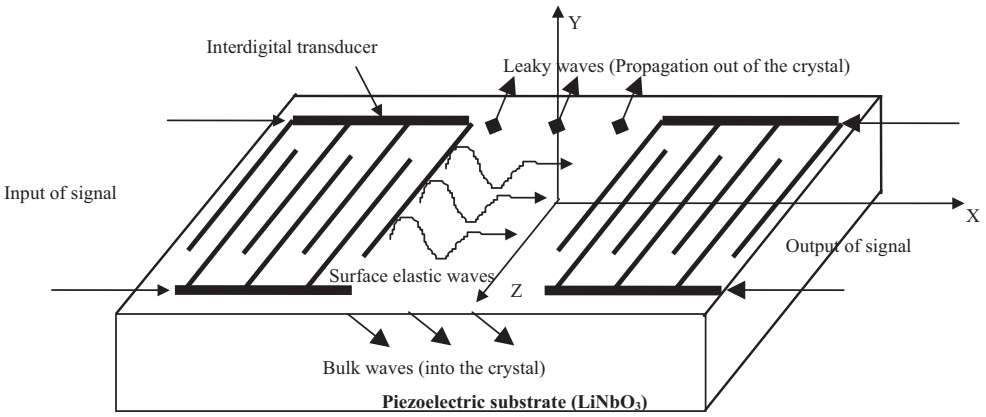

Figure 1: $LiNbO_3$ crystal excited by transducer.

The strain is bound to the relative displacements of the particles of the material environment is defined by:

$$S_{ij} = \frac{1}{2}\left(\frac{\partial U_i}{\partial X_j} + \frac{\partial U_j}{\partial X_i}\right) \tag{3}$$

where U_i represents the elastic displacement of the particle $(i = 1, 2, 3)$.

Note that in the quasi-static approximation, we can define an electric field of components:

$$E_i = -\frac{\partial U_4}{\partial X_i} \tag{4}$$

where U_4 is the electric potential (with $i = 1, 2, 3$)

In the quasi-static approximation, the Maxwell's equation amount to the Poisson's equation:

$$div \cdot \vec{D} = \frac{\partial D_i}{\partial X_i} = 0 \tag{5}$$

The movement of the particles under the action of stress (constraints), is described by the following:

$$\nabla T = \frac{\partial T_{ij}}{\partial X_i} = \rho \cdot \frac{\partial^2 U_j}{\partial t^2} \tag{6}$$

where ρ is the mass density of medium.

Replacing (3) and (4) in (1) and (2), we obtain:

$$T_{ij} = C_{ijkl} \cdot \frac{1}{2}\left(\frac{\partial U_k}{\partial X_l} + \frac{\partial U_l}{\partial X_k}\right) + e_{kij} \cdot \frac{\partial U_4}{\partial X_k} \tag{7}$$

$$D_i = e_{ikl} \cdot \frac{1}{2}\left(\frac{\partial U_k}{\partial X_l} + \frac{\partial U_l}{\partial X_k}\right) - \varepsilon_{ik} \cdot \frac{\partial U_4}{\partial X_k} \tag{8}$$

Replacing (7) and (8) in (5) and (6), we obtain the piezoelectric tensorial equations:

$$C_{ijkl}\frac{\partial^2 u_k}{\partial X_i \partial X_l} + e_{lij}\frac{\partial^2 U_4}{\partial X_k \partial X_i} = \rho\frac{\partial^2 u_j}{\partial t^2} \tag{9}$$

$$e_{ikl}\frac{\partial^2 u_k}{\partial X_i \partial X_l} - \varepsilon_{ik}\frac{\partial^2 U_4}{\partial X_k \partial X_i} = 0 \tag{10}$$

3. THE FORM OF SOLUTION

Consider the following form of the surface wave (partial wave):

$$U_i = u_i \exp\left(jk \cdot \alpha_i Y\right) \exp -j\left[\omega \cdot t - k(1 + j\gamma)X\right] \tag{11}$$

where $u_i\,(i = 1, 2, 3)$ are the displacement amplitudes, $u_i\,(i = 4)$ is the amplitude of the electric potential, k is the constant of propagation, the α_i are the penetration coefficients of the wave inside

the piezoelectric substrate (Figure 1), γ is the coefficient of longitudinal attenuation and ω is the angular pulsation.

Equations (9) and (10) can be written in a matrix form as:

$$[A][U] = [0] \tag{12}$$

with $[U] = [u_1, u_2, u_3, u_4]^T$, $[A]$ is a matrix (4×4).

The determinant of the matrix $[A]$ must be zero to ensure a non trivial solution, it can be written as:

$$\sum_{i=0}^{8} \beta_i \cdot \alpha^i = 0 \tag{13}$$

where B_i depends on the piezoelectric material features (C_{ijkl}, ε_{ik}, e_{lij}) and of the acoustic velocity V_S.

The determinant of the matrix $[A]$ must be zero, we have eight complex roots ($i = 1 \ldots 8$):

$$\alpha_i = a_i + jb_i \tag{14}$$

where a_i: is the real part and b_i: is the imaginary part, with $a_m = a_{m+1}$ and $b_m = -b_{m+1}$ where $m = 1, 3, 5, 7$.

In the surface mode (or Rayleigh wave) the α_i $(i = 1 \ldots 8)$ are conjugated by pairs and only the complex roots with negative imaginary part are taken into consideration (for convergence reasons).

Let us first neglect the longitudinal attenuation ($\gamma = 0$) and insert (14) in (11) to obtain:

$$U_i = u_i \exp -(b_i k \cdot Y) \exp -j\left[\omega \cdot t - k\left(X + a_i Y\right)\right] \tag{15}$$

If we go inside the crystal (Y tends to $-\infty$), the wave U_i tends to zero. This corresponds to surface acoustic waves (S.A.W) (Figure 1). In the opposite case (Y tends to $+\infty$), U_i tends $+\infty$ (without physical signification).

4. LEAKY AND BULK WAVES

The variation of the acoustic velocity V_S allows us to obtain $b_i = 0$ (imaginary part) and (15) becomes:

$$U_i = u_i \cdot \exp -j\left[\omega \cdot t - k \cdot \left(X + a_i Y\right)\right] \tag{16}$$

The wave nature bulk waves (**B.W**) and leaky waves (**L.W**) depends on the sign of the real part of α_i (a_i).

If $\mathbf{a_i}$ is negative, we have bulk waves (Propagation inside the crystal (Figures 1 and 2)).

If $\mathbf{a_i}$ is positive, we have leaky waves (radiation out of the crystal (Figures 1 and 2)).

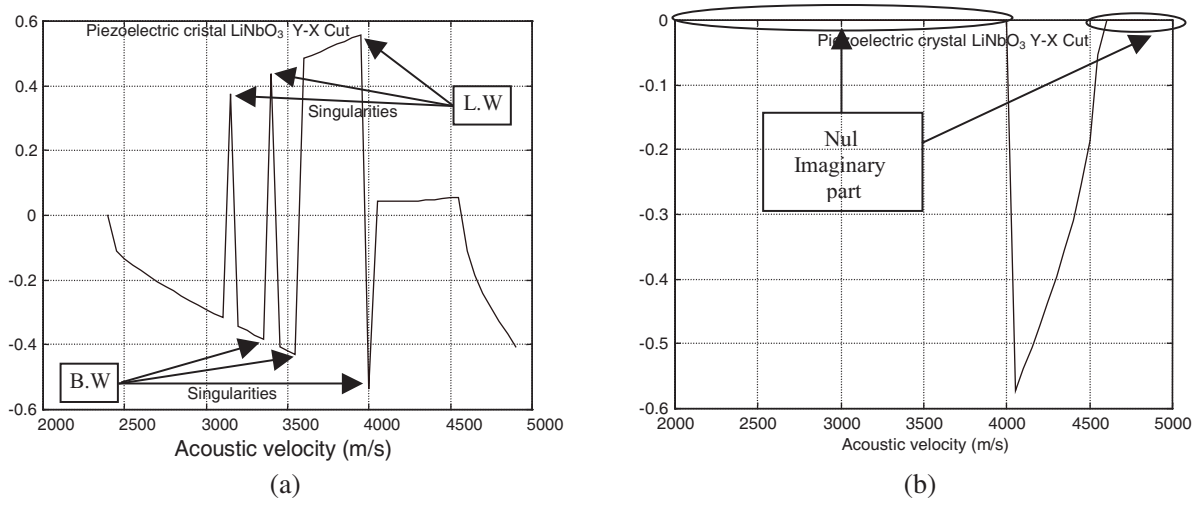

Figure 2: Penetration coefficient α_4. (a) Real part. (b) Imaginary part.

5. GENERAL FORM OF THE ACOUSTIC WAVE SOLUTION

The general form of U_i $(i = 1, 2, 3, 4)$ is expressed by:

$$U_i(k, Y) = \sum_{n=1}^{4} C_n \cdot A_i^{(n)} \cdot \exp^{-j[\omega t - k \cdot \alpha_n \cdot Y]} \tag{17}$$

where $A_i^{(n)}$ are the components of eigen vectors associated to coefficients α_n [3]

C_n are the constants determined by the traction-free boundary conditions [3].

the product $C_n \cdot A_i^{(n)}$ depends on C_{ijkl}, ε_{ik}, e_{lij} and of the acoustic velocity V_S.

For $i = 4$, we have a potential electric given by:

$$U_4(k, Y) = \sum_{n=1}^{4} C_n \cdot A_4^{(n)} \cdot \exp^{-j[\omega t - k \cdot \alpha_n \cdot Y]} \tag{18}$$

6. WAVELET TRANSFORM OF SIGNAL

The signal chosen for analysis by wavelet transform is given by Equation (18). It represents an electric potential "U_4" coupled with an elastic wave of components "U_1, U_2, U_3". This wave with the frequency "f" propagates along the X direction and guided on the free surface of the piezoelectric (Figure 1).

The space-scale type wavelet transform of U_4 (in the neighbourhood of the surface: $Y \approx 0$) is given by this convolution product [8]:

$$T_{U_4}(Y \approx 0, X, a) = U_4(Y \approx 0, X) \otimes \frac{1}{\sqrt{a}} \Psi^* \left(\frac{X}{a} \right) \tag{19}$$

where $U_4\,(Y \approx 0, X)$ is a signal in the neighbourhood of the material surface $(Y \approx 0)$.

$\Psi^*(X)$ is the complex conjugate of the wavelet (Mexican-hat): $\Psi(X) = d^2/dX^2(e^{-X^2/2})$

The frequency-scale type wavelet transform of U_4 becomes a simple product:

$$T_{U_4}(Y \approx 0, f, a) = \sqrt{a} U_4(Y \approx 0, f) \cdot \Psi^*(a \cdot f) \tag{20}$$

where $U_4\,(Y \approx 0, f)$ is the Fourier transform of a signal in the neighbourhood of the material surface

$\Psi^*(f)$ is the Fourier transform of $\Psi^*(X)$: $\Psi^*(f) = (2 \cdot \pi)^{1/2} \cdot e^{-(4 \cdot \pi^2 \cdot f^2/2)} \cdot (2 \cdot \pi \cdot f)^2$.

Replacing the expression of $\Psi^*(a \cdot f)$ in Equation (20), the wavelet transform of U_4 in this case becomes:

$$T_{U_4}(Y \approx 0, f, a) = |U_4(k, 0)| \cdot \underbrace{\sqrt{2 \cdot a \cdot \pi} \cdot e^{-\frac{4 \cdot \pi^2 a^2 \cdot f^2}{2}} \cdot (2\pi f \cdot a)^2}_{\Psi^*(a \cdot f)} \tag{21}$$

With $|U_4(k, 0)| = \sum_{n=1}^{4} C_n \cdot A_4^{(n)}$, $k = 2 \cdot \pi \cdot f / V_S$

7. RESULTS AND DISCUSSION

The detection of leaky and bulk waves appears at the level of the penetration coefficients when the acoustic velocity V_s change its value. This change results in an annulation of the imaginary parts of the penetration coefficients. We note that when the imaginary part becomes null, it appears at the level of signal wavelet transform an ***abrupt variations*** called ***pseudo-singularities***. These pseudo-singularities are not always observable. The use of the scale of this transform permits to visualise them. Once these pseudo-singularities are detected, the sign of the real part can inform us about the leaky wave ($\mathbf{a_i} > 0$) and the bulk wave ($\mathbf{a_i} < 0$).

The analysis of the signal by wavelet transform (Equation (21)) clearly shows these pseudo-singularities at the level of the contour of three-dimensional figure (the above view). This figure englobes the Wavelet Transform of "U_4", the Acoustic Velocity "V_S" and the Scale "a" with the frequency "f" as parameter (Figures 3, 4 and 5). At the frequency $f = 1\,\text{GHZ}$, it is impossible to detect the pseudo-singularities for a scale superior to 10^{-8}, In this case we can't detect the pseudo-singularities (Figure 3). For a good detection, it is necessary to reduce the scale from 10^{-8} to 10^{-10} (Figures 4 and 5), these pseudo-singularities appear more and more clearly.

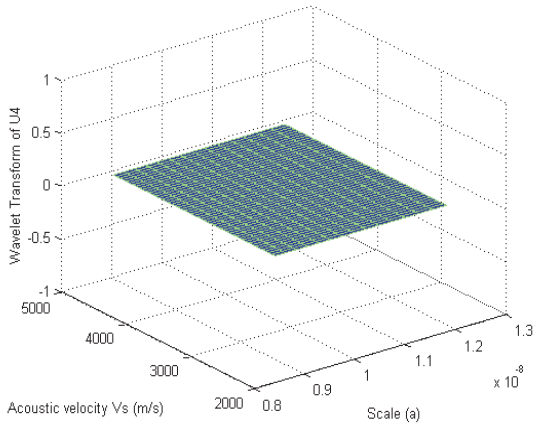

Figure 3: The wavelet transform of the U_4 Scale order (10^{-8}).

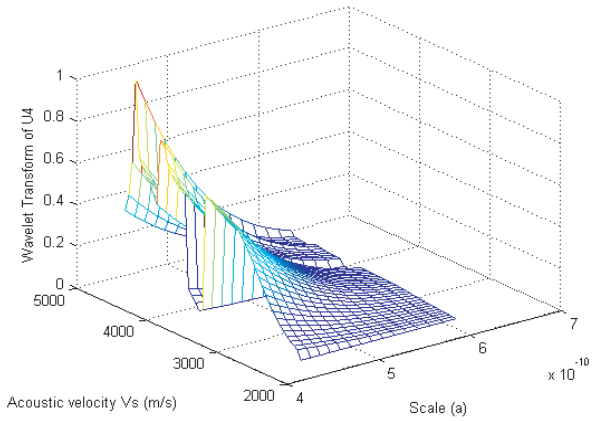

Figure 4: The wavelet transform of U_4 Scale order (10^{-10}).

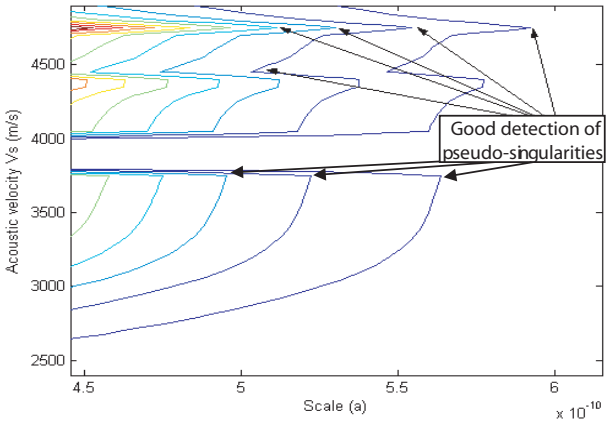

Figure 5: The above view of Figure 4 (Good detection of pseudo-singularities).

8. CONCLUSION

In this work, we have developed a model for studying the behaviour of electroacoustic waves at the level of pseudo-singularities which appear for some velocities giving the leaky and bulk waves. This model that insures the detection of pseudo-singularities using the wavelet transform. This latter has the property of being locally maximal around the points where the signal is singular or pseudo-singular. In this paper, we were interested in the influence of the scale "a" of this transform. The decrease of the scale allowed us to detect the pseudo-singularities whatever the frequency so that we can obtain all the details about the propagation of acoustic waves in particular on the leaky and bulk waves. This information can be useful for many applications such us the antenna and the oscillator devices.

REFERENCES

1. Greeb, C. A. J., et al., "Electrical coupling properties of acoustics and electric surface waves," *Physical Report*, Vol. 1, No. 5, 235–268, 1971.
2. Lakin, K. M., "Perturbation theory for electromagnetic coupling to elastic surface waves on piezoelectric substrates," *J. Appl. Phys.*, Vol. 42, No. 3, 899–906, 1971.
3. Milson, R. F., N. H. C. Reilly, and M. Redwood, "Analysis of generation and detection of surface and bulk acoustic waves by interdigital transducers," *IEEE Trans. Sonics and Ultrason.*, Vol. 24, No. 3, 147–166, 1977.
4. Jhunjhunwalla, A. and J. F. Vetelino, "Spectrum of acoustic waves emanating from an IDT on a piezoelectric half space," *Proceedings of IEEE Ultrasonics Symposium*, 945–952, 1979.

5. Yashiro, K. and N. Goto, "Analysis of generation of acoustic waves on the surface of a semi-ifinite piezoelectric solid," *IEEE Trans. Sonics and Ultrason.*, Vol. 25, No. 3, 146–153, 1978.
6. Lightil, J., *Waves in Fluid*, University Press, Cambridge, 1978.
7. Mallat, S. and W. L. Wan, "Singularity detection and processing with wavelets," *IEEE Trans. on Information Theory*, Vol. 38, 617–643, 1992.
8. Arneodo, A., F. Argoul, E. Bacry, J. Elezgaray, and J. F. Muzy, *Ondelettes, Multifractales et Turbulences*, Diderot (ed.), Art et Sciences, Paris, France, 1995.
9. Josse, F. and D. L. Lee, "Analysis of the excitation, interaction, and detection of bulk and surface waves on piezoelectric substrates," *IEEE Trans. Sonics and Ultrason.*, Vol. 29, 261–273, 1982.
10. Goodberlet, M. A. and D. L. Lee, "The excitation and detection of surface generated bulk waves," *IEEE Trans. Sonics and Ultrason.*, Vol. 31, 67–76. 1984.
11. Fusero, Y., S. Ballandras, J. Desbois, J. M. Hodé, and P. Ventura, "SSBW to PSAW conversion in SAW devices using heavy mechanical loading," *IEEE Trans. on Ultrason., Ferroelectrics, and Frequency Control*, Vol. 49, No. 6, 805–814, 2002.
12. Martin, F., "Propagation characteristics of harmonic surface skimming bulk waves on ST," *Electron Lett.*, Vol. 38, 941–942, August 2002.

Surface Latent Heat Flux (SLHF) Prior to Major Coastal and Terrestrial Earthquakes in China

Jinping Li[1,2], **Lixin Wu**[1,3], **Huanping Wu**[4], **Shanjun Liu**[3], **and Jieqing Yu**[1]

[1]Institute for GIS/RS/GPS & Subsidence Research, China University Mining & Technology
Beijing, China
[2]Department of Surveying and Engineering, Heilongjiang Institute of Technology
Harbin, China
[3]Institute for GIS/RS/GPS & Digital Mine Research, Northeastern University
Shenyang, China
[4]National Meteorological Centre, China Meteorological Administration
Beijing, China

Abstract— Recent some researches reveals that abnormal SLHF in the epicentral regions is found to appear prior to several coastal earthquake in the world, while no abnormal existence in terrestrial region far away from coast. The features of SLHF anomaly of four earthquakes occurred in the past ten years in China are studied in this paper. The analysis shows that there was abnormal SLHF occurred 2∼12 days before these earthquakes without exception. The SLHF anomaly usually occurred in the epicenter or its surrounding area, and its spatial distribution was in accordance with the local active faults. It is concluded that the SLHF anomaly can act as a valuable index for the remote sensing monitoring of tectonic activity, and it provides a useful impending messages for both costal and inland earthquakes in China.

1. INTRODUCTION

The satellite thermal infrared (TIR) imaging data have been proposed to map large linear structure and fault systems in the Earth's crust and to monitor geophysical phenomena associated with major earthquakes. TIR radiation anomaly can provide early warming information for impending earthquakes, and is considered to be a new precursor of shocking. The satellite TIR remote sensing, for the advantages of large observation area and short observation period, is becoming a promising technique for detecting earthquake and for monitoring tectonic activities. Surface Latent Heat Flux (SLHF), as an atmospheric parameter proportional to the evaporation from the Earth's surface, is dependent on meteorological parameters such as surface temperature, relative humidity, wind speed and underlaying surface. Numerous precursory geophysical parameters have been found to be associated with earthquakes that occurred in the world. These parameters can be proved to be potential precursors of earthquake even if their characteristic behavior has not been understood.

Recently, the analysis on SLHF from the epicentral areas of several coastal earthquakes in the world shows that SLHF is possible to provide meaningful anomaly index. The spatial-temporal anomalies of satellite SLHF, observed several months to several weeks before shocking, were suggested to be pre-seismic signals [1–4]. The results of SLHF anomaly investigations in coastal regions has indicated that: 1) the SLHF anomaly is sensitive to earthquake above Ms5.0, 2) the SLHF anomaly usually appears from 2∼19 days before and disappears quickly after the shocking, 3) the anomalous behavior of SLHF is not found for terrestrial earthquakes in India.

In the present paper, the SLHF behaviors of the epicentral areas of four earthquakes in China (one coastal earthquake and three terrestrial earthquakes) are analyzed to study the SLHF behavior both before and after the earthquake.

2. DATA AND PROCESSING

The details of one coastal earthquake and three terrestrial earthquakes are given in Table 1, which have been obtained from CSNDMC (http://www.csndmc.ac.cn/newweb/). The SLHF data of four earthquakes have been downloaded from the NCEP-NCAR reanalysis data of the IRI/LDEO Climate Data Library (http://iridl.ldeo.columbia.edu/). The data set is in resolution of global grid $1.8^\circ \times 1.8^\circ$. The global database of various meteorological and surface parameters are generated by taking into considering the measured values at various worldwide stations and also retrieved from satellite dada. The spatial distribution of the SLHF anomaly prior to each event has been studied in a $12^\circ \times 12^\circ$ area with the pixel covering the epicenter. The daily values of a month period prior to and after shocking from 1991 to 2007 are taken for analysis.

Table 1: Details of four earthquakes.

Place	Data	Epicenter	Magnitude (Ms)	Focal Depth
Zhangbei	01/10/1998	114.51E, 41.12N	6.3	15
Taiwan Chichi	21/09/1999	121.20E, 23.35N	7.6	8
Jiashi	24/02/2003	77.33E, 39.58N	6.8	8
Puer	06/02/2007	101.13E, 23.08N	6.7	6

Since SLHF is affected by the winds, tides and monsoon, it is spatial-temporally changed. To analyze the SLHF anomaly prior to earthquake, the perennial spatial-temporal influences are considered as background trend, and the SLHF data of 16 years (besides the shocking year) are used to calculate the mean values of SLHF for each pixel as perennial trend. The mean value during that period is used to take account of the seasonal effect. For each earthquake location, to analyze the SLHF behavior of the epicenter, the mean value of SLHF plis 1.5 time the standard deviation of SLHF were taken as background noise. To analyze the SLHF behavior of the epicenter and the adjacent regions of shocking, the procedures are as following:

1) The mean value and the standard deviation (the same month and the same day of 16 years) are calculated so as to get the background trend of each pixel.

2) The daily anomaly index of each pixel can be calculated as:

$$\mathrm{AI} = \frac{(\mathrm{SLHF}(r,t) - \overline{\mathrm{SLHF}(r)})}{\sigma_{\mathrm{SLHF}}}$$

$\mathrm{SLHF}(r,t)$ is the daily value of SLHF, $\overline{\mathrm{SLHF}(r)}$ and σ_{SLHF} are the mean value and standard deviation of each pixel respectively;

3) If $\mathrm{AI} > 1.5$, the pixel is considered to be an anomaly pixel;

4) The group of the anomaly pixels is considered to be a potential seismic active region.

3. RESULTS AND DISCUSSION

To analyze the SLHF behavior of the epicenter pixel of four earthquakes in Table 1, the temporal variation features of SHLF in epicenter pixel were obtained in Fig. 1. The solid line shows the SLHF daily values prior to and after earthquake. The dashed-dot line shows the daily mean value for 16 years. The dotted line shows daily mean of 16 years plus 1.0 time standard deviation. The dashed line shows the maximum SLHF values, which is considered as the maximum background noise daily mean of 16 years plus 1.5 time standard deviation. This background noise varies with location to location and day to day. The arrow shows the day of the main earthquake event. The result show that: 1) SLHF behavior of the epicenter pixel shows a similar trend for all the four earthquake, 2) abnormal SLHF occurred 9 days before Zhangbei earthquake (Fig. 1(a)), abnormal SLHF occurred 2 days before Chichi earthquake (Fig. 1(b)), abnormal SLHF occurred 12 days before Jiashi earthquake (Fig. 1(c)), abnormal SLHF occurred 5 days before Puer earthquake (Fig. 1(d)), 3) Prior to the main earthquake event, SLHF values have been found to be greater the sum of mean SLHF plus 1.5 time standard deviation.

The SLHF anomaly has associated with local active faults before earthquake. The spatio-temporal distribution of SLHF anomaly index of seismic active areas of two earthquakes has been analyzed.

For convenience of comparison, the spatio-temporal distribution of SLHF anomaly has been considered for two different stages of a month period prior to and after the earthquake in Zhangbei region: from 2 January 1998 to 5 January 1998 as the first stage (anomalous stage), from 6 January 1998 to 10 January 1998 as the second stage. Fig. 2 shows a spatio-temporal distribution of the SLHF anomaly index (10 days prior to the main event): 1) the SLHF anomaly appeared on north-west in epicenter on 2 January 1998, 2) the SLHF anomaly increased significantly on 3 January 1998, their distribution tended to concentrate onto the main active faults, the maximum ΔSLHF exceed 2 time standard deviation, 3) the SLHF anomaly decreased in southern of epicenter on 4 January 1998 and disappeared on 5 January, 4) the SLHF anomaly decreased in western of epicenter, but increased in eastern and the maximum ΔSLHF exceed 2 time standard deviation.

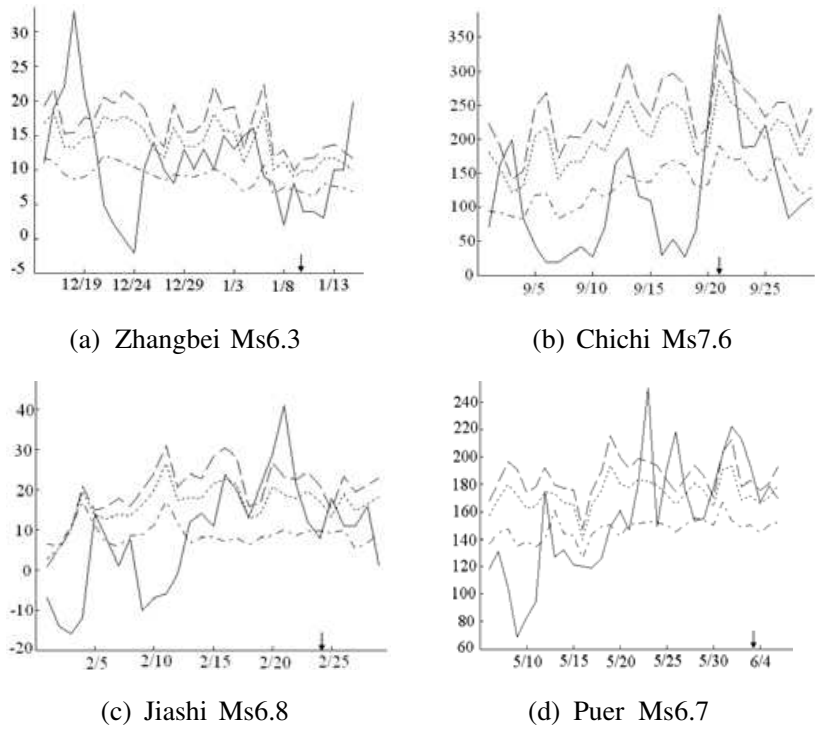

(a) Zhangbei Ms6.3 (b) Chichi Ms7.6

(c) Jiashi Ms6.8 (d) Puer Ms6.7

Figure 1: Temporal features of SHLF in the epicenters pixels of four earthquakes respectively.

During the second stage (4 days before the earthquake), the region of SLHF values decreased to normal values.

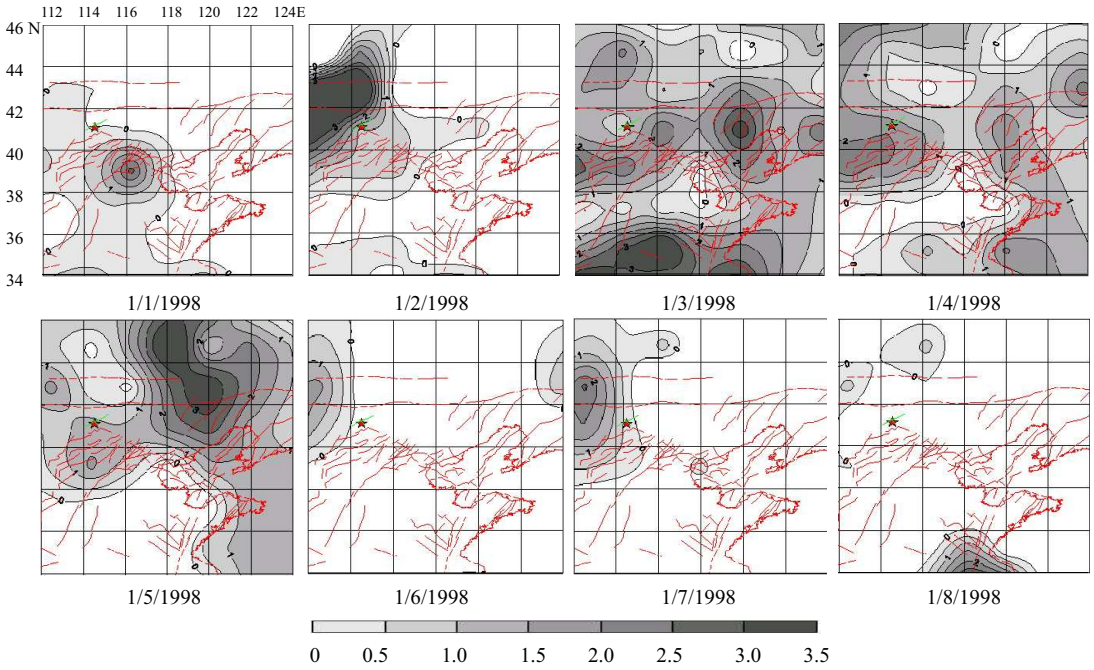

Figure 2: Spatio-temporal distribution of SLHF anomaly in the Zhangbei region.

Figure 3 shows a spatio-temporal distribution of the SLHF anomaly index in Puer region prior to the earthquake: 1) the SLHF anomaly appeared on northern and western in epicenter on 27 May 2007, the maximum ΔSLHF exceed 3 time standard deviation in northern, 2) the SLHF anomaly increased significantly from 31 January 2007 to 2 June 2007, their distribution tended to concentrate onto the main active faults, the maximum ΔSLHF exceed 2 time standard deviation

on 2 June 2007.

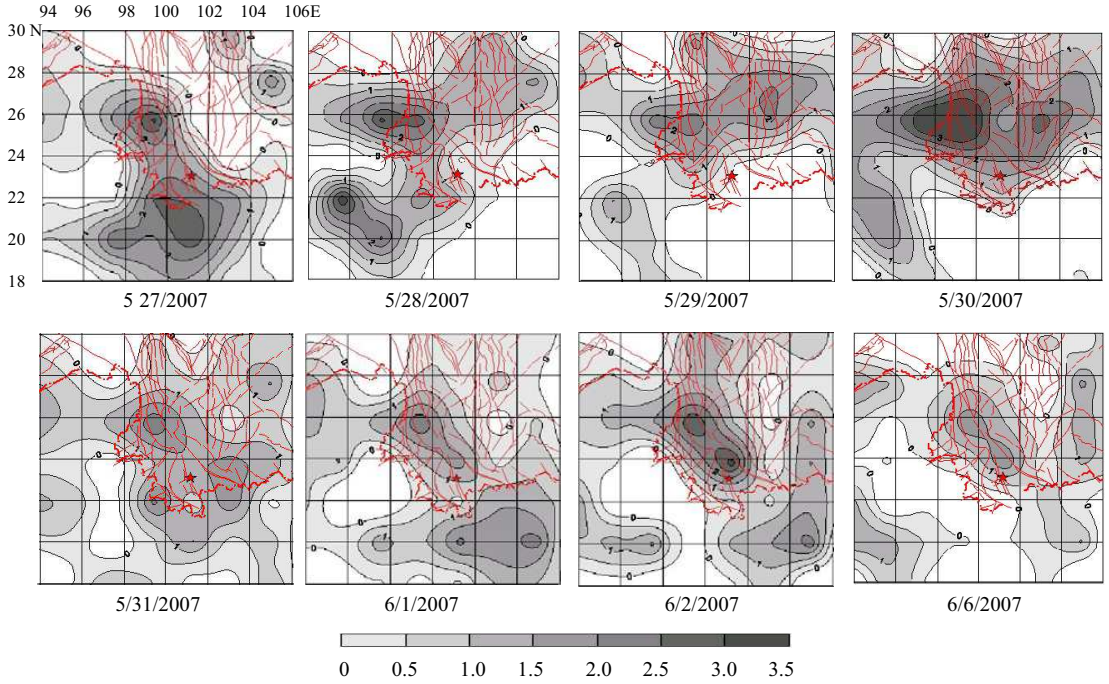

Figure 3: Time-spatial distribution of SLHF anomaly in the Puer region.

The analysis results of spatio-temporal distribution of the SLHF anomaly index show that the SLHF anomaly usually occurred in the epicenter or its surround area, and its spatial pattern was in accordance with the strike of local active faults.

4. CONCLUSIONS

The analysis of SLHF data of data the recent four earthquakes has shown anomalous behavior prior to the earthquakes. The result shows that there were abnormal SLHF occurred 2∼12 days before the earthquakes without exception. The SLHF anomaly usually occurred in the epicenter or its surround area, and its spatial pattern was in accordance with the strike of local active faults. It was concluded that the SLHF anomaly can act as a valuable index for the remote sensing monitoring of tectonic activity, and provide useful impending messages for both costal and inland earthquakes in China. It was suggested that SLHF together with other meteorological data such as surface temperature, water vapor, cloud liquid water and outgoing long wave radiation can be used for early warning of costal and territorial earthquakes.

ACKNOWLEDGMENT

This research is supported by the National Outstanding Youth Fund (No. 50525414) and NSFC (No. 50774017).

REFERENCES

1. Dey, S. and R. P. Singh, "Surface latent heat flux as an earthquake precursor," *Natural Hazards and Earth System Sciences*, Vol. 3, 749–755, 2003.
2. Cervone, G., M. Kafatos, D. Napoletani, et al., "Wavelet maxima curves of surface latent heat flux associated with two recent Greek earthquakes," *Natural Hazards and Earth System Sciences*, Vol. 4, 359–374, 2004.
3. Singh, R. P., G. Cervone, V. P. Singh, et al., "Generic precursors to coastal earthquakes: Inferences from Denali fault earthquake," *Tectonophysics*, Vol. 431, 231–240, 2007.
4. Chen, M., Z. Deng, Z. Yang, et al., "Surface latent heat flux anomalies prior to the Indonesia MW 9.0 earthquake of 2004," *Chinese Science Bulletin*, Vol. 51, No. 1, 118–120, 2006.

Temperature Dependable Microwave Dielectric Model for Moist Soils

V. L. Mironov and S. V. Fomin
Kirensky Institute of Physics, SB RAS Krasnoyarsk, Russia

Abstract— In this paper, the temperature dependable dielectric model for moist soils was developed on the basis of the generalized refractive mixing dielectric model (GRMDM) recently proposed by Mironov et al. to provide for substantially less error, as compared to the most popular model by Dobson et al.. This model was substantiated with the use of the dielectric data measured by Curtis et al.. For a specific soil type, the temperature dependable GRMDM was shown to make as accurate predictions of this value, as a function of volumetric moisture, wave frequency, and temperature, as the dielectric data measurement accuracy is. The error of dielectric predictions was tested in the range of temperatures from 10 to 40°C, frequencies from 300 MHz to 26.5 GHz, and moistures varying from those of dry soil to the ones corresponding to full soil water capacity. The Silty Sand soil tested contained 14, 9, and 77% of clay, silt and sand respectively. In addition, the error of dielectric predictions with the temperature dependable GRMDM was compared with that of Dobson's model, proving a lot more accurate predictions.

1. INTRODUCTION

Dielectric models of the soil and vegetation are [1] an essential part in the algorithms used for data processing with regard to the problems of radar and radiothermal remote sensing. At present, the semiempirical dielectric model (SDM) proposed in [2–4] has become a routine instrument for predicting permittivities of moist soils in the microwave band. Wide spread occurrence of this model in the respective literature is partly caused by its direct linkage to conventional geophysical or agro physical variables describing moist soils, which are the input parameters sufficient for dielectric predictions. This factor makes the SDM simple and convenient in practical use, so giving this model an undisputable superiority over the other dielectric models in solving inverse problems pertinent to the radar and radiothermal remote sensing.

At the same time, once the SDM was developed on the bases of limited dielectric measurements in terms of soil mineral composition and temperature range, what really needs to be analyzed about this model is its accuracy when being applied to the soil types and used in the range of temperatures falling out of the domains encountered in [2–4]. In this context, the SDM was recently shown [5–7] to generate predictions for an assemblage of soils measured in [8] with three times as large error compared to that it does in the case of the prototypal soils, thus revealing essential impact of specific soil mineral compositions on the SDM error.

Meanwhile, the impact of temperature variations on the SDM accuracy has not been analyzed yet. In this paper, this analysis is conducted in conjunction with testing the error of a newly developed temperature dependable GRMDM.

2. METHODOLOGIES OF ACCOUNTING FOR TEMPERATURE DEPENDENCE IN THE FRAME OF THE GRMDM

According to the GRMDM [5–7], dielectric constant (DC) ε' and loss factor (LF) ε'' can be calculated using the following formulas:

$$\varepsilon' = n^2 - \kappa^2, \quad \varepsilon'' = 2n\kappa \tag{1}$$

where n and κ are the refractive index and normalized attenuation coefficient.

The moist soil-water mixture refractive index (RI) and normalized attenuation coefficient (NAC) can be represented in the following form:

$$n_s = \begin{cases} n_d + (n_b - 1)\, W, & W \le W_t \\ n_d + (n_b - 1)\, W_t + (n_u - 1)\,(W - W_t)\,, & W \ge W_t \end{cases} \tag{2}$$

$$\kappa_s = \begin{cases} \kappa_d + \kappa_b W, & W \le W_t \\ \kappa_d + \kappa_b W_t + \kappa_u\,(W - W_t)\,, & W \ge W_t. \end{cases} \tag{3}$$

A set of parameters in (2) and (3) consists of: 1) maximum bound water fraction, W_t; 2) RIs n_d, n_b, n_u and NACs κ_d, κ_b, κ_u of the dry soil, bound soil water (BSW), and free soil water (FSW), respectively.

RI and NAC are the following functions of DC and LF:

$$n_p = \frac{1}{\sqrt{2}}\sqrt{\sqrt{\varepsilon_p'^2 + \varepsilon_p''^2} + \varepsilon_p'}, \tag{4}$$

$$\kappa_p = \frac{1}{\sqrt{2}}\sqrt{\sqrt{\varepsilon_p'^2 + \varepsilon_p''^2} - \varepsilon_p'}, \tag{5}$$

Here, the values $p = u$ and $p = b$ correspond to the FSW and BSW, respectively. The DC and LF of the BSW and FSW as a function of wave frequency follow the Debye formula:

$$\begin{aligned} \varepsilon_p' &= \varepsilon_\infty + \frac{\varepsilon_{0p} - \varepsilon_\infty}{1 + (2\pi f \tau_p)^2} \\ \varepsilon'' &= \frac{\varepsilon_{0p} - \varepsilon_\infty}{1 + (2\pi f \tau_p)^2} 2\pi f \tau_p + \frac{\sigma_p}{2\pi \varepsilon_r f} \end{aligned} \tag{6}$$

Here, $\varepsilon_\infty = 4.9$ is the DC in the high-frequency limit, ε_{0p} is the DC in the low frequency limit, f is the wave frequency in Hertz, τ_p is the relaxation time in second, σ_p is the effective conductivity in S/m, and ε_r is the DC for free space, which is equal to 8.854×10^{-12} F/m.

In order to make the GRMDM expressed with formulas (1)–(6) a temperature dependable dielectric model, some of the GRMDM spectroscopic parameters have to be presented as a function of temperature. The dependence of the low frequency dielectric constant limit on the temperature can be represented with the Clausiuss-Mossotii equation [9] in the form

$$\varepsilon_{0p}(T) = (1 + 2\exp(F_p(t_s) - \beta_p(t - t_s)))/(1 - \exp(F_p(t_s) - \beta_p(t - t_s))) \tag{7}$$

where β_p is the volumetric expansion coefficient, t and t_s are the current and starting temperatures by degrees centigrade. The function $F_p(t)$ can be expressed with the equation

$$F_p(t) = \ln[(\varepsilon_{p0}(t) - 1)/(\varepsilon_{p0}(t) + 2)]. \tag{8}$$

The relaxation time, in picoseconds, can be determined with the Debye relaxation formula [9] accounting for the temperature dependence:

$$\tau_p = \frac{48 \times 10^{-12}}{T} \exp\left(\frac{\psi_p}{T} - \theta_p\right) \text{ (ps)} \tag{9}$$

where the parameters, $\psi_p = \Delta H_p/R$ and $\theta_p = \Delta S_p/R$, are proportional to the activation energy, ΔH_p, and entropy of activation, ΔS_p, respectively, T is the absolute temperature, and R is the universal gas constant.

Finally, the conductivity, σ_p, has a linear dependence on the temperature, which is characteristic to the ionic solutions:

$$\sigma_p(t) = \sigma_p(t_s) + \beta_{\sigma\, p}(t - t_s). \tag{10}$$

Here, $\beta_{\sigma p}$ is the temperature incrementation coefficient for conductivity. While $\sigma_p(t_s)$ is the value of conductivity at a starting temperature, t_s. The temperature in (10) is to be assigned in degrees by centigrade. As a result, to make dielectric predictions, the temperature dependable GRMDM needs the input parameters shown in Table 1.

3. TEMPERATURE DEPENDABLE DIELECTRIC MODEL

The dielectric data available in [8] were employed to obtain the GRMDM spectroscopic parameters with the same fitting procedure as used in [5–7] for the Silty Sand soil containing by mass 14% of clay, 77% of sand, and 9% of silt. The results of this fitting at the temperatures of 10, 20, 30, and 40°C are shown in Table 2.

The data from Table 2 were fitted with formulas (7)–(10) to yield the parameters relating to the temperature dependable GRMDM, as given in Table 3, with the starting temperature being equal to 20°C.

Table 1: Temperature dependable GRMDM parameters.

n_d	Dry soil RI
κ_d	Dry soil NAC
W_t	Maximum BW fraction
$\varepsilon_{0b}(t_s)$	Starting low frequency limit DC for BSW
β_b, (K^{-1})	Volumetric expansion coefficient for BSW
ψ_b, (K)	Activation energy coefficient for BSW
θ_b	Entropy of activation coefficient for BSW
$\sigma_b(t_s)$, (S/m)	Starting conductivity for BSW
$\beta_{\sigma b}$, (S/mK)	Temperature incrementation coefficient for conductivity for BSW
$\varepsilon_{0u}(t_s)$	Starting low frequency limit DC for FSW
β_u, (K^{-1})	Volumetric expansion coefficient for FSW
ψ_u, (K^{-1})	Activation energy coefficient for FSW
θ_u	Entropy of activation coefficient for FSW
$\sigma_u(t_s)$, (S/m)	Starting conductivity for FSW
$\beta_{\sigma u}$, (S/mK)	Temperature incrementation coefficient for conductivity for FSW

Summing up it is worth noticing that the GRMDM is represented with the formulas (1)–(6) in conjunction with the spectroscopic parameters to be assigned for each temperature and taken from Table 2 as a function of temperature. While the temperature dependable GRMDM is presented with the formulas (1)–(10) in conjunction with the spectroscopic parameters, which do not depend on the temperature, as given in Table 3, nevertheless ensuring dependence of the complex dielectric constant on the temperature. In the next section, the temperature dependable GRMDM will be tested against the dielectric data from [8].

Table 2: GRMDM spectroscopic parameters at different temperatures.

Spectroscopic Parameters	**Temperatures, °C**			
	10	**20**	**30**	**40**
$\boldsymbol{n}_d$	1.5			
$\boldsymbol{\kappa}_d$	0.03952			
$\boldsymbol{W}_t$	0.071			
$\boldsymbol{\varepsilon}_{0b}$	66.5			
$\boldsymbol{\tau}_b$ (ps)	13.8	10.5	8.4	7.04
$\boldsymbol{\sigma}_b$ (S/m)	0.160	0.200	0.243	0.290
$\boldsymbol{\varepsilon}_{0u}$	103.9	100	96.4	93.1
$\boldsymbol{\tau}_u$ (ps)	11.8	8.5	6.4	5.04
$\boldsymbol{\sigma}_u$ (S/m)	0.200	0.250	0.304	0.363

Table 3: Temperature dependable GRMDM parameters for the Silty Sand soil at the starting temperature of 20°C.

$\boldsymbol{n}_d$	$\boldsymbol{\kappa}_d$	$\boldsymbol{W}_t$	$\boldsymbol{\varepsilon}_{0b}(\boldsymbol{t}_s)$	$\boldsymbol{\beta}_b$ (K^{-1})	$\boldsymbol{\psi}_b$ (K^{-1})	$\boldsymbol{\theta}_b$	$\boldsymbol{\sigma}_b(\boldsymbol{t}_s)$ (S/m)
1.5	0.03952	0.071	66.5	0	1700.983	1.623	0.2
$\boldsymbol{\beta}_{\sigma b}$ (S/mK)	$\boldsymbol{\varepsilon}_{0u}(\boldsymbol{t}_s)$	$\boldsymbol{\beta}_u$ (K^{-1})	$\boldsymbol{\psi}_u$ (K^{-1})	$\boldsymbol{\theta}_u$	$\boldsymbol{\sigma}_u(\boldsymbol{t}_s)$ (S/m)	$\boldsymbol{\beta}_{\sigma u}$ (S/mK)	
0.004	100	0.0001	2227.226	3.634	0.25	0.005	

4. VALIDATION OF THE TEMPERATURE DEPENDABLE GRMDM

To estimate the correlation between the predictions obtained with the temperature dependable GRMDM and the measured DCs and LFs borrowed from [8], the latter were plotted in Fig. 1 versus predicted ones for the whole ensemble of temperatures shown in Table 2. In their turn, the predicted values were calculated with the use of the formulas (1)–(10) and parameters shown in Table 3.

As follows from Fig. 1, over the whole variety of temperatures, moistures, and frequencies measured in [8] for the Silty Sand soil, the temperature dependable GRMDM is able to predict the DCs and LFs with error characterized by the correlation coefficients, R_{DC} and R_{LF}, and standard deviations, SD_{DC} and SD_{LF}, which are equal to: $R^2_{DC} = 0.996$, $R^2_{LF} = 0.981$, $SD_{DC} = 0.601$, $SD_{LF} = 0.401$. While the linear fits obtained are expressed in the form as follows: $\varepsilon'_m = 0.319 + 1.003\varepsilon'_p$, $\varepsilon''_m = -0.0481 + 1.0325\varepsilon''_p$, which signifies only a minor bias of the predictions obtained against the measured data.

The test conducted in the same way with the use of the GRMDM, that is, the formulas (1)–(6) and Table 1, revealed the same error in terms of the correlation coefficients, R_{DC} and R_{LF}, and standard deviations, SD_{DC} and SD_{LF}, which appeared to be equal to: $R^2_{DC} = 0.996$, $R^2_{LF} = 0.981$, $SD_{DC} = 0.606$, $SD_{LF} = 0.403$. The linear fits themselves were found to be as follows: $\varepsilon'_m = 0.0.320 + 1.004\varepsilon'_p$, $\varepsilon''_m = -0.051 + 1.033\varepsilon''_p$, which are almost identical to those corresponding to the temperature dependable GRMDM. This means that the temperature dependable GRMDM is able to provide predictions with the same accuracy as the GRMDM does.

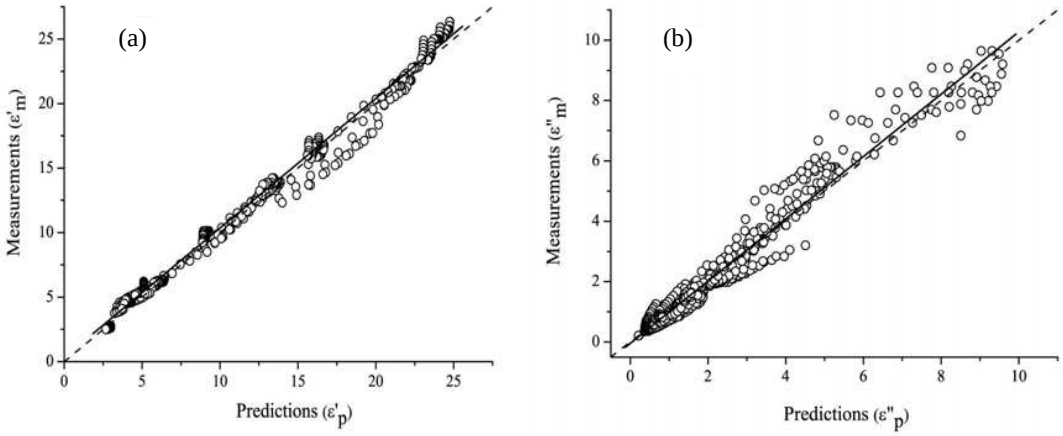

Figure 1: Correlation of the temperature dependable GRMDM predictions, ε'_p, ε''_p, for DCs (a) and LFs (b) with the measured ones, ε'_m, ε''_m, in the case of soil D measured in [7]. Solid and dotted lines represent bisectors and linear fits, respectively. Correlation coefficients, R_{DC} and R_{LF}, and standard deviations, SD_{DC} and SD_{LF}, are equal to $R^2_{DC} = 0.996$, $R^2_{LF} = 0.981$, $SD_{DC} = 0.601$, $SD_{LF} = 0.401$. The linear fits are expressed as follows: $\varepsilon'_m = 0.319 + 1.004\varepsilon'_p$, $\varepsilon''_m = -0.0481 + 1.032\varepsilon''_p$.

5. VALIDATION OF THE TEMPERATURE DEPENDABLE DOBSON'S DIELECTRIC MODEL

In order to make assessments of the predictions error regarding Dobson's dielectric model [2–4] over the whole range of temperatures available in [8] for the Silty Sand soil, the respective predictions were calculated using the formulas of Dobson's model from [2–4], with the water complex dielectric constant values as a function of temperature to be calculated according to the dielectric data and formulas available in [10]. The results of this correlation analysis are presented in Fig. 2, based on the data set for all temperatures, frequencies and moistures available in [8] for the Silty Sand soil. Although the measured and predicted values presented in Fig. 2 exhibit rather a high degree of correlation ($R = R^2_{DC} = 0.988$ for DCs and $R = 0.906$ for LFs), it should be noted that the predictions have a noticeable bias relative to the measured values, their linear fits being expressed by the following equations: $\varepsilon'_m = -0.95347 + 0.77726$, $\varepsilon''_m = 0.77612 + 0.74347\varepsilon''_p$, instead of $\varepsilon'_m = \varepsilon'_p$ and $\varepsilon''_m = \varepsilon''_p$. And, second, some values of LF predicted take negative in the range of measured values from 0.5 to 3. From the data given in Figs. 1 and 2 follows that the error of the temperature dependable GRMDM dielectric predictions is about twice as small, compared to that of the SDM.

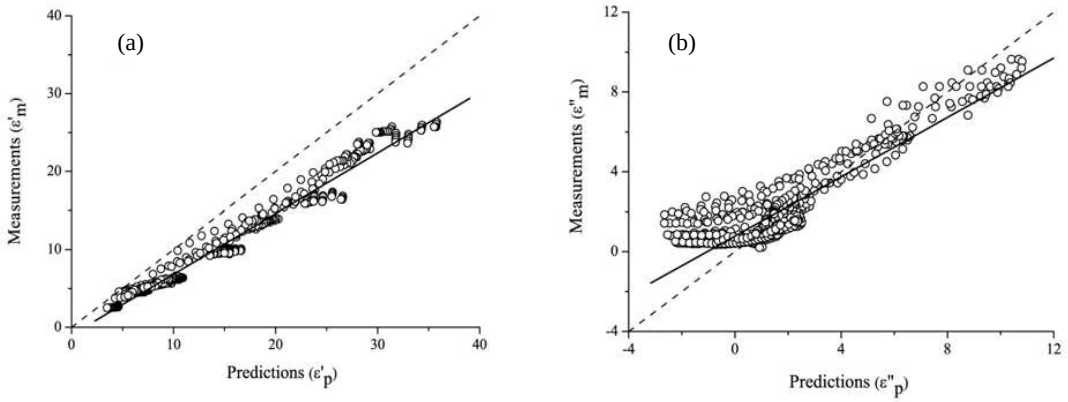

Figure 2: Correlation of the temperature dependable Dobsonfs dielectric model predictions, ε'_p, ε''_p, for DCs (a) and LFs (b) with the measured ones, ε'_m, ε''_m, in the case of the Silty Sand soil measured in [7]. Solid and dotted lines represent bisectors and linear fits, respectively. Correlation coefficients, R_{DC} and R_{LF}, and standard deviations, SD_{DC} and SD_{LF}, are equal to $R^2_{DC} = 0.988$, $R^2_{LF} = 0.906$, $SD_{DC} = 1.072$, $SD_{LF} = 0.885$. The linear fits are expressed as follows: $\varepsilon'_m = -0.953 + 0.777\varepsilon'_p$, $\varepsilon''_m = 0.776 + 0.743\varepsilon''_p$.

6. CONCLUSIONS

The temperature dependable GRMDM proved to ensure dielectric predictions in the temperature range from 10 to 40°, using the spectroscopic parameters not dependable on the temperature, with the same accuracy as the GRMDM does with the use of the temperature dependable spectroscopic parameters. In terms of standard deviation, the error of the temperature dependable GRMDM dielectric predictions was found to be twice as small, compared to that of the SDM.

REFERENCES

1. Ulaby, F. T., R. K. Moor, and A. K. Fung, *Microwave Remote Sensing, Active and Passive*, Vol. 3, Artech House, Dedham, MA, 1986.
2. Dobson, M. C., F. T. Ulaby, M. T. Hallikainen, and M. A. El-Rayes, "Microwave dielectric behavior of wet soil — Part II: Dielectric mixing models," *IEEE Trans. Geosci. Remote Sensing*, Vol. 23, No. 1, 35–46, 1985.
3. Peplinski, N. A., F. T. Ulaby, and M. C. Dobson, "Dielectric properties of soils in the 0.3–1.3 GHz range," *IEEE Trans. Geosci. Remote Sensing*, Vol. 33, No. 3, 803–807, 1995.
4. Peplinski, N. A., F. T. Ulaby, and M. C. Dobson, "Correction to 'Dielectric properties of soils in the 0.3–1.3 GHz range'," *IEEE Trans. Geosci. Remote Sensing*, Vol. 33, No. 6, 1340, 1995.
5. Mironov, V. L., L. G. Kosolapova, and S. V. Fomin, "Phisically and mineralogically based spectroscopic dielectric model for moist soils," Preprint 842F (in English), Russian Academy of Sciences Siberian Branch L.V. Kirensky Institute of Physics, Krasnoyarsk, Russia, 2007.
6. Mironov, V. L., L. G. Kosolapova, and S. V. Fomin, "Soil dielectric model accounting for contribution of bound water spectra through clay content," *PIERS online*, Vol. 4, No. 1, 31–35, 2008.
7. Mironov, V. L., L. G. Kosolapova, and S. V. Fomin, "Validation of the soil dielectric spectroscopic models with input parameters based on soil composition," *Proc. IGARSS*, Barcelona, Spain, 2007.
8. Curtis, J. O., C. A. Weiss, Jr., and J. B. Everett, "Effect of soil composition on dielectric properties," Technical Report, EL-95-34, December 1995.
9. Dorf, R. C., Ed., *The Electrical Engineering Handbook*, 2nd ed., CRC Press LLC, Boka Raton, FL, 1997.
10. Stogryn, A., "Equation for calculation the dielectric constant of saline water," *IEEE Trans. Microwave Theory Tech.*, Vol. 19, 733–736, 1971.

Monioring of Satellite Thermal Pattern in the Azores Current Area

Shigehisa Nakamura

Kyoto University, Japan

Abstract— In relation to problems on monitoring of satellite thermal pattern of relation to ocean front evolution, a specific example is introduced to give one of the supporting data obtained in the sea area of the Azores in the northeastern Atlantic. A simplified model is shown for understanding the sea surface temperature pattern observed in-situ. This result is effective to encourage the author's modeling.

1. INTRODUCTION

This work is an extensive part of the author's research project on monitoring if satellite thermal pattern in the ocean front evolution.

In relation to this project, the author has had an information from one of the scientist in the Azores. The Azores group has reported on a problem of the Azores current separates the colder and fresher waters in the northeastern Atlantic. They have noticed about the sea surface temperature pattern in-situ in their interested sea are could be well related to the satellite thermal pattern in the satellite signal of the infrared band received out of the sea surface.

The author's model for realizing satellite thermal pattern of an ocean front evolution is taken to be well supported by this specific case. So that, a more advanced research might be effective to find a key to this application.

2. DATA SOURCE

The author is now introducing a simple model for illustrating sea surface thermal pattern observed in the ocean by this time not only in the area of the northwestern Pacific but also a specific case in the Azores area of the northeastern Atlantic.

The specific case of the sea surface temperature pattern was informed personally by one of the scientists in the University of Azores. This pattern was obtained by an observation in-situ which was studied comparing the satellite thermal pattern of the sea surface obtained by analyzing the signals of the infrared band radiated out of the sea surface. The Azores research group has compared to find them to be consistent each other.

On the other hand, referring to the author's related research by this time, this specific case of the Azores seems to support the author's model for ocean front evolution studied on the bases of the author's monitoring system by directly receiving of the satellite signal at a station where a simple system has been available to use an antenna and a processing function.

3. OCEAN FRONT MODEL

The author introduces a model of ocean front evolution first.

Now, assume that a cold water mass encountering to a warm water mass forms an ocean front. Consider a straight line form case of an ocean front. An undulation of a straight ocean front is a conditional trigger of an ocean front evolution. A small amplitude undulation evolves to form a kink, filament, and an entrapped core water.

In this work, a case of the entrapped core water in an encircled filament is formed by the ocean front.

Assuming a case of no water masses interaction across the front, the encircled water in the core of the considering filament may be taken as if it were a form of eddy. There are some concept of eddy though the author considers that this filament formation to be taken as an eddy like front evolution, as found in A of Figure 1. In this case, a couple of eddy like front evolution can be seen. However, one of them is simply taken in our interest for our purpose. This spiral pattern can be found by the satellite just at the time when this pattern is in the foot print of the sensor mounted on the satellite.

Next, consider about a thermal pattern on the sea surface along a survey line A–A for a line of X=A (cf. Figure 1).

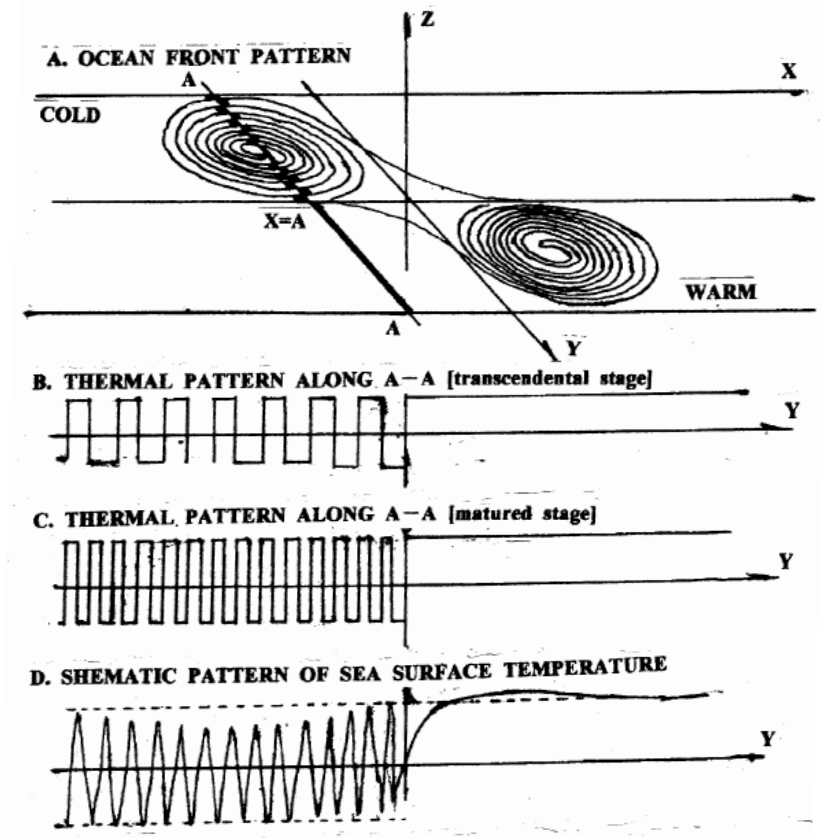

Figure 1: A model of ocean front evolution for intruded filament which is a stage of forming a couple of eddies. A — Ocean front pattern with a core of a matured stage; B — A thermal pattern along a line A–A of sea surface in a transcendental stage of model; C — A thermal pattern along a line A–A of sea surface in a matured stage of model; D — A schematic thermal pattern of the sea surface temperature observed in the Azores area.

Then, a thermal pattern on the sea surface in the interested ocean area must be a form of a case similar to that of B as shown in Figure 1. In a case of a matured stage of the encircled filamentation, The case of C rather than the case of B might be possible to appear.

In the actual ocean, some interactions and exchange processes are found across the front. Exactly speaking, the two water masses contacts a frontal face of the 3 dimensional shape.

In fact, no thermal pattern with a harshe edges is seen (cf. cases B or C in Figure 1), though a rounded thermal pattern of the sea surface temperature is usually found as shown in case D of Figure 1.

4. AZORES OBSERVATION

The research group of the University of Azores, has surveyed to obtain a specific thermal pattern on the sea surface temperature in-situ along a survey line where was in a foot print of the satellite sensor in the northeastern Atlantic.

A part of their group's survey has been analyzed and reported. The author has informed about the pattern of the sea surface along one of their survey lines. This was personally informed to the author by Professor Ana Martins (the University of Azores), the leader of the survey group, when she had a chance to discuss here on the problems related to ocean front. Their research has covered not only the satellite monitoring but also surveys in-situ, numerical modeling of current field in their interested field area. The other oceanographic factors are their interest so that several other data are also introduced though the author is not to introduce the other informations from them. With this, it could easy to see that the water masses have complicated motions though the specific thermal pattern is found easily.

The author has noted first an ocean front evolution referring to the cases found in the area of the northwestern Pacific. Then, he could find his model could be taken applicable to the other cases in the other ocean area. This might be a key to introduce a model good for a universal application.

5. CONCLUSIONS

The author introduced the sea surface thermal pattern monitored by the satellites in order to see what problems should be considered for the problems of an ocean front evolution. This work is a special reference to the case of the sea surface thermal pattern along a survey line which was in the foot print of a satellite, referring to a project which has been promoted by the survey group of the University of Azores. The sea surface thermal pattern observed along a survey line in the northeastern Atlantic seems to support the author's model of an ocean front evolution. Even though, it is necessary to consider a 3 dimensional problem in practice. A more advanced research is expected.

Radiometric Measurements of Maximum Bound Water Fraction in Soil

V. L. Mironov, **P. P. Bobrov**, **and A. S. Yascheko**
Kirensky Institute of Physics, SB, RAS, Krasnoyarsk, Russia

Abstract— The radiothermal method of simultaneous sensing both the maximum bound water fraction in the soil and the bulk soil moisture has been proposed and experimentally substantiated. The method is based on soil emissivity measurements for thawed and frozen soils during a short time before and after freezing.

1. INTRODUCTION

So far, the radiometric remote sensing of moist soils has been focused on retrieving only volumetric soil moisture [1], with almost no studies having been developed to remotely sense hydrological properties of soils, such as the maximum bound water fraction (MBWF) retained by a given type of soil. This situation can be partly attributed to using in respective moisture retrieving algorithms the semiempirical dielectric model [2–4], in which the MBWF was not explicitly introduced as a distinct value to be determined. At the same time, recently, the MBWF as a hydrological soil parameter was proposed to be used in the generalized refractive mixing dielectric model (GRMDM) for moist soils [5], which made possible, at least in principle, deriving the MBWF from radiometric or radar remote sensing data. In this paper, a method of radiometric measurements of the MBWF is considered, using the GRMDM as a radiophysics basis.

2. MEASUREMENT METHODOLOGY

First, on the basis of the GRMDM parameters given for a variety of soils in [6, 7], there were established the regression dependences of the real, n_t, and imaginary, κ_t, parts of the soil complex refractive index on the MBWF, with soil volumetric moistures being equal to the MBWF. These equations can be expressed in the following form:

$$n_t = (f, T, W_t) = a\,(f, T)\,W_t + b,$$
$$\kappa_t = (f, T, W_t) = c\,(f, T)\,W_t + d,$$

where f and T are the wave frequency and physical temperature, respectively. Coefficients b and d do not depend on the frequency and temperature ($b = 1.65$, $d = 0.11$), as they concern dry soil. At the temperature of 20°C and frequency of 1.67; 6; and 6.9 GHz, the factors a and c are equal to: $a = 5.21$; 4.97; and 4.93 and $c = 0.77$; 0.86; and 0.89, respectively.

Second, according to the GRMDM, at a given total volumetric moisture, W, the emissivity for moist soils was expressed through the real and imaginary parts of the complex refractive index, which can be written in the form

$$n = (f, T, W_t, \Delta W) = n\,(f, T, W_t) + (n_\Delta\,(f, T) - 1)\,\Delta W,$$
$$\kappa = (f, T, W_t, \Delta W) = \kappa\,(f, T, W_t) + \kappa_\Delta\,(f, T)\,\Delta W,$$

where $n_\Delta(f, T)$ and $\kappa_\Delta(f, T)$ are respectively the real and imaginary parts of the complex refractive index of free soil water, which is present in soil in excess of the MBWF, $\Delta W = W - Wt$. If the surface of soil is smooth, the emissivity, χ, is given by the equation

$$\chi = 1 - \left|\frac{\cos\varphi_1 - \dot{n}\cos\varphi_2}{\cos\varphi_1 + \dot{n}\cos\varphi_2}\right|^2 \tag{1}$$

where $\dot{n}$ stands for the complex refractive index of the soil, φ_1 and φ_2 are the angles of incidence in air and refraction in soil, respectively. As seen from (1), the emissivity appears to be a known function of four arguments, $\chi = \chi(f, T, Wt, \Delta W)$, provided the functions $n_\Delta(f, T)$ and $\kappa_\Delta(f, T)$ are determined from some other consideration.

Third, to derive the MBWF, it was proposed to measure the brightness temperature T_B of thawed soil just before and after freezing, with the depth of frozen layer being equal to, or greater

then, the depth of sensing, and the temperature of soil being confined in a narrow range around the freezing point, T_f. From these measurements, the soil emissivity can be found with the following formula: $\chi = T_B/T_f$.

As follows from [8], the values $n_t(f, T, W_t)$ and $\kappa_t(f, T, W_t)$ undergo only minor variations with the temperature, so that they were estimated at the temperature of 20°C with the use of data presented in [6]. While, in the case of thawed soil, the values of $n_\Delta(f, T) = n_q(f, T)$ and $\kappa_\Delta(f, T) = \kappa_q(f, T)$ were calculated using the Debye formula for liquid water, according to [9]. While in the case of frozen soil, they were supposed to be equal to the real and imaginary parts of the complex refractive index of the ice: $n_\Delta(f, T) = n_c = 1.77$ and $\kappa_\Delta(f, T) = \kappa_c = 0.02$. In the final analysis, the system of two transcendental equations was obtained, $\chi_q = \chi_q(f, T, W_t, W_q)$ and $\chi_c = \chi_c(f, T, W_t, W_c)$, which is to be resolved with regard to the MBWF, W_t, and liquid water fraction, $W_q = 0.917W_c$, using χ_q, and χ_c measured as input values.

3. VALIDATION OF MEASUREMENT METHODOLOGY

To validate the proposed methodology, the emissivities at 6.0, 6.9, and 8.2 GHz for three soil plots having different values of W_t were measured in the thawed and frozen conditions. Simultaneously, the MBWFs and bulk volumetric moistures for all soil types were determined as reference values with the use of weight analysis, in case of bulk moisture, $W_t + \Delta W$, and moist soil dielectric measurements, like in [5], in case of the MBWF, W_t. At the frequencies of 6.0, 6.9, and 8.2 GHz the depth of sensing is small enough for the upper layer of the soil to get frozen without occurring noticeable decrease of its temperature, in regard with the temperature of freezing. Testing plot soils had different clay and humus contents thus ensuring variations in the values of MBWF from 0.1 to 0.17.

Figure 1: The view of the radiometric system.

Plots number 1, 2, having nearly homogeneous moisture profile due to artificial irrigation, and 3, with noticeable moisture gradient, were measured at nadir and 45 degree of arc incidence angle, respectively. The surface roughness of plots 1 and 2 was ignored because a special smoothing procedure had been applied before radiobrightness measurement.

From the start of freezing, the radiobrightness temperature grew in the course of night time, experiencing some oscillations as a function of time (see Fig. 2), which were caused by wave interference in a frozen layer of the soil. In the process of relaxation oscillations, the radiobrightness observed was approaching to the value, which corresponds to the case of soil homogeneously frozen in the limits of sensed depth. This value and the physical temperature of soil, were used for calculating the emissivity of frozen soil, χ_2.

Testing plot number 3 was measured in a succession of three freezing/thawing cycles. The emissivity for this plot is presented in Fig. 3. During the whole cycle of measurement, the soil moisture varied from 0.35 $\mathrm{cm}^3/\mathrm{cm}^3$, in the layer from 0 to 1 cm, to 0.25 $\mathrm{cm}^3/\mathrm{cm}^3$, in the layer from 2 to 5 cm, and the surface of soil had not been smoothed in advance.

To calculate brightness temperature T_B, we implemented a coherent model representing the soil as a stratified dielectric medium consisting of elementary layers with uniform complex permittivity, $\varepsilon = \varepsilon' - j\varepsilon''$. The reflectivity factor of this media was calculated using an iterative procedure as

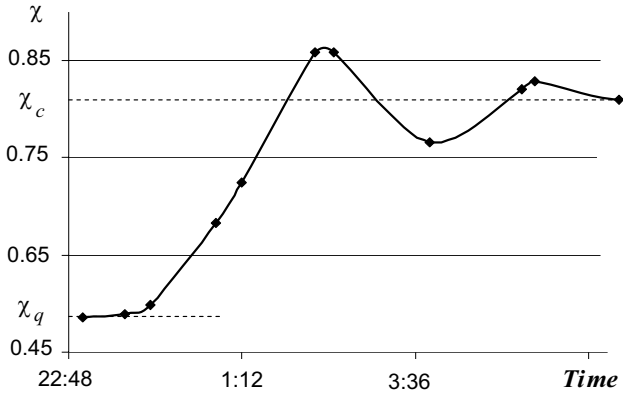

Figure 2: Emissivity related to plot 2 as a function of time in the process of freezing (see Table 1) measured at the frequency of 8.2 GHz.

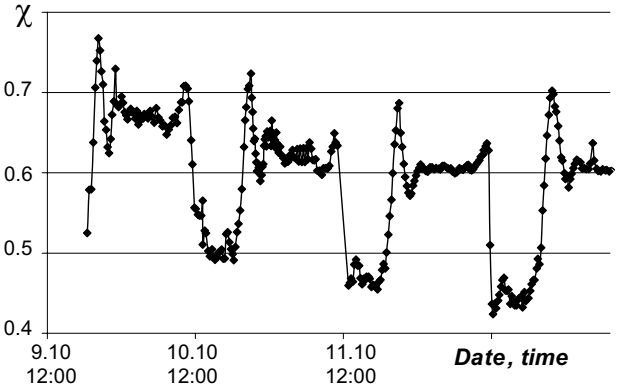

Figure 3: Emissivity related to plot 3 in the process cyclic freezing/thawing measured at frequency of 6.9 GHz.

given by the formula

$$r_0' = \frac{r_0 + r_1' \exp(-2jk_{z1}\Delta Z_1)}{1 + r_0 r_1' \exp(-2jk_{z1}\Delta Z_1)}, \tag{2}$$

where r_0' — reflectivity factor regarding the surface of multilayered soil, r_0 — Fresnel reflectivity factor relating to this boundary, r_1' — reflectivity factor regarding the multilayer soil below the depth of ΔZ_1, which is the thickness of the 1-st layer, $k_{z1} = k_0\sqrt{\varepsilon_1 - \sin^2\theta}$ — transverse component of the complex wave number in the 1-st layer, $k_0 = 2\pi/\lambda_0$ — wave number in vacuum, ε_1 — permittivity of the 1-st layer. Then the brightness temperature T_B of the soil with rough surface can be determined with the use of the formula

$$T_B = \left(1 - \left|r_0'\right|^2 \exp\left(-h\right)\right) T \tag{3}$$

where T is the thermodynamic soil temperature, h — the parameter of roughness. The latter was derived from fitting the radiobrightness measured before freezing with that calculated by the formulas (2) and (3), with the profiles of temperature and moisture in the soil having been simultaneously measured and an appropriate soil dielectric model employed. As a result, at the frequency of 6.9 GHz, the value of this parameter appeared to be of $h = 0.73$. As shown in [10], in the case of thawed soils, with the decrease of moisture, the roughness parameter, h, slightly increases, thus suggesting the value of h to increase in the process of freezing as well. However, the theoretical estimations proved the roughness parameter to be nearly constant in the process of freezing. In processing the radiobrightness data measured the roughness parameter was considered to be of the same value for the thawed and frozen soils.

Soils of plots 1 and 2 had homogeneous moisture profiles. Therefore, a good agreement of the MBWF and total moisture data obtained from the radiometric measurements and direct measurements was observed (see Table 1). Though, as seen from Table 1, the error of remote sensing data increased in the case of plot 3, which had a noticeable moisture gradient of moisture with depth.

Nevertheless, data for the MBWF appeared to be less affected by the gradient of moisture, as compared to those related to the bulk moisture.

In Table 1, are shown the values of bulk soil moisture determined by direct measurement for the layer with thickness of 4 cm. At the same time, in the process of freezing, the motion of moisture toward the freeze/thaw boundary was present, thus causing the decrease in emissivity χ_1 of both thawed and frozen soil in a succession of freezing/thawing cycles, which is well observed in Fig. 3.

Table 1: Measured values of χ_q and χ_c, retrieved values of the MBWF, W_t, and bulk volumetric moistures, W.

Plot	χ_q	χ_c	f, GHz	W_t, cm³/cm³		W, cm³/cm³	
				remote sensing data	direct data	remote sensing data	direct data
1	0.714	0.813	6.0	0.16	0.17	0.265	0.27
2	0.690	0.842	6.0	0.11	0.10	0.27	0.28
2	0.560	0.812	8.2	0.09	0.10	0.32	0.28
3	0.502	0.621	6.9	0.15	0.13	0.29	0.34
3	0.476	0.605	6.9	0.14	0.13	0.29	0.34
3	0.443	0.609	6.9	0.15	0.13	0.34	0.33

4. CONCLUSIONS

The experimental testing of the methodology proposed in this paper for radiothermal measurements of both the maximum bound water fraction and bulk soil moisture values showed good accuracy in the case of small moisture gradients present in the soil. This technique seems to be so far a unique one, allowing to remotely sense hydrological properties of the soil with acceptable accuracy. The method can be applied to perform measurements over large territories with both airborn and spaceborn radiothermal instruments.

It should be noted that the methodology needs to be improved in terms of accuracy to cover the soils with noticeable moisture gradients. In this case, multi-frequency measurements may prove to be helpful

REFERENCES

1. Wigneron, J.-P., Y. Kerr, P. Waldteufel, et al., "L-band microwave emission of the biosphere (L-MEB) model: Description and calibration against experimental data sets over crop fields," *Remote Sensing of Environment*, Vol. 107, 639–655, 2007, www.elsevier.com/locate/rse.
2. Dobson, M. C., F. T. Ulaby, M. T. Hallikainen, and M. A. El-Rayes, "Microwave dielectric behavior of wet soil — Part II: Dielectric mixing models," *IEEE Trans. Geosci. Remote Sensing*, Vol. 23, No. 1, 35–46, 1985.
3. Peplinski, N. A., F. T. Ulaby, and M. C. Dobson, "Dielectric properties of soils in the 0.3–1.3 GHz range," *IEEE Trans. Geosci. Remote Sensing*, Vol. 33, No. 3, 803–807, 1995.
4. Peplinski, N. A., F. T. Ulaby, and M. C. Dobson, "Correction to 'Dielectric properties of soils in the 0.3–1.3 GHz range'," *IEEE Trans. Geosci. Remote Sensing*, Vol. 33, No. 6, 1340, 1995.
5. Mironov, V. L., M. C. Dobson, V. H. Kaupp, S. A. Komarov, and V. N. Kleshchenko, "Generalized refractive mixing dielectric model for moist soils," *IEEE Trans. Geosci. Remote Sensing*, Vol. 42, No. 4, 773–785, 2004.
6. Mironov, V. L., "Spectral dielectric properties of moist soils in the microwave band," *Proc. IGARSS'04*, Vol. 5, 3474–3477, Anchorage, USA, 2004.
7. Mironov, V. L., L. G. Kosolapova, and S. V. Fomin, "Soil dielectric model accounting for contribution of bound water spectra through clay content," *PIERS Online*, Vol. 4, No. 1, 31–35, 2008.
8. Mironov, V. L., S. A. Komarov, and V. N. Kleshchenko, "Microwave dielectric spectroscopy for bound water in saline soil," *Proc. IGARSS'05*, Vol. 5, 3196–3199, Seoul, Korea, 2005.
9. Ulaby, F. T., R. K. Moor, and A. K. Fung, *Microwave Remote Sensing, Active and Passive*, Vol. 3, Artech House, Dedham, MA, 1986.

10. Wigneron, J.-P., Y. Ker, and L. Laguerre, "A simple parameterization of the L-band microwave emission from rough agricutural soil," *IEEE Trans. Geosci. Remote Sensing*, Vol. 39, No. 2, 1697–1707, 2001.

New Method of Permanent Scatterers Selection for Changing City

Shibo Qu[1,2,3], **Yanping Wang**[1,2], **Wen Hong**[1,2], **and Fang Cao**[1,2]
[1]National Key Laboratory of Microwave Imaging Technology, China
[2]Institute of Electronics, Chinese Academy of Sciences, China
[3]The Graduate University of Chinese Academy of Sciences
No. 19, Bei Si Huan Xi Lu, Beijing 100190, China

Abstract— Permanent scatterers interferometry (PSI) is a technique to exploit the temporal and spatial characteristics of interferometric signatures collected from point targets to accurately map surface deformation histories, terrain heights, and relative atmospheric path delays. Among PS processing steps, permanent scatterers selection is the first one. It will strongly affect the other following processing steps, and be considered as the most important one. In this paper, we present a new PS selection method using temporal variation information intended to detect permanent scatterers for changing city.

1. INTRODUCTION

Permanent scatterers interferometry is a technique to exploit the temporal and spatial characteristics of interferometric signatures collected from point targets to accurately map surface deformation histories, terrain heights, and relative atmospheric path delays. It is a complicated technique composed several processing steps: PS selection, pixel triangulation, phase unwrapping ... [1], each step can affect the monitoring results to some extent. Among these steps, permanent scatterers selection is the first step. It will strongly affect the other following processing steps. So it is most important in PS technique.

Many methods have been developed for selecting permanent scatterers. These selection methods are based on pixel amplitude stability, pixel phase stability, and also spatial coherence. Coherence has been widely used as an indicator of interferometry quality. So the spatial coherence is used to obtain the maximum likelihood estimator of the coherence magnitude, and provides an estimation of the accuracy of the pixel's phase for each interferogram that is not dependent on the number of images available. The required estimation window decreases the spatial resolution, also can cause loss of isolated scatterers which could be selected with the amplitude or phase criteria. On the other hand, the selection based on amplitude presented by Ferretti estimates the phase standard deviation of every pixel from its temporal amplitude stability, which preserves the maximum spatial resolution of the images and allows detecting single isolated scatterers smaller than a resolution cell. These two methods are widely used by all researchers, and proved their effectiveness in most tests.

2. TRADITIONAL PERMANENT SCATTERERS SELECTION METHOD

For PS processing steps, choosing enough permanent scatterers with high reliability is the most important step. Permanent scatterers are the points with high stability, their back scattering character are steady or not easily changed in long-term monitoring. Besides the good temporal stable character, permanent scatterers also have good stability when the interferometric baseline changed from more than ten to more than a thousand miles. Based on this character, there are mainly two permanent scatterers selection methods:

(1) Coherence method

Based on coherence, we can choose out enough high coherent points as permanent scatterers, which coherence is above a certain threshold. The estimation window decreases the spatial resolution, also can cause loss of isolated permanent scatterers. So we should trade off between estimation window size and good resolution. Theoretically, we can select permanent scatterers with high interferometric phase stability using coherence. Using coherence as a criterion is considered as the most direct PS selection method. Coherence can be illustrated as following equation [2].

$$\gamma = \frac{\left| \sum_{i=1}^{m} \sum_{j=1}^{n} M(i,j) S^*(i,j) \right|}{\sqrt{\sum_{i=1}^{m} \sum_{j=1}^{n} |M(i,j)|^2 \sum_{i=1}^{m} \sum_{j=1}^{n} |S(i,j)|^2}} \tag{1}$$

Here, M and S stand for pixels of two interferometric single look complex acquisitions data respectively. And * stands for conjugate operator. Generally, points of bigger coherence value correspond to the higher stability scatter points. Estimation windows have affected coherence value greatly in this PS selection method. The bigger the estimation window, the better the estimation is. But this could decrease resolution to some extent, leading to the loose of some isolated good PS points. On the other hand, the smaller estimation window can decrease the reliability of coherence estimation, which is also unfavorable for PS selection. So, the effectiveness of this method is greatly depends on the size of estimation window. This could be considered its primary deficient of coherence method.

(2) Amplitude deviation method

Amplitude deviation method is based on the theory that permanent scatterers often have good amplitude stability. This method presented by Ferretti estimates the phase standard deviation of every pixel from its temporal amplitude stability [3]. Then choose a proper threshold of amplitude standard deviation as a criterion for permanent scatterers selection. This method can be seriously affected by the number of data sets. When the available data set is small, statistical amplitude dispersion can not reflect the scatterers amplitude variation exactly, then it can pass the error into permanent scatterers selection. Large amount of data set is needed for this method.

Amplitude coefficient of variation is widely used as a symbol of scatterers phase stability. For an ordinary point in SAR image, we can define amplitude standard deviation as $\frac{\mathrm{std}(V)}{E[V]}$, $\mathrm{std}(V) = \sqrt{E[V^2] - E[V]^2}$, $E[V]$ is mean value. We then choose a proper threshold, normally used value between 0.2 to 0.3. When standard deviation is above this threshold, we identify these corresponding points as permanent scatterers.

The above two methods all have their disadvantages. For coherence method, thought it has a significant physical meaning, but the estimation window caused resolution loose. This is a handicap for permanent scatterers selection especially for space born SAR image, which resolution is low. For amplitude deviation method is a technique based on isolated pixel calculation, which preserved space resolution well. This method is effective for a large stacks data process.

3. NEW PERMANENT SCATTERERS SELECTION METHOD

These traditional PS selection methods have limitations, because they have not taken new building or house-breaking into consideration. The selection methods using amplitude stability and spatial coherence are not considered the temporal amplitude variation; often mis-select new buildings as non-permanent scatterers. We can see clearly from the equations used as criterion for PS selection, one value method will mis-select the points have only one or two big changes but demonstrate high stability in other time. But in many areas, especially in many developing cities, many buildings are newly built, rebuilt, or disappeared for reprogramming the city. Cities change almost every year. Here two pictures following are examples of the changing city as Figure 1 shows. This new method is intended to solve this problem.

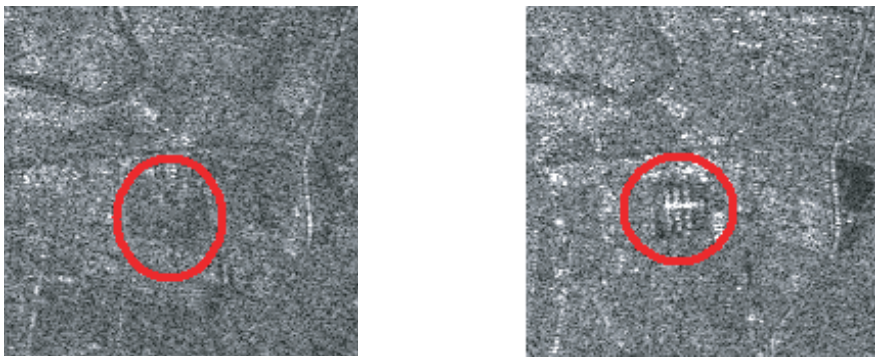

Figure 1: Example of changing city: circled points showed an area from nothing to some new buildings.

We use pixel amplitude of SAR image to judge phase noise in high signal to noise ratio circumstances. This can be illustrated as follows: For pixels in SAR images, if real part and imaginary

part all have standard deviation σ_n, then amplitude of the pixel can be Rice distribution:

$$f_A(a) = \frac{a}{\sigma_n^2} I_0\left(\frac{ag}{\sigma_n^2}\right) e^{-(a^2+g^2)/2\sigma_n^2} \quad a > 0 \tag{2}$$

Here, g stands for backscatter energy, is a positive real number. I_0 is Bessel function. For points with low signal to noise ratio (SNR, g/σ_n), the amplitude of the pixels can demonstrates Rayleigh distribution instead of Rice distribution. For points with high signal to noise ratio ($g/\sigma_n > 4$), the amplitude of the pixel can be Gauss distribution. Especially when $\sigma_n << g$, then:

$$\sigma_A \cong \sigma_{nR} = \sigma_{nl} \tag{3}$$

$$\sigma_v \cong \frac{\sigma_{nl}}{g} \cong \frac{\sigma_A}{m_A} = D_A \tag{4}$$

As we can see from the equations above, we can use pixel amplitude dispersion of SAR image to judge phase noise for high signal to noise points. Our historical method is based on this theory, can be simply illustrate from the following simulation of temporal variation of certain pixel. We use an array of number to simulate the pixel's amplitude change in a long time. a = [0.1 0.2 0.1 0.15 0.16 0.8 0.9 0.85 0.8 0.9 0.8 0.9 0.85 0.8 0.9 0.8 0.9 0.85 0.8 0.9], the mean value is 0.6703, and amplitude standard deviation $\frac{\text{std}(V)}{E(V)}$ is 0.47198. It can be a simulation of a point from nothing to a manmade building. Before or after its building, this point demonstrates stable amplitude characters, which is permanent scatterers character. But When we used amplitude deviation method to select PS point, amplitude standard deviation is 0.47198, which could be usually bigger than the threshold (normally between 0.2 and 0.3), and mis-select as non-PS point.

We then calculate its amplitude standard deviation using the three values around, it is shown in the Figure 2 right. There is a pinnacle between five and six, other point's deviations are small, and the mean deviation value is 0.1969. But this point has a typical character of PS point, except for one big change in the array. So our method re-select this kind of points as PS points.

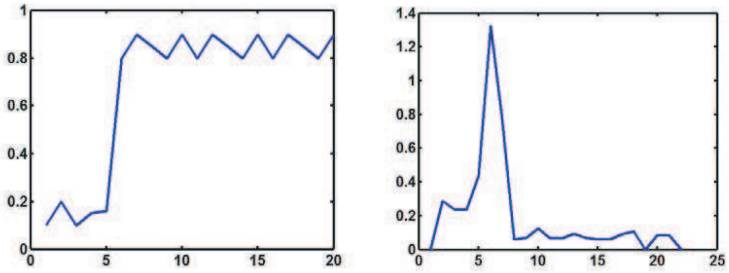

Figure 2: Left: amplitude of the simulated point. Right: deviation of this point calculated from relatively small data sets around.

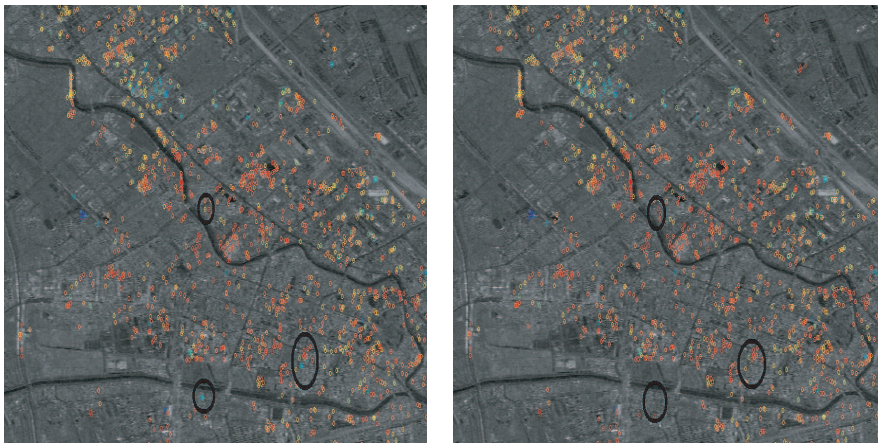

Figure 3: New method (left) and amplitude deviation method (right) comparison.

Figure 4: Corresponding position of re-selected points in Google Earth.

4. EXPERIMENT AND CONCLUSION

These analyses above are mainly focused on ideal simulation. In order to prove the effectiveness of our method we apply it on space born SAR data. Our experiment data is from Envisat ASAR, from April 25 in 2003 to Jan. 4 in 2008. These 26 acquisitions covered Tianjin area in China. We compared this new method to amplitude deviation method, amplitude deviation method selects 1621 PS, and our new method selects 1674 PS in the same area. As we can see from the Figure 3, it can re-select these newly building points successfully. The bold black circles make three of them more significantly. The last picture is the three re-selected points corresponding position in google earth. As shown in the picture, these points we highlighted in bold red circles are actually new buildings. We have check out that the left point at bottom is a new uptown in Tianjin, which have been built mainly in 2003 and 2004. Comparing to the long monitoring time span, nearly six years, its variation did not change its permanent scatterers character. Our method select it back successfully.

ACKNOWLEDGMENT

This work is supported by 07QNCX-1161 and MITL2007-06.

We would like to thank ESA for data providing under Dragon Project, especially thank Rita for her patient help for data acquisition.

REFERENCES

1. Ferretti, A., C. Prati, and F. Rocca, "Permanent scatterers in SAR interferometry," *Geoscience and Remote Sensing, IEEE Transactions*, Vol. 39, 8–20, 2001.
2. Ferretti, A., C. Prati, and F. Rocca, "Nonlinear subsidence rate estimation using permanent scatterers in differential SAR interferometry," *IEEE Transactions on Geoscience and Remote Sensing*, Vol. 38, 2202–2212, 2000.
3. Kampes, B. M., *Radar Interferometry: Persistent Scatterer Technique*, German Aerospace Center (DLR), Germany, 2006.
4. Marotti, L., A. Parizzi, N. Adam, and K. Papathanassiou, "Coherent vs. Persistent Scatterers: A case study," *Proceedings of EUSAR2008*, Kostas Papathanassiou, Germany, June 2008.

Time-domain Double Diffraction for UWB Signals

Peng Liu, **Jianying Wang**, **and Yunliang Long**
Department of Electronics & Communication Engineering
Sun Yat-Sen University, Guangzhou 510275, China

Abstract— In this paper, a heuristic time-domain uniform theory of diffraction (TD-UTD) coefficient for a double wedge obstruction is proposed. The coefficient is obtained by taking the inverse Laplace transform of the corresponding frequency domain (FD) solution that incorporates higher-order diffracted field. The early-time approximations are employed to heuristically establish the double TD-UTD coefficients for the analysis of the diffraction by dispersive obstacle wedge. The proposed closed form time domain solution is in good agreement with the numerical inverse fast Fourier transform (IFFT) of the FD solution.

1. INTRODUCTION

Ultra-wideband (UWB) systems have gained worldwide popularity in recent years due to its unique features. Accurate channel models are vital for performance evaluation and the design of UWB communications systems. Given the very wideband nature of UWB signals (i.e., up to tens of GHz of frequency bandwidth), it is more advantageous to analyze UWB channel model directly in the time domain (TD) where all the detail features that need to be calculated in an UWB system, such as the number of the multipath, the delay, the power, and the distortion of each path can be easily obtained.

Time-domain UWB multipath propagation channel model can characterize the most important electromagnetic wave propagation mechanisms, such as reflection, transmission and diffraction. Many papers have addressed the issue on the TD reflection [1] and TD transmission coefficient [2]. The Time domain UTD (TD-UTD) for a single straight perfectly conducting wedge was calculated in [3], whereas a general solution of TD-UTD coefficient for a curved perfectly conducting wedge was presented in [4]. However, in complicated environment, the transmitted signals usually undergo multiple diffractions before reaching the receiving antenna. So it is necessary to extend the single diffraction solution to a multiple-diffraction solution.

The contribution of this paper is to extend a single diffraction case to a multiple diffraction solution. By incorporating time domain higher order diffracted field, this work derives the impulse response of a double wedge diffraction configuration in a closed form. Furthermore, the early-time approximations are employed to heuristically establish the double TD-UTD coefficients [6]. And for the validity of our proposed solution, the TD solution is compared with the corresponding FD solution by applying the IFFT. The results show a very good agreement between the two solutions.

2. THEORY

2.1. Frequency Domain Model

The finite conductivity diffraction coefficients are given by [5] as

$$D(L,n;\phi,\phi') = D^{(1)} + R_0 R_n D^{(2)} + R_0 D^{(3)} + R_n D^{(4)} \tag{1}$$

where $R_{0,n}$ are the Fresnel reflection coefficients for the 0 and n face of a wedge, respectively. According to [5], double UTD coefficient in FD can be expressed as

$$E_{\mathrm{UTD}} = \frac{E_0 e^{-jks_T}}{s_T}\sqrt{\frac{s_T}{s_1 s_2 s_3}}\sum_{m=0}^{\infty}\frac{1}{m!}\left(\frac{-1}{jks_2}\right)^m \frac{\partial^m D_1(\phi_1,\phi_1')}{\partial\phi_1^m}\frac{\partial^m D_2(\phi_2,\phi_2')}{\partial\phi_2'^m} \tag{2}$$

where D_1 and D_2 are the diffraction coefficients for the first and second wedge, $\frac{\partial^m D_1}{\partial\phi_1^m}$ and $\frac{\partial^m D_2}{\partial\phi_2'^m}$ are the derivatives of the coefficients with respect to ϕ_1 and ϕ_2', as presented in [5], when dealing with multiple diffraction, higher order diffraction field might be required for a good result. For the double-diffracted examples in this paper, however, the first-order ($m = 0$) and the second-order field ($m = 1$) give good enough result. The calculation of each individual component of (2) when $m = 1$ can be found in [7]. Moreover, a special case of double diffraction with two-joined wedges also will be considered, it is illustrated in Fig. 2. Here, the second wedge is illuminated at the grazing incidence by the field from the first wedge. Consequently, the factor of 1/2 in Fig. 2 is used for grazing incidence.

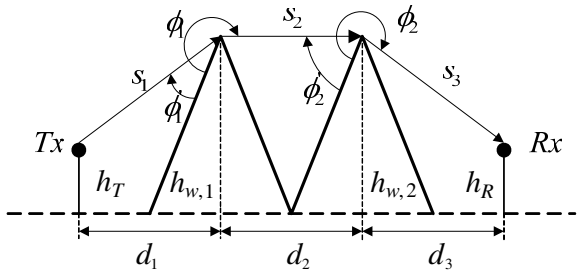

Figure 1: Ray geometry for diffraction by two wedges.

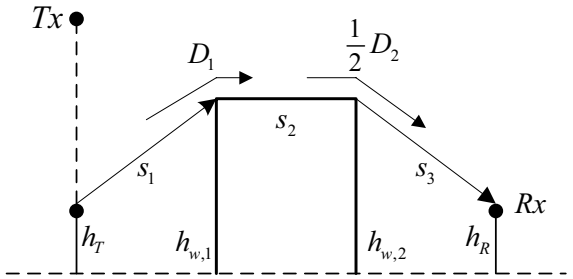

Figure 2: Diffraction by two joined wedge when using a factor of 1/2 for grazing incidence.

2.2. Time Domain Model

Following the formula above in (1), the TD-UTD coefficient for a lossy wedge can be written as

$$D_{s,h}(t) = d_1(t) + r_0(t) * r_n(t) * d_2(t) + r_0(t) * d_3(t) + r_n(t) * d_4(t) \tag{3}$$

where $r_0(t)$ and $r_n(t)$ are the TD reflection coefficients for the 0 and n face of a wedge, respectively, and the $d_i(t)$ components is given by

$$d_i(t) = \frac{-1}{2n\sqrt{2\pi}} \cot(\gamma_i) \frac{X_i}{\sqrt{\pi c t}\left(t + \frac{X_i}{c}\right)}, \quad X_i = 2Ln^2 \sin^2(\gamma_i) \tag{4}$$

where L is the distance parameter, $n\pi$ is the exterior angle of the wedge. c is the speed of light and γ_i relates to the angle of incidence and diffraction.

In the formula of (3), the time domain reflection coefficients are incorporated into the diffraction coefficient for the lossy wedge cases. But sometimes the TD versions of the reflection coefficients and their derivatives are cumbersome for calculation. In [6], the early time approximations are introduced to build the TD-UTD heuristic coefficients. This early time approximations are based on the fact that the UTD is an asymptotic formulation, valid in the limit $\omega \to \infty$. And considering that the Fresnel reflection coefficients are the functions of the complex permittivity ($\varepsilon = \varepsilon_r - j\sigma/\omega\varepsilon_0$) of the lossy obstacle, it proposes to treat the complex permittivity in the limit $\omega \to \infty$ (i.e., $\varepsilon \approx \varepsilon_r$, with negligible frequency variation), which means to assume that the Fresnel reflection coefficients do not vary with ω. Such reflection coefficient can be written as

$$R_{H,V} = \frac{\sin\varphi - a_{H,V}\sqrt{\varepsilon_r - \cos^2\varphi}}{\sin\varphi + a_{H,V}\sqrt{\varepsilon_r - \cos^2\varphi}} \tag{5}$$

where $a_H = 1$ and $a_V = 1/\varepsilon_r$, corresponding to the horizontal and vertical polarization, $\varphi = \phi'$ for the 0 face, $\varphi = n\pi - \phi$ for the n face. By using the formula of (5), the derivation of the TD-UTD heuristic coefficients is quite straightforward. It has been confirmed in [6] that the early time approximations work very well for the single diffraction cases. In this paper, the early time approximation is also applied to the establishment of the TD double diffraction coefficients. Then by taking the inverse Laplace transform of (2), the time domain double diffraction coefficients can be expressed as

$$h(t) = \sqrt{\frac{1}{s_T s_1 s_2 s_3}} \times \left[D_1(t) * D_2(t) - \frac{1}{s_2} d_1^f(t) * d_2^f(t)\right] * \delta\left(t - \frac{s_T}{c}\right) \tag{6}$$

where $D_1(t)$ and $D_2(t)$ (defined by (3)) are the single time domain diffraction coefficient corre-

sponding to the first and second wedge.

$$\begin{aligned} d_1^f(t) &= L^{-1}\left\{\frac{1}{\sqrt{jk}}\frac{\partial D_1}{\partial \phi_1}\right\} \\ &= \frac{-L}{\sqrt{2\pi}}\left[F_s^{(1)}(t) - R_0R_nF_s^{(2)}(t) + R_0F_s^{(3)}(t) - R_nF_s^{(4)}(t)\right] \\ &\quad + \frac{c}{2n\sqrt{2\pi}}\left[R_0\frac{\partial R_n}{\partial \varphi}\cot(\gamma_2)\frac{\sqrt{a_2}}{\sqrt{(t+a_2)}} + \frac{\partial R_n}{\partial \varphi}\cot(\gamma_4)\frac{\sqrt{a_4}}{\sqrt{(t+a_4)}}\right] \end{aligned} \tag{7}$$

and

$$\begin{aligned} d_2^f(t) &= L^{-1}\left\{\frac{1}{\sqrt{jk}}\frac{\partial D_2}{\partial \phi_2'}\right\} \\ &= \frac{-L}{\sqrt{2\pi}}\left[-F_s^{(1)}(t) + R_0R_nF_s^{(2)}(t) + R_0F_s^{(3)}(t) - R_nF_s^{(4)}(t)\right] \\ &\quad + \frac{-c}{2n\sqrt{2\pi}}\left[\frac{\partial R_0}{\partial \varphi}R_n\cot(\gamma_2)\frac{\sqrt{a_2}}{\sqrt{(t+a_2)}} + \frac{\partial R_0}{\partial \varphi}\cot(\gamma_3)\frac{\sqrt{a_3}}{\sqrt{(t+a_3)}}\right] \end{aligned} \tag{8}$$

$$F_s^i = \frac{\sqrt{a_i}}{2\left(t+a_i\right)^{3/2}}\cdot u(t), \quad a_i = 2Ln^2\sin^2(\gamma_i)/c \tag{9}$$

with R_0 and R_n defined by (5). Noting that for the special case in Fig. 2, the factor of 1/2 is also used in the time domain formulas for the grazing incidence.

3. NUMERICAL RESULTS

Throughout the paper, the second order derivative of Gaussian pulse is used as the incident pulse which can be mathematically expressed as

$$s = \left[1 - 4\pi\left(\frac{t-t_c}{\tau}\right)^2\right]\exp\left(-2\pi\left(\frac{t-t_c}{\tau}\right)^2\right) \tag{10}$$

where τ is the parameter used to control the width of the pulse, t_c is the time shift to put the pulse in the middle of the window, we use $\tau = 0.414\,\text{ns}$ and $t_c = 1.5\,\text{ns}$. Fig. 3 is the time domain incident pulse shape. In our simulation, hard polarization was assumed. The received signal $r(t)$ can be calculated by the equation $r(t) = s(t) * h(t)$.

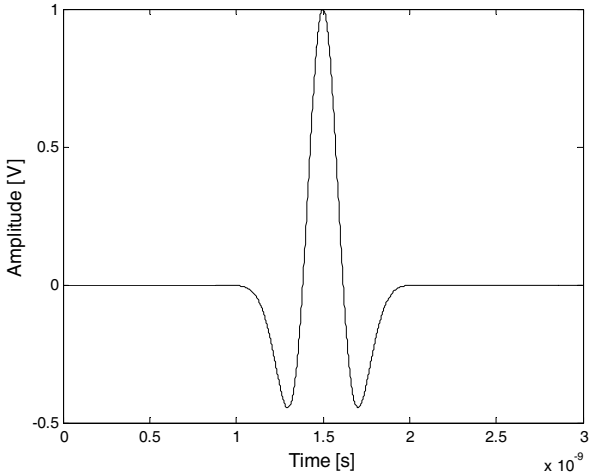

Figure 3: Second-order Gaussian pulse used as incident pulse $s(t)$.

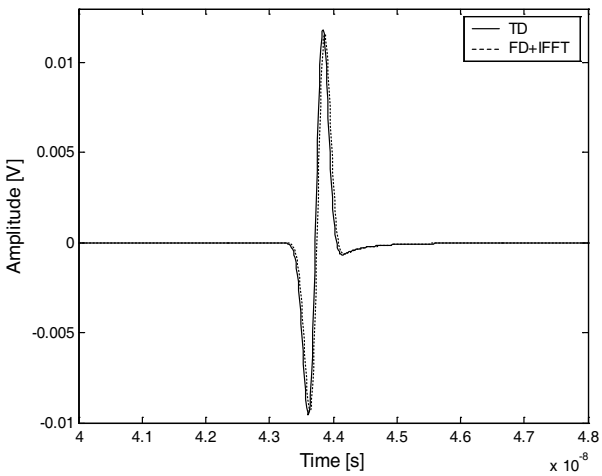

Figure 4: Pulse waveforms of the received signal at the receiver Rx in Fig. 1.

As illustrated in Fig. 1, a simple environment that only consists of two wedges was simulated and the environment parameters are as follows: height of the wedges $h_{w,1} = h_{w,2} = 4\,\text{m}$, height of

transmitter $h_T = 3\,\mathrm{m}$, height of the receiver $h_R = 1\,\mathrm{m}$, distances between wedges, the transmitter and the receiver $d_1 = d_2 = d_3 = 4\,\mathrm{m}$, the two wedges have the same internal angle $\pi/3$, the relative permittivity $\varepsilon_r = 15$ and the conductivity $\sigma = 0.012\,\mathrm{S/m}$. In Fig. 4, the solid curve denoted as "TD" is calculated by performing direct convolution, the dash line is calculated by performing an IFFT of the FD formulations. As we can see from Fig. 4, the received pulse shape is greatly distorted. Fig. 4 also shows that our time domain results are in well agreement with the frequency domain results, which validate our derivation in Section 2.

In Fig. 2, another special case of double diffraction with two-joint wedge was studied. The environment parameters remain the same with the Fig. 1 except the internal angle ($\pi/2$ in Fig. 2). The factor of $1/2$ is used for the second wedge for the grazing incidence. Noting that when $h_t \geq h_{w,1}$, besides a doubly diffracted ray, a singly diffracted ray has also been involved. It is confirmed again in Figs. 5 and 6 that both techniques essentially provide the same result.

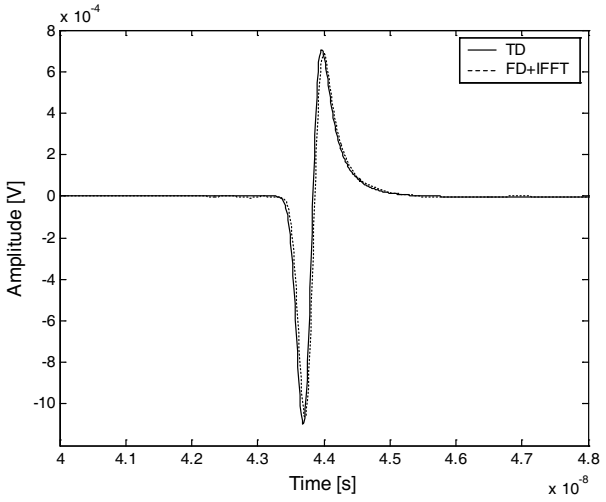

Figure 5: Pulse waveforms of the received signal at the receiver Rx in Fig. 2, when $h_T = 3\,\mathrm{m}$.

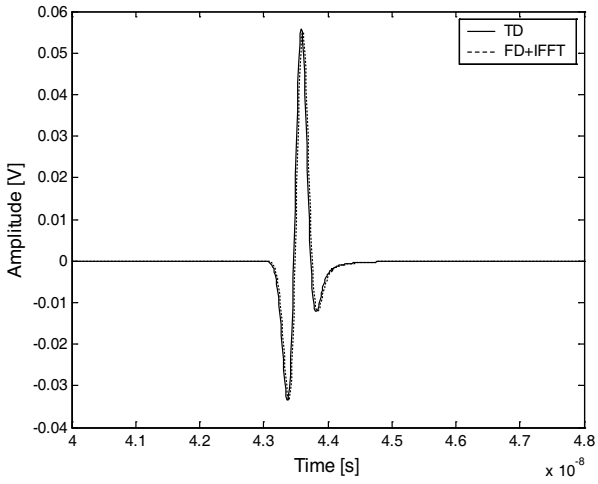

Figure 6: Pulse waveforms of the received signal at the receiver Rx in Fig. 2 with single diffraction involved, when $h_T = 5\,\mathrm{m}$.

4. CONCLUSIONS

This paper derives closed form expressions in the time domain for a double wedge diffraction that can be easily extended to a multiple diffraction solution. The obtained analytical model can model the channel with better accuracy and is very simple to use. Early time approximations are also employed to heuristically establish the double TD-UTD coefficients without any compromise on the accuracy of the results. The numerical results show that our proposed time domain results agree well with the frequency results that are widely adopted in the literature with the TD solution being more efficient in computation time and more accurate and straightforward for the analysis of pulse distortion.

ACKNOWLEDGMENT

This work was supported by the Natural Science Foundation of Guangdong (8151027501000102) and by NSFC-Guangdong (U0635003).

REFERENCES

1. Barnes, P. R. and F. M. Tesche, "On the direct calculation of a transient plane wave reflected from a finitely conducting half space," *IEEE Trans. Electromagn. Compat.*, Vol. 33, No. 2, 90–96, May 1991.
2. Qiu, R. C., "A generalized time domain multipath channel and its application in ultra-wideband (UWB) wireless optimal receiver design — Part II: Physics-based system analysis," *IEEE Trans. Veh. Techn.*, Vol. 54, No. 5, 2312–2324, Nov. 2004.
3. Veruttipong, T. W., "Time domain version of the uniform GTD," *IEEE Trans. Antennas Propagat.*, Vol. 38, No. 11, 1757–1764, Nov. 1990.

4. Rousseau, P. and P. Pathak, "Time-domain uniform geometrical theory of diffraction for a curved wedge," *IEEE Trans. Antennas Propagat.*, Vol. 43, No. 12, 1375–1382, Dec. 1995.
5. Holm, P. D., "A new heuristic UTD diffraction coefficient for nonperfectly conducting wedges," *IEEE Trans. Antennas Propagat.*, Vol. 48, 1211–1219, Aug. 2000.
6. Schettino, D. N., F. J. S. Moreira, and C. G. Rego, "Heuristic TD-UTD coefficients for the transient analysis of diffraction by lossy conducting wedges," *12th Biennial IEEE Conference on Electromagnetic Field Computation (CEFC 2006)*, 272, Miami, FL, USA, May 2006.
7. Luebbers, R. J., "A heuristic UTD slope diffraction coefficient for rough lossy wedge," *IEEE Trans. Antennas Propagat.*, Vol. 37, 206–211, Feb. 1989.

Coherent Terahertz Smith-Purcell Radiation from a Two-section Model

Zongjun Shi[1], **Ziqiang Yang**[1], **Feng Lan**[1], **Xi Gao**[1], **Zheng Liang**[1], **and D. Li**[2]

[1]Institute of High Energy Electronics, University of Electronic Science and Technology of China
Chengdu, Sichuan 610054, China
[2]Institute for Laser Technology, 2-6 yamada-oka, suita, Osaka 565-0871, Japan

Abstract— This paper presents a two-section model to produce beam bunching and obtain coherent Terahertz (THz) Smith-Purcell (SP) radiation. Based on the mechanism of Cherenkov oscillator, a continuous beam is bunched in the first section without external signal. In the second section, the coherent THz Smith-Purcell (SP) radiation is stimulated by the bunched beam interacting with open grating. The particle-in-cell (PIC) simulations show that the beam is effectively bunched and the strongest radiation is observed at 51° with the frequency of 194 GHz in this scheme.

1. INTRODUCTION

The THz sources, a currently active research area, are of importance in a variety of applications to biophysics, medical, and materials science [1, 2]. The coherent SP radiation is a promising alternative in the development of a compact, tunable, and high power THz device. However it is necessary to improve the performance of such kinds of devices.

Recently, in a companion article [3–16], the SP radiation mechanism and characteristic are discussed. They conclude that the high quality bunches is the key to generate the coherent SP radiation.

We have previously presented a study of obtaining coherent THz SP radiation from a two-section grating system [17]. By an external input signal the electron beam is bunched in traveling wave domain in the first section of the model. To obtain compact and relatively inexpensive coherent THz source, we will explore in this article how to generate the bunches mainly based on the mechanism of Cherenkov oscillator.

This paper is organized as follows: Section 2 contains a description of the physical model. In Section 3, the simulations are carried out using a CHIPIC code [18], we analyze the physical process of generating THz radiation. The Simulations and results are described in Section 4. The conclusions are given in Section 5.

2. THE PHYSICAL MODEL

A schematic diagram of the two-section model [17] is given in Fig. 1. The system consists of a grating with a flat conducting roof and an open grating. The main parameters of the grating and electron beam are summarized in Table 1.

The dispersion curve of the first section is shown in Fig. 2. In Fig. 2, the operating point P is indicated, with $f = 97$ GHz, i.e., the intersection of the dispersion relation with the beam line for

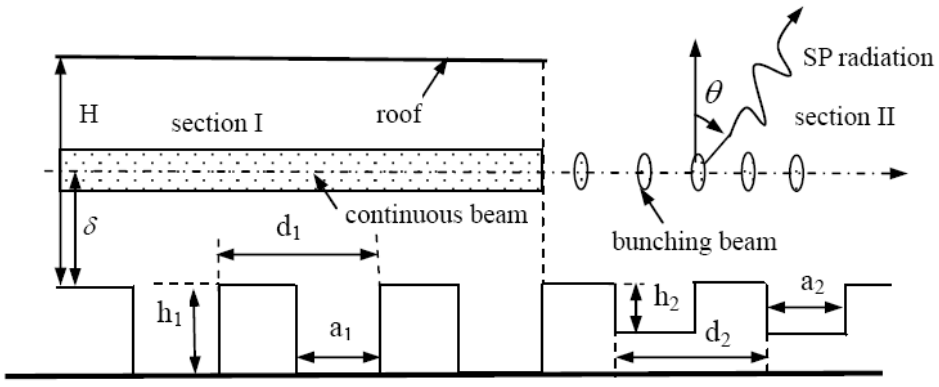

Figure 1: Schematic illustration of the physical model.

Table 1: Main parameters for the two-section model.

Parameters	First section	Second section
Beam energy	40 keV	
Current density	200 A/m	
Beam thickness	0.4 mm	
Beam-grating distance	$\delta = 0.3$ mm	
Grating period	$d_1 = 0.5$ mm	$d_2 = 0.8$ mm
Grating groove depth	$h_1 = 0.625$ mm	$h_2 = 0.24$ mm
Grating groove width	$a_1 = 0.25$ mm	$a_2 = 0.24$ mm
Number of period	$N_1 = 89$	$N_2 = 20$
Grating roof height	$H = 0.75$ mm	
External magnetic field	2 T	

40 keV electrons. Obviously, the first section Operates like a diffraction oscillator. Then it can be bunch the electrons without input signal.

In the second section, the coherent SP radiation is stimulated by the bunched beam. The frequency of SP radiation [20] observed at the angle θ as shown in Fig. 1 is

$$f = |n| \frac{c}{d} \left(\frac{1}{\beta} - \sin\theta \right)^{-1}, \tag{1}$$

where f is the frequency of the radiation, n is the order of the radiation, d is the grating period, βc is the electron velocity, c is the speed of light.

3. PIC SIMULATIONS

3.1. Descriptions of the Simulation Geometry

The simulations are carried out using a CHIPIC code [19]. It is a finite-difference, time-domain code for sufficiently simulating plasma physics process. The geometry for simulations is given in Fig. 3. The surface of the grating and the roof are assumed to consist of a perfect conductor whose rectangular grooves are parallel and uniform in the z direction. A sheet electron beam propagates along the x-direction. It is a perfect beam produced from a small cathode located at the left boundary of the simulation area. The beam-wave interaction and radiation propagation happen in the vacuum box. The boundary is enclosed with absorbers. At the end of the first section, there is an attenuator, which prevents most of the electromagnetic wave from reaching the second section.

The simulation parameters of the grating and the electron beams are shown in Table 1. The parameters of the first section grating are the same as those in a previous the article [17]. Since

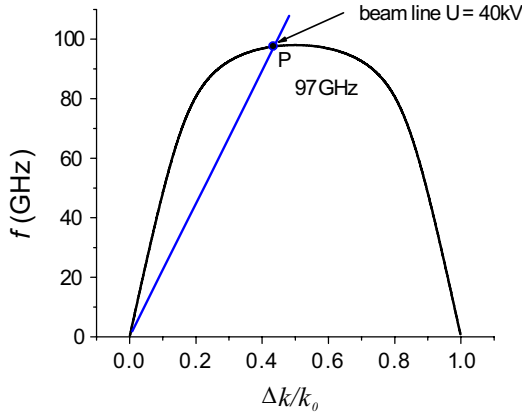

Figure 2: Dispersion curves of the grating with a flat conducting roof.

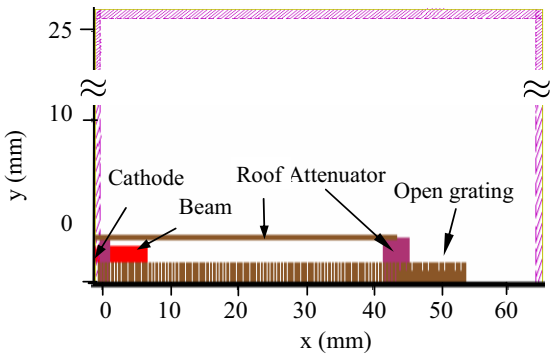

Figure 3: Simulation geometry.

it is a two-dimensional simulation, it assumes that all fields and currents are independent of the z-direction. The current density is 200 A per meter. To operate the first section as an oscillator the beam voltage is 40 kV.

3.2. Generation of Periodic Bunches

To illustrate the beam bunching, we show the phase-space plots and energy modulation of the electrons at time 3 ns, as shown in Fig. 4. The PIC simulations show that the bunching can be clearly observed as functions of both space and time. From Fig. 4(b), we note that appreciable energy modulation is visible and the mean beam energy reduction is about 2 keV due to the beam-wave interaction.

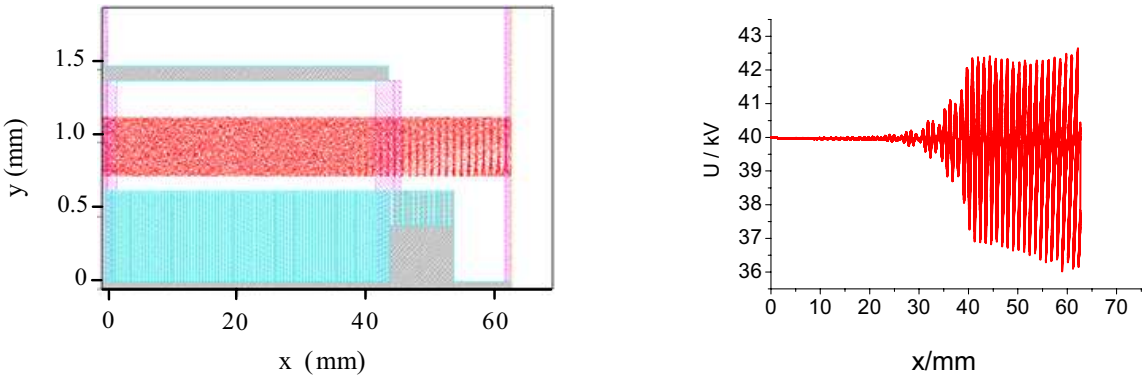

Figure 4: Phase-space distribution: Fig. 4(a) density of electrons in the x-y plane at 3 ns, bunching is evident. Fig. 4(b) kinetic energy-x density at the same time.

The modulation of the current displayed in Fig. 5. The Fig. 5(a) shows that the bunching current gets maximum at the center of open grating. In Fig. 5(b), one clearly sees the bunching current is stable in time after about 1.3 ns. The simulation results show that a continuous beam is effectively bunched by the first section.

3.3. Coherent THz Radiation

Here we focus on the radiation from the bunched beam interacting with the open grating. We observe the coherent SP radiation emitted at harmonics of the bunching frequency of 97 GHz. We use a grating having 12 periods. The B_z detector is placed at the distance 21.25 mm from the center of the open grating. Because only the second harmonic radiation frequency 194 GHz is allowed frequency of the first order ($|n| = 1$), we observe the distributions of the evanescent wave and the SP radiation wave, as illustrated in Fig. 8. From the fast-Fourier-transform (FFT) amplitude observed by the B_z detectors, we know that the dominant radiation is the second harmonic of the

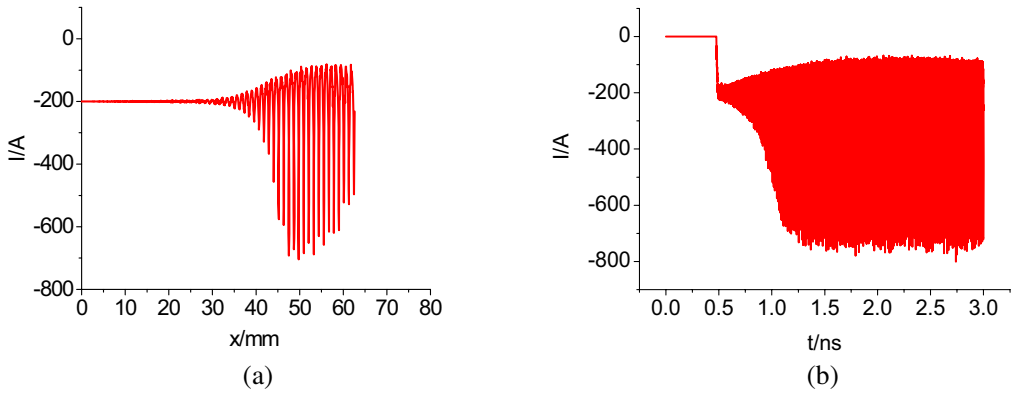

Figure 5: Current evolution as functions of both space and time: Fig. 5(a) current as a function of x direction at 3 ns, Fig. 5(b) current as a function of time at the center of open grating.

bunching frequency, which peaks at the angle of about 51° corresponding to the SP radiation angle predicted by Eq. (1). Of course, due to the beam-wave interaction which reduces the value of the particle velocity, there is a slight discrepancy between the simulation data for the radiation angle of 51° and the theoretical value 48° of the basic SP equation. According to the Fig. 6, we know the evanescent wave radiation reaches maximum at the angle of about −90° corresponding to the left end of the open grating, where it undergoes partial reflection and partial diffraction. This is due to the evanescent wave being backward wave.

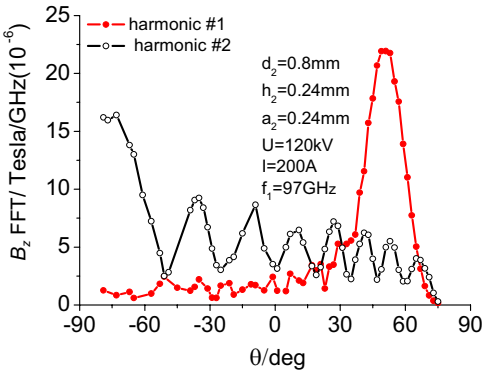

Figure 6: The peak of FFT amplitude of B_z as a function of angle, detected at the distance 21.25 mm from the open grating center.

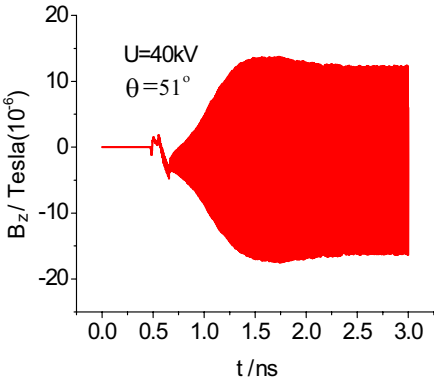

Figure 7: Time signal of B_z observed at point 21.25 mm and 51° from the open grating center.

In Fig. 7, we show evolution of magnetic field $B_z(t)$ and the corresponding FFT at angle 51° shown in Fig. 8. The time signal shows rapid growth after 1 ns. From the contour plot of Fig. 9, one can easily understand that the dominant second harmonic radiates at the angle of about 51°, in agreement with what is shown in Fig. 8.

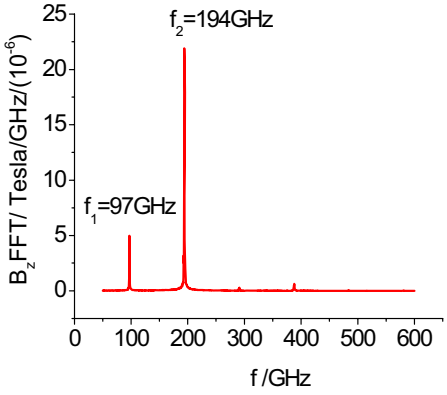

Figure 8: FFT of time signal corresponding to Fig. 7.

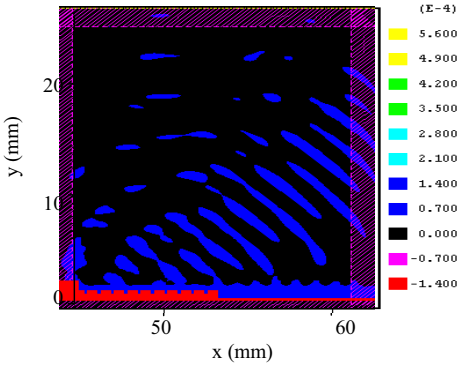

Figure 9: Contour map of B_z, $t = 2.6$ ns.

4. CONCLUSIONS

In this paper, we have presented a study of obtaining coherent THz SP radiation from a two-section grating system. Based on mechanism of Cherenkov oscillator, a continuous beam is effectively bunched through the first section. In the second section, the coherent SP radiation has been obtained by the bunched electrons interacting with the open grating. The strongest radiation is observed at 51° and the radiation frequency is 194 GHz at the simulation parameters. The coherent THz SP radiations are emitted at frequencies that are integer multiples of the bunching wave frequency, and at the corresponding SP angles. The results show that process is stable in time and along the grating. The coherent SP radiation will occur in the other frequency band when proper parameters are chosen. In this scheme, the periodic bunches are generated by itself instead of the input signal, and the cost of the source will be reduced.

ACKNOWLEDGMENT

This work was supported by National Natural Science Foundation of P. R. China (60571020).

REFERENCES

1. Mickan, S. P. and X.-C. Zhang, *Int. J. High Speed Electron. Syst.*, Vol. 13, 601, 2003.
2. Siegel, P. H., *IEEE Trans. Microwave Theory Tech.*, Vol. 50, 910.
3. Kim, K. J. and S. B. Song, *Nucl. Inst. Methods A*, Vol. 475, 158, 2001.
4. Andrews, H. L., J. E. Walsh, and J. H. Brownell, *Nucl. Inst. Methods A*, Vol. 483, 478, 2002.
5. Doria, A., G. P. Gallerano, E. Giovenale, G. Messina, V. B. Asgekar, G. Doucas, and M. F. Kimmitt, *Nucl. Inst. Methods A*, Vol. 475, 318, 2001.
6. Doria, A., G. P. Gallerano, E. Giovenale, G. Messina, G. Doucas, M. F. Kimmitt, and H. L. Andrews, *Nucl. Inst. Methods A*, Vol. 483, 263, 2002.
7. Andrews, H. L. and C. A. Brau, *Phys. Rev. ST Accel. Beams*, Vol. 7, 070701, 2004.
8. Andrews, H. L., C. H. Boulware, C. A. Brau, and J. D. Jarvis, *Phys Rev. ST Accel. Beams 8*, 050703, 2005.
9. Gover, A., *Phys. Rev. ST Accel. Beams*, Vol. 8, 030701, 2005.
10. Gover, A. and E. Dyunin, *Phys. Rev. ST Accel. Beams*, Vol. 8, 030702, 2005.
11. Donohue, J. T. and J. Gardelle, *Phys. Rev. ST Accel. Beams*, Vol. 8, 060702, 2005.
12. Donohue, J. T. and J. Gardelle, *Phys. Rev. ST Accel. Beams*, Vol. 9, 060701, 2006.
13. Korbly, S. E., A. S. Kesar, J. R. Sirigiri, and R. J. Temkin, *Phys. Rev. Lett.*, Vol. 94, 054803, 2005.
14. Li, D., Z. Yang, K. ImassKi, and G.-S. Park, *Appl. Phys. Lett.*, Vol. 88, 201501, 2006.
15. Li, D., Z. Yang, K. Imasaki, and G.-S. Park, *Phys. Rev. ST Accel. Beams*, Vol. 9, 040701, 2006.
16. Kumar, V. and K.-J. Kim, *Phys. Rev. E*, Vol. 73, 020501, 2006.
17. Shi, Z., Z. Yang, Z. Liang, et al., *Nucl. Inst. Methods A*, Vol. 578, No. 3, 543, 2007.
18. Di, J., D.-J. Zhu, S.-G. Liu, et al., "Electromagnetic field algorithm of the CHIPIC code," 2005.
19. Freund, H. P. and T. M. Abu-Elfadl, *IEEE Plasma Sci.*, Vol. 32, 1015, 2004.
20. Smith, S. J. and E. M. Purcell, *Phys. Rev.*, Vol. 92, 1069, 1953.

Modeling the Electromagnetic Scattering from a Dielectrically Filled Groove Using the Method of Auxiliary Sources

Naamen Hichem and Taoufik Aguili
Département Technologie de l'information et de communications
Ecole nationale d'ingénieurs de Tunis, Tunisia

Abstract— Scattering of electromagnetic waves from a 2D groove filled with a lossy dielectric in an infinite conducting plane is modeled using the method of auxiliary sources. The scattering structure contain two mediums (perfectly electric conductor and the lossy dielectric) considered as strongly coupled.

According to the MAS, in order to approximate the electromagnetic fields in each domain, fictitious current sources verifying the Helmoltz equation in the considered domain are introduced and distributed around the physical boundary.

Three bases of AS must be taken into account, the satisfaction of the respective boundary conditions between the dielectric, the PEC and the upper free space model the strong coupling affecting the structure.

Therefore, the scattered field is the superposition of the scattered fields by the two mediums.

The implementation code was realized with Mathematica, and the numerical results (RCS, near field) agree very well with references.

The MAS in conjunction with the EM coupling model is able to analyze the scattering from finite gratings.

1. INTRODUCTION

The method of auxiliary sources MAS is a numerical technique used extensively to solve problems involving boundaries [1]. The MAS is based on the fact that the EM fields within each domain are expressed as a linear combination of analytical solutions of Helmholz equation. These particular solutions constitute the base of auxiliary sources placed along the auxiliary contour surrounded by the physical one [2].

The MAS is applied to model the scattering by a PEC half space groove filled with a dielectric, illuminated by a TMz monochromatic plane wave. In order to simplify the presentation, we have initially decomposed the whole structure in two globally coupled parts.

The satisfaction of the boundary conditions lead to a linear system having as solution the amplitude and phase of the different auxiliary sources [3].

The implementation code realized with Mathematica justifies the above mentioned technique to model the coupling between the groove and the filled dielectric.

Numerical results (RCS, pattern field) reveal good agreement with references [5, 6].

At the end, we have numerical results justifying the technique and the possibility to extend it to periodically filled groove (gratings . . .).

An $e^{j\omega t}$ time convention is assumed and suppressed throughout the paper.

2. FORMULATION

A TMz monochromatic plane wave illuminate under the φ_i incidence a dielectrically filled groove (Fig. 1).

In the purpose to clarify the technique handled to model the initial structure, we decompose it as indicated in (Fig. 2).

Three bases of auxiliary sources are needed to evaluate the total scattered field: as shown in (Fig. 2), the first one behind the boundary groove generates the scattered field in the medium1, the second located inside the dielectric and radiate outside in the first medium and the third one is distributed outside the dielectric boundary and acts inside it. The total scattered field in the medium1 is the superposition of the fields scattered by the groove and the dielectric, of course after resolving the linear system having as unknowns the auxiliary currents.

The incident transverse magnetic wave has an electric field:

$$E_{inc}(x, y) = E_{oi}\vec{z}\exp[jk_0(x\cos(\varphi_i) + y\sin(\varphi_i))] \tag{1}$$

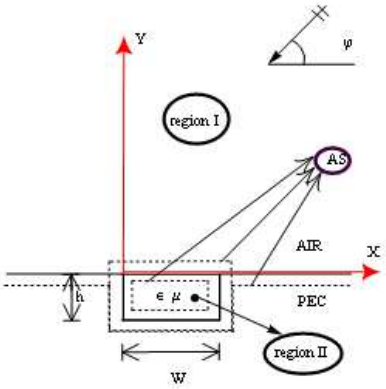

Figure 1.

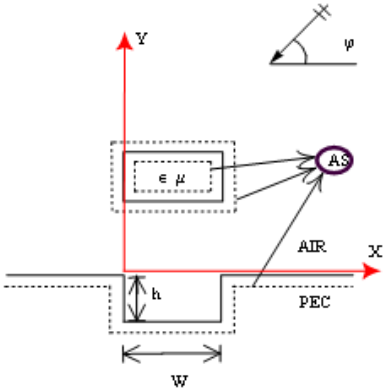

Figure 2.

Here, z denote unit vector in the z direction, since the incident electric field is z directed and independent of z with uniform structure along z, then we deduce that the scattered field is z directed too, reducing the scattering problem to a bidirectional one.

For the dielectric and the PEC, the auxiliary sources are regularly distributed along the auxiliary contour surrounded by the physical one on which are positioned the collocation points.

An auxiliary source $(\mathbf{x}_n, \mathbf{x}_n)$ produce an electric field expressed as:

$$E_{sn}(x,y) = A_n \vec{z} H_0^{(2)} \left[k_0 \sqrt{(x-x_n)^2 + (y-y_n)^2} \right] \tag{2}$$

where, $H_0^{(2)}(.)$ is the Hankel function of the second kind of first order and A_n the complex current.

According to the standard impedance boundary condition (SIBC), the tangential component of the total electric field must be continuous on the boundary [4], then for the PEC:

$$n_{PEC} \wedge E_{total} = 0 \tag{3}$$

And for the dielectric boundary:

$$n_{DIEL} \wedge E_{inside} = n_{DIEL} \wedge E_{outside} \tag{4}$$

$$n_{DIEL} \wedge H_{inside} = n_{DIEL} \wedge H_{outside} \tag{5}$$

Applying (3) on the PEC boundary and (4), (5) on the dielectric we obtain a linear system composed of $3N$ equations. Where, the unknowns' A_n mentioned before represent the complex currents and N the number of auxiliary sources per base.

For every groove collocation point m and dielectric collocation point n, the continuity equations yield to:

$$E_{1(m)}^{inc} + E_{1(m)}^{I} + E_{1/2(m)}^{I} = 0 \tag{6}$$

$$E_{2(n)}^{inc} + E_{2(n)}^{I} + E_{2/1(n)}^{I} = E_{2(n)}^{II} \tag{7}$$

$$n_2 \wedge \left(H_{2(n)}^{inc} + H_{2(n)}^{I} + H_{2/1(n)}^{I} \right) = n_2 \wedge H_{2(n)}^{II} \tag{8}$$

The indices 1 and 2 refers respectively to the groove and the dielectric,

$E_{1(m)}^{inc}$ is the incident electric field just on the groove collocation m.

$E_{1(m)}^{I}$ in the total electric field radiated by the groove auxiliary base on the collocation point m.

$E_{1/2(m)}^{I}$ is the total electric field radiated by the inside dielectric auxiliary base and evaluated just on the groove collocation point m.

$E_{2(n)}^{inc}$ is the incident electric field just on the dielectric collocation n.

$E_{2(n)}^{I}$ is the total electric field radiated by the inside dielectric auxiliary base on the collocation point n.

$E_{2/1(n)}^{I}$ is the total electric field radiated by the groove auxiliary base and evaluated just on the dielectric collocation point n.

$E^{II}_{2(n)}$ is the total electric field radiated by the outside dielectric auxiliary base on the collocation point n.

Repeating these conditions for different collocation points, we obtain the following square matrix:

$$\begin{pmatrix} Z_{11} & Z_{12} & 0 \\ Z_{21} & Z_{22} & Z_{23} \\ Z_{31} & Z_{32} & Z_{33} \end{pmatrix}$$

We obtain a linear system composed of $3N$ equations that gives as solution the amplitude and phase of the complex currents.

3. NUMERICAL RESULTS

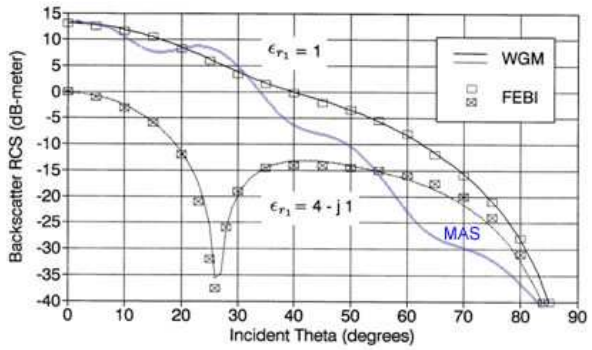

Figure 3: Backscattering 2-D RCS for TM Incidence on a Rectangular Groove with $W = 1.0\,\mathrm{m}$ and $d = 0.25\,\mathrm{m}$. Comparing calculations using MAS to those from (FEBI) Approach in [6] at $f = 300\,\mathrm{MHz}$ for: $\varepsilon_r = 1$ (vacuum).

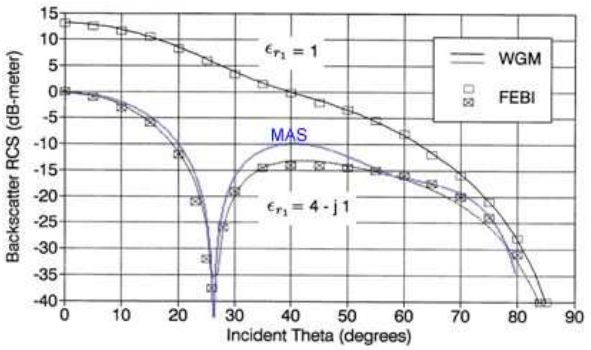

Figure 4: Backscattering 2-D RCS for TM Incidence on a Rectangular Groove with $W = 1.0\,\mathrm{m}$ and $d = 0.25\,\mathrm{m}$. Comparing calculations using MAS to those from (FEBI) Approach in [6] at $f = 300\,\mathrm{MHz}$ for: $\varepsilon_r = 4 - j1$ (lossy dielectric).

4. CONCLUSION

The MAS is applied is this paper to model coupling between a PEC groove and a lossy dielectric. Numerical results show good agreement with references. According to the MAS we can superpose two different auxiliary bases acting with different frequencies.

We are working about the application of this technique to a periodic grating.

REFERENCES

1. Shubitidze, F., H. T. Anastassiu, and D. I. Kaklamani, "An improved accuracy version of the method of auxiliary sources for computational electromagnetics," *IEEE Transactions on Antennas and Propagation*, Vol. 52, No. 1, January 2004.
2. Anastassiu, H. T., et al., "Electromagnetic scattering analysis of coated conductors with edges using the method of auxiliary sources (MAS) in conjunction with the standard impedance boundary condition (SIBC)," *IEEE Transactions on Antennas and Propagation*, Vol. 50, No. 1, January 2002.
3. Kaklamani, D. I. and T. Hristos, "Aspects of the method of auxiliary sources (MAS) in computational electromagnetics," *IEEE Transactions on Antennas and Propagation*, Vol. 44, No. 3, June 2002.
4. Harrington, R. F., *Time Harmonic Electromagnetic Fields*, McGraw-Hill, New York, 1961.
5. Volakis, J. L., et al., *Finite Element Method for Electromagnetics, Antennas, Microwave Circuits and Scattering Applications*, 132, 296.
6. Morgan, M. A., et al., "Mode expansion solution for scattering by a material filled rectangular groove," *Progress In Electromagnetics Research*, PIER 18, 1–17, 1998.

Analysis of Two-dimensional Scattering by a Finite Periodic Array of Conducting Cylinders Using the Method of Auxiliary Sources

Naamen Hichem and Taoufik Aguili
Département Technologie de l'information et de communications
Ecole nationale d'ingénieurs de Tunis, Tunisia

Abstract— According to the method of auxiliary sources and for conducting bodies, the scattered field is the summation of radiated fields by a set of auxiliary sources distributed on a fictitious inner contour near the physical one and satisfying the Helmoltz equation outside the considered domain [3].

The satisfaction of boundary conditions leads to the unknown complex currents. The MAS applied to model coupling between a finite array of infinitely and parallel conducting cylinders, illuminated by a monochromatic plane wave. The coupling modeled by the mutual satisfaction of the boundary conditions just on the collocation points of every cylinder [6].

In the purpose to decrease the computational cost and to alleviate calculus, we suppose that every cylinder is coupled only to the eight neighbouring cylinders. The partial coupling implementation full simplifies the global matrix expression.

The comparison between the results obtained (RCS, field pattern) according to global and partial coupling for the same array reveals good agreement with references.

In this paper, we validate the MAS applicability for the global coupling and the approximation validity for the partial coupling for a finite array of conducting cylinders.

1. INTRODUCTION

Generally, the method of auxiliary sources is used to solve problems involving one scatterer. For an array, we extend the MAS technique by subdividing the array in a finite number of different scatterers, each one acts according the distributed auxiliary sources around his boundary [1].

The boundary satisfaction on every part leads to a linear system having as unknowns the auxiliary currents.

The above mentioned technique is applied to model the scattering by a finite array of conducting and parallel infinite cylinders illuminated by a TMz monochromatic wave.

The electromagnetic coupling between the different cylinders is tacked into account by the mutual satisfaction of the boundary conditions [7].

The exact or global coupling between different parts entrains the calculus to a completely filled matrix, leading a difficult computation.

In the purpose to decrease the computational cost, we suppose that every cylinder is coupled only with the eight neighboring one. The mathematical development show that the global matrix is fully simplified and the implementation code realized by Mathematica justify the low computational cost achieved by this approximation.

Numerical results (RCS, pattern field) reveal good agreement with references.

An $e^{j\omega t}$ time convention is assumed and suppressed throughout the paper.

2. FORMULATION

A TMz monochromatic plane wave illuminate under the φ_i incidence a finite two-dimensional array of K.L infinite, PEC, circular cylinders positioned in the xOy plane (Fig. 1).

The incident transverse magnetic wave has an electric field:

$$E_{inc}(x,y) = E_{oi}\vec{z}\exp\left[jk_0\left(x\cos(\varphi_i) + y\sin(\varphi_i)\right)\right] \tag{1}$$

Here, z denote unit vector in the z direction, since the incident electric field is z directed and independent of z with uniform cylinders along z, then we deduce that the scattered field is z directed too, reducing the scattering problem to a bidirectional one.

For every cylinder, the auxiliary sources are regularly distributed along the auxiliary contour and surrounded by the physical one on which are positioned the collocation points [2].

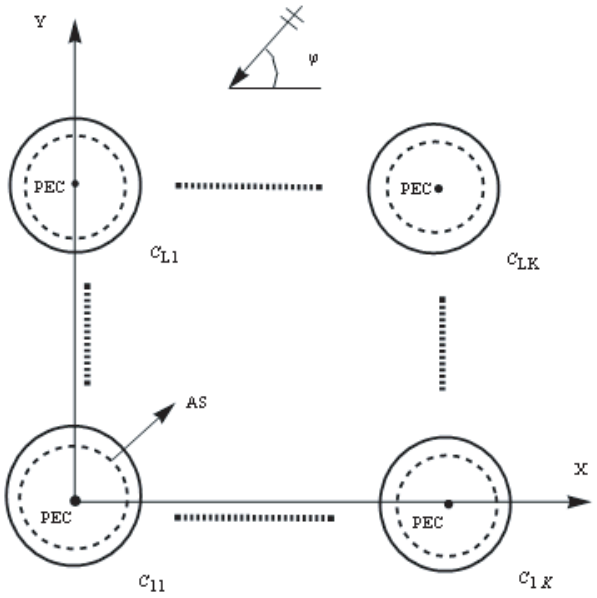

Figure 1: Array of K.L conducting cylinders.

An auxiliary source (x_n, y_n) produces an electric field expressed as:

$$E_{sn}(x,y) = A_n \vec{z} H_0^{(2)} \left[k_0 \sqrt{(x-x_n)^2 + (y-y_n)^2} \right] \tag{2}$$

where, $H_0^{(2)}[.]$ is the Hankel function of the second kind of zero order and A_n the complex current.

According to the standard impedance boundary condition (SIBC), the tangential component of the total electric field must be continuous on the boundary, then for a PEC [4]:

$$n \wedge E_t = 0 \tag{3}$$

Applying this boundary condition on every cylinder, we obtain a linear system of K.L equations:

$$E_{pq} + \sum_{i \neq p} \sum_{j \neq q} E_{pq/ij} + E_{inc/pq} = 0 \tag{4}$$

E_{pq} is the total electric field generated by all the auxiliary sources of the C_{pq} cylinder.

$E_{pq/ij}$ is the total electric field generated by all the auxiliary sources of C_{ij} cylinder and calculated on C_{pq}.

$E_{inc/pq}$ is the incident electric field on C_{pq} cylinder.

2.1. Global Coupling

The linear system (4) traduce the fact that the electric field on each collocation point take into account the contribution of all the auxiliary sources present in the array.

Let us consider a collocation point m^{pq} on C_{pq} then:

$$E_{inc(m)} = E_{oi} \exp\left[j k_0 \left(x_m \cos(\varphi_i) + y_m \sin(\varphi_i) \right) \right] \tag{5}$$

$$E_{pq(m)} = \sum_{n^{pq}=1}^{N^{pq}} A_n^{pq} H_0^{(2)} \left[k_0 R_{mn}^{pq/ij} \right] \tag{6}$$

$$E_{pq/ij(m)} = \sum_{n^{ij}=1}^{N^{ij}} A_n^{ij} H_0^{(2)} \left[k_0 R_{mn}^{pq/ij} \right] \tag{7}$$

$R_{mn}^{pq/ij}$ represents the distance between the collocation m of C_{pq} and the auxiliary source n of C_{ij}.

A_n^{ij} represents the current of the auxiliary source n of C_{ij}.

Developing these expressions in (4) we obtain:

$$\sum_{n^{pq}=1}^{N^{pq}} A_n^{pq} H_0^{(2)}\left[k_0 R_{mn}^{pq/ij}\right] + \sum_{i\neq p}\sum_{j\neq q}\sum_{n^{ij}=1}^{N^{ij}} A_n^{ij} H_0^{(2)}\left[k_0 R_{mn}^{pq/ij}\right] = -E_{inc(m)}^{pq} = V_m^{pq} \tag{8}$$

We obtain a linear system composed of N.K.L equations that gives the solution the amplitude and phase of the complex currents.

2.2. Partial Coupling

In this part, we take into account only the coupling between the considered cylinder and the eight neighboring one. The Equation (8) will take the following form:

$$\sum_{n^{pq}=1}^{N^{pq}} A_n^{pq} H_0^{(2)}\left[k_0 R_{mn}^{pq/ij}\right] + \sum_{i=p\pm1}\sum_{j=q\pm1}\sum_{n^{ij}=1}^{N^{ij}} A_n^{ij} H_0^{(2)}\left[k_0 R_{mn}^{pq/ij}\right] = -E_{inc(m)}^{pq} = V_m^{pq} \tag{9}$$

The matrix will be fully simplified because only eight lines around the diagonal will be different from zero.

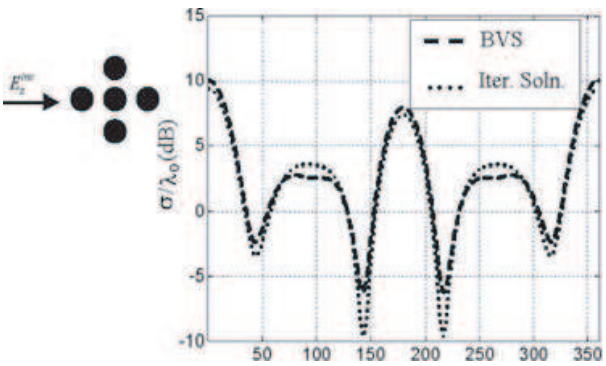

Figure 2: The RCS of five perfectly conducting cylinders each of radius = 0.1λ, and their centers are separated by 0.5λ, due to a plane wave incident at $\varphi = 180°$.

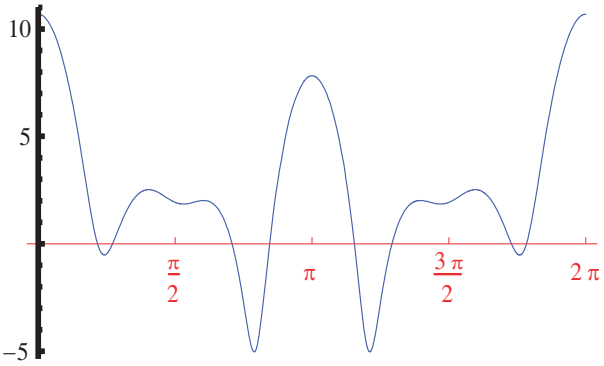

Figure 3: The RCS according to MAS for the same structure in Fig. 2.

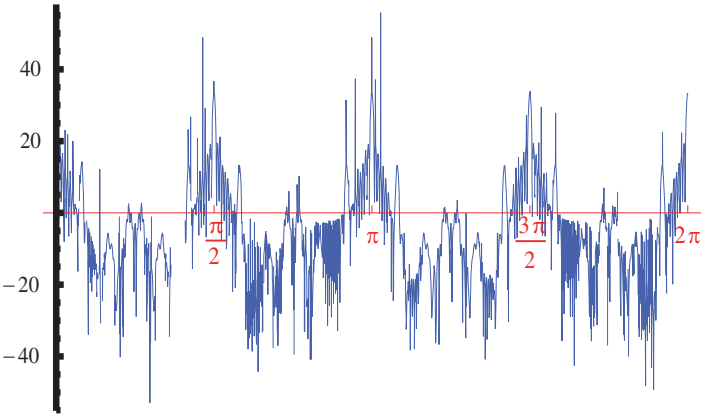

Figure 4: The RCS of 10.10 perfectly conducting cylinders each of radius = 0.5λ, and their centers are separated by 3λ, due to a plane wave incident at $\varphi = 90°$ (global coupling).

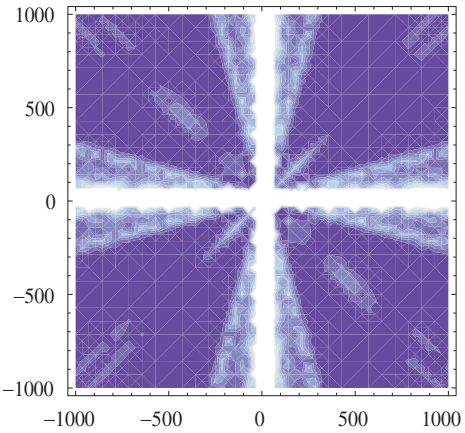

Figure 5: Far scattered field by 10.10 conducting cylinders (global coupling).

3. NUMERICAL RESULTS

The reference [8] as shown in Fig. 2 applied foe five conducting cylinders have an RCS identical to the MAS one.

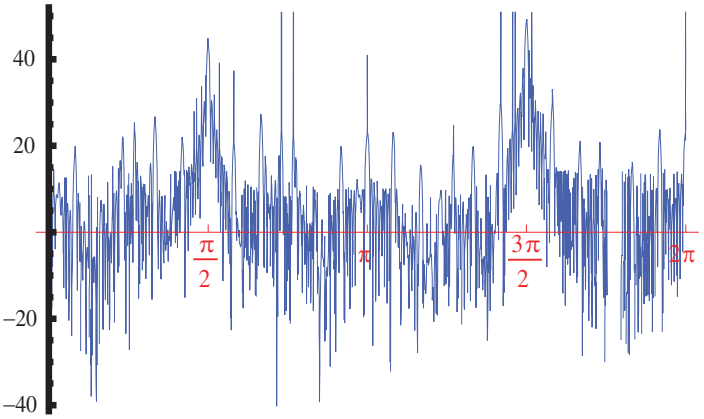

Figure 6: The RCS of 10.10 perfectly conducting cylinders each of radius = 0.5λ, and their centers are separated by 3λ, due to a plane wave incident at $\varphi = 90°$ (partial coupling).

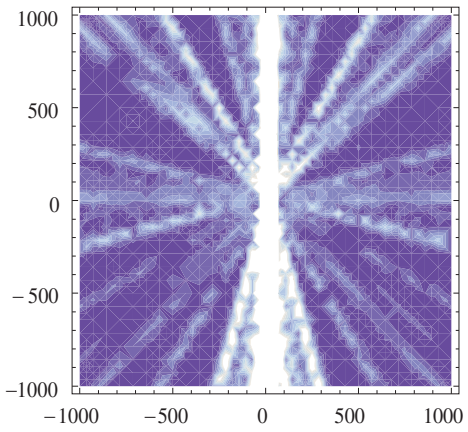

Figure 7: Far scattered field by 10.10 conducting cylinders (partial coupling).

4. CONCLUSIONS

The aforementioned numerical results valid the applicability of the MAS for the scattering properties by a finite linear array of conducting cylinders with no restriction on the cylinders size and spacing.

The global and partial coupling applied to a 10.10 conducting cylinders array have almost the same RCS and this can be explained by the fact that the number of auxiliary sources per wavelength is not sufficient (5 per wavelength).

REFERENCES

1. Shubitidze, F., H. T. Anastassiu, and D. I. Kaklamani, "An improved accuracy version of the method of auxiliary sources for computational electromagnetics," *IEEE Transactions on Antennas and Propagation*, Vol. 52, No. 1, January 2004.
2. Anastassiu, H. T., et al., "Electromagnetic scattering analysis of coated conductors with edges using the method of auxiliary sources (MAS) in conjunction with the standard impedance boundary condition (SIBC)," *IEEE Transactions on Antennas and Propagation*, Vol. 50, No. 1, January 2002.
3. Kaklamani, D. I. and H. T. Anastassiu, "Aspects of the method of auxiliary sources (MAS) in computational electromagnetics," *IEEE Transactions on Antennas and Propagation*, Vol. 44, No. 3, June 2002.
4. Harrington, R. F., *Time Harmonic Electromagnetic Fields*, McGraw-Hill, New York, 1961.
5. Henin, B. H., A. Z. Elsherbeni, and M. H. Al Sharkawy, "Oblique incidence plane wave scattering from an array of dielectric cylinders," *Progress In Electromagnetic Research*, PIER 68, 261–279, 2007.
6. Elsherbeni, A. Z. and M. Hamid, "Scattering by parallel conducting circular cylinders," *IEEE Transactions on Antennas and Propagation*, Vol. 35, No. 3, March 1987.
7. Munk, B. A., *Finite Antenna Arrays and FSS*, IEEE Press, Wiley Interscience, 2003.
8. Al Sharkawy, M. H., A. Z. Elsherbeni, and S. F. Mahmoud, "Electromagnetic scattering from parallel chiral cylinders of circular cross-sections using an iterative procedure," *Progress In Electromagnetics Research*, PIER 47, 87–110, 2004.

Single Scattering Properties of Ice Particles in mm/sub-mm Waveband: Effects of Refractive Index and Shapes

Xinxin Xie and Jungang Miao
Electromagnetics Laboratory, School of Electronic Information and Engineering
Beijing University of Aeronautics and Astronautics, Beijing 100191, China

Abstract— The effects of refractive index and shape on single scattering properties of ice particles are investigated in this paper. Mie theory is employed to simulate the effects of refractive index for ice spherical particles in the mm/sub-mm waveband. Mean deviations of scattering properties, caused by uncertainties in the real part and the imaginary part of refractive index, are calculated respectively. The discrete dipole approximation (DDA) method is used to calculate the scattering properties of bullets and Koch-fractals of the first generation.

1. INTRODUCTION

Cirrus clouds play an important role in the radiation balance of the earth [1]. Their distributions and microphysical parameters are vital to the global circulation models. Many kinds of ice crystals exist in cirrus clouds, including considerable amount of non-spherical shapes, like plate, pyramid, polyhedron, solid or hollow column, bullet and bullets aggregation, etc. The scattering and absorption characteristics of these ice particles are essential in performing radiative transfer in simulations and retrieving physical parameters of cirrus clouds.

Analytical and numerical methods, which have been tested to be valid and accurate for regular shapes like spheroids etc., have been applied for calculating scattering properties of ice particles. For irregularly-shaped particles, scattering properties can be simulated by volume integral equation methods such as DDA method [2, 3], etc. Since using spheroids to simulate the scattering characteristics of non-spherical ice particles in cirrus clouds introduces significant deviations of brightness temperature in microwave radiative transfer, it is necessary to model scattering properties of ice particles in realistic shapes in cirrus clouds. The scattering properties of ice particles depend on many other factors like crystal shape, refractive index, size parameter, orientation, etc.

This study employs Mie theory and DDA method to study the effects of refractive index and shape, respectively. In Section 2, Mie theory is employed to compute the effects of refractive index for ice spherical particles in mm/sub-mm waveband. In Section 3, the DDA method is briefly described and the emphasis is given on scattering properties of non-spherical ice particles, namely bullets and Koch-fractals (first generation). Finally, conclusions are given in Section 4.

2. EFFECTS OF REFRACTIVE INDEX

Refractive index, expressed as the square root of complex permittivity, plays a key role in calculating the scattering properties of ice particles in radiative transfer. An accurate knowledge of refractive index is required to perform radiative transfer; however, uncertainties in environmental factors and measurement errors may result in deviations of refractive index. This can take effects on the scattering characteristics of ice particles.

A model for pure ice permittivity [4] is employed in this study. The permittivity of pure ice $\varepsilon = \varepsilon' + i\varepsilon''$, at the frequency of 89 GHz, is $3.15 + \mathrm{i}0.0047$ at the temperature of $-30°\mathrm{C}$. Refractive index m is equal to $1.7748 + \mathrm{i}0.0013$.

Based on Mie theory, we simulated the effects of refractive index for ice spherical crystals. The results at 89 GHz are shown in Figures 1–3. In Figure 1, the optical efficiencies and asymmetry factor, calculated in the interval of $\pm 5\%$ uncertainty in the real part of complex permittivity or of $\pm 20\%$ in the imaginary part, is monotonously increasing or decreasing at the radius of 300 μm. Figure 2 shows the optical efficiencies and asymmetry factor are as a function of sphere radii. The relative errors are given when the permittivity ε has $\pm 5\%$ uncertainty in the real part and $\pm 20\%$ uncertainty in the imaginary part, in the left panel and right panel of Figure 2 respectively. The mean deviations of optical efficiencies and asymmetry factors are demonstrated in Figure 3. The radii are calculated in the range from 20 μm to 1000 μm since the equivalent-volume spherical radii of realistic ice particles are less than 1000 μm. Here we suppose the imaginary part of the ice permittivity lying in the interval between $80\% \times 0.0047$ and $120\% \times 0.0047$ uniformly, the real part between $95\% \times 3.15$ and $105\% \times 3.15$. Optical efficiencies and asymmetry parameters are

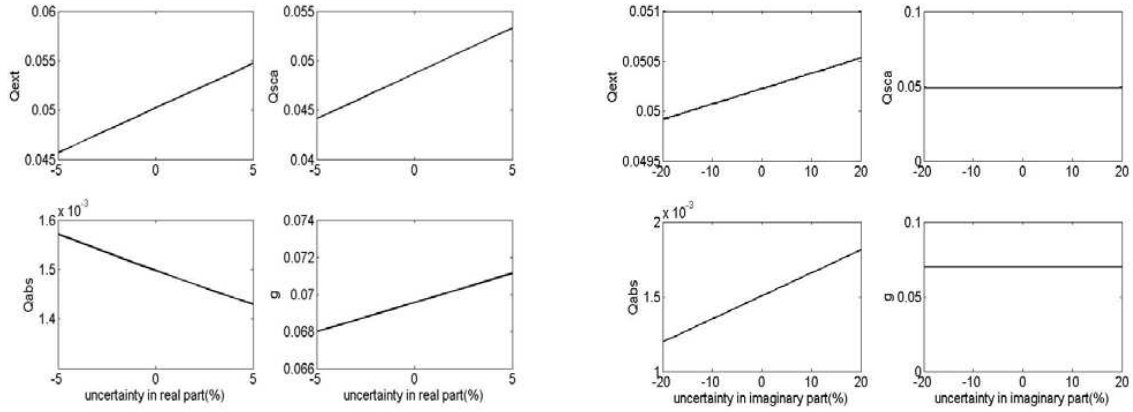

Figure 1: Optical efficiencies and asymmetry parameter g as a function of uncertainty in the real part of permittivity and in the imaginary part when the spherical radius is 300 μm.

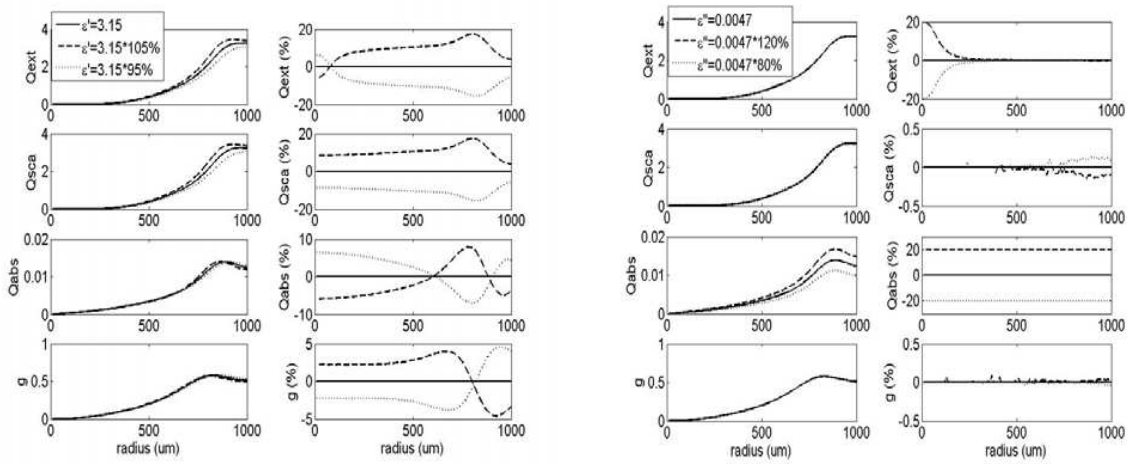

Figure 2: Optical efficiencies and asymmetry parameter g as a function of spherical radii at 89 GHz. Left Panel is scattering properties calculated as uncertainty of ±5% in the real part and relative errors of optical efficiencies and asymmetry factor while right Panel of ±20% in the imaginary part.

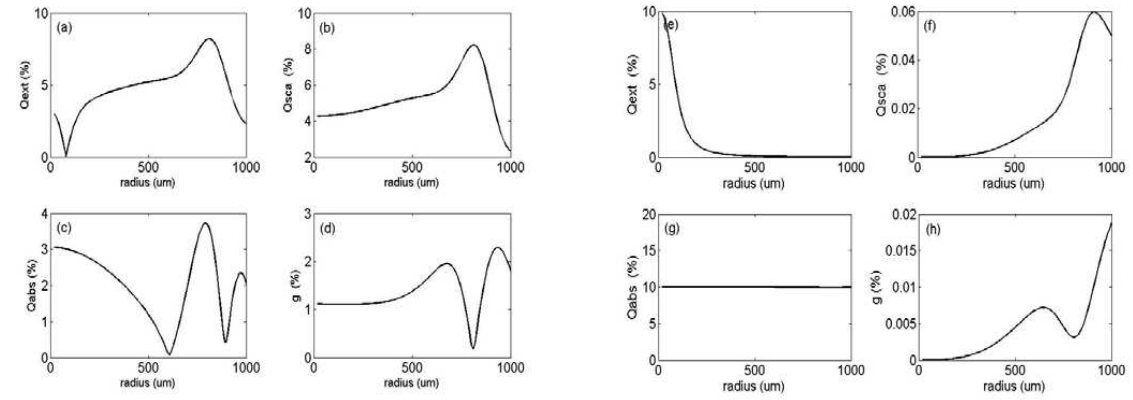

Figure 3: ±5% uncertainty in the real part of permittivity results in mean deviations at 89 GHz (Panel a-d) and ±20% uncertainty in the imaginary part (Panel e-h).

slightly influenced by uncertainty of ±20% in the imaginary part, since the mean deviations are all less than 1.0% at 89 GHz in Panel e-h of Figure 3. The uncertainty in the imaginary part of permittivity mainly affects absorption efficiencies, and results in significant deviations in absorption efficiencies. Mean deviation of extinction efficiencies is greater at small particle size. When the radii of ice particles are greater than 200 μm, mean deviation of extinction efficiencies declines since the extinction of the incidence is greatly caused by scattering rather than absorption at larger

particle sizes. While uncertainty in the real part of permittivity results in error up to about 8% in extinction and scattering efficiencies at some radii, for the real part of permittivity is a significant parameter in calculating size parameter in Mie theory.

3. EFFECTS OF SHAPE

The DDA method [2, 3], is a widely used approach to calculate non-spherical particle's scattering properties. In the DDA algorithm, a particle is divided into an array of dipoles. Each dipole is excited by the sum field of the incident field and the electric fields contributed by other dipoles of the particle. In this paper, we used DDSCAT 6.1 package [3] to simulate the effects of different particle shapes. The criterion $|m|kd < 0.5$ is satisfied, where m is refractive index of the material, k is the wave number in vacuum and d is the distance between two dipoles.

Figure 4: The geometry of ice particles. Left panel is bullet, and right panel is Koch-fractals (first generation).

We perform the calculation at 89 GHz to observe the effects of different particle shapes. At 89 GHz the refractive index of pure ice is $1.7748 + \mathrm{i}0.0013$ at a supposed temperature of $-30°$C. In Figure 4, it shows the geometric shapes of ice particles, which are studied in this paper. To determine the scattering properties of randomly oriented ice particles, we averaged the results for $8 \times 7 \times 12$ orientations ($\beta \times \theta \times \varphi$, β, θ and φ are angles used to specify the particle orientations, where β is from 0° to 180°, θ from 0° to 180°, and φ from 0° to 360°). The Koch-fractals of first generation is deterministic. We suppose that the height of a pyramid is a half of the hexagon radius for bullets and the relationship between length L and diameter D satisfies the power law as follows [5],

$$D = \begin{cases} 0.7L & L \leq 100\,\mu\mathrm{m} \\ 6.96L^{0.5} & 100\,\mu\mathrm{m} < L < 3000\,\mu\mathrm{m} \end{cases} \tag{1}$$

The scattering characteristics of bullets are revealed by Panel a-d of Figure 5 and the differences of scattering properties between the equivalent-volume spheres and bullets are given by Panel e-f, Koch-fractals by Figure 6. The range of large dimensions for bullets and Koch-fractals is about from 50 μm to 3000 μm. The equivalent-volume spherical radii of the two particles are all less than 800 μm and greater than 20 μm. The extinction efficiencies, scattering efficiencies, absorption

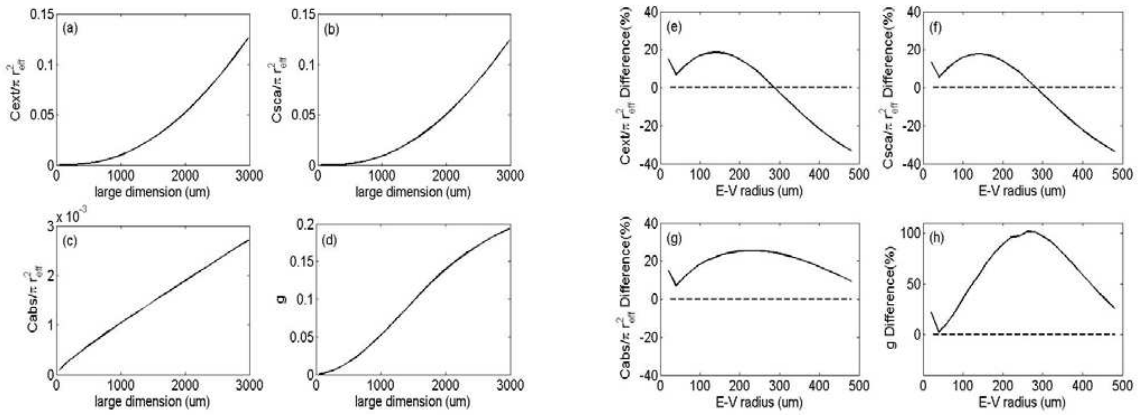

Figure 5: The optical efficiencies and asymmetry parameters g are as a function of large dimension for bullets at 89 GHz in Panel a-d. The difference of scattering properties between bullets and equivalent-volume spheres is as a function of equivalent-volume spherical radius in Panel e-f. r_{eff} is the radius of the equivalent-volume sphere.

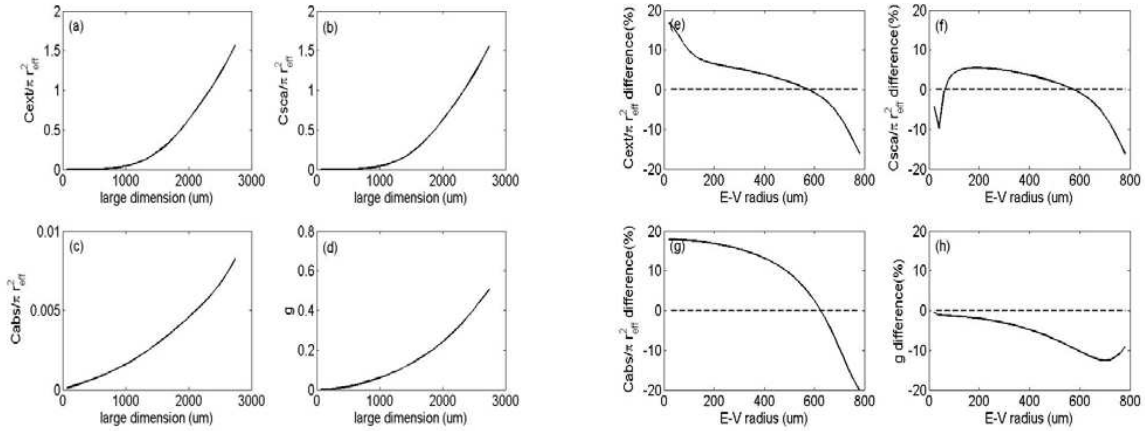

Figure 6: Same as Figure 5 except the particle shape is Koch-fractals.

efficiencies and asymmetry factors are increasing as the large dimension grows in Figures 5–6. As the large dimension increases, the extinction and scattering efficiencies of Koch-fractals grow more quickly than bullets. Different shapes results in significant different scattering properties, as demonstrated in Figure 5 and Figure 6.

4. CONCLUSIONS

Base on the calculations, it can be found that the mean deviations of scattering characteristics are less than 10% introducing uncertainties of ±20% in the imaginary part of permittivity and of ±5% in the real part. The scattering efficiencies for non-spherical ice particles are increasing as the dimensions grow since the radii of the equivalent-volume sphere existing in the natural clouds are all less than 1000 µm. The shape of ice particles appears to have greater effects on the scattering properties than refractive index. The scattering properties of different shapes with large dimensions are quite different, up to a factor of 10 at some sizes.

ACKNOWLEDGMENT

The authors thank B. T. Draine and P. J. Flatau for providing the DDSCAT 6.1 package. This research is supported by the National Natural Science Fund for Distinguished Young Scholars Grant 40525015.

REFERENCES

1. Liou, K. N., "Influence of cirrus clouds on weather and climate process: A global perspective," *Mon. Weather. Rev.*, Vol. 114, 1167–1199, 1986.
2. Purcell, E. M. and C. R. Pennypacker, "Scattering and absorption of light by non-spherical dielectric grains," *J. Astrophys.*, Vol. 186, 705–714, 1973.
3. Drain, B. T. and P. J. Flatau, "User guide for the discrete dipole approximation code DDSCAT 6.1," http://www.astro.princeton.edu/∼draine/DDSCAT.6.0.html, 2004.
4. Hufford, G., "A model for the complex permittivity of ice at frequency below 1 THz," *International Journal of Infrared and Millimeter Waves*, Vol. 12, No. 7, 677–682, 1991.
5. Auer, A. H. and D. L. Veal, "The dimensions of ice crystals in natural clouds," *J. Atmos. Sci.*, Vol. 27, 919–926, 1970.
6. Bohren, C. F. and D. R. Huffman, *Absorption and Scattering of Light by Small Particles*, Wiley-Interscience, New York, 1983.

Radio-frequency Characteristics of a Printed Rectangular Helix Slow-wave Structure

Chengfang Fu, **Yanyu Wei**, **Wenxiang Wang**, **and Yubin Gong**
National Key Laboratory of High Power Vacuum Electronics
University of Electronic Science and Technology of China, Chengdu 610054, China

Abstract— A new type of printed rectangular helix slow-wave structure (SWS) is investigated using the field-matching method and the electromagnetic integral equations at the boundaries. The radio-frequency characteristics including the dispersion equation for transverse-antisymmetric (odd) modes of this structure are analysed. The numerical results agree well with the results obtained by the EM simulation software HFSS. It is shown that the dispersion of the rectangular helix circuit is weakened, the phase velocity is reduced after filling the dielectric materials in the rectangular helix SWS. As a planar slow-wave structure, this structure has potential applications in compact TWTs.

1. INTRODUCTION

Recently, there is an increasing interest in the study on miniaturization of TWTs for potential applications in millimeter wave radar, communications and electronic wars [1, 2]. With the requirement of a large amount of compact TWTs, the fabrication technique with increasing reliability, improved repeatability and small tolerance is necessary. Fortunately, the micro-electro-mechanical systems (MEMS) can meet these requirements, which results in innovative TWT designs based on this technology. As the key component of beam-wave interaction of a TWT for exciting microwave energy, the slow-wave structure (SWS) directly influences the TWT's properties. Thus, the investigation on the novel compact slow-wave interaction structures based upon MEMS technique is more important. Though the conventional circular helix is so far the best structure for wide bandwidth and low dispersion, it is not compatible with MEMS technology. A related structure in planar configuration was studied in Refs. [2–7]. An investigation of the rectangular helix SWS printed on dielectric substrates and incorporating the shields, considering the width, as far as we know, has not appeared in the literature.

In this Letter, a field theory of the rectangular helix printed on dielectric substrates incorporating metal shields is obtained using the electromagnetic integral equations at the boundaries. The dispersion equation of transverse-antisymmetric (odd) modes of this structure in high power applications are derived using the sheath model [8], and the effect of the dielectric parameters on the slow wave characteristics based on the finite wide model is investigated.

2. THEORY

A rectangular helix on dielectric substrates shielded by metal shields is shown in Fig. 1. It encompasses a rectangular geometry, thus the configuration can be described in terms of a rectangular coordinate system (x, y, z), where $2a$ and $2b$ are the height and width of the rectangular helix cross section, respectively, $2c$ and $2d$ are the height and width of the rectangular shield screen, respectively, L is the helix period, ψ is the pitch angle and $\tan\psi = L/2/(a+b)$, respectively. In the sheath helix approximation [8], the four side surfaces are represented as unidirectionally conducting (UC) screens (Fig. 1(b)), which are separated by a distance $2a$ in the x-direction and $2b$ in the y-direction, respectively. In general the media inside and outside the helix have different permittivities, the medium 1 inside the helix with dielectric constant ε_{r1} and magnetic permeability μ_0, and the medium 2 between the helix and the metal shields with dielectric constant ε_{r2} and magnetic permeability μ_0. Special cases are of particular interest and are examined in detail, they are normal helix ($\varepsilon_{r1} > \varepsilon_{r2}$) and inverted helix ($\varepsilon_{r1} < \varepsilon_{r2}$). And the helix direction of the structure is shown in detail in Fig. 1(a).

Due to the anisotropic conducting boundary conditions of the rectangular helix, all the solutions in the helix with a rectangular cross section are hybrid modes (both TE and TM modes are required). Considering the symmetry of the rectangular helix together with Maxwell's equations, one finds that the solution of the problem must be either even or odd if x and y are taken in conjunction. Thus the structure admits of two independent solutions: transverse symmetric (even) modes and transverse antisymmetric (odd) modes [3]. In the former type, the transverse field

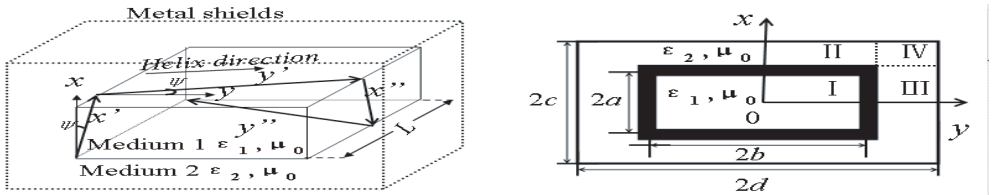

Figure 1: (a) Rectangular helix structure and (b) the rectangular Sheath helix model.

components are symmetrical with respect to x and y, while the longitudinal field component E_z and H_z are antisymmetrical. Similarly, in the latter type of modes, the opposite is true. The symmetry also ensures that only a quarter of the structure need considering for analysis. The quarter structure is divided into four regions: region I ($0 < x < a$ and $0 < y < b$), region II ($a < x < c$ and $0 < y < b$), region II ($0 < x < a$ and $b < y < d$) and region IV ($a < x < c$ and $b < y < d$). For simplification reasons in the following analysis, the weak fields in region IV are neglected.

With omitting $e^{j\omega t - j\beta z}$, where ω is the angular frequency, the longitudinal components for odd modes in each region can be obtained by solving wave equations in a rectangular coordinate system as follows:

(1) Region I ($0 < x < a$ and $0 < y < b$):

$$\begin{aligned} E_{1z} &= A\cosh(u_1 x)\cosh(v_1 y), \\ H_{1z} &= B\cosh(u_1 x)\cosh(v_1 y); \end{aligned} \tag{1}$$

(2) Region II ($a < x < c$ and $0 < y < b$):

$$\begin{aligned} E_{2z} &= C\sinh u_2(c-x)\cosh(v_2 y), \\ H_{2z} &= D\cosh u_2(c-x)\cosh(v_2 y); \end{aligned} \tag{2}$$

(3) Region III ($0 < x < a$ and $b < y < d$):

$$\begin{aligned} E_{3z} &= E\cosh(u_3 x)\sinh v_3(d-y), \\ H_{3z} &= F\cosh(u_3 x)\cosh v_3(d-y); \end{aligned} \tag{3}$$

(4) Region IV ($a < x < c$ and $b < y < d$):

$$\begin{aligned} E_{4z} &= G\sinh u_4(c-x)\sinh v_4(d-y), \\ H_{4z} &= H\cosh u_4(c-x)\cosh v_4(d-y); \end{aligned} \tag{4}$$

where A, B, C, D, E, F, G, and H in (1), (2), (3), and (4) are the amplitude constants. The transverse field components can be expressed in terms of the longitudinal components of the fields with the aid of the Maxwell equations.

According to the Sheath model [8], the boundary conditions at the interface are represented as follows:

(1) The tangential components of electric field are continuous at $x = a$ and $y = b$;

$$\int_{-b}^{b} E_{1z}\,|_{x=a}\,dy = \int_{-b}^{b} E_{2z}\,|_{x=a}\,dy, \tag{5}$$

$$\int_{-b}^{b} E_{1y}\,|_{x=a} dy = \int_{-b}^{b} E_{2y}\,|_{x=a}\,dy, \tag{6}$$

$$\int_{-a}^{a} E_{1z}\,|_{y=b}\,dx = \int_{-a}^{a} E_{3z}\,|_{y=b} dx\,, \tag{7}$$

$$\int_{-a}^{a} E_{1x}\,|_{y=b} dx = \int_{-a}^{a} E_{3x}\,|_{y=b}\,dx. \tag{8}$$

(2) The electric field components along the helix-direction are zero, i.e.,

$$\int_{-b}^{b}(E_{1z}\sin\psi\,|_{x=a}+E_{1y}\cos\psi\,|_{x=a})dy=0, \tag{9}$$

$$\int_{-a}^{a}(E_{1z}\sin\psi\,|_{y=b}-E_{1x}\cos\psi\,|_{y=b})dx=0. \tag{10}$$

(3) Because of the singular behaviour of the fields at the corners, the boundary conditions for magnetic fields in differential form can not be used at the boundary between regions I, II and III. Here, the matching conditions we choose is that the average values of magnetic field components are continuous along the helix direction, and we have the integral equation

$$\begin{aligned}&\int_{-b}^{b}(H_{1z}\sin\psi\,|_{x=a}+H_{1y}\cos\psi\,|_{x=a})dy+\int_{-a}^{a}(H_{1z}\sin\psi\,|_{y=b}-H_{1x}\cos\psi\,|_{y=b})dx\\ =&\int_{-b}^{b}(H_{2z}\sin\psi\,|_{x=a}+H_{2y}\cos\psi\,|_{x=a})dy+\int_{-a}^{a}(H_{3z}\sin\psi\,|_{y=b}-H_{3x}\cos\psi\,|_{y=b})dx.\end{aligned} \tag{11}$$

(4) At $x=c$ and $y=d$, the field expressions already satisfy with the metallic boundary conditions. Substituting the field expressions of each region into the above boundary conditions, the characteristic equations for odd modes are obtained,

$$\begin{aligned}\frac{k_1^2\cot^2\psi}{(\beta^2-k_1^2)^2}&=\coth(u_1a)\frac{M}{N},\\ u_1\tanh(u_1a)&=v_1\tanh(v_1b),\end{aligned} \tag{12}$$

where

$$\begin{aligned}M=&\cosh(u_1a)\sinh(v_1b)\frac{1}{u_1v_1}+\sinh(u_1a)\cosh(v_1b)\frac{1}{u_1^2}\\ &+\frac{\gamma_2^2}{\gamma_1^2}\coth(u_2(c-a))\sinh(u_1a)\sinh(v_2b)\frac{1}{u_2v_2}\\ &+\frac{\gamma_3^2}{\gamma_1^2}\coth(v_3(d-b))\sinh(v_1b)\sinh(u_3a)\frac{v_1}{u_1u_3v_3},\\ N=&\sinh(u_1a)\sinh(v_1b)(\frac{u_1^2+v_1^2}{u_1v_1})+\frac{\varepsilon_2}{\varepsilon_1}\frac{\gamma_1^2}{\gamma_2^2}\coth(u_2(c-a))\cosh(u_1a)\sinh(v_2b)\frac{u_2}{v_2}\\ &+\frac{\varepsilon_2}{\varepsilon_1}\frac{\gamma_1^2}{\gamma_3^2}\coth(v_3(d-b))\cosh(v_1b)\sinh(u_3a)\frac{v_3}{u_3}.\end{aligned}$$

3. NUMERICAL RESULTS

The numerical results on the slow wave properties of a rectangular helix printed on dielectric substrates incorporating the metal shields are illustrated in the following. Fig. 2 shows the dispersion characteristics of odd modes in the rectangular helix filling of dielectric media ($\varepsilon_{r2}=2.0$) between the helix and the shield screens. Here βL is the phase shift, and k_0a is the normalized frequency. For comparison, we have also simulated the structure using a three-dimensional EM simulation code HFSS. It can be seen from Fig. 2 that the numerical calculation data from the present theory agree well with the results by HFSS simulation.

The effect of the dielectric constant ε_{r1} on the dispersion characteristics of odd modes in the normal rectangular helix are presented in Figs. 3(a) and 3(b), respectively, where $\varepsilon_{r2}=1.0$. Fig. 3(a) shows that the increase of ε_{r1} can make the phase velocity decrease and the dispersion curves become steeper.

Figure 4 shows the effect of ε_{r2} of an inverted rectangular helix SWS on the phase velocities. It is clear that, as ε_{r2} increases while $\varepsilon_{r1}=1.0$, the phase velocity decreases and the cures become flatter, the bandwidth becomes greater.

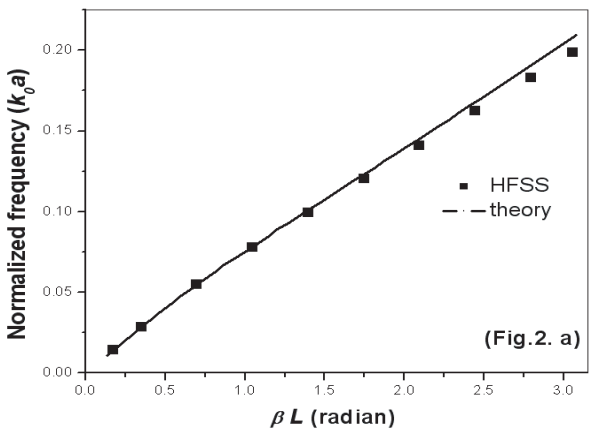

Figure 2: Dispersion curve when $b/a = 2$, $a/L = 0.75$, $a = 3\,\text{mm}$, $c/a = 2$, $d/b = 2$, $\varepsilon_{r1} = 1.0$, $\varepsilon_{r2} = 2.0$.

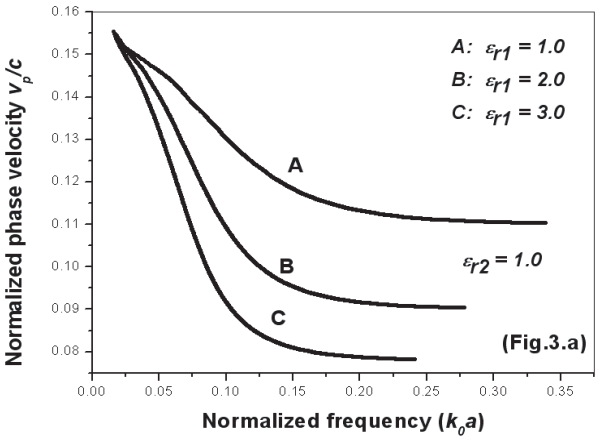

Figure 3: Phase velocity of a rectangular helix SWS when $b/a = 2$, $a/L = 0.75$, $a = 3\,\text{mm}$, $c/a = 2$, $d/b = 2$, $\varepsilon_{r2} = 1.0$.

Figure 5(a) shows the comparison of dispersion between the rectangular helix SWS in free space and dielectric-loaded cases. Here the structure dimensions are the same. It is clear that the phase velocity of the dielectric-loaded cases (A and C in Fig. 5(a)) will decrease in comparison with a free rectangular helix (B in Fig. 5(a)), and curve A is flatter than the curve C, which suggests the wider bandwidth and lower working voltage.

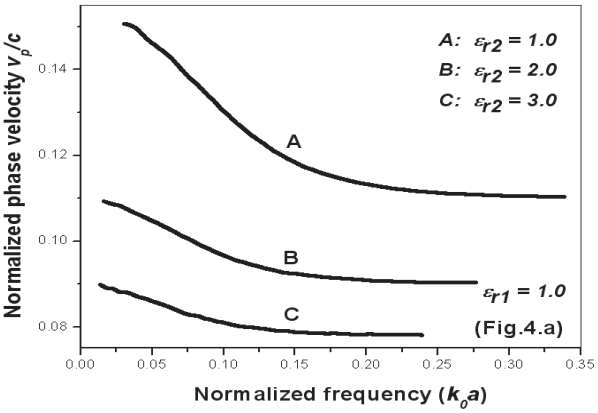

Figure 4: Phase velocity of a rectangular helix SWS when $b/a = 2$, $a/L = 0.75$, $a = 3\,\text{mm}$, $c/a = 2$, $d/b = 2$, $\varepsilon_{r1} = 1.0$.

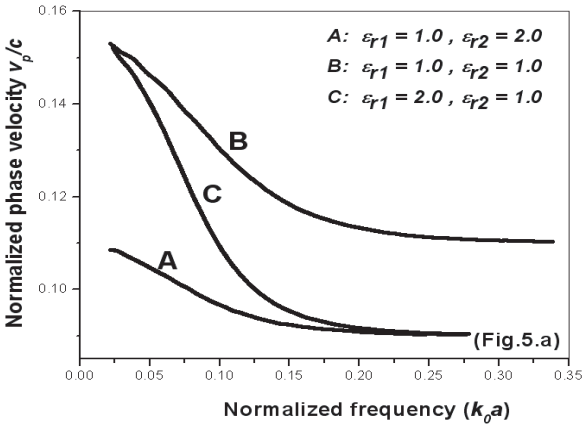

Figure 5: Phase velocity of a normal/inverted rectangular helix SWS when $b/a = 2$, $a/L = 0.75$, $a = 3\,\text{mm}$, $c/a = 2$, $d/b = 2$.

4. CONCLUSIONS

In summary, The dispersion equation for odd modes of this structure have been derived respectively and calculated numerically with the variation of the dielectric constant. The numerical results, which are in good agreement with the results from using the HFSS, reveal that weaker dispersion can be obtained by adjusting the dielectric constant of the medium of the rectangular helix structure, which may allow wider bandwidth or higher gain of a TWT. With advantages of compatibility with microwave integrated circuits, ease of fabrication based on MEMS techniques and interaction with a sheet beam, the rectangular helix structure thus holds promise for applications in compact TWTs.

REFERENCES

1. Kory, C., L. Ives, J. Booske, S. Bhattacharjee, et al., "Novel TWT interaction circuits for high frequency application", *Proc. 5th IEEE Int. Vacuum Electron. Conf.*, 51–52, Eur. Space

Agency, Apr. 2004.
2. Johnson, C. C., "Impedance and dispersion characteristics of the flattened helix," *IEEE Trans. Electron. Devices*, Vol. 6, No. 2, 189–194, 1959.
3. Arora, R. K., "Surface wave on a pair of parallel unidirectionlly conducting screens," *IEEE Trans. Antennas Propagat.*, Vol. 14, 795–797, 1966.
4. Arora, R. K., "Field of a line source situated parallel to a surface-wave structure comprising a pair of unidirectionally conducting screens," *Can. J. Phys.*, Vol. 45, 2145–2172, 1967.
5. Chadha, D., S. Aditya, and R. K. Arora, "Field theory of planar helix traveling-wave tube," *IEEE Trans. Microwave Theory Tech.*, Vol. 31, No. 1, 73–76, 1983.
6. Chadha, D., S. Aditya, and R. K. Arora, "Study of planar-helix slow-wave structure for application to travelling-wave tubes," *IEE Proceedings*, Vol. 131, No. 1, 14–20, 1984.
7. Fu, C. F., Y. Y. Wei, W. X. Wang, and Y. B. Gong, "Dispersion characteristics of a rectangular helix slow-wave structure," accepted by *IEEE Trans. Electron Devices*.
8. Pierce, J. R., *Traveling Wave Tubes*, Princeton, New York, Van Nostrand, NJ, 1950.

Investigation of the Dielectric-loaded Folded Waveguide Traveling-wave Tube Amplifier

C. Q. Zhang, Y. B. Gong, H. R. Gong, Y. Y. Wei, and W. X. Wang
National Key Laboratory of High Power Vacuum Electronics of UESTC, Chengdu, China

Abstract— The cold-test characteristics of the dielectric-loaded folded waveguide traveling-wave tube (FWTWT) amplifier are investigated theoretically and the Pierce small-signal theory is employed to confirm the results. The linear theory for the Q-band dielectric-loaded FWTWT amplifier shows that the bandwidth is increased from 15.08% to 27.03%.

1. INTRODUCTION

The dielectric materials have long been used to improve the performance of traveling-wave tube (TWT) amplifiers [1, 2]. The FWTWT is a kind of slow-wave amplifier with moderate bandwidth and power-handling in combination. It also has the advantages of simple structure compatible to planar precise-fabrication technologies and easy coupling, which make it promising in millimeter wave as well as the Terahertz region [3, 4]. In reference [5] the dielectric and Metamaterial Effects in a Terahertz TWT amplifier have been studied by computational software. The results indicated that adding materials to a certain part of the folded waveguide didn't work well. In the present paper, a concise analytical method is employed to study the characteristics of a new type of dielectric-loaded folded waveguide.

2. THEORETICAL ANALYSES

The dielectric-loaded Folded Waveguide is formed by folding a dielectric-loaded rectangular waveguide in y-z plane, as is shown in Fig. 1. In the rectangular waveguide there are three different dielectrics along x-direction.

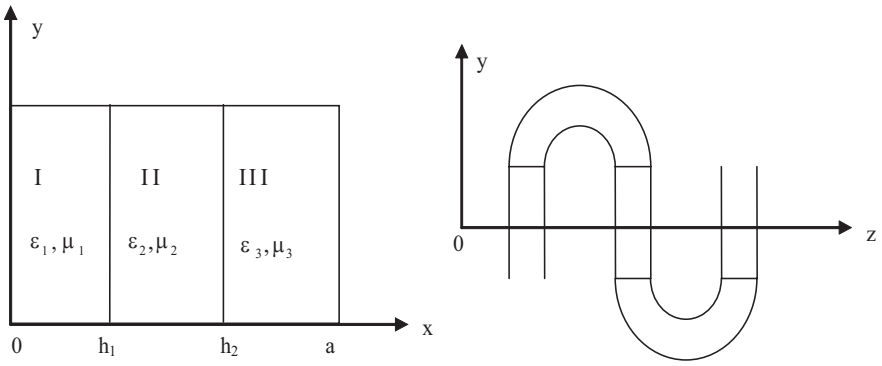

Figure 1: Schematic of dielectric-loaded folded waveguide.

The normal modes in such a rectangular waveguide structure are classified as longitudinal section electric (LSE) and longitudinal section magnetic (LSM) modes respectively, depending on whether they have a magnetic or electric field component normal to the dielectric interface (transverse x-direction).

Considerations of the boundary conditions lead to the fact that for modes having no y dependence of fields, the LSE mode is a TE mode, the only difference between them is the description method [6]. Thus, we can also assume that the mode structure is not altered in the folded guide but the axial phase velocity decreases due to propagation along a circuitous path, the phase shift per segment is given by the following expression [3]

$$\beta_{z,m}p = \beta L + \pi + 2m\pi \tag{1}$$

Differently, β represents the propagation constant of the dielectric-loaded rectangular waveguide. From above expression, the cold dispersion characteristic is achieved. It should be noticed that we do not take account of the reflections caused by waveguide bends and holes for beam which can create a stop-band but not influence our conclusions.

2.1. The Field Representation and Propagation Constant of the Dielectric-loaded Rectangular Waveguide

In region II ($h_1 \le x \le h_2$),

$$\begin{aligned} E_{y2} &= -j\omega\mu_2 k_{x2} A_2 \sin(k_{x2}x + \phi_2)\, e^{-j\beta z} \\ H_{z2} &= k_{x2}^2 A_2 \cos(k_{x2}x + \phi_2)\, e^{-j\beta z} \end{aligned} \tag{2}$$

Continuity of the field at $x = h_1$, $x = h_2$ requires

$$E_{y1}(h_1) = E_{y2}(h_1), \quad E_{y2}(h_2) = E_{y3}(h_2); \tag{3}$$

$$H_{z1}(h_1) = H_{z2}(h_1), \quad H_{z2}(h_2) = H_{z3}(h_2). \tag{4}$$

Considering the expression (3), the dispersion relations are given by:

$$\begin{aligned} \frac{k_{x1}}{\mu_1}\cot(k_{x1}h_1) &= \frac{k_{x2}}{\mu_2}\cot(k_{x2}h_1 + \phi_2) \\ \frac{k_{x2}}{\mu_2}\cot(k_{x2}h_2 + \phi_2) &= \frac{k_{x3}}{\mu_3}\cot[k_{x3}(h_2 - a)] \end{aligned} \tag{5}$$

When the frequency and the parameters of dielectrics are given, we can get the numerical values of the k_{x1}, k_{x2}, k_{x3}, ϕ_2 and then determine the propagation constant β.

2.2. Interaction Impedance

The *on*-axis interaction impedance of the nth space harmonic is expressed as

$$K_n = \frac{|E_n|^2}{2\beta_n^2 P}, \tag{6}$$

where E_n is the *on*-axis electric field of the nth space harmonic, and P is the RF power flow in the serpentine waveguide. According to the representations of the electric field in region II, we get

$$K_n = \frac{bG_m^2 \sin^2(k_{x2}x + \phi_2)}{(\beta_n p)^2 \frac{\beta}{\omega}\left(\frac{c_1 P_1}{\mu_1} + \frac{c_2 P_2}{\mu_2} + \frac{c_3 P_3}{\mu_3}\right)}, \tag{7}$$

where,

$$c_1 = \left(\frac{\sin(k_{x2}h_1 + \phi_2)}{\sin k_{x1}h_1}\right)^2, \quad c_2 = 1, \quad c_3 = \left(\frac{\sin(k_{x2}h_2 + \phi_2)}{\sin[k_{x3}(h_2 - a)]}\right)^2;$$

$$P_1 = \int_0^{h_1} \sin^2(k_{x1}x)dx, \quad P_2 = \int_{h_1}^{h_2} \sin^2(k_{x2}x + \phi_2)dx, \quad P_3 = \int_{h_2}^{a} \sin^2[k_{x3}(x - a)]dx.$$

From the representation of interaction impedance derived above we note that there is an extra term $\sin^2(k_{x2} + \phi_2)$ which indicates that the dielectrics may influence the location of the maximum electric field.

3. RESULTS AND DISCUSSIONS

We set the dielectrics in regions II and III have the same permittivity and thickness. And the region II is free from dielectric, i.e., $\varepsilon_2 = \varepsilon_0$, $\mu_2 = \mu_0$. In addition, permeability has been removed from our discussions.

3.1. The Cold-test Characteristics

The dimensions of the folded waveguide are $a = 4\,\text{mm}$, $b = 0.5\,\text{mm}$, $p = 1.42\,\text{mm}$, $l = 1.069\,\text{mm}$. The normalized phase velocity versus frequency for several dielectric constant and thickness are plotted in Fig. 2 and Fig. 3. Note that the choice of $\varepsilon_r = 1$ corresponds to the absence of any dielectric material. It is clear that the effect of the dielectric is to (1) progressively reduce the phase velocity and (2) flatten the dispersion curve. It also can be seen that the dispersion is more sensitive to the dielectric thickness. However, When an over high dielectric constant is chosen, the passband will fail to meet the design requirements. Thus, for a design it is necessary to choose the proper materials.

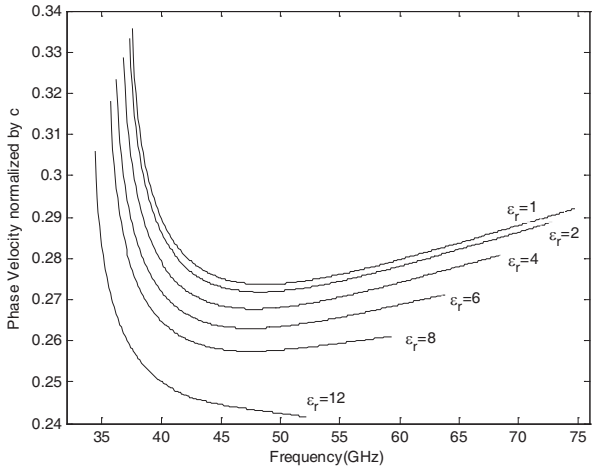

Figure 2: Normalized phase velocity for variations on dielectric constant.

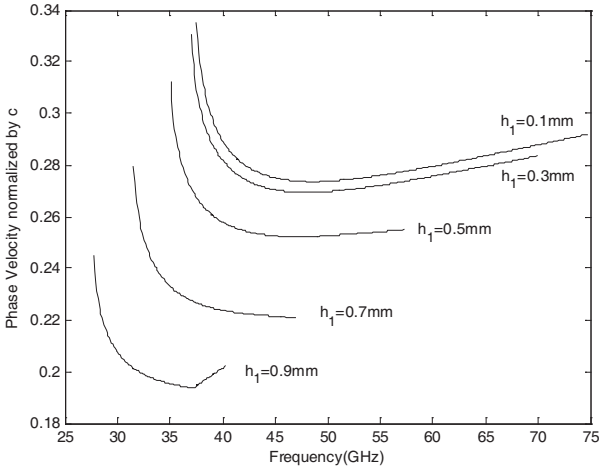

Figure 3: Normalized phase velocity for variations on dielectric thickness.

Figure 4 and Fig. 5 show the *on*-axis interaction impedance of the dielectric-loaded folded waveguide. From these illustrations we see that as the dielectric constant or thickness increases, the impedance is decreased. Since there is no dielectric in region II, this effect is mainly caused by the fact that loading dielectric reduces the cutoff frequency and shifts the pass band range. From Fig. 5, it is noted that when the value of h_1 is small ($h_1/a \leq 0.1$), the interaction impedance is influenced slightly, because the dielectrics are far away from the beam tunnel, which have small influence on the *on*-axis electric field. Like the dispersion curves, it is also seen that the interaction impedance is more sensitive to thickness.

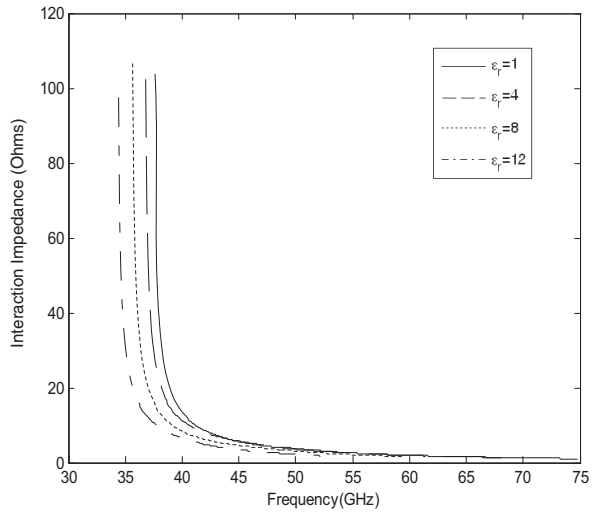

Figure 4: Interaction impedancefor variations on dielectric constant.

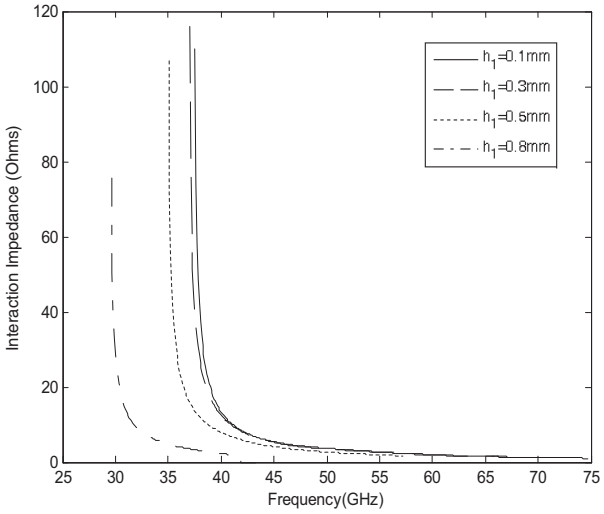

Figure 5: Interaction impedancefor variations on dielectric thickness.

3.2. Pierce Small Signal Gain

The linear theory [7] is employed to confirm the study above. The small-signal gain of the dielectric-loaded FWTWT is plotted in Fig. 6, compared to the unloaded waveguide.

The dimensions of the folded waveguide are the same as above and the parameters of dielectrics and beam are $\varepsilon_{r1} = \varepsilon_{r3} = 6$, $d_1 = d_2 = 0.4\,\text{mm}$, $U_0 = 20.5\,\text{KV}$, $I_0 = 0.17\,\text{A}$, $r_b = 0.2\,\text{mm}$, where r_b is the radius of beam. The 3 dB-bandwidth is given by the difference of the two frequencies at which $g_{\min} = 0.85 g_{\max}$ [8], where g is the growth rate in dB/cm.

It is shown that the maximum gain decreases by a small amount but there is a large increase in bandwidth. The bandwidth is increased from 15.08% to 27.03% and the operating voltage is decreased from 20.5 KV to 18.6 KV.

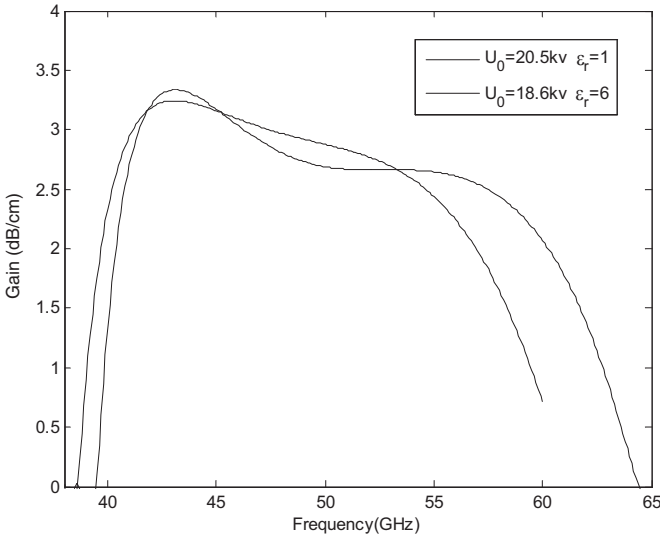

Figure 6: Small-signal gain of the dielectric-loaded FWTWT.

4. CONCLUSIONS

The characteristics of the dielectric-loaded FWTWT amplifier have been investigated. It has been shown that for the dielectric thickness where $h1/a \leq 0.1$, the interaction impedance is little affected. Accordingly, by proper choice of thickness and dielectrics, the bandwidth can be significantly increased with small influence on maximum gain. In addition, the operating voltage is decreased, which may benefit to reducing the volume of the device.

ACKNOWLEDGMENT

This research was supported by the National Natural Science Foundation of China (Grant No. 60532010, 60401005).

REFERENCES

1. Freund, H. P., E. G. Zaidman, M. A. Kodis, and N. R. Vanderplaats, "Linearized field theory of a dielectric-loaded helix traveling wave tube amplifier," *IEEE Trans. Plasma Sci.*, Vol. 24, No. 3, 895–904, 1996.
2. Garven, M., J. P. Calame, B. G. Danly, et al., "A gyrotron-traveling-wave tube amplifier experiment with a ceramic loaded interaction region," *IEEE Trans. Plasma Sci.*, Vol. 30, No. 3, 885–893, 2002.
3. Dohler, G., D. Gagne, D. Gallagher, and R. Moats, "Serpentine waveguide TWT," *IEDM*, 487–488, 1987.
4. Bhattacharjee, S., J. H. Booske, C. L. Kory, et al., "Folded waveguide traveling-wave tube sources for terahertz radiation," *IEEE Trans. Plasma Sci.*, Vol. 32, No. 3, 1002–1014, 2004.
5. Starinshak, D. P. and J. D. Wilson, "Investigating dielectric and metamaterial effects in a terahertz traveling-wave tube amplifier," *NASA/TM*-2008-215059, available electronically at http://gltrs.grc.nasa.gov.
6. Zhang, K.-Q. and D.-J. Li, *Electromagnetic Theory for Microwave and Optoelectronics*, 2nd edn., 305–314, Publishing House of Electronics Industry, Beijing, 2001.
7. Tsimring, S. E., *Electron Beams and Microwave Vacuum Electronics*, 306–316, John Wiley & Sons, Inc., Hoboken, New Jersey, 2006.
8. Ganguly, A. K., J. J. Choi, and C. M. Armstrong, "Linear theory of slow wave cyclotron interaction in double-ridged folded rectangular waveguide," *IEEE Trans. on Electron Devices*, Vol. 42, No. 2, 348–355, 1995.